

Permanent Magnet Synchronous and Brushless DC Motor Drives

Permanent Magnet Synchronous and Brushless DC Motor Drives

R. Krishnan

*Electrical and Computer Engineering Department
Virginia Tech
Blacksburg, Virginia, U.S.A.*



CRC Press

Taylor & Francis Group

Boca Raton London New York

CRC Press is an imprint of the
Taylor & Francis Group, an **informa** business

MATLAB® is a trademark of The MathWorks, Inc. and is used with permission. The MathWorks does not warrant the accuracy of the text or exercises in this book. This book's use or discussion of MATLAB® software or related products does not constitute endorsement or sponsorship by The MathWorks of a particular pedagogical approach or particular use of the MATLAB® software.

CRC Press
Taylor & Francis Group
6000 Broken Sound Parkway NW, Suite 300
Boca Raton, FL 33487-2742

© 2010 by Taylor and Francis Group, LLC
CRC Press is an imprint of Taylor & Francis Group, an Informa business

No claim to original U.S. Government works

Printed in the United States of America on acid-free paper
10 9 8 7 6 5 4 3 2 1

International Standard Book Number: 978-0-8247-5384-9 (Hardback)

This book contains information obtained from authentic and highly regarded sources. Reasonable efforts have been made to publish reliable data and information, but the author and publisher cannot assume responsibility for the validity of all materials or the consequences of their use. The authors and publishers have attempted to trace the copyright holders of all material reproduced in this publication and apologize to copyright holders if permission to publish in this form has not been obtained. If any copyright material has not been acknowledged please write and let us know so we may rectify in any future reprint.

Except as permitted under U.S. Copyright Law, no part of this book may be reprinted, reproduced, transmitted, or utilized in any form by any electronic, mechanical, or other means, now known or hereafter invented, including photocopying, microfilming, and recording, or in any information storage or retrieval system, without written permission from the publishers.

For permission to photocopy or use material electronically from this work, please access www.copyright.com (<http://www.copyright.com/>) or contact the Copyright Clearance Center, Inc. (CCC), 222 Rosewood Drive, Danvers, MA 01923, 978-750-8400. CCC is a not-for-profit organization that provides licenses and registration for a variety of users. For organizations that have been granted a photocopy license by the CCC, a separate system of payment has been arranged.

Trademark Notice: Product or corporate names may be trademarks or registered trademarks, and are used only for identification and explanation without intent to infringe.

Library of Congress Cataloging-in-Publication Data

Krishnan, R. (Ramu)
Permanent magnet synchronous and brushless DC motor drives / author, Ramu Krishnan.
p. cm.
“A CRC title.”
Includes bibliographical references and index.
ISBN 978-0-8247-5384-9 (hardcover : alk. paper)
1. Electric motors, Synchronous. 2. Brushless direct current electric motors. I. Title.

TK2787.K75 2010
621.46--dc22

2009029824

Visit the Taylor & Francis Web site at
<http://www.taylorandfrancis.com>

and the CRC Press Web site at
<http://www.crcpress.com>

To

My brothers: Govindan and Elango

My sisters: Jothi, Parvathi, and Saya

Contents

Preface.....	xvii
Acknowledgments.....	xxi
Author	xxiii
List of Symbols	xxv

PART I Introduction to Permanent Magnets and Machines and Converters and Control

Chapter 1 Permanent Magnets and Machines	3
1.1 Permanent Magnets	3
1.1.1 Demagnetization Characteristics	5
1.1.2 Operating Point and Air Gap Line	7
1.1.3 Energy Density	10
1.1.4 Energy Stored in the Magnet.....	12
1.1.5 Magnet Volume	13
1.1.6 Effect of External Magnetic Field Intensity	13
1.1.6.1 Analytical Approach.....	14
1.1.6.2 Graphical Approach.....	17
1.2 Arrangement of PMs	21
1.3 Magnetization of PMs	23
1.3.1 Radial and Parallel Magnetizations	23
1.3.2 Halbach Array	25
1.4 PM ac Machines	31
1.4.1 Machine Configurations.....	31
1.4.2 PM Rotor Types.....	34
1.4.2.1 Surface-Mounted PMSM.....	34
1.4.2.2 Surface-Inset PMSM	34
1.4.2.3 Interior PMSM.....	35
1.4.2.4 Line-Start PMSM	37
1.4.3 Hybrid Machines	38
1.4.3.1 Flux Reversal PMSM.....	39
1.4.3.2 Flux Switching Machine.....	42
1.4.3.3 PM SRM or Doubly Salient PM Machine	43
1.4.4 Concentrated Coil-Wound PMSMs	46
1.4.5 Types of PMSMs	48
1.5 Fundamentals of Synchronous Machines.....	51
1.5.1 Principle of Operation	51
1.5.2 MMF of a Coil	52

1.5.3	Sinusoidal MMF Distribution	53
1.5.3.1	Concentric Winding.....	53
1.5.3.2	Distributed Winding	53
1.5.4	Induced EMF.....	54
1.5.4.1	Winding Distribution Factor.....	57
1.5.4.2	Winding Pitch Factor.....	59
1.5.4.3	Skew Factor	61
1.5.4.4	Winding Factor.....	63
1.5.5	Types of Windings.....	64
1.5.5.1	Single-Layer Winding.....	64
1.5.5.2	Double-Layer Winding	64
1.5.6	Rotating Magnetic Field.....	66
1.5.6.1	Sinusoidal MMF Distribution.....	67
1.5.6.2	Rectangular MMF Distribution.....	71
1.6	Fundamental Synchronous Machine Relationships	71
1.6.1	Effective Air Gap	72
1.6.2	Effect of Magnet on Induced EMF	74
1.6.3	Electromagnetic Power and Torque.....	75
1.6.4	Fundamental Representation of Electromagnetic Torque.....	76
1.6.5	Machine Output Equation	78
1.6.6	Equivalent Magnet Current	81
1.6.7	Safe Peak Stator Current	82
1.6.8	Inductances.....	84
1.6.8.1	Self-Inductance per Phase.....	87
1.6.8.2	Magnetizing Inductance	87
1.6.8.3	Synchronous Inductance.....	88
1.6.8.4	d- and q-Axes Inductances	88
1.6.9	Effect of Stator Excitation on Air Gap Flux Density	89
1.7	Core Losses	92
1.7.1	Stator Core Losses.....	92
1.7.2	Eddy Current Losses	95
1.7.2.1	Eddy Current Loss in Tooth	96
1.7.2.2	Eddy Current Loss in Yoke	99
1.7.3	Evaluation of Peak Tooth and Yoke Flux Densities	100
1.7.4	Hysteresis Losses	101
1.7.5	Core Loss Measurement in the Machine.....	102
1.8	Resistive Losses.....	103
1.9	Initial Machine Design.....	105
1.10	Cogging Torque	107
1.10.1	Cause and Magnitude.....	107
1.10.2	Basics of Cogging Torque	107
1.10.2.1	General Expression for Cogging Torque	109

1.10.3	Analysis and Computation	110
1.10.4	Factors Affecting Cogging Torque.....	111
1.10.5	Mitigation Methods.....	111
1.10.5.1	Skewing	112
1.10.5.2	Varying Magnet Width	113
1.10.5.3	Varying Slot Width	114
1.10.5.4	Shifting Alternate Pair of Poles.....	114
1.10.5.5	Notching of Teeth	114
1.11	Basic Types of PMSMs Based on Flux Paths.....	115
1.12	Vibration and Noise	122
	References	123
Chapter 2	Introduction to Inverters and Their Control.....	135
2.1	Power Device.....	136
2.1.1	Power Devices and Switching	136
2.1.1.1	Power Diodes	136
2.1.1.2	MOSFET.....	137
2.1.1.3	Insulated Gate Bipolar Transistor.....	138
2.1.2	Switching of Power Devices.....	139
2.1.3	Device Losses.....	142
2.1.3.1	Conduction Loss	142
2.1.3.2	Switching Losses	143
2.2	DC Input Source.....	146
2.2.1	DC Input Source with Diode Bridge Rectifier	147
2.3	DC to ac Power Conversion.....	150
2.3.1	Single-Phase Half-Wave Inverter	150
2.3.2	Single-Phase Full-Wave Inverter	153
2.3.3	Three-Phase Inverter	155
2.4	Real Power.....	161
2.5	Reactive Power	161
2.6	Need for Inverter Control	162
2.7	Pulse Width Modulation.....	164
2.7.1	PWM Implementation	167
2.7.1.1	Reference Signal Generation	168
2.7.1.2	Sampling of Reference Signals	169
2.7.1.3	Transfer Characteristics of PWM- Controlled Inverters	171
2.7.1.4	Off-Line Optimized PWM	172
2.8	Hysteresis Current Control	173
2.9	Space Vector Modulation	176
2.9.1	Switching States of the Inverter	177
2.9.2	Principle of Space Vector Modulation	177
2.9.2.1	Transfer Characteristics of SVM- Controlled Inverters	183
2.9.3	Space Vector Modulator Implementation.....	188

2.9.4	Switching Ripple in SVM	188
2.9.4.1	Hybrid PWM Controller	192
2.10	Inverter Switching Delay	195
2.10.1	Control Modeling of the Three-Phase Inverter	207
2.11	Input Power Factor Correction Circuit	208
2.11.1	Single-Phase Power Factor Correction Circuit	208
2.11.2	Three-Phase Power Factor Correction Circuit	210
2.12	Four-Quadrant Operation	211
2.13	Converter Requirements	214
	References	215

PART II *Permanent Magnet Synchronous Machines and Their Control*

Chapter 3	Dynamic Modeling of Permanent Magnet Synchronous Machines	225
3.1	Real-Time Model of a Two-Phase PMSM	226
3.2	Transformation to Rotor Reference Frames	231
3.3	Three-Phase to Two-Phase Transformation	236
3.3.1	Unbalanced Operation	238
3.4	Zero Sequence Inductance Derivation	239
3.5	Power Equivalence	241
3.6	Electromagnetic Torque	242
3.7	Steady-State Torque Characteristics	244
3.8	Models in Flux Linkages	250
3.9	Equivalent Circuits	251
3.10	Per Unit Model	254
3.11	Dynamic Simulation	257
3.12	Small-Signal Equations of the PMSM	262
3.12.1	Derivation	262
3.13	Evaluation of Control Characteristics of the PMSM	264
3.13.1	Transfer Functions and Frequency Responses	264
3.14	Computation of Time Responses	266
3.15	Space Phasor Model	270
3.15.1	Principle	270
3.15.2	Model Derivation	270
	References	276
Chapter 4	Control Strategies for a Permanent Magnet Synchronous Machine	279
4.1	Vector Control	279
4.2	Derivation of Vector Control	280
4.2.1	Electromagnetic Torque	282

4.2.2	Stator d- and q-Axis Currents in Stator Reference Frames	283
4.2.3	Mutual Flux Linkages	283
4.2.4	Role of a Torque Angle in Machine Operations.....	284
4.2.5	Key Results.....	284
4.3	Drive System Schematic.....	285
4.3.1	Torque-Controlled Drive System	285
4.3.1.1	Hysteresis Current Controller.....	287
4.3.2	Simulation and Results of a Torque-Controlled Drive System	288
4.3.3	Speed-Controlled Drive System.....	293
4.3.3.1	Mutual Flux Programming.....	294
4.3.3.2	Torque Programming in the Flux-Weakening Region	294
4.3.4	Simulation and Results of a Speed-Controlled Drive System	296
4.4	Control Strategies	303
4.4.1	Constant ($\delta=90^\circ$) Torque Angle Control	304
4.4.2	Unity Power Factor Control.....	308
4.4.3	Constant Mutual Flux Linkages Control.....	312
4.4.4	Angle Control of Air Gap Flux and Current Phasors	314
4.4.5	Optimum Torque per Unit Current Control	317
4.4.6	Constant Power Loss Control.....	320
4.4.7	Maximum Efficiency Control	325
	References	328
Chapter 5	Flux-Weakening Operation	331
5.1	Maximum Speed	332
5.2	Flux-Weakening Algorithm.....	333
5.2.1	Indirect Control Scheme	336
5.2.2	Constant Torque Mode Controller.....	336
5.2.3	Flux-Weakening Controller	338
5.2.4	System Performance.....	339
5.3	Direct Flux Weakening	343
5.3.1	Maximum Permissible Torque Limit	344
5.3.2	Speed Control Scheme	344
5.3.3	Implementation Strategy	345
5.3.3.1	Lookup Tables Realization	346
5.3.4	System Performance.....	348
5.4	Parameter Sensitivity	349
5.4.1	Stator Resistance Variation	349
5.4.2	Rotor Flux Linkage Variation	350
5.4.3	q-Axis Inductance Variation	350
5.5	Model-Free (Parameter-Insensitive) Flux-Weakening Method.....	351

5.6	Six-Step Voltage and Constant Back EMF Control Strategies for PMSM	353
5.6.1	Constant Back EMF Control Strategy.....	354
5.6.1.1	The Basics.....	354
5.6.1.2	Maximum Current in the Flux-Weakening Region	355
5.6.1.3	Operational Boundary	355
5.6.1.4	Maximum Speed in the Flux-Weakening Region	356
5.6.2	Six-Step Voltage Control Strategy.....	356
5.6.2.1	Fundamental Analysis	357
5.6.2.2	Steady-State Current in SSV Mode	359
5.6.2.3	Operational Boundary for the SSV Control Strategy	359
5.6.2.4	Comparison.....	360
5.7	Direct Steady-State Evaluation.....	361
5.7.1	Input Voltages.....	362
5.7.2	Machine Equations in State Space Form	365
5.7.3	Boundary Matching Condition and Solution	366
5.7.4	MATLAB® Program	369
5.8	Flux Weakening in SMPM and IPM Synchronous Machines	371
5.8.1	Flux-Weakening Equations in New Base	371
	References	376
Chapter 6	Design of Current and Speed Controllers	379
6.1	Current Controller	380
6.1.1	Rotor Reference Frame Current Controllers	381
6.1.2	Stator Reference Frames Current Controller.....	382
6.1.3	Deadbeat Current Controllers	385
6.1.3.1	Deadbeat Controller.....	385
6.1.3.2	Predictive Deadbeat Controller	386
6.1.3.3	Improved Predictive Deadbeat Controller	388
6.2	Speed Controller.....	389
6.2.1	Derivation of Block Diagram	390
6.2.2	Simplified Current Loop Transfer Function.....	391
6.2.3	Speed Controller.....	393
6.2.3.1	Smoothing.....	396
	References	398
Chapter 7	Parameter Sensitivity and Compensation.....	401
7.1	Introduction	401
7.1.1	Ratio of Torque to Its Reference.....	402
7.1.2	Ratio of Mutual Flux Linkages to Its Reference	403

7.2	Parameter Compensation through Air Gap Power Feedback Control.....	404
7.2.1	Algorithm	405
7.2.2	Performance	408
7.3	Parameter Compensation by Reactive Power Feedback Control.....	413
7.3.1	Principle of the Reactive Power Feedback Compensation Scheme	414
7.3.2	Drive Schematic	414
7.3.3	Simulation Results.....	416
7.3.4	Comparison with Air Gap Power Feedback Scheme	419
	References	421
Chapter 8	Rotor Position Estimation and Position Sensorless Control	423
8.1	Current Model Adaptive Scheme	423
8.2	Sensing by External Signal Injection	428
8.2.1	Revolving Voltage Phasor Injection Scheme.....	428
8.2.2	Flux Linkage Injection in Rotating q-Axis	432
8.2.2.1	Algorithm.....	433
8.2.2.2	Demodulation	436
8.2.2.3	Observer.....	437
8.2.2.4	Implementation	438
8.2.2.5	Merits and Demerits of the Scheme	440
8.2.3	Alternating Voltage Phasor Injection	442
8.2.3.1	Sensorless Algorithm.....	442
8.2.3.2	Implementation	444
8.3	Current Model-Based Injection Scheme	447
8.4	Position Estimation Using PWM Carrier Components.....	448
8.4.1	Harmonic Voltage and Current Vectors	448
8.4.2	Rotor Position Estimation.....	449
8.4.3	Performance	450
	References	451

PART III Permanent Magnet Brushless DC Machines and Their Control

Chapter 9	PM Brushless DC Machine.....	457
9.1	Modeling of PM Brushless dc Motor	457
9.2	Normalized System Equations	460
9.3	The PMBDCM Drive Scheme.....	462
9.4	Dynamic Simulation.....	463
	References	473

Chapter 10	Commutation Torque Ripple and Phase Advancing	475
10.1	Commutation Torque Ripple	476
10.2	Phase Advancing	480
10.3	Dynamic Modeling.....	481
10.3.1	Machine Equations.....	482
	References	494
Chapter 11	Half-Wave PMBDCM Drives.....	497
11.1	Split Supply Converter Topology.....	497
11.1.1	Operation of the PMBDC Motor with the Split Supply Converter.....	498
11.1.2	Operational Modes of the Converter.....	499
11.1.3	Merits and Demerits of the PMBDC Drive with the Split Supply Converter	501
11.1.4	Design Considerations for the PMBDC Motor	502
11.1.5	Impact of the Motor Inductance on the Dynamic Performance	504
11.1.6	Winding Connections.....	505
11.1.7	Drive System Description	506
11.1.8	Modeling, Simulation, and Analysis of the PMBDC Drive System	507
11.1.8.1	Modeling of the PMBDCM with Converter Modes.....	507
11.1.8.2	Modeling of the Speed Controller	508
11.1.8.3	Steering Circuit.....	509
11.1.8.4	Current Loop Modeling.....	510
11.1.8.5	Simulation and Analysis	510
11.1.8.6	Current Commutation Angle	511
11.1.8.7	Comparison of the Half-Wave and Full-Wave Inverter-Based PMBDC Drives.....	512
11.2	C-Dump Topology	513
11.2.1	Principle of Operation of the C-Dump PMBDC Drive System	514
11.2.1.1	Motoring Operation	514
11.2.1.2	Regenerative Operation	515
11.2.2	Analysis of the C-Dump PMBDCM Drive	516
11.2.2.1	Maximum Speed.....	516
11.2.2.2	Peak Recovery Current.....	517
11.2.2.3	Energy Recovery Capacitor	517
11.2.2.4	Energy Recovery Chopper.....	518
11.2.3	Comparison with Full-Wave Inverter-Controlled PMBDCM Drive	518

11.2.4	Modeling, Simulation, and Dynamic Performance	519
11.2.4.1	Modeling.....	519
11.2.4.2	System Performance	521
11.3	Variable dc Link Converter Topology	521
11.3.1	Principle of Operation	522
11.3.2	Motoring.....	524
11.3.2.1	Regenerative Operation	524
11.3.3	System Performance.....	525
11.3.3.1	Torque Drive Performance	525
11.3.3.2	Speed-Controlled Drive Performance	526
11.3.4	Merits and Demerits.....	526
11.4	Variable Voltage Converter Topology with Buck-Boost Front-End.....	527
11.4.1	Converter Circuit.....	527
11.4.2	Operational Modes and Modeling of the PMBDC Motor Drive System	528
11.4.3	Merits and Demerits.....	530
11.4.4	Comparison with Full-Wave Inverter Drive	532
11.4.5	Design of the Inductor and Output Capacitor in the Buck-Boost Front-End	532
11.4.6	Control Strategies and Performance	534
11.4.6.1	Strategy I—Open Loop Voltage Control	534
11.4.6.2	Strategy II—Closed Loop Voltage Control	536
11.4.6.3	Strategy III—Direct Phase Current Control	536
	References	538

Chapter 12	Design of Current and Speed Controllers	541
12.1	Transfer Function of Machine and Load	541
12.2	Inverter Transfer Function	544
12.3	Transfer Functions of Current and Speed Controllers	544
12.4	Current Feedback	544
12.5	Speed Feedback.....	545
12.6	Design of Controllers.....	545
12.6.1	Current Controller	546
12.6.2	First-Order Approximation of Inner Current Loop	548
12.6.3	Speed Controller.....	549
	References	553

Chapter 13	Sensorless Control of PMBDCM Drive	555
13.1	Current Sensing	555
13.2	Position Estimation.....	556
	References	559
Chapter 14	Special Issues	561
14.1	Torque Smoothing	561
14.2	Parameter Sensitivity of the PMBDCM Drive.....	562
14.3	Faults and Their Diagnosis.....	562
14.4	Vibration and Noise.....	562
	References	563

Preface

Books on permanent magnet (PM) ac machine drives have focused primarily on the design of the machines and have covered the control and converters for these drives only in an elementary manner. In the last two decades, research and development on control strategies and their subsequent implementation have been reported in journal publications and presented at conferences. The knowledge base of these publications and conference proceedings is yet to be cohesively made available in a book through a systematic dissemination to both industrial and academic audiences. With regard to power electronics associated with these drive systems, the three-phase bridge inverter has been used as the standard for a very long time. Its understanding and control have changed significantly over time. Cost minimization has been the main focus of emerging high-volume applications and has therefore necessitated a review of the subsystem costs. While controller costs have been standardized according to their applications, the obvious targets for cost minimization are the converters and the machines. Of late, new power converter topologies are also being considered for low-cost drive systems. A book dedicated exclusively to PM ac machines with a major emphasis on the control and low-cost converter topologies would be timely. Keeping this in mind, this book has been under development for several years. The contents of this book were widely used for teaching at the doctoral level at Virginia Tech and tested at the University of Aalborg, Denmark, and industrial audiences in the United States and other countries.

This book is divided into three parts. Part I covers the fundamentals of the machines, power devices, inverters, and their control (Chapters 1 and 2). Parts II and III are devoted to the PM synchronous (Chapters 3 through 8) and brushless dc motor drives (Chapters 9 through 14), respectively.

To understand PM ac drives one must start with the fundamentals of the machine. Chapter 1 provides an elementary introduction to the characteristics of PMs and their operating points, machine rotor configurations, differences between synchronous and brushless dc machines, windings, flux density distribution in the tooth and yoke, expressions relating machine dimensions, magnet and stator excitation with torque and power output, and inductance derivations. Further, the core losses, their computation and measurement are included to cover the characterization of the machine for modeling and control strategy formulations. Greater emphasis has been placed on sinusoidal machines than on trapezoidal machines as the former are closely related to other ac machines both in functioning and in the principles of operation and control. Considering only the fundamental components of the variables, both the sinusoidal and trapezoidal PM machines are identical in their behavior. The applicability of the principles is obvious even though there are some significant differences among them. Various aspects of PM placement on the rotor, special machines with PM on the stator, and the Halbach arrangement are presented to enable readers to familiarize themselves with both the old and the new machines.

Chapter 2 contains a brief description of power devices, their switching characteristics and losses, rectifiers, and inverters. The section on inverters introduces various switching schemes, their merits and demerits, and their modeling. A description of the four-quadrant operation and its applicability to PM ac machines is included to introduce the terminology that is used frequently in the description and operation of PM ac drive systems.

The dynamic modeling of PM synchronous machines using d_{q0}-axes in rotor reference frames and also in space phasor variables is systematically derived in Chapter 3. The approach in this chapter is intuitive and assumes that the reader is familiar with elementary circuit theory and simple axes projections using trigonometry. Various aspects of the modeling are illustrated with MATLAB®-based simulation results. The dynamic model is required in subsequent developments.

The starting basis for the control of PM synchronous machines is vector control, leading to the decoupling of torque and flux channels in the machine. Additional performance requirements such as constant torque angle, unity power factor, constant mutual flux linkages, maximum torque per unit current, fixed angle between current and flux phasors, constant power loss, and maximum efficiency are superimposed on the vector controller and thus various control strategies emerge for the synchronous machine. All these control strategies and some aspects of their implementation for the PM synchronous machines are elaborated in Chapter 4.

Flux weakening is crucial to extend the speed range of PM synchronous motor drives. Various control strategies to accomplish flux weakening are provided in Chapter 5 along with implementations. Importantly, the six-step inverter operation in the flux-weakening mode is studied and compared to other methods of flux weakening based on model and model-free controllers.

The differences between interior and surface PM machines related to their performance in flux weakening as well as in the constant torque regions are derived with normalized machine parameters and are discussed.

The drives have invariably inner current control loops for torque control and hence the necessity for current controllers and their design procedure in practice. Such a procedure is derived from the transfer function obtained from block diagram reduction methods. The method establishes the similarity between the separately excited dc machine and PM synchronous machine drives, thus broadening the reader's understanding. Speed control is enforced with an outer speed feedback control loop. The design of the speed controller is analytically derived using the symmetric optimum method. The design procedure is illustrated with an example in Chapter 6.

Almost all of the control strategies are dependent on machine parameters for their implementation. Because of the sensitivity of the stator resistance, and rotor flux linkages to temperature and q-axis inductance to saturation, the consequences on drive performance and methods to overcome their effects in drive systems are studied in Chapter 7 for PM synchronous machine drives.

Position information is vital to the success of the control of PM synchronous motor drives. The position sensorless approach is very attractive from the point of view of cost and reliability. A few methods of position sensorless control are presented in Chapter 8.

Chapters 9 through 14 contain a study of PM brushless dc motor drives. Chapter 9 elaborates on the modeling and simulation of these drives. A control scheme in prevalent use is also considered in this chapter.

Chapter 10 addresses the important issues of commutation torque ripples and their computation. Flux weakening is studied as an adjunct of the method introduced to study torque generation using Fourier series.

Half-wave inverter topologies emerge to primarily cater to the low-cost and high-performance requirements of high-volume applications. Four such inverter topologies for PM brushless dc motor drives are studied in Chapter 11.

The design of current and speed controllers using a very similar approach taken for PM synchronous motor drives is considered in detail in Chapter 12. A discussion of various methods of current and position sensorless operation of PM brushless dc motor drives is provided in Chapter 13. Various secondary topics such as torque smoothing and parameter sensitivity of these drives are outlined in Chapter 14.

This book is written for engineers with bachelors' degrees, preferably in electrical engineering. The contents of this book can also be taught as a one-semester advanced course in the motor drives area, as practiced in the Electronics and Communication Engineering department, Virginia Tech.

An attempt has been made to develop a consistent method for treating various issues of analysis and design from first principles. While realizing that modeling and analysis get in the way of the flow of the subject matter, they are unavoidable in a book such as this, which is intended for engineers who face the challenges of design and development every day in their work. Wherever appropriate, MATLAB codes are developed and given to illustrate the simulation of the drive systems.

MATLAB® is a registered trademark of The MathWorks, Inc. For product information, please contact:

The MathWorks, Inc.
3 Apple Hill Drive
Natick, MA 01760-2098 USA
Tel: 508 647 7000
Fax: 508-647-7001
E-mail: info@mathworks.com
Web: www.mathworks.com

I have generously drawn on materials from published papers but with my own interpretation, particularly from Dr. G. R. Slemon and his former students, most notably from Dr. T. Sebastian and Dr. X. Liu.

Prof. J. Holtz and his associates' work on inverters, current control, and rotor position sensorless control are gratefully acknowledged.

A large number of research results from my doctoral students, past and present, are incorporated in the text. I acknowledge the use of materials from the following: Prof. P. Pillay, Dr. G. H. Rim, Dr. P. Vijayraghavan, Dr. R. Monajemy, Dr. Byeong Seok Lee, Nimal Lobo, and Jaehyuck Kim. In particular, Dr. P. Vijayraghavan, Nimal Lobo, and Ben Rudolph have been helpful with suggestions and editorial help.

The errors in this book are mine while the results of research, on which this text is built, belong to the general community of hundreds of researchers and practitioners in this field.

I am grateful to Nora Konopka, Marsha Pronin, and Frances Weeks of CRC Press and their contractors from SPi, Manju Chinnappan and Anithajohny Mariasusai, for their help, advice, and patience during the preparation of this book.

My wife, Vijaya, has been very supportive of this venture with good cheer. To her, I owe the most.

R. Krishnan

Blacksburg, Virginia

Acknowledgments

I gratefully acknowledge the following organizations for giving permission to use materials cited herein:

1. Prentice Hall, Upper Saddle River, New Jersey, for permission to use materials from their book: R. Krishnan, *Electric Motor Drives*, 2001. Particularly materials from Chapter 9 in their book are generously used in this book spread over many chapters.
2. IEEE for permission to use materials from the following papers authored or coauthored by me:
 - R. Krishnan, Control and operation of PM synchronous motor drives in the field-weakening region, *IEEE IES, IECON Proceedings (Industrial Electronics Conference)*, pp. 745–750, 1993.
 - R. Krishnan and P. Vijayraghavan, Parameter compensation of permanent magnet synchronous machines through airgap power feedback, *IEEE IES, IECON Proceedings (Industrial Electronics Conference)*, pp. 411–416, 1995.
 - R. Krishnan, S. Lee, and R. Monajemy, Modeling, dynamic simulation and analysis of a C-dump brushless dc motor drive, *IEEE Applied Power Electronics Conference and Exposition (APEC), Conference Proceedings (Cat. No. 96CH35871)*, pp. 745–750, 1996.
 - R. Krishnan, Novel single-switch-per-phase converter topology for four-quadrant PM brushless dc motor drive, *IEEE Transactions on Industry Applications*, 33(5), 1154–1161, 1997.
 - R. Krishnan and S. Lee, PM brushless dc motor drive with a new power-converter topology, *IEEE Transactions on Industry Applications*, 33(4), 973–982, 1997.
 - R. Krishnan and P. Vijayraghavan, New power converter topology for PM brushless dc motor drives, *IEEE IE, IECON Proceedings (Industrial Electronics Conference)*, pp. 709–714, 1998.
 - R. Krishnan and P. Vijayraghavan, Fast estimation and compensation of rotor flux linkage in permanent magnet synchronous machines, *IEEE IES International Symposium on Industrial Electronics*, vol. 2, pp. 661–666, 1999.
 - B. S. Lee and R. Krishnan, A variable voltage converter topology for permanent-magnet brushless dc motor drives using buck-boost front-end power stage, *Proceedings of the IEEE International Symposium on Industrial Electronics (Cat. No. 99TH8465)*, pp. 689–694, 1999.
 - R. Monajemy and R. Krishnan, Performance comparison for six-step voltage and constant back EMF control strategies for PMSM, *Conference*

- Record, IEEE Industry Applications Society Annual Meeting*, vol. 1, pp. 165–172, 1999.
- R. Monajemy and R. Krishnan, Control and dynamics of constant-power-loss-based operation of permanent-magnet synchronous motor drive system, *IEEE Transactions on Industrial Electronics*, 48(4), 839–844, 2001.
 - K. Sitapati and R. Krishnan, Performance comparisons of radial and axial field, permanent-magnet, brushless machines, *IEEE Transactions on Industry Applications*, 37(5), 1219–1226, 2001.

R. Krishnan

Author

R. Krishnan is the author of *Electric Motor Drives*, published by Prentice Hall in February 2001; its Chinese translation and an Indian edition were released in 2002 by Pearson Education, Taiwan, and Prentice Hall, India, respectively, and its international edition was released in 2001 by Prentice Hall (International Edition). He is also the author of *Switched Reluctance Motor Drives* (CRC Press, first edition, June, 2001; second edition, 2003) and the coeditor and coauthor of *Control in Power Electronics* (Academic Press, August, 2002).

Krishnan has been granted seven U.S. patents and many are still pending in the United States, Europe, and in other countries. His inventions have been prominently featured in the media including radio, TV, and newspapers such as *The Wall Street Journal*. He has served as a consultant for 18 companies in the United States. He has developed and delivered short courses for academia and industry on vector-controlled induction, permanent magnet synchronous and brushless dc, switched reluctance, and linear electric motor drive systems.

Krishnan is a recipient of the best paper prize awards from the IEEE Industry Applications Society's Industrial Drives Committee (five awards) and the Electric Machines Committee (one award). In addition, he received the first prize from the *IEEE Transactions on Industry Applications* for his paper and the 2007 Best Paper Award from the *IEEE Industrial Electronics Magazine*. His coedited book, *Control in Power Electronics*, won the best book award of the Ministry of Education and Sport, Poland, in 2003. He was awarded the IEEE Industrial Electronics Society's Dr. Eugene Mittelmann Achievement Award for Outstanding Technical Contributions to the field of industrial electronics in 2003.

Krishnan is a fellow of the IEEE and a distinguished lecturer of the IEEE Industrial Electronics Society. He is an elected senior AdCom member of the IEEE Industrial Electronics Society and served as a vice president (publications) from 2002 to 2005. He served as the general chair of the 2003 IEEE Industrial Electronics Conference, Roanoke, Virginia, and as one of the three general cochairs of the IEEE IES' ICIT 2006 in Mumbai, India. He has also delivered many keynote speeches in IEEE conferences.

Krishnan and some of his graduate scholars' inventions constituted founding technologies for three motor drives companies. He founded Panaphase Technologies, LLC, in 2002, which went through a successful merger and acquisition in 2007, and Ramu Inc., in 2008, which specializes in high-volume variable speed motor drives for home appliances, air conditioners, hand tools, wind power and automotive applications. He is also a cofounder of TransNetics, LLC, which specializes in intellectual property for linear motor drives.

Krishnan is a professor of electrical and computer engineering at Virginia Tech, Blacksburg, Virginia, and the director of the Center for Rapid Transit Systems, specializing in linear and rotating motor drives.

List of Symbols

A	State transition matrix
a_c	Area of cross section of armature conductor, m ²
A_c	Area of cross section as seen by the flux per pole, m ²
A_g	Area of cross section of air gap, m ²
A_m	Area of cross section of the magnet, m ²
A_{sl}	Linear stator current density, Amp-conductor/m
B_1	Friction coefficient, N · m/(rad/s)
B_d	Flux density at maximum energy density operating point, T, and also direct axis flux density, T
B_g	Air gap flux density, T
B_i	Intrinsic magnet flux density, T
B_ℓ	Load constant, N · m/(rad/s)
B_m	Operating magnet flux density, T
B_{m1}	Peak of the fundamental magnet flux density, T
B_{mr}	Rms value of B_{m1} , T
B_n	Normalized friction coefficient, p.u.
B_o	Flux density with magnet excitation but with no external excitation, T
B_p	Maximum magnet flux density very near to demagnetization of the magnets, T And also the peak flux density in the stator lamination in core loss section, T
B_{pk}	Peak flux density in the air gap, T
B_r	Remanent flux density, T
B_{rr}	Recoil flux density, T
B_t	Total friction coefficient, N m/(rad/s)
B_{tm}	Maximum tooth flux density, T
B_y	Yoke flux density, T
B_{ym}	Maximum yoke (back iron) flux density, T
b_y	Stator back iron thickness, m
C_f	Filter capacitance, F
C_o	Value of the C-dump capacitor, F
D	Bore diameter or inner stator diameter, m
d	Duty cycle
d^r, q^r	d- and q-axes in rotor reference frames, respectively.
e	Instantaneous induced emf, V
E	Also denotes average voltage phasor in Chapter 8, V Steady-state (rms) induced emf and also used as C-dump capacitor voltage, V
e_{as}	Induced emf in phase a (instantaneous), V
E_{as}	Steady-state rms phase a induced emf, V

e_{bs}	Induced emf in b phase (instantaneous), V
e_{cs}	Induced emf in c phase (instantaneous), V
$e_{\text{hd}}, e_{\text{hq}}$	Nonfundamental harmonic components of induced emf in d- and q-axes, respectively, V
E_m	Maximum energy density of the magnet, J/m ³
E_m	Maximum induced emf in the flux weakening region, V
e_n	Instantaneous normalized induced emf, p.u.
E_n	Normalized steady state induced emf, p.u.
E_p	Peak induced emf, V
E_p	Peak stator phase voltage in PM brushless dc machine, V
F, F^*	Modified reactive power and its reference, VAR
F	Force generated in the machine, N
$F_{\text{as}}, F_{\text{bs}}, \text{ and } F_{\text{cs}}$	Instantaneous a, b, and c phase mmfs, AT
$f_{\text{as}}(\theta_r)$	Position-dependent function in the induced emf in a phase
$f_{\text{bs}}(\theta_r)$	Position-dependent function in the induced emf in b phase
f_c	Control frequency, and PWM carrier frequency, Hz
$f_{\text{cs}}(\theta_r)$	Position-dependent function in the induced emf in c phase
F_d	Force density in the machine, N/m ² and also the mmf per pole in d-Axis winding, AT
F_e	External source mmf, AT
F_m	Magnet mmf, AT
f_n	Natural frequency, Hz
f_s	Utility supply frequency or stator frequency supply, Hz
F_s	Peak value of the resultant stator mmf per pole, AT
F_{sp}	Safe stator peak mmf per pole (that does not demagnetize the magnets), AT
f_{sn}	Normalized stator frequency, p.u.
f_r	Rotational frequency, Hz
g_d	Effective air gap length, m
g_d, g_q	Effective air gap length in direct (magnet) and quadrature axis, m
h	Average duty cycle of phase switches in half-wave converter topologies
H	Inertial constant in normalized unit, p.u.
H	Magnet field intensity, A/m
H_c	Gain of the current transducer, V/A
H_c	Magnet coercive force or coercivity at normal flux density, A/m
H_{ch}	Maximum safe field intensity without demagnetizing the magnets, A/m
H_{ci}	Intrinsic coercive force (where intrinsic flux density is zero) for magnets, A/m
H_{cl}	Maximum field intensity that will not irreversibly demagnetize the low-grade magnets, A/m
H_{cr}	Fictitious coercivity corresponding to remanent flux density of the low-grade magnets, A/m
H_{cs}	Fictitious coercivity corresponding to recoil remanent flux density of the low-grade magnets, A/m

H_e	External field intensity, A/m
H_g	Air gap field intensity, A/m
H_m	Magnet field intensity, A/m
H_o	Magnet field intensity with zero external excitation and on no load, A/m
H_p	Peak field intensity without demagnetizing the magnets, A/m
H_ω	Gain of the speed filter, V/(rad/s)
i_α, i_β	Currents in α and β frames that are rotating at assumed speed, A
i_{abc}	abc phase current vector
i_{as}	Instantaneous stator phase a current, A
i_{asn}	Normalized phase a stator current (instantaneous), p.u.
I_{avn}	Normalized average armature current, A
I_b	Base current in two-phase system, A or base current, A
I_{b3}	Base current in three-phase system, A
i_{bs}, i_{cs}	Instantaneous b and c stator phase currents, A
I_{cn}	n th harmonic capacitor current, A
I_d	Steady-state d-axis current flowing into the motional emf in rotor reference frames, A
I_{dc}	Steady-state dc link current or the inverter input current, A
i_{ds}, i_{qs}	d- and q-axes stator currents in stator reference frames, A
i_{dsi}, i_{qsi}	d- and q-axes stator currents in stator reference frames due to injected high-frequency voltage signals, A
i_{dsi}^s, i_{qsi}^s	d- and q-axes stator currents in stator reference frames due to injected high-frequency voltage signals, A
i_{dsi}^r, i_{qsi}^r	d- and q-axes stator currents in rotor reference frames due to injected high-frequency voltage signals, A
I_f	Steady-state field current or flux producing component of the stator current phasor, A
i_f	Instantaneous field current or flux producing component of the stator current phasor, A
i_{hk}	Harmonic current vector, A
i_{ip}, i_{in}	Positive and negative sequence current components resulting from injected signals, A
I_{me}	Rms per phase equivalent magnet current, A
I_{mep}	Peak per phase equivalent magnet current, A
I_n	n th harmonic current, A
i_o	Stator zero sequence current, A
I_p	Peak stator phase current in PM brushless dc machine, A
I_{ph}	Fundamental phase current, A
I_{ps}	Peak stator phase current in PM synchronous machine, A
I_q	Steady-state q-axis current flowing into the motional emf in rotor reference frames, A
I_{qc}, I_{dc}	Core loss current in the stator d- and q-axes, A
i_{qdo}	qdo current vector (q, d, and o) in stator reference frames, A
i_{qdo}^r	qdo current vector (q, d, and o) in rotor reference frames, A
i_{qds}	Stator q- and d-axes current vector in stator frames, A

$\vec{i}_{\text{qd}s}^{\text{r}}$	Stator q- and d-axes current vector in rotor reference frames, A
$I_{\text{qs}}, I_{\text{ds}}$	Steady-state stator q- and d-axes currents in stator reference frames, A
$I_{\text{qs}}^{\text{r}}, I_{\text{ds}}^{\text{r}}$	Steady-state stator q- and d-axes currents in rotor reference frames, A
I_s	Source current, A
I_{sm}	Maximum safe stator current that does not demagnetize the magnets, A
	Also denotes fundamental value of the stator current phasor under SSV strategy, A
I_{sp}	Sinusoidal peak stator phase current, A
I_{sy}	Rms current of the synchronous machine phase, A
i_{T}	Torque producing component of the stator current phasor, A
\vec{i}_f^*	Field current reference, A
i_{T}^*	Torque producing component of stator current phasor, A
\vec{i}_T^*	Reference torque producing component of stator current phasor, A
\vec{i}_s^{r}	Stator current phasor in rotor reference frames
$\vec{i}_{\text{sip}}^{\text{s}}, \vec{i}_{\text{sin}}^{\text{s}}$	Positive and negative sequence current phasor components resulting from injected signals, A
$I_{\text{T}}, I_{\text{T}}^*$	Steady-state values of i_{T} , and i_{T}^*
$\vec{i}_{\text{as}}^*, \vec{i}_{\text{bs}}^*, \vec{i}_{\text{cs}}^*$	a, b, c phase current commands, A
$i_{\text{xsn}}^{\text{r}}$	Current in rotor reference frames, and subscript x for q- or d-axis, s for stator, and n for normalized unit. Without subscript n, the variable is in SI units.
J	Total moment of inertia, kg-m ²
J_c	Current density of the armature conductor, A/m ²
J_l	Moment of inertia of load, kg-m ²
J_m	Moment of inertia of motor, kg-m ²
k	Inverse of leakage factor
K_b	Induced emf constant, V/(rad/s)
K_c	Gain of the current controller, V/A
k_d	Winding distribution factor for the fundamental
k_{dn}	Winding distribution factor for the n th harmonic
k_e	Eddy current loss constant
k_h	Hysteresis loss constant
K_i	Current loop transfer function gain
K_{is}	Integral gain of the speed controller
k_m	Ratio between mutual and self-inductances, per phase, in PMBDC machine
k_p	Winding pitch factor for the fundamental
k_{pn}	Winding pitch factor for the n th harmonic
K_i	Integral gain of the PI controller in power feedback control
K_p	Proportional gain of the PI controller in power feedback control
K_{ps}	Proportional gain of the speed controller
K_r	Inverter gain, V/V

K_s	Gain of the speed controller
k_s	Ratio of slot to tooth width
k_{sk}	Skew factor
K_t	Torque constant, N m/A
K_{vf}	Ratio between stator phase voltage and stator frequency, V/Hz
k_ω	Fundamental winding factor
K_ω	Speed feedback filter gain, V/(rad/s)
$k_{\omega n}$	n^{th} harmonic winding factor
L	Stack length, m
L, M	Stator self and mutual inductances in PM brushless machines, H
L_a	Denotes (L-M) in PM brushless dc machines, H
L_{aa}	Self-inductance of a phase winding, H
L_{ab}	Mutual inductance between phases a and b, H
L_{ac}	Mutual inductance between phases a and c, H
L_b	Base inductance, H
L_f	Filter inductance, H
L_{ma}	Magnetizing inductance per phase, H
ℓ_c	Average length of a stator phase winding, m
ℓ_g	Air gap length, m
ℓ_m	Magnet length, m
L_o	Value of inductor in energy recovery chopper in C-dump topology, H
L_q, L_d	Also denotes zero sequence inductance in machines, H
	Quadrature and direct axis stator self-inductances in rotor reference frames, H
L_{dq}	Mutual inductance between d- and q-axes, H
L_{qd}	Mutual inductance between q- and d-axes, H
L_{ql}, L_{dl}	Stator q- and d-axes leakage inductances in rotor reference frames, H
L_{qn}, L_{dn}	Normalized quadrature and direct axis stator self-inductances in rotor reference frames, p.u.
L_{qq}, L_{dd}	Self-inductance of the stator q- and d-axes stator windings in stator reference frames, H
L_s	Input source inductance, H
L_{xy}	Mutual inductance between windings given by the subscripts x and y, H
m	Modulation ratio and also used to denote the ratio between slot to pole number
N_1	Number of turns/phase with half-wave converter control
N_{co}	Cogging cycles per mechanical revolution
N_{ph}	Effective turns per phase
n_r	Rotor speed, rpm
n_s	Stator field speed or synchronous speed, rpm
N_{sp}	Number of slots per pole (and also denotes speed in rpm in Chapter 2)

o	Subscript ending with o in a variable indicates its steady-state operating point value
p	Differential operator, d/dt
P	Number of poles
P_1	Air gap power with half wave converter, rad/s
P_{1n}	Dominant harmonic resistive losses, W
P_a	Air gap power, W
P_{an}	Normalized air gap power, p.u.
P_{av}	Average input power, W
P_b	Base power, W
P_c	Armature resistive losses, W
P_{cl}	Machine copper loss with half-wave converter operation, W
P_{co}	Core losses, W
P_{cd}	Core loss density ($P_{ed} + P_{hd}$), W/unit weight
P_{ed}	Eddy current loss per unit weight, W/unit weight
P_{et}	Eddy current loss in tooth for trapezoidal magnet flux density distribution, W
P_{ets}	Eddy current loss in tooth for sinusoidal magnet flux density distribution, W
P_{ey}	Eddy current loss in yoke for trapezoidal magnet flux density distribution, W
P_{eys}	Eddy current loss in yoke for sinusoidal magnet flux density distribution, W
P_{eyn}	Ratio of P_{ey} and P_{eys}
P_{hd}	Hysteresis current loss per unit weight, W/unit weight
P_{hs}	Stator hysteresis loss, W
P_i	Input power, W
P_p	Number of pole pairs
p_i	Instantaneous input power, W
P_1	Total power losses, W
P_{1n}	Maximum power losses, W
P_m	Mechanical power output, W
P_o	Output power, W
P_{on}	Normalized power output, p.u.
P_{sc}	Stator resistive losses of a three phase machine, W and, also the conduction loss in a transistor, W
P_{scn}	Normalized stator resistive losses of a three phase machine, p.u.
P_{sw}	Switching loss in a device, W
P_{VA}	Apparent power, VA
P_a^*	Air gap power reference, W
q	Number of slots per pole per phase
Q and Q_i	Reactive power, VAR
Q_f	Filtered reactive power, VAR
Q_n, Q_{fn}	Normalized reactive and filtered reactive power, respectively, p.u.
r	Radius of the bore, m
R_1	Stator resistance/phase with half-wave converter operation, W

R_a	Twice the per phase resistance in PM brushless dc machines, Ω
R_c	Core loss resistance, Ω
R_d, R_q	Stator d- and q-axes winding resistances, Ω
R_s	Stator resistance per phase, Ω
R_{sn}	Normalized stator resistance per phase, p.u.
s	Laplace operator
S	Number of slots in the stator
S_a, S_b, S_c	a, b, c phase switching states of the inverter
T	Carrier period time, s, as well as effective turns per stator phase winding
t	Time, s
t_d	Inverter dead time, s
t_t	Time taken to vary the tooth flux density from zero to maximum value, s
t_y	Time taken to vary the yoke flux density from zero to maximum value, s
T_1, T_2	Electrical time constants of the motor, s
T_{abc}	Transformation from abc to qdo variables in rotor reference frames
T_{av}	Average torque, N·m
T_b	Base torque, N·m
T_c	Time constant of the current controller, s
T_{co}	Cogging torque for a cycle expressed in terms of a Fourier series, N·m
T_e	Air gap or electromagnetic torque, N·m
T_{ec}	Analytically computed cogging torque, N·m
T_{e1}	First-harmonic air gap torque, N·m
T_{e6}	Sixth-harmonic torque, N·m
T_{e6n}	Normalized sixth-harmonic torque, p.u.
T_{ec}	Torque reference generated by speed error, N·m
T_{ef}	Maximum air gap torque generated with the voltage and current constraints, N·m
T_{em}	m th harmonic torque in PM brushless dc machines, N·m
T_{emn}	Normalized m th harmonic torque in PM brushless dc machines, p.u.
T_{en}	Normalized air gap torque, p.u.
T_{er}	Rated air gap torque, N·m
T_{er}	Reluctance torque, N·m
T_{es}	Synchronous torque due to magnets, N·m
T_i	Time lag of the current control loop, s
T_l	Load torque, N·m
T_{ln}	Normalized load torque, p.u.
T_m	Mechanical time constant, s
T_{max}	Maximum torque limit, N·m
T_n	Peak value of n th order harmonic of cogging torque, N·m
t_{on}	Conduction time or on time of a device in a switching cycle, s

t_{off}	Device off time in a switching cycle, s
T_p	Peak value of cogging torque in a cycle, N·m
T_{ph}	(Effective) Number of turns per phase
T_r	Converter (inverter) time delay, s
$[T]$	Transformation from rotor reference frames of the qd variables to stationary reference frames
T_s	Time constant of the speed controller, s
t_s	Total switching time in a device, s
T_{ω}	Time constant of the speed filter, s
T_{abc}^s	Transformation from abc to qdo variables in the stationary reference frames
T_e^*	Torque reference, N·m
T_{en}^*	Normalized torque reference, p.u.
u	Input vector
V	Rms line-to-line voltage of the supply, V
v_α, v_β	Voltages in α and β frames that are rotating at assumed speed, A
$v_{\text{as}}, v_{\text{bs}}, v_{\text{cs}}$	Phase a, b, and c input voltages to PM brushless dc machine, V
v_{ab}	Instantaneous line-to-line voltage between phases a and b, V
V_{ab}, V_{bc}, V_{ca}	Rms line-to-line voltages between a and b, b and c, and c and a phases, V
v_{ab}, v_{bc}, v_{ca}	Instantaneous line-to-line voltages between a and b, b and c, and c and a phases, V
v_{abc}	abc voltage vector
v_{abi}	Instantaneous input converter line-to-line voltage between phases a and b, V
$v_{\text{am}}, v_{\text{bm}}, v_{\text{cm}}$	Instantaneous voltages between dc midpoint voltage and inverter midpole phases a, b, and c, V
v_{an}	Midpoint voltage for ideal inverter phase a, V
v'_{an}	Inverter phase a midpoint voltage with dead time incorporated, V
v_{anc}	Inverter phase a midpoint voltage with dead time compensation, V
v_{ao}, v_{bo}, v_{co}	Inverter midpole voltages, V
V_{as}	Stator rms voltage input per phase and also rms phase a voltage, V
V_{asn}	Normalized phase a stator voltage, p.u.
V_b	Base voltage, V
V_{b3}	Base voltage in three-phase system, V
v_c	Control voltage, V
V_c	Voltage across the capacitor, V
V_{cn}	Normalized conduction voltage drop across a transistor, p.u.
V_{cm}	Maximum control voltage, V
V_d	Diode peak voltage, V
V_{dc}	Steady-state dc link voltage, V
v_{dc}	Instantaneous dc link voltage, V
v_{ds}, v_{qs}	d- and q-axes stator voltages in stator reference frames, V
v_{dsi}, v_{qsi}	d- and q-axes injected voltages in rotor reference frames, V
V_g	Air gap volume, m ³

v_{g1}, v_{g4}	Gate signals to inverter phase a, V
v_{g1}, v_{g4}'	Modified gate signals to inverter phase a incorporating dead time, V
v'_{g1c}, v'_{g4c}	Compensated gate signals of inverter phase a to overcome the effects of dead time, V
v_{hk}	Harmonic voltage vector, V
V_i	Inverter input voltage, V
V_m	Peak supply voltage, V and also magnet volume, m ³
v_{mn}	Voltage between midpoint source and neutral of the load, V
v_o	Stator zero sequence voltage, V
V_{on}	Conduction voltage drop across transistor, V
V_{ph}	Maximum rms phase voltage output of the inverter, V
v_{qds}^r	Stator voltage vector in rotor reference frames, V
v_r	Instantaneous phase converter input voltage, V
v_{re}	Instantaneous rectifier output voltage, V
v_s	Instantaneous phase source voltage, V
V_{si}^a	Injected voltage vector in anisotropic or estimated rotor frames, V
V_{si}^s	Injected voltage vector transformed to stator reference frames, V
V_{si}^r	Injected voltage vector transformed to rotor reference frames, V
V_s	Average source voltage, V
V_t	Stator tooth volume, m ³
V_{ts}	Peak power switch voltage, V
V_y	Stator yoke (back iron) volume, m ³
V_{vs}^*	Sensor output voltage, V
v_a^r	Peak value of the phase command or reference, V
v_s^r	Stator voltage phasor in rotor reference frames
v_{sn}^r	Normalized stator voltage phasor in the rotor reference frame, p.u.
v_{xsn}^r	Voltage in rotor reference frames, and subscript x for q- or d-axis, s for stator and n for normalized unit. Without subscript n, the variable is in SI units.
v_{zs}	Zero sequence voltage, V
W_c	Coenergy, J
W_m	Energy stored in a device, J
W_s	Stator slot width, m
W_t	Stator tooth width, m
X	State variable vector
$X(0)$	Initial steady-state vector
$X(s)$	Laplace transform of input vector
$y(s)$	Laplace transform of output variable
Δi	Hysteresis current window, A
α	Stator voltage phasor angle with reference to rotor d-axis, rad
β	Ratio of actual to controller instrumented mutual inductance and also one-half of the magnet arc, rad
δ	Preceding a variable indicates small-signal variation

δ	Torque angle in synchronous machine, rad
δ^*	Torque angle command in synchronous machine, rad
$\delta\theta$	Error in rotor position, rad
$\delta\omega_m$	Change in rotor speed, rad/s
ΔQ	Change in reactive power, VAR
ϕ	Machine power factor angle, rad
ϕ_i	Input power factor angle, rad
ϕ_g	Air gap flux, Wb
ϕ_m	Peak mutual flux and also magnet flux, Wb
γ	Slot pitch or angle, rad
ξ	Coil pitch, rad
λ	Flux linkage, V-s
λ_{aa}	Flux linkage of a phase winding, V-s
λ_{af}	Armature flux linkages due to rotor magnets, V-s
λ_{af}^*	Armature flux linkages due to rotor magnets at ambient temperature, V-s
$\lambda_{afhd}, \lambda_{afhq}$	Nonfundamental harmonic flux linkages in d- and q-axes, respectively, V-s
λ_{afn}	Normalized mutual flux linkages due to rotor magnets, p.u.
$\lambda_{as}, \lambda_{bs}, \lambda_{cs}$	Flux linkages of phases a, b and c, respectively, V-s
λ_b	Base flux linkages, V-s
λ_m	Mutual air gap flux linkages, V-s
λ_m^*	Reference or command mutual air gap flux linkages, V-s
λ_{ma}	Flux linkages due to resultant mmf, V-s
λ_{mn}	Normalized mutual flux linkages, p.u.
λ_o	Stator zero sequence flux linkages, V-s
λ_p	Peak mutual flux linkages from rotor magnets (in PM brushless dc machines), V-s
$\lambda_{qs}, \lambda_{ds}$	Stator flux linkages in q- and d-axes, V-s
$\lambda_{qsi}, \lambda_{dsi}$	Stator flux linkages in q- and d-axes for injected high-frequency currents, V-s
λ_s^r	Stator flux linkage phasor in rotor reference frame, V-s
λ_{sn}^r	Normalized stator flux linkage phasor rotor reference frame, p.u.
θ	Spatial position, rad
θ_a	Phase advance angle of current in PM brushless dc machines, rad
θ_{ms}	Angle between the mutual flux and stator current phasors, rad
θ_λ	Angle between stator flux linkages phasor and rotor flux linkages phasor, rad
θ_r	Rotor position, rad
θ_s	Stator voltage phasor angle with respect to the closest switching voltage vector of the inverter, rad
θ_s^*	Also stator current phasor angle from stationary reference, rad
θ_{sk}	Stator current phasor angle command, rad
θ_{re}	Skew angle, rad
	Estimated rotor position, rad

\mathfrak{R}	Reluctance
$\mathfrak{R}_d, \mathfrak{R}_q$	Direct and quadrature axis reluctances, respectively
ρ	Saliency ratio, i.e., between q- and d-axes self-inductances and also used to denote specific resistivity of winding material
ρ_i	Mass density of the steel lamination, kg/m ³
τ_{fw}	Stator electrical time constant with full-wave converter operation, s
τ_{hw}	Stator electrical time constant with half-wave converter operation, s
τ_q, τ_d	Stator q- and d-axes stator time constant, s
τ_s	Stator time constant in surface mount PMSM, s
ω_1	Speed with half-wave converters, rad/s
ω_a	Estimated rotor and or anisotropic angular frequency, rad/s
ω_b	Base angular frequency, rad/s
ω_c	Carrier angular frequency, rad/s and also the speed of arbitrary reference frames in induction machines
ω_i	Angular frequency of the injected signal to the stator windings, rad/s
ω_m	Rotor mechanical speed, rad/s
ω_{rn}	Normalized rotor speed, p.u.
ω_{mr}	Speed signal from the output of speed filter, V
ω_r^*	Electrical rotor speed, rad/s
ω_r	Speed reference, V
ω_{rm}	Speed of model rotor frames, rad/s
ω_{rn}	Normalized rotor speed, p.u.
ω_s	Supply angular velocity, rad/s
μ_o	Permeability of air
μ_c	Permeance coefficient of the magnet
μ_{rm}	Relative permeability of the magnet
μ_r, μ_{rec}	Magnet recoil permeability
$\mu_{re}(H_m)$	External permeability of the magnet defined in Chapter 1

Part I

*Introduction to Permanent
Magnets and Machines and
Converters and Control*

1 Permanent Magnets and Machines

An introduction to permanent magnets (PMs) and their varieties, their characteristics such as demagnetization, and energy density and realization of machines with PMs is briefly presented in this chapter. Various forms of magnet placement on the rotor lead to certain unique operating characteristics of the machines and a number of such rotor configurations are discussed. PM synchronous machines (PMSMs) with magnets on the stator are of recent origin and they are covered under hybrid machines. The principle of operation of synchronous machines with PM rotors is introduced in the course of which machine fundamental relationships such as the magnetomotive force (mmf), induced emf (also known as back emf), and torque are derived for PMSMs with sinusoidal-induced emf but they can be extended along the same lines to brushless dc machines with trapezoidal-induced emf. To obtain these relationships, it is important to understand the stator windings and how the number of turns and their placement in the stator laminations affect them. Factors that affect the windings are pitch, distribution, and skew, they are evaluated and some commonly used winding types are given. The fundamental machine derivations are made from the first principles and they relate the physical dimensions of the machine and electrical and magnetic loading to output variables such as electromagnetic torque and air gap power [1–8]. In this process, the interplay of the machine variables and control variables is brought to the forefront, demonstrating the sphere of influence for the machine designer and control engineer to influence the outcome of the motor drive performance. In turn, it clearly emphasizes the need for integrated design of the motor drive system to optimize a set of performance indices dictated by a given application. Preliminary sizing of the machine and calculation of motor parameters such as inductances are derived. They are the starting points for fine-tuning the machine design mostly with finite element analysis software, which is outside the scope of this book and hence will not be covered. Core and resistive losses play crucial roles in the power density and operational torque and power of the machine and their computation is explained in detail. A special problem of the PMSMs exists in the form of cogging torque resulting from the interaction of the magnets and the stator teeth. It is described in detail along with the methods for mitigating the cogging torque.

1.1 PERMANENT MAGNETS

Materials to retain magnetism were introduced in electrical machine research in the 1950s [9–14]. There has been a rapid progress in these kinds of materials

since then. The magnetic flux density in the magnets can be considered to have two components. One is intrinsic and, therefore, due to the material characteristic depends on the permanent alignment of the crystal domains in an applied field during magnetization. It is referred to as the intrinsic flux density characteristic of the PMs. The flux density component, known as intrinsic flux density, B_i , saturates at some magnetic field intensities and does not increase with the applied magnetic field intensity. The other component of the flux density in the magnet is due to its magnetic field intensity as though the material does not exist in the presence of the applied magnetic field or in other words, is a very small component due to the magnetic field intensity in the coil in vacuum, B_h . Therefore, the flux density in the magnet material is given by

$$B_m = B_h + B_i \quad (1.1)$$

The excitation component B_h is directly proportional to magnetic field intensity, H , and given by

$$B_h = \mu_0 H \quad (1.2)$$

where H is the magnetic field intensity. In all magnetic materials, this component is very small compared to the intrinsic flux density. Combining Equations 1.1 and 1.2, the magnetic flux density can be written as

$$B_m = B_i + \mu_0 H \quad (1.3)$$

where

B_i is the intrinsic flux density

H is the magnetic field intensity

B_m is the flux density in the magnet or known as normal flux density in the magnet

A typical ceramic magnet's intrinsic and magnet flux densities are shown for the second quadrant in [Figure 1.1](#). The magnetic flux density in the second quadrant is a straight line and it can be represented in general as

$$B_m = B_r + \mu_0 \mu_{rm} H \quad (1.4)$$

where μ_{rm} is the relative permeability of the magnet. It is seen that at $H = 0$, the intrinsic and normal induction flux densities pass through the point known as remanent flux density, B_r . The intrinsic flux density in the second quadrant can be derived from the demagnetization characteristic of the magnet as follows:

$$B_i = B_m - \mu_0 H = B_r + \mu_0 H (\mu_{rm} - 1) \quad (1.5)$$

For a hard magnet with a straight line demagnetization characteristic, note that the intrinsic flux density is constant in the second quadrant, i.e., it remains "permanently magnetic" and this is termed a high-grade magnet. If the demagnetization

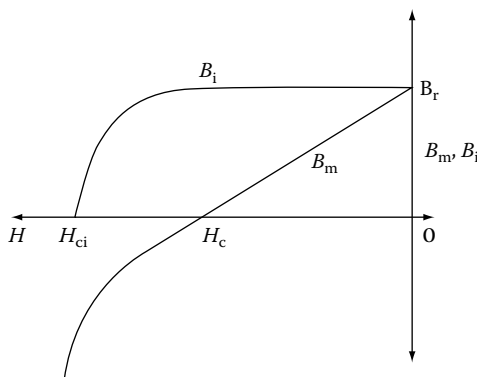


FIGURE 1.1 Typical ceramic magnet flux densities.

characteristic is not a straight line in the second quadrant, then the intrinsic flux density is not a constant, indicating that the “permanency of magnetism” is not as good as that of the high-grade magnets and, therefore, such magnets are known as low-grade PMs. The coercive force required to bring the magnet’s intrinsic flux density to zero is the intrinsic coercive force, H_{ci} , and that of the normal flux density is coercive force or coercivity, H_c , shown in Figure 1.1.

The demagnetization characteristic is the one used in analysis and design of the machines, as it includes the effect of the external magnetic field intensity that invariably comes into existence in the machine due to its winding excitation. More on this is described in later sections.

The materials that retained magnetism are known as hard magnet materials. The ability to retain permanent magnetism is found in cobalt, iron, and nickel, and they are referred to as ferromagnetic materials. Various materials such as alnico-5, ferrites (ceramics), samarium-cobalt, and neodymium boron iron are available as PMs for use in machines. The most popular ones in practice are samarium cobalt and neodymium-type magnets.

1.1.1 DEMAGNETIZATION CHARACTERISTICS

The generic $B-H$ demagnetization characteristics of these materials are shown in Figure 1.2 for second quadrant only [6]. For available PM materials in the market, the reader is referred to manufacturer data sheets that may be obtained from the manufacturer and the data will be available for complete $B-H$ characteristics in four quadrants of magnetic flux density versus magnetic field intensity and not limited to second quadrant only. Second quadrant is considered here because the magnets need not have an external excitation once they are magnetized and any magnetic field strength that may be applied through coils in an electromagnetic device is by design usually intended to reduce its flux density. Therefore, the operation of the machine and the magnets lies in the demagnetization domain. That includes the second and third quadrants of the $B-H$ characteristics. It is not usual to encounter the third quadrant in operation and hence only the second quadrant is considered here but the analysis and discussion here can be easily extended to cover the third quadrant also, if necessary.

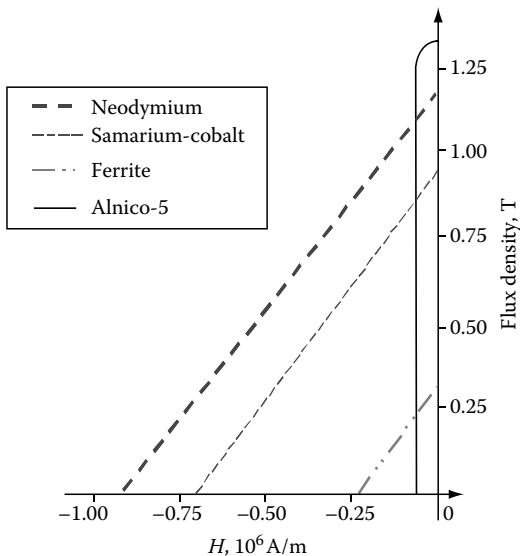


FIGURE 1.2 Second quadrant B - H characteristics of PMs. (From Krishnan, R., *Electric Motor Drives*, Figure 9.1, Prentice Hall, Upper Saddle River, NJ, 2001. With permission.)

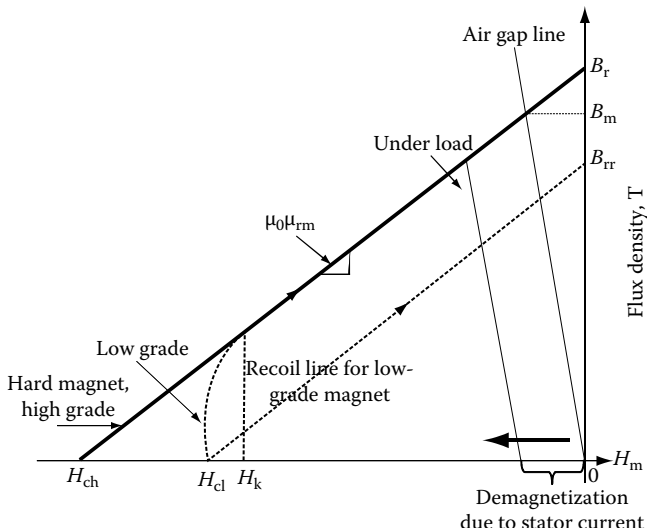


FIGURE 1.3 Operating point of magnets. (From Krishnan, R., *Electric Motor Drives*, Figure 9.2, Prentice Hall, Upper Saddle River, NJ, 2001. With permission.)

The last three listed magnets have straight-line characteristics whereas alnico-5 has the highest remanent flux density but has a nonlinear characteristic. The flux density at zero excitation is known as remanent flux density, B_r (referred to as remanence also in some texts) shown in Figure 1.3 for a generic hard PM. The low-grade magnet has a curve, usually termed as knee at low flux density and around this point, it sharply dives down to zero flux density and reaches the magnetic field strength of H_{cl} known

as coercivity. The magnetic field strength at the knee point is H_k . If the external excitation acting against the magnet flux density is removed, then it recovers magnetism along a line parallel to the original B - H characteristic. In that process, it reaches a new remanent flux density, B_{rr} , considerably lower than the original remanent flux density. The magnet has irretrievably lost a value equal to $(B_r - B_{rr})$ in its remanent flux density. Even though the recoil line is shown as a straight line, it usually is a loop and the average of the looping flux densities is represented by the straight line. In the case of a high-grade magnet, the B - H characteristic is a straight line and its coercivity is indicated by H_{ch} . The line along which the magnet can be demagnetized and restored to magnetism is known as recoil line. The slope of this line is equal to $\mu_0\mu_{rm}$ as derived from the relationship between the flux density and magnetic field intensity and where μ_{rm} is relative recoil permeability for the high-grade magnets. For samarium-cobalt and neodymium boron magnets, the recoil permeability, μ_{rm} , nearly has a value from 1.03 to 1.1. More on recoil line and demagnetization characteristics is considered in later sections with worked examples.

1.1.2 OPERATING POINT AND AIR GAP LINE

To find the operating point on the demagnetization characteristic of the magnet, consider the flux path in the machine [6]. The flux crosses from the north pole of the rotor magnet to stator through an air gap and then closes the flux path from stator to rotor south pole, via air gap. In the process, the flux crosses two times the magnet length and two times the air gap, as shown in Figure 1.4. The mmf provided by magnets is equal to the mmf received by the air gap if the mmf requirement of stator and rotor iron is considered negligible. Then

$$H_m \ell_m + H_g \ell_g = 0 \quad (1.6)$$

where

H_m and H_g are magnetic field intensities or strengths in magnet and air, respectively

ℓ_m and ℓ_g are the length of the magnet and air gap, respectively

The operating flux density on the demagnetization characteristic can be written assuming that it is a straight line as

$$B_m = B_r + \mu_0 \mu_{rm} H_m \quad (1.7)$$

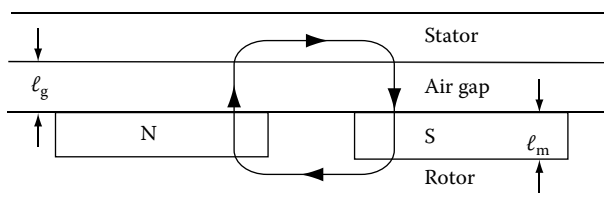


FIGURE 1.4 Simple layout of the stator and rotor of a machine. (From Krishnan, R., *Electric Motor Drives*, Figure 9.3, Prentice Hall, Upper Saddle River, NJ, 2001. With permission.)

The air gap flux density in terms of its magnetic field density is

$$B_g = \mu_0 H_g \quad (1.8)$$

Substituting for H_m from Equation 1.6 into Equation 1.7 and then substituting for H_g in terms of B_g from Equation 1.8 gives

$$B_m = B_r + \mu_0 \mu_{rm} H_m = B_r - \mu_0 \mu_{rm} \frac{H_g \ell_g}{\ell_m} = B_r - \mu_{rm} \frac{\ell_g}{\ell_m} \mu_0 H_g = B_r - \mu_{rm} \frac{\ell_g}{\ell_m} B_g \quad (1.9)$$

Neglecting leakage flux leads to

$$B_g = B_m \quad (1.10)$$

Substituting Equation 1.10 into Equation 1.9, the operating magnet flux density is derived as

$$B_m = \frac{B_r}{\left(1 + \frac{\mu_{rm} \ell_g}{\ell_m}\right)} \quad (1.11)$$

This clearly indicates that the operating flux density is always less than the remanent flux density because of the air gap excitation requirement. Note that the excitation requirements of iron and leakage fluxes are neglected in this conceptual derivation. The equation gives design guidelines. Consider an air gap flux density that is equal to remanent flux density of the magnet. In this case, the denominator of the equation has to be the one which amounts to thickness of the magnet being much higher than the product of the air gap length and relative permeability of the magnet. Approximating the relative permeability of a high-grade magnet to be 1, the thickness of the magnet has to be much larger than air gap length to equal the air gap flux density to magnet's remanent flux density. This will result in a large magnet, which is not feasible in a practical machine from viewpoints of cost and compactness of the rotor and hence the machine overall. Assuming the thickness of the magnets is far higher than that of the air gap length, which is not practical, there is another issue that makes it impractical. There will be leakage fluxes between the magnets in the air gap without connecting the stator part of the machine and it will be significant when the gap between adjacent magnets is smaller compared to the thickness of the magnets. Therefore, the practical ratio encountered between the thickness of the magnet and air gap length is from 1 to 20. The lower this ratio is, the volume of the magnet and cost will be lower and so also the power output and power density of the machine. The higher this ratio, the characteristics described in previously are higher. Increasing the ratio does not lead to proportional benefit in power output and beyond a certain ratio between

them, the benefits peak due to factors such as leakage fluxes and increasing volume and weight of the rotor, resulting in lower power density of the machine.

The operating point obtained from Equation 1.11 is shown in Figure 1.3 and the line connecting the operating flux density, B_m , and origin is known as air gap line or also load line. The slope of this line is equal to negative of a fictitious permeance coefficient, μ_c , times the permeance of the air. If the stator is electrically excited to produce demagnetization, then the load line moves toward the left and parallel to the load line as shown in the figure. The operating flux density is further reduced from B_m . Note that the permeance coefficient is derived for an operating point defined by B_m and H_m as

$$B_m = B_r + \mu_0 \mu_{rm} H_m = -\mu_0 \mu_c H_m \quad (1.12)$$

where H_m is the magnet field intensity due to stator current excitation in the machine. The permeance coefficient is then derived as

$$\mu_c = -\frac{B_r}{\mu_0 H_m} - \mu_{rm} \quad (1.13)$$

But the remanent flux density B_r can be expressed by assuming as though it is a function of operating magnetic field intensity, H_m as

$$B_r = -\mu_0 \mu_{re} (H_m) H_m \quad (1.14)$$

where $\mu_{re}(H_m)$ can be considered as external permeability and dependent on H_m . Substituting Equation 1.14 into Equation 1.13 gives the permeance coefficient as

$$\mu_c = \mu_{re} (H_m) - \mu_{rm} \quad (1.15)$$

The variations in the remanent flux density due to temperature changes as well as the impact of the applied magnetic field intensity, both of which are induced by external operating conditions, are clearly seen from this formulation of μ_c . As demagnetizing field is introduced by external operating conditions, it is seen that the permeance coefficient will decrease as the external permeability also decreases for that operating point. In hard PMs, the external permeability is in the order of 1–10 in the nominal operating region. It may be arrived at as in the following. Consider an example with a high-grade PM having a remanent flux density of 1.2 T and corresponding coercivity of -9×10^6 A/m. Let the air gap line produce, say, a flux density of 0.8 T. To find the permeance coefficient, the relative permeability of the magnet has to be evaluated, which is obtained from

$$\mu_{rm} = -\frac{B_r}{\mu_0 H_m} = -\frac{1.2}{4\pi \times 10^{-7} (-0.9 \times 10^6)} = 1.058$$

The operating magnetic field intensity for the operating flux density of 0.8 T is

$$B_m = B_r + \mu_0 \mu_{rm} H_m = 0.8 = 1.2 + (4\pi \times 10^{-7}) 1.058 H_m$$

from which

$$H_m = -0.3 \times 10^6 \text{ A/m}$$

Using this value, the permeance coefficient can be calculated as

$$\mu_c = -\frac{B_r}{\mu_0 H_m} - \mu_{rm} = 2.13$$

And likewise, for operating flux density of 1 T, the permeance coefficient is 5.32. As the operating flux density is lowered to zero, the permeance coefficient goes to zero and for higher flux densities, the permeance coefficient increases, and for realistic operating points up to 1.1 T (that is, nearly 92% of remanent flux density), it stays within a value of 10. Which brings up the point that for high-grade PMs, the permeance coefficient is in the range of 1–10 and hence it may be used as an indicator of the magnet's operating flux density.

1.1.3 ENERGY DENSITY

The energy density of the magnet is found by taking the product of its magnetic field strength and operating flux density. This measure serves to differentiate the magnets for use in machines with those having higher values preferred for high-power density machines. The peak energy operating point is optimal from the point of view of magnet utilization. The maximum energy density, E_{max} , for a hard high-grade PM shown in Figure 1.5 is derived as follows. The energy density, E_m , in terms of the product of magnet flux density, B_m , and its field intensity, H_m , is found and then taking its derivative with respect to field intensity and equating it to zero gives the condition that leads to maximum energy density. The steps to find maximum energy density are

$$E_m = B_m H_m = (B_r + \mu_0 \mu_{rm} H_m) H_m \quad (1.16)$$

Taking the derivative of this energy density as

$$\frac{dE_m}{dH_m} = 0 = B_r + 2\mu_0 \mu_{rm} H_m \quad (1.17)$$

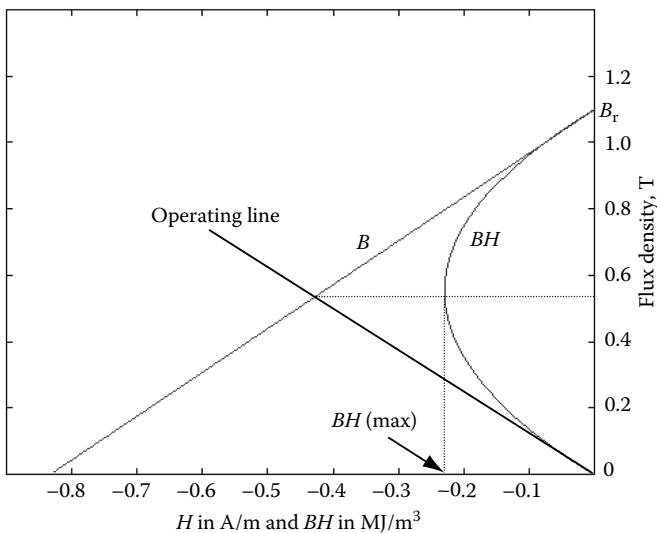


FIGURE 1.5 Energy product and preferred operating characteristics. (From Krishnan, R., *Electric Motor Drives*, Figure 9.4, Prentice Hall, Upper Saddle River, NJ, 2001. With permission.)

from which the field intensity is derived as

$$H_m = -\frac{B_r}{2\mu_0\mu_{rm}} \quad (1.18)$$

Substituting Equation 1.18 into Equation 1.16, the maximum energy density is derived as

$$E_{\text{max}} = -\frac{B_r^2}{4\mu_0\mu_{rm}} \quad (1.19)$$

Substituting Equation 1.18 into the expression for magnet flux density inserted in Equation 1.16, the flux density at which the maximum energy density available is found to be at half the remanent flux density, $0.5B_r$. The operating line for this flux density is shown in the figure giving the required magnetic field strength. Note that this operating point for maximum energy density requires a considerable amount of demagnetizing field strength from the stator excitation of the machine. Moreover, it is not practical to maintain this operating point in a variable speed machine drive as the stator currents will be varying widely over the entire torque speed region. To read the energy density in Figure 1.5, the projection of BH curve on H -axis is considered as the energy has to be negative. Some authors plot it in quadrant III to avoid confusion in this regard but here it is plotted in the second quadrant itself to keep the figure small and compact.

For a low-grade PM such as alnico, the magnet flux density and energy density characteristics are shown in [Figure 1.6](#). The flux density corresponding to maximum

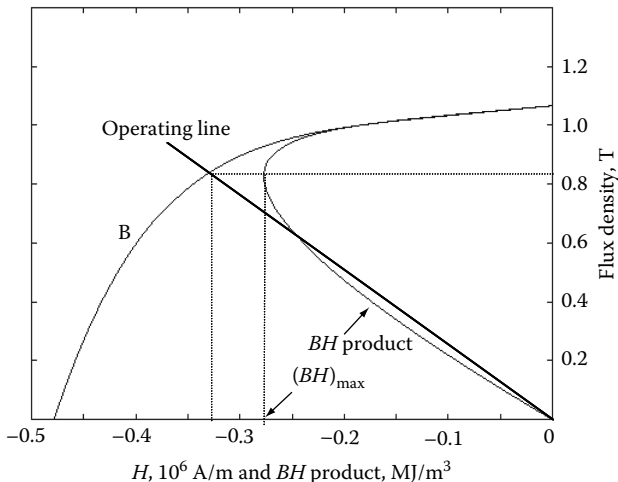


FIGURE 1.6 The energy density characteristic of an alnico magnet.

energy density is higher than half the remanent flux density in contrast to the high-grade PM characteristics. The maximum energy density is around one-tenth of the high-grade magnet's energy density is to be observed. Therefore, for high-performance applications requiring small motor weight and volume, these magnets are not preferred for use in electromagnetic devices.

1.1.4 ENERGY STORED IN THE MAGNET

Energy density gives an indication of where best to operate the magnet in a device but it is not the same as the energy stored in the magnet. From fundamental electromechanics, the energy stored in a device is given by

$$W_m = (\text{Volume}) \int H dB \quad (1.20)$$

Or energy stored per unit volume is given as

$$\frac{W_m}{\text{Volume}} = \int H dB \quad (1.21)$$

For example, consider a high-grade magnet with linear demagnetization characteristic and for that the energy stored per unit volume is

$$\frac{W_m}{\text{Volume}} = \int_0^{B_r} H dB = \int_0^{B_r} \left(\frac{B - B_r}{\mu_0 \mu_{rm}} \right) dB = -\frac{B_r^2}{2\mu_0 \mu_{rm}} = 2[(BH)_{\max}] = 2E_{\max} \text{ (J/m}^3\text{)} \quad (1.22)$$

$(BH)_{\max}$ is nothing but the maximum energy density derived in Equation 1.19 and denoted as E_{\max} .

1.1.5 MAGNET VOLUME

The volume of magnet embedded in the rotor determines the single most important cost component of the PM electrical machine, particularly in the case of the high power density magnet machines. It is critical in all applications to minimize the volume of the magnets among other things to minimize the cost of the machine as well as to have a smaller and lighter rotor. The magnet volume is found in terms of operating energy density and air gap volume as follows. Using Equation 1.6 and substituting for H_g in terms of B_g

$$B_g \ell_g = -\mu_0 H_m \ell_m \quad (1.23)$$

$$B_m A_m = B_g A_g \quad (1.24)$$

Using these ideal relationships, the magnet volume is derived as

$$V_m = A_m \ell_m = -\left(\frac{B_g A_g}{B_m}\right)\left(\frac{B_g \ell_g}{\mu_0 H_m}\right) = \frac{B_g^2 (A_g \ell_g)}{\mu_0 |B_m H_m|} = \frac{B_g^2 V_g}{\mu_0 |E_m|} \quad (1.25)$$

where

V_g is the air gap volume

E_m is the magnet operating energy density

A_m and A_g are the magnet and air gap area

Note that the equation is framed in absolute magnitude of the energy density by factoring $-H_m$ as a positive value with an absolute sign. From this relationship, it is inferred that the maximum operating energy density point of the magnet will yield the magnet with minimum volume and hence minimum cost. This is a simplified relationship since the leakage flux between the magnets is ignored and even then the result is not far off from reality for preliminary design calculation.

1.1.6 EFFECT OF EXTERNAL MAGNETIC FIELD INTENSITY

PMSMs experience a magnetic field due to the excitation of its armature windings in the stator in addition to the field due to PMs on the rotor. The interaction of these fields has a certain consequence depending on whether the fields are in the same or opposite directions. The external excitation (due to the winding excitation) is always intended for weakening the flux in the air gap. Therefore, the flux due to external excitation is directed in the opposite direction to that of the PM rotor flux. It is not usual to cumulatively compound the fluxes as it would strengthen the air gap flux and hence will result in the saturation of the stator core laminations and consequently in higher core losses. The reason for not allowing to cumulative compounding of fluxes

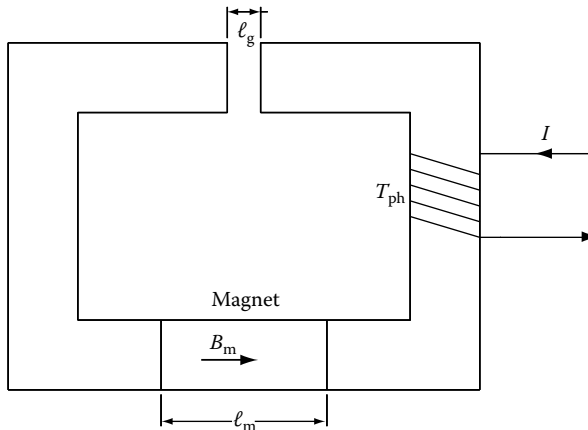


FIGURE 1.7 Simple electromagnetic device with a PM.

is that during design phase of the electrical machine, the magnet flux alone is set to provide the operating point near the knee point in the B - H (or equivalently flux versus current) characteristics of the lamination materials. Any further compounding of the flux with external excitation will move the operating point into saturation. Consider a simple electromagnetic device shown in Figure 1.7 to illustrate the effect of external magnetic field intensity. The coil has T_{ph} turns and carries a current of I . Assume that the external current is zero and hence only the field due to the PM exists. That would circulate a flux in the core in the anticlockwise direction as the magnet polarity is defined to be from left to right. If the winding is excited with a current, then the flux produced by it will traverse the core in the same direction as that of the PM flux. That would increase the flux in the core and in the air gap as the two fluxes due to the winding excitation and PM field are additive. If the current direction in the winding is opposite to that shown in figure, then the PM flux will be opposed by the external field due to the winding flux, resulting in the net reduction of the flux in the core and air gap. Two approaches, analytical and graphical, are developed in the following for the determination of the operating load flux density in the magnet when the electromagnetic device is superposed with an external excitation through a winding.

1.1.6.1 Analytical Approach

Let the magnet operating flux density is given by

$$B_m = B_r + \mu_0 \mu_{rm} H \quad (1.26)$$

and the mmf of the external source must be equal to that of the mmf requirement of the air gap and magnet. The mmf required for the iron path is neglected here to get a conceptual result. The mmf around the flux path then is written as

$$H_m \ell_m + H_g \ell_g = T_{ph} I \quad (1.27)$$

where the subscript m and g correspond to variables in magnet and air gap, and ℓ corresponds to length of the air gap and magnet with respective subscripts. The magnetic field intensity is then

$$H_m = \frac{T_{ph}I - H_g \ell_g}{\ell_m} \quad (1.28)$$

But the magnetic field intensity in the air gap is related to the air gap flux density as

$$B_g = \mu_0 H_g \quad (1.29)$$

and there is a clear relationship between the flux densities in the air gap and magnet and it can be modeled as follows. The useful flux, which is in the air gap, is always a fraction of the magnet flux, which is expressed in terms of the constant of proportionality, $1/k$, also known as leakage factor:

$$\phi_g = \frac{\phi_m}{k} \quad (1.30)$$

But the air gap and magnet flux in terms of the flux densities and areas of cross section are

$$\phi_g = B_g A_g; \quad \phi_m = B_m A_m \quad (1.31)$$

where the area of cross-section of the air gap and magnet are given as A_g and A_m , respectively. Thus defining the flux density of the air gap in terms of the magnet flux density by combining the equations from Equation 1.27 to Equation 1.31 and substituting in the magnet flux density equation of the magnet (Equation 1.26), the following is obtained:

$$B_m = \frac{1}{1 + \mu_{rm} \frac{\ell_g}{\ell_m} \frac{A_m}{A_g} \frac{1}{k}} \left[B_r + \mu_0 \mu_{rm} \frac{T_{ph}I}{\ell_m} \right] \quad (1.32)$$

In the case of a high-grade PM, note that the remanent flux density is directly proportional to coercive force as the demagnetization characteristic is a straight line and can be expressed as

$$B_r = -\mu_0 \mu_{rm} H_c q \text{ or alternately } qB_r = \mu_0 \mu_{rm} |H_c| \quad (1.33)$$

In the case of low-grade PM such as alnico, the same relationship can be used but instead of the real coercive force, a fictitious coercive force is considered for modeling. It is obtained by extending the operating line until it intersects the field intensity

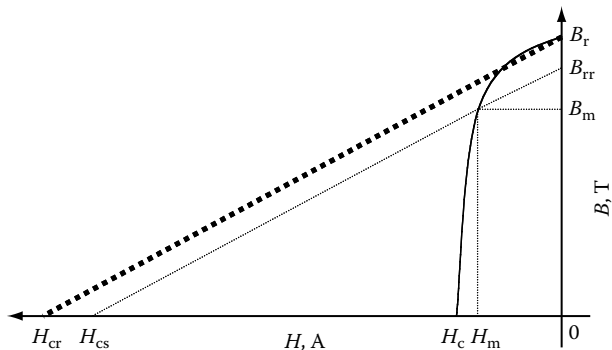


FIGURE 1.8 The alnico magnet's fictitious coercive force for an operating point.

axis and the intersecting field intensity, H_{cs} for an operating flux density of B_m and shown in Figure 1.8.

Realizing that the external mmf, the product of number of winding turns and current, over the magnet length is the external field intensity, H_e , yields the flux density equation in such terms as

$$B_m = \frac{B_r}{1 + \mu_{rm} \frac{\ell_g}{\ell_m} \frac{A_m}{A_g} \frac{1}{k}} \left[1 + \mu_0 \mu_{rm} \frac{H_e}{B_r} \right] \quad (1.34)$$

where

$$H_e = \frac{T_{ph} I}{\ell_m} \quad (1.35)$$

Substituting the remanent flux density in terms of the coercive force (real in the case of high-grade and fictitious in the case of the low-grade PMs) given in Equation 1.33 in the flux density equation (Equation 1.34) gives

$$B_m = \frac{B_r}{1 + \mu_{rm} \frac{\ell_g}{\ell_m} \frac{A_m}{A_g} \frac{1}{k}} \left[1 - \frac{H_e}{H_c} \right] = B_0 \left[1 + \frac{H_e}{|H_c|} \right] \quad (1.36)$$

where

$$B_0 = \frac{B_r}{1 + \mu_{rm} \frac{\ell_g}{\ell_m} \frac{A_m}{A_g} \frac{1}{k}} \quad (1.37)$$

where B_0 is the no load flux density, i.e., with no externally applied field intensity. From Equation 1.36, it is inferred that the external excitation reduces the flux density if the excitation is against the magnet flux. Reversing the excitation will increase the magnet flux but invariably lead to saturation of the iron core and therefore is not attempted in practice.

1.1.6.2 Graphical Approach

Instead of the analytical approach, the load flux density can also be found graphically. Such a procedure is derived here from the analytical expressions derived earlier. It is illustrated for the low-grade PM device.

The no load flux density is written as

$$B_0 = B_{rr} + \mu_0 \mu_{rm} H_o = B_{rr} \left[1 - \frac{H_o}{H_{cs}} \right] \quad (1.38)$$

where subscript “o” corresponds to operating recoil line and as shown in Figure 1.9. The remanent flux density under the new operating condition is B_{rr} and corresponding coercivity is H_{cs} , which is fictitious for low-grade magnet such as the one shown in Figure 1.8. Similarly the load flux density is derived by substituting for B_o from Equation 1.37 into Equation 1.38 as

$$B_m = B_o \left[1 - \frac{H_e}{H_{cs}} \right] = B_{rr} \left[1 - \frac{H_o}{H_{cs}} \right] \left[1 - \frac{H_e}{H_{cs}} \right] = B_{rr} + \mu_0 \mu_{rm} H_m \quad (1.39)$$

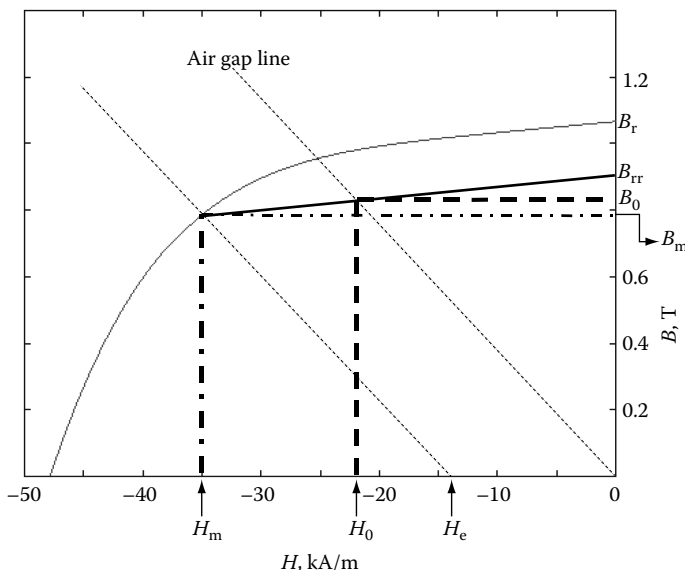


FIGURE 1.9 The magnet characteristic and operating points with and without external excitations.

On rearranging this equation to obtain the magnetic field intensity at the operating point as

$$\begin{aligned} H_m &= \frac{B_{ir}}{\mu_0 \mu_{rm}} \left[-\frac{H_o + H_e}{H_{cs}} + \frac{H_o H_e}{H_{cs}^2} \right] = -H_{cs} \left[-\frac{H_o + H_e}{H_{cs}} + \frac{H_o H_e}{H_{cs}^2} \right] = H_o + H_e - \frac{H_e}{H_{cs}} H_o \\ &= H_o + H_e + \left[\frac{B_m}{B_o} - 1 \right] H_o = H_e + \left[\frac{B_m}{B_o} \right] H_o \end{aligned} \quad (1.40)$$

Equation 1.40 is rearranged in a manner to bring out explicitly the equality of air gap line and load line with an external excitation of H_e as

$$\frac{H_m - H_e}{B_m} = \left[\frac{H_o}{B_o} \right] \quad (1.41)$$

This demonstrates that the operating flux density, B_m , is given by the line that is parallel to the air gap line that is shifted from the origin by the external magnetic field intensity generated from the excitation of the coil. Its construction is shown in Figure 1.9.

Example 1.1

A PM whose characteristics are given in Figure 1.9 is embedded in the electromagnetic device shown in Figure 1.6. The magnet is stabilized at -35 kA/m with a new remanent flux density. The relative permeability of iron is considered very large so the reluctance of the iron is zero to simplify calculations. Find the current in the coil required to operate the magnet at its stabilized operating point. The data for the device are

$$\ell_g = 0.5 \text{ mm}$$

$$\ell_m = 12 \text{ mm}$$

Leakage factor, $k = 1.25$

Magnet area = air gap area

Number of turns in the coil, $T_{ph} = 1000$

Solution

The approach to solve this problem is to find the magnet permeability from the characteristic given, then to proceed to find the new remanent flux density. Given the remanent flux density, the magnet flux density with no external excitation is found, which gives the air gap line. From this, the solution can be obtained graphically by drawing a line parallel to the air gap line that is shifted to the left of the origin by an amount equal to externally excited field intensity from the stabilized operating point. The intersection of this line on the field strength axis gives the external excitation required to demagnetize the magnet. Graphical solution is shown in Figure 1.9. Alternatively, it is evaluated analytically as in the following.

Magnet relative permeability is found from the characteristic by considering the remanent flux density and another operating point B_1 at H_1 as

$$\mu_{rm} = \frac{B_r - B_1}{\mu_0 H_1} = \frac{1.0665 - 1.033}{(4\pi \times 10^{-7}) \times (10 \times 10^3)} = 2.665$$

As the magnet is stabilized at $H_d = -35$ kA/m, which gives the magnet operating point B_m (0.7856 T), the new remanent flux density is found by drawing the recoil line, which is a line parallel to the magnet characteristic from this operating point or analytically obtained from

$$B_m = B_{rr} + \mu_0 \mu_{rm} H_m$$

and therefore the new remanent flux density (for the stabilized operating point) is

$$B_{rr} = B_m - \mu_0 \mu_{rm} H_m = 0.7856 - 4\pi \times 10^{-7} \times 2.665 \times (-35,000) = 0.9028 \text{ T}$$

The operating point of the magnet with no external excitation in the device is obtained from

$$B_o = \frac{B_{rr}}{1 + \mu_{rm} \frac{l_g}{l_m} \frac{A_m}{A_g} \frac{1}{k}} = \frac{0.9028}{1 + 2.665 \times \frac{0.5}{12} \times 1 \times \frac{1}{1.25}} = 0.8291 \text{ T}$$

Fictitious coercivity of the magnet in low-grade magnets is

$$H_{ce} = \frac{B_{rr}}{\mu_0 \mu_{rm}} = 269.5 \text{ kA/m}$$

The flux density lowered by external excitation is

$$\Delta B = \frac{B_m - B_o}{B_o} = \frac{0.7856 - 0.8291}{0.8291} = -0.05246 \text{ T}$$

The external field strength required to demagnetize the magnet is

$$H_e = -\Delta B | H_{ce} | = -0.5246 \times 269.5 \times 10^3 = -14.14 \times 10^3 \text{ A/m}$$

Mmf to create this field strength is given by

$$F_e = H_e l_m = -14.14 \times 10^3 \times 0.012 = -169.68 \text{ AT}$$

The demagnetizing current is obtained from it as

$$I = \frac{F_e}{T_{ph}} = \frac{-169.68}{1000} = -0.16968 \text{ A}$$

Example 1.2

The electromagnetic device shown in Figure 1.6 is considered for this problem. The magnet is of the neodymium variety with the remanent flux density of 1.1 T and coercivity of 0.86×10^6 A/m and has a straight line demagnetization characteristic. Determine the flux density in the air gap when the current in the coil is 10 A. The data for the device are given in Example 1.1.

Solution

The solution is very similar to the solution for Example 1.1. The graphical solution is shown in Figure 1.10.

Or analytically the solution is found as follows:

$$B_m = B_r + \mu_0 \mu_{rm} H$$

and at $B = 0$, $H = H_c = 0.86 \times 10^6$ A/m, which on substitution gives the relative permeability of the magnet as

$$\mu_{rm} = \frac{B_r}{\mu_0 H_c} = \frac{1.1}{4\pi \times 10^{-7} \times 0.86 \times 10^6} = 1.0062$$

The no load operating flux density, B_o , is obtained from

$$B_o = \frac{B_r}{1 + \mu_{rm} \frac{\ell_g}{\ell_m} \frac{A_m}{A_g} \frac{1}{k}} = \frac{1.1}{1 + 1.0062 \times \frac{0.0005}{0.012} \times 1 \times \frac{1}{1.25}} = 1.0643 \text{ T}$$

The line connecting origin and the no load flux density gives the air gap line or no load line. To evaluate the load operating flux density, a line parallel to the air

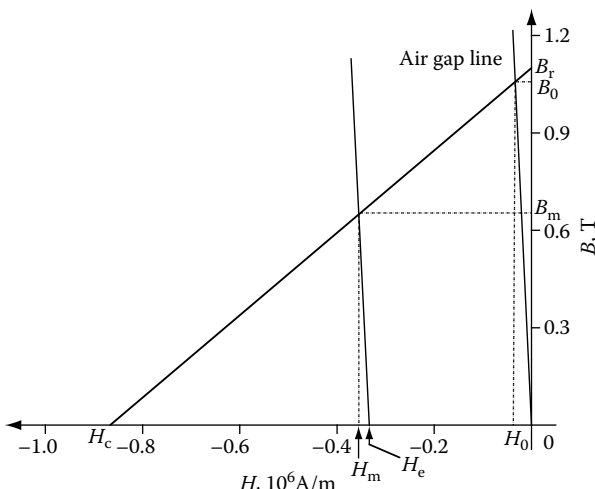


FIGURE 1.10 Operating point determination with external excitation for Example 1.2.

gap line shifted from the origin to the left by an amount equal to the external field strength (H_e) has to be drawn to intersect the demagnetization characteristic of the magnet. The external field strength is computed as follows:

The external excitation, $F_e = T_{ph}I = -1000 \times 4 = -4000$ AT

The external field strength

$$H_e = \frac{F_e}{\ell_m} = -\frac{4000}{0.012} = -0.333 \times 10^6 \text{ A/m}$$

Drawing the load line parallel to the air gap line from H_e intersects the magnet demagnetization characteristic yielding the magnet flux density B_m as 0.6575 T. Analytically the magnet load flux density is found from

$$B_m = \frac{1}{1 + \mu_{rm} \frac{\ell_g}{\ell_m} \frac{A_m}{A_g} \frac{1}{k}} \left[B_r + \mu_0 \mu_{rm} \frac{T_{ph} I}{\ell_m} \right] = 0.6575 \text{ T}$$

Note that the air gap flux density is

$$B_g = \frac{B_m A_m}{k A_g} = \frac{0.6575}{1.25} = 0.526 \text{ T}$$

1.2 ARRANGEMENT OF PMs

The magnets can be individually made in many shapes and sizes. They also come in the ring form. The ring form is the easiest to install as they can be slid on top of the steel laminated rotor and held in place by suitable means. Then they can be magnetized in any desired direction. The disadvantage of the ring magnets is that they are expensive compared to individual magnets. The individual magnets can take any shape. Each pole may consist of a number of magnet segments instead of one piece. The reason for this is that for large machines with constraints on machining of the magnet materials and charging them to magnetize, the use of a single magnet piece or segment per pole may not be possible or if possible it may not be the most economical. In some cases, a single magnet per pole is not suitable for large flux weakening range of operation. It is found that the flux weakening capability is enhanced with multisegment magnet per pole structures. They can also be stacked one on top of another with equal or varying widths to yield a desired flux distribution such as a sinusoidal or trapezoidal distribution in the air gap of the PM synchronous and brushless dc machines, respectively. The three kinds of magnet poles are shown in [Figure 1.11](#). The magnets may have varying thicknesses and widths for stacking up and note that the magnetization polarities are in the same direction for the stack.

All these arrangements have advantages and applications. Single magnet per pole is ideal for small machines. Higher power machines may use multisegment magnets

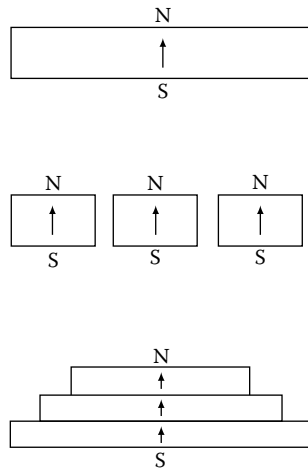


FIGURE 1.11 Realization of magnet poles with one or multiple segments.

per pole and stacked pole structures. Single magnet and multisegment magnets are prevalent in practice.

Various shapes of magnets that are in practice such as rectangular, radial, and breadloaf are shown in Figure 1.12. The radial and breadloaf types of magnets are ideal for surface mount-type of PMSMs. The air gap in the case of the radial magnets on the rotor surface is uniform, assuming that it is not partially embedded in the rotor lamination with the result that the air gap flux density is uniform. Radial magnets can come with their end surfaces being radial or parallel and accordingly they are referred to as surface radial and surface parallel magnets and they are shown in Figure 1.13. The air gap for the breadloaf magnet is nonuniform and hence the air gap flux density also being nonuniform. That allows for shaping the flux density in the air gap, which can be other than rectangular and constant over the magnet arc. This is elaborated in Section 1.3.

Rectangular magnets are commonly used in interior PM rotor construction. The recent trend is to have multiple magnets per pole in this construction to facilitate higher flux-weakening region of operation. This structure is not ideal in surface

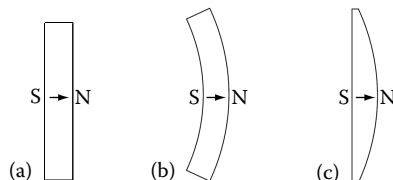


FIGURE 1.12 Various types of magnets: (a) rectangular; (b) radial; and (c) breadloaf.

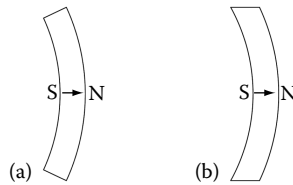


FIGURE 1.13 Radial magnets with radial and parallel surfaces. (a) Surface radial magnet and (b) surface parallel magnet.

mount machines as the desired constant air gap cannot be maintained. Other shapes are possible and open to the imagination of the designer but may be limited by manufacturing cost and techniques. The constraining factors in regard to shapes are as follows:

- Minimum material per magnet pole
- Ease of machining and construction
- Flux density distribution that is rectangular or sinusoidal

Because of these constraints, many other shapes have not seen the light of the day.

1.3 MAGNETIZATION OF PMs

PMs are magnetized [56–59] with certain orientation or direction such as radial, parallel, or any other direction. The magnetization orientation strongly influences the quality of the air gap flux density distribution and indirectly affects the power density in a given arrangement of the machine with PMs. The air gap flux density distribution influences in turn the harmonic torque generation in the machine and the presence of the harmonic torques corrodes the quality of torque output in the machine, particularly in the case of high-performance motor drives. Radial and parallel magnetization are prevalent in practice whereas other forms of magnetization are yet to make their presence felt even when they have been known to possess unique advantages in some cases.

1.3.1 RADIAL AND PARALLEL MAGNETIZATIONS

Radial and parallel magnetization are shown in [Figure 1.14](#). The normal direction to the surface is indicated by vector \mathbf{n} and the magnetization vector by \mathbf{M} . The radial magnetization is along the radius while the parallel magnetization is parallel to the edges as in the case of surface parallel magnets. But that need not be true in cases with other edge shapes. The key in that case is that the magnetization direction is horizontal as shown in the figure. The effect of two such magnetizations in a synchronous machine is shown in the form of air gap flux density versus rotor position using finite element analysis as well their flux plots in [Figure 1.15](#) for a machine

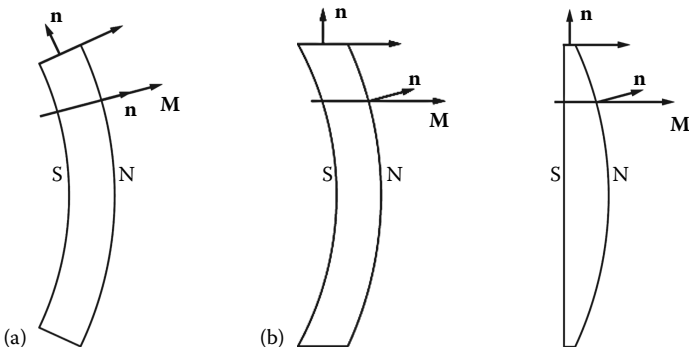


FIGURE 1.14 Magnetization of magnets. (a) Radial magnetization and (b) parallel magnetization

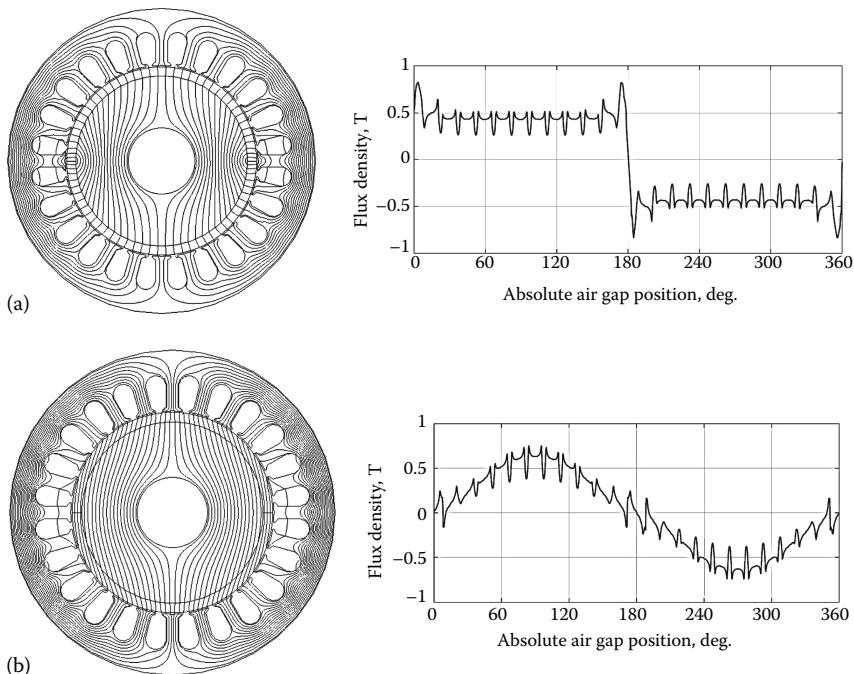


FIGURE 1.15 Flux and flux density versus rotor position for radially and parallel magnetized magnet machines. (a) Radially magnetized magnet machine. (b) Parallel magnetized magnet machine.

with 24 slots and 2 poles. The radially magnetized magnets produce a rectangular flux density distribution in the air gap whereas the parallel magnetized magnets produce a sinusoidal air gap flux density distribution. The reasons for the different flux density distributions can be explained from the following. The magnet flux leaves

the PM and enters the stator in normal direction to their surfaces. The flux density vector in the radially magnetized magnets is normal along the radial direction itself, resulting in the maximum flux flowing in the radial direction also. Therefore, the air gap flux and its density are maximum and remain uniformly constant across the magnet. In the case of the parallel magnetized magnets, the normal component of the flux density vector that enters the stator can be seen to be proportional to sine of the angle between the x -axis and the magnetization vector M at that point in the magnet with the result that the flux density distribution is sinusoidal in the air gap. There is also a tangential component of the flux density in the case of the parallel magnetized magnets embedded machine while it is zero in the radially magnetized magnet machine.

1.3.2 HALBACH ARRAY

There is also the case where the magnets need not be magnetized in radial or parallel directions but can be in any direction. Such magnetization is exploited in an arrangement due to Halbach. Radial or parallel magnetization requires a back iron for better utilization of the magnets and these are the cases that have been illustrated so far. They are also the most prevalent in practice since they are much easier to realize. Before the Halbach arrangement is considered, the radial magnet arrangement is considered again here for a plain magnet arrangement (or an array) in air and its flux paths shown in Figure 1.16. Note that the magnets are of alternate polarity. To maximize magnet utilization, iron is required on both the top and the bottom of the magnet arrangement. In a machine, one side of the magnet array faces the stator through the air gap and the other side sits on the rotor lamination, and both the stator and rotor have steel laminations.

The Halbach arrangement [60–69] (sometimes known as Halbach array) shown in Figure 1.17 is a combination of two magnet arrays: one radial magnet array and one azimuthal magnet array. The combination is made in such a way that the succeeding magnets in the combined or Halbach array have either a clockwise or counterclockwise magnetization. Its flux distribution can be arrived at by summing the

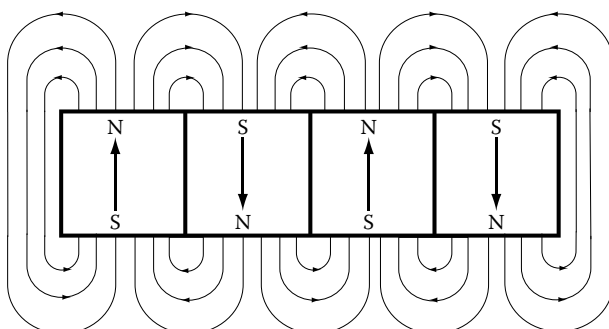


FIGURE 1.16 Radial magnet array in air.

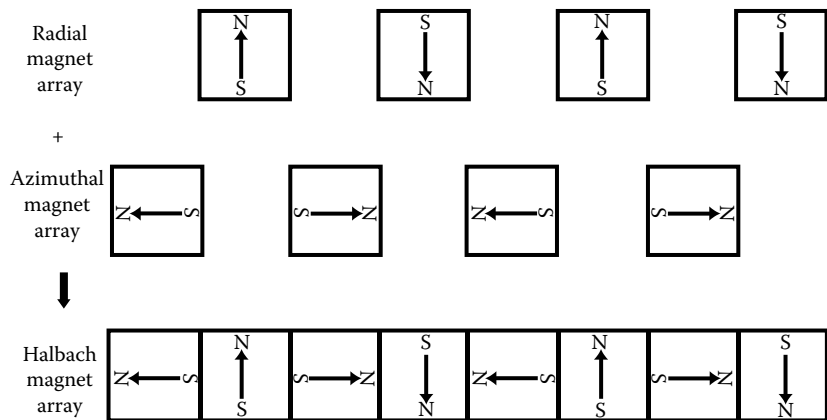


FIGURE 1.17 Halbach magnet array.

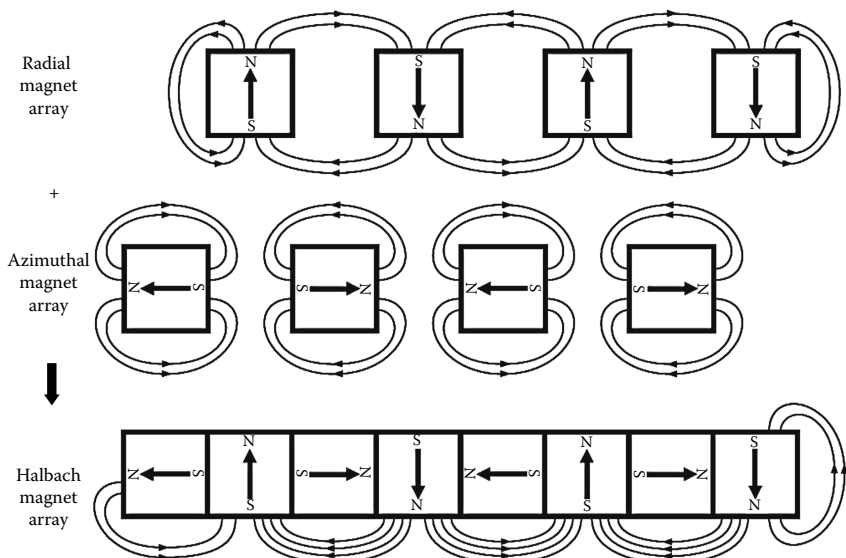


FIGURE 1.18 Flux distribution of Halbach array.

flux distributions of the radial and azimuthal magnet arrays, shown in Figure 1.18. A finite element flux plot of Halbach array with seven magnet segments is shown in Figure 1.19 illustrating that the simplified conceptual flux plots fairly correspond to reality. There are some flux lines seen on the top of the magnet array but they are very small compared to the number of flux lines at the bottom of the magnet array

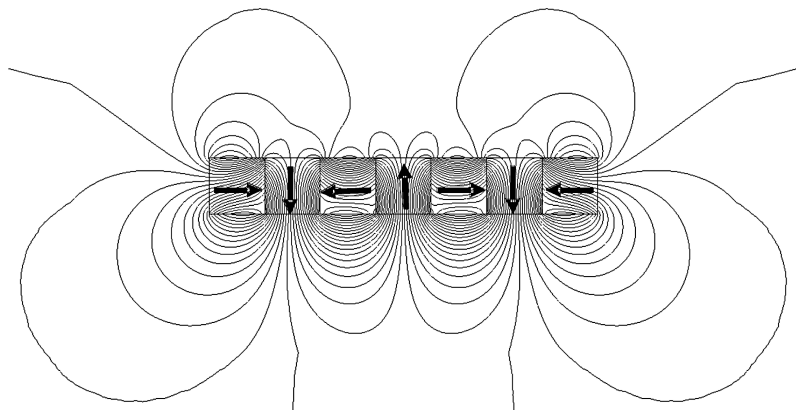


FIGURE 1.19 Flux plot from finite element analysis for Halbach array with seven magnet segments.

and hence they could be considered to be negligible on top and almost all being at the bottom of the array. From the flux distribution of this array, the following observations are made:

1. There is almost no flux at the top of the magnets, implying that back iron is not required for this ideal Halbach array.
2. The flux is much more focused than that of the radial magnet array and could be focused in any direction depending on the magnetization of the magnets and the number of magnet segments that make a pole.
3. The flux is downward (interior) or upward (exterior) depending on the orientation of the Halbach magnet segments. Clockwise orientation of north and south poles of the magnets gives upward (outward) flux distribution for conventional machines with stators and outer rotors. Similarly, anticlockwise rotation of magnet polarities gives inward flux distribution and this is preferred for machines with outer rotors and inner stators (known as inside-out machines in industrial circles).

Halbach array corresponding to case (3) are shown in the [Figures 1.20](#) and [1.21](#). Here it is shown with air surrounding the magnet array rotors to get a glimpse of the flux distribution. There are hardly any flux lines outside and inside of the magnet arrays and all the flux is concentrated in the inside (Figure 1.21) and outside (Figure 1.20) of the rotors, respectively. A small amount of leakage flux is evident in the simulations and it is usually negligible compared to the total flux on the significant or active side of the array. The same rotors with Halbach magnet arrays with inside and outside stators in synchronous machines are shown in [Figures 1.22](#) and [1.23](#) along with their air gap flux density distribution as a function of rotor position. From the figures, it becomes obvious that the leakage flux remain

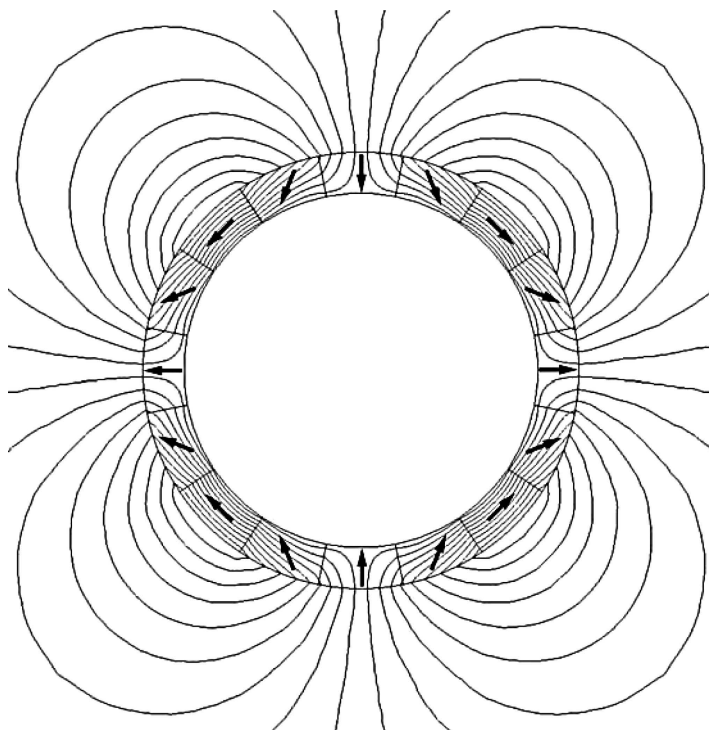


FIGURE 1.20 For outward flux distribution with Halbach array.

at low level on the inactive side of the Halbach array rotor and almost all the flux is concentrated on the side facing the stator. The leakage flux even though small is not particularly desirable in the case of the outer rotor machine and measures to curb them have to be resorted to in such cases. The flux density distribution is almost sinusoidal for the rotor, with four magnet segments per pole. The machine with inner rotor has lower flux density ripples compared to the machine with the outer rotor and this is being caused by the stator slots and saturation particularly at the edges of the teeth.

Halbach magnet arrays are realized in two ways:

1. Use of discrete magnet segments or blocks of magnetic material that are uniformly magnetized in a desired axis or direction to approximate an ideal Halbach array
2. Use of Halbach ring magnets using sintered or bonded forms by orienting anisotropic NdFeB powder during injection molding process and impulse magnetizing them with the required Halbach (sine) field distribution

The air gap flux density distribution of the inner Halbach rotor magnet arrangement is computed for varying magnet thicknesses and shown in [Figure 1.24](#). The

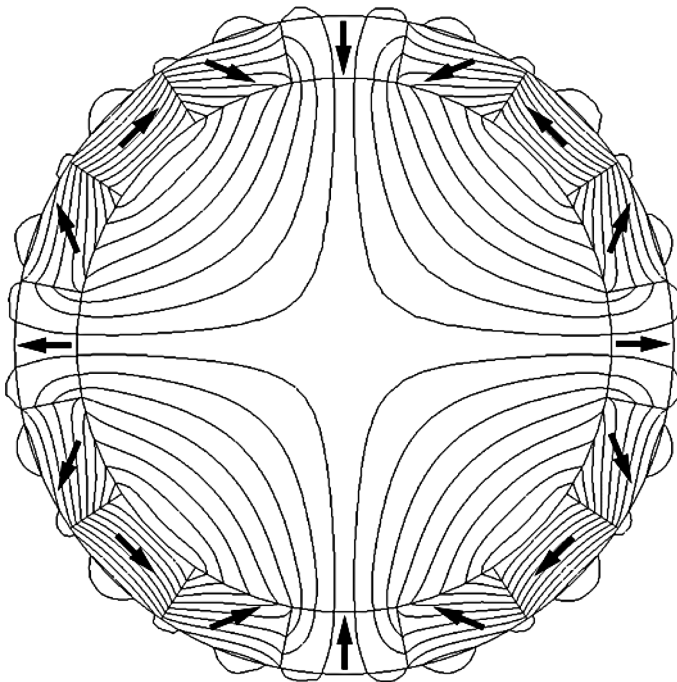


FIGURE 1.21 For inward flux distribution with Halbach array.

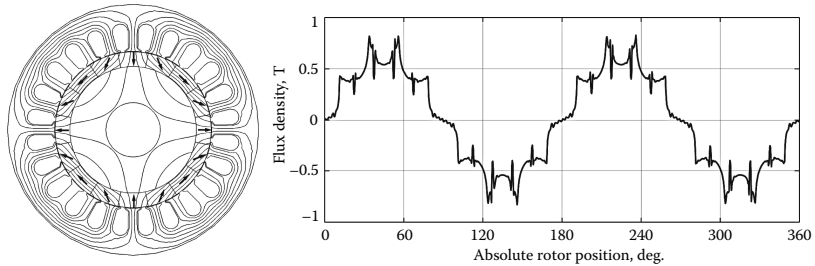


FIGURE 1.22 Inside Halbach magnet array rotor in the machine and air gap flux density distribution.

flux density distribution is almost sinusoidal when the ripples, due to the slot opening of the stator laminations, are ignored. With higher number of magnet segments per pole, the flux density distribution is expected to be much more sinusoidal. The features of the Halbach array can be summarized as follows:

1. Focusing of flux is at the heart of the Halbach array
2. Pure sinusoidal distribution for ideal Halbach array (but not possible to realize in practice)
3. Higher magnetic potential of the fundamental (1.414 times the conventional arrangement's) in a linear motor is theoretically proven

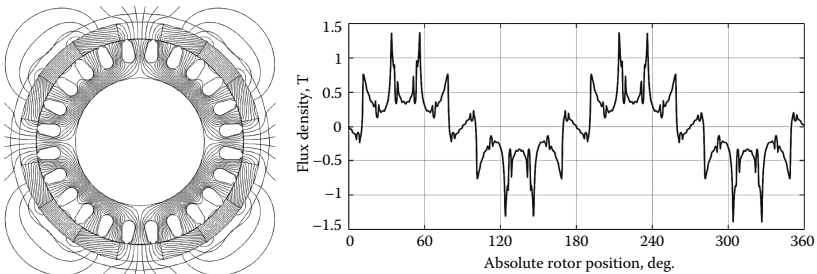


FIGURE 1.23 Inside Halbach magnet array rotor in the machine and air gap flux density distribution.

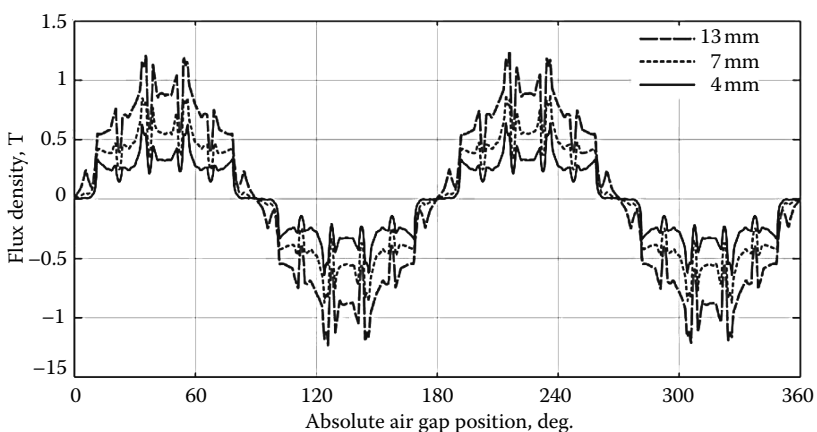


FIGURE 1.24 Air gap flux density versus rotor position for increasing magnet thickness.

4. This does not translate into 41.4% more flux in practice due to nonidealities in cylindrical environment and rotor construction; system studies for rotating PMSMs prove the previous point.
5. Further positives: No back iron is required (as flux hardly exists on one side); hence, Halbach array can be bonded directly to nonferrous substrates such as aluminum or other materials with good structural properties.
6. Since sinusoidal field distribution exists, there is no torque ripple.
7. Skewing of the stator or rotor magnets are avoided, which is a major saving in manufacturing operations.
8. Halbach array leads to high-performance positioning applications because of near zero cogging torque as it is found that cogging torque is reduced in Halbach magnet array machines to almost 20% of that of conventional magnet machines.
9. In spite of some of its unique advantages, this magnet array is yet to be exploited in commercial applications due to its complex construction and magnetization of PMs.

1.4 PM AC MACHINES

The availability of modern PM with considerable energy density led to the development of dc machines with PM field excitation in 1950s. Introduction of PMs to replace the electromagnetic poles with windings requiring an electric energy supply source resulted in compact dc machines. Likewise in synchronous machines, the conventional electromagnetic field poles in the rotor are replaced by the PM poles and by doing so the slip rings and brush assembly are dispensed with. With the advent of switching power transistor and silicon-controlled rectifier devices in the later part of 1950s, the replacement of the mechanical commutator with an electronic commutator in the form of an inverter was achieved. These two developments contributed to the development of PMSMs and brushless dc machines. The armature of the dc machine need not be on the rotor if the mechanical commutator is replaced by its electronic version. Therefore, the armature of the machine can be on the stator enabling better cooling and allowing higher voltages to be achieved as significant clearance space is available for insulation in the stator. The excitation field that used to be on the stator is transferred to the rotor with the PM poles. These machines are nothing but “an inside out dc machine” with the field and armature interchanged from the stator to rotor and rotor to stator, respectively.

1.4.1 MACHINE CONFIGURATIONS

The PMSM can be broadly classified on the basis of the direction of field flux as follows:

1. *Radial field*: The flux direction is along the radius of the machine [15–35].
2. *Axial field*: The flux direction is parallel to the rotor shaft.

The radial field PM machines are common whereas the axial field machines are coming into prominence in a small number of applications due to their higher power density and acceleration capacity than its counterpart. Note that these are very desirable features in high-performance applications. A comparison of the radial and axial PM machines for some power ranges widely encountered in practice is made and given at the end of this chapter.

The magnets can be placed in many ways on the rotor. The radial field versions [6] are shown in [Figure 1.25](#). The high power density synchronous machines have surface PMs with radial orientation whereas the interior magnet version is intended for high-speed applications. Regardless of the manner of mounting the PMs on the rotor, the basic principle of operation of the machine is same. An important consequence of the method of mounting the rotor magnets is the difference between direct and quadrature axes inductance values. It is explained as follows. The rotor magnetic axis is called direct axis and the principal path of the flux is through the magnets. Consider the permeability of high flux density PMs is almost that of the air. This results in the magnet thickness becoming an extension of air gap by that amount. The stator inductance when the direct axis or magnets are aligned with the stator winding is known as direct axis inductance. By rotating the magnets from the

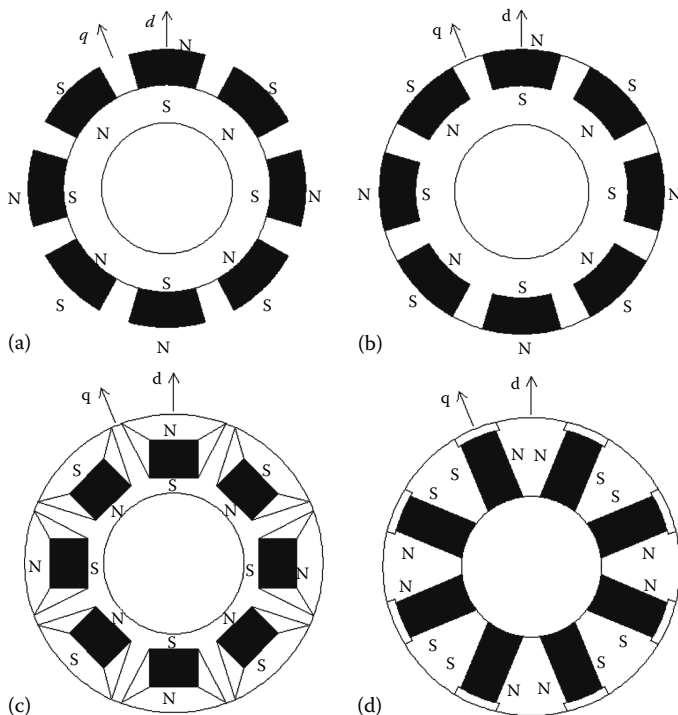


FIGURE 1.25 (a) Surface PM (SPM) synchronous machine. (b) Surface inset PM (SIPM) synchronous machine. (c) Interior PM (IPM) synchronous machine. (d) Interior PM synchronous machine with circumferential orientation. (From Krishnan, R., *Electric Motor Drives*, Figure 9.5, Prentice Hall, Upper Saddle River, NJ, 2001. With permission.)

aligned position by 90° , the stator flux sees the interpolar area of the rotor containing only the iron path and the inductance measured in this position is referred to as quadrature axis inductance. Inductance is derived from device dimensions, air gap length and number of turns as

$$L = \frac{\lambda}{I} = \frac{T_{\text{ph}}\phi}{I} = \frac{T_{\text{ph}}F}{I\Re} = \frac{T_{\text{ph}}T_{\text{ph}}I}{I\Re} = \frac{T_{\text{ph}}^2}{\Re} \quad (1.42)$$

where

T_{ph} is the number of turns

ϕ is the flux

F is the mmf

I is the current in the coil

\Re is the reluctance given by

$$\Re = \frac{\ell}{\mu_0 \mu_r A} \quad (1.43)$$

where

ℓ is the length of the flux line

A is the area of cross-section

μ_r is the relative permeability of the steel laminations

Considering only the air gap and magnet reluctance dominant (as the relative permeability of air is one and that of the high-grade PM is approximately one) and ignoring the reluctance of the iron (as its relative permeability is very high, say, in thousands, thus reducing the reluctance to negligible value compared to that of the air gap), the ratio of the direct axis and quadrature axis reluctances is derived as

$$\frac{\mathfrak{R}_d}{\mathfrak{R}_q} = \frac{\ell_g + \ell_m}{\ell_g} \quad (1.44)$$

where

ℓ_g is the air gap length

ℓ_m is the thickness of the magnet

\mathfrak{R}_d is the reluctance of the direct axis flux path

\mathfrak{R}_q is the reluctance of the quadrature axis path of the flux

From the above relationship, it is inferred that with the magnet thickness usually greater than that of the air gap length by many times, the direct axis reluctance is much higher than the quadrature axis reluctance. Or in other words, it may be stated that the effective air gap of the direct axis is multiple times that of the effective air gap of the quadrature axis. The consequence of such an unequal reluctance is reflected in the unequal inductances in the axes. As inductance is inversely proportional to the reluctance and applying it to Equation 1.44 the relationship between quadrature and direct axis inductances is obtained as

$$L_q > L_d \quad (1.45)$$

where

L_d is the inductance along magnet axis (i.e., direct axis) usually termed as direct axis inductance

L_q is the inductance along an axis in electrical quadrature (or perpendicular) to the magnet axis and termed as quadrature axis inductance

The quadrature axis inductance is always greater than that of the direct axis inductance in PMSMs. This is quite contrary to the wound rotor salient pole synchronous machine. It is because that in the wound rotor salient pole synchronous machine, the direct axis has the excitation or field coil and it is usually embedded in the rotor slots with a uniform air gap along the direct axis with salient poles having a small air gap whereas along the quadrature axis the air gap is much larger compared to the direct axis. The particular constructional difference with more air gap length in quadrature axis much larger than that of the direct axis makes the quadrature inductance much smaller than that of

the direct axis inductance in the wound rotor salient pole synchronous machine. Such inequality in inductances has a direct consequence on the operation of the machine in that in addition to synchronous torque another component torque known as reluctance torque is generated in the machine. More on this will be treated in later chapters.

1.4.2 PM ROTOR TYPES

Different ways of arranging magnets on the rotor have created many types of PMSMs and brushless dc machines. Some popular and research-type arrangements and their impact on the air gap flux density, winding inductances, and their influence on reluctance torque, which is capable of enhancing the magnet generated or synchronous torque are described in this section.

The control and operation of PM synchronous [36–41] and brushless [42–56] motor drives are considered in later chapters.

1.4.2.1 Surface-Mounted PMSM

Figure 1.25a shows the magnets mounted on the surface of the outer periphery of rotor laminations. This arrangement provides the highest air gap flux density as it directly faces the air gap without the interruption of any other medium such as part of rotor laminations. Drawbacks of such an arrangement are lower structural integrity and mechanical robustness as they are not snugly fitted into the rotor laminations to their entire thickness. PMs, in practice, are buried into the rotor laminations that provide some mechanical strength and by using Kavilor tape, the magnets are bound to the rotor, thus reinforcing the mechanical strength of the rotor and magnet combination. Machines with this arrangement of magnets are known as surface mount PMSMs. They are not preferred for high-speed applications, generally greater than 3000 rpm but machines with very small rotor diameter can be found to have speeds in the range of 50,000 rpm also. The reluctance variation between the direct and quadrature axes is fairly small in this machine as seen from its construction. Accordingly, there is very little (less than 10%) variation between the quadrature and direct axes inductances in this machine. This particular fact has consequence on the control, operation, and characteristics of the surface mount PMSM drives. The details are deferred to later sections.

1.4.2.2 Surface-Inset PMSM

Figure 1.25b shows the magnets placed in the grooves of the outer periphery of the rotor laminations, providing a uniform cylindrical surface of the rotor. In addition, this arrangement is much more mechanically robust compared to surface mount machines as the magnets do not protrude out of the rotor laminations as in the case of the synchronous permanent magnet (SPM) and therefore they are fully and mechanically embedded in the rotor giving it mechanical strength from flying out. Bracing magnets on to the rotor with tapes in the case of SPM with lateral air gaps between magnets does not give the greatest mechanical strength. Whereas in the surface inset PMSM, it is mostly unwarranted and even if it is used, it can be bound uniformly as the rotor lamination and magnet surfaces make a uniform surface unlike that of the SPM. The ratio between the quadrature and direct axes inductances can be as high as 2–2.5 in this machine. The machine with this rotor configuration is known as inset PMSM.

1.4.2.3 Interior PMSM

Figure 1.25c and d shows the placement of magnets in the middle of the rotor laminations in radial and circumferential orientations, respectively. Such a machine construction is generally referred to as interior PMSM. The interior PM rotor construction is mechanically robust and therefore suited for high-speed applications. The manufacturing of this arrangement is more complex than the surface mount or inset magnet rotors. Note that the ratio between the quadrature and direct axes inductances can be higher than that of the inset magnet rotor and generally is in the range of 3 even though there have been claims of much higher ratio for various other interior type PM rotor configurations. The interior PM rotor shown in Figure 1.25c has steel removed to create large air gaps between the magnets in the rotor. They are intended to discourage the flow of flux between adjacent PMs within the upper rotor surface. Without these air barriers known as flux barriers, the flux will flow from one magnet to the adjacent one within the rotor and thereby bypass the stator structure. It will result in reduced mutual flux linkages, and, therefore, the flux barriers are essential to this arrangement of PMs. The barriers also reduce the weight of the rotor itself thus giving the lowest rotor inertia. Consequently, it facilitates higher acceleration rates usually required in servo drives. Surprisingly, in spite of this advantage, these machines are seldom used in those applications today.

The circumferential inset PM rotor shown in Figure 1.25d seems to require a large volume of the PMs and, therefore, as such this configuration is not suitable for high energy density PMs since they are expensive. Accordingly, this configuration can only be confined to low energy density and low-cost magnets such as ferrites. Uniquely this configuration bestows a rotor arrangement that can yield a higher air gap flux density than that of the magnets themselves. It is achieved by the fact that the area of cross-section of the magnets is much larger than the rotor surface area that conducts the flux from a magnet to the stator. Because of its higher air gap flux density compared to, say, the surface mount ferrite PMSMs, this configuration is very desirable from the point of view of higher efficiency and smaller stator excitation for the same power output. But higher air gap flux density is achieved at the expense of higher rotor volume compared to that of the rotor with high energy density PMs has to be noted.

The inset magnet construction has the advantages of high mechanical robustness and a high ratio between the quadrature and direct axis inductances, respectively. Many more arrangements of the magnets on the rotor are possible and they are very rarely used in general industrial practice and hence they are not considered any further in the book.

The flux plot and flux density versus rotor position of a surface PM with radial orientation [6] are shown in the Figures 1.26 and 1.27, respectively. The dips in the flux density at various points occur because of the slot opening of the stator lamination where the reluctance is much higher and hence the flux and its density are lower.

An interior PMSM with its flux plot is shown in Figure 1.28. The flux barriers that are at the corners of the magnet increase the reluctance and hence does not encourage the flow of flux lines. Without these flux barriers, there will be significant leakage of flux between the magnets. These leakage flux lines will outskirt the stator electromagnetic circuit and therefore such leakage flux does not contribute to any torque production and hence is a waste.

One of the important points to observe in the surface and interior PM machines is that the flux in the rotor back iron does not change. The stator is cylindrical except

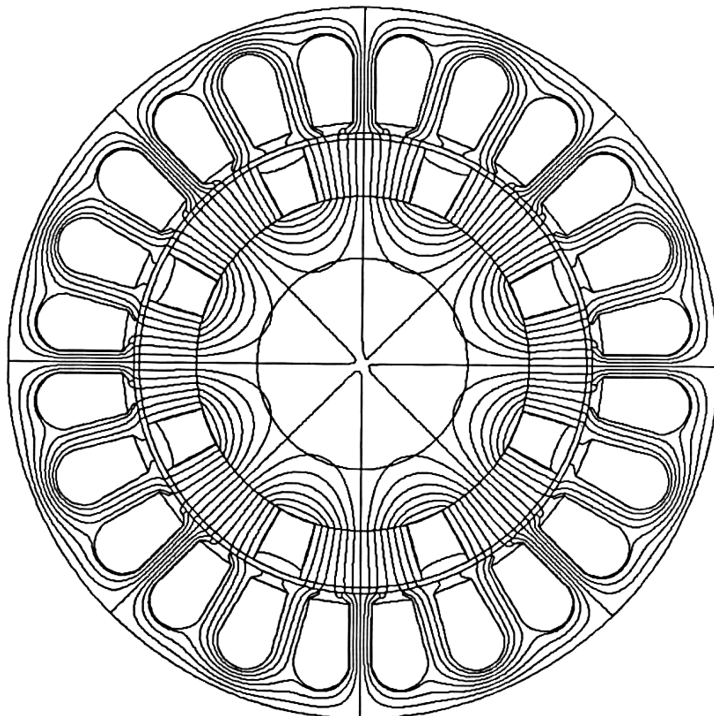


FIGURE 1.26 Flux distribution in the machine at no load. (From Krishnan, R., *Electric Motor Drives*, Figure 9.6, Prentice Hall, Upper Saddle River, NJ, 2001. With permission.)

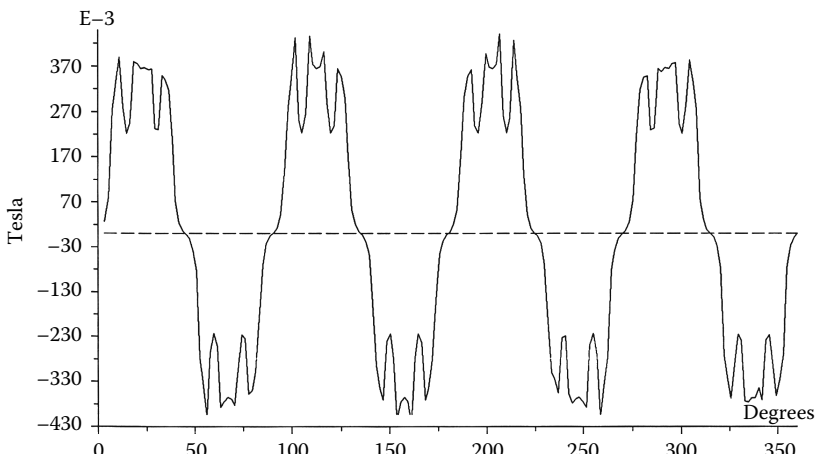


FIGURE 1.27 Radial air gap flux density profile in the machine at no load. (From Krishnan, R., *Electric Motor Drives*, Figure 9.7, Prentice Hall, Upper Saddle River, NJ, 2001. With permission.)

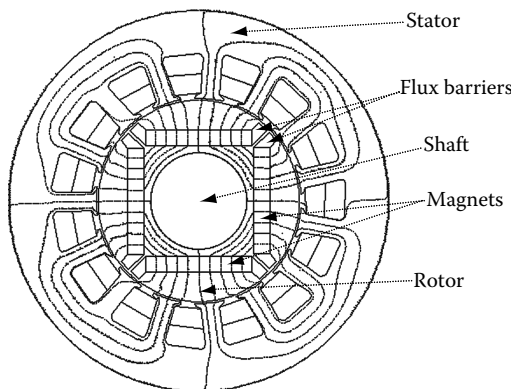


FIGURE 1.28 Flux plot of an interior PMSM.

for the stator slot openings. If the slot openings are ignored from an electromagnetic point of view, then the rate of change of flux density in the rotor back iron is zero and hence the eddy current and hysteresis losses are zero. The real situation is that there will be variations in the flux from the magnet as it encounters the stator slots and teeth with the resulting reluctance variation. It will change the flux and its density to an extent in the back iron of the rotor also resulting in some core losses but for all practical purposes, they are ignored in initial designs. Consideration of such losses is beyond the scope of this book. But the stator experiences flux density variations in various parts of its body and therefore generates core losses. Stator core losses constitute the bulk of the core losses and hence more on this will be treated in the section on core loss computation. It is relevant to remind again that in PM rotors with Halbach array, there is hardly any flux in the rotor back iron and hence the iron losses in it can be avoided. It is also practical to reduce the back iron thickness as it has to carry very little flux and thereby reduce the rotor weight, resulting in significant increase in power density and lower inertia for the machine. But this comes at the cost of fairly complex manufacturing of the rotor compared to conventional surface mount PM rotor.

1.4.2.4 Line-Start PMSM

Some PM synchronous motors are designed for constant speed applications to improve efficiency and power factor in comparison to induction and wound rotor synchronous motors. Such motors have a squirrel cage winding to provide the torque from standstill to near synchronous speed. The same cage windings also serve to damp rotor oscillations. Once the motor pulls into synchronism, the cage windings do not contribute to electrical torque as there are no induced voltages and hence no currents flow in them at zero slip.

Variable speed PM synchronous motor drives have no need for the damper windings to offset hunting and oscillation. The damping is provided by properly controlling the input currents from the inverter. This results in a compact and smaller rotor than that of the machine with damper windings. The way damping is produced in the PM synchronous motor with and without damper windings deserves a comment. The

machine with the damper windings operates to suppress the oscillations with no external feedback. The feedback comes internally through the induced emf due to the slip speed in the cage windings. Whereas in the inverter-controlled PM drives, the control has to be initiated by an external signal or feedback variable to counter the oscillation. Hence its dependence on an external feedback loop compromises reliability. Wherever reliable operation regardless of the accuracy in torque or position control is a major concern or requirement, the synchronous motor with damper windings may prove to be an intelligent choice. For example, if the load can tolerate a constant speed, then during moments of inverter failure, it is possible to bypass the inverter and connect the PMSM with damper windings to the fixed frequency utility supply. Then the machine will start as an induction motor and then pull into synchronism running at synchronous speed. Note that then the speed of the machine is determined by the stator frequency (utility frequency in this case) and will operate at a fixed speed only. This is desirable in some applications than a complete shutdown of the motor in case of inverter failure. A case in point is critical pumping applications such as in nuclear power plants or in ships. Such line start PMSMs [71–73] with cage windings have been advocated for fan and pump applications in the 1980s to improve the operational efficiency of the system with a single speed. The efficiency improvement due to the synchronous operation as compared to the induction motor operation with slip losses justified an investment in the PM rotor construction but it was felt that many low-cost applications could not justify the capital investment in the inverter. Such research and development petered out due to the lower energy cost in United States throughout the last two decades of the twentieth century.

1.4.3 HYBRID MACHINES

Homopolar machines are a class of machines having windings for ac and dc excitations on the stator itself. The rotor consists of laminations only with salient poles and has no windings or PMs. They are used for generator applications and are obtained from synchronous homopolar machines that are a subset of general class of homopolar machines. The reason to bring this introduction to homopolar machines is to show an opportunity that exists for the use of PMs in doubly salient stator and rotor machine structures. Having the field (dc excited) through a set of stator windings that are concentric wound, the rotor is freed of the burden of this winding in the rotor and a set of slip rings to inject the excitation current. A class of PMSMs has been patterned after this concept. Having the windings and PMs on the stator itself has the advantages of simpler construction and capability for very higher speed operation without any need for sleeves for holding the PMs on the rotor. Absence of sleeve lowers eddy current losses while preserving the advantages of conventional PMSMs. Three types of such machines have come into research in the last decade. The manner in which the PMs are placed makes the hybrid PM machines's features different from each other. But these machines are basically PMSMs [73–81] and their principle of control is the same. The stator and rotor have salient poles with at least a difference of two poles between them. The stator coils are concentrically wound and rotor have no windings or PMs on them. Those who are familiar with this type of machine construction know that they are referred to as variable reluctance machines or switched

reluctance machines (SRM) in literature. These machines produce torque based on their reluctance variation, i.e., varying inductances in their phases. Interested readers may consult Ref. [7] on this subject. The types of hybrid machines are created by superimposing PMs in the stator of SRMs and are based on the manner of placement of PMs:

- (i) PMs in the back iron: This machine is referred to as doubly salient permanent magnet (DSPM) machine [76].
- (ii) PMs in the stator pole faces or shoes: Such a machine is referred to as flux reversal machine (FRM) [75]. The PMs are placed with radial orientation.
- (iii) PMs within the stator poles: The permanent magnets are sandwiched in each stator pole with a circumferential orientation. These machines are referred to as flux switching machines (FSM) [78].

These machines are described in the next section. Only their principle of operation, merits, and demerits are given. Their detailed analysis and design are not considered here and interested readers are referred to respective references available at the end of this chapter. It is relevant to realize that these machines are in the early stages of development with no product lines in sight for them at this time. Because of their unique construction with the PMs situated on the stator and still endowing a brushless feature, this kind of machine holds promise particularly in very high-speed generator applications.

1.4.3.1 Flux Reversal PMSM

Principle of operation: Consider an SRM with two stator poles spaced at 180° degrees interval from each other and three rotor poles spaced at 120° interval from each other, with each stator pole having two magnets, and the magnets are attached to the stator poles with the polarities of the PM as shown in Figure 1.29. The PMs in a stator pole have opposite polarities. The diametrically opposite PMs have the same polarity in the diametrically opposite stator poles. The coils on the stator poles are concentrically wound and they are connected in series to form a single-phase winding and in the present illustration thus constituting a single-phase machine. It is to be stated here that the principle of operation of the FRM under illustration is not limited to single-phase machines and is equally applicable to multiphase machines.

Consider the machine windings are not excited and the rotor is driven in the counterclockwise direction. For the rotor position shown in Figure 1.29a, one rotor pole is in the middle of the two PMs in the top stator pole and the PMs in the bottom stator pole each straddle a rotor pole. There are two flux paths, one comprising of the top pole magnets and the top rotor pole with the flux path closing in the back of the stator pole, PMs, air gaps, and rotor pole and the second flux path comprising of the bottom pole magnets and the two remaining rotor poles with the flux path closing with the PMs, back of the stator pole, air gaps, rotor poles, and back iron of the rotor poles. In this position, the fluxes are confined to the stator and rotor poles with no linking of the stator coils, resulting in zero stator flux linkages.

Let the rotor be moved so that the top rotor pole is aligned with the left side PM by moving it from the midpoint of the two PMs. The majority of the flux from the top PM

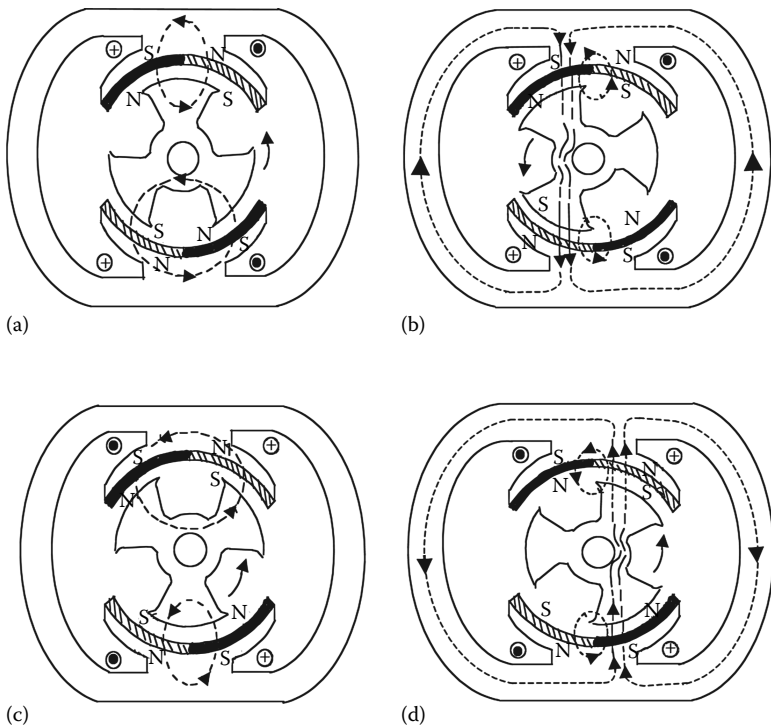


FIGURE 1.29 Illustration of FRM and its principle of operation. (a) Zero flux linkages position, (b) maximum positive flux linkages position, (c) zero flux linkages position, and (d) maximum negative flux linkages position.

goes through the top air gap, top rotor pole, bottom rotor pole, bottom air gap, bottom stator pole, stator yoke, and back to the top stator pole. This flux divides itself into two paths on either side of the stator yoke as shown in Figure 1.29b. There is also a small leakage flux as shown in the top and the bottom. It may be seen that only one PM in each pole is helpful in producing this change of flux linkage from the previous position to this new position. In between these two positions, it may be assumed that the flux and stator flux linkages are linearly rising. As the center of the rotor pole moves away from the PM, the flux and the stator flux linkages decrease also linearly as per the assumption. From the first position of no flux linkages corresponding to Figure 1.29a and the peak flux linkages corresponding to Figure 1.29b where the center of the PM and the center of the rotor pole in the top aligns, a positive change of flux linkages from zero to maximum is seen. The flux linkages are considered positive by convention as the flux goes from top to down. As the rotor moves away from the top left PM, the flux linkages decrease likewise until they become zero when two rotor poles come under the top pole and they are positioned with each facing a PM of the top stator pole as shown in Figure 1.29c. At this point, the flux is only linking the stator and rotor poles with no flux linking the stator coils.

When two rotor poles come to the top, the bottom pole is centered between the two PMs of the bottom stator pole as shown in Figure 1.29c. As the rotor moves, the bottom

rotor pole comes more under the right bottom PM, resulting in the flux flow from the bottom magnet in the bottom to top direction through the bottom rotor pole, back rotor iron, the right top rotor pole, air gap, top right PM, and to one of the stator yoke part and back to the bottom stator pole, as shown in Figure 1.29d. This produces the stator flux linkages (negative in direction), which vary with the rotor position with the maximum when the bottom rotor pole aligns with the right PM of the bottom stator pole. When the rotor pole leaves the bottom right PM, the flux linkages are reduced and become zero when the bottom stator pole faces two rotor poles as shown in Figure 1.29a. Therefore, in one rotor revolution, the stator coils experience three cycles of flux linkages variation with each cycle consisting of a variation from zero to positive maximum, from positive maximum to zero, from zero to negative maximum, and from negative maximum to zero. Bipolar flux with PMs only on the stator poles is uniquely achieved with this machine. Such a stator flux reversal appearing with magnets on the rotor in conventional PMSMs is to be kept in mind. As the flux reverses in the stator back iron and stator poles with respect to rotor position, these machines may be named as FRMs with stator permanent magnets and for brevity they are referred to as FRM.

Control: With stator flux linkages variation that is alternating, the induced emf in the stator winding is also alternating and it may be considered to be a rectangular ac voltage assuming ideal linear variation of flux linkages. When the stator winding is excited with the same polarity of the current as that of the induced emf, then the air gap power produced in the machine is positive, resulting in motoring torque in either directions of rotation. When the stator winding is excited with current that is of opposite polarity to the induced emf, then the machine is in regeneration with the machine supplying electrical power while taking the mechanical input power. Therefore, this machine with the appropriate power converter and control can operate in all the four quadrants of the torque versus speed regions of the machine.

For the sake of completeness, a three-phase FRM with six stator poles and eight rotor poles is shown in Figure 1.30. A1 and A2 constitute phase a and likewise the other coils for two of the rest of the phases. Its operational principle is similar to the single-phase FRM described earlier.

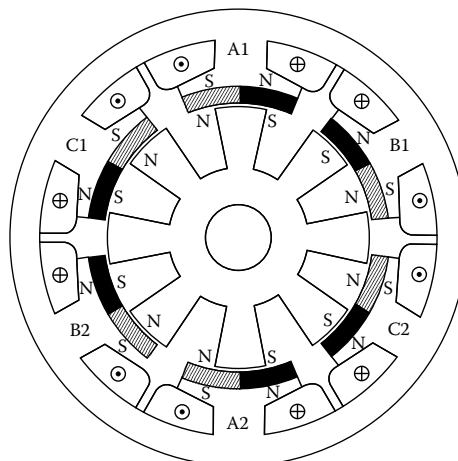


FIGURE 1.30 Three-phase FRM.

The features of the FRMs are summarized in the following:

1. They have bidirectional flux with the outcome of ac machine characteristics. The flux linkages versus current has a four-quadrant characteristic as against one quadrant for the SRM.
2. PMs are on the stator and, therefore, these machines are easier to manufacture. Also the robustness of the rotor now makes it an ideal candidate for very high-speed operation unlike the machine with the PMs on the rotor.
3. The stator and rotor poles are salient and the punching of such laminations is simpler.
4. The coils are concentric, making them easier to manufacture and install in the machine.
5. The SRM superposed with PMs in its stator poles becomes a PM brushless dc machine in all its characteristics without the distributed windings, magnets on the rotor, and hence without much of a manufacturing cost.
6. Because of the PMs in the path of the flux, and as the relative permeability of the magnet is in the range of the air, the reluctance is very large, thus making the inductance of the winding very small, resulting in a small time constant of the winding. This leads to a fast torque response, a desirable feature in high-performance applications.
7. Core losses increase in this machine compared to the SRM due both to the sweeping PM flux in the rotor iron and the presence of bipolar flux in the machine laminations.
8. The PMs may experience the elevated temperature of the stator poles, which will reduce their residual flux density, thus reducing the output of the machine. Because of the PMs, the need for keeping the temperature rise to a certain safe value for the sake of PMs in the stator poles will reduce the overall power output of the machine.
9. The harmonic torques will be fairly high in these machines and because of this fact they may not be suitable for high-performance servo applications.

Some comments are in order as to the power density of the machine and its comparison to other machines. This machine will not have the same power density as that of the PM brushless dc machine with PMs on the rotor and as well as a conventional SRM. The reasons are that only half of the PMs are in effective use at any given time in comparison to the PM brushless dc machine. With regard to SRM, the converter requirement becomes bipolar and different configurations of SRM are capable of higher power density than these machines. This machine may have some applications in high-speed generators to endow high power density where no external excitation is required contrary to SRMs that require a controlled excitation, necessitating a converter for its operation. Possible applications for FRMs are in aerospace and in automobiles.

1.4.3.2 Flux Switching Machine

Consider the PMs being placed in the middle of stator poles of a SRM as shown in [Figure 1.31](#) and let the adjacent PMs have the opposite polarity. The orientation of

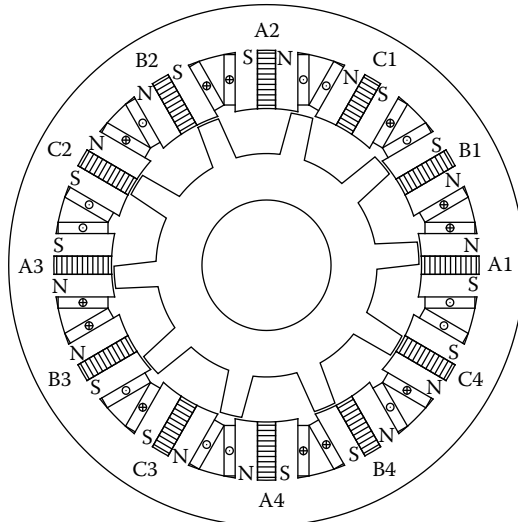


FIGURE 1.31 Three-phase flux switching PMSM.

the PMs is in the circumferential direction. Such a machine is known as FSM. This facilitates use of low energy density and low-cost magnets to provide the same power densities as that of conventional PMSMs with high energy density magnets. The effect of the PMs is to focus and enhance the flux in the machine as in other structures. The coils are concentrated with its attendant advantages of lower end turn build up, cost of manufacture, winding materials usage, and resistive losses compared to conventional PMSMs with distributed windings. The operation of the machine is no different from the FRM described earlier. The windings and magnets are magnetically in parallel with the result that the armature reaction due to armature currents has almost no effect on the operating point of the magnets. Whereas in conventional PMSMs, the opposite is true with the magnets and windings being magnetically in series. Such a distinct characteristic has enabled a high per unit inductance to be achieved in FSM compared to conventional magnet machines. This is a very highly desirable feature from the point of view of flux weakening operation as will be explained in Section 1.4.4. Further there is very little difference between the quadrature and direct axis inductances, making the reluctance torque negligible in FS machines. There are some subtle differences between the FSMs and doubly salient PM machines and they are discussed in Section 1.4.3.3. The FSMs have a four-quadrant flux versus current operation, has bipolar sinusoidal flux with the effect that the ripple torque is small or negligible when excited with a set of sinusoidal currents. Because it has a four-quadrant flux versus current operation, it is claimed to have a higher power density as compared to machines with lower number of flux versus current quadrant capability.

1.4.3.3 PM SRM or Doubly Salient PM Machine

There are many ways PMs can be placed on the SRM and one such arrangement resulted in FRM as seen in the section above. Another arrangement that only uses

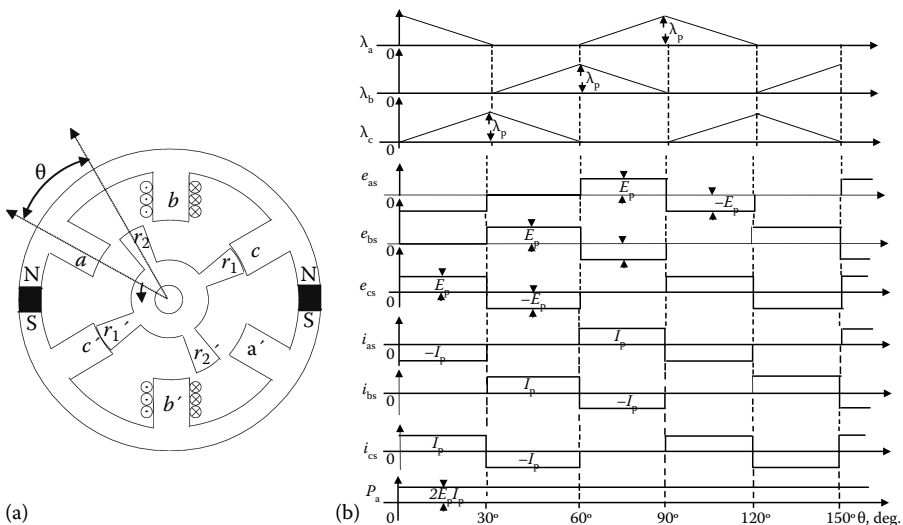


FIGURE 1.32 (a) Doubly salient permanent magnet SRM. (b) The flux linkages, induced emfs and currents air gap power of a six stator and four rotor poles PM SRM.

two quadrants of flux linkages versus current feature is shown in Figure 1.32a. In this arrangement, the PMs are placed in the stator back irons so that only a unipolar flux is possible in them. The principle of operation can be best realized first by looking at the flux linkage versus rotor position for the stator phase windings without energizing the stator windings. Then the only excitation comes from the PMs. The stator flux linkages are modulated by the rotor poles as a function of their rotor position to a larger measure and to a smaller extent as a function of the rotor and stator pole shapes. Consider the rotor poles that are 30° from stator poles of phase a, shown in Figure 1.32a. At this point, the flux in the phase a stator poles may be considered almost zero as all the magnet flux will be going through the other pair of rotor poles and phase c stator poles. Therefore, the phase a stator flux linkages is zero. As the rotor is driven away in the clockwise direction from this position of the rotor poles that is midway between the stator poles of phases a and b, the flux gradually increases in the stator poles of phase a and hence the increase in its flux linkages. Note that the flux finds its way from the c phase stator poles to the phase a stator poles. When a pair of rotor poles and phase a stator poles are aligned, the flux through the stator poles is maximum. Similarly as the rotor poles move away from the alignment of stator phase poles, the flux gradually decreases. For the sake of illustration, the increase and decrease of flux and flux linkages are assumed to be linear. When the rotor poles are away from the stator poles by 30° , note that the other pair of rotor poles is in full alignment with phase b stator poles. Therefore, all the magnet flux goes by phase b and none through phase a stator poles. From this description, it is seen that the stator flux linkages goes from zero to maximum in 30° and from maximum to zero in another 30° . For the next 30° , the stator phase a has zero flux linkages as the flux path is through phase b during this time and the rotor poles are far away from phase a poles compared to any other stator poles. Therefore, the flux linkage variation of

zero to maximum, maximum to zero, and constant at zero has a total dwell of 90° , the same as the rotor pole pitch. For every rotor rotation, each phase experiences four full cycles of such flux linkage variations in them. This is shown in [Figure 1.32b](#) assuming a constant speed of rotation of the rotor.

An emf is induced due to the varying flux linkages in each phase. Exciting the stator windings with currents of the same polarity of the induced emfs will give a PM brushless dc machine. The induced emf and current waveforms are shown in [Figure 1.32b](#). From the current and voltage waveforms, the air gap power is computed as the sum of their individual products and plotted. The air gap power under ideal conditions of these emfs and currents is a constant and so also the electromagnetic torque due to this calculation.

Even though the operation of this machine is very much like that of the PM brushless dc machine, there are significant differences and they are listed below:

1. Zero current intervals do not occur in between the positive and negative half cycles as in the case of the permanent magnet brushless dc (PMBDC) machines but a positive half cycle is followed by the negative half cycle without a period of zero interval. This has a tremendous implication in the operation and high power density aspect of this machine. The current reversal in the middle of the operation of the phase results in a loss of significant current seconds, i.e., the current integral over time or area of the current over time. The phase current of one polarity has to be brought to zero before current of another polarity in that phase can be built up and both of these operations are determined by the time constant of the phase winding. Time constant in this motor may be smaller compared to SRM, but it is not negligible and has a finite value. During the current transition, the power is almost half of what could be in normal full load current operation assuming that the current is ramping down or up linearly. Output power reduction invariably happens during this time.
2. The induced emf waveforms are not ideal and are more trapezoidal than rectangular, thereby resulting in somemore volt-second loss and hence power loss affecting detrimentally the power density of the machine.
3. The reluctance torque under ideal ac rectangular current is not used in the machine in general. It enhances the magnet synchronous torque for half the time and subtracts for the other half time in a half cycle. Even though the average of the reluctance torque is zero, it does provide a significant torque ripple, resulting in a low-performance motor drive.
4. The flux created by the stator current does not go through the magnets mainly because of their high reluctance but flows through the adjacent stator pole pair that is under excitation. Such a mode in the operation increases the flux density in the stator back iron and hence provision has to be made in the design to handle such enhanced flux densities by increasing the stator back iron thickness.

Because all of the above stated factors, the claim of power density in the tune of 1.414–2.828 times the power density of an equivalent SRM (or for that matter even

to an induction motor) may not be realistic. It is timely to present some differences between this machine and flux reversal/switching machines and they are as follows:

1. Flux versus current: Two quadrant operation for DSPMs and four quadrant for FSM/FRMs.
2. Induced emf: Trapezoidal for DSPMs and sinusoidal for FSM/FRMs.
3. Torque ripple: Commutation torque ripple can be significant in DSPMs similar to PM brushless dc machines and it is nonexistent in FSM/FRMs. Commutation torque ripple is analyzed in a later chapter.
4. Power density: DSPMs because of property 1 can have lower power density than that of the FSM/FRMs.

1.4.4 CONCENTRATED COIL-WOUND PMSMs

Around the time researchers started experimenting with PM machines having SRM stators such as doubly salient pole, flux reversal, and flux-switching machines, it became clearer that it is possible to utilize the same stators with a conventional surface-mounted PM rotor. This formidable combination of the stator to reduce the cost of winding and manufacturing complexity and the rotor to provide the high air gap flux density was waiting to be exploited. Many of the features of this machine are carried over from SRMs and they are given below:

1. Simpler construction.
2. No mutual inductance between phases endowing a higher fault tolerance in these machines, thereby removing one of the greatest disadvantages they faced in defense and critical applications.
3. Low cogging torque as it engenders high number of cogging cycles per mechanical revolution.
4. No large end connections because of concentrated coil winding, contributing to saving in copper and its losses.
5. High direct axis self-inductance that makes it possible to have lower currents to counter the magnet flux and because of that a wider flux weakening operation is obtained, a property that is very important in electric vehicle applications. An example given in Ref. [80] of a three machine with 12 stator teeth and 14 rotor poles with concentrated coil winding and a distributed coil-wound machine with 36 stator teeth and 14 rotor poles shows that the concentrated coil-wound machine has a direct axis inductance that is 6.56 times that of the distributed winding machine based on equivalent magnet flux linkage in both machines.

A 12-stator pole (teeth) with 10-magnet combination is considered for illustration of the winding connections in a three-phase PMSM, which is shown in [Figure 1.33](#). Alternately, windings may be placed on alternate stator teeth and its winding diagram is shown in [Figure 1.34](#). It appears as though that this machine may not be

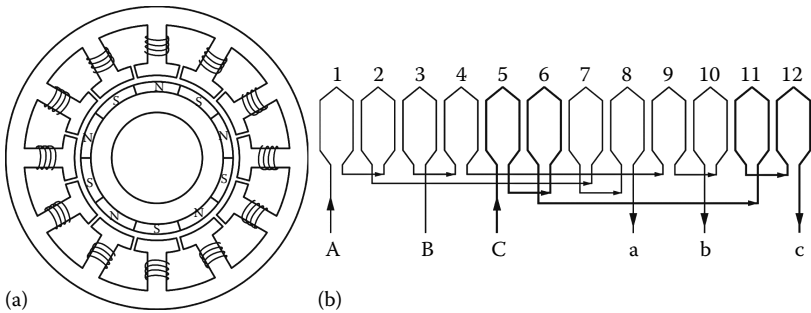


FIGURE 1.33 Concentrated coil-wound machine with 12 stator teeth and 10 rotor poles:
(a) machine schematic; (b) winding diagram.

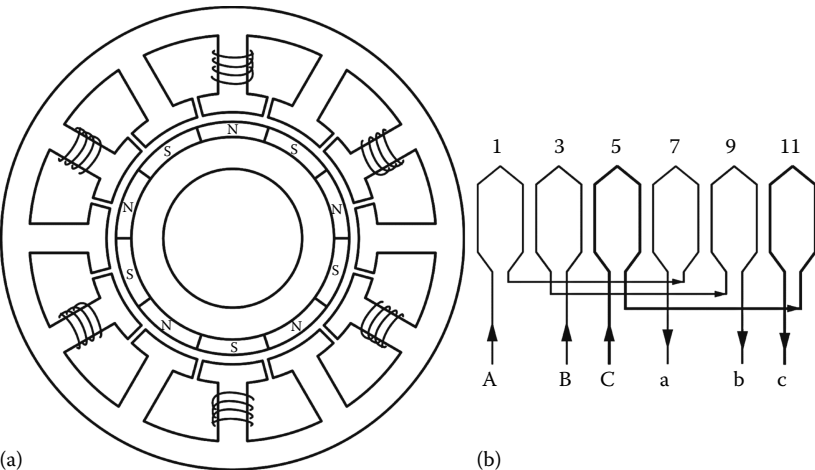


FIGURE 1.34 Previous example machine with alternate teeth wound: (a) machine schematic; (b) winding diagram.

attractive as compared to the machine with all teeth wound. But it has some advantages as illustrated with an example given in Ref. [81]:

1. Assuming equal tooth width, the winding factor is higher than that of the all teeth-wound machine. For example with 10 poles, 12-teeth machine with all teeth wound, the fundamental winding factor is 0.933 whereas for the alternate teeth-wound machine, the fundamental winding factor is 0.966.
2. For all teeth-wound machine, the phase-induced emf is more trapezoidal and has a cogging torque of less than 2%. Whereas for the alternate teeth-wound machine with equal tooth width the induced emf is a fine trapezoid with higher volt-second content than all teeth-wound machine. But its cogging torque is higher and around 5%.
3. In comparison to all teeth-wound machine, the alternate teeth-wound machine with unequal teeth width has a unity winding factor, larger constant voltage duration in its phase emf, and a higher cogging torque.

In general, it can be summarized that the modular machines have higher winding factor, more finer trapezoidal phase-induced emf, manufacturing advantage, high torque capability, and lower cogging torque because of higher cogging cycles per mechanical revolution.

The feasible pole and slot combinations for the class of concentrated coil-wound machines are as follows:

$$S = P \pm 1 \text{ for odd slots per phase}$$

$$S = P \pm 2 \text{ for even slots per phase}$$

where

S is the number of slots

P is the number of magnet poles

It is found in experimental machines that the cogging torque can be as little as 0.1% of full load torque and further it matches the torque of the distributed winding machines. It is quite likely that more of these concentrated coil-wound PMSMs with all teeth or alternate teeth wound will be available in the marketplace in time to come as they are already available in PM brushless dc machine versions.

1.4.5 TYPES OF PMSMs

The PMSMs are classified on the basis of the wave shape of their induced emf, i.e., sinusoidal and trapezoidal. The sinusoidal type is known as PMSM and the trapezoidal type are called PM dc brushless machine.

Even though the trapezoidal type of induced emfs have constant magnitude for electrical 120° both in the positive and negative half cycles, as shown in [Figure 1.35](#), the power output can be uniform by exciting the rotor phases with 120° (electrical) wide currents [41–55]. The currents cannot rise and fall in the motor windings in zero time and hence in actual operation, there are power pulsations during the turn on and turn off of the currents for each half cycle. The severity of such pulsations is absent in the sinusoidal emf type motors as their currents are sinusoidal having no step changes.

PM dc brushless machines have 15% more power density [6] than the PMSM. It can be attributed to the fact that the ratio of the rms value to peak value of the flux density in the PM dc brushless machine is higher than that of the sinusoidal PM machine. The ratio of the power outputs of these two machines is derived in the following, based on equal copper losses in their stators. Let I_{ps} and I_p be the peak values of the stator currents in the synchronous and dc brushless machine, respectively. The rms values of these currents are

$$I_{sy} = \frac{I_{ps}}{\sqrt{2}} \quad (1.46)$$

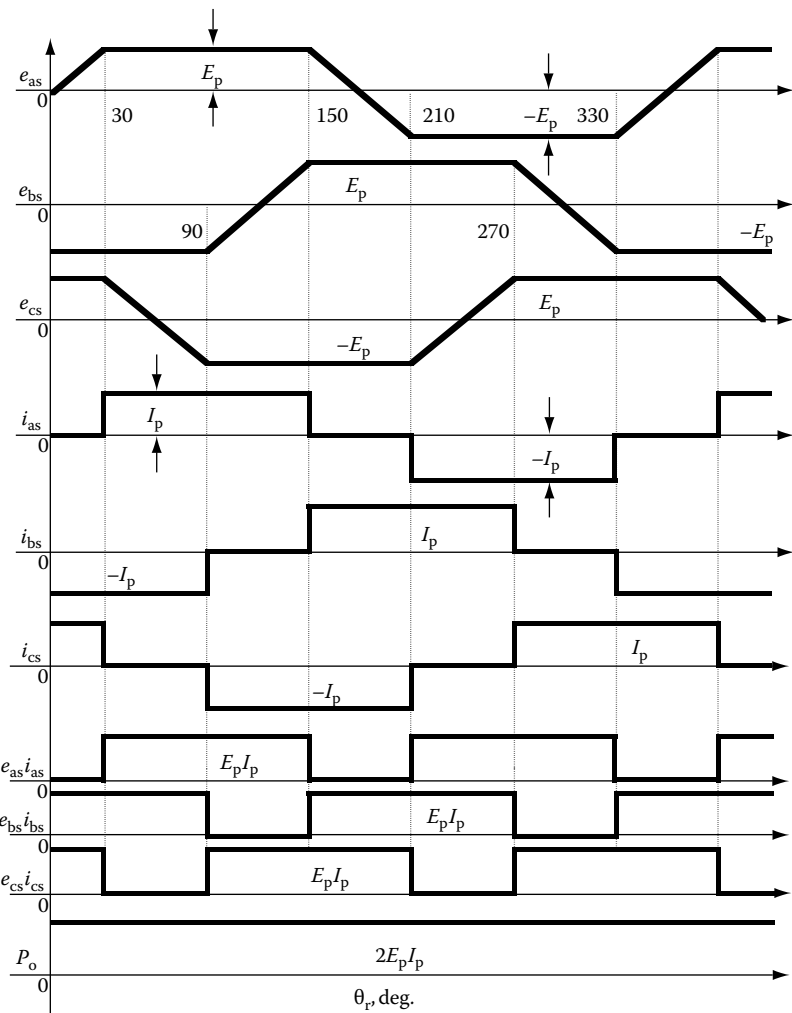


FIGURE 1.35 PM dc brushless motor waveforms. (From Krishnan, R., *Electric Motor Drives*, Figure 9.8, Prentice Hall, Upper Saddle River, NJ, 2001. With permission.)

$$I_d = I_p \sqrt{\frac{2}{3}} \quad (1.47)$$

Equating the copper losses and substituting for the currents in terms of their peak currents as

$$3I_{sy}^2 R_a = 3I_d^2 R_a \quad (1.48)$$

Substituting the rms currents in terms of the synchronous and brushless dc machine currents:

$$3\left(\frac{I_{ps}}{\sqrt{2}}\right)^2 R_a = 3\left(\sqrt{\frac{2}{3}} I_p\right)^2 R_a \quad (1.49)$$

From Equation 1.49, the relationship between the peak currents of the PMSMs and brushless dc machine is obtained as

$$I_p = \frac{\sqrt{3}}{2} I_{ps} \quad (1.50)$$

The peak values of the induced emfs in both machines are equal and denoted by E_p . From the excitation waveforms of the PM brushless dc machine, it is seen that only two phases conduct current at any time, and hence power output is contributed by only two phases at a given time. On the contrary, the PMSM has currents in all its phases, and hence power output is contributed by all the three phases.

The ratio of their power outputs is obtained from these relationships as follows:

$$\begin{aligned} \text{Power output ratio} &= \frac{\text{PM dc brushless power}}{\text{PM synchronous power}} \\ &= \frac{2 \times E_p \times I_p}{3 \times \frac{E_p}{\sqrt{2}} \times \frac{I_{ps}}{\sqrt{2}}} = \frac{2 \times E_p \times \frac{\sqrt{3}}{2} \times I_{ps}}{3 \times \frac{E_p \times I_{ps}}{2}} = 1.1547 \end{aligned} \quad (1.51)$$

Note that the power output ratio has been derived with the assumption that the power factor of the PM synchronous motor is unity.

From the waveforms of the PM dc brushless motor, it is seen that its control is simple if the absolute position of the rotor is known. Knowing the rotor position amounts to certain knowledge of the rotor field and the induced emf and hence instances of applying the appropriate stator currents for control.

The salient features of this machine are summarized as follows:

1. For equal resistive losses, it has 15.4% higher power density than the PMSMs.
2. The duty cycle of the phase currents is only two-thirds as against the one for the PMSMs. This property has strong implications in that only two transistors in an inverter conduct as against three in the PMSM drive system. The conduction and switching losses are smaller for this motor drive in comparison to PMSM drive system. Sufficient time is available for cooling of the devices in the inverter in this motor drive is a significant factor that enhances the thermal reliability of the inverter.
3. The currents are rectangular in shape having variable frequency and, therefore, they are easier to synthesize as compared to variable frequency sinusoidal currents with minimum control implementation complexity.

4. The commutation of current, which has a constant magnitude in every half cycle, is required at every one-sixth of the time period with the result that the commutation signal has to be generated only six times in an electrical cycle. The commutation signals are derived from a position sensor whose resolution has to be only six times the fundamental frequency of the motor. By contrast, the sinusoidal PMSM drive system has to have position information continuously to construct the sinusoidal current commands and the resolution of the current command determines the resolution of the position sensor. Usually, in practice, it amounts to 8, 10, and 12 bits position per revolution with the effect that the cost of the position sensor is high for PMSMs as against very low cost for PM brushless dc motor drive system.
5. The complexity of installation of the position sensors, i.e., usually Hall effect sensors in the case of PM brushless dc motor drive systems is very low as against the installation of position encoders for PMSMs, which is fairly high.
6. The torque ripple due to commutation of currents is high in these machines as against the sinusoidal PMSMs. The deviations in the induced emf waveforms from a truly trapezoid with magnitude constancy period of 120° in each half cycle and their interactions with a constant current produce a large torque ripple in these motor drive systems. In low-performance applications, torque ripple hardly matters but in high-performance applications, it becomes unacceptable. Torque ripple analysis and minimization [114–121] will be considered in later chapters on current control.

1.5 FUNDAMENTALS OF SYNCHRONOUS MACHINES

Field analysis by two-dimensional and three-dimensional finite element method or conventional analytical method with two dimensions is required for detailed analysis and design of the machine [82–101]. Such an approach is outside the scope of this book. Performance prediction of PM machines can be achieved by assuming a certain field distribution, which is tested over time and found reasonable. In it, the secondary issues, such as, uneven air gap due to manufacturing, saturation, stray flux and its paths, uneven field strength in magnets, etc., are ignored. This method is derived from first principles and it does not provide the accuracy of the two and three-dimensional field analysis approaches. But it does explicitly relate the relationship between machine dimensions, materials characteristics, and excitation variables to machine performance and their equivalent parameters. It enables engineers to derive control algorithms and to develop design optimization for the motor drive system. Such an approach is pursued here.

1.5.1 PRINCIPLE OF OPERATION

To produce electromagnetic torque, in general, a rotor flux and a stator mmf has to be present that are stationary with respect to each other but having a nonzero phase shift between them. In a PMSM, the necessary rotor flux is present due to

rotor PMs. Currents in the stator windings generate the stator mmf. The zero relative speed between the stator mmf and the rotor flux is achieved if the stator mmf is revolving at the same speed as the rotor flux, i.e., rotor speed and also in the same direction. The revolving stator mmf is the result of injecting a set of polyphase currents phase shifted from each other by the same amount of phase shift between the polyphase windings. For example, a three-phase machine with three windings shifted in space by electrical 120° from each other and injected with currents shifted by the same amount of electrical 120° between them produces a rotating magnetic field constant in magnitude and traveling at the angular frequency of the currents as will be explained in subsequent section. Basic concept of mmf, winding distribution to achieve sinusoidal mmf, and revolving magnetic field in polyphase machines are presented in this section.

1.5.2 MMF OF A COIL

Consider a stator with one turn of a coil, air gap, and rotor shown in Figure 1.36 to illustrate the concept of mmf of the winding. The magnetic flux produced by the coil has a distribution, resulting in a north and a south pole. The mmf axis is leading the physical coil axis aa' by electrical 90° . Assuming that the rotor and stator iron have infinite permeability, then it is easy to realize that the mmf produced by the coil is entirely spent to overcome the reluctance of the two air gaps in the path of the flux. Instead of only one turn, if the coil has T_{ph} turns, then the total mmf is $T_{ph}I$ (in units of amp-turns) where I is the current in the coil. The mmf versus rotor angle position can be drawn with the convention that positive mmf is required to produce a north pole and a negative mmf for the south pole. Only one half of the coil mmf is utilized to produce one pole. With this understanding, the coil mmf versus stator spatial position is shown in Figure 1.37.

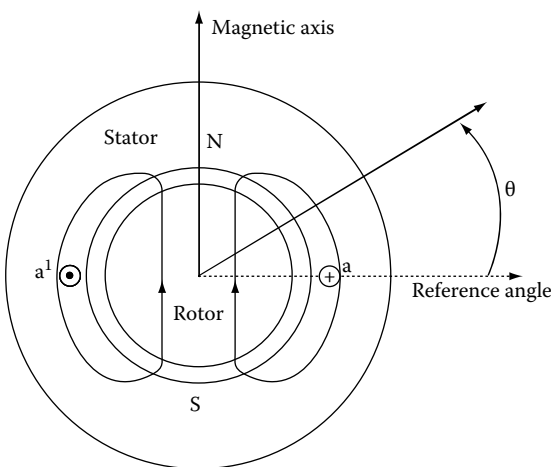


FIGURE 1.36 Simplified machine with one coil and its flux path.

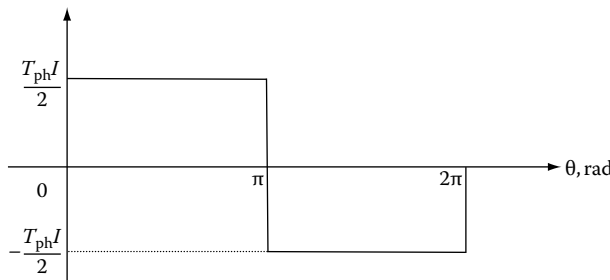


FIGURE 1.37 MMF versus air gap position for a single coil.

1.5.3 SINUSOIDAL MMF DISTRIBUTION

The mmf produced by a coil has a rectangular distribution with a dominant fundamental component. But it is also rich in harmonics that are significant in comparison to the fundamental component. The harmonics do not contribute to useful torque and, in addition, produce only losses. Hence it is important to minimize the harmonics in the stator mmf. There are two ways to achieve it and they are described in the following.

1.5.3.1 Concentric Winding

A sinusoidal mmf distribution can be achieved by a sinusoidal distribution of the windings in the slots but with different coil pitches within a pole pitch. Such a coil arrangement is known as concentric winding and shown in Figure 1.38 with its mmf diagram. The mmf of coils 11', 22', and 33' are represented as such without division by 2 as is the usual case because these coils produce only one pole, thus driving the flux across only one air gap. The phase displacement between the mmfs is the same as the spatial displacement of the coils. The resultant mmf of the phase is the sum total of the individual coil mmfs. The resultant mmf is multisteped and approximately closer to a sinusoid. If there are infinite slots, then the mmf distribution will be triangular. By varying the number of turns, a close sinusoidal mmf is obtained. The coil pitches are less than a pole pitch and decrease for coils as they progress from outer to inner slots. The advantages of the concentric winding are ease of manufacture and its ability to provide a near-sinusoidal mmf distribution. The disadvantage is that the effective turns are slightly less than the algebraic sum of the turns in the coils. Consequently a machine with this winding is saddled with added copper weight and volume and resistive losses compared to some other winding types.

1.5.3.2 Distributed Winding

In this form of winding, the number of conductors in each slot is the same and also the coil pitch is constant for all coils. Both of these features are in sharp contrast to the concentric winding. A distributed winding is shown in Figure 1.39 for illustration. There are five slots per pole per phase and its coils carry a positive current I under one pole and negative current, $-I$, in the adjacent pole. The mmf of coils in each connecting pair of slots is drawn as a rectangle with a magnitude of 0.5 TI, positive for first 180 electrical degrees and negative for next 180 electrical degrees.

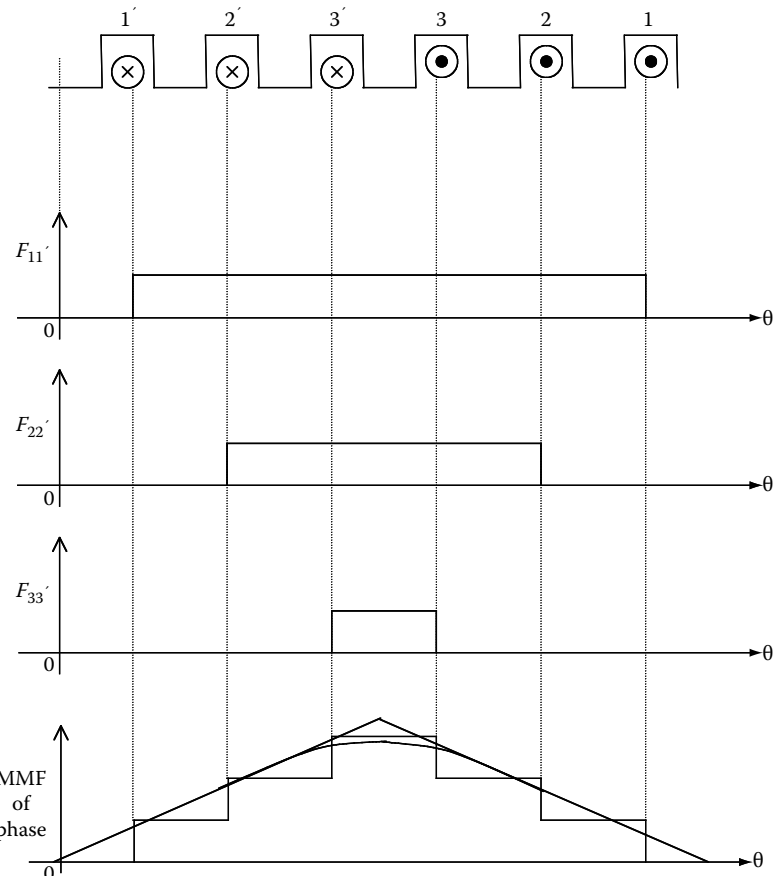


FIGURE 1.38 Concentric winding of a phase and its mmf.

The resultant mmf of the phase coil is derived from summing the individual mmfs of the coils. The advantages of this distributed winding are better utilization of the slot volume and a higher effective turns of the winding. It has the disadvantage of low copper utilization, resulting from longer end turns and higher resistive loss.

The discussion and description so far have been on a single-phase winding, its distribution, and consequent mmf generation. The next section considers ways to arrange three-phase windings in a machine. The same approach can be extended to machines that have different phase arrangements other than the three phases. The concept of induced emf in the machine winding is introduced in this section so that a meaningful approach to the realization of three-phase windings is attempted.

1.5.4 INDUCED EMF

As the coils in the stator experience a change of flux linkages caused by the moving magnets, there is an induced emf in the windings. The waveform of the induced emf

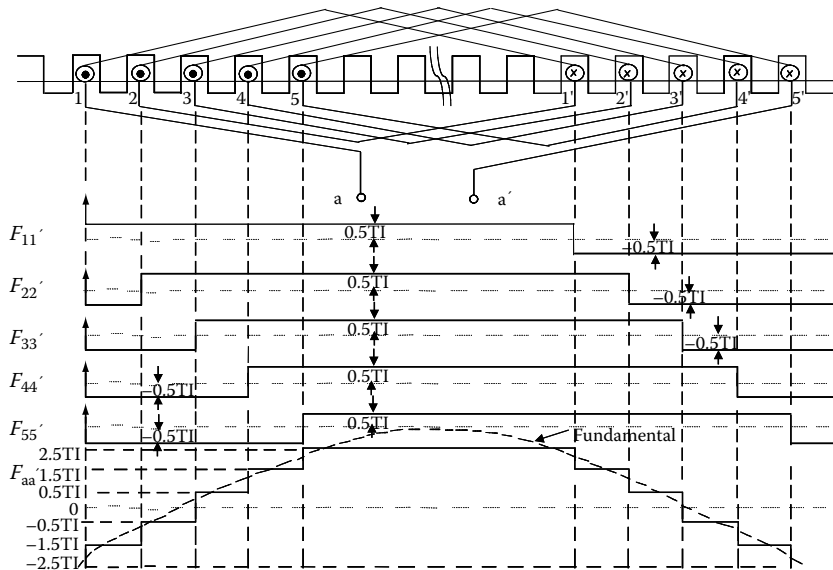


FIGURE 1.39 MMF distribution with five coils in adjacent slots.

is very dependent on the waveform of the flux linkages. The flux linkages are the product of the flux in the air gap and the number of turns associated with the flux lines. The air gap flux is directly influenced by the rotor magnet flux density and the configuration of the stator, air gap, and the rotor construction. If the rotational speed of the machine in electrical radian is ω_r and the air gap flux is sinusoidal then it can be expressed as

$$\phi = \phi_m \sin(\omega_r t) \quad (1.52)$$

Given the number of turns per phase is T_{ph} , then the flux linkages are equal to the product $T_{ph}\phi$. The induced emf is equal to the rate of flux linkages and it is derived as

$$e = -\frac{d\lambda}{dt} = -T_{ph} \frac{d\phi}{dt} = -T_{ph}\phi_m \omega_r \cos(\omega_r t) = -2\pi T_{ph}\phi_m f_r \cos(\omega_r t) \quad (1.53)$$

The rms value of the induced emf is given by

$$E = \frac{2\pi T_{ph}\phi_m f_r}{\sqrt{2}} = 4.44 T_{ph}\phi_m f_r \quad (1.54)$$

where f_r is the frequency of the emf or rotational frequency. A number of observations are made based on this emf equation. They are given below:

1. The emf is proportional to the product of the rotational frequency and air gap (or mutual flux assuming that the entire air gap flux is linking the stator), as the number of turns is a constant. This equation also gives the basic concept behind the control of the machine. Assuming that the air gap flux is constant, it is seen that the emf is influenced only by the rotational frequency of the synchronous machine. Therefore, the excitation frequency of the voltage directly controls the speed of the machine and which also lends itself to very precise speed control as the excitation frequency in the stator can be minutely regulated. Beyond a certain speed known as base speed, an increase in stator frequency will entail voltage demand exceeding the supply capability. During that operation, keeping the voltage constant and increasing the excitation frequency reduces the air gap flux, thus allowing to go to higher speed over and above the base speed. This operation is known as flux weakening.
2. To obtain a sinusoidal voltage, it is important to have a sinusoidal distribution of flux in the air gap. That is achieved with the rotor magnet pole shaping. If the air gap flux contains harmonic components, thus distorting the air gap flux from the fundamental sinusoid, then the quality of the induced emf waveform is poor. Stator slots contribute to these harmonics.

It is assumed in the derivation that the number of turns per phase is T_{ph} and in final expression it needs to be modified to take into account for conductor distribution over a number of slots, for having a coil pitch other than the pole pitch and for skewing the stator to mitigate some harmonics in air gap mmf. It is incorporated by modifying the actual number of turns with effective turns with the help of a factor known as winding factor. Derivation of this winding factor in detail is given in a later section.

For example, a three-phase machine with one coil per phase and two rotor poles is shown in [Figure 1.40a](#) to illustrate the emf induction. The three-phase windings are spatially displaced by electrical 120° from each other. If the mutual flux, i.e., the air gap flux neglecting leakage flux, is plotted for the current position, then it produces a maximum flux linkage with the phase a winding. Assuming that the mutual flux is sinusoidal, the air gap flux density, B_{gs} and mutual flux linkages for the three phases are plotted. Note that the phase shift between the flux linkages is the same as the winding phase shift. The induced emfs are obtained by taking the derivatives of the mutual flux linkages and their illustrative waveforms are shown in the Figure 1.40b. They are a set of three-phase balanced sinusoidal voltages and correspond to the PMSMs. Suppose that the mutual flux density is rectangular, then the waveforms of the machine variables are derived by similar reasoning as in the previous case and they are shown in [Figure 1.41](#). Note this case corresponds to PM brushless dc machines.

The mutual flux linkages are triangular and hence the induced emfs are rectangular, resembling the shape of the flux density. If the phase winding occupies more than one slot per pole, say for two slots, then the rectangular-induced emfs of the coils in the adjacent slots will be connected in series to provide the final phase voltage. In that case, the voltages will have zero magnitude for the overlap period covering the slot angle but double in magnitude for the rest of the duration. This kind of winding is prevalent in PM brushless dc machines.

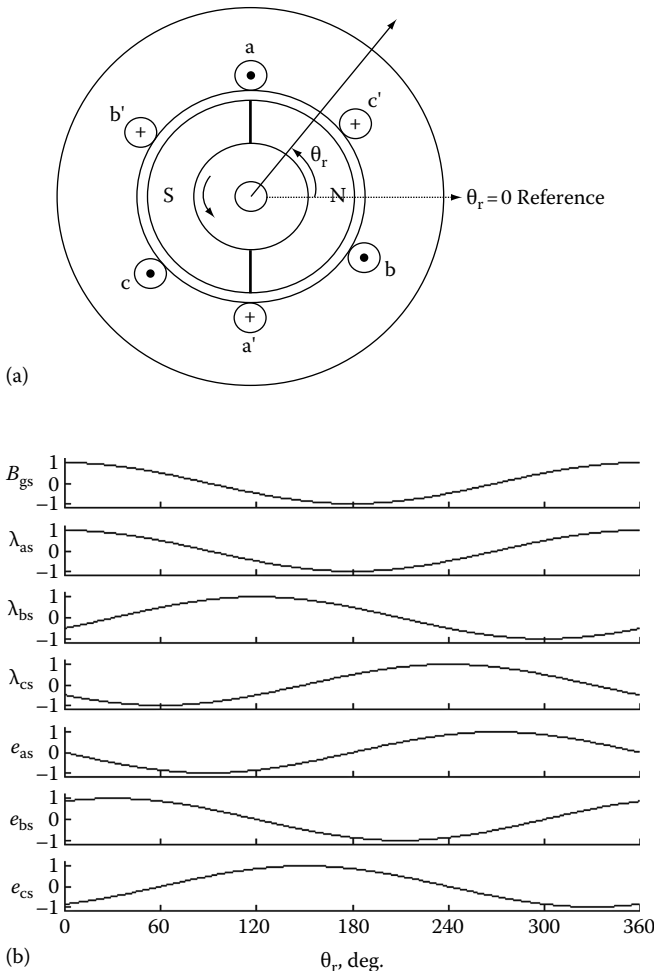


FIGURE 1.40 (a) Simple three-phase machine with sinusoidal flux density. (b) Simple three-phase machine variables.

1.5.4.1 Winding Distribution Factor

To obtain a desired mmf distribution, such as a sinusoidal distribution, it has been seen that the winding is spread or distributed over a number of slots and this case was illustrated and discussed in previous sections. Such a distribution of coils in various slots to obtain a single winding has direct consequences on the induced emf as well as mmf. The voltages induced are sinusoidal in each conductor in the slots but the induced emf in coils adjacent to each other is phase-shifted by the electrical angle of the electrical slot pitch. The slot pitch is the mechanical angle between two slots multiplied by pole pairs so as to express the slot pitch in electrical degrees. Consider a winding phase with three coils distributed over three slots under each north and south poles and it is taken that they are connected in series. When voltages induced in two adjacent slot coils, which are two phasors with a phase shift of the slot pitch

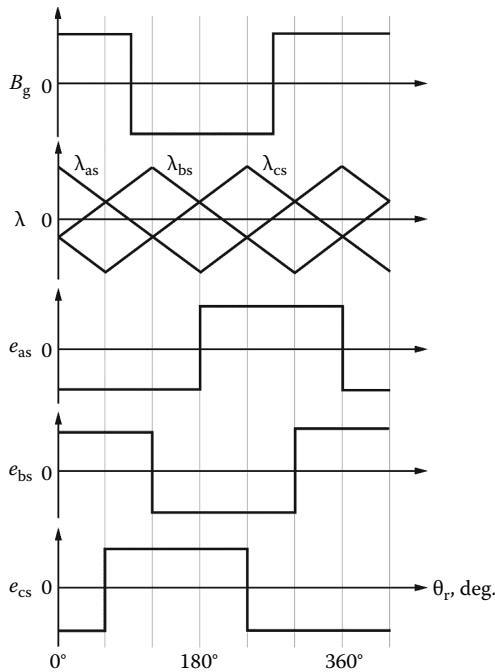


FIGURE 1.41 Three-phase machine-induced emfs and flux linkages for rectangular flux density distribution.

are added to obtain their resultant voltage, note that it is less than algebraic sum of their individual magnitudes. The same applies to any number of coils spread over a number of slots such as three in our illustration. Consider the slot pitch angle is γ in electrical degrees and the induced emfs in the three coil sides with series connected coils as E_1 , E_2 , and E_3 and note that these voltages are equal in magnitude. Note these emfs are phase-shifted from each other by the slot pitch angle. Their resultant voltage is obtained by the phasor summation shown in Figure 1.42. The resultant voltage is less than their arithmetic sum of coil side voltages is obvious from the figure. This attenuation factor is derived in general case with the coils distributed in q-slots under

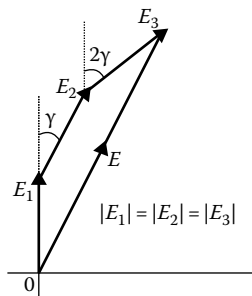


FIGURE 1.42 Effect of winding distribution.

one pole for a phase winding. The coils in one slot under the north pole is connected in series with the coils under the south pole that are separated by one pole pitch, i.e., electrical 180°, which then constitutes a turn for each conductor in the slot. If there are more conductors in a slot, then there are as many turns having a positive and negative emf of the coils under north and south poles that will be added together to form the algebraic sum since the phase shift is 180° electrical. Let the induced emf for the slot turns of the winding is E_1 and likewise for the second slot set is E_2 and for the third slot set is E_3 . Such a turn (or turns) in the slot is connected in series with the turns in the adjacent slot and so on for that phase winding. Then the attenuation factor named as distribution or breadth factor can be derived as the ratio between the phasor sum and the algebraic sum of the coil voltages:

$$k_d = \frac{\sin\left(\frac{q\gamma}{2}\right)}{q \sin\left(\frac{\gamma}{2}\right)} \quad (1.55)$$

where

q is the number of slots per pole per phase

the product $q\gamma$ represents the total breadth of the coil of a phase under one pole in the illustrated case here, $q = 3$

The distribution of the windings consequently carries over to the harmonic components of the mmf and induced emf and note in that case, the distribution angle becomes proportional to the harmonic of the fundamental frequency. Accordingly, the distribution factor for the harmonic of order n may be derived from the fundamental distribution factor as

$$k_{dn} = \frac{\sin\left(n \frac{q\gamma}{2}\right)}{q \sin\left(n \frac{\gamma}{2}\right)} \quad (1.56)$$

Table 1.1 shows the distribution factors for various slots per pole per phase including harmonics. The lower the number of slots per pole per phase, higher is the harmonic distribution factor, resulting in very little harmonic attenuations. For good sinusoidal mmf distribution and induced emf generation, it is critical that slots per pole per phase is kept as high as possible. There are other design limitations in achieving this for a given machine dimension as well as other factors such as manufacturing costs of the coil winding and its insertion.

1.5.4.2 Winding Pitch Factor

So far in the discussion, it was assumed that the coils are connected in series that are spatially apart by electrical 180°, the same as the pole pitch. The desirable outcome of such an arrangement is that the coil sides generated voltages of opposite polarity

TABLE 1.1
Distribution Factors for Various Slot per Pole per Phase

Harmonic	Slots per Pole per Phase			
	1	2	3	4
1	1	0.9659	0.9598	0.9577
3	1	0.7071	0.6677	0.6533
5	1	0.2588	0.2176	0.2053
7	1	-0.2588	-0.1774	-0.1576
9	1	-0.7071	-0.3333	-0.2706
11	1	-0.9659	-0.1774	-0.1261

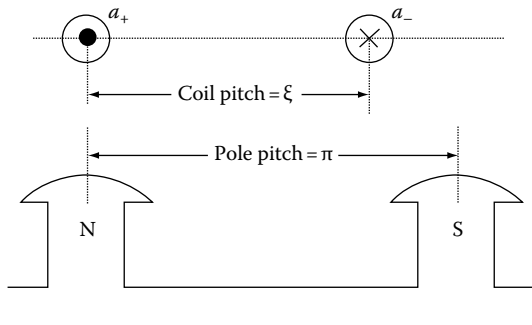


FIGURE 1.43 Short chording of the coil.

under a north and a south pole, which when connected in series gives a resultant of twice the conductor-induced emf as the phase difference between the induced emfs is 180° . If for some reason the conductors that are connected in series are not exactly spatially apart by a pole pitch as shown in Figure 1.43, then the induced emf has a phase shift other than the pole pitch, which leads to a resultant that is less than their algebraic sum. This is accounted by an attenuation factor known as pitch factor. It is done as follows.

If the coils are not separated by 180 electrical degrees but by ξ , which is the coil pitch, then the voltage induced in the coil under south pole will be phase shifted by $(180 - \xi)$ and it is the angle by which the coil is short chocked, i.e., by the amount its displacement is reduced from 180° . This is shown in Figure 1.44 for a turn under north and south poles with a coil pitch shorter than the pole pitch. The attenuation due to pitch factor is derived as

$$k_p = \sin\left(\frac{\xi}{2}\right) \quad (1.57)$$

The winding arrangement under discussion is known as fractional pitch winding. Short chording is used to reduce or eliminate harmonics in the induced emf and

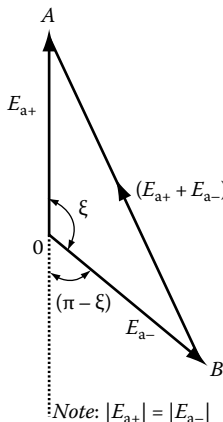


FIGURE 1.44 Resultant voltage in a short chocked turn of winding shown in previous figure.

also to minimize the length of the end turns required to connect the coils in series between the north and south poles. Minimization of end turn length also reduces the amount of copper and winding resistive losses.

The coil pitch for the n th harmonic is equal to n times the actual coil pitch and therefore, the pitch factor for n th harmonic is given by

$$k_{pn} = \sin\left(n \frac{\xi}{2}\right) \quad (1.58)$$

Elimination of a particular harmonic is achieved by choosing the coil pitch such that the pitch factor for that harmonic is equal to zero. For example, consider a coil pitch of 120° , which may be expressed as $2/3$ of the pole pitch or simply as $2/3$ coil pitch, eliminates all triplen harmonics such as $3, 6, 9, 12, \dots$, etc. But in the process the fundamental is only 86.6% and 5th, 7th, 11th harmonics have the same pitch factors as the fundamental. Likewise, $4/5$ th coil pitch eliminates the fifth harmonic and its multiples, $6/7$ th coil pitch eliminates the seventh harmonic and $10/11$ th coil pitch eliminates the 11th harmonic is shown in [Table 1.2](#). The triplen harmonics may not be of concern as the line to line voltages will not have those harmonics in a star connected winding.

1.5.4.3 Skew Factor

The stator windings are placed in slots that are skewed by half a slot or a slot pitch over its axial length. To accommodate that, the stator laminations are stacked progressively with a phase shift from each other by a small measure so that the angle between the first lamination's slot and its corresponding slot in the last lamination along the axial direction is the desired skew angle, θ_{sk} shown in [Figure 1.45](#). The winding is skewed so that certain harmonics in the induced emf are eliminated and for mostly the mitigation of cogging torque that is generated in the machine due to the effects of slotting. In that process, it also reduces the resultant fundamental voltage and other harmonics. While skewing the stator is not prevalent in PMSMs,

TABLE 1.2
Pitch Factors for Various Coil Pitches

Harmonic	Coil Pitch			
	$\frac{2}{3}$	$\frac{4}{5}$	$\frac{6}{7}$	$\frac{10}{11}$
1	0.866	0.951	0.974	0.989
3	0.000	-0.587	-0.781	-0.909
5	-0.866	0.000	0.433	0.755
7	0.866	0.5878	0.000	-0.541
9	0.000	-0.951	-0.433	0.282
11	-0.866	0.951	0.781	0.000

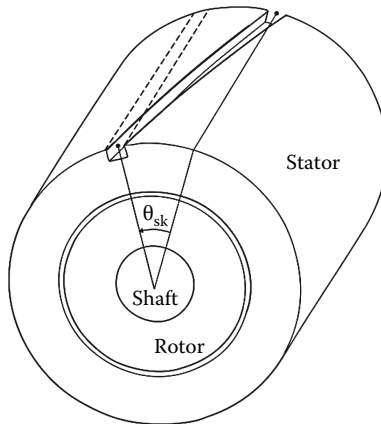


FIGURE 1.45 Skewing of the stator.

it is not unusual to encounter it in practice. The effect of the progressive skew along the axial length of the coil side can be determined as follows. If the length of the coil side is divided into very small segments, then the voltages induced in these segments are displaced from each by a small phase shift corresponding to skew angle divided by the number of segments. The segment voltages in the coil side are on the arc of the circle subtended with the phase shift angle and the resultant voltage E_r then is seen to be that of the chord, as shown in Figure 1.46 and accordingly the attenuation factor associated with skewing then is given as

$$k_{sk} = \frac{2 \sin\left(\frac{\theta_{sk}}{2}\right)}{\theta_{sk}} = \frac{\sin\left(\frac{\theta_{sk}}{2}\right)}{\frac{\theta_{sk}}{2}} \quad (1.59)$$

The skew factor for harmonics can be derived similar to that of the harmonic distribution and pitch factors.

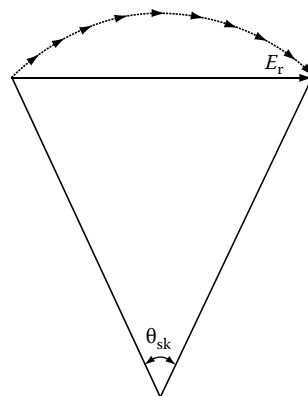


FIGURE 1.46 Resultant voltage in a coil side in skewed stator.

1.5.4.4 Winding Factor

Distribution, pitch, and skew factors reduce the available voltage in a phase winding. Distribution effect was derived assuming coil pitch is equal to pole pitch, while the effect of coil pitch that is different from the pole pitch is accounted with the pitch factor and finally winding skew is taken into consideration with the skew factor. Simultaneous presence of distribution, short chording, and skew in a winding will reduce the induced emf as well as the mmf. Overall, the effect on the induced voltage and mmf is as shown in Figure 1.47 in the form of a signal flow graph diagram. The effects due to skew, pitch, and distribution factors are combined into a single variable termed winding factor and that is given by

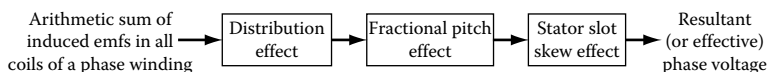
$$k_{\omega} = k_d k_p k_{sk} \quad (1.60)$$

Equivalently, the effective number of turns in the phase winding can be thought of as attenuated by the winding factor and then that effective turns are substituted in the emf equation. Therefore, the induced emf for actual T_{ph} turns per phase is given by

$$E = 4.44k_{\omega}T_{ph}\phi_m f_s = (4.44T)\phi_m f_s \quad (1.61)$$

where effective turns per phase, T , is given as

$$T = k_{\omega}T_{ph} \quad (1.62)$$



$$mE_1 \rightarrow k_d \rightarrow k_p \rightarrow k_{sk} \rightarrow E$$

FIGURE 1.47 Effects of pitch, distribution, and skew factors.

As the fundamental is only of interest at this time and assuming there is no skewing, the pitch and distribution factors are calculated for fundamental and then used to obtain the winding factor for the fundamental. The harmonic-induced emfs are calculated by substituting the respective winding factor for that harmonic as

$$k_{\omega n} = k_{dn} k_{pn} \quad (1.63)$$

And likewise the effective turns for the harmonics are computed by multiplying the harmonic winding factor with the turns per phase. Note that the peak harmonic flux for the desired harmonic order is substituted in the place of fundamental peak flux in the emf equation for the computation of induced emf and in the place of the frequency the harmonic frequencies.

1.5.5 TYPES OF WINDINGS

Having seen the implications of the distribution and variation of coil pitch of windings, it is appropriate at this stage to become familiar with some types of windings commonly found in practice in PMSMs. Coils belonging to different phases can share some of the stator. Single-layer windings have only one phase coil in any slot and do not share the slot with any other phase coils. If two phase coils share a slot, then it is a two-layer winding. Three-layer windings with three phase coils sharing slots may be found also. Single- and multilayer windings can have fractional and full pitch coils. Illustrations of single-layer full and fractional pitch coils and likewise two-layer windings are given in the following.

1.5.5.1 Single-Layer Winding

A simple two-pole, six-slot, three-phase machine with full pitched single-layer winding is shown in [Figure 1.48](#) with its phase spread and winding diagram. The slot pitch is 60° and the phase spread is the same as shown in [Figure 1.48a](#) schematically. [Figure 1.48b](#) shows only one conductor per slot and [Figure 1.48c](#) shows the slot with multiple conductors and their connection. Note that the subscript “s” indicates the start terminal of a phase and subscript “f” indicates the end terminal of a phase. The arrows indicate the induced emf direction. Note that the distribution factor for this winding is one and so also for all the harmonics. That is the disadvantage of this machine and hence it is rarely used in PMSMs but it is quite advantageously used in low-cost PM brushless dc machines to generate trapezoidal-induced emf.

A 2-pole, 12-slot, 3-phase machine is considered with a full pitch. Its schematic diagram of the stator and rotor is shown in [Figure 1.49a](#) with its winding diagram in [Figure 1.49b](#). The phase spread is 60° and the slot pitch is 30° . As the coils of each phase are spread in two slots, there is the effect of distribution with the consequence that the induced emf is attenuated. The distribution factor may be easily computed for the fundamental in this case to be 0.966 or can be obtained from [Table 1.1](#) as well.

1.5.5.2 Double-Layer Winding

The same illustration considered in the single-layer winding case is taken up for illustration here, i.e., a two-pole, six-slot, three-phase machine with full pitch coils.

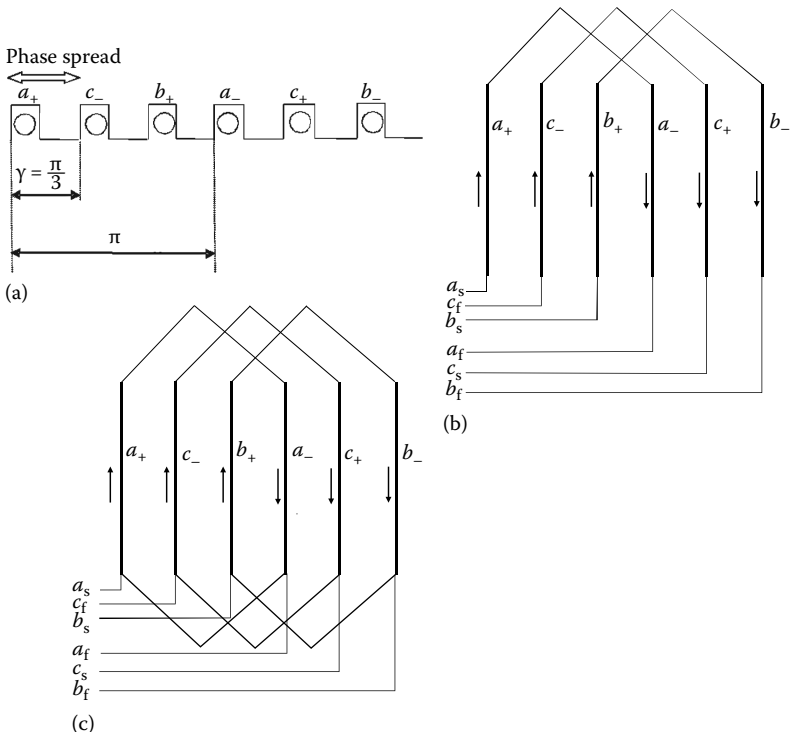


FIGURE 1.48 Single-layer winding with full pitch coils for a three-phase machine: (a) schematic layout; (b) winding diagram with a single conductor per slot; and (c) winding diagram with multiple conductors per slot.

The schematic of the coils in the stator lamination and the winding diagram are shown in Figure 1.50(a) and (b), respectively. The bold lines indicate the upper coil side and double lines indicate the lower coil side in a slot and it is assumed that each coil side has multiple conductors. Note that the phase spread is 120° and the slot angle is 60° . The distribution factor for this machine is 0.866 while the triplen harmonic distribution factors have become zero.

Consider the same machine for a fractional pitch winding having a coil pitch of 120° and the phase spread is the same as the coil pitch. The schematic layout and the winding diagram for this case are shown in Figure 1.51a and b, respectively. The distribution factor for this is 0.866 and the pitch factor also is the same with the result that the winding factor is reduced to 0.75 whereas machine with double-layer full pitch coils has a winding factor of 0.866. The harmonic winding factors become different and they are all considerably attenuated in the present case. It is unusual to have a low number of slots per pole per phase in synchronous machines (but not in brushless dc machines) such as the illustrated cases but the basics that are covered here are easily extended to such high slots per pole per phase cases. Interested readers are referred to books on electrical machines listed in the reference for further reading on winding types and their role in machine design.

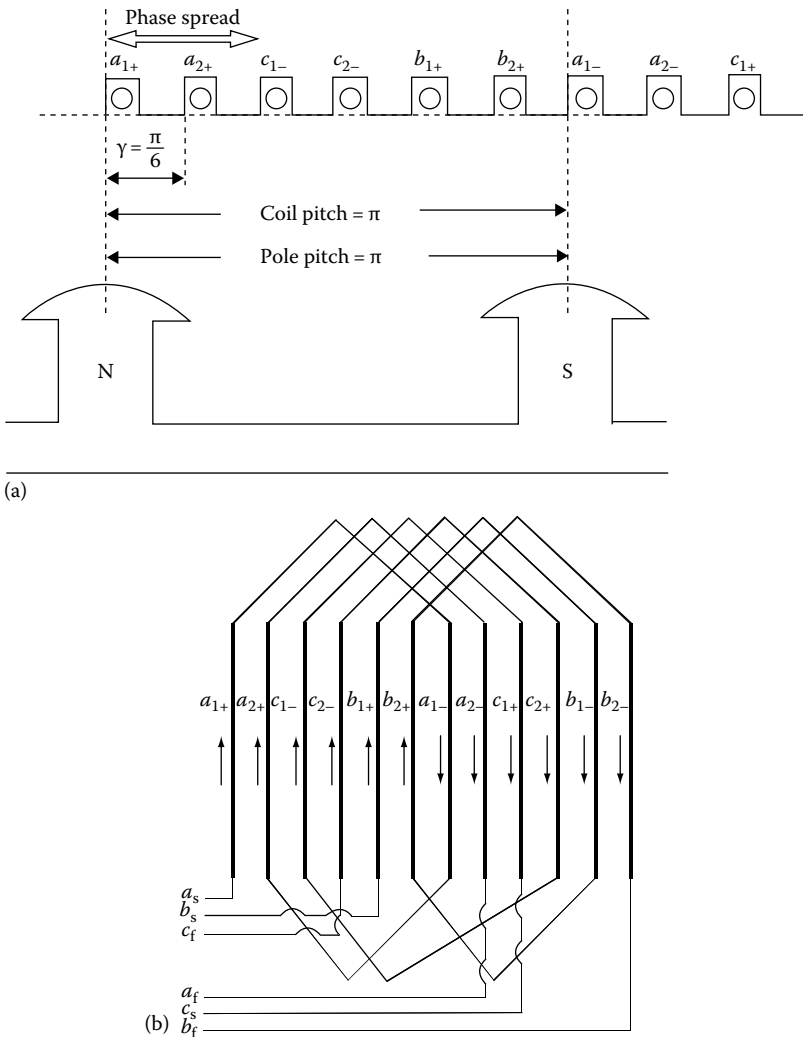


FIGURE 1.49 Single-layer winding with distribution of windings in two slots: (a) schematic; (b) winding diagram.

1.5.6 ROTATING MAGNETIC FIELD

A rotating magnetic field is produced in a machine with balanced polyphase winding when it is injected with a balanced polyphase current. Balanced polyphase winding currents mean that their sum is zero and each phase current is displaced from each other by the same phase as the windings are displaced from each other spatially. Proof of this is derived in this section considering a special case of three-phase machines as they are the most prevalent in practice but the proof is extendable to any balanced polyphase machine with balanced polyphase currents. In the process, the magnitude and phase of the rotating magnetic field are also obtained, which are of

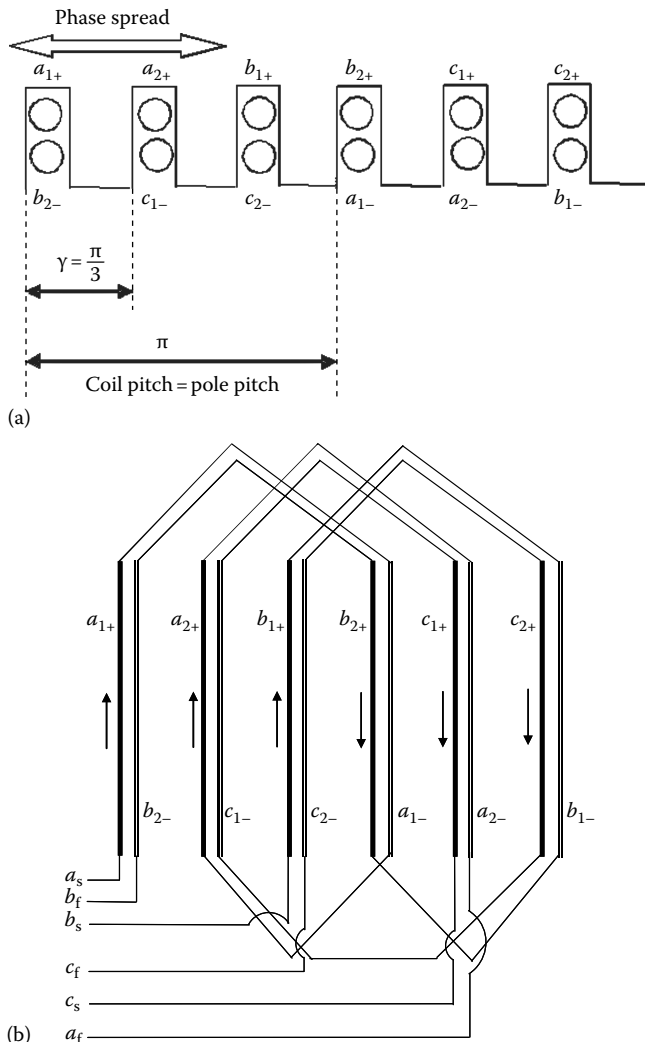


FIGURE 1.50 Double-layer winding with full pitch coils in a three-phase machine: (a) schematic layout; (b) winding diagram.

utmost importance in deriving fundamental relationships in the machine. Two cases of phase mmf distribution are considered and they are sinusoidal and rectangular as both are encountered in the PMSMs.

1.5.6.1 Sinusoidal MMF Distribution

Consider a balanced three-phase winding sinusoidally distributed over the space. A balanced three-phase winding has equal number of turns in each phase and has a spatial displacement of 120° electrical between successive phase windings. Let these phase currents also be balanced in that they have equal peaks, I_m , have an angular

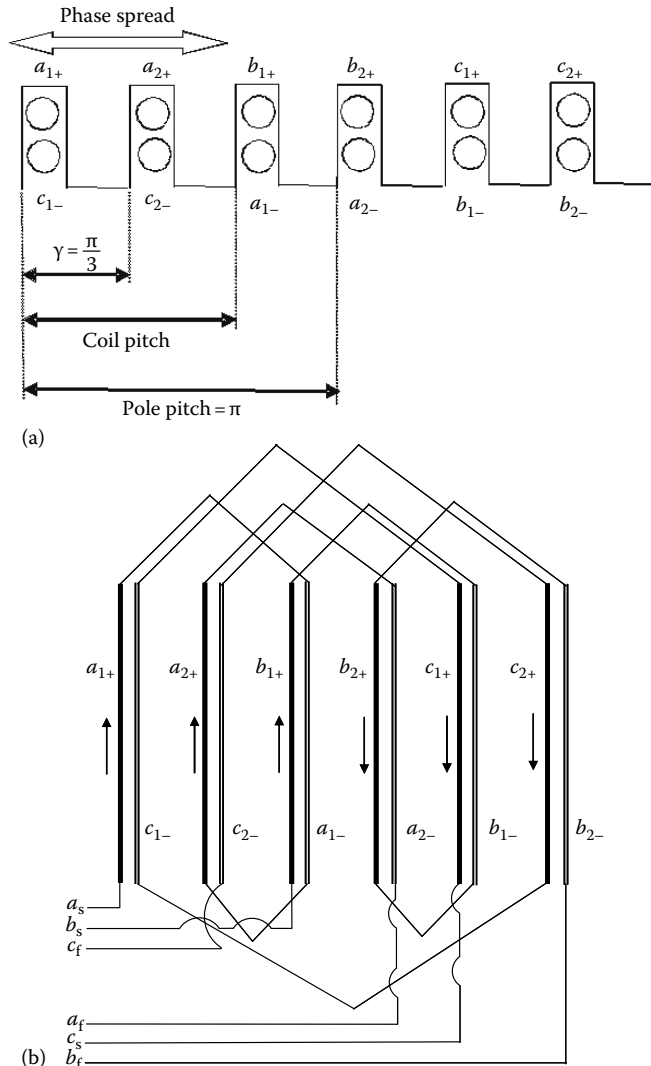


FIGURE 1.51 Double-layer winding with fractional pitch: (a) layout schematic; (b) winding diagram.

frequency ω_s and shifted in phase from each other by electrical 120° . Then these stator currents are written as

$$i_{as} = I_m \sin(\omega_s t)$$

$$i_{bs} = I_m \sin\left(\omega_s t - \frac{2\pi}{3}\right) \quad (1.64)$$

$$i_{cs} = I_m \sin\left(\omega_s t + \frac{2\pi}{3}\right)$$

If T_{ph} is the effective number of turns in each phase including the effects of pitch, distribution, and skew factors, then the individual phase mmfs per pole corresponding to the spatial position θ are given by

$$\begin{aligned} F_{\text{as}} &= \frac{T_{\text{ph}}I_m}{P} \sin(\theta) \sin(\omega_s t) \\ F_{\text{bs}} &= \frac{T_{\text{ph}}I_m}{P} \sin\left(\theta - \frac{2\pi}{3}\right) \sin\left(\omega_s t - \frac{2\pi}{3}\right) \\ F_{\text{cs}} &= \frac{T_{\text{ph}}I_m}{P} \sin\left(\theta + \frac{2\pi}{3}\right) \sin\left(\omega_s t + \frac{2\pi}{3}\right) \end{aligned} \quad (1.65)$$

Note that considering a two-pole machine and infinitely permeable iron in the stator and rotor, the mmf, $T_{\text{ph}}I_m$ overcomes the reluctance of two air gaps, one under each pole, to set up the magnetic flux. Hence half of the magnitude of the mmf supports the flux in each air gap, which is equal to the mmf per pole. Extending this case to P -pole machine, the mmf magnitude per pole is obtained as $T_{\text{ph}}I_m/P$. The phase mmfs are shown in Figure 1.52 and they are directed along the magnetic axis of the respective phases. It is from the direction of the currents in the coils of the phases and the flux distribution that both the magnetic axis as well as the direction of the mmf are derived. They are derived based on the understanding gained from an earlier section on the mmf generated from a single coil.

The resultant stator mmf is given by the sum of the individual phase mmfs. Prior to that the individual phase mmfs are decomposed into forward and backward rotating components as

$$\begin{aligned} F_{\text{as}} &= \frac{T_{\text{ph}}I_m}{P} \sin(\theta) \sin(\omega_s t) = \frac{1}{2} \frac{T_{\text{ph}}I_m}{P} \left[\cos(\theta - \omega_s t) - \cos(\theta + \omega_s t) \right] \\ F_{\text{bs}} &= \frac{T_{\text{ph}}I_m}{P} \sin\left(\theta - \frac{2\pi}{3}\right) \sin\left(\omega_s t - \frac{2\pi}{3}\right) = \frac{1}{2} \frac{T_{\text{ph}}I_m}{P} \left[\cos(\theta - \omega_s t) - \cos\left(\theta + \omega_s t - \frac{4\pi}{3}\right) \right] \\ F_{\text{cs}} &= \frac{T_{\text{ph}}I_m}{P} \sin\left(\theta + \frac{2\pi}{3}\right) \sin\left(\omega_s t + \frac{2\pi}{3}\right) = \frac{1}{2} \frac{T_{\text{ph}}I_m}{P} \left[\cos(\theta - \omega_s t) - \cos\left(\theta + \omega_s t - \frac{2\pi}{3}\right) \right] \end{aligned} \quad (1.66)$$

When these phase mmfs are summed up to obtain the resultant mmf of the machine, the backward rotating components add to zero and the sum of the forward rotating components result in

$$F_s = F_{\text{as}} + F_{\text{bs}} + F_{\text{cs}} = \frac{3}{2} \frac{T_{\text{ph}}I_m}{P} \cos(\theta - \omega_s t) \quad (1.67)$$

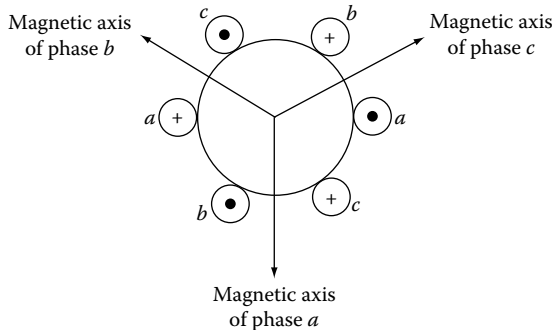


FIGURE 1.52 Three-phase windings with currents and their magnetic axes.

The resultant stator mmf has a constant magnitude but varies sinusoidally. It is maximum when the stator position and angular position of the current phasor coincides. That is, the speed of the resultant field is equal to the angular speed of the stator currents. If the rotor is also revolving, say at angular speed of the stator excitation, then the relative speed between the stator mmf and rotor flux is zero. This satisfies a necessary condition for electromagnetic torque generation. A graphical illustration of the revolving magnetic field production is shown in Figure 1.53 and the plotted mmf is for all the poles and not per pole. To obtain the mmf per pole from this figure, the resultant mmf is divided by the number of poles, P . It is also seen from the figure that variation of stator current phasor angle by 90° has also moved the stator mmf by the same angle in the clockwise direction. The phase sequence is abc for the current phasors and the direction of rotation of the current phasors is in the clockwise direction as defined in the equations for currents. Because of the resultant mmf's rotation at a speed equal to the angular frequency of the input currents, the field is termed as revolving or rotating magnetic field in literature.

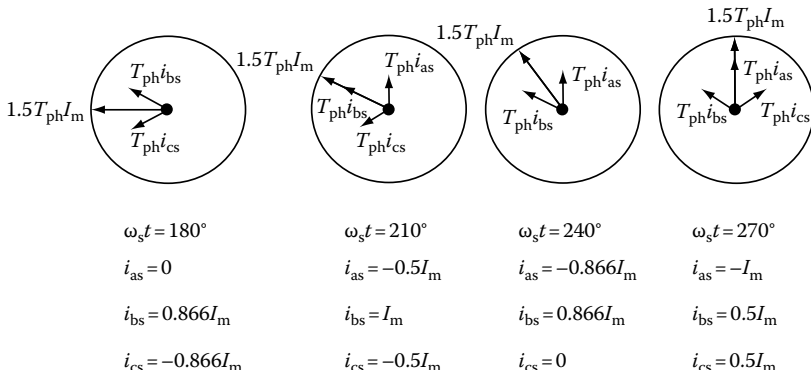


FIGURE 1.53 Graphical illustration of the revolving magnetic field in a three-phase machine.

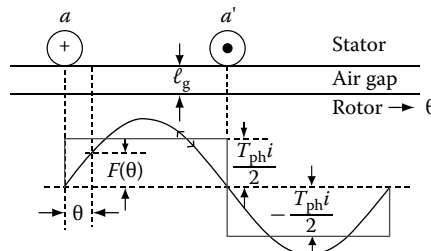


FIGURE 1.54 MMF diagram with its fundamental for a stator winding with T_{ph} turns carrying a current i .

1.5.6.2 Rectangular MMF Distribution

So far the treatment is based on the sinusoidal distribution of phase windings. This is not the case in PM brushless dc machines where the coils are concentrated in one or two slots per pole per phase with the consequence that the phase mmf is rectangular as shown in Figure 1.54. Under such a circumstance, the rotating magnetic field's peak magnitude is not the same as derived in the above. It is derived as follows by considering only the fundamental field. Consider the rectangular mmf of magnitude $T_{ph}I_m/P$ and its fundamental component is equal to $(4/\pi)(T_{ph}I_m/P)$ for each phase obtained from Fourier series decomposition of the rectangular mmf. When this is substituted in the development of resultant mmf computation described in the development for the sinusoidally distributed winding case, it is found that the resultant mmf per pole is equal to $1.909 T_{ph}I_m/P$. Comparing this to the sinusoidally distributed magnetic field strength of $1.5T_{ph}I_m/P$, it is found that for equal number of turns and current, the rectangular mmf distributed magnetic field resultant is 27% higher. Looking at this impressive result in another way, the sinusoidally distributed windings require 27% higher effective turns compared to that of the rectangular mmf distributed or concentric windings.

The resultant mmf derivation strictly for any winding distribution can be computed by first computing the mmf for each phase derived in Section 1.5.6.1 and then finding its fundamental component by Fourier series analysis for final derivation of the resultant mmf. Such an approach is particularly desirable in machines that are designed for variable speed applications driven from an inverter supply that contributes considerable harmonics, which may have consequences in losses and heating with the inevitable derating of the machine capacity. The derivation and explanation only pertain to the fundamental mmf due to concentrated windings. Harmonic mmfs can be ascertained from the Fourier components. They are not probed for the present here.

1.6 FUNDAMENTAL SYNCHRONOUS MACHINE RELATIONSHIPS

This section and others that follow consider some fundamental relationships relating to induced emf, torque, and power to machine and magnet dimensions, excitation current, and flux density, leading to a physical understanding of the machine. Output power equation is also derived to enable sizing of the machine. Equivalent

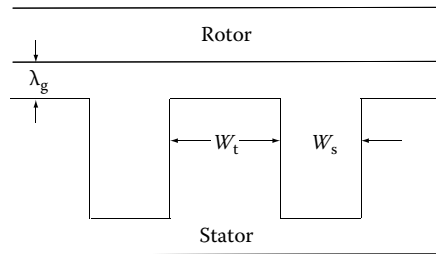


FIGURE 1.55 Illustration of a part of the machine cores.

stator current-induced magnetic field to match rotor field due to the PMs is derived for use in the equivalent circuit of a PMSM. Safe operating peak stator current is computed based on the demagnetization characteristics of the PMs. Equivalent circuit characterization requires self, magnetizing, synchronous, direct, and quadrature axes inductances and they are derived analytically and presented in this section. Finally, the effect of stator excitation on air gap flux density in presence of rotor PM field is illustrated to gain an insight into the operating air gap magnetic field and its control.

The key to all the derivations is the air gap flux density. It is affected by slotting of the stator lamination as it makes the air gap nonuniform. The effective air gap to account for such nonuniformities is to introduce a correction factor to the physical air gap. That is frequently used in all the subsequent sections and accordingly its treatment is discussed immediately in the following section.

1.6.1 EFFECTIVE AIR GAP

The effective air gap length is slightly different from the actual air gap. The effective air gap considers the effect of slotting in the stator core in that the flux density in the air gap across the slot and tooth are very different. Therefore, the air flux density decreases on an average due to slotting of the stator core compared to a cylindrical surface without any slots. Accordingly to reflect that in calculations, the air gap is modified from that of the actual air gap by a coefficient known as Carter coefficient. It expresses the ratio between the flux density in the air gap without slotting to the flux density with slotting on the stator core. Carter's coefficient is determined by the slot width, W_s , and tooth width, W_t , and air gap length, ℓ_g , and they are shown for a small part of the machine in Figure 1.55. For one sided slotting, i.e., for the slotting of stator core only, the effective air gap is

$$g_d = C \ell_g \quad (1.68)$$

where Carter coefficient C is given by

$$C = \frac{W_s + W_t}{W_s(1-\sigma) + W_t} = \frac{1}{1-\sigma \frac{W_s}{W_s + W_t}} \quad (1.69)$$

where

$$\sigma = \frac{2}{\pi} \left\{ \tan^{-1} \left(\frac{W_s}{2\ell_g} \right) - \frac{\ell_g}{W_s} \ln \left[1 + \left(\frac{W_s}{2\ell_g} \right)^2 \right] \right\} \quad (1.70)$$

\ln is the logarithm to base e.

In these two equations, note that the ratio between the slot width and air gap and ratio between the slot width and slot pitch are nondimensional and hence they are used in the plot of Carter coefficient shown in Figure 1.56. The impact of the ratio between the slot width and air gap on Carter coefficient is shown in Figure 1.57

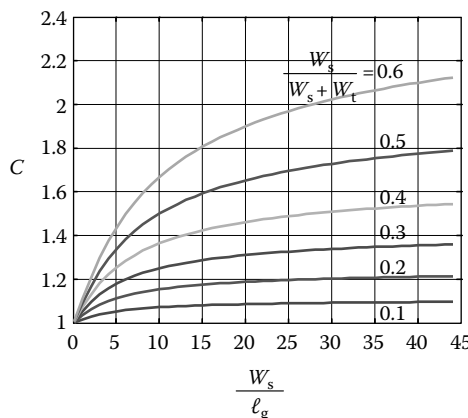


FIGURE 1.56 Carter coefficient for slotted stator and PM rotor.

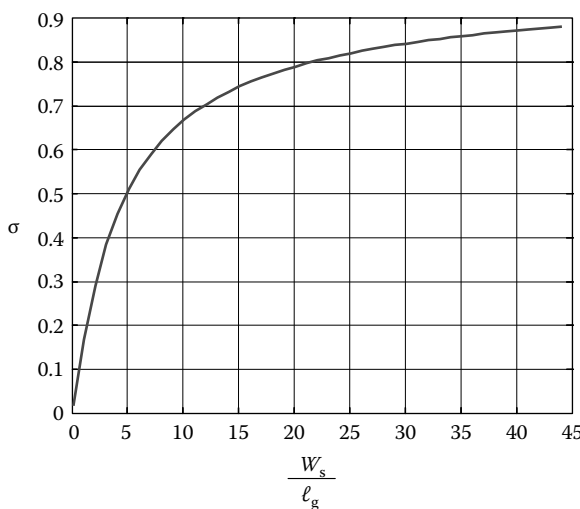


FIGURE 1.57 Impact of slot width and air gap on Carter's coefficient through the intermediary variable σ .

through the relationship σ . With increasing ratio between the slot width and air gap, the intermediary variable σ saturates and comes closer to 0.9, resulting in saturating Carter coefficient for the set of slot widths expressed in nondimensional unit with the aid of slot pitch that is the sum of the slot and tooth widths. The optimal value of the slot width to slot pitch is half and most practical values are around it.

The slotting effect of the rotor is negligible in the case with PMs as the air gap flux density is mainly due to the magnets and the majority of the flux is confined through magnets rather than through the iron separating the magnets that may be considered as tooth in the rotor. This may not be justifiable in rotors with a large number of magnets as well as in the case with interior PM machines. Similar to the stator slotting effect, the rotor slotting can be accounted if necessary.

1.6.2 EFFECT OF MAGNET ON INDUCED EMF

The magnet's thickness (or sometimes referred to as magnet length, which is entirely different from stack length), its arc or width and its operating flux density are the variables that play a crucial role in the determination of the air gap flux density and in the induced emf. The effect of magnet thickness on the operating point to find the magnet flux density has been considered in the earlier sections. The effect of the other two variables, magnet arc and magnet flux density, on the induced emf is derived in this section.

Consider the magnet has an arc of 2β in the machine. Its flux density will have a constant magnitude of B_m over 2β in the positive half cycle and $-B_m$ over 2β in the negative half cycle as shown in Figure 1.58 for a surface mount magnet rotor. Its fundamental, which is a sinusoid will have a peak, B_{m1} , obtained by using Fourier analysis as

$$B_{m1} = \frac{4}{\pi} B_m \sin \beta \quad (1.71)$$

The peak-induced emf is given by

$$E_m = 2\pi f_s (T_{ph} k_{\omega}) \phi_{m1} \quad (1.72)$$

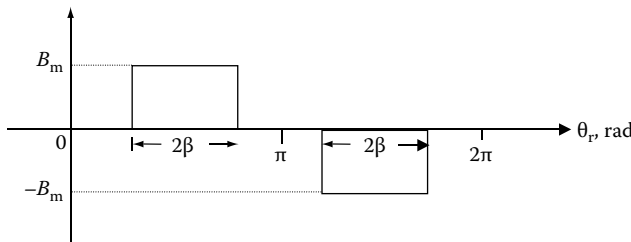


FIGURE 1.58 Air gap flux density for surface mount magnet machine.

where ϕ_{m1} is the peak fundamental flux in the machine. It is essential at this stage to find the peak flux. It is derived in a later section (1.6.8) and its result is used here. Assuming it is produced by the magnet, the peak fundamental flux is given by

$$\phi_{m1} = \frac{B_{m1}DL}{(P/2)} \quad (1.73)$$

where D is the bore or inner diameter of the stator lamination and L is the effective length of the stator laminations assembled in a stack.

Substituting for peak flux density in terms of the magnet flux density in the flux equation and then using that in the induced emf equation gives

$$E_m = \frac{4}{\pi} k_\omega T_{ph} D L B_m \omega_m \sin \beta \quad (1.74)$$

Note that the mechanical angular speed appears in the equation because the angular stator frequency divided by pairs of poles that appears in the equation is nothing but the angular mechanical speed itself. This equation describes the induced emf and its relationship to machine dimensions, winding turns, magnet flux density and magnet arc, and rotational speed. Then the next step is to compute the output power of the machine.

1.6.3 ELECTROMAGNETIC POWER AND TORQUE

If E_m is leading the rotor flux by 90° and the stator current leads the rotor flux by δ (known as torque angle), then the real air gap or electromagnetic power is computed from the real part of the three-phase power [87] where the phase power is the product of the rms induced emf and conjugate of the rms current given by

$$\begin{aligned} P_a &= \operatorname{Re} \left[3 \left\{ \frac{E_m}{\sqrt{2}} \frac{(I_m)^*}{\sqrt{2}} \right\} \right] = \operatorname{Re} \left[\frac{3}{2} E_m \angle 90^\circ \cdot I_m \angle -\delta \right] \\ &= \frac{3}{2} E_m I_m \sin \delta = \left(\frac{3}{2} \frac{4}{\pi} k_\omega T_{ph} D L \sin \beta \right) B_m I_m \omega_m \sin \delta \end{aligned} \quad (1.75)$$

from which the torque is derived as

$$\begin{aligned} T_e &= \frac{P_a}{\omega_m} = \frac{3}{2} \left(\frac{4}{\pi} k_\omega T_{ph} \right) (D L) (B_m \sin \beta) I_m \sin \delta \\ &= \frac{3}{2} (D L) \left(\frac{4}{\pi} k_\omega T_{ph} I_m \right) (B_m \sin \beta) \sin \delta \end{aligned} \quad (1.76)$$

Noting that the effective turns of a sinusoidally distributed winding for the concentrated winding with T_{ph} can be written in the form of $\left(\frac{4}{\pi}k_{\omega}T_{ph}\right)$ and that can be termed as N_s turns per phase. In this case, the torque can be written as

$$T_e = \frac{3}{2}(DL)(B_m \sin \beta)(N_s I_m) \sin \delta \quad (1.77)$$

This expression shows that the torque is determined by the product of bore diameter and stack length, mmf, magnet flux density and magnet arc angle, and finally the control angle between the rotor magnetic field (same as rotor) and current phasor. The machine designer has control over the bore diameter, stack length, magnet flux density by choice of the magnets and its arc, and the number of winding turns per phase. The inverter designer cooperates with the machine designer in choosing the number of turns based on the phase voltage that can be delivered from the inverter and its ac or dc supply inputs. Based on these variables, the inverter design is achieved. Finally the control system designer controls the magnitude of current and the torque angle, δ , to deliver specified torque at various speeds. In all, this expression clearly identifies the interaction of the electromagnetics, power electronics, and control system and hence the role of various subsystem engineers to design the machine and to operate it as a variable speed motor drive.

Many different forms of this expression can be found in various publications and care must be taken to understand the definitions of various variables before the expression can be confidently exploited in the design. For example, another version [3] of the torque expression is presented in the following which is derived from the one derived earlier as

$$\begin{aligned} T_e &= \frac{3}{2}(DL)(B_m \sin \beta)(N_s I_m) \sin \delta \\ &= \frac{3}{2}(2rL)\left(B_{m1} \frac{\pi}{4}\right)\left(N_s I_s \sqrt{2}\right) \sin \delta \\ &= \frac{3}{2}\left(I_s \sqrt{2}\right)\left(\frac{\pi r L B_{m1} N_s}{2}\right) \sin \delta \end{aligned} \quad (1.78)$$

where

I_s is the stator phase rms current and is equal to $I_m/\sqrt{2}$

r is the radius of the bore

1.6.4 FUNDAMENTAL REPRESENTATION OF ELECTROMAGNETIC TORQUE

An alternate form of torque expressed as an interaction of the stator and rotor (in this case, magnet) mmfs is more fundamental than other derivations and that is derived as follows from the previous representations.

The peak fundamental magnet flux density can be expressed in the form of a magnet mmf as

$$B_{m1} = \frac{\mu_0 F_m}{g_d} \quad (1.79)$$

where

F_m is the magnet mmf

g_d is the effective air gap length in the magnet axis

The peak fundamental flux density is expressed in terms of the remanent flux density as given in Equation 1.10 and for that the magnet operating flux density is required and derived as

$$B_m = \frac{B_r (\ell_m / \mu_{rm})}{C \ell_g + \ell_m / \mu_{rm}} = \frac{B_r \ell_m}{g_d \mu_{rm}} \quad (1.80)$$

where C is Carter coefficient for correcting the air gap for stator slotting effect and

$$g_d = \frac{\ell_m}{\mu_{rm}} + C \ell_g \quad (1.81)$$

where g_d is the effective air gap length in magnet or d-axis and using the previous three equations, the magnet mmf is derived as

$$F_m = \frac{B_{m1} g_d}{\mu_0} = \left(\frac{4}{\pi} B_m \sin \beta \right) \frac{g_d}{\mu_0} \quad (1.82)$$

The relationship between the magnet flux density and its fundamental flux density can be seen from Figure 1.59. The magnet flux density can be substituted from this in terms of the magnet mmf in the torque expression [161,162] as

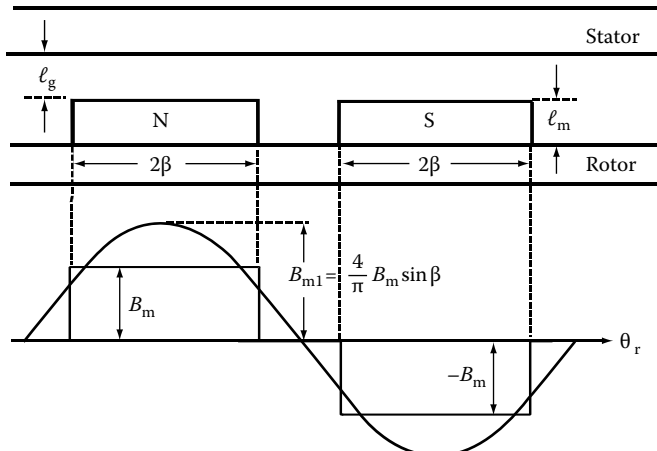


FIGURE 1.59 Relationship between the magnet flux density and its fundamental.

$$\begin{aligned}
 T_e &= \frac{3}{2} \left(\frac{4}{\pi} k_{\omega} T_{ph} \right) (DL) (B_m \sin \beta) I_m \sin \delta \\
 &= 2(DL) \left(\frac{P}{2} \right) \left(\frac{3}{2} \frac{k_{\omega} T_{ph} I_m}{P} \right) \left(\frac{4}{\pi} B_m \sin \beta \right) \sin \delta \\
 &= 2\mu_0 \left(\frac{DL}{g_d} \right) \left(\frac{P}{2} \right) F_s F_m \sin \delta \quad (\text{N} \cdot \text{m}) \quad (1.83)
 \end{aligned}$$

where F_s is peak value of the resultant stator mmf per pole and derived earlier as

$$F_s = \frac{3}{2} \frac{k_{\omega} T_{ph} I_m}{P} 1q \quad (\text{amp-turns/pole}) \quad (1.84)$$

The magnet mmf, F_m , is given by Equation 1.82. The torque representation now is a cross product of the stator and rotor mmfs and containing the crucial physical dimensions given by bore diameter, stack length, and air gap, and number of poles in a given machine. The gearing effect of the pole pairs is evident in this expression, a preferred representation by practicing engineers.

1.6.5 MACHINE OUTPUT EQUATION

In spite of this fundamental torque expression, which gives a clear insight into the torque generation process, this may not be very handy in the design process as most of the designers prefer to express the torque in terms of the linear current density and air gap flux density due to magnet and machine bore volume, which lends itself to the initial design process in sizing the machine very quickly with very few calculations and to the well-known machine power output equation. It is derived in the following from the original torque expression.

Consider the definition of linear current density as ampere-conductors per meter of bore periphery with the current considered in its rms value. The total number of conductors in the three machine is $3(2T_{ph})$ as each turn has two conductors. It is distributed in the stator around a periphery of $2\pi r$ meters and hence the linear current density is defined to be

$$A_s = \frac{3(2T_{ph})}{2\pi r} I_s \quad (\text{amp-conductors/m}) \quad (1.85)$$

Accounting for the winding factor and only considering the fundamental value of the linear current density yields

$$A_{s1} = k_{\omega} A_s = k_{\omega} \frac{3(2T_{ph})}{2\pi r} I_s \quad (\text{amp-conductor/m}) \quad (1.86)$$

Substituting the mmf in terms of the linear current density in the torque, Equation 1.76 yields

$$\begin{aligned}
 T_e &= \frac{3}{2} \left(\frac{4}{\pi} k_{\omega} T_{ph} \right) (DL) (B_m \sin \beta) I_m \sin \delta \\
 &= \frac{3}{2} (DL) \left(k_{\omega} T_{ph} I_s \sqrt{2} \right) \left(\frac{4}{\pi} B_m \sin \beta \right) \sin \delta \\
 &= \frac{3}{2} \sqrt{2} (2rL) \left(\frac{2\pi r}{6} A_{s1} \right) (B_{m1}) \sin \delta \\
 &= \sqrt{2} (rL) (\pi r A_{s1}) (\sqrt{2} B_{mr}) \sin \delta \\
 &= (2\pi r^2 L) B_{mr} A_{s1} \sin \delta \quad (N \cdot m) \tag{1.87}
 \end{aligned}$$

where B_{mr} is the rms value of the B_{m1} and given as $B_{mr} = B_{m1}/\sqrt{2}$. The force generated is obtained from this [164] as

$$F = \frac{T_e}{r} = (2\pi r L) B_{mr} A_{s1} \sin \delta \quad (N) \tag{1.88}$$

Force manifests itself on the bore surface and accordingly the force density linking the force and surface area is of interest to designers and it is derived in those terms from Equation 1.88 as

$$F_d = \frac{F}{\text{surface area}} = \frac{F}{2\pi r L} = B_{mr} A_{s1} \sin \delta \quad (N/m^2) \tag{1.89}$$

From the force density expression given by Equation 1.89, its maximum can be derived easily as the maximum value of $\sin \delta$ can only be one and hence the maximum force density is $B_{mr} A_{s1}$ (N/m^2). Key observations can be made of these various important indices and the torque expression that have been derived and they are as follows:

1. Torque is the product of linear current density, air gap flux density due to magnet, and sine of the torque angle and proportional to twice the cylindrical volume of the bore when the linear current and air gap flux densities are expressed in rms values. If they are expressed in peak values, then the torque is only proportional to cylindrical volume as the multiplier 2 goes away.
2. The implication of this expression is that the torque is uniquely given by the volume of the bore and therefore, for a given size, it is easy to estimate once the torque capability of the machine. This is assuming that the other two variables of linear current and air gap flux densities are given.

3. The upper limits for linear current and air gap flux densities are available given the cooling arrangement and for specified magnets. For example, consider nominally the maximum flux density in the stator tooth is 1.6 T and for a slot width of 50% of the slot pitch, the air gap flux density can only be at 0.8 T. From these limits, it is easy to calculate the bore volume for the specified torque.
4. The force produced is only on the periphery of the rotor bore and it is proportional to the surface area of the rotor bore. This naturally leads to the realization that force density is the product only of air gap flux density, linear current density, and the sine of the torque angle. The maximum force density possible out of the machine is only equal to the product of the linear current and air gap flux densities. Such a theoretical maximum is important to determine so that initial sizing of the machine can be estimated in a shortest amount of time with the least amount of computation. It becomes handy when engineers are given power density specifications by the customers and they can quickly determine whether a PMSM is feasible for the required application.
5. The actual force density and hence the torque have to be adjusted for factors such as cooling arrangements and resulting current densities, magnet flux leakage, machine tolerances, etc. In spite of the assumptions surrounding these expressions, the fact that they have immense value in practical design is known to designers for a long time.

The output of a machine in terms of its key physical dimensions, speed, and electric and magnetic loadings enables sizing and initial design of the machine where the electric loading is seen as the linear current density. A particular cooling arrangement, for example, limits the linear current density and therefore for this condition, the machine dimensions in terms of the bore or inner stator diameter and length of iron, known as stack length, are to be determined. Of particular interest to the designer is the minimum value of the stack length and bore diameter from which they can compute the overall motor diameter and length of the machine for a given specification. This process is termed sizing. The understanding of the output equation is a standard first step in the machine design procedure and that provides a mechanism to bring the interplay of magnetic and electric loading capacities in determining the size of the machine. The electromagnetic torque multiplied by the mechanical rotor speed in rad/s gives the electromagnetic power (known as air gap power) output of the machine. Therefore, the air gap power of the machine is then

$$P_a = \omega_m T_e = (2\pi r^2 L) \omega_m B_{mr} A_{sl} \sin \delta \quad (1.90)$$

The factor 2 can be dispensed with using the peak instead of rms values for the flux and linear current densities. Then it is seen that the air gap power output is proportional to the bore volume. For a specified air gap power, with all other variables being constant, it can be inferred from this expression that the bore volume is inversely proportional to rotational speed. The key to machine size and volume

reduction is found here. The higher the rotational speed, the machine size and weight are smaller and vice versa is evident. In applications where both the weight and volume minimization are of prime requirements, it is usual to come across operational speeds in the range of 15,000–40,000 rpm such as in aircraft actuators.

1.6.6 EQUIVALENT MAGNET CURRENT

In some of the modeling of the PMSMs, the PMs are represented by a current source. This lends it to use the existing models of conventional synchronous machines with wound rotors with ease. Further, this provides a way to relate to calculating the demagnetizing current for the magnets. To enable those familiar with such modeling of machines, the magnet is modeled as a current source with a rms current I_{me} as follows. The peak fundamental magnet flux density is

$$B_{\text{m1}} = \frac{4}{\pi} B_{\text{m}} \sin \beta \quad (1.91)$$

This can be assumed to be produced by an equivalent three-phase winding of T_{ph} turns per phase, very similar to the stator, to counter the magnet flux density and its mmf has to be equal to

$$F_{\text{m}} = \frac{3}{2} \frac{T_{\text{ph}} I_{\text{mep}}}{P} \quad (1.92)$$

where I_{mep} is the peak current. The peak fundamental magnet flux density then can be rewritten as

$$B_{\text{m1}} = \mu_0 \frac{F_{\text{m}}}{g_{\text{d}}} = \mu_0 \frac{3}{2} \frac{\sqrt{2} I_{\text{mep}} T_{\text{ph}}}{g_{\text{d}} P} = \frac{4}{\pi} B_{\text{m}} \sin \beta \quad (1.93)$$

where

B_{m} is the magnet flux density

g_{d} is the effective air gap

the equivalent magnet current in its rms value, I_{me} , is

$$I_{\text{me}} = \frac{4\sqrt{2}}{3\pi} \frac{g_{\text{d}} P B_{\text{m}}}{\mu_0 T_{\text{ph}}} \sin \beta \quad (1.94)$$

The magnet operating flux density can be obtained from first principles described in Sections 1.1.2 and 1.6.4 and given in Equations 1.11 and 1.80 as

$$B_{\text{m}} = \frac{B_r (\ell_{\text{m}} / \mu_{\text{rm}})}{C \ell_g + \ell_{\text{m}} / \mu_{\text{rm}}} = \frac{B_r \ell_{\text{m}}}{g_{\text{d}} \mu_{\text{rm}}} \quad (1.95)$$

Substituting for the air gap along the magnet axis, g_d in the magnet equivalent current expression, the magnet equivalent rms current in terms of the remanent flux density, phase winding turns, magnet length and magnet arc is obtained as

$$I_{\text{me}} = \frac{4\sqrt{2}}{3\pi} \frac{PB_r \ell_m}{\mu_0 \mu_r T_{\text{ph}}} \sin \beta \quad (1.96)$$

1.6.7 SAFE PEAK STATOR CURRENT

The peak stator current is determined by the maximum current that will not demagnetize the magnets. That amounts to not allowing the operation to slide into the nonlinear part of the demagnetization characteristic, as shown in Figure 1.60 with the boundary being that between linear and nonlinear operating points given by (H_p, B_p) . Note that this operating point for a certain magnet resides in third quadrant of the B - H characteristic and B_p is negative. B_p is written as

$$B_p = \mu_0 \mu_r H_p + B_r \quad (1.97)$$

The stator current that can produce a flux density to counter this may be assumed as I_{sp} and that is peak current. Then the mmf produced by this current is

$$F_{\text{sp}} = \frac{3}{2} \frac{T_{\text{ph}} I_{\text{sp}}}{P} \quad (1.98)$$

Considering the path of the flux through magnets, stator iron, and two air gaps, the mmf in this closed path is zero and written as

$$2 \left[H_c \ell_m + F_{\text{sp}} + H_g \left(g_d + \frac{\ell_m}{\mu_r} \right) \right] = 0 \quad (1.99)$$

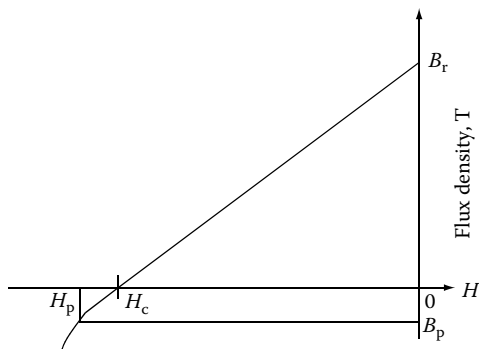


FIGURE 1.60 Demagnetization characteristic with maximum current operating point.

At peak operating condition the air gap field intensity is

$$H_g = \frac{B_p}{\mu_0} \quad (1.100)$$

The peak allowable flux density just before demagnetization obtained from Equation 1.97 assuming linear demagnetization characteristic is given by

$$B_p = (H_p - H_c) \mu_0 \mu_r \quad (1.101)$$

and then combining the above two Equations 1.100 and 1.101, the air gap filed intensity is

$$H_g = (H_p - H_c) \mu_r \quad (1.102)$$

From the mmf relationships given in Equations 1.97 and 1.98, the safe stator peak mmf is derived as

$$F_{sp} = (H_c - H_p) \mu_r \left(g_d + \frac{\ell_m}{\mu_r} \right) - H_c \ell_m = \frac{3T_{ph}}{2P} I_{sp} \quad (1.103)$$

Then the rms value of the maximum stator current is derived from it as

$$I_{sm} = \frac{I_{sp}}{\sqrt{2}} = \frac{\sqrt{2}P}{3T_{ph}} \left[g_d \mu_r (H_c - H_p) - H_c \ell_m \right] \quad (1.104)$$

This current is the absolute maximum that the machine can be subjected to under all circumstances. The magnet characteristics have to be for the operating temperature and not for nominal operational conditions must be kept in mind as coercive forces will become smaller with the result that the maximum stator current can vary from its nominal maximum value calculated for ambient conditions. Precautions must be in place to limit the fault currents within these limits so as to have the machine to resume operation after the fault is cleared. In critical applications, it may be required to coordinate the protection of the machine with online computation of maximum current allowable for all operating conditions by monitoring the temperature and accordingly using the correct magnetic characteristics in the computation and together with margins for tolerances in air gap and magnet length. Such monitoring and protection techniques may not cost much with software control except for the temperature sensors and most of them are very inexpensive. Winding factor is ignored in the effective number of turns plugged in Equation 1.104 but that only makes the peak current computation conservative, which is good from a design point of view.

1.6.8 INDUCTANCES

Machine models depend on phase inductances [102–113] and also on the direct and quadrature axis inductances. Analytical derivations relating the machine dimensions to various inductances are the most important information that designers require to provide them to power conversion and control engineers to do their respective tasks. These expressions are developed from first principles and their accuracy is fairly astonishing given the simplicity of their derivations with all the assumptions. But it is not surprising as the air gap in the PM machines are far more than that of other machines because of manufacturing constraints and the magnets have permeabilities that are close to that of air, resulting in high air gap and magnet path reluctance for this machine. The high reluctance due to the air gap is more dominant than that of the iron in these machines in comparison to other machines whose reluctance is not simple to compute. Therefore, higher accuracy is made possible in predicting these machine inductances. To make these derivations, basics such as representation of sinusoidal distributed winding, flux in a winding turn, and the mutual flux linkage associated with a winding due to a flux in the air gap or magnets have to be derived for easier sailing through this section. They are considered in the subsections (a), (b), and (c) as follows:

(a) *Sinusoidal winding distribution*: It is shown in figure under two poles in Figure 1.61. The conductors are distributed with sinusoidal weighting of turns and let the total number of turns in the phase is equal to T_{ph} . It can be represented for an arbitrary spatial position θ by

$$N_s(\theta) = \frac{T_{ph}}{2} \cos(P_p \theta) \quad (1.105)$$

where P_p is the number of pairs of poles. The total number of conductors can be obtained by integrating the above expression from its lower to upper limits as

$$\text{Conductors per pole} = \int_{-(\pi/2P_p)}^{\pi/2P_p} N_s(\theta) d\theta = \int_{-(\pi/2P_p)}^{\pi/2P_p} \frac{T_{ph}}{2} \cos(P_p \theta) d\theta = \frac{T_{ph}}{P_p} \quad (1.106)$$

Therefore, the total number of turns in a pole pair is equal to the number of conductors in it divided by 2. That gives the total number of turns per pole pair as T_{ph}/P_p .

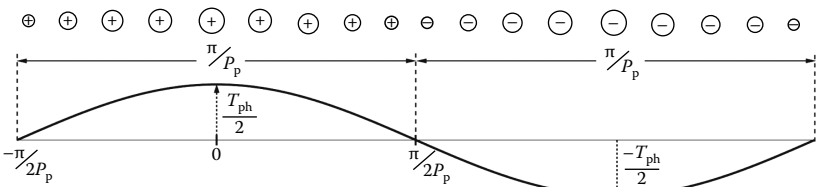


FIGURE 1.61 Sinusoidal distribution of winding.

(b) *Flux linkage in a turn:* The flux linkage in a turn is nothing but the flux connecting to a winding turn. It is obtained from flux density, stack length, and bore radius as

$$\lambda_t = \int_{\theta}^{\theta + \pi/P_p} B(\theta) Lr d\theta \quad (1.107)$$

where

λ_t is the flux linkage in a turn

$B(\theta)$ is the flux density at a given electrical spatial position

L is the stack length

r is the bore radius. The flux density can be represented in the air gap as

$$B(\theta) = B_{pk} \cos(\omega t + \alpha - P_p \theta) \quad (1.108)$$

where

ω is the electrical rotor speed

α is the angle between the center of the pole or d-axis of the magnet and stator phase winding

Then the flux linkage in the turn or the flux in the turn is given by substituting for the flux density in the integral equation over a pole as

$$\begin{aligned} \lambda_t &= \int_{-(\pi/2P_p)}^{\pi/2P_p} B(\theta) Lr d\theta \\ &= \int_{-(\pi/2P_p)}^{\pi/2P_p} B_{pk} \cos(\omega t + \alpha - P_p \theta) Lr d\theta \\ &= 2 \frac{B_{pk} Lr}{P_p} \sin(\omega t + \alpha - P_p \theta) \\ &= \phi_m \sin(\omega t + \alpha - P_p \theta) \end{aligned} \quad (1.109)$$

where on inspection, the peak flux in the turn or flux linkage associated with a turn is given by

$$\phi_m = 2 \frac{B_{pk} Lr}{P_p} = \frac{B_{pk} DL}{P_p} = \frac{B_{pk} DL}{\frac{P}{2}} = 2 \frac{B_{pk} DL}{P} \quad (1.110)$$

where

D is the bore diameter

P is the number of poles

(c) *Mutual flux linkage between flux on the rotor or air gap and stator winding:* In the previous derivation, the flux per turn was evaluated for specific values and instead, it may be derived for any stator spatial and rotor position as in the following and then it could be used to compute the entire flux linkage in the stator phase winding due to rotor magnet flux or due to its own or due to the resultant mmf of the stator windings. The flux linkage for a turn covering arbitrarily any spatial position over a pole is

$$\begin{aligned}\lambda_t &= \int_{-\pi}^{\theta+\pi/P_p} B_{pk} \cos(\omega t + \alpha - P_p\theta) Lr d\theta \\ &= -2 \frac{B_{pk} Lr}{P_p} \sin(\omega t + \alpha - P_p\theta) \\ &= -\phi_m \sin(\omega t + \alpha - P_p\theta)\end{aligned}\quad (1.111)$$

The flux linkage in the entire stator phase winding is derived from the flux linkage in a turn by multiplying it with the sinusoidal distributed winding and integrating them over a pole. The result has to be multiplied by pairs of poles so that all the turns for them are included in the flux linkage computation. It is given as

$$\begin{aligned}\lambda_{ma} &= P_p \int_{-(\pi/2)}^{\pi/2} N_s(\theta) \lambda_t \\ &= P_p \int_{-(\pi/2)}^{\pi/2} \frac{T_{ph}}{2} \cos(P_p\theta) \{-\phi_m \sin(\omega t + \alpha - P_p\theta)\} d\theta \\ &= \frac{\pi T_{ph}}{4} \phi_m \sin(\omega t + \alpha)\end{aligned}\quad (1.112)$$

The results of the three subsections are used in the following to compute the self, magnetizing, and then the direct axis inductance of the PMSM. The self-inductance is defined as the inductance of a phase winding due to its own excitation with all other phases not being excited. Consider effective turns per phase for fundamental, N_{ph} , instead of the number of turns per phase winding, T_{ph} , in all derivations. Note that, for a distributed winding, the effective number of turns per phase is

$$N_{ph} = k_{wl} T_{ph} \quad (1.113)$$

In the case of full-pitch winding because of rectangular mmf distribution, the effective number of turns for fundamental only is

$$N_{ph} = \frac{4k_{wl} T_{ph}}{\pi} \quad (1.114)$$

Therefore, care must be exercised to use these values for specific windings in the machines.

1.6.8.1 Self-Inductance per Phase

The self-flux linkages of a winding due to its own excitation is computed from the air gap flux linkage per turn and then using it to obtain the phase flux linkages as using the subsection (c) result and substituting appropriately:

$$\lambda_{aa} = \frac{\pi N_{ph}}{4} \phi_g \quad (1.115)$$

where ϕ_g is the air gap flux and similar to ϕ_m given by

$$\phi_g = 2 \frac{B_g D L}{P} \quad (1.116)$$

and the peak air gap flux density is computed from the phase mmf and air gap as

$$B_g = \mu_o H_g = \mu_o \frac{N_{ph} I_m}{P l_g} \quad (1.117)$$

Combining the three expressions, the self-flux linkages of phase a are

$$\lambda_{aa} = \frac{\pi}{4} \mu_o \frac{Lr}{l_g} \left[\frac{N_{ph}}{P_p} \right]^2 I_m \quad (1.118)$$

from which the self-inductance per phase is derived as

$$L_{aa} = \frac{\lambda_{aa}}{I_m} = \frac{\pi}{4} \mu_o \frac{Lr}{l_g} \left[\frac{N_{ph}}{P_p} \right]^2 (H) \quad (1.119)$$

1.6.8.2 Magnetizing Inductance

It is defined as the phase inductance due to resultant mmf from excitation in all phases. The only difference between this and the self-inductance is that the mmf is the resultant mmf and its value in a three-phase machine is equal to 1.5 times the value of single-phase mmf. This changes the flux density, flux, and then the flux linkages of the single-phase excitation case results to uniformly 1.5 times. The magnetizing inductance consequently is 1.5 times that of the self-phase inductance and given by

$$L_{ma} = L_{aa} = \frac{\lambda_{ma}}{I_m} = \frac{3\pi}{8} \mu_o \frac{Lr}{l_g} \left[\frac{N_{ph}}{P_p} \right]^2 (H) \quad (1.120)$$

1.6.8.3 Synchronous Inductance

Synchronous inductance is the sum of the phase-magnetizing inductance and phase leakage inductance. The calculation of leakage inductance is omitted here and it may be used from standard texts. Negligence of leakage inductance in computations hardly affects results in many practical cases and for initial designs their computations are not usually resorted to.

1.6.8.4 d- and q-Axes Inductances

The machine model developed in Chapter 3 has two axes, known as direct and quadrature axes. Correspondingly the machine inductances and parameters have to correspond to this axis with stator windings on the axis. This will be elaborated later, but the inductances are derived here to exploit the continuity in development of inductances in this section. The d-axis equivalent air gap is given by Equation 1.81 and is denoted as g_d from here. The d-axis winding is considered to have $(3/2)T_{ph}$ turns, distributed sinusoidally, having a current i_{ds} generating a mmf:

$$F_d = \frac{3}{2} \frac{T_{ph}}{P} i_{ds} \sin \theta \quad (1.121)$$

From this expression, the d-axis flux density is obtained as

$$B_d = \mu_0 \frac{F_d}{g_d} = \frac{\mu_0}{g_d} \frac{3}{2} \frac{T_{ph}}{P} i_{ds} \sin \theta \quad (1.122)$$

The flux is given by

$$\phi_d = B_d A_c \quad (1.123)$$

where A_c is the area of the cross-section as seen by the flux per pole given by

$$A_c = \frac{2LD}{P} \quad (1.124)$$

The flux linkages is derived as

$$\lambda_d = \frac{\pi}{4} \left(\frac{3}{2} T_{ph} \right) \phi_d \quad (1.125)$$

The $\pi/4$ factor appears because the flux and the conductor distribution are sinusoidal and integrating their product gives $\pi/4$ times the apparent flux linkages as shown in subsection result (b) and (c). The direct axis inductance is derived by combining equations from Equations 1.122 to 1.125 and can then be written as

$$L_d = \frac{\lambda_d}{I_{ds}} = 1.125\pi\mu_0 \left(\frac{T_{ph}}{P} \right)^2 \frac{DL}{g_d} \quad (1.126)$$

This result [102] is kept in the same form that was made originally so that readers can see the identity. The same result is obtained by substituting for change in effective number of turns in d axis from N_{ph} to $1.5N_{ph}$, in Equation 1.118 resulting in

$$L_d = \left(\frac{3}{2} \right)^2 L_{aa} = \left(\frac{3}{2} \right)^2 \frac{\pi}{4} \mu_o \frac{Lr}{\ell_g} \left[\frac{T_{ph}}{P_p} \right]^2 \quad (1.127)$$

By substituting for pairs of poles in number of poles and converting the radius to diameter, it is seen that the expressions for direct axis inductance are identical.

Similarly the q-axis inductance is found as

$$L_q = 1.125\pi\mu_0 \left(\frac{T_{ph}}{P} \right)^2 \frac{DL}{g_q} \quad (1.128)$$

where g_q is the air gap in the q-axis and it equals the air gap only as it does not contain the magnet. Quadrature axis air gap, g_q is, therefore, much smaller than that on the direct axis equivalent air gap, g_d , with the result that the quadrature axis inductance is always higher than that of the direct axis inductance in PMSMs.

Machine parameters such as inductances and rotor flux linkages are required to develop the equivalent circuits from which the performance of the machines can be predicted. The development of equivalent circuits for machines and steady state [157–160] and dynamic performance computations are given in later chapters.

1.6.9 EFFECT OF STATOR EXCITATION ON AIR GAP FLUX DENSITY

The stator excitation is usually neglected in the core loss estimation by considering only the flux density due to rotor magnets alone. It is valid at low loads where the stator excitation is very small. At normal and higher stator excitations, the flux densities in various parts of the stator body vary significantly from the flux densities due to the rotor magnets alone demonstrated here. Effective air gap between the stator and rotor is computed from air gap, and magnet thickness and its relative permeability. The stator mmf phasor is positioned from the rotor flux density by the control angle, δ , and it is used to derive the air gap flux density due to stator mmf. Then the sum of the rotor flux density and the air gap flux density due to the stator excitation gives the resultant air gap flux density. Three such plots for the control angles of -90° , -120° , and -180° are shown in Figure 1.62a through c. The magnet arc is 120° for these plots. The control angles considered correspond to regeneration in the machine and likewise the plots for motoring are similar and can be obtained by the same procedure. Few observations are in order and they are as follows:

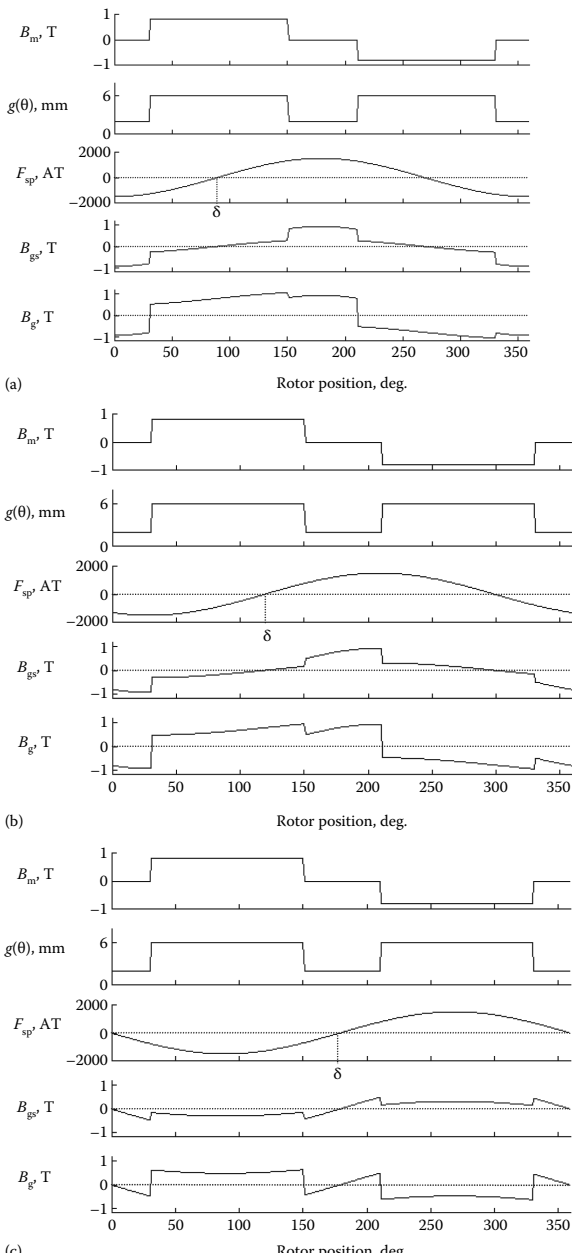


FIGURE 1.62 Air gap flux density waveforms for various control angles with stator excitation: (a) $\delta = -90^\circ$; (b) $\delta = -120^\circ$; (c) $\delta = -180^\circ$.

1. The air gap flux density is no more rectangular and it has additional variations at 150° and 330° . The consequence of such additional variations is that the eddy current losses increase in the machine. It is apparent from the tooth and air gap flux densities plotted for -120° control angle and shown in Figure 1.63.
2. The air gap flux density is considerably reduced for control angle of -180° and shows a decreasing trend from -90° onward. This clearly indicates that it is the only way by which flux weakening is possible in these machines. Such a flux weakening has the consequence of diverting the stator current to reduce the flux density due to the rotor magnets and therefore a part of the stator current is not usually available for torque generation in its entirety. Stated in another way, to produce the same torque under flux weakening condition as under constant flux operation, the stator current has to increase in this machine. It is in contrast to other machines where the stator current may decrease or stay the same to produce the flux weakening while maintaining the same torque. This is a big drawback with these machines in flux-weakening operational range.
3. The air gap torque resulting from the interaction of the air gap flux density and stator excitation will hardly be constant over an electrical cycle as the flux density is neither purely sinusoidal nor rectangular and when they interact with stator excitations that are sinusoidal or rectangular, invariably harmonic torque ripples appear. Such harmonic torque components could be easily eliminated if the air gap flux density is either sinusoidal or rectangular, which is not possible and in that case modifying the stator excitation to yield constant torque is an option. A deterioration of electromagnetic torque performance is inevitable because of air gap flux density distortion due to stator excitation.

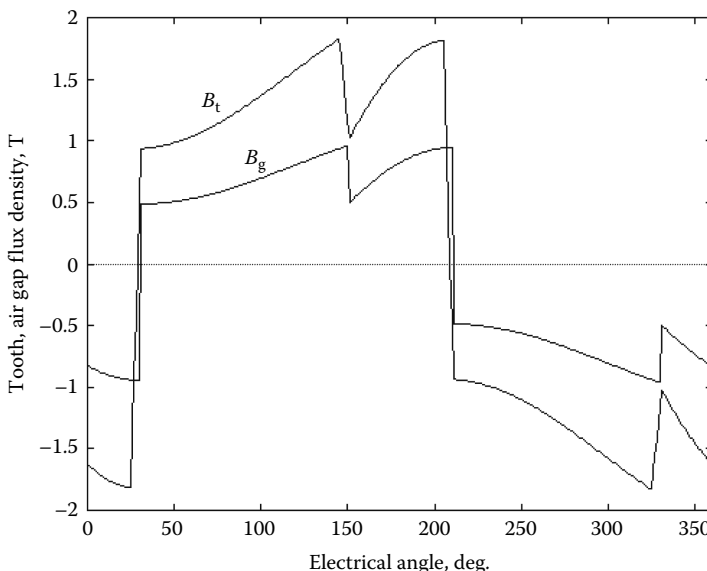


FIGURE 1.63 Tooth and air gap flux densities for -120° control angle.

Saturation of the iron may occur at higher operating currents and for certain torque angle operation. Usually saturation reduces the torque constant and inductances and invariably increases the core losses [122–126]. Reduction of torque constant in saturation means that the torque per input ampere is not at the same level it is at when saturation does not occur. It is a good practice not to operate machines in deep saturation.

1.7 CORE LOSSES

Core losses are not negligible in PMSMs and brushless dc machines. Given the literature [127–145] and mostly lack of it on this topic, engineers may be persuaded to think otherwise. It can be computed either with finite element analysis techniques using one of the commercially available softwares or by using analytical expressions. The former approach is suitable if the final machine dimensions are available and only one computation needs to be made for core losses. It becomes obvious immediately that is time consuming for optimization of machine and inevitable that the analytical route is more productive. Further the designers need to relate the physical dimensions and material characteristics to core losses to gain an understanding to minimize them by innovations in the machine itself and in the suitable selection of materials too. Machine design optimization becomes even easier with this route as it involves only seconds for each iteration as compared to minutes (two-dimensional cases) or even hours (three-dimensional cases) with the finite element analysis methods. To facilitate the understanding of the core losses, the analytical approach is embraced in the following presentation. Only stator core losses are being dealt in the treatment. The rotor core losses are not taken up for the simple reason that ideally there are no flux reversals in the back iron and therefore no significant losses can occur in it and in the small teeth section of the interstice between the magnets facing the air gap. But such is not the case in high-speed applications for it not only has core losses but also has pole face losses due to current harmonics injected in the stator windings, which get reflected on the magnets. Usually for low-speed machines with low pole numbers, it is not unusual to ignore them for the initial design or sizing. Then it is incorporated during fine-tuning of the final design either by analytical or finite element techniques. For computation of rotor core losses strictly in the iron, the approach for the stator core losses computation may be gainfully used. As for pole face losses, it is entirely a different issue and it is left to the reader to delve into it in existing literature and in-house design procedures.

1.7.1 STATOR CORE LOSSES

The core losses in the machine have two components, i.e., hysteresis and eddy current losses. The core losses occur due to time variations in flux density experienced in the core. The hysteresis loss is the result of the inherent B – H material characteristics and is proportional to the product of frequency and flux density with the flux density raised to a power n , generally termed as Steinmetz constant. When the lamination cores experience a change in the flux density because of a change in the flux and hence flux linkages. Note that the flux is equal to the product of the flux density and the area of the cross-section of the core. As the flux linkage changes with time, the cores have an emf induced in

them. The induced emf generates a current in the core depending on the resistance of the core, resulting in losses that are termed the eddy current losses. To evaluate the eddy current losses, it is important to find the emf induced in the core and hence necessary to calculate flux densities in the various parts of the core. The eddy current losses are then proportional to the square of the induced emf and hence proportional to square of the product of frequency and flux density. Then the eddy current loss is

$$P_{ed} \propto (f_s B_p)^2 \propto (\omega_s B_p)^2 \quad (1.129)$$

which then can be written as

$$P_{ed} = k_e \omega_s^2 B_p^2 \text{ (W/unit weight)} \quad (1.130)$$

where

k_e is the loss proportionality constant that accounts for volume to weight conversion and all other particular constants associated with magnetic materials

B is the peak flux density and fundamental angular frequency of applied voltage is ω_s

Based on Equation 1.130, the steel manufacturers provide eddy current loss per unit weight, say in W/kg, versus peak flux density for various frequencies. From these manufacturer's graphs and data, the eddy current loss proportionality constant can be computed for a given flux density and frequency.

Hysteresis loss arises from energy lost in core material in its $B-H$ loop for each cycle of operation and therefore it is directly dependent on operating frequency. But the area enclosed in the core material's $B-H$ loop from fundamentals is known to be energy loss density per unit volume and it is proportional to the operating flux density as well as to frequency. Then the hysteresis loss, in general, can be represented in Watts per unit weight, say, W/kg, in line with the manufacturer's data sheets, as

$$P_{hd} = k_h \omega_s B_p^n \text{ (W/unit weight)} \quad (1.131)$$

where

k_h is hysteresis loss density proportionality constant

n is known as Steinmetz constant

The value of n ranges from 1.5 to 2.5 and is dependent on peak operating flux density and material characteristics.

The total core loss/unit weight (which is core loss density) is the sum of the eddy current and hysteresis loss components and given as

$$P_{cd} = P_{hd} + P_{ed} \quad (1.132)$$

A partial surface-mounted PMSM is shown in [Figure 1.64](#) for illustration of flux distribution in the machine. The no load tooth and back iron or yoke flux densities are shown in [Figure 1.65](#). The flux densities have finite changes and do not have discontinuities as shown in the approximated diagram but will be rounded off with smooth

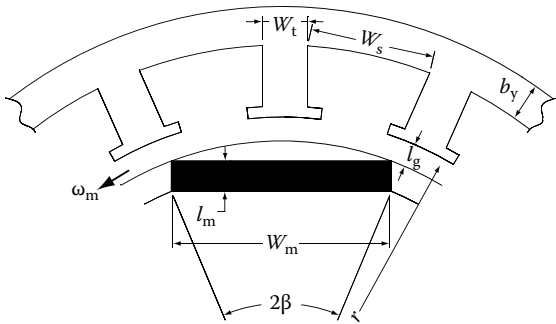


FIGURE 1.64 Surface mounted PMSM details for core loss computation.

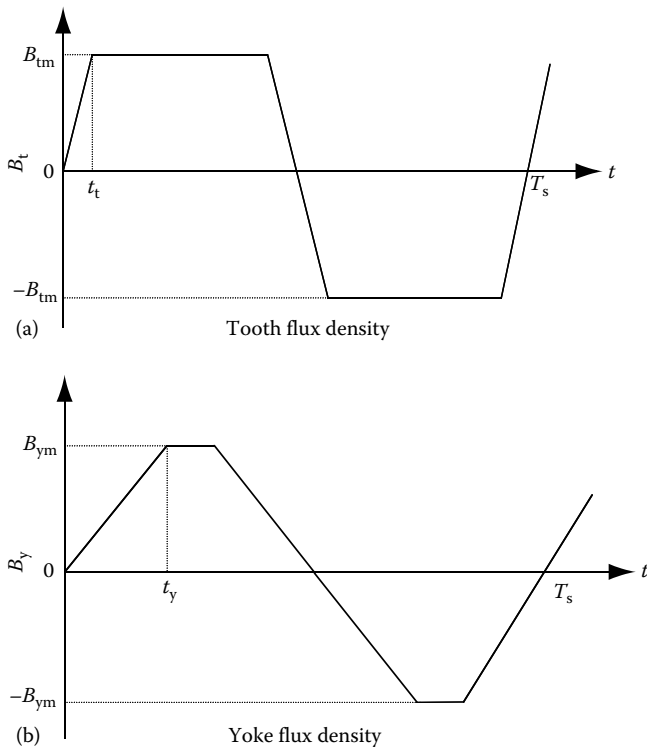


FIGURE 1.65 Tooth and yoke flux density waveforms.

changes in the corners. Note that the rotor flux density does not undergo changes and hence ideally the rotor core losses are nonexistent. Therefore, the core losses occur in the stator iron alone. Note that there are rotor pole face losses due to the stator time harmonic fields produced by the stator excitation. For the present, these losses are ignored in this treatment.

1.7.2 EDDY CURRENT LOSSES

Eddy current losses occur in the stator teeth and back iron of the stator. The effect of rotational losses due to the rotation of the flux density in the back of the teeth is yet to be fully understood and documented. Therefore, for this matter, it is not considered in this chapter any further. The eddy current losses have been traditionally derived assuming a sinusoidal flux density. The average eddy current loss is calculated as follows [137]. Let the instantaneous flux density in a part of the iron is

$$B = B_p \sin \omega_s t \quad (1.133)$$

and its rate of change is given by

$$\frac{dB}{dt} = \omega_s B_p \cos \omega_s t \quad (1.134)$$

The average eddy current loss density is then given by

$$\left(\frac{dB}{dt} \right)_{av}^2 = \frac{1}{2\pi} \int_0^{2\pi} \left(\frac{dB}{dt} \right)^2 d(\omega_s t) = \frac{(\omega_s B_p)^2}{2\pi} \int_0^{2\pi} \cos^2(\omega_s t) d(\omega_s t) = \frac{(\omega_s B_p)^2}{2} \text{ (W/kg)} \quad (1.135)$$

Substituting for the square of the product of the frequency and peak flux density from Equation 1.130 in terms of the eddy current loss density and its proportionality constant in the right-hand side of Equation 1.34, the eddy current loss density in terms of the rate of change of flux density is derived as

$$P_{ed} = 2k_e \left(\frac{dB}{dt} \right)_{av}^2 \text{ (W/kg)} \quad (1.136)$$

This formulation with rate of change of flux density is quite useful when the flux density deviates from sinusoid as in the case of the PMSM and it is adapted in the analytical approach derived in this section. Further the flux density only due to PMs is considered in this approach and the flux density contribution due to stator winding excitation is ignored in this section but has been discussed in Section 1.6.9. This method of deriving the eddy current losses is primarily the work of Slemmon and Liu [137]. Results neglecting the effect of stator excited flux density are proven to correlate with measured results keeping the torque angle of 90° only. From the earlier flux density plots, it can be seen that the rate of change of air gap flux density is marginally affected for this particular torque angle as compared to operation with torque angles other than 90°. In interior PMSM, and even in surface mount PMSM, there is a great advantage in operation with torque angles greater than 90° and it is proven in later chapters. Then under these circumstances, this simplified analysis for eddy current loss and hence core loss calculation may not hold. In spite of such a shortcoming, the analytical method has the benefit of relating the machine dimensions and variables to core losses providing an insight into core loss

reduction during the design stage of the machine itself with appropriate machine design changes.

The steel manufacturers give the core loss density data in terms of the W/kg and to correspond with the data sheets, the core loss can be represented using Equations 1.35 and 1.36 as

$$P_e = (\rho_i V) P_{ed} = (\rho_i V) k_e (\omega_s B_p)^2 = (\rho_i V) 2k_e \left(\frac{dB}{dt} \right)_{av}^2 \quad (1.137)$$

where

ρ_i is the mass density of the steel core material in kg/m³

V is the steel core volume in m³ and their product gives the weight of the core material in kg

In the following, eddy current losses in the stator teeth and yoke are derived first and then hysteresis loss is estimated. Both of them require computation of peak tooth and yoke flux densities, which, in turn, are computed from the air gap flux density. An illustrated example from [137] is given to smooth any computational glitch in the understanding. The calculation of loss coefficients is also discussed in brief. Core loss measurement is introduced to enable engineers plan experiments.

1.7.2.1 Eddy Current Loss in Tooth

The tooth flux density rises from zero to a peak value of B_{tp} , shown in Figure 1.65a as the leading edge of the rotor magnet, say, north pole passes by the tooth. When the tooth is fully covered by the magnet, its flux density does not change and remains constant at B_{tp} until the magnet's trailing edge starts to leave the tooth when the flux decreases from B_{tp} to zero. Similar is the case for the south pole passing by the tooth but its flux density is of opposite polarity and its shape is identical to that of the previous case. The time taken for the tooth flux density to change from zero to its peak value is t_t and given by

$$t_t = \frac{\text{Width of tooth}}{\text{Rotor velocity}} = \frac{W_t}{r\omega_m} = \frac{W_t \frac{P}{2}}{r\omega_s} = \frac{PW_t}{2r\omega_s} \quad (1.138)$$

where

r is the air gap radius

ω_m and ω_s are the mechanical rotor and electrical stator angular frequencies, respectively

W_t is the tooth width

The rate of change of flux density, then, is given by

$$\frac{dB}{dt} = \frac{B_{tm}}{t_t} = \frac{2r\omega_s}{PW_t} B_{tm} \quad (1.139)$$

In one electrical cycle, it is seen that there are four such variations in flux density and during these times, the eddy current loss occurs. The time duration for which the eddy current loss happens in a fraction of the fundamental electrical cycle and expressed in terms of the eddy current loss duty cycle in tooth derived as

$$d_{et} = \frac{4t_t}{T_s} = 4 \frac{PW_t}{2r\omega_s} \frac{1}{\frac{1}{f_s}} = 2 \frac{PW_t}{r\omega_s} \frac{\omega_s}{2\pi} = \frac{PW_t}{\pi r} \quad (1.140)$$

Therefore, the eddy current loss in the tooth can be written as

$$P_{et} = \rho_i V_t \left\{ 2k_e \left(\frac{dB}{dt} \right)_{av}^2 \right\} d_{et} = \frac{8k_e \rho_i V_t}{\pi} \left(\frac{r}{PW_t} \right) (\omega_s B_{tm})^2 \text{ (W)} \quad (1.141)$$

where

ρ_i is the mass density of the tooth steel given in kg/m³

V_t is the volume of the teeth in m³

Note that the rate of change of flux density and the duty cycle are substituted in terms of machine dimensions and variables to yield the final expression.

It can be seen that eddy current loss can be reduced significantly by varying the rate of change of flux density in the teeth. It can be achieved in two ways:

1. *Shaping the rotor magnets:* Such an action has the effect of making the flux density sinusoidal, which in turn has a lower rate of change compared to the trapezoidal tooth flux density. Then the eddy current loss amounts to

$$P_{ets} = k_e \rho_i V_t (\omega_s B_{tm})^2 \text{ (W)} \quad (1.142)$$

2. *Optimization of number of slots and slot width:* Decreasing the slot numbers per pole and making the slot width equal to tooth width reduces the eddy current loss nearly to that of the loss with sinusoidal tooth flux density. As the number of slots is made close to the number of poles, the tooth flux density becomes close to a triangular wave with the smooth top of a sinusoid. Hence its rate of change is much reduced in comparison to the trapezoidal flux density.

The effect of optimizing the slot number and slot opening is demonstrated as follows. Let N_{sp} is the number of slots per pole and the width of the slot is k_s times the width of the tooth. Then the tooth width is related to the air gap radius by

$$2\pi r = N_{sp} P (W_t + W_s) = N_{sp} P (1 + k_s) W_t \quad (1.143)$$

which on substitution in eddy current loss equation results in

$$\begin{aligned}
 P_{et} &= \left(\frac{4k_e \rho_i V_t}{\pi^2} \right) N_{sp} (1+k_s) (\omega_s B_{tm})^2 \\
 &= (k_e \rho_i V_t) (\omega_s B_{tm})^2 \left[\frac{4}{\pi^2} N_{sp} (1+k_s) \right] \\
 &= P_{ets} \left[\frac{4}{\pi^2} N_{sp} (1+k_s) \right]
 \end{aligned} \tag{1.144}$$

where P_{ets} is the eddy current loss in the tooth with a sinusoidal flux density. The ratio of the eddy current loss between trapezoidal and sinusoidal tooth flux density distribution then is derived as

$$\frac{P_{et}}{P_{ets}} = \frac{4}{\pi^2} N_{sp} (1+k_s) \tag{1.145}$$

This shows clearly that eddy current loss in tooth can be made equal to that of the sinusoidal flux density case if the number of slots per pole is reduced close to one (but never to one), which is not uncommon in many PM brushless dc machines and the slot width is made equal or preferably less than the tooth width, which is also prevalent in practice. The effect of slot per pole and the ratio between the slot and tooth width on eddy current loss is shown in Figure 1.66. Machines with higher

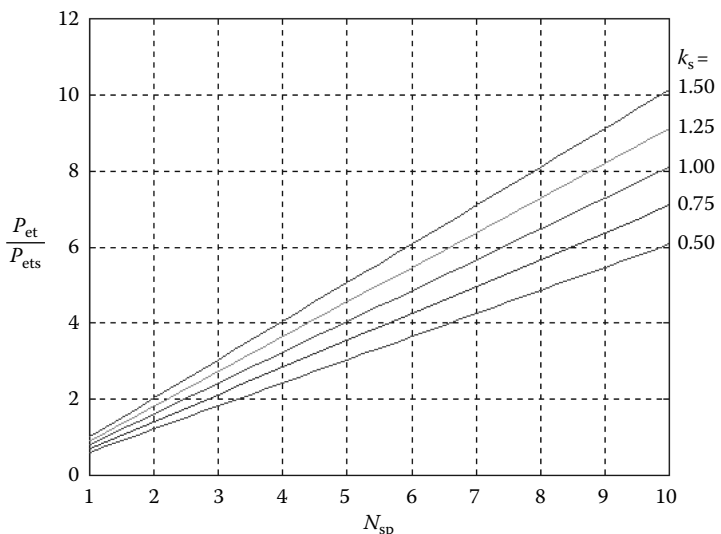


FIGURE 1.66 Tooth eddy current loss ratio versus number of slots per pole versus ratio of slot to tooth width.

slots per pole and trapezoidal flux density in the teeth have multiple times the eddy current loss of the machines with sinusoidal flux density distribution in their teeth. A higher number of slots per pole is preferable to obtain a near sinusoidal-induced emf in the machine phases but it is highly undesirable considering tooth current eddy loss.

1.7.2.2 Eddy Current Loss in Yoke

The flux density in the yoke is approximated as a trapezoidal waveform and shown in Figure 1.65b. Consider a point on the yoke. As north pole comes toward it, the flux density is falling from a maximum value B_{ym} to zero when half of the rotor magnet pole arc passes this point. Then for the other half of the pole arc passing, the flux density falls from zero to negative maximum, $-B_{ym}$. After that the flux density remains constant at $-B_{ym}$ until the south pole of the magnet comes across the point. Therefore, the time taken for the flux density to rise from zero to B_{ym} is derived as

$$t_y = \frac{\text{Half width of magnet}}{\text{Rotor velocity}} = \frac{W_m/2}{r\omega_m} = \frac{\left(\frac{2\beta r}{2}\right)P}{r\omega_s} = \frac{P\beta}{2\omega_s} \quad (1.146)$$

where 2β is the magnet arc in electrical degrees. The total time for flux density changes is $4t_y$ in one electrical cycle and the rate of change of flux density therefore is given by using Equation 1.146:

$$\frac{dB_y}{dt} = \frac{B_{ym}}{t_y} = 2 \frac{B_{ym}\omega_s}{P\beta} \quad (1.147)$$

The eddy current loss in the yoke then is given by

$$P_{ey} = \rho_i V_y \left[2k_e \frac{4t_y}{T_s} \left(\frac{dB_y}{dt} \right)_{av}^2 \right] = k_e \rho_i V_y \left[\frac{8}{\pi\beta} (\omega_s B_{ym})^2 \right] \quad (1.148)$$

Compared to a sinusoidal flux density eddy current loss, the trapezoidal yoke flux density based eddy current loss can be derived as

$$P_{eyn} = \frac{P_{ey}}{P_{eys}} = \frac{k_e \rho_i V_y \left[\frac{8}{\pi\beta} (\omega_s B_{ym})^2 \right]}{k_e \rho_i V_y (\omega_s B_{ym})^2} = \frac{8}{\pi\beta} \quad (1.149)$$

The normalized yoke eddy current loss versus magnet arc is shown in Figure 1.67. Beyond a magnet arc of 145° , the eddy current loss decreases in comparison to the sinusoidally distributed flux density-based eddy current loss in the yoke. The loss ratio falls within a range of 1.7–2.8 p.u. during the usual design range for magnet arcs.

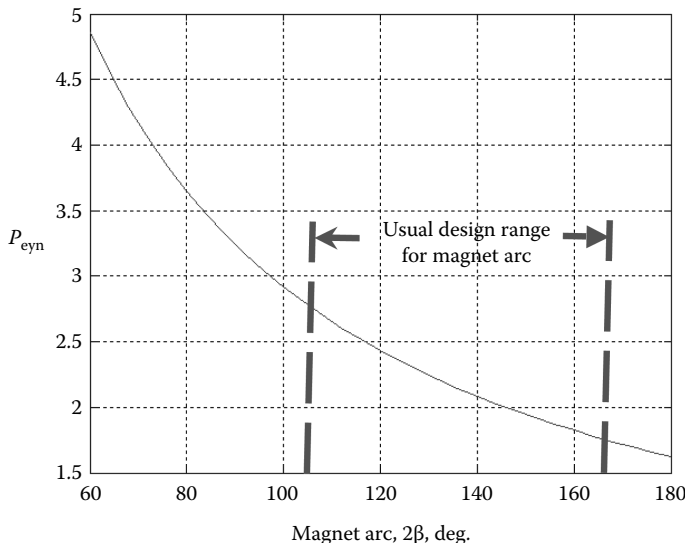


FIGURE 1.67 Normalized yoke eddy current loss versus magnet arc.

1.7.3 EVALUATION OF PEAK TOOTH AND YOKE FLUX DENSITIES

The maximum flux densities in the tooth and yoke are evaluated from the residual magnet flux density and average flux density. The average air gap flux density can be derived from the residual magnet flux density using the permeance coefficient of the magnetic circuit explained elsewhere. Let g be the effective air gap length on the magnet axis taking into account the effects of slotting with Carter's coefficient. Then the average air gap flux density is derived as

$$B_g = \frac{B_r}{1 + \mu_{rm} \frac{g}{l_m}} \quad (1.150)$$

The peak tooth flux density, neglecting fringing, can be approximated by making use of the fact that the air gap flux over a slot pitch enters the tooth and is carried in it. It is given as

$$B_{tm} = \frac{W_t + W_s}{W_t} B_g \quad (1.151)$$

where W_t and W_s are the tooth and slot widths, respectively. Similarly, the peak yoke flux density is found by equating the air gap and yoke flux obtained multiplying their flux densities with their respective areas of cross-section as

$$B_{ym} = \frac{W_m}{2b_y} B_g \quad (1.152)$$

where

- W_m is the width of the magnet
- b_y is the back iron thickness

1.7.4 HYSTERESIS LOSSES

The hysteresis losses of the tooth and yoke of the stator are found using the following equations:

$$P_{hs} = k_h \rho_i [V_t B_{tm}^n + V_y B_{ym}^n] \omega_s \quad (W) \quad (1.153)$$

where

- k_h is the hysteresis loss density
- n is the Steinmetz constant

They, together with k_e , are obtained from magnetic steel manufacturer's data by using the general core loss density formulation of

$$P_{cd} = P_{hd} + P_{cd} = k_h \omega_s B_p^n + k_e \omega_s^2 B_p^2 \quad (W/kg) \quad (1.154)$$

The constants may be extracted by curve fitting the data. It is not unusual to design a machine for frequencies at which manufacturer's core loss test data may not be available. In that case, an experimental setup to measure the core loss of the laminations at desired frequencies is unavoidable. The accurate determination of the core losses is very crucial in high-speed machine designs as it will be much more significant than that of other losses in the machine.

Example 1.3

Consider the machine and steel data given in [167]. Compute the stator core losses versus speed in rpm using the analytical expressions derived in the above. The machine details are

- Air gap radius, $r = 58.5$ mm
- Stack length, $L = 76$ mm
- Outer stator diameter, $D_o = 95$ mm = $2r_o$
- Yoke thickness, $b_y = 17.4$ mm
- Tooth depth, $t_h = 17.2$ mm
- Tooth width, $W_t = 5.3$ mm
- Effective air gap = 2 mm
- Magnet thickness, $l_m = 6.3$ mm
- Magnet arc, $2\beta = 120^\circ$ electrical
- Number of slots, $N_s = 36$
- Number of poles, $P = 4$
- Air gap flux density, $B_g = 0.79$ T
- Peak tooth flux density, $B_{tm} = 1.53$ T
- Peak yoke flux density, $B_{ym} = 1.2$ T
- Hysteresis loss density, $k_h = 5.8 \times 10^{-3}$

Eddy current loss density, $k_e = 9.3 \times 10^{-6}$

Steinmetz constant, $n = 1.93$

Steel mass density, $\rho_i = 7650 \text{ kg/m}^3$

Solution

$$\text{Teeth volume} = N_s W_t t_h L = 2.494 \times 10^{-4} \text{ m}^3$$

$$\text{Yoke volume} = \pi(r_o^2 - (r+t_h)^2)L = 7.866 \times 10^{-4} \text{ m}^3$$

$$\text{Magnet width, } W_m = W_{m_0} = \left(r - \frac{l_m}{2} - \frac{g}{2} \right) \frac{2\alpha}{P/2} = 0.0569 \text{ m}$$

$$\text{Slot width} = \frac{2\pi r}{N_s} - W_t = 0.0049 \text{ m}$$

The core loss versus speed is shown in Figure 1.68 up to a maximum speed of 3000 rpm corresponding to the stator frequency of 100 Hz for the surface mount PMSM.

1.7.5 CORE LOSS MEASUREMENT IN THE MACHINE

The test machine requires an auxiliary motor to drive it in this method. The no load loss of the auxiliary motor is measured by running it alone and its input power is measured for each speed. Its copper losses are evaluated separately. Then the test machine is coupled to the auxiliary motor and driven on no load with its stator windings open circuited. Measuring the torque output of the auxiliary motor and multiplying with the rotor speed gives the test machine's core, friction, and windage losses. If the torque transducer is not available, then the input power to the auxiliary motor is measured and the no load losses excluding the no load copper losses of

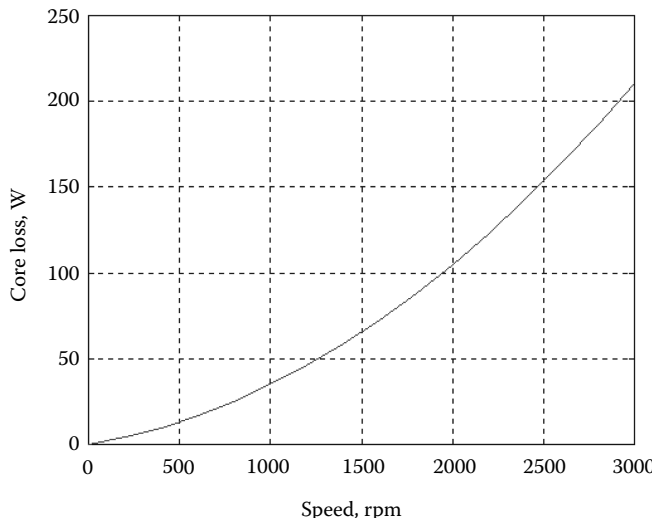


FIGURE 1.68 Core loss versus speed for a surface mount PMSM.

the auxiliary motor is subtracted from it and then its own present copper losses are subtracted to obtain the sum total of the core, frictional, and windage losses of the test machine. To separate the core losses from the frictional and windage losses of the test machine, the test machine's rotor is replaced with an identical test machine rotor but without the magnets on it and filled preferably with equivalent nonmagnetic material of same weight in the place of magnets and driven by the auxiliary motor repeating the measurements. The measured power output of the auxiliary motor gives the frictional and windage losses of the test machine.

1.8 RESISTIVE LOSSES

The stator windings produce losses whenever they carry a current. They are referred to in common parlance as copper losses. Given the rising cost of the copper, many new products may have to use aluminum in the not too distant future and hence it may be better to retain the term resistive losses hereafter. The resistance per phase winding is computed from the number of turns T_{ph} , material specific resistivity ρ , average length of a conductor ℓ_c that is half of a winding turn, and area of cross section of the coil a_c , by computing the resistance for one conductor and then multiplying it with the total number of conductors:

$$R_s = \rho \frac{\ell_c}{a_c} (2T_{ph}) \quad (\Omega) \quad (1.155)$$

Resistance has to be corrected for both operating temperature and for frequency effect of shrinking skin depth with its attendant increase in its value.

The resistive losses for a three-phase machine with stator rms phase currents of I_s are

$$P_{sc} = 3I_s^2 R_s = 3\rho \frac{I_s^2}{a_c^2} (\ell_c a_c) (2T_{ph}) = 3\rho J_c^2 V_c \quad (\text{W}) \quad (1.156)$$

where

J_c is the conductor current density in the coil

V_c is the volume of winding material be it copper or aluminum and they are given as

$$V_c = (\ell_c a_c) (2T_{ph}) \quad (\text{m}^3) \quad (1.157)$$

$$J_c = \frac{I_s}{a_c} \quad (\text{A/m}^2) \quad (1.158)$$

The implication of the stator resistive loss expression is that it shows for a fixed volume of winding material as it must be the case for a given stator lamination design where the slot volume is already defined, varying the number of turns perface reduces the conductor area, increases the current density, and inevitably the resistive losses.

The outcome will require thermal redesign to address the issue as well a reduction in machine efficiency, which has become a premium requirement recently. In comparing machines, particularly in industrial setting, it is crucial to maintain volume of winding material apart from other variables constant. Unless such elementary precaution is taken, it is difficult to arrive at a meaningful conclusion regarding the cost comparison of the competing designs and competing machines. Note that the expression for stator resistive losses and its implication are applicable to all electrical machines except the number of phases has to be modified in cases other than three phases.

In design optimization, it is very useful to derive the resistive losses in terms of the linear current density apart from the conductor current density, bore radius, and stack length so that common terms can be found between it and the power output expression in the machine. Specification of resistive losses as a percentage of power output for design optimization leads to the use of both the power output and resistive loss expressions. In tune with that, the resistive losses are reformulated as

$$P_{sc} = 3I_s^2 R_s = 3I_s^2 \rho \left(\frac{\ell_c}{a_c} \right) (2T_{ph}) \quad (W) \quad (1.159)$$

But the length of one conductor of a phase winding can be written for a distributed winding as equal to the stack length and one half of the build across the stator pole pitch, which in turn can be written in terms of the bore radius. But the build can be very accurately estimated and can be taken as a constant for the specified number of turns and stator lamination and stack length. It is factored by parameter a and the length of one conductor is expressed as

$$\ell_c = \left(L + \frac{2\pi r}{P} a \right) (m) \quad (1.160)$$

The factor a can handle all the cases of short pitch winding in a distributed winding. For concentrically wound machines, appropriate factor and build width across the stator pole have to be modified. The stator copper losses then are

$$P_{sc} = 3I_s^2 \rho \left(\frac{\ell_c}{a_c} \right) (2T_{ph}) = 3 \frac{I_s}{a_c} \rho (T_{ph} I_s) \left(2L \left\{ 1 + \frac{2\pi r}{P} a \right\} \right) \quad (W) \quad (1.161)$$

The stator mmf can be expressed in terms of fundamental linear current density with a subscript “1” from its definition as

$$A_{s1} = k_{w1} \frac{3(2T_{ph})}{2\pi r} I_s \quad (\text{amp-conductor/m}) \quad (1.162)$$

Substituting for mmf in terms of the linear current density, the stator copper losses are

$$P_{sc} = 6J_c A_{sl} \rho \frac{2\pi r}{6k_{w1}} \left(L \left\{ 1 + \frac{2\pi r}{P} a \right\} \right) = \left(\frac{\rho \left\{ 1 + \frac{2\pi a}{bP} \right\}}{k_{w1}} \right) (2\pi r^2) J_c A_{sl} \quad (\text{W}) \quad (1.163)$$

where $L = br$ and b represents the ratio between the stack length and bore radius. Dividing the stator resistive losses by rated or nominal output power derived in Equation 1.90 in Section 1.6.5 expresses the stator copper losses in nondimensional units denoted as per unit (p.u.). The torque angle is assumed to be 90° as this is a reasonable assumption for all types of PMSMs. Then the stator resistive losses in p.u. are given by

$$P_{scn} = \frac{P_c}{P_a} = \frac{kr^2 J_c A_{sl}}{2\pi b r^3 A_{sl} B_{mr} \omega_{mr}} = \left(\frac{k}{2\pi b} \right) \left(\frac{J_c}{B_{mr}} \right) \frac{1}{r} \frac{1}{\omega_{mr}} \quad (\text{p.u.}) \quad (1.164)$$

and

$$k = \frac{2\pi \rho \left(b + \frac{2\pi a}{P} \right)}{k_{w1}} \quad (1.165)$$

where

ω_{mr} in rad/s is the rated speed of the PMSM

P_{scn} is the normalized value of stator resistive losses

Use of this expression is explained in the following section on initial machine design

1.9 INITIAL MACHINE DESIGN

Machine power output, emf, inductances, resistive losses, and core losses in their relationship to physical dimensions and material characteristics have been derived so far. A simple illustration to do an initial design is presented in this section. Readers are cautioned that it is not the procedure for final design that is carried out in practice. A standard industrial design procedure involves many more crucial tasks such as thermal and mechanical designs, verifications with finite element analysis, computational fluid dynamics, comprehensive optimization to save materials by minimizing the machine dimensions and weight, and system optimization including inverter, control, and load subsystems [161–177].

It is usual to specify resistive losses as a per cent of the rated output power. Many other performance indices can be incorporated in the design but for the present illustration, it is limited to stator resistive losses.

Consider an example with the following data:

$P_a = 50 \text{ kW}$, $P_{scn} = 0.02 \text{ p.u.}$, $\omega_{mr} = 188.5 \text{ rad/s}$, $k_{w1} = 0.9$, $P = 4$, $a = 1.5$, $\rho = 2.5 \times 10^{-8} \Omega \cdot \text{m}$, let $b = 2$, $J_c = 4 \text{ A/mm}^2$.

Here the ratio between the stator stack length to bore radius has been fixed as 2 but its optimum need not be at this chosen value but may be seen later that it is closer to optimum value. From the equation on the normalized stator resistive losses and k , they are evaluated for the given variables and constants as

$$k = \frac{2\pi\rho \left(b + \frac{2\pi a}{P} \right)}{k_{w1}} = \frac{2 \times 2.5 \times 10^{-8} \left(2 + \frac{2\pi \times 1.5}{4} \right)}{0.9} = 0.76 \times 10^{-6} \quad (1.166)$$

After the evaluation of k , the bore radius is the only unknown in the normalized stator resistive losses equation and it is evaluated to be 91.7 mm. From the radius and assumed value of the ratio between stack length and bore radius, the stack length is evaluated. Changing only the ratio between the stack length and rotor bore radius, b from the current value of 2 to (1) 1.5 and (2) 1.6, the bore radius is evaluated as (1) 108.2 mm and (2) 112.6 mm for the cases considered. The varying bore radius has a significant impact on the linear current density in these cases and it is as for case (1) 39.08 kA/m and (2) 28.098 kA/m and they are computed from

$$P_{sc} = \left(\frac{\rho \left\{ 1 + \frac{2\pi a}{bP} \right\}}{k_{w1}} \right) (2\pi r^2) J_c A_{s1} = kr^2 J_c A_{s1} \quad (\text{W}) \quad (1.167)$$

Criteria for the ratio between stack length and rotor bore radius: It is obtained by minimizing resistive loss, minimizing length, and maximizing enclosed air gap area for maximum torque production. All of these performance indices are mutually contradictory and the optimum value is obtained provided the pole sides are square so as to minimize the factor a with the result that the stack length to bore radius ratio [167] is

$$\frac{L}{r} = \frac{2\pi a}{P} \quad (1.168)$$

Caution has to be exercised that this optimum need not be useful for all applications and mostly useful in general purpose industrial applications but not in special purpose applications such as aerospace and defense sector.

From the ac or dc supply voltage to the rectifier inverter or inverter subsystem, respectively, the line to line voltage and phase voltage of the PMSM is determined. From induced emf equation and magnet characteristics, magnet arc, stack length L , bore radius r , and the number of turns are evaluated. The phase current is determined from the linear current density equation having r , number of turns, and winding factor. The stator and rotor laminations are evaluated based on the above and considering mechanical constraints. This completes the initial electromagnetic design of the PMSM.

1.10 COGGING TORQUE

The nature of cogging torque and its cause, methods of analysis, and computation and methods for its mitigation are presented in this section [146–155].

1.10.1 CAUSE AND MAGNITUDE

An electromagnetic torque exists in PM machines even when there is no excitation of the stator windings. This arises due to the interaction between the rotor PM field and the stator teeth. As the rotor magnet is approaching or leaving a tooth, the field around it is changing, resulting in a change of coenergy in the air space between the magnet and tooth. The change in coenergy results in a net torque. This torque is sometimes referred to as detent or cogging torque in the literature. The cogging torque may also be thought of as a reluctance torque due to the reluctance variation presented by the tooth and slot to the magnet current source. Its period is the same as the slot pitch in general during most of the measurements but it is not the case, which is derived later. The cogging torque is alternating and almost symmetric about its angular axis.

Improper design of the machines results in cogging torque that may be as high as 25% of the rated torque. But in many commercially available machines, it has a nominal value of 5%–10% of the rated torque. A number of high-performance applications necessitate cogging torque not to exceed 1% or 2% of the rated torque. Therefore, methods of analysis and computation of the cogging torque and an understanding arising out of such analysis are required to design optimally machines meeting the specifications.

1.10.2 BASICS OF COGGING TORQUE

Consider a stator with two teeth and rotor with two PMs for an arbitrary rotor position, as shown in Figure 1.69. For the case under consideration, assume that the stator

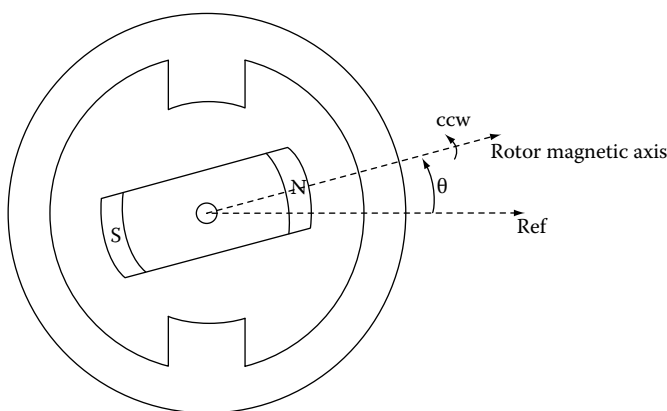


FIGURE 1.69 A simple PM machine with two teeth and two rotor poles.

windings are not excited and rotor is fitted with two magnets with their magnetization as shown. Counterclockwise direction of rotation is considered here for illustrating the generation of cogging torque. When the rotor is in reference position at 0° , it may be surmised that the force and hence the torque on the rotor is zero. It is known as a detent position. It is known as unstable detent position because the rotor cannot stay in this position because of its attraction to a minimum reluctance position. Such a minimum reluctance position corresponds to rotor magnets in alignment with the stator teeth at rotor positions of 90° and 270° . This attraction force between the magnets and the teeth has a component that produces circumferential force, resulting in a torque. It is rising nonlinearly from a reference position and reaches a maximum not at 45° but closer toward the stator teeth and becomes zero at 90° where the rotor reaches a stable detent position, as shown in Figure 1.70. It is stable in the sense that rotor can stay in this position indefinitely provided there is no significant external load applied on the rotor. When disturbed around the stable detent position, the rotor tends to align with stator teeth so as to be in a minimum reluctance position. To move the rotor beyond 90° , force has to be exerted. Hence it corresponds to a negative torque generation by convention and it is shown in the second half cycle in Figure 1.70. Note that the cogging cycle has achieved a full cycle in 180° , i.e., half the revolution for the machine with two stator teeth and two PMs. The cogging torque cycles per revolution N_{co} is two for this machine. From this understanding, the cogging torque cycles per mechanical revolution can be generalized for a stator with S slots and P rotor poles with the following points:

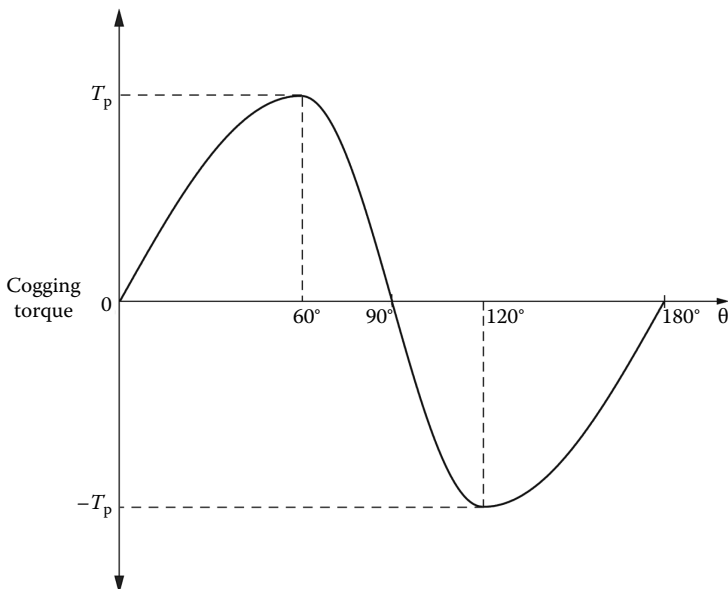


FIGURE 1.70 Cogging torque versus rotor position for the simple machine considered.

1. If $m = S/P$ is an integer, then that many slots interact simultaneously with PMs. Hence there is no phase shift for all the slots producing this cogging cycle, and, accordingly the cogging cycles per mechanical revolution, $N_{co} = mP$.
2. If m is not an integer, and S is even, two diametrically slots produced cogging torque add, resulting in reduced cogging cycles by half, i.e., $N_{co} = (S/2)P$.
3. If m is not an integer, and S is odd, then each slot produces a cogging cycle for each pole with the result of cogging frequency $N_{co} = SP$.
4. The above various cases can be stated concisely for all cases as follows:
 - a. Cogging cycles per mechanical revolution (CPMR), $N_{co} = \text{LCM}(S,P)$.

For example, the cogging cycles per mechanical revolution, is given in Table 1.3 for some machines with distributed and concentric types of windings found in practice. Contrary to common perception, the cogging cycles are higher for concentric-wound machines, i.e., the machines with projecting stator poles given the same number of stator teeth and rotor poles compared to distributed winding machines. This fact has enormous implications.

Higher cogging cycles are preferred since cogging torque magnitude decreases with increasing cogging frequencies. Note that the concentrically wound machine (say $S = 12, P = 10$) has almost the same cogging cycles as the machine ($S = 36, P = 8$) with finely distributed windings. The distributed and concentric-wound machines differ much in their manufacturing complexity and that, in turn, contributes to both cost and reliability implications in favor of concentric-wound machines. Further, the concentric-wound machines offer better flux weakening capabilities compared to its counterpart. Both of these facts drive the research and development of concentric-wound PMSMs and brushless dc machines.

1.10.2.1 General Expression for Cogging Torque

The cogging torque has a fundamental frequency of N_{co} and no subharmonics can be present in the cogging torque with the result that it is modeled as a Fourier sum of harmonics starting from fundamental to other higher order harmonics as

TABLE 1.3
CPMR for Various Machines with Different Winding Types

S	P	$N_{co} = \text{LCM}(S,P)$	Winding Type
8	12	24	Distributed
8	10	40	Concentric
18	12	36	Distributed
27	6	54	Distributed
12	10	60	Concentric
36	8	72	Distributed

$$T_{\text{co}} = \sum_{n=1}^{\infty} T_n \sin(nN_{\text{co}}\theta + \varphi_n) \quad (1.169)$$

where $n = 1$ corresponds to fundamental T_1 , giving the peak fundamental of the cogging torque and θ is the mechanical rotor position. This torque series can be evaluated by analytical derivation, finite element computation, or from experimental data. Regardless, the equation can be used to elicit some characteristics for mitigating the cogging torque in the PM machines and this is illustrated in Section 1.10.5.1.

1.10.3 ANALYSIS AND COMPUTATION

The cogging torque can be computed by calculating the coenergy around the region of interest, i.e., around the edges of the magnet in proximity to the nearest tooth and slot opening. The relevant equations from electromechanics are [2]

$$T_{\text{ec}} = \frac{dW_c}{d\theta} \quad (1.170)$$

where the coenergy is given by

$$W_c = \int \frac{B_\theta^2}{2\mu_0} d(v_r) \quad (\text{J}) \quad (1.171)$$

Note that the integral is with respect to the volume, v_r , corresponding to the region of interest.

Even though there are some analytical methods to predict the cogging torque, their prediction accuracy is not sufficient for use in a comprehensive design of the machine intended for high-performance applications. It is usual to employ a two-dimensional finite element analysis package to optimize a design for reduced cogging torque. In that case, Maxwell stress tensor on air gap volume can be computed to yield the cogging torque as

$$T_{\text{ec}} = \frac{L}{\ell_g \mu_0} \int_{S_g} r B_n B_t \, ds \quad (1.172)$$

where

L is the active rotor length

ℓ_g is the air gap length

r is the dummy radius

B_n and B_t are the normal and tangential flux densities of the air gap, respectively

S_g is the air gap surface area

LS_g equals the air gap volume

1.10.4 FACTORS AFFECTING COGGING TORQUE

Machine design variables and manufacturing related issues affect cogging torque. Magnet strength, stator slot width, irregularities in manufacturing, and impact on materials during manufacturing predominantly affect cogging torque, among others. A brief introduction to them is given to help avoid the pitfalls during design and realization of the PMSMs.

Magnet strength: The operating remanent flux density determines the air gap flux that is critical in determining the magnitude of the cogging torque. The remanent flux density is affected by temperature and also the initial charging of the magnets. Both of these factors affect the cogging torque; the former dependent on the operating conditions and the latter permanently.

Slot width: This is determined based on the criterion to maximize torque generation. Usually the slot opening is equal to tooth width in conventional design. Although that is beneficial from the output point of view, it does not take into account the cogging torque affected by this design variable as the cogging torque is solely due to the interaction of the magnets and slot openings. Note that the cogging torque is zero for machines with zero slot opening but that may not be practical in most machines. A minimum opening has to be provisioned for winding placement. The key in the design process is to determine what this minimum is while simultaneously maximizing the output torque. After winding insertion in slots, it is quite feasible to place magnetic wedges in the slot opening to reduce the cogging torque. This may increase the manufacturing cost of machine.

There are machines with no stator teeth (toothless or slotless or ironless machines) that have practically no cogging torque. The retention of windings with no teeth on the stator presents manufacturing challenges. These machines may be found in small power ranges, say a few watts, than in integral hp.

Manufacturing irregularities: The accuracy of placement of magnets in the rotor affects the cogging torque more than the magnet dimensional accuracy. But both have influence on the cogging torque but in that order only.

Manufacturing impact on materials: Various items enter into this picture. Stator lamination isotropy is affected by punching, stamping, grain orientation, method of stacking, using welds, holes and bolts, and other forms of interlocking. They all introduce anisotropies in stator laminations, resulting in reduction of cogging cycles to equal the slot number instead of CPMR, which is larger than the number of slots. The consequence is that invariably the cogging torque increases with decreasing cogging cycles per revolution. An additional factor due to manufacturing tolerances and due to imperfections in the bearings is the rotor eccentricity in the machine. Not only does this contribute to unbalanced radial forces but also constrains the cogging cycles to equal the number of slots rather than to the CPMR.

1.10.5 MITIGATION METHODS

A number of methods exist to attenuate the cogging torque during the machine design phase itself. They are skewing of the stator laminations or rotor magnets, varying slot width, varying magnet width, shifting alternate pair of poles, and notching of teeth. Briefly they are described in this section.

1.10.5.1 Skewing

Skewing was introduced in Section 1.5.4. Skewing [156] is phase shifting of the stator laminations or PMs along the axial direction in radial flux machines. It is usual to come across one half or one slot pitch skewing of the stator or rotor PMs in PM brushless dc and synchronous machines in servo drives industry. This method does not completely eliminate cogging torque in all machines. The correct skew angle that can eliminate the cogging torque can be found from the cogging torque expression by nulling the cogging torque. Consider the skew angle to span the entire cogging cycle and that amounts to

$$\theta_{co} = \theta_{sk} = \frac{2\pi}{N_{co}} \quad (1.173)$$

When stator laminations are skewed [156] with this angle, the cogging torque is obtained as

$$\begin{aligned} T_{sk} &= \frac{1}{\theta_{sk}} \int_0^{\theta_{sk}} T_{co}(\theta) d\theta = \frac{1}{\theta_{sk}} \sum_{n=1}^{\infty} \int_0^{2\pi/N_{co}} T_n \sin(nN_{co}\theta + \phi_n) d\theta \\ &= \frac{1}{\theta_{sk}} \sum_{n=1}^{\infty} \left[\frac{-T_n \cos(nN_{co}\theta + \phi_n)}{nN_{co}} \right]_0^{2\pi/N_{co}} = 0 \end{aligned} \quad (1.174)$$

The cogging torque for the chosen skew angle is reduced to zero. As the stator is skewed by one slot pitch, the rotor angle for the skewed end varies over the stack length. The cogging torque generated for this varying angle within a slot pitch corresponds to each and every rotor angle that is specific to cogging torque over one of its cycle. The net cogging torque generated over the length of the skewed slot pitch is then the sum of the cogging torque for one cycle that amounts to zero and hence the desired result. Further it is seen that not only the fundamental of the cogging torque but the entire cogging torque is eliminated by this method. The cogging torque never exactly is zero in practice because of fringing effects and effects due to unavoidable machining tolerances of magnets and stator laminations. The disadvantages of skewing are (a) that it reduces the fundamental-induced emf as seen earlier, hence reduces output power, which in turn reduces the output torque, (b) increases leakage inductance and stray losses, and (c) increases the manufacturing complexity by increasing the number of operations involved in the fabrication of the stator.

Another alternative is to skew the magnets on the rotor. It is not desired due to complexity of manufacturing. An alternative approach to rotor magnet skewing is to have multiple magnets per pole along the stack length (axial direction) and have their phase shifted from each other. It is illustrated in [Figure 1.71](#). Let the number of PMs segments per pole be N . The phase shift between each segment, θ_{ss} and it is given in terms of the desired skew angle as

$$\theta_{ss} = \frac{\theta_{sk}}{N} \quad (1.175)$$

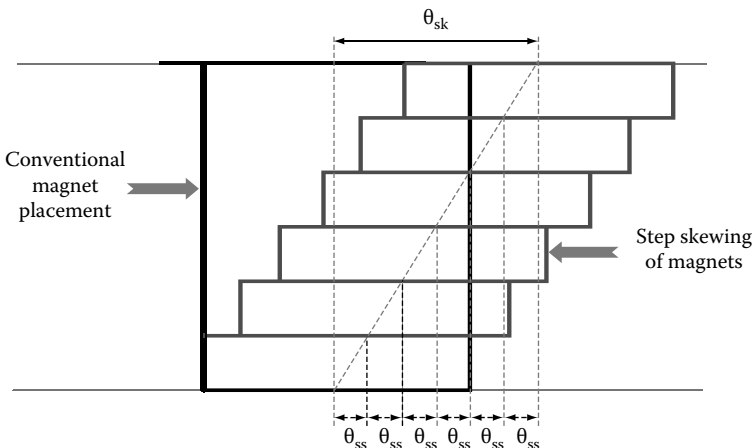


FIGURE 1.71 Step skewing of rotor magnets.

The figure illustrates a case of step magnet skewing with six magnet steps per pole. Keeping the first segment in line with the equivalent single magnet per pole place, it is seen that the other five segments are shifted from each other by the phase shift angle starting with the first segment. It may seem that only five times the phase shift has been effected instead of six times the phase shift. But the angle subtended by the center of the first segment to the sixth segment shows that effectively six times the phase shift to equal to desired skew angle is attained.

The cogging torque for N -step skewing of rotor magnets can be derived as

$$T_{co}(\theta) = \sum_{n=1}^N \sum_{k=1}^{\infty} T_{ck} \sin \left\{ ks \left[\theta - (n-1) \frac{2\pi}{N_{co}} \right] \right\} \quad (1.176)$$

It is deduced from this that all harmonics of the cogging torque are eliminated except the multiples of N th harmonic in the cogging torque. This is an additional disadvantage of step magnet skewing along with all other disadvantages of stator skewing. But it does reduce the cogging torque comparable to stator skewing. A higher number of segments is advantageous but invariably it is accompanied by higher number of manufacturing operations and hence cost.

Both types of magnet and stator skewing in PM brushless dc machines reduce the flat top portion of the induced emf, making it more sinusoidal than rectangular. Injected with a rectangular ac current, the torque ripple increases with skewing, which is not a desirable outcome.

1.10.5.2 Varying Magnet Width

This is easier to accommodate in the production process. The width of the magnet, in general, to reduce the cogging torque, is represented as

$$W_m = (n + x) \lambda_{sl} \quad (1.177)$$

where

n is an integer

λ_{sl} is the slot pitch

x is a number that reduces the cogging torque, which is dependent on the method of magnetization such as radial or parallel and rotor construction such as inset or surface mount or interior PM rotors

There is a slight disadvantage in this method that the magnet width is slightly higher than conventional designs by a fraction, x , of the slot pitch. This usually is not such a formidable penalty in many designs. Every machine design has to be studied to determine x that satisfies the cogging torque and ripple torque specifications is to be noted.

1.10.5.3 Varying Slot Width

Another design variable that is available for reducing the cogging torque is the slot width. It has been found that the ratio between the slot width and the slot pitch near 0.5 is approximately optimal. Also this is also optimal from the design consideration of maximizing the fundamental output torque.

1.10.5.4 Shifting Alternate Pair of Poles

Studies have shown that shifting an alternate pair of poles relative to other pair of poles by an angle equal to a slot pitch reduces the cogging torque as well as the commutation torque pulsation. This method came into existence when cogging torque was optimized with varying magnet width and slot opening, and it was found that the commutation torque ripple increased in magnitude and compromised the quality of electromagnetic torque of the machine. The disadvantage of this method is that there is a small asymmetry introduced in the construction of the rotor between adjacent poles.

1.10.5.5 Notching of Teeth

Dummy slots can be introduced by notching the teeth, as shown in Figure 1.72, and this increases the number of interactions between the rotor PMs and the created miniteeth and slots. The slots that are created on the teeth are not as deep as the regular slots having the windings but for the purpose of cogging torque mitigation they serve as slots. The notches in teeth are easy to make during punching of stator laminations. These notches introduce cogging torque cycles of their own with a phase shift given by

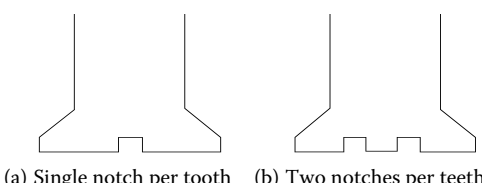


FIGURE 1.72 Notching of stator teeth with one and two notches per tooth: (a) single notch per tooth and (b) two notches per teeth.

$$\phi_{no} = \frac{2\pi}{s(N_n + 1)} \quad (1.178)$$

where N_n is the number of notches per stator tooth. The cogging torque generated with notches is superposed on the cogging torque of the conductor-carrying slots to obtain the resultant cogging torque. Firstly, the dummy slots have increased the cogging cycles with the attendant consequence that they can mitigate the cogging torque. The cogging torque harmonic multiples of $(N_n + 1)$ of the dummy slots all add and their frequency is increased while all other higher harmonics are cancelled in the resultant torque. This enables the reduction of cogging torque magnitude. In order for notching to be effective in reducing the cogging torque, it is important that certain guidelines be followed. Otherwise, the cogging torque may even increase. The guideline in this regard [151] is that the highest common factor between $(N_n + 1)$ and number of cogging cycles during the rotation of a slot pitch, N_p be equal to 1 expressed as

$$\text{HCF}[(N_n + 1)], N_p = 1 \quad (1.179)$$

where

$$N_p = \frac{P}{\text{HCF}[S, P]} \quad (1.180)$$

and HCF is the highest common factor. The harmonics deleted by the introduction of notching are the highest order than that of $(N_n + 1)$ and its multiples.

Alternately, dummy teeth can be introduced in the midst of regular slots containing windings. This poses a significant problem as the slot volume for winding is reduced. But a class of machines known as modular machines is introduced in research literature with concentrated coil windings that have alternate teeth wound, leaving alternate teeth to be free of coils and they serve as dummy teeth. Note that the dummy teeth need not have the same width as the regular teeth. From a manufacturing point of view, this type of introducing dummy teeth is very viable and also has the additional advantage of increasing the direct axis inductance.

All the discussion regarding cogging torque may become academic with the impending market arrival of salient pole concentric wound (alternately known as concentrated coil wound) PM machines that are capable of having very small cogging torque. But conventional machine designs may still use one or other of the techniques that have been discussed in this section.

1.11 BASIC TYPES OF PMSMs BASED ON FLUX PATHS

The machines that have been discussed so far have flux flowing from the rotor to stator and vice versa through air gap in radial direction. Machines are constructed that have flux flow along the axial direction of the shaft and they are known as axial

flux machines or pancake machines [178–184] in industrial circles. Such a machine with one stator and one rotor and two stators and one rotor are shown in Figure 1.73a and b, respectively. Each of these machines can be considered as a stack and such multiple stacks can be cascaded for increasing the power and this was realized in the automotive industry in the late 1960s for developing a line of various power trains for various models. Such a concept has gained momentum again in the 1990s for naval propulsion applications even in the multimegawatt range of power. The construction is much simpler in concept than in practice. The stator iron is laminated in the radial direction and resembles concentric rings that usually have a constant slot width and tapered teeth because the magnets are pie-shaped and its area of cross-section facing the air gap grows along the radial direction. Such an arrangement of the slots and teeth makes the radial flux density in the teeth constant. The axial flux machine with single rotor and single stator has the disadvantage of having attraction force between the stator and magnets and uneven forces due to manufacturing tolerances and they are mostly eliminated in the machine having two stators one on each side of the rotor and one rotor or vice versa. The machine with a single stator and rotor has back irons in both whereas the one with two stators and one rotor has no back iron in the rotor but has back irons in the stator. Because of two stators, its power density is higher than the other machine with one stator. The key to this machine construction is the way the laminations are assembled. It has presented a formidable problem over the years but manufacturing solutions have been around to mitigate the complexities of manufacturing the laminations and their assembly. Unquestionably, the radial field machines are superior in the simplicity of manufacture and assembly and hence their overwhelming popularity and presence in the market place. However, the axial flux machines have some advantages and they are shown via an example covering four types of axial flux machines with their counterpart radial flux machine. All machines have trapezoidal-induced emf to work as a PM brushless dc machine. A brief description of the four different types of axial flux PM brushless dc machines together with the radial flux machine for comparison [182] is given in the following:

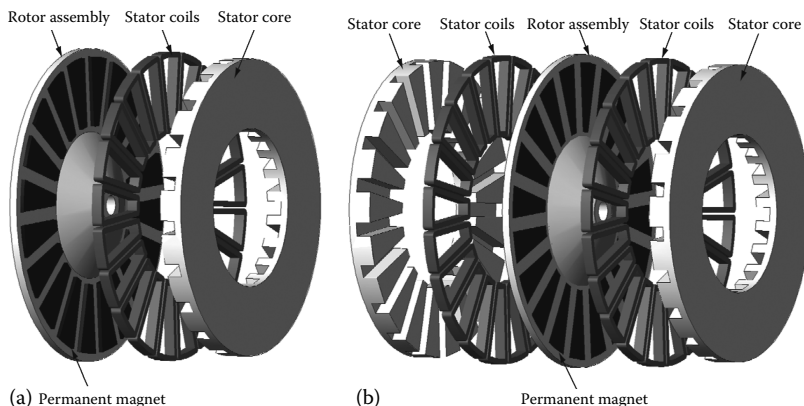


FIGURE 1.73 Axial flux PM machines: (a) one stator and rotor; (b) two stators and one rotor.

1. *Type A, conventional radial field:* This is a typical radial flux brushless dc motor with the PM structure rotating inside the stationary armature windings. The stator is made up of electrical-grade steel laminations with distributed windings. The rotor is cylindrical in shape with a shaft on which the bearings are mounted.
2. *Type B, axial field single air gap:* It has a single air gap. The stator is made up of electrical-grade steel laminations and distributed windings. In all the axial field machines, the rotor rotates beside the stator with the flux crossing the air gap in an axial direction.
3. *Type C, axial field dual air gap:* It has two air gaps. There are two stator assemblies on either side of the rotor.
4. *Type D, axial field slot less single air gap:* This is an axial field slot less motor with a single air gap. The only steel in the magnetic circuit is in the rotor yoke and in the stator yoke or back iron. As the machines do not have teeth, there is a large air gap compared to other types. To drive the flux across the air gap, which comprises the windings too, these machines are usually made with high-energy rare-earth magnets. They are expensive to make and have very low natural thermal capability. Their main advantage claimed in earlier times is that the cogging torque is zero as there are no teeth to interact with the magnets. That concern for cogging torque has diminished with the use of various techniques mentioned earlier and very recently with the appearance of concentrated coil-wound machines. They have pushed the slot less machines to very limited and narrow band of applications.
5. *Type E, axial field slot less dual air gap:* This is an axial field slot less motor with two air gaps. There is no back iron in the rotor and the magnet flux crosses two air gaps as in the case of Type C and has the same advantages as that.

The following power ratings are chosen for comparison: $\frac{1}{4}$, 1, 3, 5, and 10kW for the shaft output power. All the machines are designed using 375V dc as the rated supply voltage. The rated speed is chosen to be 1000rpm with a no-load maximum speed of 2000rpm for all the machines except the $\frac{1}{4}$ kW machine. The rated speed was 2000rpm for these machines, with a 3000rpm no-load speed at 375V dc. All the designs used high-energy, rare-earth, sintered Nd–Fe–B magnets. The winding currents are assumed to be limited at rated speed. The no-load speed of 2000rpm corresponds to a motor back emf constant, K_e , of about 187 V/krpm, line to line. This parameter is also chosen so that the sizing comparison can be made for machines that can be replaced for a certain application, making the replacement transparent to the motor drive electronics. All the performance calculations are made using a three-phase, six-step inverter drive and the induced emf of all the machines are assumed to be trapezoidal. The $\frac{1}{4}$ kW machine used a combination of 12 slots, 8 poles while all the other slotted designs used 24 slots and 8 poles. The following design variables are held constant in each power range of the machines: The slot fill factor S_f in percent, the flux density in the steel B in T, air gap flux density B_g in T, phase resistance R_{ph} , number of conductors in parallel, and their wire gauge AWG, and magnet thickness ℓ_m in mm. Only slot less machines have very high fill factor as there are no slots. For example, only parameters corresponding to 1kW alone are shown in [Table 1.4](#). The

air gap flux density is less than half of the other designs for the slot less machines and that is unavoidable due to the larger air gap to accommodate windings but somewhat compensated by its ability to accommodate large number of turns and accordingly their phase winding resistances are higher than that of other types.

The magnet thickness for higher powers are not kept the same in the case of slot less machines as they tend to have poor air gap flux density without the additional magnet thickness in designs for machines with higher output power than 1 kW. Therefore, magnet thickness is doubled in such cases and an illustrative case of 3 kW design is given in Table 1.5.

The steel flux density is kept below 1.2 T so the loss per unit weight is nearly the same in all these designs for comparison. The active iron volume is taken to be the volume of the stator teeth, stator back, iron, and rotor back iron. The active weight is considered to be the weight of the active volume. This approach neglects additional material required for the housing, shaft, bearings, and cooling fan as they are specific to a given application. Comparison based on major machine dimensions, power density in terms of both power output per unit active volume and power output per unit active weight, and torque per unit inertia that gives the acceleration capability of the machine, total losses versus power output is made in the following.

TABLE 1.4
1.0kW Design

Parameters	A	B	C	D	E
S_f	52	53	53	92	91
B	1.15	1.19	1.2	1.18	1.18
B_g	0.88	0.88	0.88	0.42	0.45
R_{ph}	1.0	0.9	0.9	1.4	1.4
AWG	1#18	1#18	1#18	1#18	1#18
ℓ_m	4	4	4	4	4

Source: Sitapati, K. and Krishnan, R., *IEEE Trans. Indus. Appl.*, 37, 1219, 2001. With permission.

TABLE 1.5
3.0kW Design

Parameters	A	B	C	D	E
S_f	61	64	61	90	90
B	1.15	1.15	1.15	1.15	1.15
B_g	0.92	0.88	0.88	0.40	0.58
R_{ph}	0.21	0.22	0.22	0.36	0.32
AWG	2#16	2#16	2#16	2#16	2#16
ℓ_m	4	4	4	8	8

Source: Sitapati, K. and Krishnan, R., *IEEE Trans. Indus. Appl.*, 37, 1219, 2001. With permission.

TABLE 1.6
Length (mm)

Power kW, rpm, Nm	A	B	C	D	E
0.25, 2000, 1	92	38	45	25	32
1.0, 1000, 10	110	45	48	27	35
3.0, 1000, 30	120	62	65	43	52
5.0, 1000, 50	160	74	77	55	65
10.0, 1000, 100	190	102	110	87	85

Source: Sitapati, K. and Krishnan, R., *IEEE Trans. Indus. Appl.*, 37, 1219, 2001. With permission.

TABLE 1.7
Outer Diameter (mm)

Power kW, rpm, Nm	A	B	C	D	E
0.25, 2000, 1	100	120	110	150	150
1.0, 1000, 10	120	130	130	170	160
3.0, 1000, 30	180	170	170	215	220
5.0, 1000, 50	190	190	190	250	230
10.0, 1000, 100	290	255	245	330	320

Source: Sitapati, K. and Krishnan, R., *IEEE Trans. Indus. Appl.*, 37, 1219, 2001. With permission.

Dimensional advantage: The active length and outside diameter of the machines are given in Tables 1.6 and 1.7, respectively. There is a striking advantage in reduced length of the axial flux machines in comparison to radial flux design. This translates into reduced active volume, weight and core losses. That becomes evident when those indices are discussed.

Magnet weight: An important consideration in design is to minimize the weight of the PMs and performance in that is shown in Figure 1.74 with the advantage going to radial flux machines and closely matched by single air gap axial flux machines. All others have higher magnet weights.

Losses: The combined resistive and core losses versus output power is shown in Figure 1.75. There are no differences between the radial and regular axial flux machines other than that of the slot less design in their loss profile. Note that all other losses are not considered here in this comparison.

Torque per unit inertia: This indicates acceleration capability of the machine and hence its capability for speed of response to commands. The performance for this category is shown in Figure 1.76. In this case, the axial flux machines reign supreme compared to radial flux machines. This index is one of their strongest suits and hence ideal for servo applications where speed of response is valued at a premium.

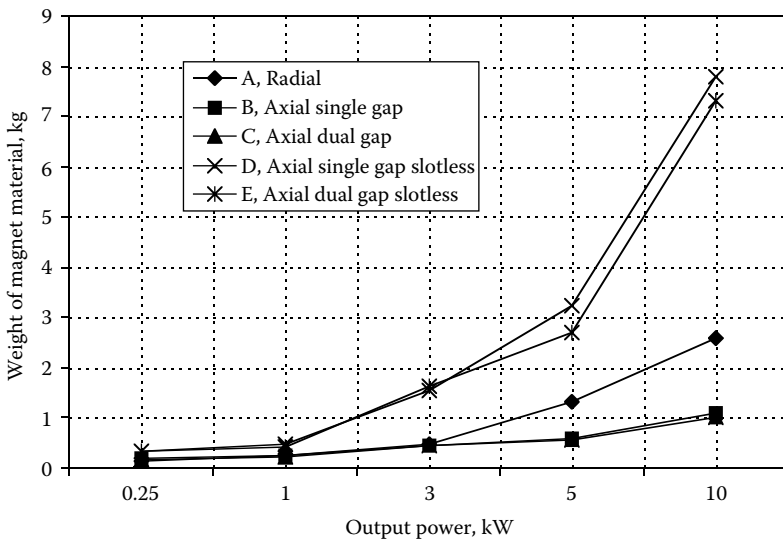


FIGURE 1.74 Magnet weight versus output power. (From Sitapati, K. and Krishnan, R., *IEEE Trans. Indus. Appl.*, 37, 1219, 2001. With permission.)

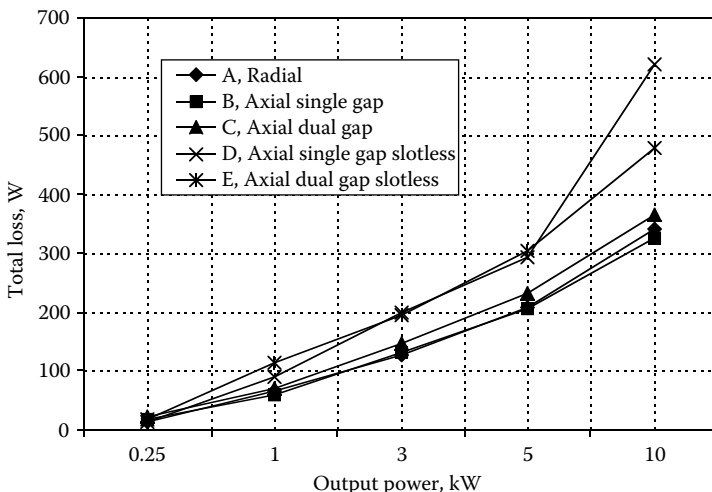


FIGURE 1.75 Sum total of core and resistive losses versus output power. (From Sitapati, K. and Krishnan, R., *IEEE Trans. Indus. Appl.*, 37, 1219, 2001. With permission.)

Power per unit active weight: Figure 1.77 shows the variation of the ratio of power per unit active weight for each of the designs. The active weight consists of the copper and iron weight required by the magnetic circuit. At higher power levels, this index for radial field motor ratio drops away from the axial field machines. The difference is within 20%–25% from their axial counterparts. That may be significant in some applications such as aerospace where per unit weight and volume measures predominate all other performance indices.

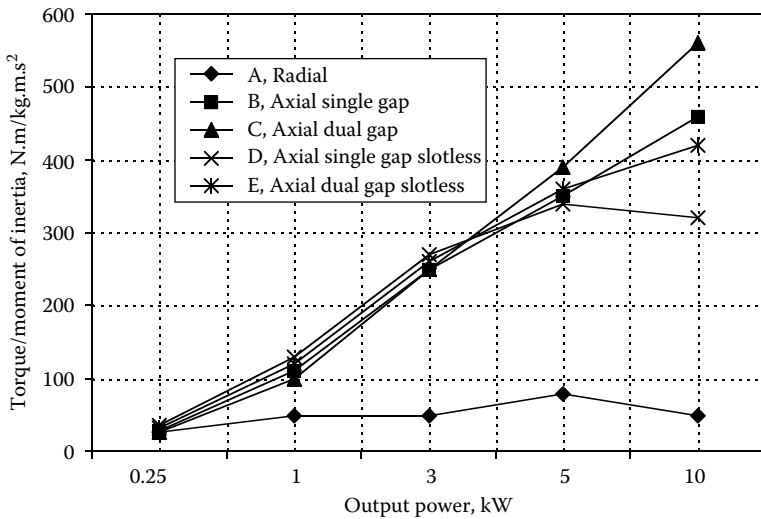


FIGURE 1.76 Torque per unit moment of inertia versus output power. (From Sitapati, K. and Krishnan, R., *IEEE Trans. Indus. Appl.*, 37, 1219, 2001. With permission.)

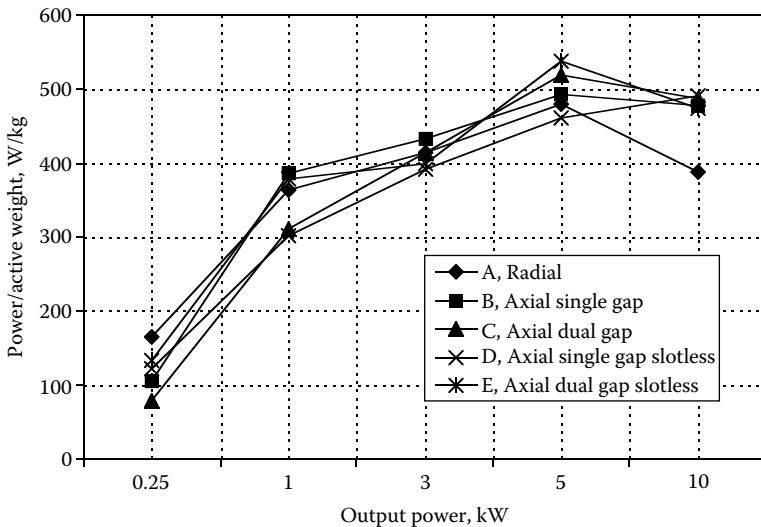


FIGURE 1.77 Power/active weight versus output power. (From Sitapati, K. and Krishnan, R., *IEEE Trans. Indus. Appl.*, 37, 1219, 2001. With permission.)

Power per unit active volume: Figure 1.78 shows the variation of the ratio of power per unit active volume for each of the designs. The active volume is the volume of the magnets, stator, and rotor laminations and windings. It can be seen that the radial field motor is inferior compared to other motor types for all the power levels considered. The power per active volume grows significantly for the axial field machines with the output power in the range that is studied. It is as much as by 1.6–5

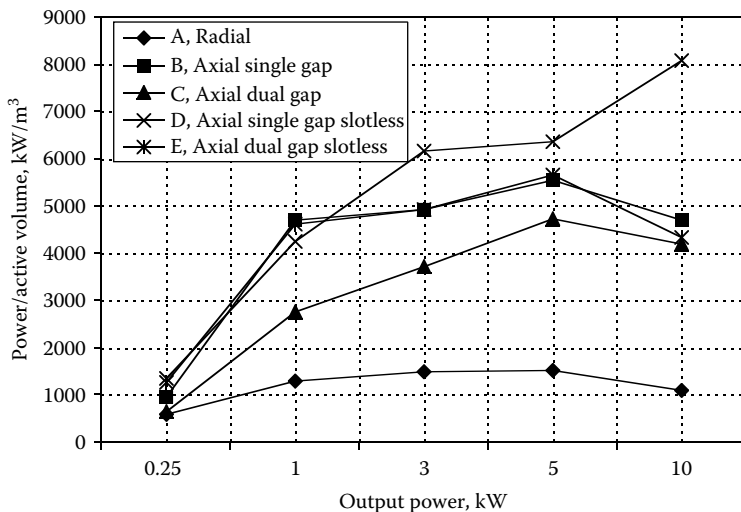


FIGURE 1.78 Power per unit active volume versus output power. (From Sitapati, K. and Krishnan, R., *IEEE Trans. Indus. Appl.*, 37, 1219, 2001. With permission.)

times that of the radial flux power density. This makes the axial motor a good choice where space is limited especially at large power levels that can be encountered plenty in defense and aerospace sectors.

From this discussion, the axial flux machines have some advantages in high acceleration rate, high power densities in terms of power per unit active volume, and power per unit active weight and lower length. There is no significant advantage in core and resistive losses but certainly has disadvantages in having higher magnet weight compared to radial flux machines, and complex manufacturing and assembly requirements. Axial field machines are being considered in several applications where the power density requirements are very high such as in aerospace, aviation, marine, and some traction applications including that of the hybrid electric vehicles, a recent application to join others, due to their compact size. Their demand in commercial applications is increasing as the complexity of manufacturing is rapidly decreasing with innovative designs. It can be safely said at this time that given the manufacturing complexity, the axial flux machines may not be in the race for high-volume and low-cost applications.

1.12 VIBRATION AND NOISE

The PM machines, particularly the synchronous type, have low vibration and noise because of low torque pulsation. Even low-cost applications such as automotive and household appliances require low acoustic noise from the variable motor drives being introduced in the market place. Research work [184–186] is very limited in this field, but it is progressing due to recent interest on the part of the manufacturers of the motor drives to meet the emerging or pending regulations. Interested readers are encouraged to refer to literature in this field beyond that which is cited here.

REFERENCES

Books

1. T. Kenjo and S. Nagamori, *Permanent-Magnet and Brushless DC Motors*, Clarendon Press, Oxford, U.K., 1986.
2. G. R. Slemon and A. Straughen, *Electric Machines*, Addison Wesley, Reading, MA, 1980.
3. T. J. E. Miller, *Brushless Permanent-Magnet and Reluctance Motor Drives*, Oxford Science Publishers, Oxford, U.K., 1989.
4. D. C. Hanselman, *Brushless Permanent Magnet Motor Design*, McGraw Hill, New York, 1994.
5. J. R. Hendershot and T. J. E. Miller, *Design of Brushless Permanent-Magnet Motors*, Marcel Dekker, New York, 1996.
6. R. Krishnan, *Electric Motor Drives*, Prentice Hall, Upper Saddle River, NJ, 2001.
7. R. Krishnan, *Switched Reluctance Motor Drives*, CRC Press, Boca Raton, FL, 2001.
8. J. F. Gieras, M. Wing, and G. F. Gieras, *Permanent Magnet Motor Technology: Design and Applications*, CRC Press, Boca Raton, FL, 2002.

Early Papers

9. H. Wagnessonner, Investigations on synchronous machines with permanent magnets for the pole system, *Archiv fur Elektrotechnik*, 33, 385–401, 1939.
10. F. W. Merrill, Permanent-magnet excited synchronous motors, *Transactions of the American Institute of Electrical Engineers, Power Apparatus and Systems*, 74(Part 3, 16), 1754–1759, 1955.
11. J. F. H. Douglas, Current loci of permanent-magnet synchronous motors: An extension of Blondel theory, *Transactions of the American Institute of Electrical Engineers, Part III (Power Apparatus and Systems)*, 78, 76–78, 1959.
12. G. Bauerlein, Brushless DC motor with solid-state commutation, *IRE International Convention Record*, 10(Part 6), 184–190, 1962.
13. D. P. M. Cahill and B. Adkins, Permanent-magnet synchronous motor, *Proceedings of the Institution of Electrical Engineers, Part A. Power Engineering*, 190(38), 483–491, 1962.
14. W. Volkrodt, The permanent-magnet synchronous motor, *Proceedings of the Institution of Electrical Engineers*, 110(7), 1276, 1963.

Machines

15. K. J. Binns, M. A. Jabbar, and G. E. Parry, Choice of parameters in the hybrid permanent magnet synchronous motor, *Proceedings of the Institution of Electrical Engineers*, 126(8), 741–744, 1979.
16. M. A. Rahman, High efficiency permanent magnet synchronous motors, *Industry Application Society IEEE-IAS Annual Meeting*, pp. 561–564, 1979.
17. K. J. Binns and M. A. Jabbar, A high field permanent magnet synchronous motor, *International Conference on Electrical Machines*, pp. 304–311, 1979.
18. N. Boules, W. R. Canders, and H. Weh, Analytical determination of slotting effect on field distribution and eddy current losses in the magnets of permanent-magnet synchronous machines, *Archiv fur Elektrotechnik*, 62(4–5), 283–293, 1980.
19. K. Miyashita, S. Yamashita, S. Tanabe et al., Development of a high speed 2-pole permanent magnet synchronous motor, *IEEE Transactions on Power Apparatus and Systems*, PAS-99(6), 2175–2183, 1980.
20. M. A. Rahman, Permanent magnet synchronous motors—a review of the state of design art, *International Conference on Electrical Machines*, pp. 312–319, 1980.

21. P. H. Trickey, Performance calculations on polyphase permanent magnet synchronous motors, *International Conference on Electrical Machines*, pp. 330–336, 1980.
22. H. Weh, High power synchronous machines with permanent magnet excitation, *International Conference on Electrical Machines*, pp. 295–303, 1980.
23. H. Weh and N. Boules, Field analysis for a high power, high speed permanent magnet synchronous machine of the disc construction type, *Electric Machines and Electromechanics*, 5(1), 25–37, 1980.
24. K. J. Binns and M. A. Jabbar, High field self-starting permanent magnet synchronous motor, *IEE Proceedings B (Electric Power Applications)*, 128(3), 157–160, 1981.
25. N. A. Demerdash, R. H. Miller, T. W. Nehl et al., Comparison between features and performance characteristics of fifteen HP samarium cobalt and ferrite based brushless DC motors operated by same power conditioner, *IEEE Transactions on Power Apparatus and Systems*, PAS-102(1), 104–112, 1983.
26. T. M. Jahns, Torque production in permanent-magnet synchronous motor drives with rectangular current excitation, *IEEE Transactions on Industry Applications*, IA-20(4), 803–813, 1984.
27. M. Jufer and P. Poffet, Synchronous motor with permanent magnets and solid iron rotor, *Proceedings of the International Conference on Electrical Machines*, pp. 598–602, 1984.
28. M. A. Jabbar, T. S. Low, and M. A. Rahman, Permanent magnet motors for brushless operation, *Conference Record—IAS Annual Meeting (IEEE Industry Applications Society)*, pp. 15–19, 1988.
29. U. K. Madawala, A. W. Green, and J. T. Boys, Brushless ironless DC machine, *IEE Conference Publication*, pp. 440–445, 1990.
30. C. C. Jensen, F. Profumo, and T. A. Lipo, A low-loss permanent-magnet brushless DC motor utilizing tape wound amorphous iron, *IEEE Transactions on Industry Applications*, 28(3), 646–651, 1992.
31. E. Favre, M. Jufer, and C. Fleury, Five-phase permanent magnet synchronous motor, *PCIM '93 Europe. Official Proceedings of the Twenty-Third International Intelligent Motion Conference*, pp. 475–487, 1993.
32. M. H. Nagrial, Synthesis of DC brushless motors with slotless windings for optimum performance, *International Conference on Electrical Machines in Australia Proceedings*, pp. 92–100, 1993.
33. S. Morimoto, H. Awata, M. Sanada et al., Interior permanent magnet synchronous motors mainly using reluctance torque, *Transactions of the Institute of Electrical Engineers of Japan, Part D*, 119-D(10), 1177–1183, 1999.
34. R. Hanitsch, D. Lammel, and I. Draheim, Benefits of the use of bonded softmagnetic material for brushless DC motors, *Proceedings of the Universities Power Engineering Conference*, p. 35, 2000.
35. J. F. Gieras and J. Zadrozny, Small permanent-magnet brushless motors—State of the art, *Electromotion*, 9(4), 217–229, 2002.

PM Synchronous Motor Drives

36. H. Grotstollen and G. Pfaff, Brushless 3-phase AC servo-drives with permanent magnet excitation, *Elektrotechnische Zeitschrift ETZ*, 100(24), 1382–1386, 1979.
37. K. J. Binns, B. Sneyers, G. Maggetto et al., Rotor-position-controlled permanent magnet synchronous machines for electrical vehicles, *International Conference on Electrical Machines*, pp. 346–357, 1980.
38. H. Grotstollen, G. Pfaff, A. Weschta et al., Design and dynamic behaviour of a permanent-magnet synchronous servo-motor with rare-earth-cobalt magnets, *International Conference on Electrical Machines*, pp. 320–329, 1980.

39. S. Ogasawara, M. Nishimura, H. Akagi et al., A high performance AC servo system with permanent magnet synchronous motor, *Proceedings IECON '84. 1984 International Conference on Industrial Electronics, Control and Instrumentation (Cat. No. 84CH1991-9)*, pp. 1111–1116, 1984.
40. S. Morimoto, K. Hatanaka, Y. Tong et al., High performance servo drive system of salient pole permanent magnet synchronous motor, *Conference Record of the 1991 IEEE Industry Applications Society Annual Meeting (Cat. No. 91CH3077-5)*, pp. 463–468, 1991.

PM Brushless dc Motor Drives

41. M. Sato and V. V. Semenov, Adjustable speed drive with a brushless DC motor, *Transactions on IGA*, IGA-7(4), 539–543, 1971.
42. N. Sato, A brushless DC motor with armature induced voltage commutation, *IEEE Transactions on Power Apparatus and Systems*, PAS-91(4), 1485–1492, 1972.
43. J. R. Woodbury, The design of brushless DC motor systems, *IEEE Transactions on Industrial Electronics and Control Instrumentation*, IECI-21(2), 52–60, 1974.
44. E. Persson, Brushless DC motors in high performance servo systems, *Proceedings of the 4th Annual Symposium on Incremental Motion Control Systems and Devices*, pp. 1–15, 1975.
45. B. V. Murty, Fast response reversible brushless DC drive with regenerative braking, *Conference Record of the Industry Applications Society IEEE-IAS-1984 Annual Meeting (Cat. No. 84CH2060-2)*, pp. 445–450, 1984.
46. R. Spee and A. K. Wallace, Performance characteristics of brushless DC drives, *Conference Record of the 1987 IEEE Industry Applications Society Annual Meeting (Cat. No. 87CH2499-2)*, pp. 1–6, 1987.
47. A. K. Wallace and R. Spee, The effects of motor parameters on the performance of brushless DC drives, *PESC 87 Record: 18th Annual IEEE Power Electronics Specialists Conference (Cat. No. 87CH2459-6)*, pp. 591–597, 1987.
48. A. G. Jack, P. P. Acarnley, and P. T. Jowett, The design of small high speed brushless DC drives with precise speed stability, *Conference Record of the 1988 Industry Applications Society Annual Meeting (IEEE Cat. No. 88CH2565-0)*, pp. 500–506, 1988.
49. A. Kusko and S. M. Peeran, Definition of the brushless dc motor, *Conference Record—IAS Annual Meeting (IEEE Industry Applications Society)*, pp. 20–22, 1988.
50. T. Miller, Brushless permanent-magnet motor drives, *Power Engineering Journal*, 2(1), 55–60, 1988.
51. G. Henneberger, Dynamic behaviour and current control methods of brushless DC motors with different rotor designs, *EPE '89. 3rd European Conference on Power Electronics and Applications*, pp. 1531–1536, 1989.
52. R. Hanitsch and A. K. Daud, Contribution to the design and performance of brushless DC motors with one winding, *Proceedings of the 25th Universities Power Engineering Conference*, pp. 273–276, 1990.
53. G. Liu and W. G. Dunford, Comparison of sinusoidal excitation and trapezoidal excitation of a brushless permanent magnet motor, *Fourth International Conference on Power Electronics and Variable-Speed Drives (Conf. Publ. No. 324)*, pp. 446–450, 1990.
54. R. Krishnan, R. A. Bedingfield, A. S. Bharadwaj et al., Design and development of a user-friendly PC-based CAE software for the analysis of torque/speed/position controlled PM brushless DC motor drive system dynamics, *Conference Record of the 1991 IEEE Industry Applications Society Annual Meeting (Cat. No. 91CH3077-5)*, pp. 1388–1394, 1991.

55. P. Pillay and R. Krishnan, Application characteristics of permanent magnet synchronous and brushless DC motors for servo drives, *IEEE Transactions on Industry Applications*, 27(5), 986–996, 1991.

Magnetization Methods and Fixtures

56. A. Cassat and J. Dunfield, Brushless DC motor. Permanent magnet magnetization and its effect on motor performance, *Proceedings, Annual Symposium—Incremental Motion Control Systems and Devices*, p. 64, 1991.
57. G. W. Jewell and D. Howe, Computer-aided design of magnetizing fixtures for the post-assembly magnetization of rare-earth permanent magnet brushless DC motors, *IEEE Transactions on Magnetics*, 28(5 pt 2), 3036–3038, 1992.
58. A. Cassat and J. Dunfield, Permanent magnets used in brushless dc motors. The influence of the method of magnetization, *Proceedings of the Annual Symposium on Incremental Motion Control System and Device*, p. 109, 1993.
59. G. W. Jewell and D. Howe, Impulse magnetization strategies for an external rotor brushless DC motor equipped with a multipole NdFeB magnet, *IEE Colloquium on Permanent Magnet Machines and Drives (Digest No. 030)*, pp. 6/1–6/4, 1993.

Halbach PM Arrangement

60. J. Ofori-Tenkorrang and J. H. Lang, A comparative analysis of torque production in Halbach and conventional surface-mounted permanent-magnet synchronous motors, *IAS '95. Conference Record of the 1995 IEEE Industry Applications Conference. Thirtieth IAS Annual Meeting (Cat. No. 95CH35862)*, pp. 657–663.
61. M. Marinescu and N. Marinescu, Compensation of anisotropy effects in flux-confining permanent-magnet structures, *IEEE Transactions on Magnetics*, 25(5), 3899–3901, 1989.
62. K. Atallah and D. Howe, Application of Halbach cylinders to brushless AC servo motors, *IEEE Transactions on Magnetics*, 34(4 pt 1), 2060–2062, 1998.
63. R. F. Post and D. D. Ryutov, Inductrack: A simpler approach to magnetic levitation, *IEEE Transactions on Applied Superconductivity*, 10(1), 901–904, 2000.
64. Z. Q. Zhu and D. Howe, Halbach permanent magnet machines and applications: A review, *IEE Proceedings—Electric Power Applications*, 148(4), 299–308, 2001.
65. S. R. Holm, H. Polinder, J. A. Ferreira et al., Comparison of three permanent magnet structures with respect to torque production by means of analytical field calculations, *International Conference on Power Electronics, Machines and Drives (IEE Conf. Publ. No. 487)*, pp. 409–414.
66. P. H. Mellor and R. Wrobel, Optimisation of a brushless motor excited by multi-polar permanent magnet array, *International Electric Machines and Drives Conference (IEEE Cat. No. 05EX1023C)*, pp. 649–654, 2005.
67. S.-M. Jang, H.-W. Cho, S.-H. Lee et al., The influence of magnetization pattern on the rotor losses of permanent magnet high-speed machines, *IEEE Transactions on Magnetics*, 40(4 II), 2062–2064, 2004.
68. T. R. Ni Mhiochain, J. M. D. Coey, D. L. Weaire et al., Torque in nested Halbach cylinders, *IEEE Transactions on Magnetics*, 35(5 pt 2), pp. 3968–3970, 1999.
69. D. L. Trumper, M. E. Williams, and T. H. Nguyen, Magnet arrays for synchronous machines, *IAS'93. Conference Record of the 1993 IEEE Industry Applications Conference Twenty-Eighth IAS Annual Meeting (Cat. No. 93CH3366-2)*, pp. 9–18, 1993.

Line Start PM Machines

70. T. J. E. Miller, Synchronization of line start permanent magnet AC motors, *IEEE Transactions on Power Apparatus and Systems*, PAS-103(7), 1822–1829, 1984.

71. A. M. Osheiba and M. A. Rahman, Performance of line-start single phase permanent magnet synchronous motors, *Conference Record of the 1987 IEEE Industry Applications Society Annual Meeting (Cat. No. 87CH2499-2)*, pp. 104–108, 1987.
72. V. B. Honsinger, Permanent magnet machines: Asynchronous operation, *IEEE Transactions on Power Apparatus and Systems*, PAS-99(4), 1503–1509, 1980.

Hybrid Machines

73. B. J. Chalmers, L. Musaba, and D. F. Gosden, Synchronous machines with permanent magnet and reluctance rotor sections, *ICEM 94. International Conference on Electrical Machines*, pp. 185–189, 1994.
74. R. P. Deodhar, S. Andersson, I. Boldea et al., Flux-reversal machine: A new brushless doubly-salient permanent-magnet machine, *IEEE Transactions on Industry Applications*, 33(4), 925–934, 1997.
75. X. Luo and T. A. Lipo, Synchronous/permanent magnet hybrid AC machine, *IEEE Transactions on Energy Conversion*, 15(2), 203–210, 2000.
76. Y. Liao, F. Liang, and T. A. Lipo, A novel permanent magnet motor with doubly salient structure, *IEEE Industry Applications Conference*, Houston, TX, pp. 308–314, Oct. 1992.
77. F. Magnussen and H. Lendenman, Parasitic effects in PM machines with concentrated windings, *IEEE Transactions on Industry Applications*, 43(5), pp. 1223–1232, 2007.
78. D. Ishak, Z. Q. Zhu, and D. Howe, Comparative study of permanent magnet brushless motors with all teeth and alternative teeth windings, *IEE Conference Publication*, pp. 834–839, 2004.
79. X. Zhu, M. Cheng, and W. Li, Design and analysis of a novel stator hybrid excited doubly salient permanent magnet brushless motor, *ICEMS 2005: Proceedings of the Eighth International Conference on Electrical Machines and Systems*, pp. 401–406, 2005.
80. A. M. El-Refaie and T. M. Jahns, Comparison of synchronous PM machine types for wide constant-power speed range operation, *Conference Record—IAS Annual Meeting (IEEE Industry Applications Society)*, pp. 1015–1022, 2005.
81. D. Ishak, Z. Q. Zhu, and D. Howe, Permanent-magnet brushless machines with unequal tooth widths and similar slot and pole numbers, *IEEE Transactions on Industry Applications*, 41(2), pp. 584–590, 2005.

Field Analysis and Performance Prediction of Machines

82. F. A. Fouad, T. W. Nehl, and N. A. Demerdash, Magnetic field modeling of permanent magnet type electronically operated synchronous machines using finite elements, *IEEE Transactions on Power Apparatus and Systems*, PAS-100(9), 4125–4135, 1981.
83. V. Honsinger, The fields and parameters of interior type AC permanent magnet machines, *IEEE Transactions on Power Apparatus and Systems*, pp. 867–876, 1982.
84. N. Boules, Field analysis of PM synchronous machines with buried magnet rotor, *ICEM '86 Munchen. International Conference on Electrical Machines*, pp. 1063–1066, 1986.
85. B. J. Chalmers, S. K. Devgan, D. Howe et al., Synchronous performance prediction for high-field permanent magnet synchronous motors, *ICEM '86 Munchen. International Conference on Electrical Machines*, pp. 1067–1070, 1986.
86. Z. Deng, I. Boldea, and S. A. Nasar, Fields in permanent magnetic linear synchronous machines, *IEEE Transactions on Magnetics*, MAG-22(2), 107–112, 1986.
87. T. Sebastian, G. R. Slemon, and M. A. Rahman, Modelling of permanent magnet synchronous motors, *IEEE Transactions on Magnetics (USA)*, pp. 1069–1071, 1986.
88. J. De La Ree and N. Boules, Torque production in permanent-magnet synchronous motors, *IEEE Transactions on Industry Applications*, 25(1), 107–112, 1989.

89. Z. Q. Zhu and D. Howe, Analytical determination of the instantaneous airgap field in a brushless permanent magnet DC motor, *International Conference on Computation in Electromagnetics (Conf. Publ. No. 350)*, pp. 268–271, 1991.
90. Z. Q. Zhu, D. Howe, E. Bolte et al., Instantaneous magnetic field distribution in brushless permanent magnet dc motors. Part I: Open-circuit field, *IEEE Transactions on Magnetics*, 29(1), 124–135, 1993.
91. Z. Q. Zhu and D. Howe, Instantaneous magnetic field distribution in brushless permanent magnet DC motors. II. Armature-reaction field, *IEEE Transactions on Magnetics*, 29(1), 136–142, 1993.
92. Z. Q. Zhu and D. Howe, Instantaneous magnetic field distribution in brushless permanent magnet dc motors. Part III: Effect of stator slotting, *IEEE Transactions on Magnetics*, 29(1), 143–151, 1993.
93. Z. Q. Zhu and D. Howe, Instantaneous magnetic field distribution in permanent magnet brushless dc motors. Part IV: Magnetic field on load, *IEEE Transactions on Magnetics*, 29(1), 152–158, 1993.
94. Z. Q. Zhu, D. Howe, and J. K. Mitchell, Magnetic field analysis and inductances of brushless DC machines with surface-mounted magnets and non-overlapping stator windings, *IEEE Transactions on Magnetics*, 31(3 pt 1), 2115–2118, 1995.
95. N. Bianchi, Radially-magnetised interior-permanent-magnet synchronous motor for high-speed drive: An analytical and finite-element combined design procedure, *Electromotion*, 6(3), 103–111, 1999.
96. K. F. Rasmussen, J. H. Davies, T. J. E. Miller et al., Analytical and numerical computation of air-gap magnetic fields in brushless motors with surface permanent magnets, *IEEE Transactions on Industry Applications*, 36(6), 1547–1554, 2000.
97. J. F. Gieras and I. A. Gieras, Performance analysis of a coreless permanent magnet brushless motor, *Conference Record—IAS Annual Meeting (IEEE Industry Applications Society)*, pp. 2477–2482, 2002.
98. D. Howe, Z. Q. Zhu, and C. C. Chan, Improved analytical model for predicting the magnetic field distribution in brushless permanent-magnet machines, *IEEE Transactions on Magnetics*, 38(1 II), 229–238, 2002.
99. W. Zhu, S. Pekarek, B. Fahimi et al., Investigation of force generation in a permanent magnet synchronous machine, *IEEE Transactions on Energy Conversion*, 22(3), 557–565, 2007.
100. D. Ishak, Z. Q. Zhu, and D. Howe, Unbalanced magnetic forces in permanent magnet brushless machines with diametrically asymmetric phase windings, *Conference Record—IAS Annual Meeting (IEEE Industry Applications Society)*, pp. 1037–1043, 2005.
101. V. Gangla and J. de la Ree, Electromechanical forces and torque in brushless permanent magnetic machines, *IEEE Transactions on Energy Conversion*, 6(3), 546–552, 1991.

Machine Inductances

102. T. Sebastian, Steady state performance of variable speed permanent magnet synchronous motors, *Ph.D. Thesis, Supervised by G. R. Slemon, University of Toronto, Canada*, 1986.
103. N. A. Demerdash, T. M. Hijazi, and A. A. Arkadan, Computation of winding inductances of permanent magnet brushless DC motors with damper windings by energy perturbation, *IEEE Transactions on Energy Conversion*, 3(3), 705–713, 1988.
104. A. Consoli and A. Raciti, Experimental determination of equivalent circuit parameters for PM synchronous motors, *Electric Machines and Power Systems*, 20(3), 283–296, 1992.
105. G. Henneberger, S. Domack, and J. Berndt, Influence of end winding leakage in permanent magnet excited synchronous machines with asymmetrical rotor design, *Sixth International Conference on Electrical Machines and Drives (Conf. Publ. No. 376)*, pp. 305–311, 1993.

106. J. F. Gieras, E. Santini, and M. Wing, Calculations of synchronous reactances of small permanent-magnet alternating-current motors: Comparison of analytical approach and finite element method with measurements, *IEEE Transactions on Magnetics*, 34(5 pt 2), 3712–3720, 1998.
107. K. Atallah, Z. Q. Zhu, D. Howe et al., Armature reaction field and winding inductances of slotless permanent-magnet brushless machines, *IEEE Transactions on Magnetics*, 34(5 pt 2), 3737–3744, 1998.
108. Y. S. Chen, Z. Q. Zhu, D. Howe et al., Accurate prediction and measurement of dq-axis inductances of permanent magnet brushless ac machines, *Proceedings of the Universities Power Engineering Conference*, vol. 1, pp. 177–180, 1999.
109. H. P. Nee, L. Lefevre, P. Thelin et al., Determination of d and q reactances of permanent-magnet synchronous motors without measurements of the rotor position, *IEEE Transactions on Industry Applications*, 36(5), 1330–1335, 2000.
110. T. Senju, Y. Kuwae, N. Urasaki et al., Accurate parameter measurement for high speed permanent magnet synchronous motors, *2001 IEEE 32nd Annual Power Electronics Specialists Conference (IEEE Cat. No. 01CH37230)*, pp. 772–777, 2001.
111. T. Senju, K. Kinjo, N. Urasaki et al., Parameter measurement for PMSM using adaptive identification, *ISIE 2002. Proceedings of the 2002 IEEE International Symposium on Industrial Electronics (Cat. No. 02TH8608C)*, pp. 711–716, 2002.
112. T. J. E. Miller, J. A. Walker, and C. Cossar, Measurement and application of flux-linkage and inductance in a permanent-magnet synchronous machine, *IEE Conference Publication*, pp. 674–678, 2004.
113. Y. S. Chen, Z. Q. Zhu, and D. Howe, Calculation of d- and q-axis inductances of PM brushless ac machines accounting for skew, *IEEE Transactions on Magnetics*, 41(10), 3940–3942, 2005.

Torque Ripple Analysis and Minimization

114. H. Le-Huy, R. Perret, and R. Feuillet, Minimization of torque ripple in brushless DC motor drives, *IEEE Transactions on Industry Applications*, IA-22(4), 748–755, 1986.
115. P. Pillay and R. Krishnan, Investigation into the torque behavior of a brushless dc motor drive, *Conference Record—IAS Annual Meeting (IEEE Industry Applications Society)*, pp. 201–208, 1988.
116. R. Carlson, A. A. Tavares, J. P. Bastos et al., Torque ripple attenuation in permanent magnet synchronous motors, *Conference Record—IAS Annual Meeting (IEEE Industry Applications Society)*, pp. 57–62, 1989.
117. R. Carlson, M. Lajoie-Mazenc, and J. C. D. S. Fagundes, Analysis of torque ripple due to phase commutation in brushless DC machines, *IEEE Transactions on Industry Applications*, 28(3), 632–638, 1992.
118. J. Y. Hung and Z. Ding, Design of currents to reduce torque ripple in brushless permanent magnet motors, *IEE Proceedings B (Electric Power Applications)*, 140(4), 260–266, 1993.
119. D. C. Hanselman, Minimum torque ripple, maximum efficiency excitation of brushless permanent magnet motors, *IEEE Transactions on Industrial Electronics*, 41(3), 292–300, 1994.
120. N. Bianchi and S. Bolognani, Reducing torque ripple in PM synchronous motors by pole-shifting, *ICEM 2000 Proceedings. International Conference on Electrical Machines*, pp. 1222–1226, 2000.
121. M. Dai, A. Keyhani, and T. Sebastian, Torque ripple analysis of a PM brushless dc motor using finite element method, *IEEE Transactions on Energy Conversion*, 19(1), 40–45, 2004.

Effects of Saturation

122. E. Richter and T. W. Neumann, Saturation effects in salient pole synchronous motors with permanent magnet excitation, *Proceedings of the International Conference on Electrical Machines*, pp. 603–606, 1984.
123. B. J. Chalmers, Influence of saturation in brushless permanent-magnet motor drives, *IEE Proceedings, Part B: Electric Power Applications*, 139(1), 51–52, 1992.
124. B. J. Chalmers, Z. Dostal, L. Musaba et al., Experimental assessment of a permanent-magnet synchronous motor representation including Q-axis saturation, *Sixth International Conference on Electrical Machines and Drives (Conf. Publ. No. 376)*, pp. 284–288, 1993.
125. S. Morimoto, T. Ueno, M. Sanada et al., Effects and compensation of magnetic saturation in permanent magnet synchronous motor drives, *IAS'93. Conference Record of the 1993 IEEE Industry Applications Conference Twenty-Eighth IAS Annual Meeting (Cat. No. 93CH3366-2)*, pp. 59–64, 1993.
126. B. Frenzell, R. Hanitsch, and R. M. Stephan, Saturation effects in small brushless DC motors. A simplified approach, *Sixth International Conference on Power Electronics and Variable Speed Drives (Conf. Publ. No. 429)*, pp. 99–102, 1996.

Losses in PM Motors

127. B. Davat, H. Rezine, and M. Lajoie-Mazenc, Eddy currents in solid rotor permanent magnet synchronous motors fed by voltage inverter, *Electric Machines and Electromechanics*, 7(2), 115–124, 1982.
128. A. K. Nagarkatti, O. A. Mohammed, and N. A. Demerdash, Special losses in rotors of electronically commutated brushless DC motors induced by non-uniformly rotating armature MMFS, *IEEE Transactions on Power Apparatus and Systems*, PAS-101(12), 4502–4507, 1982.
129. C. Mi, G. R. Slemon, and R. Bonert, Modeling of iron losses of permanent-magnet synchronous motors, *IEEE Transactions on Industry Applications*, 39(3), 734–742, 2003.
130. C. C. Mi, G. R. Slemon, and R. Bonert, Minimization of iron losses of permanent magnet synchronous machines, *IEEE Transactions on Energy Conversion*, 20(1), 121–127, 2005.
131. T. J. E. Miller and R. Rabinovici, Back-EMF waveforms and core losses in brushless DC motors, *IEE Proceedings—Electric Power Applications*, 141(3), 144–154, 1994.
132. Z. Q. Zhu, K. Ng, N. Schofield et al., Analytical prediction of rotor eddy current loss in brushless machines equipped with surface-mounted permanent magnets. II. Accounting for eddy current reaction field, *ICEMS'2001. Proceedings of the Fifth International Conference on Electrical Machines and Systems (IEEE Cat. No. 01EX501)*, pp. 810–813, 2001.
133. Z. Q. Zhu, K. Ng, and D. Howe, Analytical prediction of stator flux density waveforms and iron losses in brushless DC machines, accounting for load condition, *ICEMS'2001. Proceedings of the Fifth International Conference on Electrical Machines and Systems (IEEE Cat. No. 01EX501)*, pp. 814–817, 2001.
134. D. Ishak, Z. Q. Zhu, and D. Howe, Eddy-current loss in the rotor magnets of permanent-magnet brushless machines having a fractional number of slots per pole, *IEEE Transactions on Magnetics*, 41(9), 2462–2469, 2005.
135. K. Atallah, Z. Q. Zhu, and D. Howe, An improved method for predicting iron losses in brushless permanent magnet DC drives, *IEEE Transactions on Magnetics (USA)*, pp. 2997–2999, 1992.
136. G. R. Slemon and X. Liu, Core losses in permanent magnet motors, *IEEE Transactions on Magnetics*, 26(5), pp. 1653–1655, Sept. 1990.

137. K. Ng, Z. Q. Zhu, N. Schofield et al., Analytical prediction of rotor eddy current loss in brushless permanent magnet motors, *32nd Universities Power Engineering Conference. UPEC '97*, pp. 49–52, 1997.
138. V. Hausberg and S. Moriyasu, Tooth-ripple losses in high speed permanent magnet synchronous machines," *Transactions of the Institute of Electrical Engineers of Japan, Part D*, 117-D(11), 1357–1363, 1997.
139. D. Fang and T. W. Nehl, Analytical modeling of eddy-current losses caused by pulse-width-modulation switching in permanent-magnet brushless direct-current motors, *IEEE Transactions on Magnetics*, 34(5), 3728–3736, 1998.
140. N. Urasaki, T. Senju, and K. Uezato, A novel calculation method for iron loss resistance suitable in modeling permanent-magnet synchronous motors, *IEEE Transactions on Energy Conversion*, 18(1), 41–47, 2003.
141. N. Urasaki, T. Senju, and K. Uezato, Investigation of influences of various losses on electromagnetic torque for surface-mounted permanent magnet synchronous motors, *IEEE Transactions on Power Electronics*, 18(1), 131–139, 2003.
142. A. Cassat, C. Espanet, and N. Wavre, BLDC motor stator and rotor iron losses and thermal behavior based on lumped schemes and 3-D FEM analysis, *IEEE Transactions on Industry Applications*, 39(5), 1314–1322, 2003.
143. M. Crivii and M. Jufer, Eddy-current losses computation for permanent-magnet synchronous motors, *Electromotion*, 13(1), 31–35, 2006.
144. S. Heung-Kyo, K. Tae Heoung, S. Hwi-Beom et al., Effect of magnetization direction on iron loss characteristic in brushless DC motor, *Proceedings of the International Conference on Electrical Machines and Systems 2007*, pp. 815–817, 2007.

Cogging Torque

145. B. Ackermann, J. H. H. Janssen, R. Sottek et al., New technique for reducing cogging torque in a class of brushless DC motors, *IEE Proceedings, Part B: Electric Power Applications*, 139(4), 315–320, 1992.
146. Y. Kawashima and Y. Mizuno, Reduction of detent torque for permanent magnet synchronous motor by magnetic field analysis, *Symposium Proceedings EVS-11. 11th International Electric Vehicle Symposium. Electric Vehicles: The Environment-Friendly Mobility*, pp. 8–10, 1992.
147. Z. Q. Zhu and D. Howe, Analytical prediction of the cogging torque in radial-field permanent magnet brushless motors, *IEEE Transactions on Magnetics*, 28(2), 1371–1374, 1992.
148. E. Favre, L. Cardoletti, and M. Jufer, Permanent-magnet synchronous motors: A comprehensive approach to cogging torque suppression, *IEEE Transactions on Industry Applications*, 29(6), 1141–1149, 1993.
149. T. Ishikawa and G. R. Slemon, A method of reducing ripple torque in permanent magnet motors without skewing, *Transactions on Magnetics*, 29(2), 2028–2031, March 1993.
150. N. Bianchi and S. Bolognani, Design techniques for reducing the cogging torque in surface-mounted PM motors, *IEEE Transactions on Industry Applications*, 38(5), pp. 1259–1265, 2002.
151. C. S. Koh and J.-S. Seol, New cogging-torque reduction method for brushless permanent-magnet motors, *IEEE Transactions on Magnetics*, 39(6), 3503–3506, 2003.
152. M. S. Islam, S. Mir, and T. Sebastian, Issues in reducing the cogging torque of mass-produced permanent-magnet brushless DC motor, *IEEE Transactions on Industry Applications*, 40(3), 813–820, 2004.
153. J. F. Gieras, Analytical approach to cogging torque calculation of PM brushless motors, *IEEE Transactions on Industry Applications*, 40(5), 1310–1316, 2004.

154. R. Islam, I. Husain, A. Fardoun et al., Permanent magnet synchronous motor magnet designs with skewing for torque ripple and cogging torque reduction, *Conference Record of the 2007 IEEE Industry Applications Conference—Forty-Second IAS Annual Meeting*, pp. 1552–1559, 2007.

Skew

155. A. Cassat, M. Williams, and D. MacLeod, Effect of skew on brushless dc motor exciting forces, *Proceedings of the Annual Symposium on Incremental Motion Control System and Device*, p. 148, 1993.

Steady-State Analysis

156. A. V. Gumaste and G. R. Slemon, Steady-state analysis of a permanent magnet synchronous motor drive with voltage source inverter, *IEEE Transactions on Industry Applications*, IA-17(2), 143–151, 1981.
157. G. R. Slemon and A. V. Gumaste, Steady-state analysis of a permanent magnetic synchronous motor drive with current source inverter, *IEEE Transactions on Industry Applications*, IA-19(2), 190–197, 1983.
158. T. Sebastian and G. R. Slemon, Operating limits of inverter-driven permanent magnet motor drives, *IEEE Transactions on Industry Applications*, IA-23(2), 327–333, 1987.
159. V. B. Honsinger, Performance of polyphase permanent magnet machines, *IEEE Transactions on Power Apparatus and Systems*, PAS-99(4), 1510–1518, 1980.

Design and Optimization of Machines

160. X. Liu and G. R. Slemon, An improved method of optimization for electrical machines, *IEEE Transactions on Energy Conversion*, 6(3), 492–496, 1991.
161. G. R. Slemon and X. Liu, Modeling and design optimization of permanent magnet motors, *Electric Machines and Power Systems*, 20(2), 71–92, 1992.
162. T. J. E. Miller, Design of PM synchronous and brushless DC motors, *Proceedings of the IECON '93. International Conference on Industrial Electronics, Control, and Instrumentation (Cat. No. 93CH3234-2)*, pp. 731–738, 1993.
163. G. R. Slemon, On the design of high-performance surface-mounted PM motors, *IEEE Transactions on Industry Applications*, 30(1), 134–140, 1994.
164. J. F. Gieras and M. Wing, Design of synchronous motors with rare-earth surface permanent magnets, *ICEM 94. International Conference on Electrical Machines*, pp. 159–164, 1994.
165. E. Hemead, R. Hanitsch, G. Duschl et al., Study of brushless DC motors in different configurations—using different kinds of permanent magnets, *32nd Universities Power Engineering Conference. UPEC '97*, pp. 37–40, 1997.
166. Z. Q. Zhu, K. Ng, and D. Howe, Design and analysis of high-speed brushless permanent magnet motors, *Eighth International Conference on Electrical Machines and Drives (Conf. Publ. No. 444)*, pp. 381–385, 1997.
167. T. Higuchi, J. Oyama, E. Yamada et al., Optimization procedure of surface PM synchronous motors, *IEEE Transactions on Magnetics*, 33(2 pt 2), 1943–1946, 1997.
168. M. Jufer, Slotless and slotted brushless DC motors. Technique performances and comparison, *Electromotion*, 4(1–2), 69–79, 1997.
169. Y. Honda, T. Higaki, S. Morimoto et al., Rotor design optimization of a multi-layer interior permanent-magnet synchronous motor, *IEE Proceedings: Electric Power Applications*, 145(2), 119–124, 1998.
170. Y. S. Chen, Z. Q. Zhu, and D. Howe, Slotless brushless permanent magnet machines: Influence of design parameters, *IEEE Transactions on Energy Conversion*, 14(3), 686–691, 1999.

171. R. Hanitsch and R. C. Okonkwo, On the design of brushless DC linear motors with permanent magnets, *PCIM '99. Europe. Official Proceedings of the Thirty-Fifth International Intelligent Motion Conference*, pp. 183–187, 1999.
172. Y. S. Chen, Z. Q. Zhu, D. Howe et al., Design and analysis of PM brushless AC machines with different rotor topologies for field-weakening operation, *34th Universities Power Engineering Conference*, pp. 169–172, 1999.
173. J.-A. Wu, D.-Q. Zhu, and X.-J. Jiang, Calculating torque of concentrated winding brushless PM motor, *Advanced Technology of Electrical Engineering and Energy*, 22(3), 59–63, 2003.
174. N. Bianchi, S. Bolognani, and F. Luise, Analysis and design of a PM brushless motor for high-speed operations, *IEEE Transactions on Energy Conversion*, 20(3), 629–637, 2005.
175. J. F. Gieras and U. Jonsson, Design of a high-speed permanent-magnet brushless generator for microturbines, *Electromotion*, 12(2–3), 86–91, 2005.
176. Y. Pang, Z. Q. Zhu, and D. Howe, Analytical determination of optimal split ratio for permanent magnet brushless motors, *IEE Proceedings: Electric Power Applications*, 153(1), 7–13, 2006.

Axial Field Machines

177. R. Krishnan and A. J. Beutler, Performance and design of an axial field PM synchronous motor servo drive, *Conference Record. 1985 IEEE Industry Applications Society Annual Meeting (Cat. No. 85CH2207-9)*, pp. 634–640, 1985.
178. H. Takano, T. Ito, K. Mori, A. Sakuta, and T. Hirasa, Optimum values for magnet and armature winding thickness for axial field PM brushless dc motors, *IEEE Transactions on Industry Applications*, pp. 157–162, 1990.
179. F. Caricchi, F. Crescimbini, A. Di Napoli et al., Development of a IGBT inverter driven axial-flux PM synchronous motor drive, *EPE '91. 4th European Conference on Power Electronics and Applications*, pp. 482–487, 1991.
180. F. Caricchi, F. Crescimbini, and O. Honorati, Low cost compact PM machine for adjustable speed applications, *IEEE Transactions on Industry Applications*, pp. 464–470, 1996.
181. K. Sitapati and R. Krishnan, Performance comparisons of radial and axial field, permanent-magnet, brushless machines, *IEEE Transactions on Industry Applications*, 37(5), 1219–1226, 2001.
182. A. Cavagnino, M. Lazzari, F. Profumo et al., A comparison between the axial flux and the radial flux structures for PM synchronous motors, *IEEE Transactions on Industry Applications*, 38(6), 1517–1524, 2002.
183. J. F. Gieras, R.-J. Wang, and M. J. Kamper, *Axial Flux Permanent Magnet Brushless Machines*, Kluwer Academic Publishers, Dordrecht, the Netherlands, 2004.

Noise and Vibration in Machines

184. Z. Q. Zhu and D. Howe, Analytical models for predicting noise and vibration in brushless permanent magnet DC motors, *Proceedings of the 25th Universities Power Engineering Conference*, pp. 277–280, 1990.
185. Y. S. Chen, Z. Q. Zhu, and D. Howe, Vibration of PM brushless machines having a fractional number of slots per pole, *IEEE Transactions on Magnetics*, 42(10), 3395–3397, 2006.
186. J. F. Gieras, C. Wang, J. C. S. Lai et al., Analytical prediction of noise of magnetic origin produced by permanent magnet brushless motors, *Proceedings of IEEE International Electric Machines and Drives Conference, IEMDC 2007*, pp. 148–152, 2007.

2 Introduction to Inverters and Their Control

The subsystem that made the widespread possible use of permanent magnet (PM) drives is the standard power electronic converter modules. To provide variable speed in the machine, variable frequency of the stator currents is required, which is achieved with an inverter. The inverter requires a dc voltage input, which, in a majority of the cases, is obtained from an ac supply by rectification with a diode bridge. The ac supply input is single phase for applications ranging from fractional hp to 1 hp, and over 1 hp, three-phase ac supply is preferred. Three-phase machines and three-phase inverters are predominant in applications. Drawing sinusoidal ac line currents from the utility supply and unity power factor requirements are coming to the forefront in large drives. To meet these needs, ac to dc front end converters are changing from diode bridge rectifiers to controllable bridge converters and these are presented in this chapter. Other than front end converters, there has hardly been any change in the power electronic subsystems, for PM drives over the last four decades. This chapter introduces devices, their switching behavior, gating circuits, protection circuits, ac to dc and dc to ac power conversion subsystems, and their control. Particular emphasis is laid on the effect of dead time, which is introduced between the activation of the top and bottom switching device in the inverter on the voltage and current waveforms and its compensation. In low-speed control systems including operation at zero speed, the nonlinearity of the inverter due to dead time as well as other aspects such as device voltage drops affect the quality of performance, particularly in sensorless position control systems. With this in view, compensation of dead time and device voltage drops to obtain linear characteristics of an inverter is presented in detail. The voltage and current control are enforced through the inverter with one of the popular schemes: pulse width modulation (PWM), hysteresis control, and space vector modulation. The fundamentals of these schemes are detailed. PWM control requires sampling of control signal. Two sampling schemes and their implications in practice are elucidated. The most significant in the inverter control has been the advent of space vector modulation. It is described in detail to enable engineers to develop a variety of implementation schemes to suit application exigencies. A hybrid scheme that unifies pulse width and space vector modulations gives enormous flexibility for implementation to control inverter losses and is described in this chapter. The control modeling of the inverter is developed for use in system transfer functions and controller designs. Resonant, multilevel, and matrix converters are not dealt with in this chapter as they not prevalent in the PM synchronous and brushless dc motor drives.

2.1 POWER DEVICE

2.1.1 POWER DEVICES AND SWITCHING

Since the advent of semiconductor power switches, the control of voltage, current, power, and frequency has become cost-effective [1–5]. The precision of control has been enhanced with the use of integrated circuits, microprocessors, and VLSI circuits in control circuits. Some of the popular power devices such as diodes, metal oxide semiconductor field-effect transistors (MOSFETs), and insulated gate bipolar transistors (IGBTs), and their symbols and capabilities are described below. These devices are commonly used in PM synchronous and brushless dc motor drives. The device physics and their functioning in detail are outside the scope of this chapter and interested reader is referred to other sources.

2.1.1.1 Power Diodes

It is a PN device with two terminals. When its anode potential is higher than the cathode potential by its on-state voltage drop, known as positive biasing, the device turns on and conducts current. The device on-state voltage drop is typically 0.7 V. When the device is reverse biased, i.e., the anode is less positive than the cathode, the device turns off and goes into blocking mode. The current through the diode goes to zero and then reverses and resurfaces to zero during the turn off [5] mode as shown in Figure 2.1.

Reversal of current occurs because the reverse bias leads to the reverse recovery of charge in the device. The minimum time taken for the device to recover its reverse voltage blocking capability is t_{rr} and the reverse recovery charge contained in the diode is Q_{rr} shown as the area during the reverse current flow. The diode does not have forward voltage blocking capability beyond its on-state voltage drop. The only way by which a conducting diode can be turned off is by reverse biasing it, i.e., by applying a negative voltage across its anode and cathode. Note that diodes are not controllable from a low-level signal like other devices.

Diodes having a reverse recovery time from a few to tens of microseconds are deemed to be slow switching devices. They are used in applications where their switching time, which is the sum of turn on and turn off times, is negligible compared to their conduction time. So these diodes find application as rectifiers used to convert an ac source into a dc source. Such diodes are known as power diodes. The power diodes are available in ratings of kiloampere and kilovolt and their switching frequency is usually limited to utility line frequency.

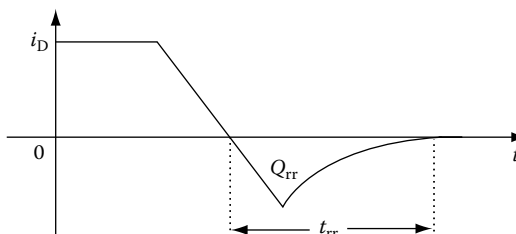
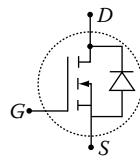


FIGURE 2.1 Diode current during turn off. (From Krishnan, R., *Electric Motor Drives*, Figure 1.1, Prentice Hall, Upper Saddle River, NJ, 2001. With permission.)

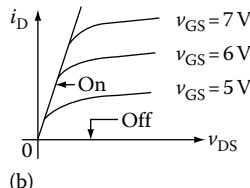
For fast switching applications, fast recovery diodes with reverse recovery times in tens of nanoseconds with ratings of several 100 A, at several 100 V but with a higher on-state drop of 2–3 V are available. They are usually used in fast switching rectifier with voltages higher than 60–100 V and in inverter applications. In case of low-voltage switching applications of less than 60–100 V, Schottky diodes are used. They have on-state voltage drop of 0.3 V, thus enabling higher efficiency in power conversion compared to the fast recovery diodes and power diodes.

2.1.1.2 MOSFET

This device is a class of field-effect transistor requiring lower voltages for turn on and turn off and is capable of higher switching frequency in the range of 30 kHz to 1 MHz [5]. The device is available at 100 A at 100–200 V, and 10 A at 1000 V. The device behaves like a resistor when in conduction and, therefore, can be used as a current sensor, thus eliminating a separate current sensing device such as a Hall effect current sensor in a drive system, leading to cost savings and compactness of the electronics package. The device always comes with an antiparallel body diode and sometimes referred to as parasitic diode that is not ultrafast and has a higher voltage drop. The device has no reverse voltage blocking capability because of its body diode. The device symbol for an N-channel MOSFET and its characteristics, drain current, i_D , versus drain to source voltage, v_{DS} , for various gate source voltages, v_{GS} , are shown in Figure 2.2. The gate source voltage is usually limited by upper value of 20 V. To provide immunity against noise switching, it is desirable to reverse bias the gate source voltage, say, to -5 V or about in practice. That ensures that the noise voltage has to overcome the barrier of this negative bias plus the threshold gate voltage for it to turn on the device. Low-cost drives do not have the luxury of having an additional negative logic power supply for reverse biasing the gate. Many industrial drives require such protection.



(a)



(b)

FIGURE 2.2 Schematic of (a) an N-channel MOSFET and (b) characteristics. (From Krishnan, R., *Electric Motor Drives*, Figure 1.5, Prentice Hall, Upper Saddle River, NJ, 2001. With permission.)

The gate signal is applied with reference to source terminal. The gate signals are generated from a micro or digital signal processor and, in general, the processor may not have the capacity to drive the gate with the required voltage level and current capability. Therefore, a circuit for level shifting the processor's output voltage of 5–15 V with significant current capability at turn on instants (up to a few milliseconds, varying with different applications) is required between the processor output and gate input, known as gate drive amplifier circuit. The input to the gate drive amplifier circuit is isolated from its input logic level signal because the logic level input signals have a common power supply whereas various gate drives are tied to different MOSFET sources where voltages may be at different levels. This isolation is provided using single-chip optoisolators for low voltages (<300 V), or by dc–dc converter circuits with high-frequency transformer link (<1000 V) or fiber optic links for high voltages (>1000 V). Different demarcating voltages for various types of isolation may be found in practice.

It is common to incorporate overcurrent, undervoltage, and overvoltage protection in the gate drive circuit. The current is sensed from the voltage drop across drain source and the voltage protection is offered by sensing the dc input voltage to the converter circuit. They can be inexpensively sensed with resistors. A typical gate drive circuit then may be represented as in Figure 2.3. In many gate drive circuits, the current and voltage protection signals can be combined with gate input signal, say by an AND circuit prior to the amplification stage of the gate signal. In such a case, care has to be exercised in having very little time delay between the AND circuit and amplification circuit so that instantaneous protection is not compromised by this time delay. The gate drive circuits are available in single chip package and they are usually used in low-voltage (<350 V dc link) converter circuits. For other voltages, the gate drive circuit is invariably custom developed to fit a certain application with features varying from one circuit to another.

2.1.1.3 Insulated Gate Bipolar Transistor

It is a three-element device with the desirable characteristics of a MOSFET from the viewpoint of gating, and a transistor in conduction with a reverse voltage blocking capability. Its symbol is given in [Figure 2.4](#). Current available ratings of these

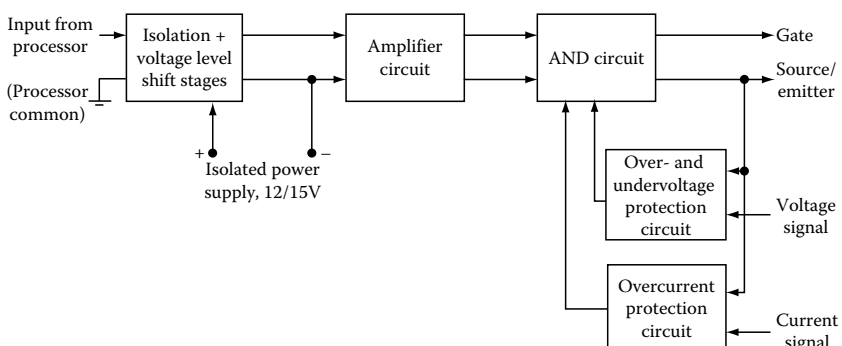


FIGURE 2.3 Gate drive circuit schematic.

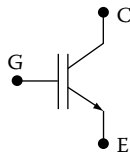


FIGURE 2.4 IGBT symbol. (From Krishnan, R., *Electric Motor Drives*, Figure 1.6, Prentice Hall, Upper Saddle River, NJ, 2001. With permission.)

devices are 1.2 kA at 3.3 kV and 0.6 kA at 6.6 kV with on-state voltage drop of 5 V. Higher currents at reduced voltages with much less on-state conduction voltage drops are available. It is expected that further augmentation commercially in the maximum current (1 kA) and voltage (15 kV) ratings will occur in the near future. The switching frequency is usually around 20 kHz for many of the devices and its utilization at high power is at low frequency because of switching losses and electromagnetic interference (EMI) concerns.

2.1.2 SWITCHING OF POWER DEVICES

The understanding of device switching in transient is of importance in the design of the converter as it relates to its losses, efficiency of the converter and the motor drive system, and finally in the thermal management of the power converter package. The transient switching of the devices during turn on and turn off is illustrated in this section, considering a generic device [5].

A device applies voltage to a load to build up or sustain or reduce current in it. Therefore, a supply voltage can be idealized by a voltage source. As for the load, consider it inductive. This is the case in ac motor drives as the machines are inherently inductive. For one period of switch conduction, which is in the order of tens of microseconds to a few milliseconds, the load current can be approximated by an ideal current source. Therefore, the circuit for switching is illustrated with ideal voltage and current sources and shown in Figure 2.5. The magnitudes of the voltage and current sources are V_s and I_s , respectively.

Initially the power switch is in off (nonconduction or blocking state) condition and the voltage across it is equal to source voltage. The path for source current, I_s , is provided by the diode across it. Consider the switching device is turned on by applying a positive voltage V_G to the gate. There is no change in voltage or current in the device for a time, known as delay time, t_{d1} . At the end of this delay time, the source current has an additional path for its flow besides the diode across it. The current in the device starts to increase linearly from zero to I_s in time t_{rc} , known as current rise time. During this time, note that the diode is conducting (the voltage across it is almost zero or conduction voltage) and hence the voltage across the device is equal to source voltage. This source voltage forces the transfer of current from diode to device, resulting in the current build up in switching device. The current rise in the switching device is limited by the current source, I_s . The diode current is reduced to zero when the device current attains the magnitude of I_s . The voltage across the device falls linearly from V_s to its conduction voltage drop V_{on} , in time, t_{fv} (the voltage fall time) and by the same measure, the voltage across the diode rises from zero to source voltage.

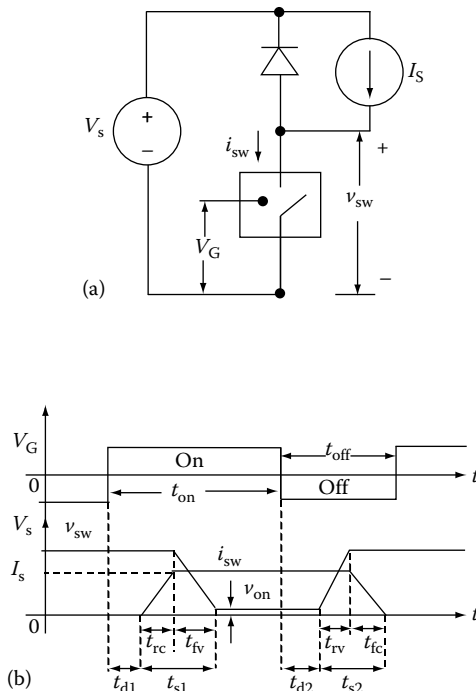


FIGURE 2.5 Switching circuit and waveforms: (a) switching circuit; (b) switching waveforms. (From Krishnan, R., *Electric Motor Drives*, Figure 1.7, Prentice Hall, Upper Saddle River, NJ, 2001. With permission.)

The sum of the current rise and voltage fall times is the turn on switching transient time, and note that during this time the device loss is very high. When it is averaged over a cycle, the switching loss is usually small. During device conduction, the voltage across the device is its conduction voltage drop (i.e., usually in the order of 1–3 V depending on the device) and during the conduction time, note that the power loss is smaller. The comparative magnitudes of the switching and conduction losses become clear when they are quantified later in this section. For most of the motor drives, the conduction losses are predominant and much higher than the switching losses.

When the gating signal goes to the turn off condition, the switching device responds with a turn off delay time of t_{d2} . Then the device voltage rises linearly to V_s in t_{rv} , which forward biases the diode initiating the current transfer from the switching device to the diode. The current in the device remains constant during the rise in voltage across it. The current transfer is completed in t_{fc} known as device current fall time. The sum of the voltage rise time across the switching device and current fall time is the turn off transient time during which the device loss is very high. The performance as described similarly is applicable to a diode as the diode is also a switching device. It turns on with a forward bias of its anode with respect to the cathode. The major difference between the diode and any other controllable

switching device is that the latter is accessed and controlled by a logic level low-voltage signal through its gate (or base). An additional difference is that when the diode is being turned off, the current in the diode will go through zero and reverse for a short duration, known as reverse recovery time, and then come back to zero. During this reverse recovery time, the voltage source is shorted by the diode and the controllable switching device. This only lasts for a few nanoseconds in fast turn off (or fast recovery) diodes. Such a high current pulse, normally tolerable in industrial systems, poses serious problems in systems where such signals may cause EMI and source identification. Inductor provides mitigation for this problem.

Consider the connecting wires (cables) between the voltage source and current source, current source and the controllable switch, and the controllable switch and voltage source. They constitute transmission lines and accordingly, each of them has a resistance, inductance, and a capacitance, which are distributed. A reasonable lumped parameter model of the circuit with the nonidealities of the connections can be visualized as shown in Figure 2.6. The elements of connecting cables are parasitic as they are not intended and desired by the designer and they impact the circuit performance in adverse ways as discussed later. The cable inductances and capacitances store energy and the resistances dissipate causing a lower circuit operational efficiency. The stored energy in the inductances requires an alternate path when the device is being turned off. It is to avoid the adverse effect of device failure from an open circuit with a current-carrying inductor. Inductance slows the current rise in the device during turn on and more importantly generates a voltage determined by the rate of change of current that adds up with the source voltage, thus creating an overvoltage across during the turn off instant and in that interval. In effect, it requires that the switch voltage be higher than the source voltage, resulting in poorer utilization of the device voltage. An alternate view of this is that the device volt-ampere rating is much more than what is effectively used in power transfer from the source to the load. To mitigate the effects of parasitic inductances, the length of connecting cables between devices, current source, and voltage source should be minimized. Also placing capacitor across the voltage source but on the side closer to devices (across terminals p and O in Figure 2.6) will also greatly benefit such efforts.

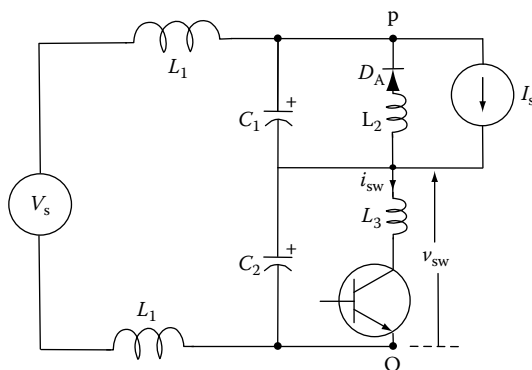


FIGURE 2.6 Circuit with approximate modeling of connecting cables.

The parasitic capacitances particularly across the devices discharge the stored energy to the devices when they are being turned on. At that instant, the device effectively short circuits the voltage across the parasitic capacitance, thus forcing a surge of a current during device turn on. This may last only for a short duration, as the energy involved is very small but nevertheless stresses the device by an overcurrent. Parasitic capacitances also slow the rate of change of voltage across the device when the device is being turned off thus keeping the device within safe dv/dt limits. With the modern devices having a large dv/dt capability, role of parasitic capacitances is not critical to limit rate of change of voltage during turn off time.

The switching illustrated is known as hard switching as current and voltage transitions occur in the device at full source voltage and current, respectively, during turn on and turn off periods. Resonant and soft switching circuits enable switching transitions at zero voltage and current, reducing or almost eliminating the switching losses. It is shown later that switching losses are not dominant in a majority of the industrial and commercial PM synchronous and brushless dc motor drives and hence schemes and circuits to reduce switching losses are not considered in these drives in general. But many of these circuits are not economical at present and generally are not considered in motor drives applications and, therefore, in this text also any further.

2.1.3 DEVICE LOSSES

The illustration and discussion in the previous section, identify the conduction and switching losses and their generation in the device. These losses are derived approximately as follows for the purpose of quantifying the losses, and having them beforehand helps so that the converter losses can be estimated and necessary cooling may be designed within a given packaging volume determined by the application. While exact predetermination of losses is not possible because of the varying operational conditions of the power converter driving a machine, it is essential for a design to have the upper values that may be encountered in practice, however, approximation of the estimation of losses is as every designer knows than none at all. Some of the approximations can be eliminated as they are introduced here to get some physical insight but some, such as the varying temperature and cooling that is encountered in actual operation, cannot be avoided.

2.1.3.1 Conduction Loss

Consider the energy loss during conduction of the device and it is

$$E_{sc} = I_s V_{on} [t_{on} + t_{d2} - t_{s1} - t_{d1}] \quad (2.1)$$

Compared to nominal conduction time in a circuit, all other times are small in Equation 2.1. Then it is fair to assume that turn on time is equal to turn off delay time and $t_{on} \gg t_{s1}$. With these approximations, the conduction energy loss is

$$E_{sc} = I_s V_{on} [t_{on} + t_{d2} - t_{s1} - t_{d1}] \approx V_{on} I_s t_{on} \quad (2.2)$$

And conduction power loss is derived by dividing the conduction energy loss with the switching period given as t_c . The switching period is the sum of the conduction (t_{on}) and nonconduction (t_{off}) times of the controllable switch. Hence the conduction power loss is

$$P_{sc} = \frac{E_{sc}}{t_{on} + t_{off}} = \frac{E_{sc}}{t_c} = V_{on}I_s \frac{t_{on}}{t_{on} + t_{off}} = V_{on}I_s d \quad (2.3)$$

where d is the duty cycle of the controllable switch given by

$$d = \frac{t_{on}}{t_{on} + t_{off}} \quad (2.4)$$

Note that duty cycle can assume values only between zero and one and it is nondimensionalized in terms of its unit. From Equation 2.3, it is seen that conduction loss is proportional to duty cycle since the conduction voltage drop is almost a constant in IGBT (but not certainly in MOSFET which is current dependent). In case of the MOSFET, conduction loss can be written as

$$P_{sc} = I_s^2 R_{DS} d \quad (2.5)$$

where R_{DS} is the drain to source resistance of the device and conduction voltage drop is given by the product of current and R_{DS} . From a conduction loss point of view, IGBTs are much preferred over MOSFETs for voltages over 350V as easily seen from the derivations. These equations have to be interpreted in the light of the assumptions that have been made. For more accurate evaluation of losses, the data sheet of the manufacturer taking together all hitherto ignored switching nonidealities should be considered.

2.1.3.2 Switching Losses

The device losses during turn on and turn off instants are known as switching losses. From [Figure 2.5](#), they are derived as

$$E_{sw} = 0.5I_s V_s [t_{s1} + t_{s2}] \quad (2.6)$$

The power loss due to switching is then obtained by averaging over switching period as

$$P_{sw} = \frac{1}{2} V_s I_s \frac{t_{s1} + t_{s2}}{t_c} = \frac{1}{2} V_s I_s f_c (t_{s1} + t_{s2}) = \frac{1}{2} V_s I_s f_c t_s \quad (2.7)$$

where the switching frequency also known as PWM or carrier frequency or simply PWM frequency is given by

$$f_c = \frac{1}{t_{on} + t_{off}} = \frac{1}{t_c} \quad (2.8)$$

and total switching time is given by

$$t_s = t_{s1} + t_{s2} \quad (2.9)$$

Switching loss is proportional to switching frequency if the switching times are assumed to be constants. To decrease the switching loss, it is imperative that the switching frequency is kept small along with the switching times of the device chosen. The latter is being continuously improved by device manufacturers. The switching times (sum of on and off switching times) for a MOSFET is in the order of 100 ns whereas for an IGBT it is in the order of 1–2 μ s. Because of the lower switching times, MOSFETs are preferred devices at high switching frequency operation. Lack of high current rating at high voltages with small drain to source resistances in MOSFETs makes them unsuitable for motor drives with ratings higher than 1 kW. Exceptions to this rule are found in specialty applications, more on the defense than on the commercial or industrial domains. Over this power level of 1 kW, IGBTs are invariably used and particularly so in PM synchronous and brushless dc motor drives.

An important point to observe is that switching losses are constant given a fixed switching frequency and device current. This is in variance with conduction loss, which is proportional to the duty cycle of the device. To assess the comparative significance of the conduction and switching losses within the total loss of the device, their ratio is found from Equations 2.3 and 2.7 as

$$\frac{P_{sc}}{P_{sw}} = d \left(\frac{2V_{on}}{V_s} \right) \frac{1}{(t_s/t_c)} = d \frac{V_{cn}}{t_{sn}} \text{ (p.u.)} \quad (2.10)$$

where the normalized conduction voltage drop and normalized total switching times are given by

$$V_{cn} = d \left(\frac{2V_{on}}{V_s} \right) \text{ (p.u.); } t_{sn} = \frac{t_s}{t_c} = f_c t_s \text{ (p.u.)} \quad (2.11)$$

Considering IGBT devices and visualizing the relationship with the following observations are in order:

$$(i) \quad \frac{1}{50} > V_{cn} > \frac{1}{500} \quad (2.12)$$

The higher and lower limits come from devices that are capable of operating at 170 and 1000 V dc source voltages, respectively.

- (ii) For these voltage ranges, the normalized total switching time can be observed for respective high and low switching frequencies (say from 20 to 1 kHz) as

$$\frac{1}{500} < t_{\text{sn}} < \frac{1}{200} \quad (2.13)$$

Using Equations 2.12 and 2.13, the ratio of conduction to switching losses is shown against $V_{\text{cn}}/t_{\text{sn}}$ for various duty cycles in Figure 2.7. The upper bound for $V_{\text{cn}}/t_{\text{sn}}$ is 10 for low-voltage and high-frequency devices and lower bound is 0.4 for low-frequency and high-voltage devices.

From Figure 2.7, some key observations on the ratio between losses are as follows:

1. Conduction loss dominates when switching frequency is smaller and vice versa is true for switching losses.
2. If higher voltage devices are to be operated at high frequency, then their switching losses will be high and that would affect the thermal junction temperature thus lowering the current rating of the device.
3. PM synchronous and brushless dc motor drives are usually operated from dc supplies obtainable from 120 or 230 V ac supply inputs. Thus they fall into $V_{\text{cn}}/t_{\text{sn}}$ values of 5–10. In this region, conduction loss predominates over switching losses and, therefore, the switching losses do not play a critical role in the power converter design for these motor drives.

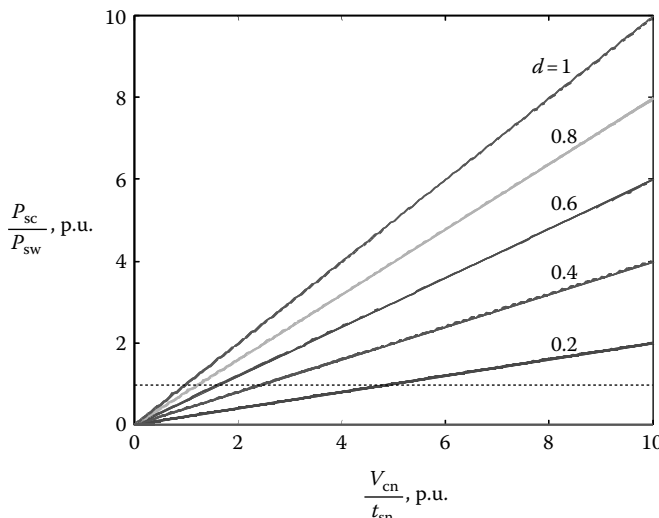


FIGURE 2.7 Ratio of conduction and switching losses versus ratio of normalized conduction voltage and switching times for various duty cycles.

The power switches are used in the circuits to control energy flow from source to load and vice versa. Its study is known as static power conversion. The details of power conversion are not the objectives of this book and many good texts are available on this topic. Some are listed in references at the end of this chapter. As and when necessary, a brief description and working of power converters are included in this text to the extent that is relevant to the scope of this book.

2.2 DC INPUT SOURCE

PM synchronous and brushless dc motor drives require variable voltage/current input at variable frequency to deliver variable speed operation. As the utility power source has constant frequency and voltage, it cannot be directly used in these machines. Various methods exist to obtain a variable voltage/current, variable frequency power supply from a fixed frequency, and voltage ac power source. They are given in the following.

Direct conversion: From fixed frequency ac supply to variable frequency, source conversion can be obtained with one-stage power conversion. The converters that facilitate such direct conversion are known as matrix converters. For a three-phase matrix converter realization, 18 self-commutating switches and diodes are required. Currently, the cost and complexity of control of the matrix converters preclude their use in industrial applications. These converters, because of this and the fact that they are not prevalent in practice, are not covered in this book.

Indirect conversion: This is a two-stage power conversion process involving first a utility ac to variable or fixed dc conversion (rectification) and then a dc to variable voltage/current, variable frequency ac conversion (inversion). The rectifier may be controlled or uncontrolled type. The uncontrolled rectifier with diodes only provides a constant dc voltage. This is the most prevalent in practice because of its low-cost implementation. The controlled rectifier with self-commutating devices provides a variable dc voltage. In spite of its higher cost and complexity in control, this is upcoming in a few applications where its operational flexibility in providing variable voltage, ac input current shaping, and output ripple reduction are highly required. The inverter stage consists of self-commutating devices such as MOSFETs or IGBTs and only six devices are required. This type of indirect conversion is the most popular in PM synchronous and brushless dc motor drive systems. The stages of power conversion are further elaborated in the following.

From a power utility ac source, dc output is derived through two basic methods using static power converters. They are as follows:

1. A diode bridge rectifier to convert the ac source voltage into a fixed dc voltage.
2. A controllable bridge that converts the ac source voltage to a variable dc voltage by a PWM controlled power converter with bidirectional power handling capacity.

Both these methods are outlined in the following sections.

2.2.1 DC INPUT SOURCE WITH DIODE BRIDGE RECTIFIER

The input to the dc to ac stage converter popularly known as inverter comes from either a battery or a rectified ac supply. The rectified ac is the prevalent form of input. The ac input is rectified through a diode bridge and its output is filtered to keep the dc voltage a constant.

A single-phase rectification circuit is shown in Figure 2.8. During positive half cycles of input voltage, v_s (with terminal r positive compared to terminal y) diodes D_1 and D_6 conduct and during negative half cycles of v_{ry} , diodes D_3 and D_4 conduct. The conduction is for electrical 180° assuming that the load is purely resistive and ideal diodes with zero conduction voltage drops. But the rectifier charges a capacitor to smooth the pulsating rectified voltage, which then is fed to an inverter driving the machine. The capacitor charges up to the peak of the supply input voltage and then due to the load, the charge in the capacitor decreases, resulting in a gradual decrease of capacitor voltage, v_{dc} . The capacitor does not start charging until the input supply voltage is higher than that of instantaneous v_{dc} . The charging current lasts until the capacitor voltage matches the peak supply input voltage. Because of this phenomenon, the current conduction duration is very small, resulting in peaky waveform. The deleterious effects of such narrow current pulses are high peak capacitor current rating, and higher harmonic currents. They can be mitigated if the input current is spread over the entire cycle and made sinusoidal and preferably in phase with supply input voltage giving a unity power factor. Such circuits to provide sinusoidal input current at unity power factor are discussed in Section 2.11.

A three-phase bridge rectifier is shown in Figure 2.9a. Only one input line voltage is larger in magnitude compared to two other line voltages at a given time. For example, let v_{ry} be much larger than v_{by} and v_{rb} as shown in Figure 2.9b. In this case, diodes D_1 and D_6 are turned on with the result that the line voltage v_{ry} is applied to the filter input, v_{re} . After 60° (electrical), note that v_{rb} becomes much larger and positive compared to all other input line voltages. This forward biases diodes D_1 and D_2 , resulting in their conduction. Note that diode D_1 is already on from previous 60° of conduction. With the turn on of D_2 and the fact that v_{by} is negative results in reverse biasing D_6 , forcing it to turn off. Similarly in the subsequent 60°, D_1 will be turned off and D_3 will be turned on while D_2 continues to conduct during this period. The

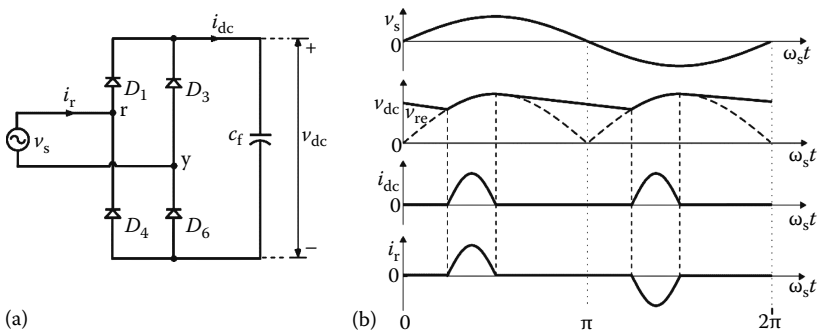


FIGURE 2.8 Single-phase rectifier and its operational waveforms: (a) diode rectifier circuit; (b) operational waveforms.

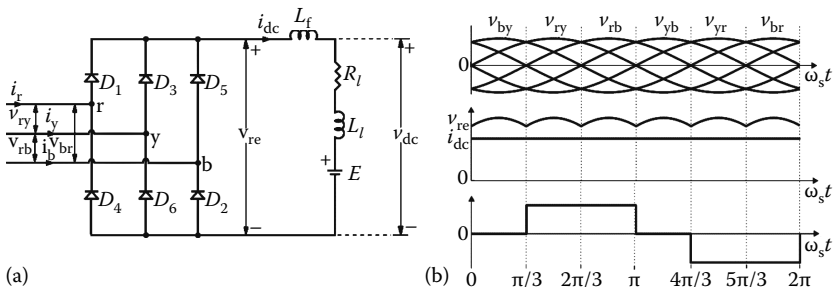


FIGURE 2.9 Three-phase diode bridge rectifier and its operational waveforms: (a) three-phase diode bridge rectifier circuit; (b) operational waveforms.

sequence of diode conduction is D_1, D_2, D_3, D_4, D_5 , and D_6 for one electrical cycle with two diodes conducting any time. Thus the rectification process happens in this converter. It may be seen that only two diodes conduct at a given time and each diode conducts only 120° in a cycle with the resulting duty cycle of $1/3$. The dc output voltage can be derived by averaging the applied input line voltage for 60° as

$$v_{dc} = \frac{1}{\left(\frac{\pi}{3}\right)} \int_{\pi/3}^{2\pi/3} v_{ry} d\theta = \frac{1}{\left(\frac{\pi}{3}\right)} \int_{\pi/3}^{2\pi/3} V_m \sin \theta d\theta = \frac{3}{\pi} V_m = \frac{3}{\pi} \sqrt{2}V = 1.35V \quad (2.14)$$

where

V is the line-to-line rms voltage (commonly referred as line voltage)

V_m is the peak line-to-line voltage and referred to as peak line voltage in power systems

The integration is carried from $\pi/3$ to $2\pi/3$ since v_{ry} becomes the largest line voltage compared to any other line voltages only during this time interval. The full rectification consists of such six 60° conductions from possible six line voltages obtained from the three line voltages and their counterparts with a phase shift of 180° .

The filter comprises of the inductor, L_f and capacitor, C_f , which is an electrolytic capacitor. This filter smooths the rectified voltage. In smaller motor drives, the inductor is not used for cost and compact packaging reasons. If an inductor is absent in the filter, there will be an inrush current when the bridge rectifier is energized. To avoid such inrush, it is usual to use resistors in the place of inductors and after charging the capacitor, resistors can be bypassed. The filter capacitor is the most vulnerable and one of the most expensive components in the drive system. Its life is affected by the ripple current and it has a much shorter life compared to other components. This poses a clear drawback in applications where maintenance access is denied. Under such rare circumstances, direct conversion process of fixed ac to variable ac with matrix converters is desirable.

A sample of rectifier ac input phase voltage, phase current and its frequency contents is shown in Figure 2.10 for various values of input inductor (zero, small, and infinite

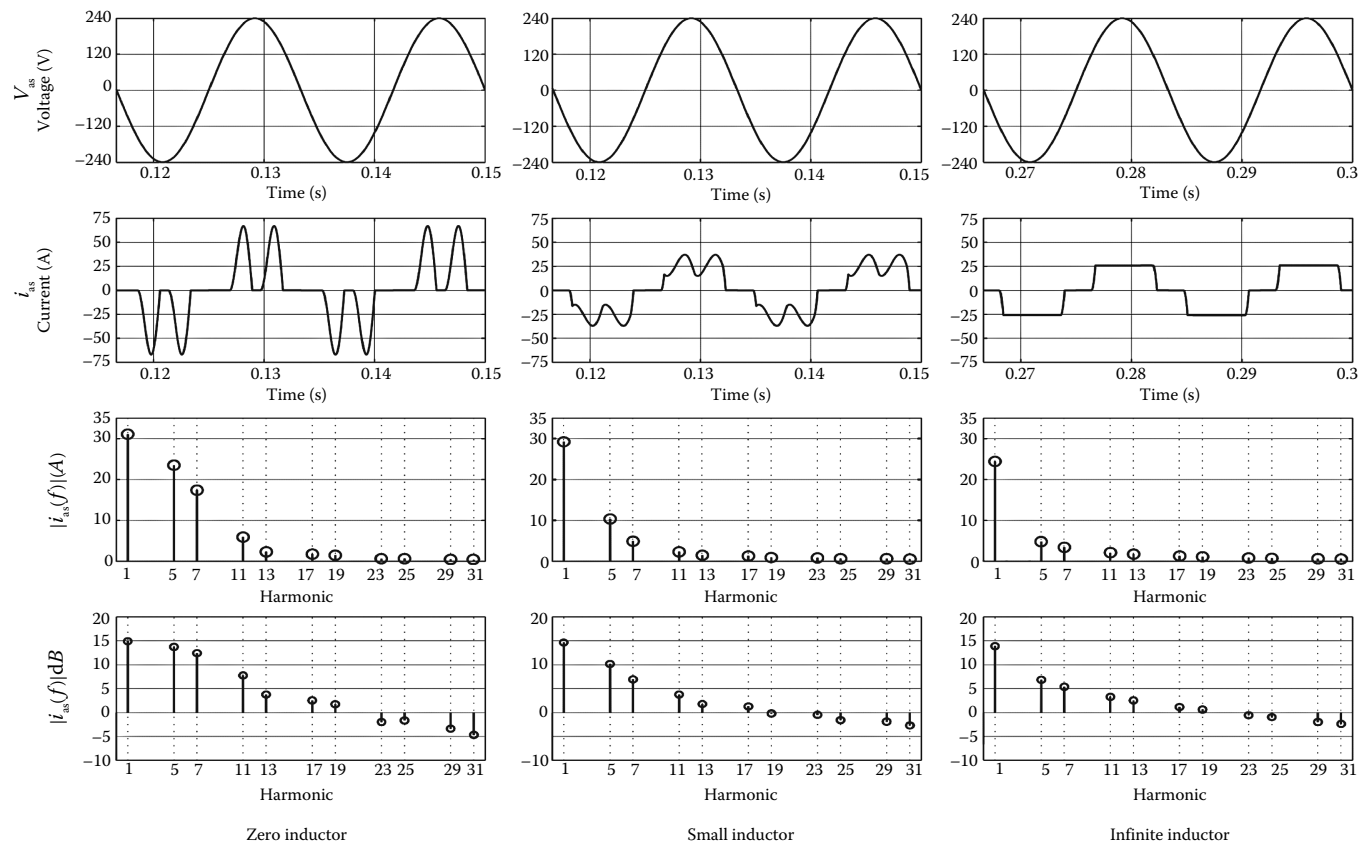


FIGURE 2.10 Input ac voltage and current in a three-phase diode bridge rectifier with inductive and capacitive output filter supplying a load. Zero inductor, small inductor, and infinite inductor.

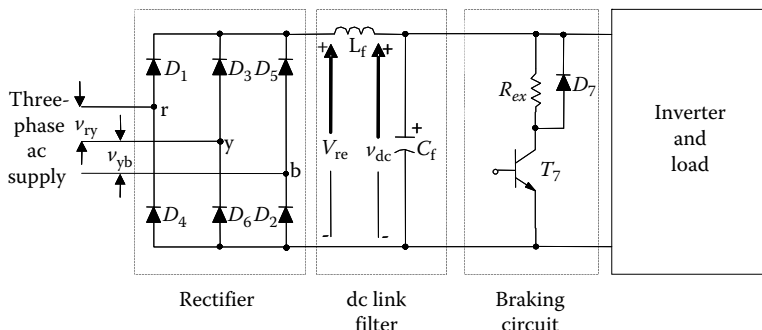


FIGURE 2.11 Front end of the inverter circuit.

inductors) on the dc output side. Even infinite inductance does not get a sinusoidal input current and the ac input current has immense higher order harmonics as seen from FFT. They are undesirable in a power system as there are no counterparts of the harmonics in the utility input, thus causing the harmonic currents to circulate in the power system unhindered. Higher harmonics generate significant interference and losses in the system. Hence the need for elimination of the higher harmonics in the system. It can be accomplished by making the input current sinusoidal in shape with negligible harmonics and it is treated in the subsection on power factor correction (Section 2.11).

The use of the diode bridge has the advantage of near unity fundamental power factor, but it draws a nonsinusoidal current, thereby affecting the power quality of the utility source. The merits of diode bridge rectifiers are compactness, high reliability, and low cost. It has the disadvantage in that it cannot send power from the dc link into ac mains. In that case, the regenerative energy (the energy received from the machine via inverter and sent to the dc link) has to be dissipated in the braking resistor, shown in Figure 2.11 by controlling the duty cycle of the switch T_7 by PWM. The simple diode bridge rectifier does not regulate the dc output voltage when the input ac voltages vary. It is clearly a disadvantage in inverter drives as the rectifiers impact the size of the dc link capacitor.

2.3 DC TO AC POWER CONVERSION

Consider an ac voltage and resulting current in an inductive circuit shown in Figure 2.12. There are four distinct regions of operation in a cycle and they are listed in Table 2.1.

Casting them in current versus voltage representation, various regions translate into current voltage quadrants as shown in Figure 2.13. That means for a converter to handle ac power conversion it must be capable of operating in all four quadrants. A simple realization of such a dc to ac power conversion circuit is described in the following.

2.3.1 SINGLE-PHASE HALF-WAVE INVERTER

For the treatment here, a dc source is given, which may be obtained from many ways as discussed in the previous section or derived from a battery. As the input source

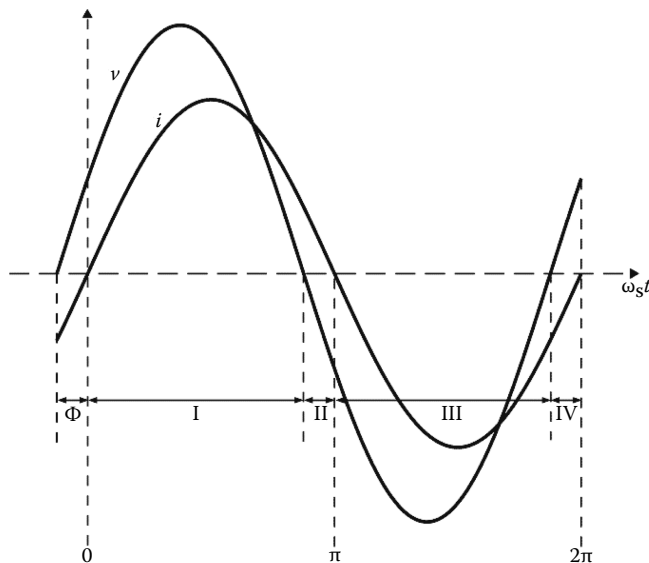


FIGURE 2.12 Single-phase ac voltage and current waveforms in an inductive load.

TABLE 2.1

Single-Phase Voltage and Current Relationship in an Inductive Circuit

Region	Voltage	Current	Power	Voltage/Current Quadrants
I	>0	>0	>0	I
II	<0	>0	<0	II
III	<0	<0	>0	III
IV	>0	<0	<0	IV

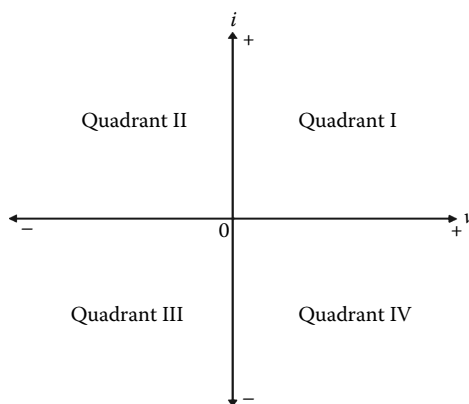


FIGURE 2.13 Quadrant designation of voltage-current operation.

is dc, it can supply only real power. But an ac system entails reactive power for nonresistive loads and this reactive power must be generated by the converter only. For this converter to handle all four quadrants, the converter must have on the minimum two transistors, one to conduct positive current and the other negative current with dc sources for each of the transistor to work with. This accounts for quadrants I and III but the remaining quadrants can be realized by having antiparallel diodes to the transistors as shown in Figure 2.14. These antiparallel diodes conduct current in a direction opposite to the transistors' current while maintaining the same polarity of the voltage across the load.

The operation can be explained considering an inductive load. For quadrant I operation, turn on T_1 , thus making the load voltage equal $v_{dc}/2$, leading to a current in load. When T_1 is turned off, the current in the load is carried by the diode D_4 , resulting in the load voltage being $-v_{dc}/2$. This corresponds to quadrant II operation with positive current and negative voltage in the load. Continued quadrant II operation will null the load current. Then reversal of current and voltage in the load is achieved by turning on T_4 , corresponding to quadrant III where the current and voltage are negative. With the current being continuous, turning off T_4 will forward bias D_1 , resulting in the voltage across the load becoming $v_{dc}/2$. A reversal of voltage across the load has occurred while maintaining the current (negative) in the same direction as in quadrant III. This operation corresponds to quadrant IV with negative current and positive voltage across the load. The operation is summarized in Table 2.2 for handy reference.

There are some disadvantages with this circuit for dc to ac power conversion and they are given below:

1. Full dc source voltage is not used, as only half its magnitude is being applied at any given instant across the load. This is known as voltage derating in the literature. The disadvantage of this is that for a given power conversion, the load current has to be doubled since the voltage is halved. Higher current involves higher conduction and higher winding resistive losses in the load

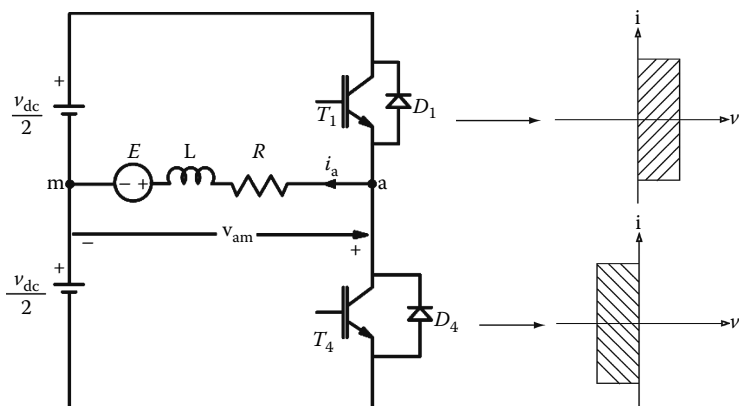


FIGURE 2.14 DC to ac power converter with minimum switches.

TABLE 2.2
Operational Modes of the dc to ac Power Converter

Modes	T_1	T_4	D_1	D_4	Initial Current	i_a	v_{am}	Quadrant
1	On	Off	Off	Off	≥ 0	>0	$\frac{V_{dc}}{2}$	I
2	Off	Off	Off	On	>0	>0	$-\frac{V_{dc}}{2}$	II
3	Off	On	Off	Off	≤ 0	<0	$-\frac{V_{dc}}{2}$	III
4	Off	Off	On	Off	<0	<0	$\frac{V_{dc}}{2}$	IV

machine, leading to poor machine and converter operational efficiencies as well as higher thermal cooling arrangements for the power converter with increased heat sink or cooling fan or cooling liquid circulation.

2. The voltage across the load is either $+v_{dc}/2$ or $-v_{dc}/2$ but a zero can never be applied with this converter. This will generate higher current ripples. For example, during positive half cycle of the load current, the applied voltage will consist of many positive and negative source voltage application intervals instead of only positive source voltage and zero voltage intervals thus contributing to higher current ripple.

In spite of its disadvantages, this circuit has some applications with its unique merit of having only two transistors for dc to ac power conversion. The process of dc to ac power conversion is known as inversion and the circuits for such power conversion go by the name of inverters. The converter that is discussed goes under the name of half-wave inverter as it uses only half the dc source voltage. Set of T_1 and T_4 with their antiparallel diodes D_1 and D_4 is known as a phase leg. This circuit has limited degrees of control freedom and full source voltage is not used and such limitations can be overcome in its full-wave version described in the following section.

2.3.2 SINGLE-PHASE FULL-WAVE INVERTER

The limitations of the half-wave inverter are overcome by adding another phase leg (say b) as shown in Figure 2.15. Turning on T_1 and T_6 enables current i_a to flow from a to b, say, positive direction, and the resulting load voltage is v_{dc} . Turning off T_1 when current is flowing to the load forward biases diode D_4 . The current in inductor cannot be turned off instantaneously and during turn off of T_1 , an alternate path for current flow has to be provided. This is diode D_4 , which is forward biased by the voltage induced by the rate of change of current in the inductance. Then diode D_4 , load and transistor T_6 form a closed circuit enabling the current i_a to flow. In this interval, the voltage across the load is zero, assuming that the devices are ideal and hence their

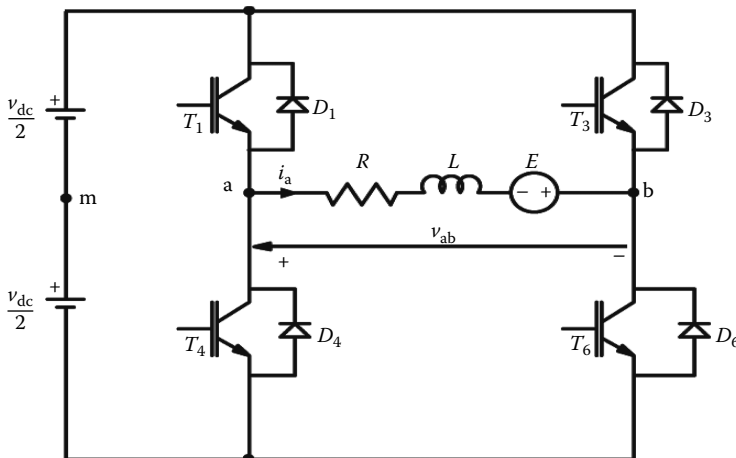


FIGURE 2.15 Full-wave single-phase inverter.

conduction voltage drops are negligible. If the transistor T_6 is also turned off when there is current in the circuit, then the diode D_3 is forward biased with the effect that the current flows back to the dc source via D_4 , load and D_3 . During this mode of operation, the load voltage is $-v_{dc}$. Including this mode, the circuit provides $-v_{dc}$, 0 and $+v_{dc}$ across the load for positive current flow. Note that this has three degrees of freedom and full source voltage application capability. Similarly with transistors T_3 and T_4 switching, negative load current (i.e., current flowing from b to a) with positive, zero or negative voltage across the load can be applied. Zero voltage is obtained by turning on transistors T_1 and T_3 or transistors T_4 and T_6 simultaneously, regardless of the current in the load. If there is current, say, positive current, then transistor T_1 and diode D_3 are conducting it when T_6 is turned off. Turning off transistor T_6 and turning on transistor T_3 does not interfere with flow of current through diode D_3 . With zero current in the load, turning on transistors T_1 and T_3 provides zero voltage across the load. The operational conditions are summarized in Table 2.3 for the single-phase inverter.

Mode 2 has zero power input but generates output power. For example, consider a dc machine as load. During this mode 2, due to the presence of positive current in the machine, a positive torque is developed in the machine and if the machine is rotating in the positive direction, the machine outputs positive power. Hence it is justifiable to denote this operational mode as belonging to quadrant I.

Note that an artificial midpoint m in the dc source is indicated in this inverter (Figure 2.15) and it has no purpose other than that the single-phase full-wave inverter is derived from two single-phase half-wave inverters, for understanding and for modeling. Because of zero voltage generation capability across the load, it is easy to visualize that an effective variable output voltage is obtained by varying the duration of positive, zero, and negative voltage ($+v_{dc}$, 0, and $-v_{dc}$) applications. The effective output voltage is independently controlled. Only device turn on and turn off times together with the number of times they are switched in each cycle determine

TABLE 2.3
Single-Phase Inverter Operational Modes

Modes	T_1	T_4	T_3	T_6	D_1	D_4	D_3	D_6	Initial Current	i_a	v_{ab}	Quadrant
1	On	Off	Off	On	Off	Off	Off	Off	≥ 0	>0	v_{dc}	I
2	Off	Off	Off	On	Off	On	Off	Off	>0	>0	0	I
3	Off	On	Off	On	Off	On	Off	Off	>0	≥ 0	0	I
4	Off	On	Off	On	Off	Off	Off	Off	0	0	0	
5	On	Off	Off	Off	Off	Off	On	Off	>0	>0	0	I
6	On	Off	On	Off	Off	Off	On	Off	>0	>0	0	I
7	On	Off	On	Off	Off	Off	Off	Off	0	0	0	
8	Off	Off	Off	Off	Off	On	On	Off	>0	>0	$-v_{dc}$	II
9	Off	On	On	Off	Off	Off	Off	Off	≤ 0	<0	$-v_{dc}$	III
10	Off	Off	On	Off	On	Off	Off	Off	<0	<0	0	III
11	On	Off	On	Off	On	Off	Off	Off	<0	<0	0	III
12	On	Off	On	Off	Off	Off	Off	Off	0	0	0	
13	Off	On	Off	Off	Off	Off	Off	On	<0	<0	0	III
14	Off	On	Off	On	Off	Off	Off	On	<0	<0	0	III
15	Off	On	Off	On	Off	Off	Off	Off	0	0	0	
16	Off	Off	Off	Off	On	Off	Off	On	<0	<0	v_{dc}	IV

the limitation of the voltage magnitude control. Given ideal switching devices, the voltage control is unconstrained by any other factor. The frequency of the output voltage is controlled by the speed with which all four quadrants are traversed by the switching of the inverter. The frequency of the load voltage can be independently controlled and it is not a function of the effective voltage. It is only constrained by the device speed and loss characteristics. Designers consider these factors in estimating and rating the maximum voltage and frequency available from an inverter.

Three units of single-phase full-wave inverter can be used to feed and control a three-phase machine. It is not usual to use such a three-phase full-wave inverter. It requires 12 active devices and cost of such a power converter is considered expensive for most of the applications. There are some applications in critical motor drives such as in aircraft and defense applications where independent control of machine phases is desirable in the face of faults. In most of the industrial drives, it is fairly common to come across an inverter with three-phase legs assembled to provide variable voltage/current and variable frequency to ac machines. Such an inverter, its operation, and control are presented in sufficient detail in following sections.

2.3.3 THREE-PHASE INVERTER

To understand its basic operation, assume the dc link voltage is constant in the three-phase inverter circuit shown in [Figure 2.16](#). Each of the phase leg is independently operated.

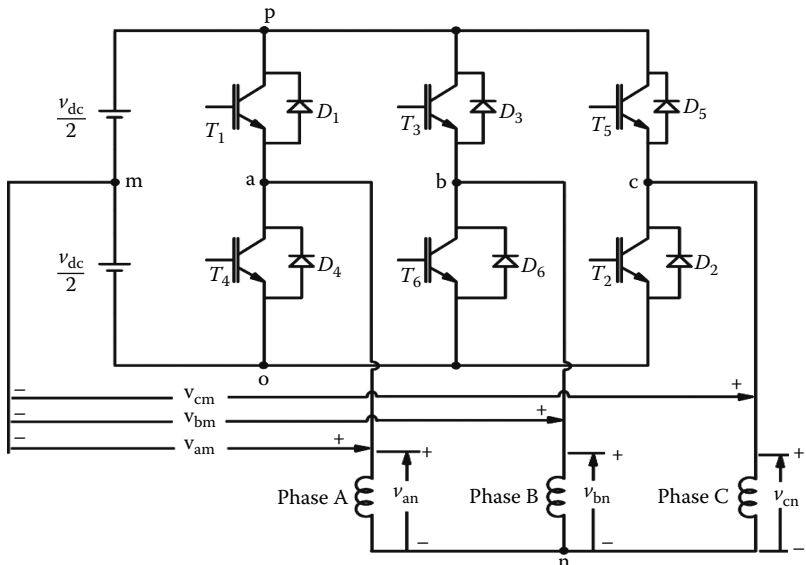


FIGURE 2.16 Three-phase inverter.

The midpoint voltages are derived dependent upon the switching status of the upper or lower devices in the phase legs. It is assumed that one switch in each phase leg is turned on at a given time. When a switch (top/bottom) is turned off, the current in that phase is transferred to the other device's (bottom/top) antiparallel diode. Sufficient time, known in literature as dead time, has to be provided between the turn on (top/bottom) of a device and turn off (bottom/top) of a device in each phase leg to avoid a short circuit of the dc supply voltage. The top/bottom device's complement is bottom/top device. The reason for complementary switching (when one is on the other is off in a phase leg) is that load voltages will be well defined regardless of the current in them. Without the complementary switching, voltage control of the inverter is not possible.

Consider the dc source voltage to be split in to two halves and the midpoint of the source voltage be *m*. The midpoint of the inverter phase legs are *a*, *b*, and *c*. The inverter midpoint voltages with respect to dc source midpoint are v_{am} , v_{bm} , and v_{cm} . They vary depending on the state of the transistors T_1 and T_4 , T_3 and T_6 , and T_5 and T_2 , respectively. For example, let T_1 be on and T_4 be off, then

$$v_{am} = \frac{v_{dc}}{2} \quad (2.15)$$

If transistor T_1 is off and transistor T_4 is on, then

$$v_{am} = -\frac{v_{dc}}{2} \quad (2.16)$$

The midpoint voltage as defined above only has two output states, i.e., either $+\frac{v_{dc}}{2}$ or $-\frac{v_{dc}}{2}$. If the midpoint voltages are defined with respect to negative of the dc bus 0, then for example,

$$\begin{aligned} v_{ao} &= v_{dc} \text{ for } T_1 \text{ on and } T_4 \text{ off} \\ &= 0 \text{ for } T_4 \text{ on and } T_1 \text{ off} \end{aligned} \quad (2.17)$$

They are derived with the assumption that the devices are ideal. Sometimes, this basis is advantageous and it is used in later sections.

The line-to-line voltages can be derived from the midpoint voltages as

$$v_{ab} = v_{am} - v_{bm} \quad (2.18)$$

$$v_{bc} = v_{bm} - v_{cm} \quad (2.19)$$

$$v_{ca} = v_{cm} - v_{am} \quad (2.20)$$

The line voltages can also be derived from the phase voltages as

$$v_{ab} = v_{an} - v_{bn} \quad (2.21)$$

$$v_{bc} = v_{bn} - v_{cn} \quad (2.22)$$

$$v_{ca} = v_{cn} - v_{an} \quad (2.23)$$

where

v_{ab} , v_{bc} , and v_{ca} are the various line voltages

v_{an} , v_{bn} , and v_{cn} are the phase voltages

From these equations, the phase voltages are derived assuming that the system is balanced, i.e., the sum of the currents and voltages is equal to zero. In many texts, the phase voltages are also symbolized as

$$v_{as} = v_{an} \quad (2.24)$$

$$v_{bs} = v_{bn} \quad (2.25)$$

$$v_{cs} = v_{cn} \quad (2.26)$$

and they in terms of the line voltages are given as

$$v_{as} = \frac{v_{ab} - v_{ca}}{3} \quad (2.27)$$

$$\nu_{\text{bs}} = \frac{\nu_{\text{bc}} - \nu_{\text{ab}}}{3} \quad (2.28)$$

$$\nu_{\text{cs}} = \frac{\nu_{\text{ca}} - \nu_{\text{bc}}}{3} \quad (2.29)$$

Consider a switching pattern for an inverter consisting of 180° positive and negative duration of voltage out of each phase leg with 120° phase displacement between the phase legs shown in Figure 2.17. The midpoint voltages of the phase legs mirror

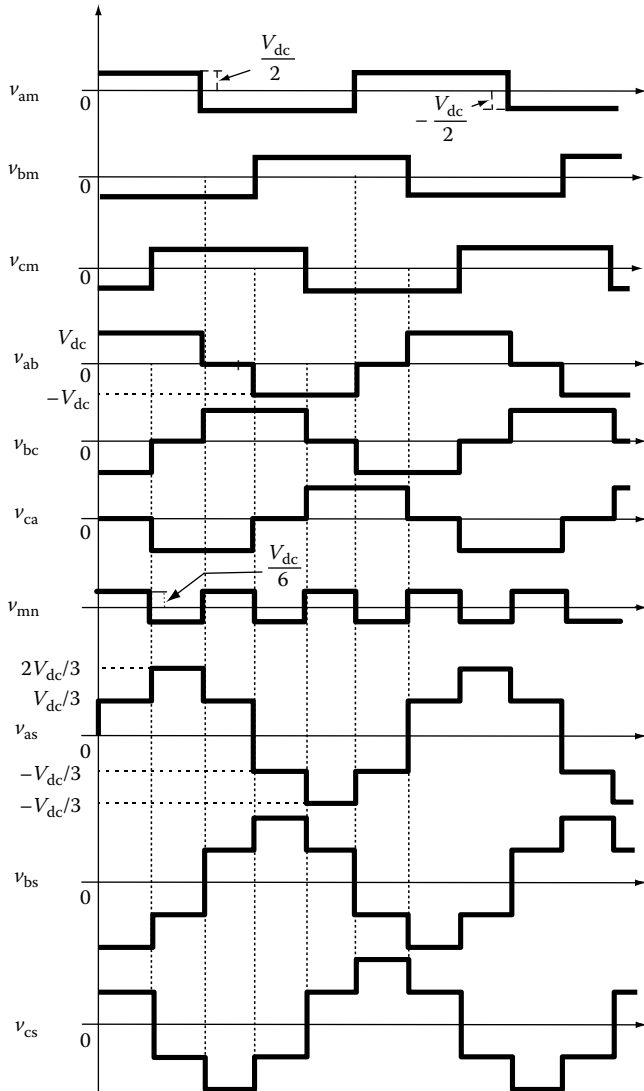


FIGURE 2.17 Inverter waveforms for a simple switching.

the switching signals to the transistors and, therefore, the switching signals are not shown separately in the figure. The line-to-line voltages are derived from the difference between the phase leg voltages, and phase voltages are derived from the line-to-line voltages using the expressions derived earlier. The voltage between the midpoint of the dc source and load neutral is derived as in the following.

From the switching signals, two distinct cases are identified:

- (i) One top transistor in one-phase leg and two bottom transistors in two other phase legs are conducting
- (ii) Two top transistors in two-phase legs and one bottom transistor are conducting in the third phase leg

Solving for the two cases and finding the voltage between the midpoint of the dc source and load neutral solves this issue. Corresponding to case (i), let T_1 , T_6 , and T_2 conduct. Then the voltage equations are

$$\frac{v_{dc}}{2} + v_{an} + v_{nm} = 0 \quad (2.30)$$

$$\frac{v_{dc}}{2} + v_{mn} + v_{nb} = 0 \quad (2.31)$$

$$\frac{v_{dc}}{2} + v_{mn} + v_{nc} = 0 \quad (2.32)$$

From these equations, the voltage between the midpoint of dc source and load neutral is derived as

$$v_{mn} = -\frac{v_{dc}}{6} \quad (2.33)$$

Similarly for case (ii), say, corresponding to transistors T_1 , T_3 , and T_2 conduction, the equations are derived as

$$\frac{v_{dc}}{2} + v_{an} + v_{nm} = 0 \quad (2.34)$$

$$\frac{v_{dc}}{2} + v_{mn} + v_{bn} = 0 \quad (2.35)$$

$$\frac{v_{dc}}{2} + v_{mn} + v_{nc} = 0 \quad (2.36)$$

Then the resulting voltage between the midpoint of dc source and load neutral is

$$v_{mn} = \frac{v_{dc}}{6} \quad (2.37)$$

Therefore, the voltage between the dc source midpoint and load neutral is $v_{dc}/6$ or $-v_{dc}/6$ when one top and two bottom devices are conducting or vice versa, respectively, and it is a third harmonic of the output. With this voltage, it is easy to derive the phase voltages and from them, it is seen that they are six stepped.

The line-to-line voltages when resolved into Fourier components have the following form:

$$v_{ab}(t) = \frac{2\sqrt{3}}{\pi} V_{dc} \left(\sin \omega_s t - \frac{1}{5} \sin 5\omega_s t + \frac{1}{7} \sin 7\omega_s t - \dots \right) \quad (2.38)$$

$$v_{bc}(t) = \frac{2\sqrt{3}}{\pi} V_{dc} \left\{ \sin(\omega_s t - 120^\circ) - \frac{1}{5} \sin(5\omega_s t - 120^\circ) + \frac{1}{7} \sin(7\omega_s t - 120^\circ) - \dots \right\} \quad (2.39)$$

$$v_{ca}(t) = \frac{2\sqrt{3}}{\pi} V_{dc} \left\{ \sin(\omega_s t + 120^\circ) - \frac{1}{5} \sin(5\omega_s t + 120^\circ) + \frac{1}{7} \sin(7\omega_s t + 120^\circ) - \dots \right\} \quad (2.40)$$

The phase voltages are shifted from the line voltages by 30° and their peak values are $(2/\pi)V_{dc}$. The peak phase voltage plays an important role in the definition of modulation ratio of the PWM and modulation index of the space vector modulation and it will be recalled a number of times in this chapter. When the output voltage is varied by means of PWM, the output voltage is expressed in terms of this phase peak voltage, giving way to a ratio between them known as modulation ratio, a non-dimensional factor. Modulation ratio is helpful in evaluating the efficacies of various PWM techniques in the control of inverter and through that the performance of various ac machines including that of the PM synchronous machines (PMSM) and PM brushless dc machines. The fundamental only produces the useful torque and hence that alone need to be considered for the steady-state performance evaluation of the inverter-fed ac motor drives. In this regard, use of rms value is the norm. Then the fundamental rms phase voltage for the six-stepped waveform is obtained as

$$V_{ph} = V_{as} = \frac{v_{as}}{\sqrt{2}} = \frac{2}{\pi} \frac{V_{dc}}{\sqrt{2}} = 0.45 V_{dc} \quad (2.41)$$

Practical systems have to contend with the fluctuations in the dc link voltage because of ac input voltage changes with the result that the available maximum phase voltages from the inverter also fluctuate. Consequence is reflected in the motor drive characteristics in terms of lower base speed delivering base torque obtained with reduced voltage, which is undesirable, and likewise an increase in the higher base speed at base torque with increased dc link voltage, which is a positive. Diode-bridge based ac to dc power conversion front end is incapable of maintaining a constant dc link voltage under this circumstance. Power factor correction circuits endow a constant dc link voltage, thus delivering desired motor drive characteristics for specified

fluctuations in the ac input to the drive system front end. Cost increases accompany such front ends for ac to dc power conversion and that has to be balanced with the specifications of the motor drive characteristics.

2.4 REAL POWER

The dc link transfers real power to the inverter and then on to the machine. Assuming ideal switching devices in the inverter, and negligible harmonic powers, the input power to the synchronous motor or for that matter to any load of the inverter considering only the fundamental is

$$P_i = V_{dc} I_{dc} = 3V_{ph}I_{ph} \cos \phi_1 \quad (2.42)$$

where

I_{dc} is the average steady-state dc link current

I_{ph} is the phase current

ϕ_1 is the fundamental power factor angle in the machine or load of the inverter

Substituting for V_{ph} from Equation 2.41 into Equation 2.42, the dc link current is obtained as

$$I_{dc} = 1.35I_{ph} \cos \phi_1 \quad (2.43)$$

2.5 REACTIVE POWER

AC machines require reactive power for its operation. Since the dc link can supply only real power and not the reactive power, then the reactive power must be supplied by the inverter. Switching of the inverter with control of fundamental voltage ensures a voltage source, which in turn supplies the reactive machine load. Hence the inverter can be considered a reactive power generator. Inverter also enables the control of the voltage phase angle. The facility to turn on and off the phase voltage and hence the current allows the inverter to vary the phase angle of the voltages and consequently the currents. This should not be misinterpreted as the power factor angle but the voltage's phasor position itself and more on this becomes evident in the section dealing with space vector modulation (see [Section 2.9](#)). The ability to control the phase of the voltage has been endowed by solid state power switching and has enormous impact on the control of ac machines.

Given the real power defined in the previous equation, the fundamental input reactive power demand of the machine is derived as

$$Q_i = 3V_{ph}I_{ph} \sin \phi_1 \quad (2.44)$$

The inverter handles both the real and reactive power. Combining the two gives apparent power whose unit is volt-amp (VA). Because of phasor relationship, the

sum of the two components of apparent power results in $3V_{\text{ph}}I_{\text{ph}}$. This constitutes the apparent power rating of the inverter and this is the rating that is accounted for in the computation of the cost and pricing of the inverter. For a given power, stator current increases for a low operating power factor, resulting in higher inverter rating. Unity power factor operation provides the minimum current requirement and note that it is not possible in induction motor drives as the machines require significant magnetizing currents. On the contrary, PMSMs are capable of unity power factor operation as discussed in Chapter 4. Because of the difference in power factor, for equivalent power output, it can be inferred that the PM synchronous motor will have lower stator current compared to the induction motor. Lower current means lower volt–amp rating of the inverter, lower resistive losses, and higher efficiency in PM synchronous motors drives as compared to the induction motor drives.

2.6 NEED FOR INVERTER CONTROL

Inverter switching is controlled to provide desired output voltage at a certain frequency. The speed of the machine is directly proportional to the frequency of the machine can be proved from the first principles as in the following:

$$f_s = \frac{PN_{\text{sp}}}{120} \quad (2.45)$$

where

f_s is the frequency of the stator phase voltage/current in Hz

N_{sp} is the speed in revolutions per minute (rpm)

P is the number of rotor poles

The speed in mechanical rad/s is given by

$$\omega_m = \frac{2\pi N_{\text{sp}}}{60} = \frac{2\pi}{60} \frac{120f_s}{P} = \frac{2\pi f_s}{P/2} = \frac{\omega_s}{P_p} \quad (2.46)$$

where

P_p is the number of pairs of poles

ω_m is the speed in mechanical rad/s

ω_s is the speed in electrical rad/s

This establishes the relationship between the machine speed and stator frequency and for variable speed operation, the necessity for varying the stator frequency in ac machines. But this alone is not sufficient to control the speed of the machine as it does not relate to the mutual flux, for example, which is very crucial for operation in regard to maximizing the torque and for providing a larger torque versus speed operational envelope. It is explained in the following. In all electrical machines, the basis for speed control is obtained from the induced emf expression. For the PMSM, the induced emf is derived in Chapter 1 and given as

$$E = 4.44T_{ph}\phi_m f_s \quad (2.47)$$

where

T_{ph} is the number of turns per phase

ϕ_m is the peak mutual flux

E is the rms induced emf per phase

This establishes that the induced emf is directly proportional to frequency, which could be written in terms of the rotor speed, note that the frequency is varied, which entails a proportional variation in induced emf as long as the mutual flux is maintained constant. This usually is the case to obtain maximum torque and some exceptions to this are dealt within Chapter 4. Ignoring the voltage drops due to phase resistance and leakage reactance leads to the induced emf being equal to applied phase voltage. That amounts to the fact that a variation in frequency entails a variation in the applied voltage to keep the mutual flux constant. The ratio between the induced emf and frequency is proportional to the mutual flux and that relationship cannot be changed arbitrarily without affecting torque generation. It is never allowed to exceed the value of the maximum flux permitted in the machine due to limitations on material characteristics. Varying from zero to rated applied voltage in proportion to the stator frequency, the mutual flux is kept constant and thereby constant torque for rated or nominal stator current is obtained and this mode of operation is denoted as constant torque operation. The maximum speed in this mode of operation is known as base or rated speed. When the induced emf equals or exceeds the available applied voltage, energy transfer between the dc link and machine through inverter becomes impossible. Therefore, the mutual flux can be reduced in inverse proportion to speed so that the induced emf is controlled and its magnitude made to be equal or lower than that of the available maximum applied voltage to the phase. This is known as flux weakening and this mode of operation enables the machine to go beyond base speed to achieve a certain maximum speed. Note that the ratio between a constant applied voltage and increasing frequency in this mode results in decreasing mutual flux. But nearly equal values of induced emf and applied voltage will not allow energy transfer from inverter to machine, and therefore, the control is exercised in the manner of phase shifting the applied voltage with respect to the induced emf so that energy can flow from the dc link to machine via inverter. From this discussion, it is seen that the constant torque control mode requires a smooth variation of voltage applied to the machine along with finer frequency control. The flux weakening operation requires phase control of applied voltage/current and frequency control. Therefore, the inverter has to act on the commands of magnitude, phase, and frequency of the output voltages and currents. This section presents some methods to achieve such control of the inverter and they are the following:

1. PWM
2. Hysteresis control
3. Space vector modulation

2.7 PULSE WIDTH MODULATION

The control of harmonics and variation of the fundamental component can be achieved by varying the duration of applied input voltage to the machine. It is realized by changing the pulse width to gate signals of the inverter and it is known as PWM. A number of PWM schemes have been in use in motor drives [6–45]. All the PWM schemes, in general, aim to maximize the fundamental harmonics and selectively eliminate a few lower harmonics. Some PWM schemes are discussed in this section.

Figure 2.18 shows sample waveforms of phase a and its midpoint voltage for the inverter given in [Figure 2.16](#). The intersections of the carrier signal v_c (usually a bidirectional triangular waveform) and the commanded fundamental voltage reference v_a^* (usually a sinusoidal waveform) provide the switching signals to the base drive of the inverter switches. The switching logic for one phase is summarized as

$$\begin{aligned} v_{am} &= \frac{1}{2} V_{dc}, \quad v_c < v_a^* \\ &= -\frac{1}{2} V_{dc}, \quad v_c > v_a^* \end{aligned} \quad (2.48)$$

The fundamental of this midpoint voltage is

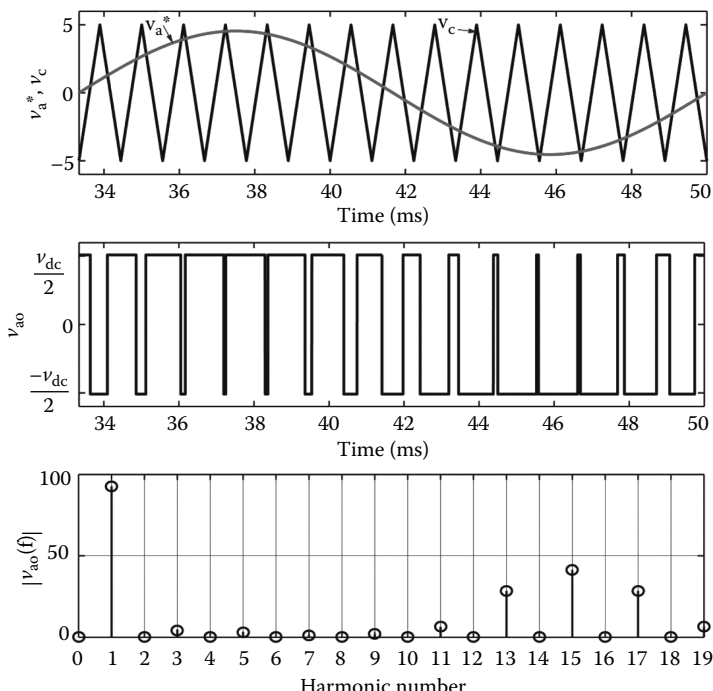


FIGURE 2.18 Sinusoidal PWM.

$$v_{\text{am}1} = \frac{V_{\text{dc}}}{2} \frac{v_a^*}{v_{\text{cp}}} \quad (2.49)$$

where

v_a^* is the peak value of the a phase reference or command signal
 v_{cp} is the peak value of the triangular carrier signal

The resulting output follows the frequency and phase of the reference signal. The modulation index or ratio is defined by

$$m = \frac{v_a^*}{v_{\text{cp}}} \quad (2.50)$$

which substituted in Equation 2.49 gives

$$v_{\text{am}1} = m \frac{V_{\text{dc}}}{2} \quad (2.51)$$

Varying modulation index changes the fundamental amplitude and varying the frequency of reference v_a^* changes the output frequency. The ratio between the carrier and reference frequencies, f_c/f_s , changes the harmonics. To eliminate a large number of lower harmonics, f_c has to be very high. Note that this will entail high switching losses and a considerable derating of the supply voltage because many turn on and turn off intervals cut sizably the volt-second area from the maximum available output volt-second and hence decreases the available output voltage. It is usual to have a fixed value for f_c , say 9 up to the base frequency of the ac machine and then reduced values of f_c because higher harmonic torque pulsations do not significantly affect the motor drive performance at high speed. The carrier and reference signals have to be synchronized to eliminate the beat frequency voltage appearing at the output.

A typical relationship between carrier and reference frequencies is shown in Figure 2.19 [5]. At low frequencies, less than 40 Hz, the carrier frequency may be

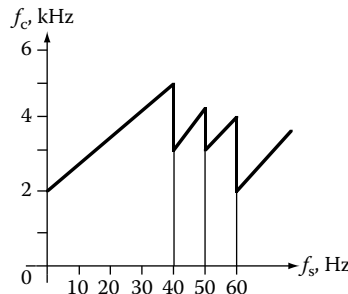


FIGURE 2.19 Relationship between carrier and fundamental stator frequency. (From Krishnan, R., *Electric Motor Drives*, Figure 7.38, Prentice Hall, Upper Saddle River, NJ, 2001. With permission.)

fixed or a variable to have the synchronization feature. The number of steps in variation of carrier frequencies is dependent on the specified output harmonic spectrum at various stator frequencies.

When the modulating signal rises above the magnitude of the carrier signal peak, the mode of operation is known as overmodulation. The gain of the inverter becomes nonlinear under such operating conditions and the magnitude of the fundamental output voltage does not rise in proportion to the modulating signal. It is crucial to have a higher fundamental and in step with modulating signal to have a highly responsive inverter for control applications. Operational waveforms in overmodulation region are given in Figure 2.20. Note the fundamental magnitude from the spectrum. It could be improved by many methods.

An alternative sinusoidal PWM strategy is shown in Figure 2.21 to boost the fundamental magnitude. The reference signal contains the fundamental and its third harmonic with a smaller magnitude for the third harmonic compared to the fundamental. As the third harmonic is canceled in the line-to-line voltages of a star-connected system, the fundamental is enriched in this strategy. Many variations of this are possible with accompanying advantages in higher fundamental voltage and reduced number of switching. The same peak reference command or modulating signal as given for the overmodulation case and shown in previous example and figure is considered for third harmonic injection example. Note that the fundamental has increased and the modulating signal is modified to be lower than the peak magnitude of the carrier signal. The higher harmonic spectrum has changed but not very much. Note also that by varying the magnitude of the third harmonic, the shape of the command or modulating signal is modified to resemble that of a trapezoid. This

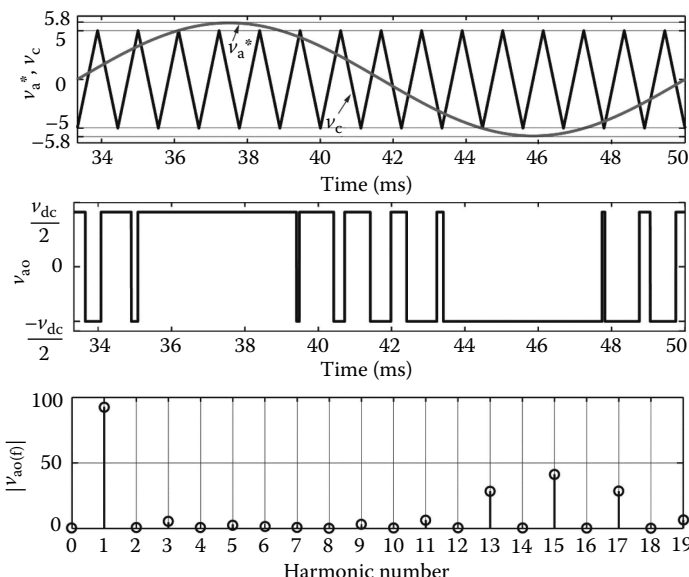


FIGURE 2.20 Overmodulation operation of the inverter.

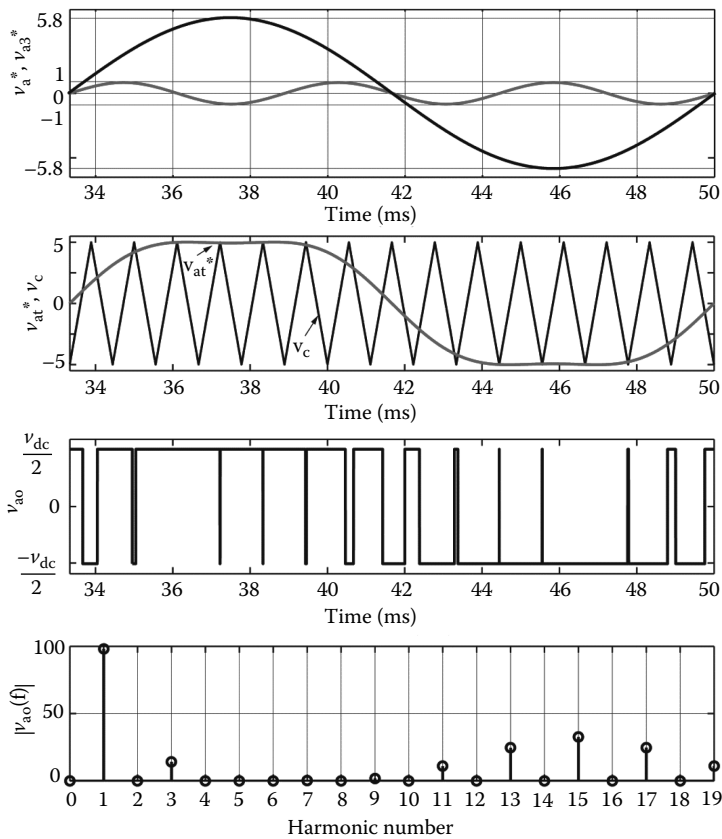


FIGURE 2.21 Alternate sinusoidal PWM strategy.

is the basis for use of trapezoidal reference voltages to maximize the fundamental output voltages in the past in motor drive applications. More importantly, it may be observed that the beginning and ending parts of the modulating signal rise and fall sharply, respectively, compared to a sinusoid. Because of it, the time duration of the resulting midpoint voltage duration is longer thus packing a larger volt-second, giving way to higher fundamental magnitude. A sample set of PWM-controlled mid-pole, line, phase and control voltages in normalized units is shown in [Figure 2.22](#) to illustrate commonly encountered waveforms in PWM operation of the motor drive.

2.7.1 PWM IMPLEMENTATION

The implementation of PWM takes many forms but there are certain underlying factors that are common to all PWM schemes. They are (1) generation of command signals for interaction with PWM carrier signals and (2) sampling of the commands to generate the PWM duty cycles. They are considered in this section.

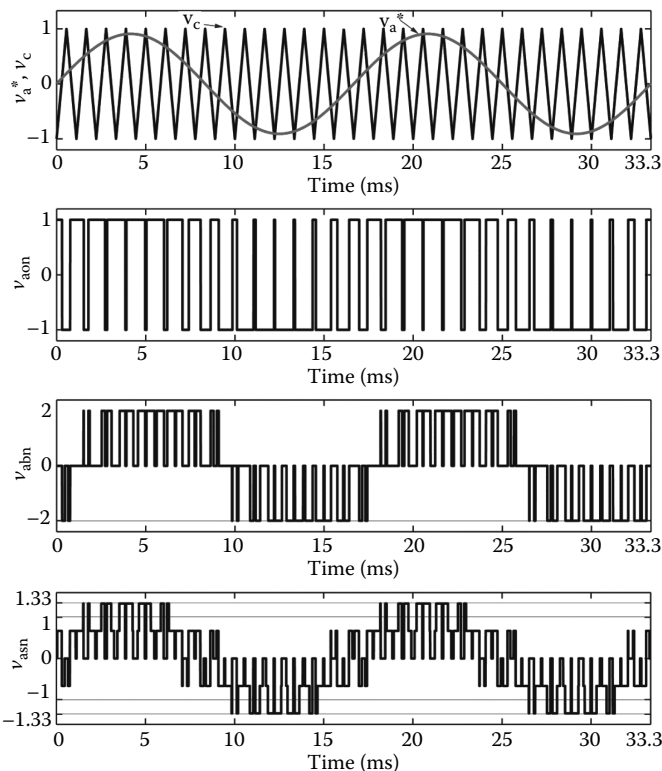


FIGURE 2.22 A sample set of voltage waveforms in normalized units.

2.7.1.1 Reference Signal Generation

The reference signals to act on the bidirectional triangular carrier frequency signals are derived depending on the nature of the drive system. In PMSM and PM brushless motor drives, control of the motor drives is exercised through the stator currents and hardly in the form of stator voltages. It is because the torque is directly proportional to currents either in stator frames or in rotor frames and control of torque gives the control in speed and position. Hardly phase voltages are the commands in these motor drives but that may be the case in some induction motor drives. That being the case, the case pertinent to the PMSM drives is illustrated in the following discussion. Consider a torque-controlled PMSM drive system where the torque reference is decomposed into stator current references and for the moment, it is assumed so is the case and this process is dealt in detail in Chapter 4. To amplify these stator current references through the inverter, the phase currents are sensed and compared to their respective references to generate errors in phase currents. These current errors are forced to zero through a proportional plus integral (PI) controller in each of the phase. The PI controller is taken for illustration but many other controllers such as state variable and intelligent controllers are feasible and they are all available in literature. Regardless of the nature of the controller, the outcome of the current

controller is a signal that will demand the phase voltage to follow in such a way that the current error in that phase is reduced to zero. Therefore, the current controller's output is a voltage signal and it will vary very fast and this is the reference signal to interact with the PWM carrier signal to generate gate pulses with variable duty cycles for the devices in a phase leg of the inverter. Similar is the case for each and every phase of the motor drive. The resulting motor drive is current controlled from a voltage source and may be deemed to be a current source. If the speed of response of the current feedback control is fast, it may resemble more of a soft current source and if it is slack, then it goes to resemble that of a hard current source. There are some advantages associated with the current source feeding a motor drive. A short circuit across inverter output lines will not have detrimental consequence on the inverter. While this is the biggest advantage, the drawback is that a sudden open circuit is dangerous to it, as a large voltage will be generated due to inductances in machine will be applied across the devices, leading to their destruction. Small dummy loads can overcome such difficulty with very little associated cost to the drive system. The schematic of the motor drive with inner current feedback loops and controllers is shown in Figure 2.23. More discussion on the current controllers and their designs is provided in Chapter 6. Only two-phase currents are sensed and in a three-phase three-wire system; the sum of the phase currents being zero, the third phase current is constructed using this fact. The processing circuit provides this option and is intended to include the filters for all individual phase currents too.

2.7.1.2 Sampling of Reference Signals

The gate signal pulse width is generated by the intersection of the reference voltage and the PWM carrier signal shown as bidirectional triangular waveform in Figure 2.24. The intersections of these two signals can be found accurately if the reference is continuously monitored, which amounts to that being infinitely sampled. It is only possible in analog implementation. Presently most of the implementations are digital processor-based and it is impossible to have infinite sampling and even a large sampling of the reference signals given the fact that the same processor is used for

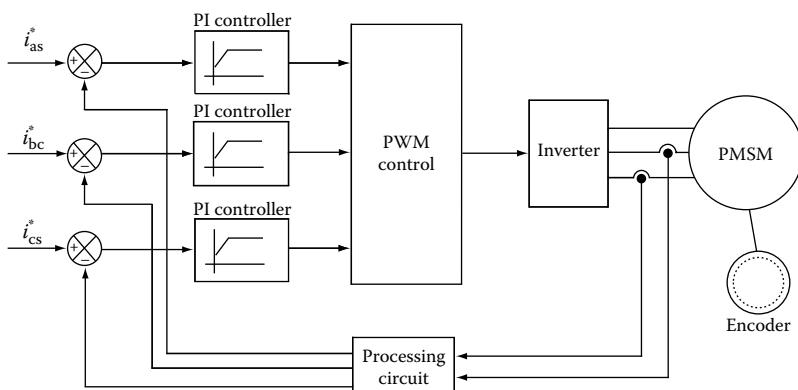


FIGURE 2.23 PWM-based current control of a PMSM drive.

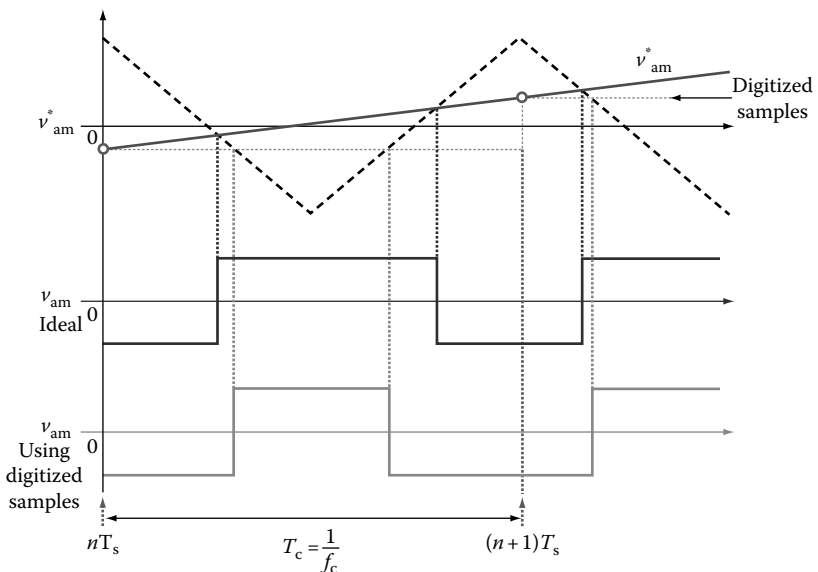


FIGURE 2.24 Symmetric sampling case.

motor drive system control too. Two cases of sampling are prevalent and they are (1) at carrier PWM frequency denoted as symmetric sampling and (2) sampling at twice the carrier frequency known as unsymmetric sampling. They are discussed in regard to their implementation in the following.

1. *Symmetric sampling:* The sampling is done at the rate of carrier PWM frequency and it is assumed that it is done at the instant of positive peak of the PWM carrier signal shown in Figure 2.24. It is seen that the actual and digitized samples intersecting with the carrier PWM signal provide two gate pulses of different widths. A significant discrepancy in the gate pulse duration exists that will translate into loss of volt-second in the case using the sampled signal, resulting in large settling time for the average output voltage to match the reference. Error can be large in the case of modulating signals with fast variations, for example, in the case of controllers having high gains and machines with very small inductances. Note that the gate pulse arising out of use of digitized sample is symmetric about the negative peak of the carrier PWM signal and hence its name.
2. *Unsymmetric sampling:* When the sampling is doubled to carrier PWM frequency and done at negative and positive peak instants of the carrier signal, the correction in the pulse widths of the gate control signals is faster resulting in error reduction. The gate signal pulses are not symmetric about the center of the carrier signal as shown in Figure 2.25 and hence the name. There will always be an error between this and ideal analog methods and the key is to find ways to minimize these errors.

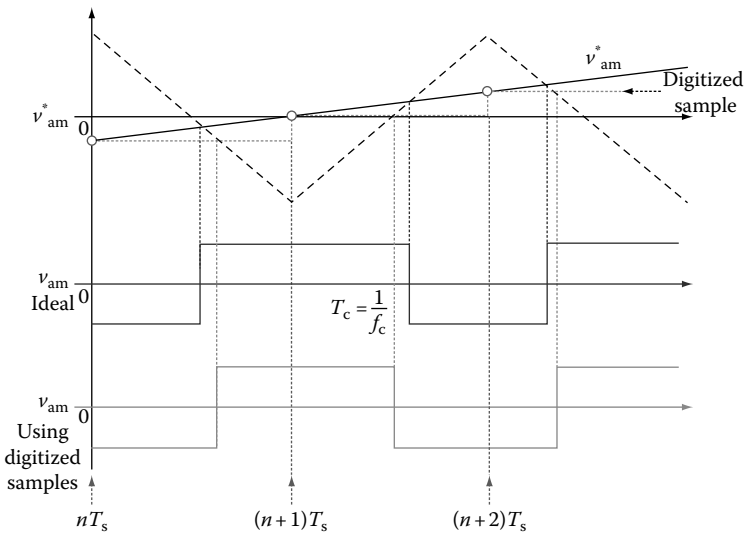


FIGURE 2.25 Unsymmetric sampling case.

The upcoming field programmable gate array (FPGA) implementations have sampling rates of 100 MHz with the result that it almost resembles the analog implementation. For many stand-alone motor drive controllers, the cost of using FPGA is not justifiable but many high performance and critical applications may incorporate the FPGA controllers in near future.

2.7.1.3 Transfer Characteristics of PWM-Controlled Inverters

Transfer characteristics are based on PWM with sinusoid as the modulating signal and computed for the entire cycle of the modulating signal. It is easily visualized that as the peak of the sinusoid exceeds the peak of the carrier PWM, there is no switching involved in the inverter leg with the result that the midpole voltage remains at its maximum (positive or negative the case may be). That gives an output line-to-line voltage greater than normally obtainable with the peak of the modulation signal that is smaller than or equal to the peak of the carrier PWM signal. The relationship is derived in the following. The fundamental output voltage is determined by the modulation ratio (MR) and it is independent of frequency. The relationship is very crucial to the control of the inverter. The line-to-line rms voltage is derived from the midpole voltage V_{am1} as

$$V_e = \frac{\sqrt{3}}{\sqrt{2}} V_{am1} = \frac{\sqrt{3}}{\sqrt{2}} m \frac{V_{dc}}{2} = 0.612mV_{dc} \quad (2.52)$$

where

m is the modulation ratio

V_{dc} is the dc link voltage or input voltage to the inverter

The modulation ratio from Equation 2.52 can be written as

$$m = \frac{\left(\frac{\sqrt{2}}{\sqrt{3}}V_{\ell}\right)}{\left(\frac{V_{dc}}{2}\right)} = \frac{\sqrt{2}V_{ph}}{\left(\frac{V_{dc}}{2}\right)} = \frac{V_p}{\left(\frac{V_{dc}}{2}\right)} \quad (2.53)$$

where V_p is the peak phase voltage. From this equation, it is seen that the modulation ratio is the ratio between fundamental peak phase voltage and the midpole voltage with respect to dc source midpoint input. It is seen by this definition that the modulation ratio is normalized with respect to midpoint of dc source input. The line-to-line voltage output is linear for the modulation ratio from zero to one. Beyond that range, the output voltage increases but not linearly and it is known as overmodulation region. This region from this value to maximum line-to-line voltage value is divided into two subregions. In the subregion where the modulation ratio is between 1 and 1.154, it is quasilinear, and the line-to-line rms voltage at $m=1.154$ is derived as

$$V_{\ell} = \frac{\sqrt{3}}{\sqrt{2}} m \frac{V_{dc}}{2} = \frac{\sqrt{3}}{\sqrt{2}} \left(1.154 \frac{V_{dc}}{2} \right) = 0.707 V_{dc} \quad (2.54)$$

and it corresponds to a peak phase voltage given by

$$V_{am1} = \frac{2}{3} V_{dc} \sin 60^\circ = \frac{V_{dc}}{\sqrt{3}} = 0.577 V_{dc} \quad (2.55)$$

For modulation ratios higher than 1.154, the output voltage enters saturation region with maximum line-to-line voltage corresponding to six-step operation given at a modulation ratio of 3.24 with a rms line-to-line voltage of $0.78V_{dc}$. With the derived break points of the modulation ratio of 1, 1.54, and 3.24, the rms line-to-line voltage in terms of the dc link voltage versus modulation ratio is shown in [Figure 2.26](#). Such a relationship is achievable with a frequency ratio between the carrier and modulation signals, known as modulation frequency ratio, greater than or equal to 15. The nonlinear relationship between the output line-to-line voltage versus modulation ratio clearly indicates that it is highly undesirable in high-performance control applications and its effects particularly in the overmodulation range in the form of sluggish currents and corresponding behavior in torque generation with the resulting slow dynamic performance.

2.7.1.4 Off-Line Optimized PWM

High power motor drives in the range of 0.5 MW and above have very different requirements. Lower power drives are pulse width modulated in the range of 2–20 kHz, the higher frequencies at the lowest end of the power rating and lowest at the medium power rating. Two kilohertz PWM is not a feasible solution in many

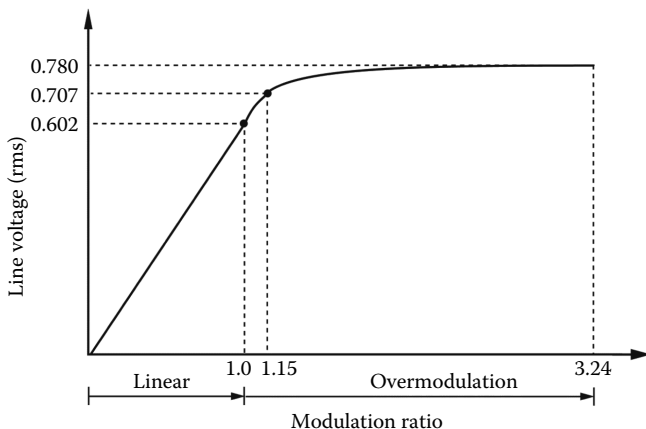


FIGURE 2.26 Line voltage versus modulation ratio of the three-phase inverter.

high power motor drives. The switching losses are significant in them as the voltage is medium-level voltage and so also the resulting EMI from switching at high frequencies that are unacceptable on many fronts including their ability to interfere with communication networks around and outside the plant over a long distance. The solution has to be found in low PWM switching in the range of 360–600 Hz of the inverter. Then selective harmonic elimination together with maximization of fundamental requires optimization of the PWM switching. That usually is not feasible with sine triangle intersection method. Off-line optimized and memory-embedded PWM is required in that case and it is almost universal in high power motor drives. The optimization process and implementation are discussed in [47]. Such high-power PM motor drives are not prevalent in the field and, therefore, their inverter control is not being considered here.

2.8 HYSTERESIS CURRENT CONTROL

The PWM current controller by sampling the input control (or modulating) voltage determines the duty cycle once in a carrier cycle. This is the case in all processor-based control systems. In between two consecutive switching, note the control voltage can exceed the maximum limit and if the PWM controller is sampled and held once a switching cycle, then the voltage (or current) is controlled on an average but not on an instantaneous basis. Continuous sampling leading to continuous duty cycle variation is possible in analog PWM controllers but then this may lead to more than one switching per carrier cycle and hence not desirable from the point of view of inverter losses. It is then fair to say that instantaneous voltage/current control is not exercised in the PWM current controller. The hysteresis controller overcomes this drawback by converting a voltage source into a fast-acting current source. The actual current is controlled within a narrow band of excursion from its desired value in the hysteresis controller. The hysteresis window determines the allowable or pre-set deviation of current Δi . Commanded current and actual current are shown in

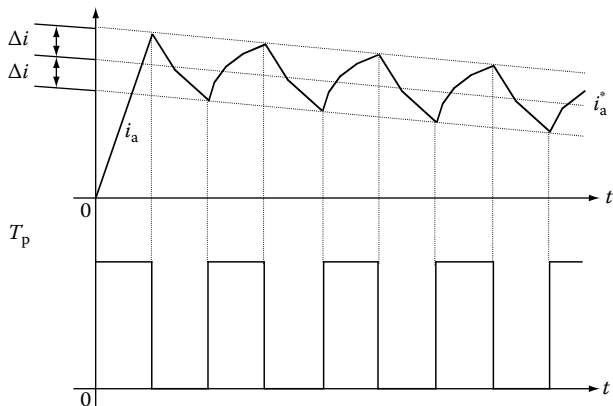


FIGURE 2.27 Illustration of hysteresis control action.

Figure 2.27 with the hysteresis windows and gate signals. The applied voltage to the load is determined by the following logic:

$$i_a \leq i_a^* - \Delta i, \quad \text{set } v_0 = V_s \quad (2.56)$$

$$i_a \geq i_a^* + \Delta i, \quad \text{reset } v_0 = 0 \quad (2.57)$$

The hysteresis window, Δi , can be externally set either a constant or made a fraction of the stator current itself by proper programming. The switching frequency is a varying quantity unlike the constant frequency in the PWM controller. This has the disadvantage of higher switching losses in the devices with increased switching frequency. The control is considered to be simple as it is dependent on the magnitude of instantaneous current peak and the set current window only. Because of its instantaneous response and simplicity of control realization, the hysteresis current controllers are the staple of the academic research laboratories but they are seldom found in industrial products.

Performance of hysteresis current controller with varying hysteresis current windows is shown in [Figure 2.28](#). The current windows are 0.02, 0.04, 0.1, 0.12, 0.15, and 0.2 times that of the peak of the phase current reference. With decreasing hysteresis current windows, the switching frequency increases as expected. The tracking of the current reference is instantaneous but the phase current deviates from the reference by hysteresis current window on both sides of the reference value.

A qualitative comparison of the PWM and hysteresis controllers is summarized in [Table 2.4](#). The disadvantages of the hysteresis controller can be overcome, say, by limiting the switching frequency, varying the hysteresis window adaptively to the changing load conditions and as a function of the current magnitude that is commanded.

A natural question that may arise at this juncture is why not combine the best features of hysteresis control scheme in providing instantaneous response with the

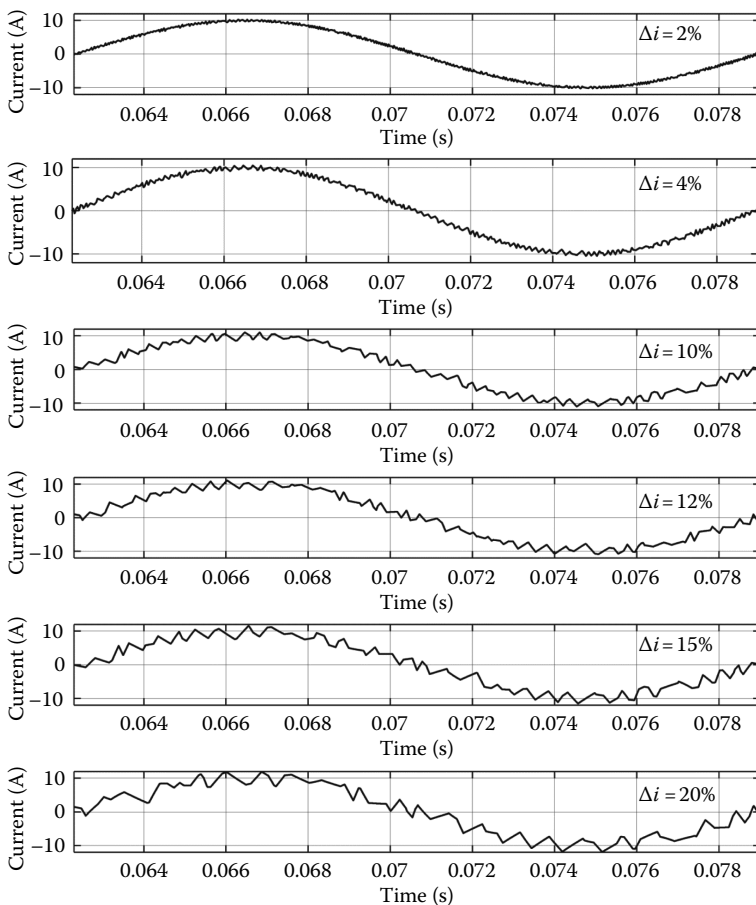


FIGURE 2.28 Phase a current for varying hysteresis current windows.

TABLE 2.4
Comparison of Current Controllers

Characteristics	Current Controllers	
	Hysteresis	PWM
Switching frequency	Varying	Fixed at carrier frequency
Speed of response	Fastest	Fast
Ripple current	Adjustable	Fixed
Filter size	Dependent on Δi	Usually small
Switching losses	Usually high	Low

constant switching carrier-based PWM switching. A hybrid current control scheme using the combination of PWM and hysteresis current control schemes to exploit the best features of them in switched reluctance motor drives was reported. Fast response with hysteresis current control was used to raise the current to its desired value and thereafter it is maintained by PWM switching with fixed carrier switching to minimize switching losses. The hybrid switching scheme may not be applicable in ac motor drives is to be noted.

2.9 SPACE VECTOR MODULATION

PWM control is the first scheme to be applied on a large scale for control of inverter and it reigned for over a quarter century. During that time, the understanding of the ac motor drive and its performance was evolving. There was fair comprehension of steady-state operation and its control but limited knowledge of transient operation, resulting in instability and inverter failure because of immense dynamic currents being drawn during the load or speed transients. Not surprisingly, in mid-1970s and later, the inverter used to be called “a short circuit waiting to occur” in some parts of the literature. In the late 1960s and early 1970s, efforts were made to understand the dynamics of the ac machines. It all started on the premise that independent control of flux and torque is the hallmark of the separately excited dc motor drive that gives a very high dynamic and steady-state performance. An equivalent control of that in ac motor drives, if found, can overcome entirely the problems associated with the dynamic transients of the motor drive. The key to this step did lie in the understanding of the ac machines as an equivalent separately excited dc machine. This required the ac machine model to be reduced into a set of single stator and rotor windings, thus freeing the conventional modeling and reality of three-phase stator and rotor windings. Kovac and Racz developed a three-phase machine model to provide such a result known as space phasor model (SPM) of the machine. Consider three-phase windings supplied with balanced three-phase currents and note that only two currents are independent as the sum of the three currents are zero. The three-phase currents and hence the magnetomotive forces (mmfs) of the three-phase windings can be resolved along a fictitious two axes that are perpendicular to each other and designated as quadrature and direct axes, popularly known as q- and d-axes in literature. Resolving the resultant of the q- and d-axes currents and mmfs gives a current phasor and a mmf phasor that are rotating at synchronous angular speed with constant magnitude. Likewise, the rotor currents can also be transformed into a rotor current phasor as well as its mmf. In the final analysis, the three-phase stator and rotor currents as well as its stator mmf and rotor mmf have been transformed into a single stator current and rotor current phasor and a resultant mmf phasor, respectively, with the result that they can be viewed as though they are produced by one stator and one rotor winding. If the machine takes a single stator current space phasor, then the inverter supplying the current must be generating it as a space phasor but not simply as a set of three-phase currents. Hence the inverter may be viewed as a voltage and or current space phasor generator but not as a three-phase voltage or current generator as was the pre-1980s understanding that constrained to think of its control as a set of three single-phase PWM or hysteresis control system. This

understanding of the inverter as a voltage/current phasor generator further imports the notion that the inverter is not only controlling the magnitude and angular velocity but also the angular position of the voltage and current phasor as the mere fact that a space phasor is in fact consists of three these variables. The position variable that the inverter is exercising control over has the most dramatic impact on the dynamics of the motor drive. This new understanding of the inverter thanks to Holtz came into being from the understanding of the machine model and its dynamics into the inverter understanding and its control. This invention singly and uniquely had one of the most powerful effects in obtaining the highest steady state and dynamic performance of the ac machines, particularly induction machines, and in taking the control of the inverter to new heights in terms of lowering harmonics and losses, and making it a linear amplifier to obtain high dynamic performance even in cases without a rotor position sensor in the feedback control systems. Note that any voltage space phasor can by synthesized with the control of inverter switching by considering the requested voltage phasor's magnitude and position. This approach does not use individual pulse width modulators for each machine phase. The process of this control and its procedure for realization [46–91] are given below.

2.9.1 SWITCHING STATES OF THE INVERTER

Consider the inverter shown in [Figure 2.29](#) [5]. The terminal voltage of phase a, V_a , with respect to negative of the dc supply is considered and it is determined by a set of switches, S_a , consisting of T_1 and T_4 as shown in [Table 2.5](#).

When the switching devices T_1 and T_4 and their antiparallel diodes are off, V_a is indeterminate. Such a situation is not encountered in practice and hence has not been considered. The switching of S_b and S_c sets for line b and c can be similarly derived. The total number of switching states possible with S_a , S_b , and S_c are eight and they are elaborated in the [Table 2.6](#) using the relationships (Equations 2.27 through 2.29) containing the phase and line-to-line voltages as well the q- and d-axes voltages derived from the phase voltages given in the following:

$$\left. \begin{aligned} v_{qs} &= v_{as} \\ v_{ds} &= \frac{1}{\sqrt{3}} (v_{cs} - v_{bs}) = \frac{1}{\sqrt{3}} v_{cb} \end{aligned} \right\} \quad (2.58)$$

The stator q- and d-voltages for each state are shown in [Figure 2.30](#). The voltage phasor, v_s , is the resultant of the q- and d-axes voltages. The limited states of the inverter create distinct discrete movement of the stator voltage phasor, v_s . An almost continuous and uniform voltage phasor generation is feasible with the following algorithm.

2.9.2 PRINCIPLE OF SPACE VECTOR MODULATION

Consider that a voltage phasor v_s is commanded. Its position is in between two switching voltage vectors, say v_1 and v_6 , and has a relative phase of θ_s from v_1 , as

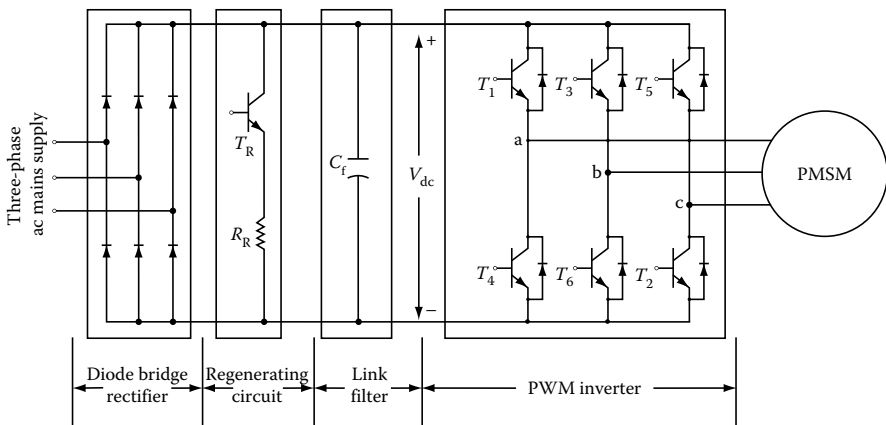


FIGURE 2.29 Power circuit configuration of the PMSM drive. (From Krishnan, R., *Electric Motor Drives*, Figure 8.8, Prentice Hall, Upper Saddle River, NJ, 2001. With permission.)

TABLE 2.5
Switching States of Inverter Phase Leg a

T_1	T_4	S_a	V_a
On	Off	1	V_{dc}
Off	On	0	0

Source: Krishnan, R., *Electric Motor Drives*, Table 8.1, Prentice Hall, Upper Saddle River, NJ, 2001. With permission.

shown in Figure 2.31. The commanded voltage phasor can only be realized with the use of the neighboring switching voltage vectors and in this case v_1 and v_6 . Taking these switching vectors for a fraction of time as it is not possible to take the fraction of them, and then combining them through the load gives the desired command space voltage phasor. Accordingly, v_s can be synthesized as the vector sum of av_1 and bv_6 where a and b are fractional constants. Then, the voltage phasor, v_s is derived by taking geometric projections given by

$$v_s = av_1 + bv_6 \quad (2.59)$$

$$a = \frac{v_s}{v_1} \left[\cos \theta_s - \frac{1}{\sqrt{3}} \sin \theta_s \right] \quad (2.60)$$

$$b = \frac{2}{\sqrt{3}} \frac{v_s}{v_6} \sin \theta_s \quad (2.61)$$

$$v_1 = v_6 = \frac{2}{3} v_{dc} \quad (2.62)$$

TABLE 2.6
Inverter Switching States and Machine Voltages

States	S_a	S_b	S_c	V_a	V_b	V_c	V_{ab}	V_{bc}	V_{ca}	V_{as}	V_{bs}	V_{cs}	V_{qs}	V_{ds}
I	1	0	0	V_{dc}	0	0	$-V_{dc}$	0	$-V_{dc}$	$\frac{2V_{dc}}{3}$	$-\frac{V_{dc}}{3}$	$-\frac{V_{dc}}{3}$	$\frac{2V_{dc}}{3}$	0
II	1	0	1	V_{dc}	0	V_{dc}	V_{dc}	$-V_{dc}$	0	$\frac{V_{dc}}{3}$	$-\frac{2V_{dc}}{3}$	$\frac{V_{dc}}{3}$	$\frac{V_{dc}}{3}$	$\frac{V_{dc}}{\sqrt{3}}$
III	0	0	1	0	0	V_{dc}	0	$-V_{dc}$	V_{dc}	$-\frac{V_{dc}}{3}$	$-\frac{V_{dc}}{3}$	$\frac{2V_{dc}}{3}$	$-\frac{V_{dc}}{3}$	$\frac{V_{dc}}{\sqrt{3}}$
IV	0	1	1	0	V_{dc}	V_{dc}	$-V_{dc}$	0	V_{dc}	$-\frac{2V_{dc}}{3}$	$\frac{V_{dc}}{3}$	$\frac{V_{dc}}{3}$	$-\frac{2V_{dc}}{3}$	0
V	0	1	0	0	V_{dc}	0	$-V_{dc}$	V_{dc}	0	$-\frac{V_{dc}}{3}$	$\frac{2V_{dc}}{3}$	$-\frac{V_{dc}}{3}$	$-\frac{V_{dc}}{3}$	$-\frac{V_{dc}}{\sqrt{3}}$
VI	1	1	0	V_{dc}	V_{dc}	0	0	V_{dc}	$-V_{dc}$	$\frac{V_{dc}}{3}$	$\frac{V_{dc}}{3}$	$-\frac{2V_{dc}}{3}$	$\frac{V_{dc}}{3}$	$-\frac{V_{dc}}{\sqrt{3}}$
VII	0	0	0	0	0	0	0	0	0	0	0	0	0	0
VIII	1	1	1	V_{dc}	V_{dc}	V_{dc}	0	0	0	0	0	0	0	0

Source: Krishnan, R., *Electric Motor Drives*, Table 8.1, Prentice Hall, Upper Saddle River, NJ, 2001.
With permission.

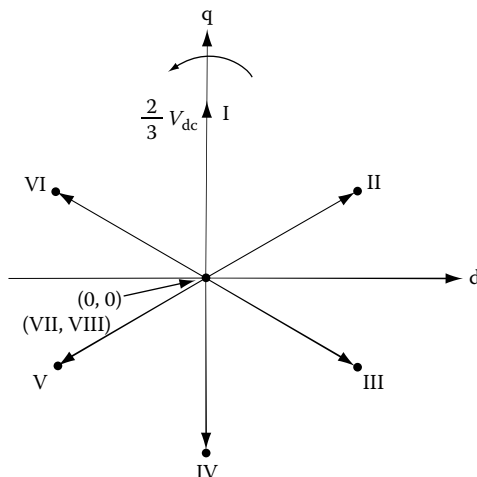


FIGURE 2.30 The inverter output voltages corresponding to switching states. (From Krishnan, R., *Electric Motor Drives*, Figure 8.9, Prentice Hall, Upper Saddle River, NJ, 2001. With permission.)

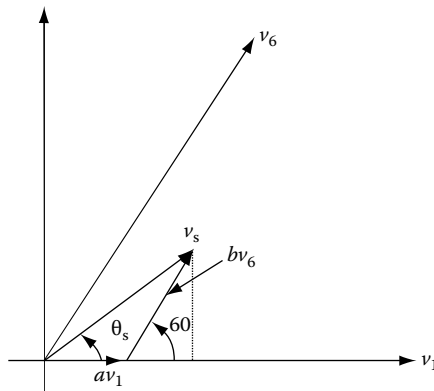


FIGURE 2.31 Synthesis of a voltage phasor from adjacent switching voltage vectors.

If the carrier frequency is f_c and one PWM period (also known as sampling period in literature), T_c is given by

$$T_c = \frac{1}{f_c} \quad (2.63)$$

and it is related to the time for switching v_2 and v_1 as

$$T_c = (a + b + c)T_c \quad (2.64)$$

where cT_c is the duration of zero vector application. The physical interpretation is obtained by multiplying the Equation 2.59 with T_c implying that the volt-second desired is provided by three vectors v_1 , v_6 , and v_0 with durations of aT_c , bT_c , and cT_c , respectively. The computed v_1 , v_6 , and v_0 are converted into switching signals and symmetrically placed from the midpoint, as shown in Figure 2.32 for a switching period, T_c . Only one switching vector is activated at any given time in any time interval corresponding to fractions of aT_c , bT_c , and cT_c for the first half of the sampling period and deactivated in the second half of the sampling period again corresponding to the remaining fractions of aT_c , bT_c , and cT_c time intervals, thereby minimizing the switching losses in the inverter. Note that switching vector activation or deactivation means one transistor turned off (on) and the other complementary transistor in that leg turned on (off) depending on the switching scheme and whether voltage or current is controlled. Thus the control involves one turn off (on) and may be one turn on switching loss in a phase leg of the inverter. There will be two instances in each phase leg and six in all three phases with the result there are six turn on and may be six turn off switching losses of the inverter transistors in a sampling (or carrier) period. The latter six switchings are not necessary if currents are controlled and if they are continuous on top of that. Then the diodes that are placed antiparallel to the devices to be activated carry the current automatically, thereby obviating the necessity to turn on the transistor.

Note that the zero vectors are placed in the middle for half cT_c and there is an advantage in doing so. That will be demonstrated in the Figure 2.33 by deriving the

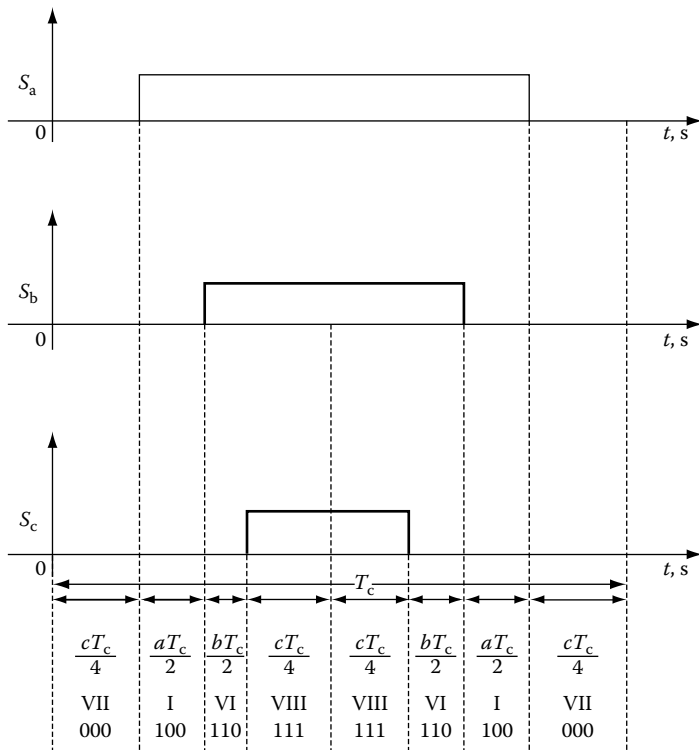


FIGURE 2.32 Switching signal derivation for a period from voltage vectors v_1 , v_6 , and v_0 .

line-to-line and phase voltages of a three-phase system from the SVM switching vectors. Both the line voltages and phase voltages (shown in dotted lines) are symmetrically split into two equal halves and placed in each half sampling period with the result that their frequencies have doubled. Its distinct advantage is demonstrated in the following illustration. Consider the case where there is only one pulse per switching period and the case where the pulse is split into two and placed with zero voltage interval so that the total duration of the on pulse is the same in both cases as shown in Figure 2.34a and b, respectively. The latter case has doubled the frequency of the applied voltage is to be noted. The current ripple can be derived as

$$\Delta i = \frac{V}{L} \Delta t \quad (2.65)$$

Given the same magnitude of voltage and an on time in the first case and half the on time in the second case, it becomes obvious that the current ripple is half in the latter case compared to the first case current ripple. The placement of zero voltage intervals in between the voltage pulses has decreased the current ripple. Likewise, it is seen that the freedom endowed by SVM to place the zero voltage vector in the middle has bifurcated the voltages into two equal halves with zero voltages in the middle, thus doubling the frequency and halving the current ripple. This is of

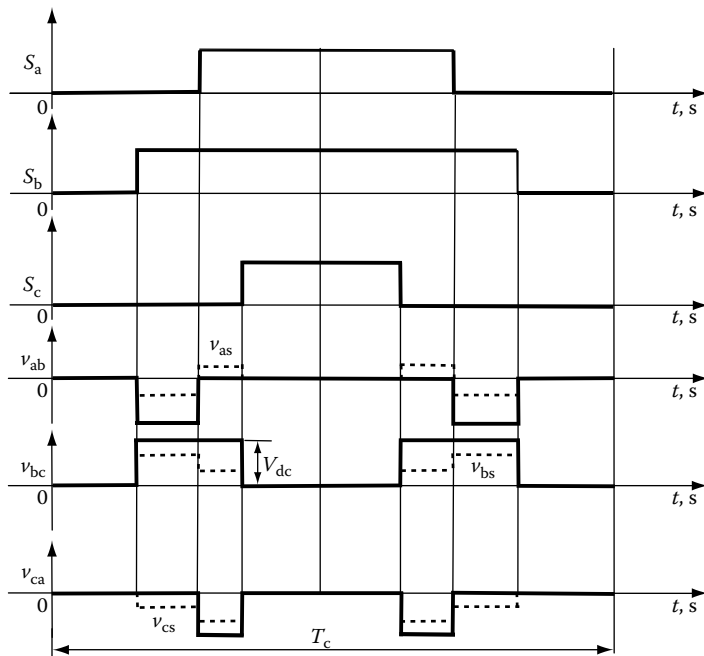


FIGURE 2.33 Derivation of line and phase voltages from SVM with zero vectors in the middle.

enormous consequence in ac motor drives since it reduces the torque ripple and also the magnetic losses associated with ripple currents in the machine. The most important point to note here is that the SVM affords the freedom to place zero voltage vectors both at the ends as well as in the middle of the switching period.

The placement of zero vectors in the middle of the switching cycle can be eliminated by taking that amount of zero voltage vector duration to the beginning and end of the switching cycles by keeping, say, one of the switching vector of a phase leg either at zero state or at one state as shown in Figure 2.35a and b, respectively. The total zero voltage vector duration has not changed in both the cases as well as in the case with zero voltage vector in the middle of the switching cycle case too. The number of switchings has reduced to four in both cases with the result that the switching losses in the inverter devices have been reduced to two-thirds of the case with zero voltage vector in the middle of the switching period. But this advantage comes at the expense of higher current ripple magnitude as shown by looking at the line-to-line and phase voltages for one case of reduced switching in Figure 2.36. The line-to-line and phase voltages are single pulses in the entire switching cycle and there are no two equal halves as in the case of the SVM with zero voltage vector in the middle of the switching period. There is no doubling of frequency of the voltages and hence the current ripple is not halved as in the previous case. Even though the current ripple is doubled, this SVM can be advantageously employed at higher speeds where the torque ripple is not of major concern in variable speed motor drives. At low speeds and for applications such as

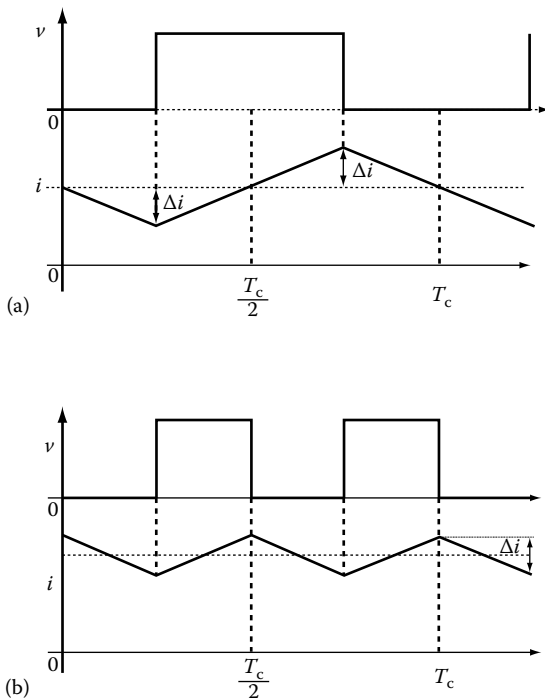


FIGURE 2.34 Effect of zero voltage placement on the current ripple for two cases: (a) single pulse per period; (b) two pulses per period.

positioning servos, the SVM with zero voltage vector in the beginning, midst and end of the carrier cycle can be resorted to minimize the current and hence torque ripple.

Space vector modulation avoids the conflicts generated by three individual pulse width modulators or hysteresis controllers. Given six nonzero and two zero discrete and distinct switching vectors, the best switching choice is being made with this approach. Variations of space vector modulation with overmodulation and other optimal switching strategies may be referred to in the literature.

2.9.2.1 Transfer Characteristics of SVM-Controlled Inverters

The transfer relationship is between the rms line-to-line voltage and modulation index and note this is different from the modulation ratio of the PWM controller. The modulation index, m_i , is defined as the ratio between the peak value of the fundamental voltage phasor and feasible maximum fundamental phase voltage in an inverter and given as

$$m_i = \frac{V_s}{\frac{2}{\pi} V_{dc}} \quad (2.66)$$

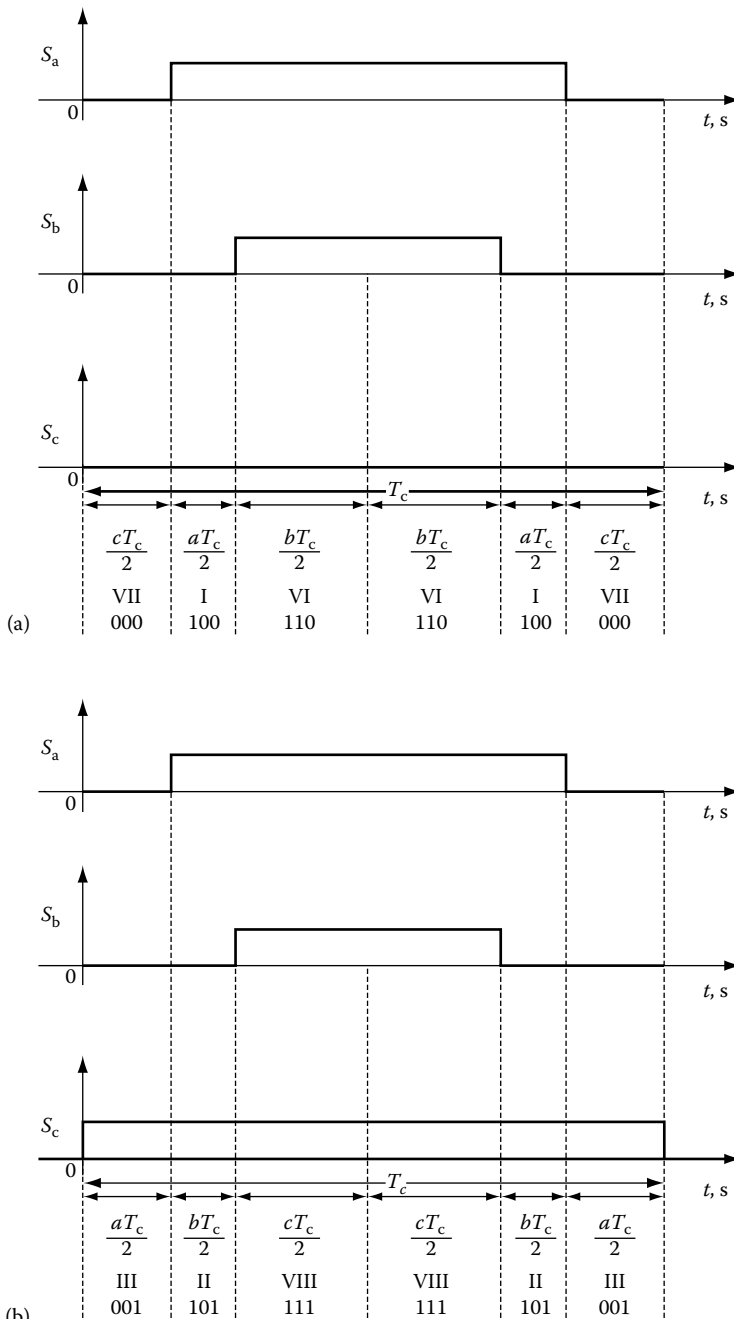


FIGURE 2.35 Constant zero or one switching vector cases in SVM. (a) One switching vector always zero. (b) One switching vector always one.

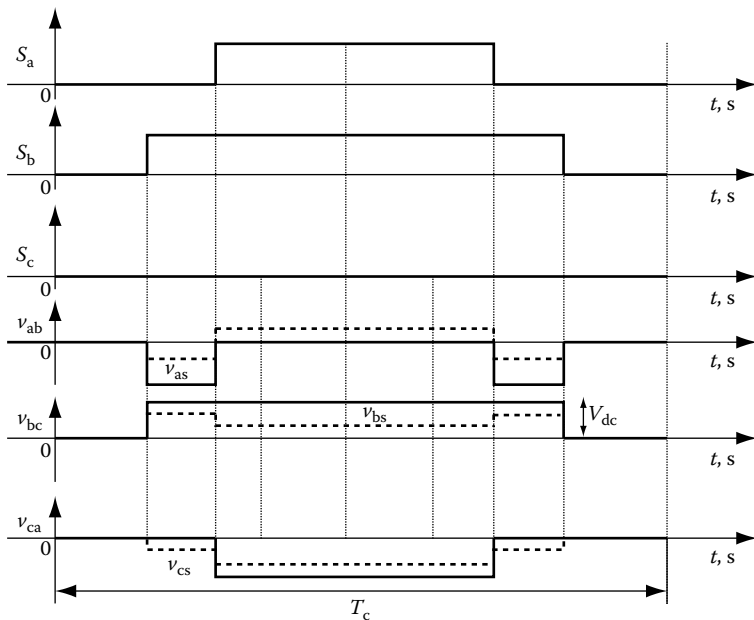


FIGURE 2.36 Reduced switching SVM and its line-to-line and phase voltages.

The ratio between the voltage phasor output and the magnitude of switching vector contains the modulation index as

$$\frac{v_s}{\frac{2}{3}V_{dc}} = \frac{v_s}{\frac{\pi}{3}\left(\frac{2}{\pi}V_{dc}\right)} = \frac{3}{\pi}m_i \quad (2.67)$$

It is attenuated by the factor $3/\pi$. Because of this factor, for example, the output voltage phasor in terms of the switching vectors is represented as in the following:

$$v_s = \frac{3}{\pi}m_i\left(\frac{2}{3}V_{dc}\right) = \frac{3}{\pi}m_i v_k \quad k = 1, 2, \dots, 6 \quad (2.68)$$

where v_k represents any one of the switching vectors. This makes sense in that the output voltage phasor is the result of the switching vectors multiplied by its modulation index but consistently attenuated by a factor $3/\pi$.

For various values of phase voltages, the modulation index and corresponding rms line-to-line output voltages are evaluated and given in [Table 2.7](#).

The relationship between the output voltage phasor and modulation index is highly linear in this case compared to the transfer relationship in PWM-controlled inverter over the entire range of the modulation index. This particular feature in SVM-controlled inverter is attractive in control applications where the linear relationship

TABLE 2.7
Relationship between the Phase Peak Fundamental and Modulation Index

v_s	Modulation Index	Rms Line-to-Line Voltage
$\frac{V_{dc}}{2}$	$\frac{\frac{V_{dc}}{2}}{\frac{2}{\pi}V_{dc}} = 0.785$	$0.612V_{dc}$
$\frac{2}{3}V_{dc} \sin 60^\circ = \frac{1}{\sqrt{3}}V_{dc}$	$\frac{\frac{V_{dc}}{\sqrt{3}}}{\frac{2}{\pi}V_{dc}} = 0.907$	$0.707V_{dc}$
$\frac{2}{\pi}V_{dc}$	$\frac{\frac{2}{\pi}V_{dc}}{\frac{2}{\pi}V_{dc}} = 1$	$0.78V_{dc}$

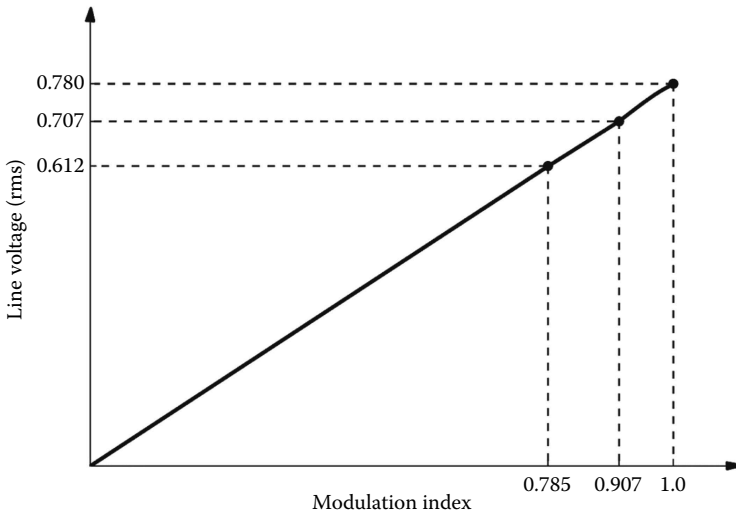


FIGURE 2.37 Transfer characteristic of SVM-controlled inverter.

guarantees a constant gain as against a varying gain of the inverter. Varying gain of the inverter in control applications deteriorates the control performance in terms of the bandwidth and sluggish responses. The transfer relationship is shown in Figure 2.37. They can also be better represented in the switching vector diagram as shown in Figure 2.38. The maximum voltage phasor locus is derived assuming that the zero vector switching is not resorted to giving the sum of a and b of adjacent vectors is equal to one and refer to Figure 2.31 to get the definition for a and b. Then a relationship between a and output voltage phasor is derived as in the following:

$$a_{v1} + b_{v6} = v_s \quad (2.69)$$

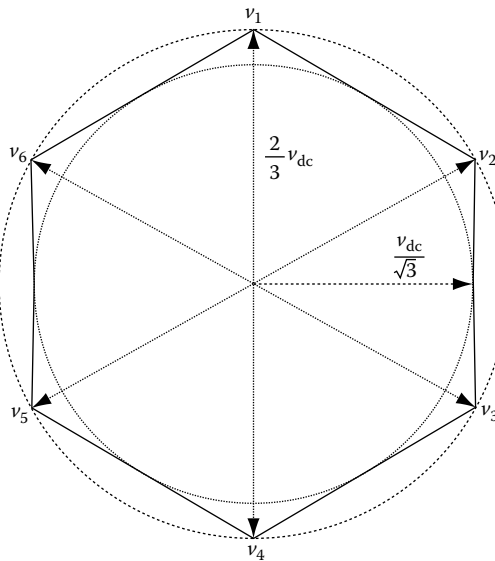


FIGURE 2.38 The maximum output voltage phasor of SVM-controlled inverter with no zero vector switching.

and the switching vectors can be represented as

$$v_1 = v_l + j0 = \frac{2}{3} V_{dc} \quad (2.70)$$

$$v_6 = v_l (\cos 60^\circ + j \sin 60^\circ) = v_l (0.5 + j0.866) \quad (2.71)$$

Hence from these relationships, the output voltage phasor is given by

$$(a + 0.5b) + j0.866b = \frac{v_s}{v_l} \quad (2.72)$$

And given the constraint of $a + b = 1$, the output voltage phasor can be derived as

$$\left(\frac{v_s}{v_l} \right) = \sqrt{a^2 - a + 1} \quad (2.73)$$

From this relationship, the locus of the output voltage phasor is derived and plotted in the figure. The inner circle corresponds to the line-to-line voltage of $0.707V_{dc}$, which gives the modulation index of 0.907 and which is also derived in [Table 2.7](#). The output voltage phasor is a curved surface with the minimum at the modulation index of 0.907. Thereafter the output line voltage varies to $0.78V_{dc}$ that corresponds to the switching vector magnitude of $(2/3)V_{dc}$, giving a modulation index of 1. From

the figure it is evident that the line voltage $0.78V_{dc}$ is unobtainable at all space phasor positions but only at switching vector locations of every 60° starting from zero. Between the modulation ratios of 0.907 and 1, line voltage magnitudes from $0.707V_{dc}$ to $0.78V_{dc}$ can be obtained for limited spatial positions and that too not very linearly. A slight nonlinearity can be observed in that region and accordingly that was shown in the transfer relationship figure. In spite of the slight nonlinearity for the modulation indices of 0.907 and higher, the SVM controller provides the most linear relationship between output line-to-line voltage and modulation index in the inverter.

2.9.3 SPACE VECTOR MODULATOR IMPLEMENTATION

Space vector modulator implementation in a PMSM drive scheme in generic form is shown in [Figure 2.39](#). The d- and q-axes voltage commands in stator reference frames give the magnitude of the voltage phasor, its angle, and the sector in which the commanded phasor resides at a given instant. From this information, the time durations of switching vectors v_1 , v_2 , and zero vector v_0 given respectively by a , b , and c are retrieved from a memory table. The gate drive signals then are extracted from this set of information again using another table stored in a memory. The sampling time T_c is an additional input to the space vector modulator module to endow a desired varying switching frequency feature that may be useful in optimizing the efficiency of the motor drive system over the entire speed torque region.

2.9.4 SWITCHING RIPPLE IN SVM

The switching ripple currents in the SVM control can be derived from the switching phasor diagram assuming the inductance L is known. Neglecting the resistive voltage drops compared to the inductive voltage drops, the rate of change of current can be written from the inductive voltage drop equation as

$$\frac{di}{dt} = \frac{v_k - v_s}{L} \quad (2.74)$$

where v_k is one of the switching vector at the given time with values of

$$\begin{aligned} v_k &= \frac{2}{3} V_{dc} && \text{for } k = 1, 2, \dots, 6 \\ &= 0 && \text{for } k = 7 \text{ and } 8 \end{aligned} \quad (2.75)$$

It may be assumed that the commanded or desired value of voltage phasor, v_s is an average within a switching cycle. Taking incremental values only gives the ripple currents over incremental times with the switching vectors applied within a switching cycle. Then the currents for each switching vector application are written as

$$\Delta i_l = \frac{v_1 - v_s}{L} aT_c \quad (2.76)$$

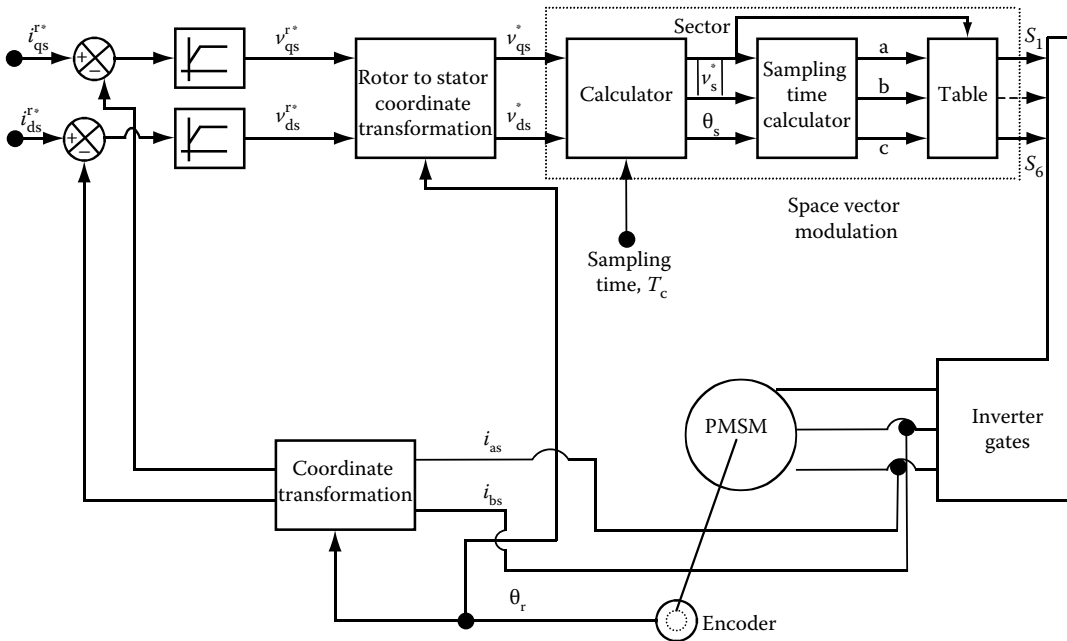


FIGURE 2.39 Generic implementation of SVM controller in a PMSM drive system.

$$\Delta i_2 = \frac{v_2 - v_s}{L} bT_c \quad (2.77)$$

$$\Delta i_o = \frac{v_7 - v_s}{L} aT_c = \frac{0 - v_s}{L} aT_c = -\frac{v_s}{L} aT_c \quad (2.78)$$

where switching vectors v_1 , v_2 , and v_7 (or v_8 as the case may be for zero vector) are applied for time durations of aT_c , bT_c , and cT_c . Note that the current ripple due to zero vector is counter to the direction of voltage command phasor and the other ripple currents are along the vector difference between the applied switching vector and the voltage command phasor. Therefore, given the switching vectors, the command voltage phasor, the vectors $v_1 - v_s$, $v_2 - v_s$ can be derived and then accordingly the ripple currents can be computed. Consider a SVM cycle shown in Figure 2.40 with switching vectors and their durations. From this switching vector diagram with all the vectors that go to make the current ripples is drawn as in Figure 2.41. Then applying the appropriate voltage vectors for the time durations indicated in the previous figure, the ripple currents for the application of $v_1 - v_s$, $v_2 - v_s$, and $-v_s$ are derived from this and shown in Figure 2.42. Note that from the steady-state operating point given by 0, the zero current vector starts from it and goes along $-v_s$ for t_1 and then switching vector v_1 is applied from t_1 to t_2 with the result that $v_1 - v_s$ causes the ripple current during this time and it is along this differential vector. Then for t_2 to t_3 interval, switching vector II is applied causing a ripple current due to $v_2 - v_s$ along this vector direction and then for time t_3 to t_4 , the zero switching vector VIII is applied causing the zero ripple current vector to move along $-v_s$ direction and that completes the half switching

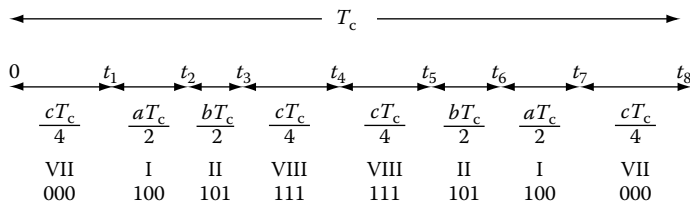


FIGURE 2.40 A typical SVM switching cycle.

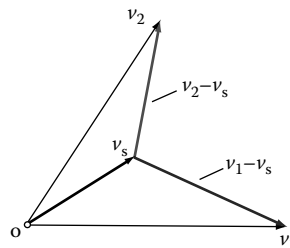


FIGURE 2.41 Switching vector diagram and differential voltage vectors to compute the current ripple.

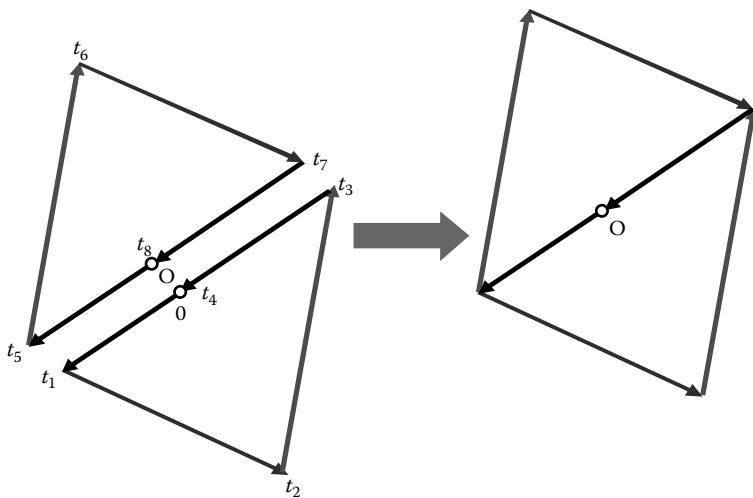


FIGURE 2.42 Derivation of ripple current vector from the switching vector diagram.

cycle and closure of the triangle. Likewise the ripple current vector diagram from t_4 to t_8 can be shown to constitute a triangle similar to the previous ripple switching triangle, which than can be combined for simplicity into one diagram merging the steady-state operating point. It is important to realize that the fundamental value of the current phasor can be obtained from the origin o of the current vector locus for each switching cycle. The fundamental current vector magnitude can be tapped off this figure by sampling at this instant, i.e., at the beginning of each SVM cycle and this comes without the need for filtering the ripple current. Bypassing the ripple current vector and its filtering that would cause delays and phase lag in the control circuits, the measured current in this method can be applied in feedback control for high-performance applications.

Likewise, consider a generic switching cycle of the reduced switching-based SVM operation shown in Figure 2.43. Its switching vector diagram and corresponding ripple current vector diagram are shown in Figure 2.44. Note that the modified SVM uses only four transitions per cycle and correspondingly the ripple current vector diagram reflects that. For higher values of the command voltage phasor with higher modulation indices, note that the ripple current vector is reduced. It is achieved with minimum number of switchings in a carrier cycle.

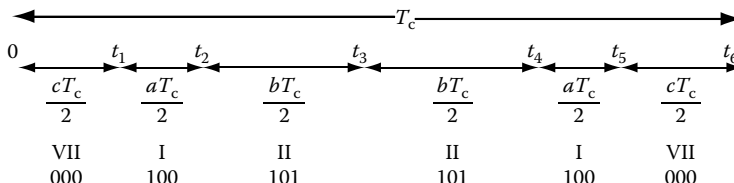


FIGURE 2.43 A generic switching cycle of modified SVM with reduced switching.

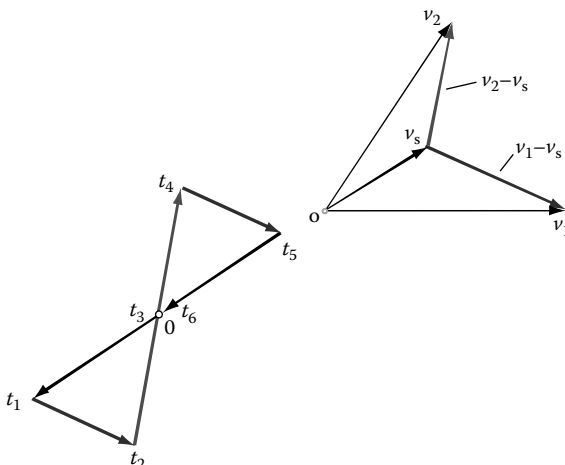


FIGURE 2.44 Switching vector diagram and the ripple current diagram.

2.9.4.1 Hybrid PWM Controller

The switching vectors are generated based on the desired space phasor voltage command consisting of a magnitude and phase angle as seen in the previous sections. But they can also be obtained by the intersection of the triangle carrier signal and the phase voltage commands as modulating signals [92–95]. This is very much similar to the traditional generation of PWM signals. In order to do that a correspondence between the switching vectors and triangle carrier-based PWM, the SVM switching vectors are projected on to the latter as shown in Figure 2.45. In the SVM switching vector signal S_c , note that the application of switching vector VIII is applied for a period of $k_o cT_c$ instead of cT_c interval and accordingly the beginning and ending of SVM cycle is generally denoted by the time intervals of $(1 - k_o)cT_c/2$. Introduction of a fraction k_o during the midperiod of the SVM generalizes the placement of the zero switching vector VIII to any time duration not equal to zero switching vector VII. It has the implication of introducing zero sequence into the midpoint voltage phase command signals and that is demonstrated in the following.

The PWM carrier period corresponds to the SVM period in this derivation and the carrier triangle carrier has positive and negative peaks of $0.5V_{dc}$. The voltage resulting out of the PWM control by intersection of the carrier triangle and a command signal with a time duration of t from the middle of the triangle is given by the equation of the triangle itself as

$$v_m^* = \frac{V_{dc}}{2} \left(\frac{4}{T_c} t - 1 \right) \quad \text{for } 0 \leq t \leq \frac{T_c}{2} \quad (2.79)$$

Normalizing it with half the dc link voltage gives the resultant midpoint voltage in normalized unit denoted as per unit (p.u.)

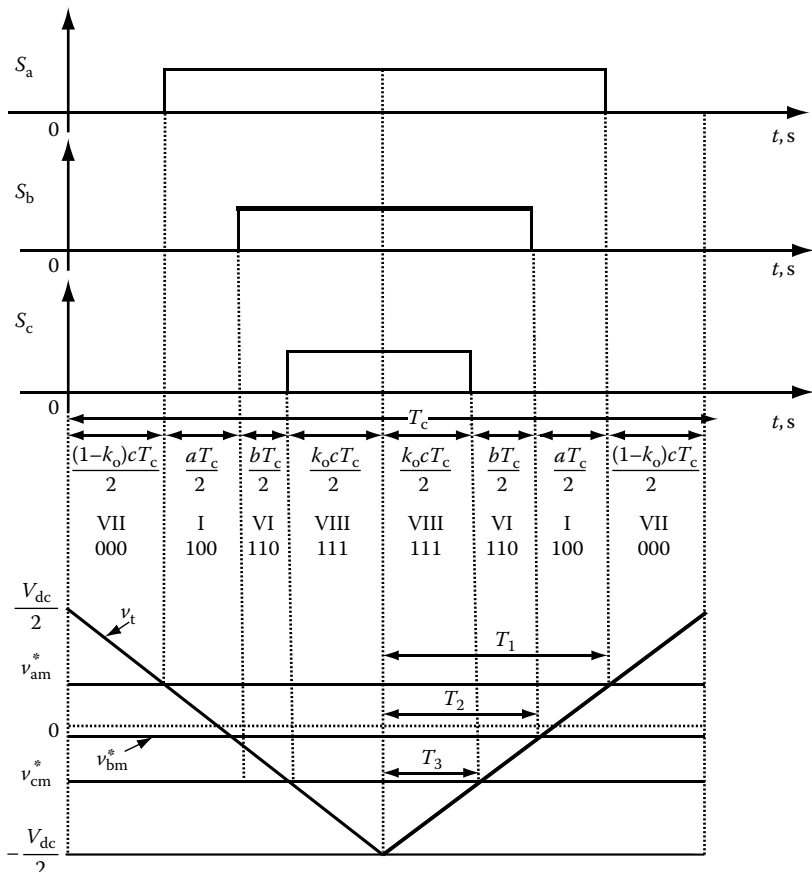


FIGURE 2.45 Derivation of SVM control through PWM method.

$$\frac{v_m^*}{V_{dc}} = v_{mn}^* = \left(\frac{4}{T_c} t - 1 \right) \text{ p.u.} \quad \text{for } 0 \leq t \leq \frac{T_c}{2} \quad (2.80)$$

The abc voltage midpoint voltage commands then are deduced from this equation by substituting the times of their durations from the midpoint of the triangle carrier given by T_1 , T_2 , and T_3 . These durations are given by the SVM switching vector time durations of

$$T_1 = (k_o c + b + a) \frac{T_c}{2} \quad (2.81)$$

$$T_2 = (k_o c + b) \frac{T_c}{2} \quad (2.82)$$

$$T_3 = k_o c \frac{T_c}{2} \quad (2.83)$$

For example, the a phase midpoint voltage command in normalized unit is given by

$$\frac{v_{am}^*}{V_{dc}} = v_{amn}^* \left(\frac{4}{T_c} t - 1 \right) = \left(\frac{4}{T_c} \{k_o c + b + a\} \frac{T_c}{2} - 1 \right) = 2(k_o c + b + a) - 1 \quad (2.84)$$

It is seen from the figure that the command line voltage between a and b applied during aT_c is given by equating the volt sec during the carrier period as

$$a \frac{T_c}{2} V_{dc} = v_{abm}^* \frac{T_c}{2} \quad (2.85)$$

On normalization and simplification it yields

$$a = \frac{v_{abm}^*}{2 \left(\frac{V_{dc}}{2} \right)} = \frac{v_{abmn}^*}{2} = \frac{1}{2} (v_{am}^* - v_{bm}^*) \quad (2.86)$$

Note that v_{am}^* and v_{bm}^* are normalized midpoint voltage commands that consist of the desired midpoint voltage and a zero sequence component. Likewise, the other fractions of time applications of the switching vectors are derived as

$$b = \frac{v_{bcmn}^*}{2} = \frac{1}{2} (v_{bm}^* - v_{cm}^*) \quad (2.87)$$

By equating the sum of the switching vector application durations to the carrier period, a relationship between the fractions a , b , and c is obtained as

$$a + b + c = 1 \quad (2.88)$$

From this equation, c can be evaluated in terms of the phase voltages from the previous two equations. The sum of the command midpoint voltages is derived in terms of the zero sequences and actual command midpoint voltages as

$$v_{am}^* + v_{bm}^* + v_{cm}^* = (v_{an}^* + v_{zs}) + (v_{bn}^* + v_{zs}) + (v_{cn}^* + v_{zs}) = (v_{an}^* + v_{bn}^* + v_{cn}^*) + 3v_{zs} \quad (2.89)$$

And noting that the sum of the actual midpoint voltage commands is zero, the sum of the command midpoint voltages equals thrice the zero sequence voltages given by

$$v_{am}^* + v_{bm}^* + v_{cm}^* = 3v_{zs} \quad (2.90)$$

Substituting for the command voltages in terms of a , b , and c and then in terms of the midpoint voltage commands yields the zero sequence voltage as

$$v_{zs} = - \left[(1 - 2k_o) + k_o v_{an}^* + (1 - k_o) v_{cn}^* \right] \quad (2.91)$$

For the standard SVM shown in [Figure 2.32](#), $k_o = 0.5$ giving the zero sequence voltage input as

$$v_{zs} = \frac{1}{2} v_{bn}^* \quad (2.92)$$

The derivations are made for sector I operation and accordingly for all other five sectors the equations can be similarly derived for the zero sequence voltage input and are generalized [92]. Once they are obtained, the effect of variation of k_o and the resulting variation of zero sequence voltage inputs on modulation index as well as on modulation ratio can be studied. Some examples of k_o variation on the voltage command waveforms are shown in [Figure 2.46](#) with the first part having constant values for the entire cycle while the second part has constant values only for one-sixth of a cycle. For $k_o = 0.5$, it is clearly seen that the zero sequence input is a third harmonic of the fundamental and moreover that harmonic is half cycle symmetric unlike in other cases for constant k_o values. That reduces the command voltage peak of 1.15 to less than or equal to 1, thereby extending the linear range of operation as in regular PWM with injected third harmonics.

Ripple current: The ripple current for PWM controlled inverter can be derived from their switching state vectors and their duration similar to the one derived for SVM-based inverter controller. Consider the timing diagram for the switching vectors given in [Figure 2.47](#) derived from the hybrid PWM controller by equating the placement of zero vectors of equal duration at each end and in the middle to be equal to $cT_c/3$ by making $k_o = 1/3$ in the hybrid PWM scheme. The ripple current diagram is derived from the switching vectors and their durations and their differences with the desired space phasor voltage as shown in [Figure 2.48](#).

The derivation of the current ripple is identical to the derivations made in the previous section for the ripple current of SVM-based inverter controller. For brevity, this is not explained here. The inference from the PWM scheme's ripple currents is that the number of switchings remains at 6 as in the case of the SVM full switching. The two halves the current vector diagram is shifted from each other with the result that the ripple currents around half carrier cycle are not symmetric and overall ripple could be higher than that of the SVM-based control.

2.10 INVERTER SWITCHING DELAY

A voltage source inverter with one phase leg is shown in [Figure 2.49](#) for illustration. Positive load current is indicated by an arrow to the load section from left to right. Transistor T_1 is turned on for a time T_{on} . In an ideal inverter with ideal switches, T_4 is turned on when T_1 is turned off. But T_1 takes a time equal to sum of storage, current fall off, and voltage rise times for it to completely turn off. If the bottom transistor is turned on before the top device is completely turned off, then both devices conduct, resulting in a short circuit of the input dc supply. It is known as shoot through fault in literature. To avoid this fault, an intentional delay is introduced

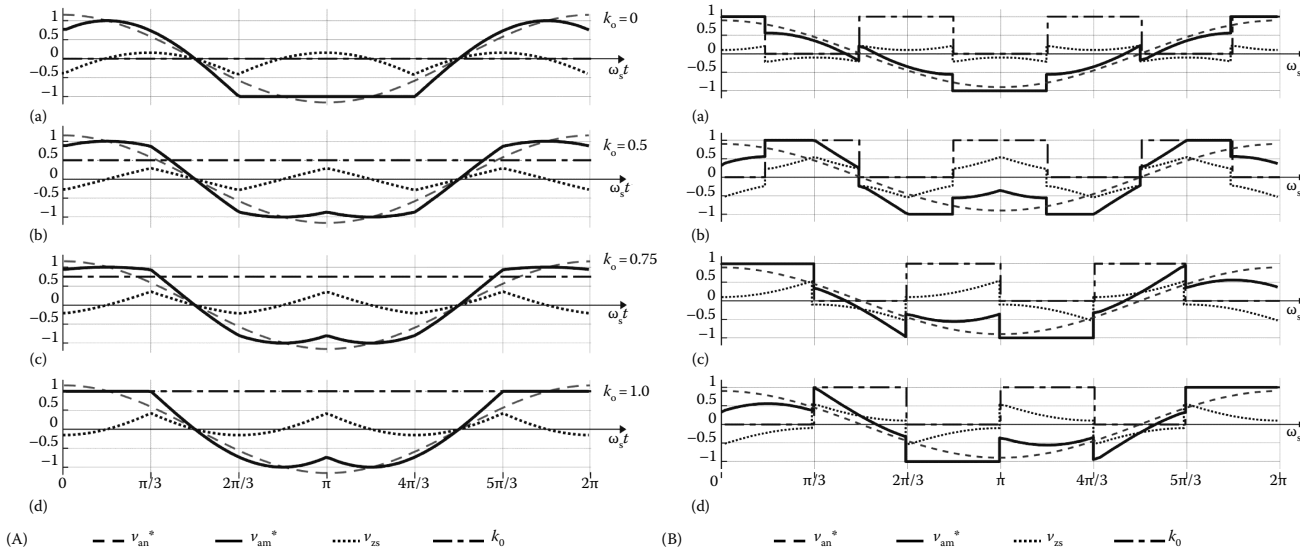


FIGURE 2.46 Effect of varying values for k_o on command voltage waveforms and zero sequence components. (A) Constant values for k_o ; (B) switched values for k_o in a cycle.

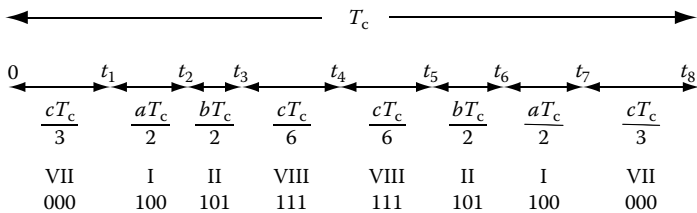


FIGURE 2.47 Switching vectors and their timing diagram.

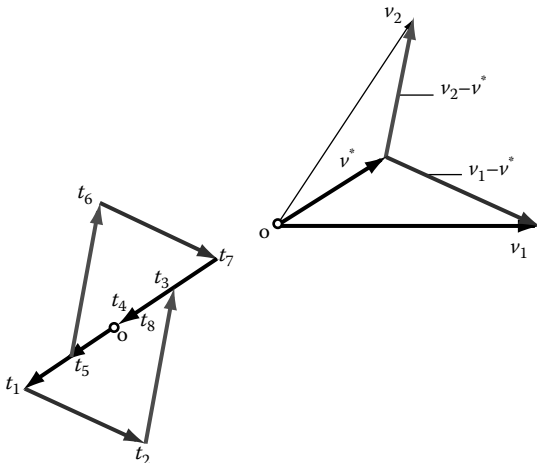


FIGURE 2.48 Derivation of ripple current of the PWM scheme.

in between the switching on and off of the top and bottom transistors in each phase leg of the inverter. This delay then has to be at least equal to the sum of the storage time, current fall time, and voltage rise time of the device. As these times vary with device operating temperature and current, it is prudent to add a safety margin to this minimum time delay. Further, this margin allows coping with the imprecise device specifications and impossibility of monitoring such variations dynamically in the controller in real time. The delay that has to be introduced goes by different names such as dead-time delay or lock out time. The dead time delay has adverse effects on the load voltage [104–127]. It is examined in the following.

Effect of dead time delay: A qualitative and approximate analysis of the effect of dead time delay on output voltage is presented. Consider ideal devices neglecting switching times so that the clarity can be preserved in the discussion. The impact on the midpoint voltage is assessed here. Note that it can be used to evaluate the effect on line voltages very easily. A dead time delay, t_d , is inserted in gate signals of both devices of a phase leg shown in Figure 2.49, whenever their states are changed from on to off and off to on conditions. Considering a continuous positive load current and an on time of t_{on} and off time of t_{off} for the top transistor (and vice versa for the bottom transistor), the gate signals are derived for the case without dead time delay

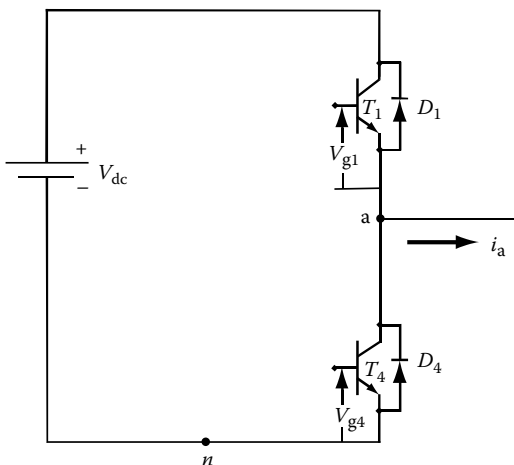


FIGURE 2.49 Single-phase leg of an inverter bridge.

and it is shown in [Figure 2.25](#). The gate signals are derived from the midpoint phase a command voltage, v_{an}^* . The top transistor's gate signal follows the midpoint voltage command whereas the bottom transistor's gate signal is the complement of the voltage command signal. Complementary switching is selected so that the midpoint voltage is well defined whether there is a load current present or not, since a voltage source inverter is considered. Note that in a voltage source inverter the output voltages have to be well defined and not the currents. The gate signals v_{g1} and v_{g4} are defined ideal gate signals. In a practical inverter, a dead time t_d is inserted during the device transitions as shown in [Figure 2.50](#) in the signals v_{g1} and v_{g4} , which are referred to as modified gate signals to illustrate the effect of the dead time delay. When bottom device turns off, the top device's turn on is delayed by t_d and likewise when top device turns off, the bottom device's turn on is delayed by the dead time. If the top device is on, the midpoint voltage is $v_s - v_{sw}$ where v_{sw} is the transistor conduction voltage drop. Here note that the voltage is measured with respect to the negative rail of the dc source. When the top device is given a gate signal to turn off, the current decreases in the device (after a time equal to the device storage time), to the same proportion that is transferred to the bottom diode, D_4 . After the complete transfer of current known as current commutation, the voltage across the top device starts to rise to match the source voltage. By the same measure, the voltage across the diode D_4 falls to its conduction value, v_d . From this instant, the midpoint voltage is $-v_d$ with respect to the negative rail of the bus voltage. If the load current is continuous, turning on T_4 has no effect on the midpoint voltage as bottom diode already is conducting the entire load current. These conduction drops of the transistors and diodes have been neglected by assuming ideal devices in [Figure 2.50](#).

From ideal and modified gate signals, the midpoint voltages are derived and denoted as v_{an} and v_{an}^* , respectively. The difference in the midpoint voltage, $(v_{an}^* - v_{an})$, between the inverter with and without time delay is indicated by Δv_{an} and it is negative and so also its average. This is the midpoint voltage that has been

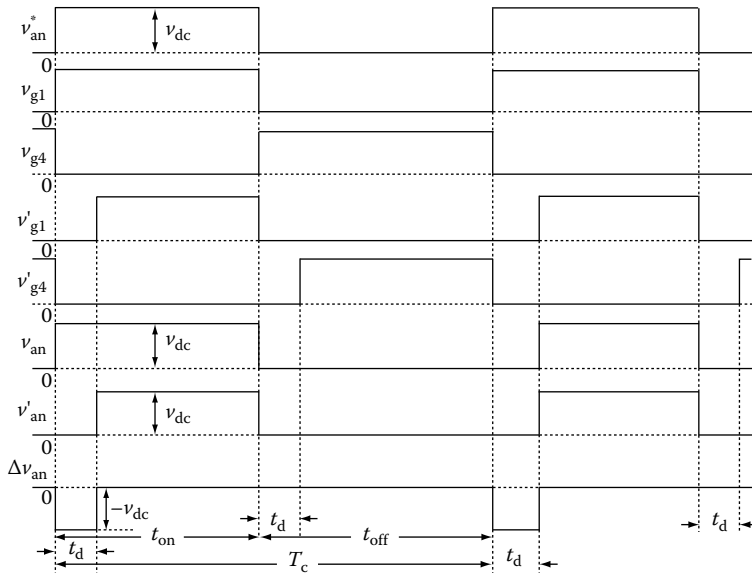


FIGURE 2.50 Effect of dead time delay on inverter for positive load current with ideal devices.

lost to the load due to the inverter dead time delay. Likewise, the effect for a negative load current is derived and shown in [Figure 2.51](#). There is a gain in midpoint and hence a gain in load voltage is seen. Based on this discussion, the following comments are in order:

- The effect of dead time delay on output voltage is determined by the duration of the dead time delay and the polarity of the load current.
- Dead time delay entails a loss of output voltage for positive load currents and a gain of output voltage for negative load currents.
- The loss/gain in output volt-second in a switching cycle is equal to $t_d V_{dc}$ where V_{dc} is the input dc voltage to the inverter and t_d is the dead time delay.
- The dead time delay is necessary only for voltage source inverter for all the time. It is not necessary for current source inverter except when the currents cross zero. This is because the current is transferred from the conducting transistor to its complementary device's diode and turning on the complement transistor has no effect whatsoever on output voltage during this time.

Replacing ideal devices with practical devices by including their switching times and conduction voltage drops, the effect of dead time delay is shown in [Figure 2.52](#) for positive load current. The load loses voltage even though there is a gain during fall time of the device and a loss during rise time of the device. Note that the deviation from the commanded voltage is very significant due to device conduction voltage drop and switching time and dead time delay. All of these make the transfer relationship between the inverter output to its command voltage very nonlinear. Similarly,

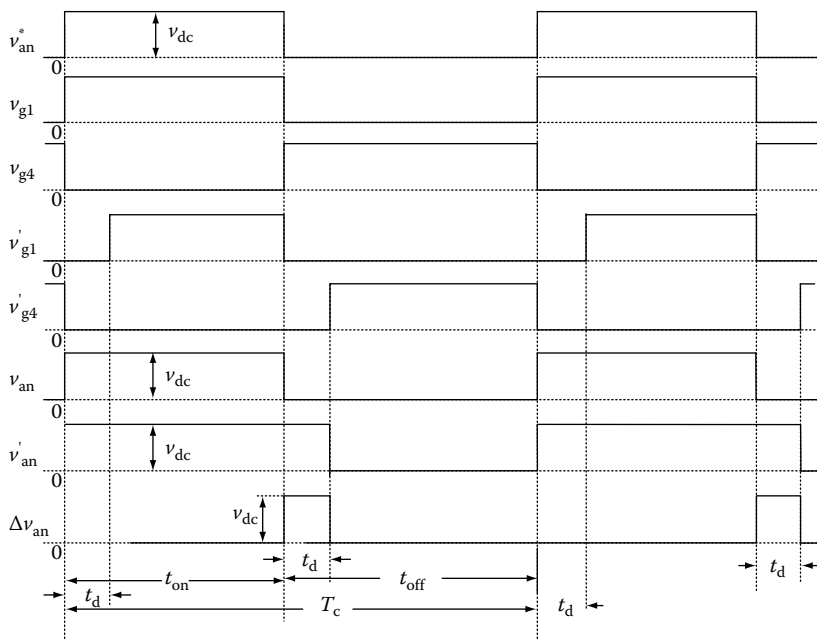


FIGURE 2.51 Effect of dead time delay on inverter for negative load current with ideal devices.

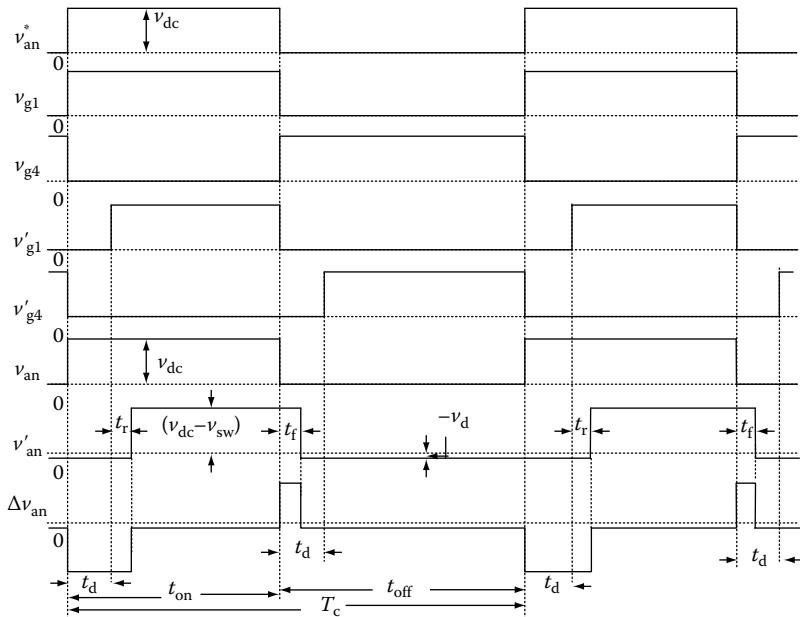


FIGURE 2.52 Dead time effects in an inverter with practical devices.

the effects can be visualized for nonideal device-based inverters for negative load current flow. Accordingly, the average voltage gain or loss is derived as

$$\begin{aligned}\Delta V &= \frac{t_d + t_r - t_f}{T_c} [V_{dc} - V_{sw}] + \frac{t_{off} + 2t_d + t_r - t_f}{T_c} V_d + \frac{T_c - t_{off} - t_d + t_f}{T_c} V_{sw} \\ &= (V_{dc} - V_{sw} + V_d) \left[\frac{t_d + t_r - t_f}{T_c} \right] + V_d \left[\frac{t_{off} + t_d}{T_c} \right] + V_{sw} \left[\frac{T_c - t_{off} - t_d + t_f}{T_c} \right] \quad (2.93)\end{aligned}$$

where V_d and V_{sw} are the diode and transistor conduction voltage drops, respectively. Many of the parameters in this expression are not constants but are dependent on device current and junction temperature. Variations in such operational variables make it difficult to predict or calculate them with precision and hence in compensating for the device dead time delay. Therefore, all compensation schemes are only approximate. Such an understanding facilitates some of the measurement/prediction problems encountered in sensorless speed and position control operation of the drive system. Additional information on this is presented in the Chapter 8 on sensorless control of PMSM drives.

Consider an inverter with generic devices having the following characteristics:

$V_{dc} = 285$ V	$t_{rv} = 100$ ns
$v_{sw} = 1.8$ V	$t_{fv} = 100$ ns
$v_d = 1.3$ V	$t_{dl} = 78$ ns
$t_d = 3$ μ s	$t_{rc} = 110$ ns
$T_c = 0.1$ ms	$t_{fc} = 265$ ns
$f_c = 10$ kHz	$t_{d2} = 340$ ns

The voltage gain/loss and inverter midpoint voltage characteristics of the inverter have been determined using Equation 2.93 for the ideal inverter and inverter with dead time delay operation and shown in Figures 2.53 and 2.54, respectively. The duty cycle is incorporated in the figure as the key variable for plotting.

The percent voltage loss is higher at low-voltage commands and smaller at high-voltage commands. Therefore, low-frequency (corresponding to low speed) operation definitely requires compensation in comparison to the high-frequency (corresponding to high speed) operation.

The effect of dead time on machine currents in a three-phase inverter fed PMSM drive is shown in Figure 2.55 for a sine triangle-based modulation scheme. The phase currents and their references are shown in the figure. The dead time delay has distorted the output currents and the distortions occur predominantly during zero crossings of the currents. As the voltages and currents are influenced by one

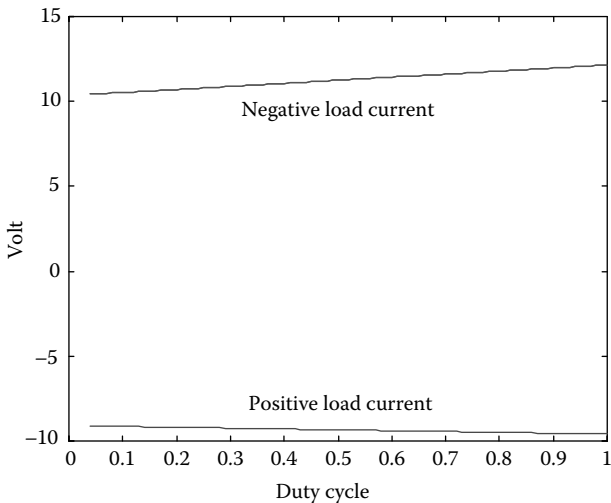


FIGURE 2.53 Voltage gain (loss) for negative (positive) current.

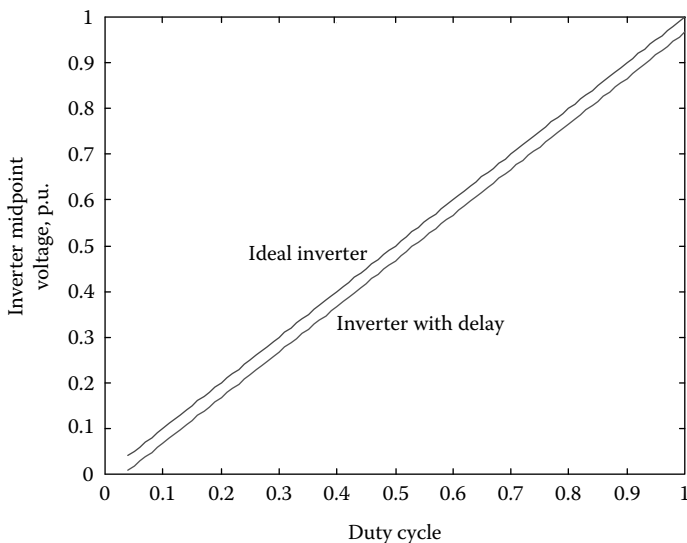


FIGURE 2.54 Inverter midpoint voltage versus duty cycle for inverter with and without dead time delay.

another, the distortions are conspicuous at every 60° , i.e., six times in one cycle as there are six zero crossings in an electrical cycle in a three-phase system for all combined phases. These distortions can cause speed oscillations at low-speed operation of a motor drive. Inability to generate distortion-free voltages and currents causes formidable problems in drives control where such inputs are assumed and required for high-performance such as in position controlled servo mechanisms. The position

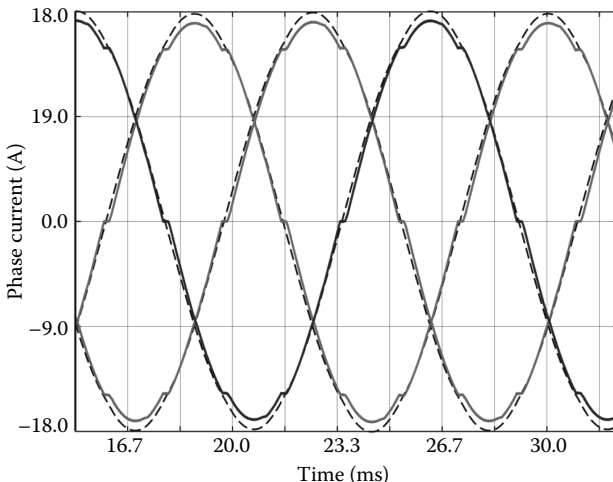


FIGURE 2.55 The effect of dead time delay in an inverter switching at 20 kHz and controlling a PMSM drive.

sensorless control and operation of the induction motor and PMSM drives have highlighted the severe drawbacks of the dead time distortion. These distortions make it difficult to estimate rotor position with reasonable accuracy. In the light of these adverse effects, it is vital to compensate for the dead time effects of the inverter. In the case of an ideal inverter, note that the output current waveforms follow exactly their commands and, therefore, they are not shown in a separate figure.

For ultrafast turn off devices, the dead time can be very small with the result that voltage gain/loss may be negligible. In that case, compensation for dead time delay may not be essential. That is not the case with many devices such as IGBTs. Apart from the dead time, the varying conduction voltage drops for various currents produce an additional nonlinearity. All these effects greatly impact transfer relationship of the inverter and the operation of the inverter-driven motor drive system.

Compensation of dead time delay effects: The compensation for the simplest case of only dead time delay is elementary. It is discussed here first neglecting the device conduction voltage drop and also the switching times to understand the concept and then these secondary adverse characteristics of the device are incorporated. It is achieved with shifting symmetrically the ideal top gate signal by dead time delay on both rising and falling edges, say for a positive load current, and the ideal bottom gate signal by twice the dead time delay only on its rising front. The inverter midpoint voltages for ideal inverter and inverter with time delay are given by v_{an} and \dot{v}_{an} , respectively. Their corresponding gate signals are given by the set of v_{g1}, v_{g4} and set of v_{g1}, v_{g4} for one phase leg of an inverter. These are carried over in each illustration to see the effect of dead time delay and its compensation on the midpoint voltages. The compensated gate signals are given as v_{g1c} and v_{g4c} for the top and bottom controllable devices. The resulting midpoint voltage with compensation, indicated by v_{anc} , is identical to its commanded value except that it is time shifted by an amount equal to the dead time delay as shown in [Figure 2.56](#). This is a drawback only if the

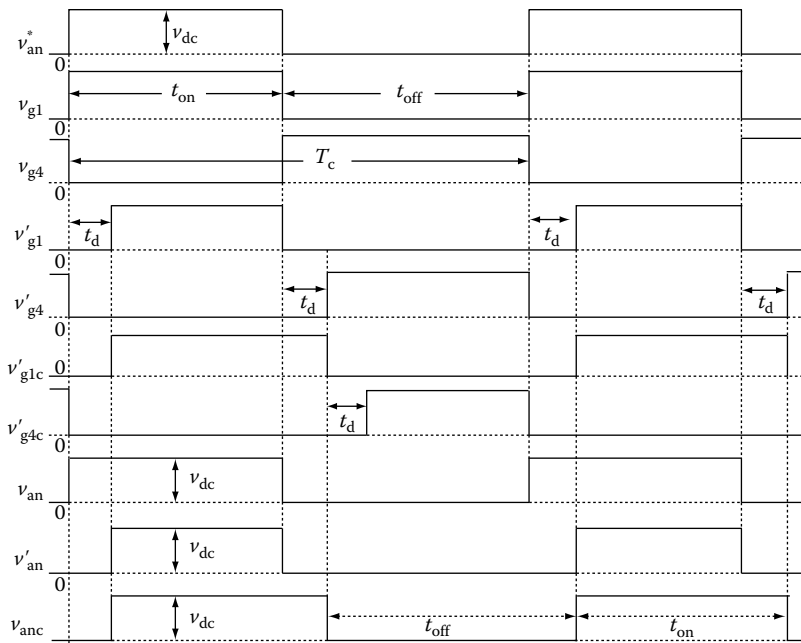


FIGURE 2.56 Compensation for dead time delay for positive load current in inverter with ideal devices.

dead time delay is large enough to prevent a drive from specific performance even after compensating for its effect in gain/loss of volt-second. If the delay is significant to the PWM carrier period, then it is prudent to include it in the inverter modeling. It is addressed in the next section on modeling.

Similarly compensation can be achieved for negative load current but not by adding but subtracting the gate signal area over a time equal to dead time delay, as against adding it for the positive load current. The gate signal duration that is subtracted from is the inverter gate signal with dead time delay instrumented, v'_{g1} . This signal is further modified for compensation by subtracting on the rising edge by a duration equal to dead time delay. Or with reference to the ideal inverter gate signal, v_{g1} , the top device gate signal duration is subtracted by an amount equal to twice the dead time delay to obtain the compensated top gate signal, v'_{g1c} . Accordingly, the compensated bottom gate signal, v'_{g4c} is separated from the top signal by dead time delay on both rising and falling edges of the compensated top gate signal. The compensation is illustrated in [Figure 2.57](#) for negative load current.

So far, the device switching times and conduction voltage drops have been ignored in the treatment of dead time delay and its compensation. They are compensated along with time delay and shown in [Figure 2.32](#). Consider the case when storage, current rise and fall, voltage fall and rise times are included in the compensation effort. For all practical purposes during the device turn on, the current rise and voltage fall times are bundled into one variable t_{sl} and device storage time t_{dl} is kept separately in this discussion. Likewise the current fall and voltage rise times are bundled into

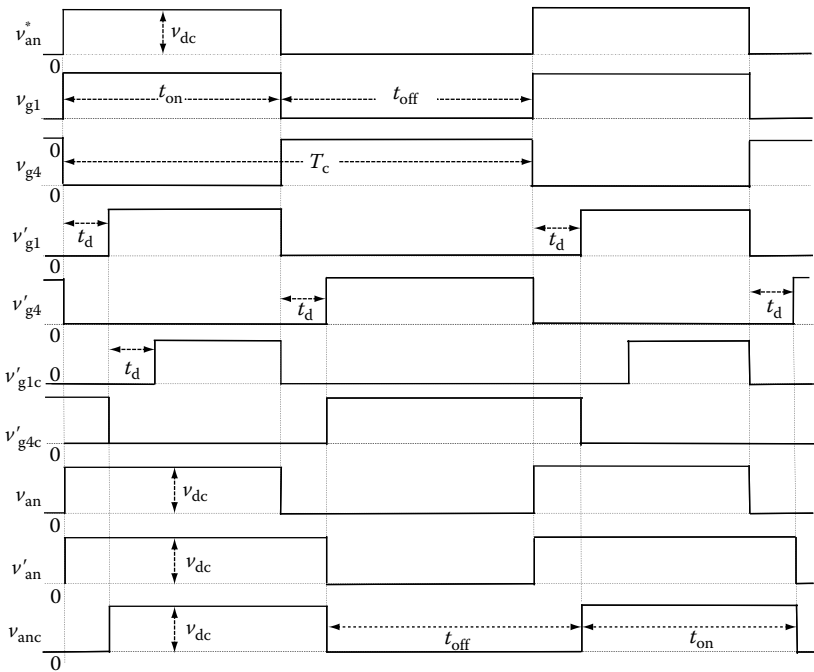


FIGURE 2.57 Compensation for dead time delay for negative load current in inverter with ideal devices.

t_{s2} and the storage time is t_{d2} during the device turn off. Consider positive load current for this part of the discussion. Whenever the device turns on, the midpoint stays near zero (or negative of the bottom diode conduction voltage drop) for a time equal to the sum of t_{d1} and t_{s1} . To compensate this effect, then the top gate signal has to be extended by the same amount of time on its falling edge. As the gate pulse was delayed by the dead time, then to compensate for that the falling edge is extended by the same amount. Therefore, the falling edge of the gate signal is extended by $(t_{d1} + t_{s1} + t_d)$. But the device when it turns off, it extends conduction by an amount equal to its turn off storage time and switching times given by the sum of t_{d2} and t_{s2} . This necessitates slicing off the rising edge of the compensated top gate signal, v'_{g1c} , by the same amount so that the final midpoint volt-second is equal to its commanded value. The compensated bottom gate signal v'_{g4c} is time shifted by dead time delay from the falling edge of the midpoint voltage or from the falling edge of the compensated top gate signal by $(t_{d2} + t_{s2} + t_d)$. This completes the compensation for the dead time delay neglecting the conduction voltage drops. They can be included by taking the average loss/gain of volt-second per switching cycle due to conduction voltage drops and then finding an equivalent time that can be added to the top gate signal. The volt-second loss to the midpoint voltage due to device conduction voltage drops equated to the compensated volt-second is given by

$$v_{dc} t_{vc} = v_{sw} t_{on} + v_d t_{off} \quad (2.94)$$

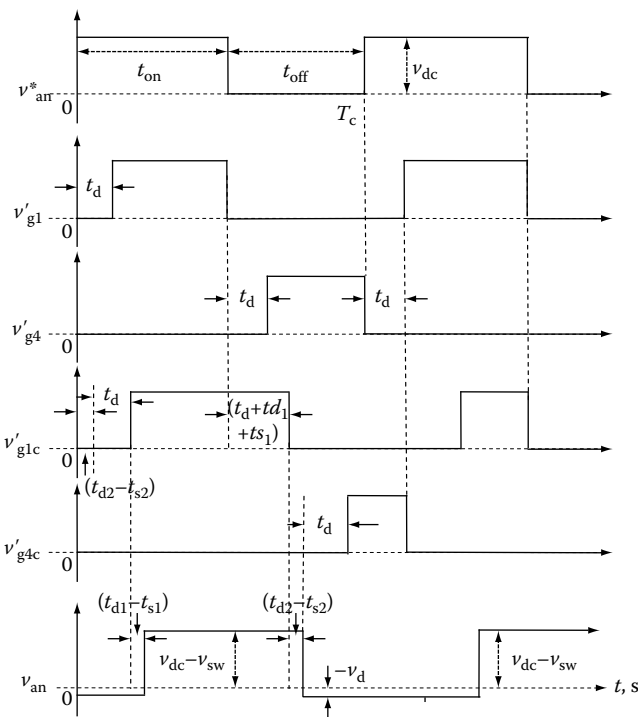


FIGURE 2.58 Compensation of dead time delay effects for positive load current with non-ideal devices.

where t_{vc} is the time to be added to the top gate signal for compensation. This is done on an average but switching cycle per cycle basis and, therefore, the error will not amount to very much in the inverter and machine dynamic performance. The addition of t_{vc} to the top gate signal is not shown in Figure 2.58 is to be noted.

The method of compensation discussed in the above is one of the techniques in practice. Many techniques for compensation have been formulated since 1987. Some are listed in the references. One of the straight forward compensation techniques is by looking at the polarity of the load current and then adding or subtracting a period equal to dead time delay to the gate signals.

The other technique is to find the voltage to be compensated for, then have its fundamental equivalent added to the command voltage to derive the compensated command voltage to generate the gate drive signals. This is known as voltage averaging method and seems to have dynamic performance problems due to the phase lag.

Another technique for time delay compensation is based on suppressing the gate drive signals. When motor or load current is continuous, turn off of top (bottom) controllable device leads to the bottom (top) diode's conduction. Therefore, there is no need to switch on the complementary controllable devices during this time and hence their gate signals can be suppressed. Therefore, there is no dead time delay needed to be instrumented in this case. But when the motor current is transitioning zero where the current continuity requirement is not met, then the dead time delay

is required and incorporated in the gate drives. This technique greatly simplifies the implementation of dead time delay compensation compared to most of the methods. Here the current polarity and accuracy near zero current are required.

It is easily seen that the motor phase current is negative when the midpoint is high and the controllable devices are off and the current is positive when the midpoint voltage is low and the controllable devices are off. Therefore, the current polarity is predicted from the measurement of the midpoint voltage, which is much less expensive than current measurement. This method then does away with current measurement and the need for current sensors.

2.10.1 CONTROL MODELING OF THE THREE-PHASE INVERTER

The converter can be considered as a black box with a certain gain and phase delay for modeling and use in control studies. The gain of the linearized controller-based converter for a maximum control voltage of V_{cm} , is given as

$$K_r = \frac{\frac{2}{\pi} V_{dc}}{V_{cm}} V/V \quad (2.95)$$

The converter is a sampled-data system. The sampling interval gives an indication of its time delay. The sampling interval corresponds to one PWM period. But the command to change switching may occur at any time within this period. Statistically on an average, the delay may be treated as one half of this interval and, in time, is equal to

$$T_r = \frac{1}{2} \times (\text{time period of one PWM cycle}) = \frac{1}{2} \times \frac{1}{f_c} \quad (2.96)$$

But other leading researchers treat this time delay to be equal to three-fourths of one PWM cycle. The justification is that there is dead time and its compensation to be accounted for as well as delays inherently involved in processing and the fact that the advocated greater delay time as against the statistical average is, to be noted, also based on their experience too. Alternatively, it is always possible to measure the delay time for a typical step signal magnitude that is encountered in the motor drive and that could be used in control modeling. The converter is then modeled with its gain and time delay as

$$G_r(s) = K_r e^{-T_r s} \quad (2.97)$$

and Equation 2.97 can also be approximated as a first-order time lag and given as

$$G_r(s) = \frac{K_r}{1 + sT} \quad (2.98)$$

For many drive system applications, the model given in Equation 2.98 is found to be adequate in practice.

2.11 INPUT POWER FACTOR CORRECTION CIRCUIT

The inverter is supplied prevalently from a rectified dc through an uncontrolled diode bridge rectifier. The distortion in the ac line supply currents, high peak currents, and resulting disturbance to the power system generated by the diode rectifier are all undesirable. Utilities if not in United States but in other countries require the power electronic manufacturers to draw sinusoidal currents with minimum distortion from their supplies as well as to have close to unity power factor operation to maximize the utilization of their installed capacity. A number of power electronic circuits became popular in late 1980s offering unity power factor correction capability together with shaping the input line currents to be sinusoidal [96–103]. Two power factor correction circuits most popular in use, one for single phase and one for three ac inputs, are discussed in this section. While both of these circuits handle power factor correction, the three-phase circuit that is presented only has the capability to handle bidirectional power flow, i.e., from inverter load to ac input and vice versa. A single-phase version of such a circuit is not presented here for lack of space but it becomes obvious from its three-phase counterpart.

2.11.1 SINGLE-PHASE POWER FACTOR CORRECTION CIRCUIT

The single-phase power factor correction circuit is shown in Figure 2.59. The rectified ac voltage, v_{re} , charges the capacitor through diode D_2 and inductor L when transistor T_1 is turned off. This resembles the conventional diode bridge rectifier operating with inductor capacitor filter. The current waveform will be better than that shown under single-phase operation without the inductor shown in Figure 2.8b and the dc current becomes increasingly flat with higher values of the inductor. For a practical inductor, the current is nonsinusoidal having higher harmonic contents. Introducing an active device on the output side of the circuit enables regulating the current in the inductor,

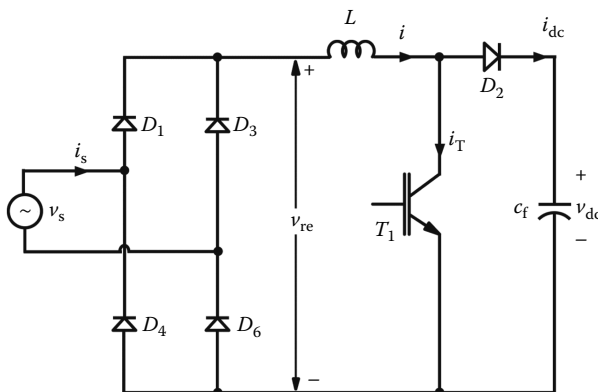


FIGURE 2.59 Circuit for single-phase rectification with power factor correction.

say, to be sinusoidal in this case while holding the capacitor voltage to any desirable level over and above that of the peak input ac voltage magnitude.

There are two modes of operation in this converter corresponding to the conduction and nonconduction of current in the transistor. Turning on the transistor enables the rectified voltage to be applied across the inductor L . During this time, energy is stored in the inductor by transferring it from ac input source. Turning off the transistor configures the circuit to have v_{re} , L , D_2 , and C in series. Because of the existing current in the inductor, diode D_2 is forward biased, resulting in flow of current from rectified voltage to the capacitor via the inductor. Energy then is transferred from the inductor and rectified dc source. When the capacitor voltage is greater than the rectified voltage, which usually is the case, mostly the energy stored in the inductor is transferred to the capacitor. The load connected across the capacitor but not shown in figure will draw its current from the capacitor when transistor T_1 is on and when it is off, the load and capacitor are charged from the stored energy in the inductor and rectified ac source. The purpose of the transistor is to shape the current in the inductor and hence the source ac current.

An outer load voltage feedback control with inner current control loop is all that is required to realize a sinusoidal input current with this converter. The current command is generated from output power requirement so that varying power demand is incorporated into the sinusoidal current magnitude to be drawn from the ac source. This current command is in the image of the ac input voltage with its magnitude supplied by the power demand. The operational waveform of the circuit is shown in Figure 2.60. The capacitor gets charged even when the input voltage is lower than the output voltage and therefore, this circuit is referred to as a boost rectifier. Sinusoidal current with zero phase from the input voltage is drawn, giving it almost a unity power factor operation. Because of this, the circuit is also known as unity power

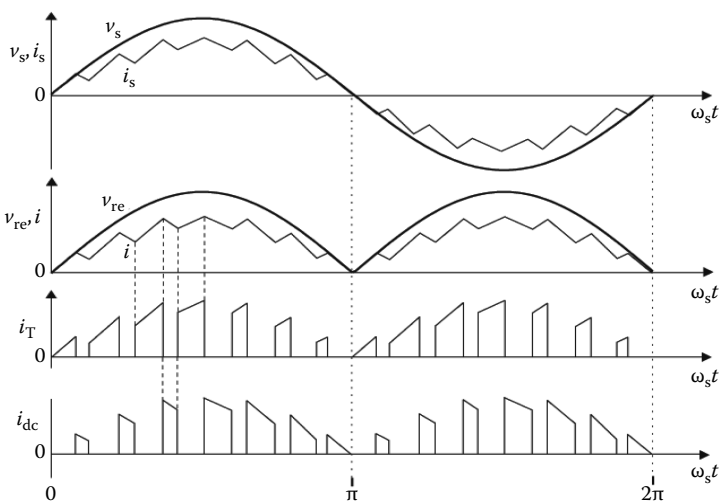


FIGURE 2.60 Source voltage and current waveforms from single-phase power factor correction circuit.

factor (UPF) boost rectifier. Other forms of single-phase UPF circuit versions are left to readers to explore.

2.11.2 THREE-PHASE POWER FACTOR CORRECTION CIRCUIT

An ac to dc power converter capable of correcting the input power factor (leading, lagging, or unity) and bidirectional power flow is shown in Figure 2.61. This circuit has self-commutating power devices with antiparallel diodes, ac input line inductances and as a unit they allow the conduction of bidirectional current. The converter and its operation have been described for operating from a dc source in the inverter section. Instead of the dc source input, this converter takes the ac source input and provides a dc source or vice versa. Thereby it works as a controlled rectifier in the first instance and an inverter in the second instance. Calling it an inverter does not fully describe the circuit features and hence it is denoted as converter circuit hereafter. Per phase equivalent circuit is shown in Figure 2.62 and its phasor diagram in Figure 2.63. With controllable switching of this converter selectively (unlike a diode bridge rectifier) the supply voltage is picked and applied for desirable durations to the dc source. That applies equally to the application of dc source voltage to the ac source because of its bidirectional flow capability and control. The current in input phase is controlled by varying the potential difference between v_s and v_r where v_s and v_r are source and converter input phase voltages, respectively. The corresponding line-to-line voltages to the source and converter are v_{ab} and v_{abi} , respectively. Their phase counterparts are v_s and v_r , respectively. The input to the inverter, i.e., after line

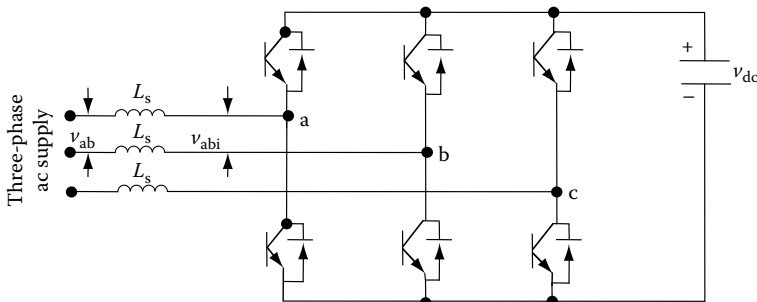


FIGURE 2.61 Power factor-corrected rectification.

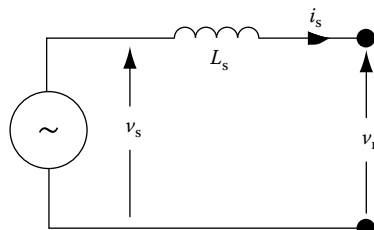


FIGURE 2.62 Per phase equivalent circuit.

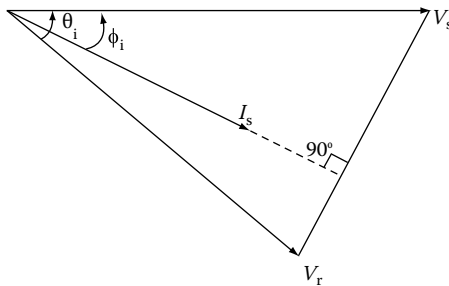


FIGURE 2.63 Phasor diagram.

inductors is the culmination of inverter switching. For a fixed current, the magnitude of v_r is constant as it is determined by the dc link voltage, v_{dc} , charged through the antiparallel diode bridge part of the converter. By varying the phase of the v_r with the converter switching, by θ_i from the input voltage, the voltage across the inductor, L_s is predetermined, which gives rise to the input current I_s as shown in Figure 2.63, and given by

$$I_s = \frac{V_s - V_r \angle -\theta_i}{j\omega_s L_s} = |I_s| \angle \phi_i \quad (2.99)$$

where ω_s is angular frequency of the input supply voltage expressed in rad/s. Therefore varying θ_i , changes I_s and its phase ϕ_i , which is the power factor angle. The power factor can be changed to leading, lagging, or unity with this power converter while maintaining a sinusoidal current with very little distortion. The resulting input current drawn from the utility will be a fundamental sinusoid superposed with ripples at switching frequency of the converter. The dominant sidebands will be at $(f_c + f_s)$ and $(f_c - f_s)$ where f_c and f_s are switching frequency of the inverter and ac supply voltage frequency, respectively. By positioning the current phasor greater than 90° away from the source voltage phasor, power flow can be reversed from the dc link to ac source. The operation of the converter is achieved with PWM, space vector modulation or hysteresis current control.

2.12 FOUR-QUADRANT OPERATION

Many applications require controlled starts and stops of the machines, such as in robotic actuation. Consider that the machine is operating at a steady speed of ω_m and it is desired to bring the speed to zero. There are two ways [5] to achieve it:

- (i) Cut off the power supply to the machine and let the rotor come to zero speed.
- (ii) The machine can be made to work as a generator, thereby the stored kinetic energy can be effectively transferred to the source. This saves energy and brings the machine rapidly to zero speed.

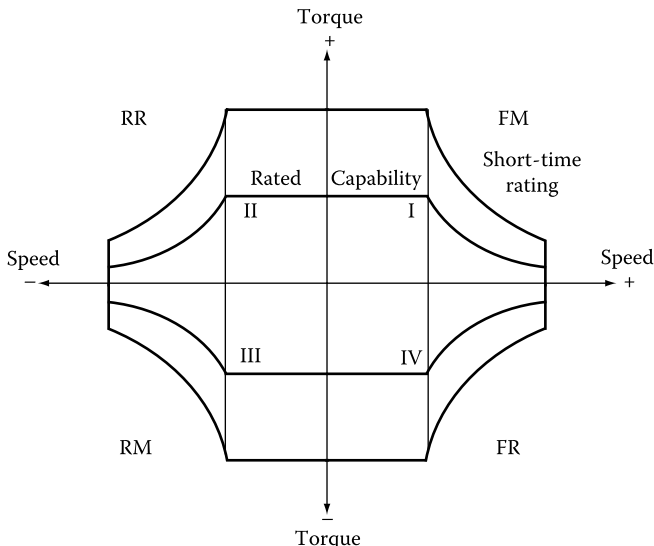


FIGURE 2.64 Four-quadrant torque–speed characteristics. (From Krishnan, R., *Electric Motor Drives*, Figure 3.4, Prentice Hall, Upper Saddle River, NJ, 2001. With permission.)

While cutting off supply produces a haphazard speed response, the second method provides a controlled braking of the machine. To make the machine operating in the motoring mode to go to the generating mode, all that needs to be done is to reverse the power flow from the machine to the power supply source. This mode of operation is termed as regenerative braking. The braking is accomplished by regeneration that implies that a negative torque is generated in the machine as opposed to the positive motoring torque. Hence, a mirror reflection of the speed–torque characteristics in I quadrant is required on the IV quadrant for regeneration, shown in Figure 2.64. The first and fourth quadrants are for one direction of rotation, say, forward motoring (FM) and forward regeneration (FR), respectively.

Some applications, such as a feed drive in machine tools, require operation in both directions of rotation. In that case, the III quadrant signifies the reverse motoring (RM) and II quadrant, the reverse regeneration (RR) mode. A motor drive capable of motoring and regeneration in both directions of rotation is referred to as a four-quadrant variable speed drive. The torque–speed characteristics of such a four-quadrant motor drive are shown in Figure 2.64. The figure contains two characteristics, one for rated operating condition and the other for short-time or intermittent operation. The short-time characteristic is used for acceleration and deceleration of the machine and it may encompass normally 50%–200% greater than the rated torque. The four-quadrant operation and its relationship to speed, torque, and power output are summarized in Table 2.8.

Figure 2.65 illustrates the speed and torque variation from a point P_1 to Q_1 and Q_1 to P_2 of the machine. On receiving the command to go from P_1 to Q_1 , the torque is changed to negative by regenerating the machine, shown by the trajectory P_1M_1 . This regeneration torque along with the load torque produces a decelerating torque. The torque is maintained at the permitted maximum levels both at field weakening

TABLE 2.8
Four-Quadrant Motor Drive Characteristics

Function	Quadrant	Speed	Torque	Power Output
Forward motoring (FM)	I	+	+	+
Forward regeneration (FR)	IV	+	-	-
Reverse motoring (RM)	III	-	-	+
Reverse regeneration (RR)	II	-	+	-

Source: Krishnan, R., *Electric Motor Drives*, Table 3.4, Prentice Hall, Upper Saddle River, NJ, 2001. With permission.

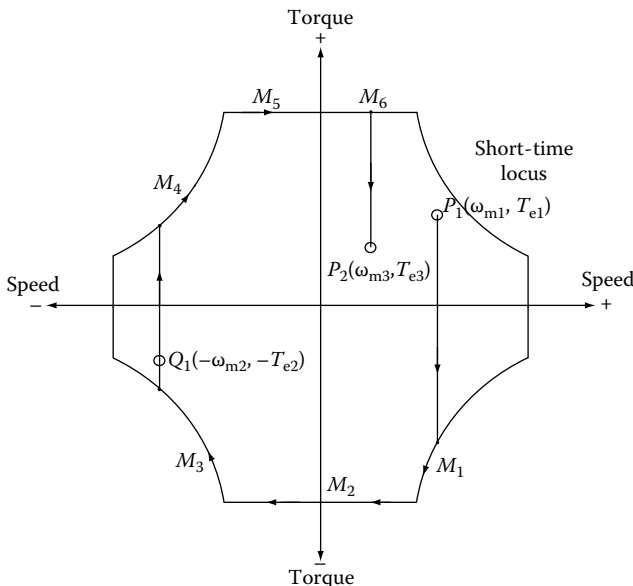


FIGURE 2.65 Changing the operating points and the use of four quadrants. (From Krishnan, R., *Electric Motor Drives*, Figure 3.5, Prentice Hall, Upper Saddle River, NJ, 2001. With permission.)

(to be explained in later chapters) and constant flux regions. As the machine decelerates, shown by the trajectory M_1M_2 , it will reach the zero speed and keeping the torque at a negative maximum will drive the motor in the reverse direction along the trajectory M_2M_3 . Once the desired speed, ω_{m2} is reached, the torque is adjusted to equal the specified value, $-T_{e2}$ along the trajectory M_3Q_1 . Similarly, to change the operating point from Q_1 to P_2 , the trajectory shown along $Q_1M_4M_5M_6P_2$ is followed.

From this illustration it is seen that the use of all quadrants of operation leads to a very responsive motor drive. Contrast this to the supply cutoff technique. In such a case, only the load torque contributes to the deceleration, which will take a longer time to stop as opposed to the combined machine and load torques in a four-quadrant motor drive leading to a faster stop.

2.13 CONVERTER REQUIREMENTS

The voltage and current requirements from the dc link side for four-quadrant operation of the PM synchronous and dc brushless machine are derived as follows. The schematic of the PMSM drive system is shown in Figure 2.66. The input voltage to the inverter, v_i , is assumed to be constant. The speed is proportional to the stator frequency and its polarity is determined by the phase sequence. Consider the FM speed is positive and the corresponding phase sequence is abc. For FM, the torque and speed are positive and the power output and input have to be positive. Therefore the average input current to the inverter, i_i , has to be positive since the input voltage is positive and the machine takes the power from the source and transfers it to the load. When the machine is regenerating in the forward direction, i.e., operating in the fourth quadrant, the speed is positive but the torque is negative. Therefore, the average input dc current to the inverter has to be negative to get the power to be negative. Similarly the quadrants III and II can be reasoned. The only change from the first and the fourth quadrant operation is that the direction of rotation is negative and hence the phase sequence is acb for the second and third quadrants of operation. From this observation, the average input dc current to the inverter and the phase sequence of the motor supply from the inverter for four-quadrant operation are summarized in Table 2.9.

The operational modes and the resultant quadrants of operation have been identified for single-phase inverter in an earlier section. Similarly, the quadrants of operation of the inverter and their modes of operation can be derived. The quadrants of operation of the inverter that directly correspond to those of the machine can be easily verified.

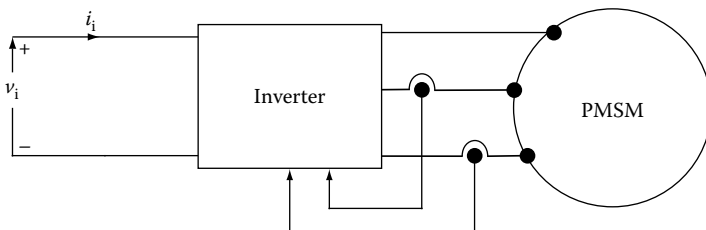


FIGURE 2.66 Schematic of the PMSM drive system.

TABLE 2.9

DC Input Current and Phase Sequence Requirements of the Inverter for Four-Quadrant Operation of the PMSM and PMBDCM Drive Systems

Operation	Speed	Torque	Phase Sequence	dc Source Current	Power Output
FM	+	+	+ (abc)	+	+
FR	+	-	+ (abc)	-	-
RM	-	-	- (acb)	+	+
RR	-	+	- (acb)	-	-

REFERENCES

Basics

1. M. Rashid, *Power Electronics: Circuits, Devices, and Applications*, 3rd ed., Prentice Hall, Upper Saddle River, NJ, 2003.
2. R. W. Erickson and D. Maksimovic, *Fundamentals of Power Electronics*, 2nd ed., Springer, New York, 2001.
3. N. Mohan, T. M. Undeland, W. P. Robbins, *Power Electronics: Converters, Applications, and Design*, 3rd edn., John Wiley & Sons, New York, 2002.
4. M. Kazmierkowski, R. Krishnan, and F. Blaabjerg, *Control in Power Electronics*, Academic Publishers, Norwell, MA, 2002.
5. R. Krishnan, *Electric Motor Drives*, Prentice Hall, Upper Saddle River, NJ, 2001.

PWM

6. S. B. Dewan and S. A. Rosenberg, Output voltage in three-phase pulsewidth-modulated inverters, *IEEE Transactions on Industry and General Applications*, IGA-6(6), 570–579, 1970.
7. S. B. Dewan and J. B. Forsythe, Harmonic analysis of a synchronized pulse-width-modulated three-phase inverter, *IEEE Transactions on Industry Applications*, IA-10(1), 117–122, 1974.
8. B. K. Bose and H. A. Sutherland, A high performance pulsewidth modulator for an inverter-fed drive system using a microcomputer, *IEEE Transactions on Industry Applications*, IA-19(2), 235–243, 1983.
9. J. Holtz, P. Lammert, and W. Lotzkat, High-speed drive system with ultrasonic MOSFET PWM inverter and single-chip microprocessor control, *IEEE Transactions on Industry Applications*, IA-23(6), 1010–1015, 1987.
10. J. W. Kolar, H. Ertl, and F. C. Zach, Minimizing the current harmonics RMS value of three-phase PWM converter systems by optimal and suboptimal transition between continuous and discontinuous modulation, *PESC '91 Record. 22nd Annual IEEE Power Electronics Specialists Conference (Cat. No. 91CH3008-0)*, pp. 372–381, 1991.
11. J. W. Kolar, H. Ertl, and F. C. Zach, Influence of the modulation method on the conduction and switching losses of a PWM converter system, *IEEE Transactions on Industry Applications*, 27(6), 1063–1075, 1991.
12. F. P. Dawson and S. B. Dewan, Transistor voltage source inverter for induction heating, *Journal of the Institution of Electronics and Telecommunication Engineers*, 37(1), 111–123, 1991.
13. S. Iida, Y. Okuma, S. Masukawa et al., Study on magnetic noise caused by harmonics in output voltages of PWM inverter, *IEEE Transactions on Industrial Electronics*, 38(3), 180–186, 1991.
14. W. G. Dunford and J. D. van Wyk, Harmonic imbalance in asynchronous PWM schemes, *IEEE Transactions on Power Electronics*, 7(3), 480–486, 1992.
15. Y. Iwaji and S. Fukuda, A pulse frequency modulated PWM inverter for induction motor drives, *IEEE Transactions on Power Electronics*, 7(2), 404–410, 1992.
16. W. G. Dunford and J. D. van Wyk, Subharmonic components in an asynchronous PWM-scheme with digital pulse modulation, *Transactions of the South African Institute of Electrical Engineers*, 84(3), 210–217, 1993.
17. A. Boglietti, G. Griva, M. Pastorelli, et al., Different PWM modulation techniques indexes performance evaluation, *ISIE'93—Budapest. IEEE International Symposium on Industrial Electronics. Conference Proceedings (Cat. No. 93TH0540-5)*, pp. 193–199, 1993.
18. R. J. Kerkman, T. M. Rowan, D. Leggate, et al., Control of PWM voltage inverters in the pulse dropping region, *IEEE Transactions on Power Electronics*, 10(5), 559–565, 1995.

19. N. A. Rahim, T. C. Green, and B. W. Williams, Simplified analysis of the three-phase PWM switching converter, *Proceedings of the 1995 IEEE IECON. 21st International Conference on Industrial Electronics, Control, and Instrumentation (Cat. No. 95CH35868)*, pp. 482–487, 1995.
20. J. Dixon, S. Tepper, and L. Moran, Practical evaluation of different modulation techniques for current-controlled voltage source inverters, *IEE Proceedings—Electric Power Applications*, 143(4), 301–306, 1996.
21. L. Yen-Shin and S. R. Bowes, A new suboptimal pulse-width modulation technique for per-phase modulation and space vector modulation, *IEEE Transactions on Energy Conversion*, 12(4), 310–316, 1997.
22. F. Blaabjerg, J. K. Pedersen, and P. Thoegersen, Improved modulation techniques for PWM-VSI drives, *IEEE Transactions on Industrial Electronics*, 44(1), 87–95, 1997.
23. K. Gi-Taek and T. A. Lipo, VSI-PWM rectifier/inverter system with a reduced switch count, *IEEE Transactions on Industry Applications*, 32(6), 1331–1337, 1996.
24. A. M. Hava, R. J. Kerkman, and T. A. Lipo, A high-performance generalized discontinuous PWM algorithm, *IEEE Transactions on Industry Applications*, 34(5), 1059–1071, 1998.
25. A. M. Hava, R. J. Kerkman, and T. A. Lipo, Carrier-based PWM-VSI overmodulation strategies: Analysis, comparison, and design, *IEEE Transactions on Power Electronics*, 13(4), 674–689, 1998.
26. S. M. Ali and M. P. Kazmierkowski, PWM voltage and current control of four-leg VSI, *IEEE International Symposium on Industrial Electronics Proceedings ISIE'98 (Cat. No. 98TH8357)*, pp. 196–201, 1998.
27. A. M. Hava, R. J. Kerkman, and T. A. Lipo, Simple analytical and graphical methods for carrier-based PWM-VSI drives, *IEEE Transactions on Power Electronics*, 14(1), 49–61, 1999.
28. C. Dae-Woong and S. Seung-Ki, Minimum-loss strategy for three-phase PWM rectifier, *IEEE Transactions on Industrial Electronics*, 46(3), 517–526, 1999.
29. Y. X. Gao and D. Sutanto, A method of reducing harmonic contents for SPWM, *Proceedings of the IEEE 1999 International Conference on Power Electronics and Drive Systems. PEDS'99 (Cat. No. 99TH8475)*, pp. 156–160, 1999.
30. A. M. Hava, S. Seung-Ki, R. J. Kerkman et al., Dynamic overmodulation characteristics of triangle intersection PWM methods, *IEEE Transactions on Industry Applications*, 35(4), 896–907, 1999.
31. D. G. Holmes and B. P. McGrath, Opportunities for harmonic cancellation with carrier-based PWM for a two-level and multilevel cascaded inverters, *IEEE Transactions on Industry Applications*, 37(2), 574–582, 2001.
32. C. B. Jacobina, A. M. Nogueira Lima, E. R. C. da Silva et al., Digital scalar pulse-width modulation: A simple approach to introduce nonsinusoidal modulating waveforms, *IEEE Transactions on Power Electronics*, 16(3), 351–359, 2001.
33. O. Ojo, The generalized discontinuous PWM scheme for three-phase voltage source inverters, *IEEE Transactions on Industrial Electronics*, 51(6), 1280–1289, 2004.
34. L. Yen-Shin and S. Fu-San, Optimal common-mode Voltage reduction PWM technique for inverter control with consideration of the dead-time effects-part I: Basic development, *IEEE Transactions on Industry Applications*, 40(6), 1605–1612, 2004.
35. S. R. Bowes and D. Holliday, Comparison of pulse-width-modulation control strategies for three-phase inverter systems, *IEE Proceedings—Electric Power Applications*, 153(4), 575–584, 2006.
36. C. Kyu Min, O. Won Seok, K. Young Tae et al., A new switching strategy for pulse width modulation (PWM) power converters, *IEEE Transactions on Industrial Electronics*, 54(1), 330–337, 2007.
37. S. R. Bowes and D. Holliday, Optimal regular-sampled PWM inverter control techniques, *IEEE Transactions on Industrial Electronics*, 54(3), 1547–1559, 2007.

38. A. Cataliotti, F. Genduso, A. Raciti et al., Generalized PWM-VSI control algorithm based on a universal duty-cycle expression: Theoretical analysis, simulation results, and experimental validations, *IEEE Transactions on Industrial Electronics*, 54(3), 1569–1580, 2007.
39. J. W. Kolar, U. Drozenik, J. Biela et al., PWM converter power density barriers, *Transactions of the Institute of Electrical Engineers of Japan, Part D*, 128D(4), 468–480, 2008.

Random PWM

40. J. K. Pedersen and F. Blaabjerg, Digital quasi-random modulated SFAVM PWM in an AC-drive system, *IEEE Transactions on Industrial Electronics*, 41(5), 518–525, 1994.
41. R. L. Kirlin, A. M. Trzynadlowski, M. M. Bech et al., Analysis of spectral effects of random PWM strategies for voltage-source inverters, *EPE'97. 7th European Conference on Power Electronics and Applications*, pp. 146–151, 1997.
42. Y. S. Lai, New random technique of inverter control for common mode voltage reduction of inverter-fed induction motor drives, *IEEE Transactions on Energy Conversion*, 14(4), 1139–1146, 1999.
43. V. Blasko, M. M. Bech, F. Blaabjerg, et al., A new hybrid random pulse width modulator for industrial drives, *APEC 2000. Fifteenth Annual IEEE Applied Power Electronics Conference and Exposition (Cat. No. 00CH37058)*, pp. 932–938, 2000.
44. M. M. Bech, F. Blaabjerg, and J. K. Pedersen, Random modulation techniques with fixed switching frequency for three-phase power converters, *IEEE Transactions on Power Electronics*, 15(4), 753–761, 2000.
45. A. M. Trzynadlowski, M. M. Bech, F. Blaabjerg et al., Optimization of switching frequencies in the limited-pool random space vector PWM strategy for inverter-fed drives, *IEEE Transactions on Power Electronics*, 16(6), 852–857, 2001.

Space Vector Modulation

46. J. T. Boys and P. G. Handley, Harmonic analysis of space vector modulated PWM waveforms, *IEE Proceedings B (Electric Power Applications)*, 137(4), 197–204, 1990.
47. J. Holtz and E. Bube, Field-oriented asynchronous pulse-width modulation for high-performance AC machine drives operating at low switching frequency, *IEEE Transactions on Industry Applications*, 27(3), 574–581, 1991.
48. A. Khambadkone and J. Holtz, Low switching frequency and high dynamic pulsedwidth modulation based on field-orientation for high-power inverter drive, *IEEE Transactions on Power Electronics*, 7(4), 627–632, 1992.
49. V. R. Stefanovic and S. N. Vukosavic, Space-vector PWM voltage control with optimized switching strategy, *Conference Record of the IEEE Industry Applications Society Annual Meeting (Cat. No. 92CH3146-8)*, pp. 1025–1033, 1992.
50. P. Enjeti and B. Xie, A new real time space vector PWM strategy for high performance converters, *Conference Record of the IEEE Industry Applications Society Annual Meeting (Cat. No. 92CH3146-8)*, pp. 1018–1024, 1992.
51. D. G. Holmes, The general relationship between regular-sampled pulse-width-modulation and space vector modulation for hard switched converters, *Conference Record of the IEEE Industry Applications Society Annual Meeting (Cat. No. 92CH3146-8)*, pp. 1002–1009, 1992.
52. J. Holtz, Pulsewidth modulation—A survey, *IEEE Transactions on Industrial Electronics*, 39(5), 410–420, 1992.
53. J. Holtz, W. Lotzkat, and A. M. Khambadkone, On continuous control of PWM inverters in the overmodulation range including the six-step mode, *IEEE Transactions on Power Electronics*, 8(4), 546–553, 1993.

54. J. Holtz and B. Beyer, Optimal synchronous pulsewidth modulation with a trajectory-tracking scheme for high-dynamic performance, *IEEE Transactions on Industry Applications*, 29(6), 1098–1105, 1993.
55. J. Holtz, Pulsewidth modulation for electronic power conversion, *Proceedings of the IEEE*, 82(8), 1194–1214, 1994.
56. J. Holtz and B. Beyer, Optimal pulsewidth modulation for AC servos and low-cost industrial drives, *IEEE Transactions on Industry Applications*, 30(4), 1039–1047, 1994.
57. V. Vlatkovic and D. Borojevic, Digital-signal-processor-based control of three-phase space vector modulated converters, *IEEE Transactions on Industrial Electronics*, 41(3), 326–332, 1994.
58. S. N. Vukosavic and M. R. Stojic, Reduction of parasitic spectral components of digital space vector modulation by real-time numerical methods, *IEEE Transactions on Power Electronics*, 10(1), 94–102, 1995.
59. J. Holtz and B. Beyer, Fast current trajectory tracking control based on synchronous optimal pulsewidth modulation, *IEEE Transactions on Industry Applications*, 31(5), 1110–1120, 1995.
60. S. Jul-Ki and S. Seung-Ki, A new overmodulation strategy for induction motor drive using space vector PWM, *APEC '95. Tenth Annual Applied Power Electronics Conference and Exposition. Conference Proceedings 1995. (Cat. No. 95CH35748)*, pp. 211–216, 1995.
61. R. Akkaya, G. Yildirmaz, and R. Gulgun, A space vector modulation technique with minimum switching loss for VSI PWM inverters, *PEMC '96. 7th International Power Electronics and Motion Control Conference, Exhibition, Tutorials. Proceedings*, pp. 352–355, 1996.
62. K. Yamamoto and K. Shinohara, Comparison between space vector modulation and subharmonic methods for current harmonics of DSP-based permanent-magnet AC servo motor drive system, *IEE Proceedings—Electric Power Applications*, 143(2), 151–156, 1996.
63. D. G. Holmes, The significance of zero space vector placement for carrier-based PWM schemes, *IEEE Transactions on Industry Applications*, 32(5), 1122–1129, 1996.
64. S. R. Bowes and L. Yen-Shin, The relationship between space-vector modulation and regular-sampled PWM, *IEEE Transactions on Industrial Electronics*, 44(5), 670–679, 1997.
65. A. Haras, Space vector modulation in orthogonal and natural frames including the overmodulation range, *EPE'97. 7th European Conference on Power Electronics and Applications*, pp. 337–342, 1997.
66. R. H. Ahmad, G. G. Karady, T. D. Blake, et al., Comparison of space vector modulation techniques based on performance indexes and hardware implementation, *Proceedings of the IECON'97 23rd International Conference on Industrial Electronics, Control, and Instrumentation (Cat. No. 97CH36066)*, pp. 682–687, 1997.
67. F. Blaabjerg, S. Freysson, H. H. Hansen et al., A new optimized space-vector modulation strategy for a component-minimized voltage source inverter, *IEEE Transactions on Power Electronics*, 12(4), 704–714, 1997.
68. A. M. Trzynadlowski, R. L. Kirlin, and S. F. Legowski, Space vector PWM technique with minimum switching losses and a variable pulse rate [for VSI], *IEEE Transactions on Industrial Electronics*, 44(2), 173–181, 1997.
69. J. F. Moynihan, M. G. Egan, and J. M. D. Murphy, Theoretical spectra of space-vector-modulated waveforms, *IEE Proceedings—Electric Power Applications*, 145(1), 17–24, 1998.
70. A. M. Trzynadlowski, M. M. Bech, F. Blaabjerg et al., An integral space-vector PWM technique for DSP-controlled voltage-source inverters, *IEEE Transactions on Industry Applications*, 35(5), 1091–1097, 1999.

71. S. R. Bowes and S. Grewal, Novel harmonic elimination PWM control strategies for three-phase PWM inverters using space vector techniques, *IEE Proceedings—Electric Power Applications*, 146(5), 495–514, 1999.
72. L. Hyeoun-Dong, L. Young-Min, and S. Seung-ki, Elimination of a common mode voltage pulse in converter/inverter system modifying space-vector PWM method, *Transactions of the Korean Institute of Electrical Engineers, B*, 48(2), 89–96, 1999.
73. G. Narayanan and V. T. Ranganathan, Synchronised PWM strategies based on space vector approach. I. Principles of waveform generation, *IEE Proceedings—Electric Power Applications*, 146(3), 267–275, 1999.
74. G. Narayanan and V. T. Ranganathan, Synchronised PWM strategies based on space vector approach. II. Performance assessment and application to V/f drives, *IEE Proceedings—Electric Power Applications*, 146(3), 276–281, 1999.
75. G. M. Lee and L. Dong-Choon, Implementation of naturally sampled space vector modulation eliminating microprocessors, *Proceedings IPEMC 2000. Third International Power Electronics and Motion Control Conference (IEEE Cat. No. 00EX435)*, pp. 803–807, 2000.
76. G. Narayanan and V. T. Ranganathan, Overmodulation algorithm for space vector modulated inverters and its application to low switching frequency PWM techniques, *IEE Proceedings—Electric Power Applications*, 148(6), 521–536, 2001.
77. G. Narayanan and V. T. Ranganathan, Extension of operation of space vector PWM strategies with low switching frequencies using different overmodulation algorithms, *IEEE Transactions on Power Electronics*, 17(5), 788–798, 2002.
78. G. Narayanan and V. T. Ranganathan, Two novel synchronized bus-clamping PWM strategies based on space vector approach for high power drives, *IEEE Transactions on Power Electronics*, 17(1), 84–93, 2002.
79. C. Attaianese, D. Capraro, and G. Tomasso, High efficiency SVM technique for VSI, *7th International Workshop on Advanced Motion Control. Proceedings (Cat. No. 02TH8623)*, pp. 269–274, 2002.
80. A. Cataliotti, F. Genduso, and G. R. Galluzzo, A new over modulation strategy for high-switching frequency space vector PWM voltage source inverters, *ISIE 2002. Proceedings of the 2002 IEEE International Symposium on Industrial Electronics (Cat. No. 02TH8608C)*, pp. 778–783, 2002.
81. J. Klima, Analytical closed-form solution of a space-vector modulated VSI feeding an induction motor drive, *IEEE Transactions on Energy Conversion*, 17(2), 191–196, 2002.
82. H. Pinheiro, F. Botteron, C. Rech et al., Space vector modulation for voltage-source inverters: a unified approach, *IECON - 2002. 2002 28th Annual Conference of the IEEE Industrial Electronics Society (Cat. No. 02CH37363)*, pp. 23–29, 2002.
83. H. Krishnamurthy, G. Narayanan, R. Ayyanar et al., Design of space vector-based hybrid PWM techniques for reduced current ripple, *APEC 2003. Eighteenth Annual IEEE Applied Power Electronics Conference and Exposition (Cat. No. 03CH37434)*, pp. 583–588, 2003.
84. H. Bai, Z. Zhao, S. Meng, et al., Comparison of three PWM strategies-SPWM, SVPWM & one-cycle control, *Fifth International Conference on Power Electronics and Drive Systems (IEEE Cat. No. 03TH8688)*, pp. 1313–1316, 2003.
85. R. P. Burgos, G. Chen, F. Wang et al., Minimum-loss minimum-distortion space vector sequence generator for high-reliability three-phase power converters for aircraft applications, *Conference Proceed the 4th International Power Electronics and Motion Control Conference (IEEE Cat. No. 04EX677)*, pp. 1356–1361, 2004.
86. M. Jasinski, M. P. Kazmierkowski, and M. Zelechowski, Unified scheme of direct power and torque control for space vector modulated AC/DC/AC converter-fed induction motor, *EPE-PEMC 2004 11th International Power Electronics and Motion Control Conference*, pp. 1–32, 2004.

87. B. Hariram and N. S. Marimuthu, Space vector switching patterns for different applications—A comparative analysis, *2005 IEEE International Conference on Industrial Technology (IEEE Cat. No. 05TH8844C)*, pp. 1444–1449, 2005.
88. S. Zeliang, T. Jian, G. Yuhua et al., An efficient SVPWM algorithm with low computational overhead for three-phase inverters, *IEEE Transactions on Power Electronics*, 22(5), 1797–1805, 2007.
89. L. Dalessandro, S. D. Round, U. Drottenik, et al., Discontinuous space-vector modulation for three-level PWM rectifiers, *IEEE Transactions on Power Electronics*, 23(2), 530–542, 2008.
90. D. Paire, M. Cirrincione, M. Pucci et al., Current harmonic compensation by three-phase converters controlled by space vector modulation, *IECON 2008—34th Annual Conference of IEEE Industrial Electronics Society*, pp. 2307–2313, 2008.
91. Y. Wenxi, H. Haibing, and L. Zhengyu, Comparisons of space-vector modulation and carrier-based modulation of multilevel inverter, *IEEE Transactions on Power Electronics*, 23(1), 45–51, 2008.

Hybrid PWM—Space Vector Modulation

92. S. Jian and H. Grotstollen, Optimized space vector modulation and regular-sampled PWM: a reexamination, *IAS'96. Conference Record of the 1996 IEEE Industry Applications Conference, Thirty-First IAS Annual Meeting (Cat. No. 96CH25977)*, pp. 956–963, 1996.
93. V. Blasko, Analysis of a hybrid PWM based on modified space-vector and triangle-comparison methods, *IEEE Transactions on Industry Applications*, 33(3), 756–764, 1997.
94. C. Dae-Woong, K. Joohn-Sheok, and S. Seung-Ki, Unified voltage modulation technique for real-time three-phase power conversion, *IEEE Transactions on Industry Applications*, 34(2), 374–380, 1998.
95. G. Narayanan, V. T. Ranganathan, D. Zhao et al., Space vector based hybrid PWM techniques for reduced current ripple, *IEEE Transactions on Industrial Electronics*, 55(4), 1614–1627, 2008.

Power Factor Correction

96. J. W. Kolar, H. Ertl, K. Edelmoser et al., Analysis of the control behaviour of a bidirectional three-phase PWM rectifier system, *EPE '91. 4th European Conference on Power Electronics and Applications*, pp. 95–100, 1991.
97. J. Holtz and L. Springob, Reduced harmonics PWM controlled line-side converter for electric drives, *IEEE Transactions on Industry Applications*, 29(4), 814–819, 1993.
98. M. Hengchun, C. Y. Lee, D. Boroyevich et al., Review of high-performance three-phase power-factor correction circuits, *IEEE Transactions on Industrial Electronics*, 44(4), 437–446, 1997.
99. M. Malinowski, M. P. Kazmierkowski, S. Hansen et al., Virtual-flux-based direct power control of three-phase PWM rectifiers, *IEEE Transactions on Industry Applications*, 37(4), 1019–1027, 2001.
100. V. Blasko and I. Agirman, Modeling and control of three-phase regenerative AC–DC converters, *Proceedings of the 40th IEEE Conference on Decision and Control (Cat. No. 01CH37228)*, pp. 2235–2240, 2001.
101. A. V. Stankovic and T. A. Lipo, A novel control method for input output harmonic elimination of the PWM boost type rectifier under unbalanced operating conditions, *IEEE Transactions on Power Electronics*, 16(5), 603–611, 2001.

102. M. Malinowski, M. P. Kazmierkowski, and A. M. Trzynadlowski, A comparative study of control techniques for PWM rectifiers in AC adjustable speed drives, *IEEE Transactions on Power Electronics*, 18(6), 1390–1396, 2003.
103. M. Cichowlas, M. Malinowski, M. P. Kazmierkowski et al., Active filtering function of three-phase PWM boost rectifier under different line voltage conditions, *IEEE Transactions on Industrial Electronics*, 52(2), 410–419, 2005.

Dead Time and Its Compensation

104. R. C. Dodson, P. D. Evans, H. T. Yazdi et al., Compensating for dead time degradation of PWM inverter waveforms, *IEE Proceedings B (Electric Power Applications)*, 137(2), 73–81, 1990.
105. T. Sukegawa, K. Kamiyama, K. Mizuno et al., Fully digital, vector-controlled PWM VSI-fed AC drives with an inverter dead-time compensation strategy, *IEEE Transactions on Industry Applications*, 27(3), 552–559, 1991.
106. J. Seung-Gi and P. Min-Ho, The analysis and compensation of dead-time effects in PWM inverters, *IEEE Transactions on Industrial Electronics*, 38(2), 108–114, 1991.
107. C. Jong-Woo and S. Seung-Ki, A new compensation strategy reducing voltage/current distortion in PWM VSI systems operating with low output voltages, *IEEE Transactions on Industry Applications*, 31(5), 1001–1008, 1995.
108. C. Jong-Woo and S. Seung-Ki, Inverter output voltage synthesis using novel dead time compensation, *IEEE Transactions on Power Electronics*, 11(2), 221–227, 1996.
109. D. Leggate and R. J. Kerkman, Pulse-based dead-time compensator for PWM voltage inverters, *IEEE Transactions on Industrial Electronics*, 44(2), 191–197, 1997.
110. T. Baumann, Identification and compensation of the dead time behaviour of an inverter, *EPE'97. 7th European Conference on Power Electronics and Applications*, pp. 228–232, 1997.
111. A. Munoz-Garcia and T. A. Lipo, On-line dead time compensation technique for open-loop PWM-VSI drives, *APEC '98. Thirteenth Annual Applied Power Electronics Conference and Exposition (Cat. No. 98CH36154)*, pp. 95–100, 1998.
112. L. Ben-Brahim, The analysis and compensation of dead-time effects in three phase PWM inverters, *IECON '98. Proceedings of the 24th Annual Conference of the IEEE Industrial Electronics Society (Cat. No. 98CH36200)*, pp. 792–797, 1998.
113. S. H. Kim, T. S. Park, J. Y. Yoo et al., Dead time compensation in a vector-controlled induction machine, *PESC 98 Record. 29th Annual IEEE Power Electronics Specialists Conference (Cat. No. 98CH36196)*, pp. 1011–16, 1998.
114. A. R. Munoz and T. A. Lipo, On-line dead-time compensation technique for open-loop PWM-VSI drives, *IEEE Transactions on Power Electronics*, 14(4), 683–689, 1999.
115. C. M. Wu, L. Wing-Hong, and H. Shu-Hung Chung, Analytical technique for calculating the output harmonics of an H-bridge inverter with dead time, *IEEE Transactions on Circuits and Systems I: Fundamental Theory and Applications*, 46(5), 617–627, 1999.
116. K. Hyun-Soo, M. Hyung-Tae, and Y. Myung-Joong, On-line dead-time compensation method using disturbance observer, *IEEE Transactions on Power Electronics*, 18(6), 1336–1345, 2003.
117. W. Zhigan and Y. Jianping, A novel dead time compensation method for PWM inverter, *Fifth International Conference on Power Electronics and Drive Systems (IEEE Cat. No. 03TH8688)*, pp. 1258–1263, 2003.
118. S. Bolognani, M. Ceschia, P. Mattavelli et al., Improved FPGA-based dead time compensation for SVM inverters, *Second IEE International Conference on Power Electronics, Machines and Drives (Conference Publication No. 498)*, pp. 662–667, 2004.

119. L. Ben-Brahim, On the compensation of dead time and zero-current crossing for a PWM-inverter-controlled AC servo drive, *IEEE Transactions on Industrial Electronics*, 51(5), 1113–1118, 2004.
120. C. Attaianese, V. Nardi, and G. Tomasso, A novel SVM strategy for VSI dead-time-effect reduction, *IEEE Transactions on Industry Applications*, 41(6), 1667–1674, 2005.
121. A. Cichowski and J. Nieznanski, Self-tuning dead-time compensation method for voltage-source inverters, *IEEE Power Electronics Letters*, 3(2), 72–75, 2005.
122. K. Liu, J. Zhang, and H. Zhang, Dead time compensation for general-purpose inverters, *Proceedings of the Eighth International Conference on Electrical Machines and Systems (IEEE Cat. No. 05EX1137)*, pp. 1482–5, 2005.
123. N. Urasaki, T. Senju, T. Kinjo et al., Dead-time compensation strategy for permanent magnet synchronous motor drive taking zero-current clamp and parasitic capacitance effects into account, *IEE Proceedings—Electric Power Applications*, 152(4), 845–853, 2005.
124. C. Chan-Hee, C. Kyung-Rae, and S. Jul-Ki, Inverter nonlinearity compensation in the presence of current measurement errors and switching device parameter uncertainties, *IEEE Transactions on Power Electronics*, 22(2), 576–583, 2007.
125. Q.-J. Wang, H.-A. Wu, W.-D. Jiang et al., Realization of a symmetrical SVM pattern with dead time compensation for three-level inverter, *Power Electronics*, 41(10), 84–86, 2007.
126. N. Urasaki, T. Senju, K. Uezato et al., Adaptive dead-time compensation strategy for permanent magnet synchronous motor drive, *IEEE Transactions on Energy Conversion*, 22(2), 271–280, 2007.
127. J. Sabate, L. J. Garce, P. M. Szczesny et al., Dead-time compensation for a high-fidelity voltage fed inverter, *IEEE Power Electronics Specialists Conference*, pp. 4419–4425, 2008.

Part II

Permanent Magnet Synchronous Machines and Their Control

3 Dynamic Modeling of Permanent Magnet Synchronous Machines

Variable speed drives are converter-fed and are therefore from finite sources due to the limitations of the switch ratings and filter sizes, unlike infinite utility sources. This results in their inability to supply large transient power. Hence, the need to evaluate the dynamics of converter-fed variable speed drives to assess the adequacy of the converter switch ratings and the converters for a given machine and their interaction to determine the excursions of currents in the converter and machine. The dynamic model could be put to use in the design to evaluate the instantaneous effects of varying voltages/currents, stator frequencies and torque disturbance on the machine and drive systems.

The dynamic model of the permanent magnet synchronous machine (PMSM) is derived using a two-phase motor in direct and quadrature (hereafter referred to as dq) axes. This approach is desirable because of the conceptual simplicity obtained with only one set of two windings on the stator. The rotor has no windings, only magnets. The magnets are modeled as a current source or a flux linkage source, concentrating all its flux linkages along only one axis. The flux linkages of the stator q and d windings are derived from first principles. The physical modeling of the machine is developed from which the circuit model is derived. The inherent connection between the field and the circuit model is shown in the present approach. The derived model in the stator frames is unsuitable for use in the analysis as the winding inductances are dependent on the rotor position. Constant inductance for windings is obtained by a transformation to the rotor by replacing the stator windings with a fictitious set of dq windings rotating at the electrical speed of the rotor. The equivalence between the three-phase machine and its model using a set of two-phase windings is derived from a simple observation and graphical projections, and this approach is suitable for extending it to model an n phase machine where n is greater than 2, with a two-phase machine. The concept of power invariance is introduced whereby the power in the three-phase machine and its equivalent two-phase model must be equal. The transformation from the two-phase to the three-phase variables of voltages, currents, or flux linkages is derived in a generalized way. Derivations for electromagnetic torque involving the currents and flux linkages are given. The differential equations describing the PMSM are nonlinear. To exploit the immense treasures of the linear control theory for stability and controller design studies, it is important to linearize by perturbing the machine equations around a steady-state operating point. The resulting equations are known as small-signal equations. The model that flows from this procedure

is the small-signal model of the PMSM, and this model is derived in this chapter. Algorithms and flowcharts are given to compute the eigenvalues, transfer functions, and frequency responses of the PMSM. For the sake of completeness, a space phasor model is derived from the dynamic model in direct and quadrature axes. The space phasor model is compact only in a nonsalient or cylindrical rotor machine and therefore it is not usually employed in interior permanent magnet (PM) machines, which have rotor saliency. Because the space phasor model powerfully evokes a similarity and equivalence between the PMSM and dc machines from modeling and control points of view, it is included here. This leads to a control of the PMSM drive that is equivalent to the control of dc machines; a concept known as vector control. The various stages of the dynamic modeling of the three-phase PMSM are shown in Figure 3.1. Examples are included in this chapter to illustrate the fundamental concepts.

A limited set of references for PMSM dynamic models [1–8], circuit parameters and equivalent circuits [9–13], loss modeling [14–15], and finite element-based models [16–17] is given at the end of this chapter.

3.1 REAL-TIME MODEL OF A TWO-PHASE PMSM

The following assumptions are made to derive the dynamic model:

1. The stator windings are balanced with sinusoidally distributed magnetomotive force (mmf).
2. The inductance versus rotor position is sinusoidal.
3. The saturation and parameter changes are neglected.

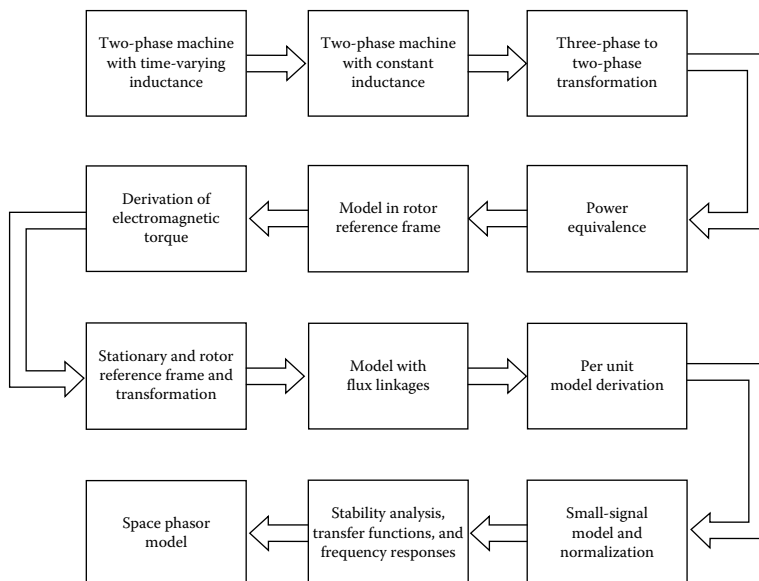


FIGURE 3.1 Procedural steps in the dynamic modeling and study of the three-phase PMSM.

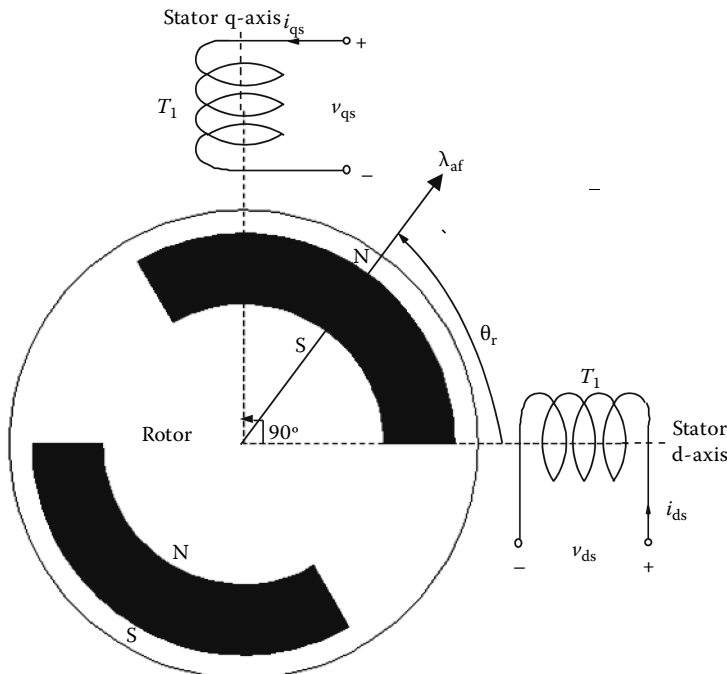


FIGURE 3.2 Two-phase PMSM.

A two-phase PMSM stator with windings and rotor with PMs is shown in Figure 3.2. The windings are displaced in space by 90 electrical degrees and the rotor winding is at an angle θ_r from the stator d-axis winding. It is assumed that the q-axis leads the d-axis to a counterclockwise direction of rotation of the rotor. The currents and voltages of the stator and rotor windings are marked in Figure 3.2. A pair of poles is assumed for this figure, but it is applicable with slight modification for any number of pairs of poles. Note that θ_r is the electrical rotor position at any instant obtained by multiplying the mechanical rotor position by pairs of electrical poles.

The d- and q-axes stator voltages are derived as the sum of the resistive voltage drops and the derivative of the flux linkages in the respective windings as

$$v_{qs} = R_q i_{qs} + p\lambda_{qs} \quad (3.1)$$

$$v_{ds} = R_d i_{ds} + p\lambda_{ds} \quad (3.2)$$

where

p is the differential operator, d/dt

v_{qs} and v_{ds} are the voltages in the q- and d-axes windings

i_{qs} and i_{ds} are the q- and d-axes stator currents

R_q and R_d are the stator q- and d-axes resistances

λ_{qs} and λ_{ds} are the stator q- and d-axes stator flux linkages

The stator winding flux linkages can be written as the sum of the flux linkages due to their own excitation and mutual flux linkages resulting from other winding current and magnet sources. Note that the rotor flux linkages have a component along the quadrature and direct axes as the rotor flux linkages are assumed to be concentrated along the axis on the instantaneous rotor position. Then the q and d stator flux linkages are written as

$$\lambda_{qs} = L_{qq}i_{qs} + L_{qd}i_{ds} + \lambda_{af} \sin \theta_r \quad (3.3)$$

$$\lambda_{ds} = L_{dq}i_{qs} + L_{dd}i_{ds} + \lambda_{af} \cos \theta_r \quad (3.4)$$

where θ_r is the instantaneous rotor position. The windings are balanced and therefore their resistances are equal and denoted as $R_s = R_q = R_d$. The d and q stator voltages can then be written in terms of the flux linkages and resistive voltage drops as

$$v_{qs} = R_s i_{qs} + i_{qs} p L_{qq} + L_{qq} p i_{qs} + L_{qd} p i_{ds} + i_{ds} p L_{qd} + \lambda_{af} p \sin \theta_r \quad (3.5)$$

$$v_{ds} = R_s i_{ds} + i_{qs} p L_{qd} + L_{qd} p i_{qs} + L_{dd} p i_{ds} + i_{ds} p L_{dd} + \lambda_{af} p \cos \theta_r \quad (3.6)$$

The various inductances are explained as follows. L_{qq} and L_{dd} are the self-inductances of the q- and d-axes windings, respectively. The mutual inductances between any two windings are denoted by L with two subscripts where the first subscript denotes the winding at which the emf is measured due to the current in the other winding indicated by the second subscript. For example, L_{qd} is the mutual inductance between the q- and d-axes windings measured on the q-axis winding with a current in the d-axis winding. The symmetry of the q- and d-axes windings ensures that L_{qd} and L_{dq} are equal.

The inductances are functions of the rotor position and they are derived as follows for the PMSM. Consider the case of the d-axis inductance when the rotor position is at zero. At that position, the magnets are aligned with the d-axis stator winding. The length of the flux path in air is increased by the magnets' thickness in this position. The relative permeability of the magnets is almost equal to the relative permeability of air, and therefore the reluctance of the flux in this path is increased and hence the winding inductance is decreased. The reluctance of the iron path is ignored for the conceptualization of this reluctance. This position corresponds to the minimum inductance position and is denoted as L_d . As the rotor is moved in the counterclockwise direction, the reluctance decreases, and hence the inductance increases until the rotor position reaches 90 electrical degrees. At that position, the d-axis flux path does not encounter the magnets at all but encounters the iron in the rotor and air gaps on both sides. Therefore, at this position, named the quadrature position, the inductance of the d-axis winding is maximum. The inductance at this position is denoted as L_q . Because the windings are distributed to provide the sinusoidal mmf, the self-inductances can be modeled as sinusoidal functions of twice the rotor position from the d-axis to correspond with the physical reality described above. Hence the self-inductances of the q- and d-axes windings are written in terms of the maximum winding inductances at the q and d positions and the rotor position as

$$L_{qq} = \frac{1}{2} [(L_q + L_d) + (L_q - L_d) \cos(2\theta_r)] \quad (3.7)$$

$$L_{dd} = \frac{1}{2} [(L_q + L_d) - (L_q - L_d) \cos(2\theta_r)] \quad (3.8)$$

This representation gives, for instance, L_{dd} at $\theta_r = 0$ as L_d and $\theta_r = 90^\circ$ as L_q , as reasoned in the discussion. They then are compactly represented as

$$L_{qq} = L_1 + L_2 \cos(2\theta_r) \quad (3.9)$$

$$L_{dd} = L_1 - L_2 \cos(2\theta_r) \quad (3.10)$$

where L_1 and L_2 are given as

$$L_1 = \frac{1}{2} (L_q + L_d) \quad (3.11)$$

$$L_2 = \frac{1}{2} (L_q - L_d) \quad (3.12)$$

The mutual inductance between the q- and d-axes windings is zero if the rotor is cylindrical and smooth, as the flux set up by a current in one winding will not link with the other winding displaced in space by 90° . In a PM machine that has magnets placed inside the rotor, there is saliency and because of that a part of the d-axis winding flux will link with the q-axis winding as the uneven reluctance provides a path for flux through the q-axis winding. When the rotor position is zero and as well as 90° , the mutual coupling is zero but is maximum when rotor position is -45° . From the figure, it is inferred that at this position, the d-axis positively couples most of its flux to the q-axis winding. Therefore, assuming a sinusoidal variation, the mutual inductance between q- and d-axes windings is given by

$$L_{qd} = \frac{1}{2} (L_d - L_q) \sin(2\theta_r) = -L_2 \sin(2\theta_r) \quad (3.13)$$

Note that in a wound rotor salient pole structure, the air gap is minimum in the winding axis, resulting in $L_d > L_q$. In PMSM, $L_q > L_d$ always, even with surface mount magnet rotor structures. The q-axis inductance is greater than the d-axis inductance as in practical machines the rotor magnets always have an arc less than 180 electrical degrees with the interpolar space of iron that provides a low reluctance path for flux. The variations in the q- to d-axis inductance are normally small in surface mounted magnet motors and are in the order of 5%–15%, whereas in the interior PMSMs, they can be as much as 200% and higher.

Substituting the self- and mutual inductances in terms of the rotor position into the stator voltage equations will result in a large number of terms that are rotor position dependent. The final machine equations then are

$$\begin{bmatrix} v_{qs} \\ v_{ds} \end{bmatrix} = R_s \begin{bmatrix} i_{qs} \\ i_{ds} \end{bmatrix} + \begin{bmatrix} L_1 + L_2 \cos 2\theta_r & -L_2 \sin 2\theta_r \\ -L_2 \sin 2\theta_r & L_1 - L_2 \cos 2\theta_r \end{bmatrix} \frac{d}{dt} \begin{bmatrix} i_{qs} \\ i_{ds} \end{bmatrix} + 2\omega_r L_2 \begin{bmatrix} -\sin 2\theta_r & -\cos 2\theta_r \\ -\cos 2\theta_r & \sin 2\theta_r \end{bmatrix} \begin{bmatrix} i_{qs} \\ i_{ds} \end{bmatrix} + \lambda_{af} \omega_r \begin{bmatrix} \cos \theta_r \\ -\sin \theta_r \end{bmatrix} \quad (3.14)$$

Note that the third term exists because of saliency, i.e., when $L_q \neq L_d$. In surface mount magnet machines, the inductances are equal and, therefore, L_2 is zero and the third term in the above equation vanishes. Also disappearing in the matrix's second term are the position-dependent terms, resulting in a simple expression for surface mounted magnet machines in stator reference frames. It is then given by

$$\begin{bmatrix} v_{qs} \\ v_{ds} \end{bmatrix} = R_s \begin{bmatrix} i_{qs} \\ i_{ds} \end{bmatrix} + \begin{bmatrix} L_1 & 0 \\ 0 & L_1 \end{bmatrix} \frac{d}{dt} \begin{bmatrix} i_{qs} \\ i_{ds} \end{bmatrix} + \lambda_{af} \omega_r \begin{bmatrix} \cos \theta_r \\ -\sin \theta_r \end{bmatrix} \quad (3.15)$$

Note that in the salient pole PMSMs, the inductances are rotor position dependent. Then the solution of such equation becomes cumbersome in spite of the greater availability of the computational power and moreover, the equations in their present form do not provide insight into machine dynamics. If the rotor position dependency is eliminated by transformation, then the equations may become manageable to obtain fundamental results such as equivalent circuit, block diagram, transfer functions, and, most of all, the steady-state equations and a phasor diagram. They are crucial to the understanding of the machine and its performance both in its steady state and dynamic operation. The next step is to obtain by a transformation the stator voltage equations without the rotor position-dependent terms. Before this is addressed, one relevant point of importance from the derived models is addressed in the following.

From Equations 3.3 and 3.4, the flux linkages are written compactly as

$$\begin{bmatrix} \lambda_{qs} \\ \lambda_{ds} \end{bmatrix} = \begin{bmatrix} L_{qq} & L_{qd} \\ L_{dq} & L_{dd} \end{bmatrix} \begin{bmatrix} i_{qs} \\ i_{ds} \end{bmatrix} + \lambda_{af} \begin{bmatrix} \sin \theta_r \\ \cos \theta_r \end{bmatrix} \quad (3.16)$$

Stator currents usually consist of a fundamental and higher harmonic components that are either intended (in the case of signal injections for diagnostic purposes) or unintended (in the case of pulse width modulation). A distinction has to be made, then about the relevancy of this equation for various components of the currents. The above equation is relevant for fundamental components as the flux linkages due to the rotor magnets are at a fundamental frequency. When considering the harmonics, either the switching or injected kinds identified with an additional subscript i to the variables, note that there is no harmonic component due to the rotor magnets and hence that term will not be there and what is then left is given in the following:

$$\begin{bmatrix} \lambda_{qsi} \\ \lambda_{dsi} \end{bmatrix} = \begin{bmatrix} L_{qq} & L_{qd} \\ L_{dq} & L_{dd} \end{bmatrix} \begin{bmatrix} i_{qsi} \\ i_{dsi} \end{bmatrix} = \begin{bmatrix} L_1 + L_2 \cos 2\theta_r & -L_2 \sin 2\theta_r \\ -L_2 \sin 2\theta_r & L_1 - L_2 \cos 2\theta_r \end{bmatrix} \begin{bmatrix} i_{qsi} \\ i_{dsi} \end{bmatrix} \quad (3.17)$$

This derivation is based on the assumption that the machine is operating in the linear region. If the machine is under a saturated operating condition, which is in the nonlinear domain, the fundamental and harmonic flux linkages cannot be separated for respective excitations because the principle of superposition is no longer valid. Therefore, in order to exploit these expressions for injected flux linkages due to injected currents, the machine operation is limited to the linear domain of operation. That is not a problem as the PMSMs have a lower saturation up to the rated current levels, and if any saturation creeps in, it is in small measure because of the large air gap and the magnet's equivalent air-like gap. Note that the relationship between the flux linkages and currents is uniquely determined by the matrix containing the rotor position terms. From this relationship, given the injected currents, the rotor position can be evaluated if the flux linkages are known. The emphasis on this aspect of operating with injected signals and on the corresponding flux linkages equations to extract rotor position from inductance measurements either directly or indirectly have gained importance in recent times. Such an approach makes the motor drive system independent of rotor position sensors that are expensive, less reliable, require space for mounting, and labor, and are a source of failure for entire system operations. These equations will be recalled frequently in Chapter 8 which is on the sensorless operation of the PMSM drive systems.

3.2 TRANSFORMATION TO ROTOR REFERENCE FRAMES

Reference frames are very much like observer platforms in that each platform gives a unique view of the system at hand as well as a dramatic simplification of the system equations. For example, consider for the purposes of control, that it is desirable to have the system variables as dc quantities although the actual variables are sinusoidal. This could be accomplished by having a reference frame revolving at the same angular speed as that of the sinusoidal variable. As the reference frames are moving at an angular speed equal to the angular frequency of the sinusoidal supply, the differential speed between them is reduced to zero, resulting in the sinusoid being perceived as a dc signal from the reference frames. Then, moving to that plane, it becomes easier to develop a small-signal equation out of a nonlinear equation as the quiescent or operating point is described only by dc values which then leads to the linearized system around an operating point. For now, it is easier to synthesize a compensator for the system using standard linear control system techniques. Note that the independent rotor field position determines the induced emf and affects the dynamic system equations of both the wound rotor and the PMSMs. Therefore, looking at the entire system from the rotor, i.e., rotating reference frames, the system inductance matrix becomes independent of the rotor position, thus leading to the simplification and compactness of the system equations. Such advantages are many when using the reference frames.

Reference frames rotating at the speed of the rotor are hereafter referred to as rotor reference frames. The relationship between the stationary reference frames denoted by d- and q-axes and the rotor reference frames denoted by d^r- and q^r-axes

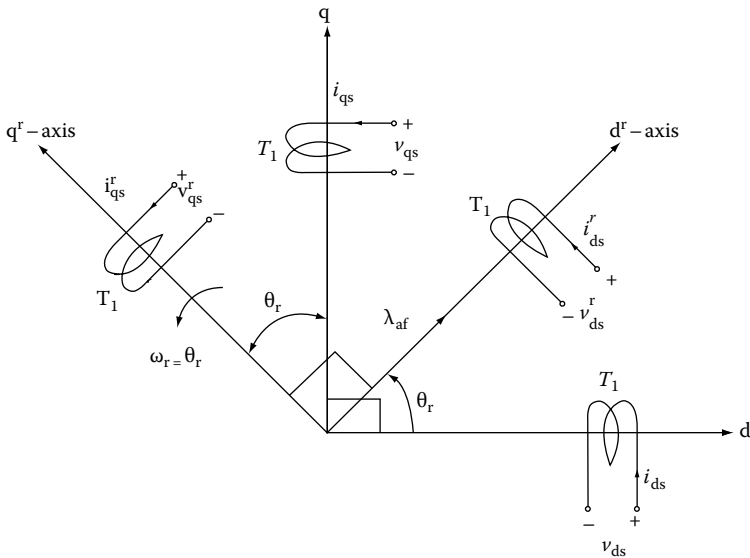


FIGURE 3.3 Stationary and rotor reference frames.

are shown in Figure 3.3. From now on, the three-phase machine is assumed to have balanced windings and balanced inputs.

The transformation to obtain constant inductances is achieved by replacing the actual stator and its windings with a fictitious stator having windings on the q^r - and d^r -axes as shown in Figure 3.3. In that process, the fictitious stator will have the same number of turns for each phase as the actual stator phase windings and should produce the equivalent mmf. The actual stator mmf in any axis (say q or d) is the product of the number of turns and current in the respective axis winding. It is equated, respectively, to the mmf produced by the fictitious stator windings on the q - and d -axes. For example, the actual q -axis mmf is equated to the mmf contributed by the fictitious q - and d -axes mmfs along the actual q -axis. It is found that, by the projection of these fictitious q - and d -axes mmfs onto the q -axis of the actual stator winding one gets the q -axis mmf of the actual stator winding. Similarly, the same procedure is repeated for the d -axis of the actual stator winding. This leads to a cancellation of the number of turns on both sides of the q - and d -axes stator mmf equations, resulting in a relationship between the actual and fictitious stator currents. The relationship between the currents in the stationary reference frames, i.e., the actual winding currents and the rotor reference frames currents, i.e., the fictitious currents is written as

$$i_{qds} = [T^r] i_{qds}^r \quad (3.18)$$

where

$$i_{qds} = [i_{qs} \quad i_{ds}]^t \quad (3.19)$$

$$i_{qds}^r = [i_{qs}^r \quad i_{ds}^r]^t \quad (3.20)$$

and

$$T^r = \begin{bmatrix} \cos \theta_r & \sin \theta_r \\ -\sin \theta_r & \cos \theta_r \end{bmatrix} \quad (3.21)$$

The speed of the rotor reference frames is

$$\dot{\theta}_r = \omega_r \quad (3.22)$$

where $\dot{\theta}_r$ is the time derivative of the electrical rotor position in rad/s.

Likewise, the relationship between the stationary and rotor reference frames' voltages is derived as

$$v_{qds} = [T^r] v_{qds}^r \quad (3.23)$$

where

$$v_{qds} = [v_{qs} \quad v_{ds}]^t \quad (3.24)$$

$$v_{qds}^r = [v_{qs}^r \quad v_{ds}^r]^t \quad (3.25)$$

Substituting Equations 3.18 through 3.23 into Equations 3.5 and 3.6, the PMSM model in rotor reference frames is obtained as

$$\begin{bmatrix} v_{qs}^r \\ v_{ds}^r \end{bmatrix} = \begin{bmatrix} R_s + L_q P & \omega_r L_d \\ -\omega_r L_q & R_s + L_d P \end{bmatrix} \begin{bmatrix} i_{qs}^r \\ i_{ds}^r \end{bmatrix} + \begin{bmatrix} \omega_r \lambda_{af} \\ 0 \end{bmatrix} \quad (3.26)$$

where ω_r is the rotor speed in electrical radians per second. This equation is in a form where the voltage vector is equal to the product of the impedance matrix and the current vector, with an additional component due to the motional emf of the rotor flux linkages. Note that the impedance matrix has constant inductance terms and is no longer dependent on the rotor position. Some of the impedance matrix elements are dependent on the rotor speed, and only when they are constant as in a steady state, does the system of equations become linear. In the case of varying rotor speed and if its variation is dependent on the currents, then the system of equations becomes nonlinear. It is derived later that the electromagnetic torque is a function of the winding currents, and rotor speed is determined by the electromagnetic and load torques along with load parameters such as inertia and friction. In that case, it can be seen that the PMSM system is nonlinear because there are products of two state variables such as the rotor speed and one

of the currents in the stator voltage equations, and a product of two currents in the torque expression.

The relationship between the stator currents in the rotor reference frames and the actual stator dq currents is given by

$$i_{qds}^r = [T^r]^{-1} i_{qds} \quad (3.27)$$

The next section contains the derivation of the electromagnetic torque in terms of the current variables in arbitrary reference frames.

Example 3.1

The parameters of a two-phase PMSM are as follows:

$$R_s = 1.2 \Omega, L_q = 12 \text{ mH}, L_d = 5.7 \text{ mH}, \lambda_{af} = 123 \text{ mWb-T}, P = 4.$$

Find the stator currents when (i) the rotor is locked and (ii) the rotor is running at 188.5 rad/s. The input to the two-phase machine may be considered to be a set of balanced two-phase voltages at 60 Hz.

Solution

Case (i): Rotor speed is zero.

The balanced stator input voltages are assumed to be

$$V_{qs} = V_m \sin(\omega_s t)$$

$$V_{ds} = V_m \cos(\omega_s t)$$

where $V_m = 10 \text{ V}$ and $\omega_s = 2\pi 60 \text{ rad/s}$. The rotor reference stator voltages are obtained by using the inverse transformation as

$$v_{qds}^r = [T^r]^{-1} v_{qds} = \begin{bmatrix} \cos \theta_r & -\sin \theta_r \\ \sin \theta_r & \cos \theta_r \end{bmatrix} v_{qds} = \begin{bmatrix} 1 & 0 \\ 0 & 1 \end{bmatrix} \begin{bmatrix} V_{qs} \\ V_{ds} \end{bmatrix}$$

as $\theta_r = \omega_r t + \theta_i$ where θ_i is the initial rotor position and is assumed to be zero for this example. As the rotor speed is zero, the rotor position becomes zero. With that, the stator voltage equations in the rotor reference frames are

$$\begin{bmatrix} V_{qs}^r \\ V_{ds}^r \end{bmatrix} = \begin{bmatrix} R_s + L_q p & 0 \\ 0 & R_s + L_d p \end{bmatrix} \begin{bmatrix} i_{qs}^r \\ i_{ds}^r \end{bmatrix}$$

In steady state with sinusoidal input conditions, $p = j\omega_s$, which is the angular frequency of the input voltages in the actual stator and in the rotor reference based

stator windings. Then by solving the stator currents in the rotor reference frames using phasors, the currents obtained as are

$$I_{qs}^r = \frac{V_{qs}^r}{R_s + j\omega_s L_q} = \frac{10}{\sqrt{2}} \frac{1\angle 0^\circ}{1.2 + j377 * 0.012} = 1.529 \angle -75.14^\circ$$

$$I_{ds}^r = \frac{V_{ds}^r}{R_s + j\omega_s L_d} = \frac{10}{\sqrt{2}} \frac{1\angle 90^\circ}{1.2 + j377 * 0.0057} = 2.873 \angle +29.19^\circ$$

where the capital letters are used for the rms currents in a steady state. The instantaneous currents are given by

$$i_{qs} = (1.529\sqrt{2}) \sin(\omega_s t - 75.14^\circ)$$

$$i_{ds} = (2.873\sqrt{2}) \cos(\omega_s t + 29.19^\circ)$$

Note that the rotor reference frame stator currents and the actual stator currents are one and the same under the condition of zero rotor speed as derived above.

Case (ii): Rotor speed = 188.5 rad/s.

$$\text{Rotor electrical speed} = \omega_r = \omega_m P/2 = 377 \text{ rad/s (elec)} = \omega_s$$

$$v_{qds}^r = [T^r]^{-1} v_{qds} = \begin{bmatrix} \cos \theta_r & -\sin \theta_r \\ \sin \theta_r & \cos \theta_r \end{bmatrix} \begin{bmatrix} V_m \sin(\omega_s t) \\ V_m \cos(\omega_s t) \end{bmatrix} = \begin{bmatrix} 0 \\ V_m \end{bmatrix} = \begin{bmatrix} 0 \\ 10 \end{bmatrix}$$

as $\theta_r = \omega_r t = \omega_s t$ in this case. Note that the sinusoidal input voltages appear as dc in the rotor reference frame stator windings. In steady state, the output must correspond to the input as it is a linear system. Therefore, a dc input will produce a dc output in the steady state of a linear system. Hence, the derivatives of the q- and d-axes currents are zero in the rotor reference frames. With these conditions, the stator voltage equations in the rotor reference frames are reduced to

$$\begin{bmatrix} V_{qs}^r \\ V_{ds}^r \end{bmatrix} = \begin{bmatrix} R_s & \omega_r L_d \\ -\omega_r L_q & R_s \end{bmatrix} \begin{bmatrix} I_{qs}^r \\ I_{ds}^r \end{bmatrix} + \begin{bmatrix} \omega_r \lambda_{af} \\ 0 \end{bmatrix}$$

from which the currents are found as

$$I_{qs}^r = -3.83 \text{ A}$$

$$I_{ds}^r = -20.51 \text{ A}$$

The actual stator currents are obtained from the transformation $[T^r]$ as

$$\begin{bmatrix} i_{qs} \\ i_{ds} \end{bmatrix} = [T^r] \begin{bmatrix} i_{qs}^r \\ i_{ds}^r \end{bmatrix} = \begin{bmatrix} \cos \theta_r & \sin \theta_r \\ -\sin \theta_r & \cos \theta_r \end{bmatrix} \begin{bmatrix} -3.83 \\ -20.51 \end{bmatrix} = \begin{bmatrix} -20.87 \sin(\theta_r + 10.58^\circ) \\ -20.87 \cos(\theta_r + 10.58^\circ) \end{bmatrix}$$

Example 3.2

Find the stator currents in the rotor reference frames where the actual stator currents are given as (i) $i_{qs} = I_m \sin(\omega_r t + \delta)$; $i_{ds} = I_m \cos(\omega_r t + \delta)$ with a phase sequence of dq and (ii) a reversed phase sequence of qd.

Solution

Assume that the direction of rotation for the phase sequence dq is counterclockwise and positive and hence for the phase sequence of qd, the direction of rotation is clockwise and negative. In the first case, the rotor position is positive and in the second case the rotor position is negative in the transformation matrix because of our assumption in the derivation of the transformation matrix. Therefore, the stator currents in the rotor reference frames are derived as follows.

Case (i):

$$\begin{bmatrix} i_{qs}^r \\ i_{ds}^r \end{bmatrix} = [T^r]^{-1} \begin{bmatrix} i_{qs} \\ i_{ds} \end{bmatrix} = \begin{bmatrix} \cos \omega_r t & -\sin \omega_r t \\ \sin \omega_r t & \cos \omega_r t \end{bmatrix} \begin{bmatrix} I_m \sin(\omega_r t + \delta) \\ I_m \cos(\omega_r t + \delta) \end{bmatrix} = \begin{bmatrix} I_m \sin \delta \\ I_m \cos \delta \end{bmatrix}$$

Case (ii): The rotor position is negative as per the convention adopted and hence the transformation matrix has its position terms and the input currents in their rotor positions contain a negative sign. In this condition, the dq-axes currents do not change from the previous case as the machine is in the reverse motoring mode of operation:

$$\begin{bmatrix} i_{qs}^r \\ i_{ds}^r \end{bmatrix} = [T^r]^{-1} \begin{bmatrix} i_{qs} \\ i_{ds} \end{bmatrix} = \begin{bmatrix} \cos(-\omega_r t) & -\sin(-\omega_r t) \\ \sin(-\omega_r t) & \cos(-\omega_r t) \end{bmatrix} \begin{bmatrix} I_m \sin(-\omega_r t + \delta) \\ I_m \cos(-\omega_r t + \delta) \end{bmatrix} = \begin{bmatrix} I_m \sin \delta \\ I_m \cos \delta \end{bmatrix}$$

3.3 THREE-PHASE TO TWO-PHASE TRANSFORMATION

The model that has been so far developed is for a two-phase PMSM. PMSMs with three phases are prevalent but two-phase machines are rarely used in industrial applications. A dynamic model for the three-phase PMSM can be derived from the two-phase machine if the equivalence between the three and two phases is established. The equivalence is based on the equality of the mmf produced in the two-phase and three-phase windings and on equal current magnitudes. [Figure 3.4](#) shows the three-phase and two-phase windings.

Assuming that each of the three-phase windings has T_1 turns per phase, and equal current magnitudes, the two-phase windings will have $3T_1/2$ turns per phase

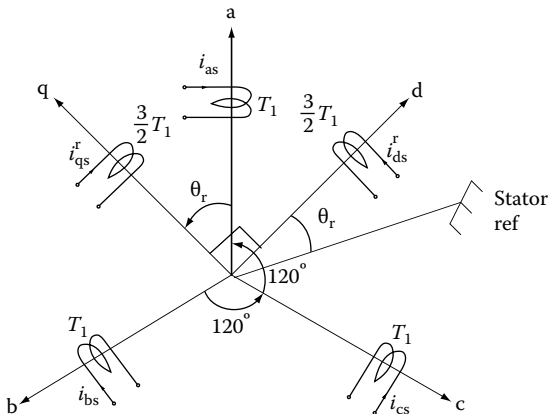


FIGURE 3.4 Two- and three-phase stator windings.

for mmf equality. The d- and q-axes mmfs are found by resolving the mmfs of the three phases along the d- and q-axes. The common term, i.e., the number of turns in the winding, is canceled on either side of the equations leaving the current equal. The q-axis here is assumed to be lagging behind the a-axis by θ_r . The relationship between d_{qo} and abc currents is

$$\begin{bmatrix} i_{qs}^r \\ i_{ds}^r \\ i_o \end{bmatrix} = \frac{2}{3} \begin{bmatrix} \cos \theta_r & \cos \left(\theta_r - \frac{2\pi}{3} \right) & \cos \left(\theta_r + \frac{2\pi}{3} \right) \\ \sin \theta_r & \sin \left(\theta_r - \frac{2\pi}{3} \right) & \sin \left(\theta_r + \frac{2\pi}{3} \right) \\ \frac{1}{2} & \frac{1}{2} & \frac{1}{2} \end{bmatrix} \begin{bmatrix} i_{as} \\ i_{bs} \\ i_{cs} \end{bmatrix} \quad (3.28)$$

The current i_o represents the imbalances in the a, b, and c phase currents and may be recognized as the zero sequence component of the current. Equation 3.28 can be expressed in a compact form by

$$i_{qdo}^r = [T_{abc}] i_{abc} \quad (3.29)$$

where

$$i_{qdo}^r = [i_{qs}^r \quad i_{ds}^r \quad i_0]^t \quad (3.30)$$

$$i_{abc} = [i_{as} \quad i_{bs} \quad i_{cs}]^t \quad (3.31)$$

and the transformation from abc to qdo variables is

$$\begin{bmatrix} T_{abc} \end{bmatrix} = \frac{2}{3} \begin{bmatrix} \cos \theta_r & \cos\left(\theta_r - \frac{2\pi}{3}\right) & \cos\left(\theta_r + \frac{2\pi}{3}\right) \\ \sin \theta_r & \sin\left(\theta_r - \frac{2\pi}{3}\right) & \sin\left(\theta_r + \frac{2\pi}{3}\right) \\ \frac{1}{2} & \frac{1}{2} & \frac{1}{2} \end{bmatrix} \quad (3.32)$$

The zero sequence current, i_0 , does not produce a resultant magnetic field. The transformation from the two-phase stator currents in rotor reference frames to three-phase stator currents can be obtained as

$$i_{abc} = [T_{abc}]^{-1} i_{qdo}^r \quad (3.33)$$

where

$$\begin{bmatrix} T_{abc} \end{bmatrix}^{-1} = \begin{bmatrix} \cos \theta_r & \sin \theta_r & 1 \\ \cos\left(\theta_r - \frac{2\pi}{3}\right) & \sin\left(\theta_r - \frac{2\pi}{3}\right) & 1 \\ \cos\left(\theta_r + \frac{2\pi}{3}\right) & \sin\left(\theta_r + \frac{2\pi}{3}\right) & 1 \end{bmatrix} \quad (3.34)$$

This transformation could also be thought of as a three (abc) axis to a new three (qdo) axis transformation and, for the uniqueness of the transformation from one set of axes to another set of axes including imbalances in the abc variables, there is a requirement of three variables such as the dqr. The reason for this is that it is easy to convert three abc variables to two qd variables if the abc variables have an inherent relationship among themselves such as equal phase displacement and magnitude. Therefore, in such a case, there are only two independent variables in abc and the third is the dependent variable obtained as the negative sum of the other two variables. Hence a qd to abc transformation is unique under that circumstance. When the abc variables have no such inherent relationship, then there are three distinct and independent variables and hence the third variable cannot be recovered from the knowledge of the other two variables only. It also means that they are not recoverable from the two dq variables but require another variable such as the zero sequence component to recover the abc variables from the dqr variables.

3.3.1 UNBALANCED OPERATION

Under voltage or current imbalance in the three-phase windings, the inherent relationship between the three-phase currents, which is, that their sum is equal to zero,

does not hold any more. Then, the only way that they can be represented in dq variables is by adding the zero sequence term. This step is very similar to the case of induction machine modeling except that only stator windings only are involved here. The zero sequence voltage is written as

$$v_0 = R_s i_0 + p\lambda_0 = R_s i_0 + L_0 p i_0 \quad (3.35)$$

where

λ_0 is the zero sequence flux linkages

L_0 is the zero sequence inductance

i_0 is the zero sequence current

Note that the zero sequence current goes through the stator resistance. The derivation for the zero sequence inductance, in terms of the phase self- and mutual inductances, is given elsewhere. It could be derived from the stator inductance matrix in the abc frames and then converted into dqa frames using the transformation derived above.

In a balanced three-phase machine, the sum of the three-phase currents is zero and given as

$$i_{as} + i_{bs} + i_{cs} = 0 \quad (3.36)$$

leading to a zero sequence current of zero value

$$i_0 = \frac{1}{3}(i_{as} + i_{bs} + i_{cs}) = 0 \quad (3.37)$$

With Equations 3.28 and 3.29, the equivalence between the two-phase and three-phase PMSMs is established. It is instructive to know that the derived transformation is applicable to currents, voltages, and flux-linkages.

3.4 ZERO SEQUENCE INDUCTANCE DERIVATION

In this section, the zero sequence inductance is derived as it is required in fault studies that create imbalance in the voltages and currents. The derivation can be made in two ways: (1) starting from the flux linkages of the three-phase machine windings and using the transformation from abc to qdo to obtain the flux linkages in the qdo axes and then extracting the zero sequence inductance from the zero sequence flux linkages and (2) inversely, the zero sequence inductance and hence zero sequence flux linkages can be assumed and together with the q- and d-axes flux linkages, the three-phase winding flux linkages can be obtained by the transformation from qdo to abc axes and then the phase inductances can be derived from which the relationship between the zero sequence inductance and phase self- and mutual inductances can be established. The second option is chosen here as it does not require the derivation of phase inductances from the physical machine but makes use of the existing dq flux linkages relationships to show that nothing more is required to derive the zero sequence flux linkage and

inductance. Note that by this approach the derived phase self- and mutual inductances, and that derived using physical reasoning are identical.

It is sufficient to derive the a-phase flux linkages from the qdo flux linkages. It is assumed that the zero sequence flux linkages is given and defined as in Equation 3.31. The a-phase flux linkages is given by using the $[T_{abc}]^{-1}$ transformation as

$$\lambda_{as} = \lambda_{qs}^r \cos \theta_r + \lambda_{ds}^r \sin \theta_r + \lambda_0 \quad (3.38)$$

where the qdo flux linkages are given elsewhere by

$$\lambda_{qs}^r = L_q i_{qs}^r \quad (3.39)$$

$$\lambda_{ds}^r = L_d i_{ds}^r + \lambda_{af} \quad (3.40)$$

$$\lambda_0 = L_0 i_0 \quad (3.41)$$

After substituting these flux linkages in the a-phase flux linkages expression, the qdo axes currents in the rotor reference frames can be written in terms of the abc phase currents using the transformation T_{abc} and, the simplification of the expression yields the a-phase flux linkages as

$$\begin{aligned} \lambda_{as} = & i_{as} \left[\frac{2}{3} \left\{ \frac{L_0}{2} + \frac{L_q + L_d}{2} + \frac{L_q - L_d}{2} \cos 2\theta_r \right\} \right] \\ & + i_{bs} \left[-\frac{2}{3} \left\{ -\frac{L_0}{2} + \frac{L_q + L_d}{4} + \frac{L_q - L_d}{2} \cos 2(\theta_r + 30^\circ) \right\} \right] \\ & + i_{cs} \left[-\frac{2}{3} \left\{ -\frac{L_0}{2} + \frac{L_q + L_d}{4} + \frac{L_q - L_d}{2} \cos 2(\theta_r + 150^\circ) \right\} \right] \\ & + \lambda_{af} \sin \theta_r \end{aligned} \quad (3.42)$$

The a-phase flux linkages can be written in terms of the self- and mutual flux linkages and the corresponding inductances and currents as

$$\lambda_{as} = L_{aa} i_{as} + L_{ab} i_{bs} + L_{ac} i_{cs} + \lambda_{af} \sin \theta_r \quad (3.43)$$

By viewing Equations 3.38 and 3.39, the self- and mutual inductances are found to be as follows:

$$L_{aa} = \frac{2}{3} \left\{ \frac{L_0}{2} + \frac{L_q + L_d}{2} + \frac{L_q - L_d}{2} \cos 2\theta_r \right\} = L_{a1} + L_{a2} \cos 2\theta_r \quad (3.44)$$

$$L_{ab} = -\frac{2}{3} \left\{ -\frac{L_0}{2} + \frac{L_q + L_d}{4} + \frac{L_q - L_d}{2} \cos 2(\theta_r + 30^\circ) \right\}$$

$$= -\{L_{m1} + L_{a2} \cos 2(\theta_r + 30^\circ)\} \quad (3.45)$$

$$L_{ac} = -\frac{2}{3} \left\{ -\frac{L_0}{2} + \frac{L_q + L_d}{4} + \frac{L_q - L_d}{2} \cos 2(\theta_r + 150^\circ) \right\}$$

$$= -\{L_{m1} + L_{a2} \cos 2(\theta_r + 150^\circ)\} \quad (3.46)$$

where

L_{aa} is the self-inductance of phase a

L_{ab} is the mutual inductance between phases a and b

L_{ac} is the mutual inductance between phases a and c and also

$$L_{a1} = \frac{L_0}{3} + \frac{L_q + L_d}{3} \quad (3.47)$$

$$L_{a2} = \frac{L_q - L_d}{3} \quad (3.48)$$

$$L_{m1} = -\frac{L_0}{3} + \frac{L_q + L_d}{6} \quad (3.49)$$

from which L_q , L_d , and L_0 are derived from the phase self- and mutual inductance components as

$$L_q = L_{a1} + L_{m1} + \frac{3}{2} L_{a2} \quad (3.50)$$

$$L_d = L_{a1} + L_{m1} - \frac{3}{2} L_{a2} \quad (3.51)$$

$$L_0 = L_{a1} - 2L_{m1} \quad (3.52)$$

It is important to note that the zero sequence inductance is part of the constant term in the phase inductances whereas the q and direct axis inductances do not contain the zero sequence inductance. Therefore, the zero sequence inductance can only be derived from the phase self- and mutual inductances and hence their measurements are necessary to obtain it.

3.5 POWER EQUIVALENCE

The power input to the three-phase machine has to be equal to the power input to the two-phase machine to have meaningful interpretation in the modeling, analysis, and

simulation. Such an identity is derived in this section. The three-phase instantaneous power input is

$$p_i = v_{abc}^t i_{abc} = v_{as} i_{as} + v_{bs} i_{bs} + v_{cs} i_{cs} \quad (3.53)$$

From Equations 3.29 and 3.33, the abc phase currents and voltages are transformed into their equivalent two axes currents and voltages as

$$i_{abc} = [T_{abc}]^{-1} i_{qdo}^r \quad (3.54)$$

$$v_{abc} = [T_{abc}]^{-1} v_{qdo}^r \quad (3.55)$$

Substituting Equations 3.54 and 3.55 into Equation 3.53, the power input is obtained as

$$p_i = (v_{qdo}^r)^t ([T_{abc}]^{-1})^t [T_{abc}]^{-1} i_{qdo}^r \quad (3.56)$$

Expanding the right-hand side of Equation 3.56, the power input in the dqr variables is

$$p_i = \frac{3}{2} [(v_{qs}^r i_{qs}^r + v_{ds}^r i_{ds}^r) + 2v_0 i_0] \quad (3.57)$$

For a balanced three-phase machine, the zero sequence current does not exist and hence the power input is compactly represented by

$$p_i = \frac{3}{2} [v_{qs}^r i_{qs}^r + v_{ds}^r i_{ds}^r] \quad (3.58)$$

The input power given by Equation 3.58 remains valid for all reference frames provided the voltages and currents correspond to the frames under consideration.

3.6 ELECTROMAGNETIC TORQUE

The electromagnetic torque is the most important output variable that determines the mechanical dynamics of the machine such as the rotor position and speed. Therefore, its importance cannot be overstated in all the simulation studies. It is derived from the machine matrix equation by looking at the input power and its various components such as resistive losses, mechanical power, and the rate of change of stored magnetic energy. Elementary reasoning leads to the fact that there cannot be a power component due to the introduction of reference frames. Similarly, the rate of change of stored magnetic energy could only be zero in steady state. Hence, the output power is the difference between the input power and the resistive losses in a steady

state. Note that dynamically, the rate of change of stored magnetic energy need not be zero. Based on these observations, the derivation of the electromagnetic torque is made as follows.

The dynamic equations of the PMSM can be written as

$$V = [R]i + [L]pi + [G]\omega_r i \quad (3.59)$$

where the vectors and matrices are identified by observation. By premultiplying Equation 3.55 by the transpose of the current vector, the instantaneous input power is

$$p_i = i^t V = i^t [R]i + i^t [L]pi + i^t [G]\omega_r i \quad (3.60)$$

where

$[R]$ matrix consists of resistive elements

$[L]$ matrix consists of the coefficients of the derivative operator p

$[G]$ matrix has elements that are the coefficients of the electrical rotor speed, ω_r

The term $i^t [R]i$ gives stator and rotor resistive losses. The term $i^t [L]pi$ denotes the rate of change of stored magnetic energy. Therefore, what is left of the power component must be equal to the air gap power, given by the term $i^t [G]\omega_r i$. From the fundamentals, it is known that the air gap power has to be associated with the rotor speed. The air gap power is the product of the mechanical rotor speed and air gap or electromagnetic torque. Hence, the air gap torque, T_e , is derived from the terms involving the rotor speed, ω_m , in mechanical rad/s, as

$$\omega_m T_e = P_a = i^t [G]i \times \omega_r = i^t [G]i \frac{P}{2} \omega_m \quad (3.61)$$

where P is the number of poles. Canceling speed on both sides of the equation leads to an electromagnetic torque that is

$$T_e = \frac{P}{2} i^t [G]i \quad (3.62)$$

Substituting $[G]$ in Equation 3.62 with the observation from Equation 3.26, the electromagnetic torque is obtained as

$$T_e = \frac{3}{2} \frac{P}{2} \left[\lambda_{af} + (L_d - L_q) i_{ds}^r \right] i_{qs}^r \text{ (N·m)} \quad (3.63)$$

The factor 3/2 from the power equivalence condition is introduced on the right-hand side of Equation 3.63 between the three-phase and two-phase PMSMs.

Alternately, the air gap torque can also be derived by multiplying the q- and d-axes stator voltages with the q- and d-axes stator currents, respectively. Then they represent the instantaneous input power of the machine:

$$\begin{aligned}
 P_i &= \frac{3}{2} \left[v_{qs}^r i_{qs}^r + v_{ds}^r i_{ds}^r \right] \\
 &= \frac{3}{2} \left[R_s [(i_{qs}^r)^2 + (i_{ds}^r)^2] + \{L_q i_{qs}^r p i_{qs}^r + L_d i_{ds}^r p i_{ds}^r\} + \omega_r \{\lambda_{af} + (L_d - L_q) i_{ds}^r\} i_{qs}^r \right] \quad (3.64)
 \end{aligned}$$

Looking at the right-hand side of the equation for input power, the terms representing the stator resistive losses, rate of change of magnetic energy stored, and the air gap power becomes obvious. Dividing the air gap power over the mechanical rotor speed results in the air gap torque that is identical to the previous equation. The factor 3/2 has been introduced to account for the power equivalence of the three-phase machine obtained from the power of the two-phase machine as discussed previously.

3.7 STEADY-STATE TORQUE CHARACTERISTICS

A salient pole PMSM is considered in order to generalize the steady-state characteristics of the machine. A set of balanced polyphase currents is assumed to be the input to the stator windings and is given by

$$I_{qs} = I_m \sin(\omega_r t + \delta) \quad (3.65)$$

$$I_{ds} = I_m \cos(\omega_r t + \delta) \quad (3.66)$$

By using the inverse of the transformation matrix T^r , the stator currents in the rotor reference frames are obtained as (as in Example 3.2)

$$I_{qs}^r = I_m \sin \delta \quad (3.67)$$

$$I_{ds}^r = I_m \cos \delta \quad (3.68)$$

And substituting these into the torque expression, the air gap torque is obtained as

$$\begin{aligned}
 T_e &= \frac{3}{2} \frac{P}{2} \left[\lambda_{af} + (L_d - L_q) I_{ds}^r \right] I_{qs}^r = \frac{3}{2} \frac{P}{2} \left[\lambda_{af} + (L_d - L_q) I_m \cos \delta \right] I_m \sin \delta \\
 &= \frac{3}{2} \frac{P}{2} \left[\lambda_{af} I_m \sin \delta + \frac{1}{2} (L_d - L_q) I_m^2 \sin 2\delta \right] \quad (3.69)
 \end{aligned}$$

where δ is termed the torque angle as it directly influences the air gap torque. Note that the torque has two terms. The first term gives the torque as a result of the interaction of the rotor magnet and the q-axis stator current in rotor reference frames and is usually referred to as the synchronous torque, T_{es} . The second term contains the reluctance variation and the torque due to that, is known as the reluctance torque, T_{er} . These two terms are written separately and the air gap torque as a function of these two as

$$T_{es} = \frac{3}{2} \frac{P}{2} \lambda_{af} I_m \sin \delta \quad (3.70)$$

$$T_{er} = \frac{3}{2} \frac{P}{2} \left[\frac{1}{2} (L_d - L_q) \right] I_m^2 \sin 2\delta \quad (3.71)$$

$$T_e = T_{es} + T_{er} \quad (3.72)$$

For a typical machine, the air gap torque and its individual components are shown in Figure 3.5 as a function of the torque angle when the stator current phasor is maintained at 1.29 p.u. The stator current phasor is the resultant of the quadrature and direct axes currents and its magnitude is given by the peak value of the d and q currents, I_m . The sum of the synchronous and reluctance torques yields the air gap torque and note that its peak is at a torque angle greater than 90°. The reluctance torque is the single contributor to this effect, affecting the peak of the air gap torque and the torque angle at which it occurs. The reluctance torque enhances the air gap torque in the torque angle region between 90° and 180° and reduces the torque from 0° to 90° of torque angle. Therefore, an operation in the first 90° is not attempted in these machines and the preferred torque angle is between 90° and 180°. Note that the maximum torque that is obtainable with a current magnitude is the point corresponding to the dotted line. It may be seen from Figure 3.6 that the angle at which the maximum torque occurs changes for various stator current magnitudes. The loci of the torque angle versus the maximum torque as a function of stator current magnitude are important in the optimum torque per unit current operation of the machine. It is shown in Chapter 4 that the maximum torque per unit current is one of the

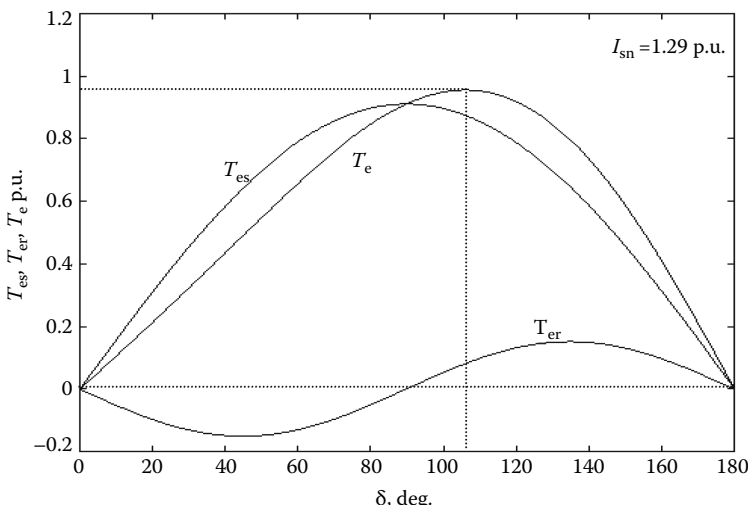


FIGURE 3.5 Reluctance, synchronous and air gap torques versus torque angle for stator current magnitude of 1.29 p.u.

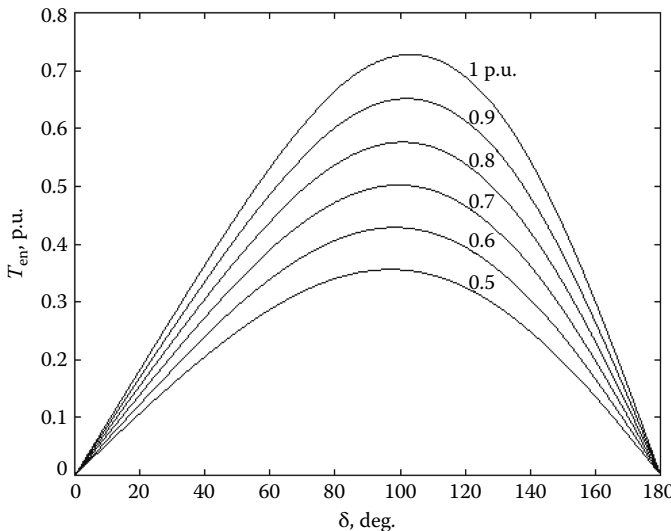


FIGURE 3.6 Air gap torque versus torque angle for various stator currents.

many performance indices for the optimal operation of the machine. But satisfying the maximum torque per unit current performance index does not necessarily mean that the machine satisfies other performance indexes such as maximum efficiency, maximum power factor, and minimum power converter volt-ampere ratings. In fact, it could be performing poorly in one or all of these aspects. More on this aspect is presented in the chapter on the control of PMSMs.

The MATLAB® code for computing the air gap torque versus torque angle for various stator current magnitudes is given in the following. Interested readers can separate the air gap torque into its component synchronous and reluctance torques from this program by plotting those variables only or all of them on the same figure as shown in [Figure 3.5](#).

```
% Steady state torque versus angle characteristics for constant
stator
%      current phasors.
%
clear all;close all;
m=0;
% Data starts here
Rs=1.2;                                % Stator resistance per phase
lq=0.0125;                               % Q axis inductance
ld=0.0057;                               % D axis inductance
ro=lq/ld;                                 % Saliency ratio
Rc=416;                                  % Core loss resistance
lamaf=0.123;                             % Rotor flux linkages
Pb=121;                                   % Base power loss
Tb=2.43;                                  % Base torque
Ib=4.65;                                  % Base current
P=4;                                      % Number of poles
```

```
w=(2*pi*3500/60)*P/2; % Electrical rotor speed
%Pb is rated loss. Actual base power is 890W for this machine.
% Computation starts here
for isn=2.325:0.465:4.65;
    m=m+1;
    n=1;
    for del = 0:0.05:180;
        delt=del*pi/180;
        ide=isn*cos(delt);
        iqe=isn*sin(delt);
        tes(m,n)=0.75*P*iqe*lamaf/Tb; % Synchronous torque, p.u.
        ter(m,n)=0.75*P*iqe*ld*(1-ro)*ide/Tb; % Reluctance torque, p.u.
        te(m,n)=tes(m,n)+ter(m,n); % Air gap torque, p.u.
        delta(n)=del;
        n=n+1;
    end
end
% Computation ends here and plotting begins
plot(delta,te,'k'); % Air gap torque vs. angle
figure(2);
plot(delta,te,delta,tes,delta,ter) % Rel., syn. and air gap torque vs. %angle
```

Example 3.3

Using the PMSM parameters given in the previous example, derive the steady-state rotor reference frame and stationary reference frame currents and electromagnetic torque when the three-phase stator voltages are given by

$$V_{as} = V_m \sin \omega_r t$$

$$V_{bs} = V_m \sin \left(\omega_r t - \frac{2\pi}{3} \right)$$

$$V_{cs} = V_m \sin \left(\omega_r t + \frac{2\pi}{3} \right)$$

where ω_r is the rotor electrical speed and is given as $2\pi 60$ rad/s. The machine is assumed to have constant rotor speed and peak phase voltage, $V_m = 10$ V.

Solution

The abc to qdo transformation to the rotor reference frames is given as

$$\begin{bmatrix} V_{qs}^r \\ V_{ds}^r \\ V_0 \end{bmatrix} = [T_{abc}] \begin{bmatrix} V_{as} \\ V_{bs} \\ V_{cs} \end{bmatrix}$$

Substituting these and solving the d- and q-axes stator voltages in the rotor reference frames,

$$\begin{bmatrix} V_{qs}^r \\ V_{ds}^r \\ V_0 \end{bmatrix} = [T_{abc}] \begin{bmatrix} V_{as} \\ V_{bs} \\ V_{cs} \end{bmatrix} = \begin{bmatrix} 0 \\ V_m \\ 0 \end{bmatrix}$$

The d- and q-axes stator voltages are dc quantities and hence the responses will be dc quantities too as the system is linear. Hence

$$pI_{qs}^r = pI_{ds}^r = 0$$

as the currents are constant in the rotor reference frames. These currents are obtained by inverting the impedance matrix and premultiplying them with the input voltage vector. The currents in the rotor frames are then obtained as

$$\begin{bmatrix} I_{qs}^r \\ I_{ds}^r \end{bmatrix} = \begin{bmatrix} R_s & \omega_r L_d \\ -\omega_r L_q & R_s \end{bmatrix}^{-1} \left\{ \begin{bmatrix} V_{ds}^r \\ V_{qs}^r \end{bmatrix} - \begin{bmatrix} \omega_r \lambda_{af} \\ 0 \end{bmatrix} \right\} = \begin{bmatrix} -6.91 \\ -17.72 \end{bmatrix} \quad (\text{A})$$

Note that capital letters are used for the voltage and current variables as the system is in a steady state. The phase currents are obtained from the dq-axis rotor reference frame stator currents, by using the inverse transformation of T_{abc} given elsewhere in the text as

$$\begin{bmatrix} i_{as} \\ i_{bs} \\ i_{cs} \end{bmatrix} = \begin{bmatrix} \cos \theta_r & \sin \theta_r \\ \cos \left(\theta_r - \frac{2\pi}{3} \right) & \sin \left(\theta_r - \frac{2\pi}{3} \right) \\ \cos \left(\theta_r + \frac{2\pi}{3} \right) & \sin \left(\theta_r + \frac{2\pi}{3} \right) \end{bmatrix} \begin{bmatrix} I_{qs}^r \\ I_{ds}^r \end{bmatrix} = \begin{bmatrix} 19.02 \sin(\theta_r + 2.77) \\ 19.02 \sin(\theta_r + 0.68) \\ 19.02 \sin(\theta_r + 4.86) \end{bmatrix}$$

where θ_r is the rotor position and also the position of the rotor flux linkages at a given instant. The electromagnetic torque is given by

$$T_e = \frac{3}{2} \frac{P}{2} [\lambda_{af} + (L_d - L_q) I_{ds}^r] I_{qs}^r = -4.865 \text{ (N·m)}$$

The stator voltages and currents in the abc and rotor reference frames and electromagnetic torque are shown in [Figure 3.7](#).

The sinusoidal voltages in the rotor reference frames appear as constants as the rotor angular velocity and the angular frequency of the supply voltages are the same and hence their relative speed is zero with respect to each other. The dc dq stator voltages produce the dc dq currents, which on recovery in the abc frames appear as sinusoids. The electromagnetic torque is negative, indicating that the machine

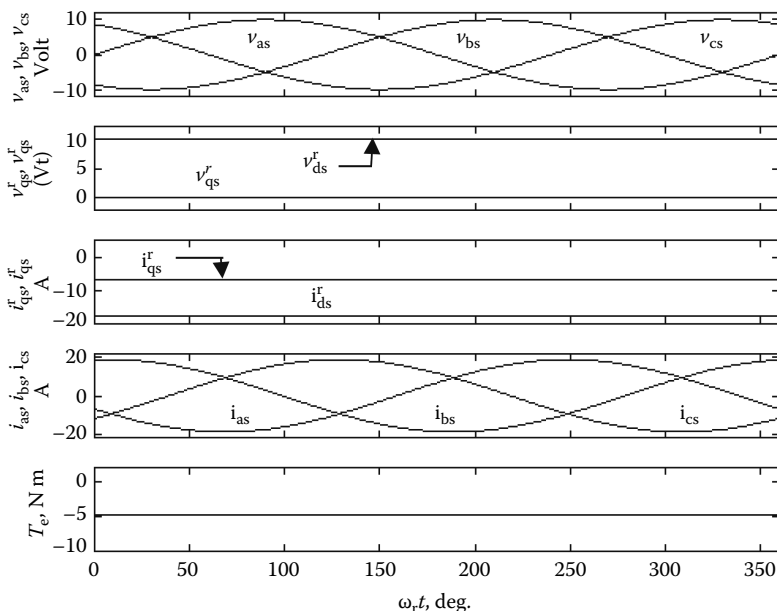


FIGURE 3.7 The rotor reference frame and abc frames based stator voltages and currents and electromagnetic torque at constant speed.

is generating and hence supplying power to the source. The MATLAB program is given in the following for this problem:

```
% Solution of abc to qd voltages and then solving for currents.
% Rotor speed is constant.
%
close all;clear all;
rs=1.2, lq=0.012;ld=0.0057;lamaf=0.123;p=4;vm=10;
wr=2*pi*60;n=1
for angle=0:0.25:360           % Do loop starts here
    theta=angle*pi/180;         % Angle is converted from deg to rad.
    v=[vm*sin(theta); vm*sin(theta-2*pi/3);
       vm*sin(theta+2*pi/3)]; % abc voltage column vector
    T=2/3*[cos(theta) cos(theta-2*pi/3)
            cos(theta+2*pi/3)]; % Transformation matrix from abc to
                           % qdo
    sin(theta) sin(theta-2*pi/3)sin(theta+2*pi/3); % in rotor reference
                           % frames
    0.5                      0.5          0.5];
    vqdo=T*v;                 % qdo voltages in rotor ref. frames
    vqd=vqdo(1:2);            % only qd voltages in rotor ref. %frames
    A=[rs wr*ld ;-wr*lq rs]; % Impedance matrix
    C=[-wr*lamaf;0];          % Motional emf vector
    iqrd=A^-1*(vqd+C);       % qd currents in rotor ref. frames
    Te(n)=0.75*p*(lamaf+(ld-lq)*
                  iqrd(2))*iqrd(1);      % Air gap torque
    iqqs(n)=iqrd(1);
```

```

ids(n)=iqd(2);
vqs(n)=vqd(1);vds(n)=vqd(2);
vas(n)=v(1);vbs(n)=v(2);vcs(n)=v(3);
T1=[cos(theta) sin(theta); % Inverse transformation from rotor
    cos(theta-2*pi/3)
    sin(theta-2*pi/3); % ref. frames to abc frames
    cos(theta+2*pi/3) sin(theta+2*pi/3)];
iabc=T1*igd; % abc phase current vector
ias(n)=iabc(1); ibs(n)=iabc(2); ics(n)=iabc(3);
thet(n)=angle;
n=n+1;
end
subplot(5,1,1); % Plotting in the format shown but
plot(thet,vas,'k',thet,vbs,
    'k',thet,vcs,'k'); % legends are differently done
axis([0 360 -12 12]);set(gca,'xticklabel',[]);
subplot(5,1,2);
plot(thet,vqs,'k',thet,vds,'k');
axis([0 360 -2 12]);set(gca,'xticklabel',[]);
subplot(5,1,3);
plot(thet,iqs,'k',thet,ids,'k');
axis([0 360 -20 5]);set(gca,'xticklabel',[]);
subplot(5,1,4);
plot(thet,ias,'k',thet,ibs,'k',thet,ics,'k');
axis([0 360 -22 22]);set(gca,'xticklabel',[]);
subplot(5,1,5);
plot(thet,Te,'k');axis([0 360 -10 2]);

```

3.8 MODELS IN FLUX LINKAGES

The dynamic equations of the PMSM in rotor reference frames can be represented using flux linkages as variables. Even when the voltages and currents are discontinuous, the flux linkages are continuous. This gives the advantage of differentiating these variables with numerical stability. In addition, the flux linkages representation is used in motor drives to highlight the process of decoupling of the flux and torque channels in the PMSMs. The stator and rotor flux linkages in rotor reference frames are defined as

$$\lambda_{qs}^r = L_q i_{qs}^r \quad (3.73)$$

$$\lambda_{ds}^r = L_d i_{ds}^r + \lambda_{af} \quad (3.74)$$

From these equations, the stator currents in the rotor reference frames can be represented in terms of the flux linkages and inductances.

Then the q- and d-axes stator voltages in terms of these flux linkages in the rotor reference frames are as follows:

$$v_{qs}^r = \frac{R_s}{L_q} \lambda_{qs}^r + p\lambda_{qs}^r + \omega_r \lambda_{ds}^r \quad (3.75)$$

$$v_{ds}^r = \frac{R_s}{L_d}(\lambda_{ds}^r - \lambda_{af}) + p\lambda_{ds}^r - \omega_r \lambda_{qs}^r \quad (3.76)$$

These equations can be represented in the form of equivalent circuits and also in the form of a block diagram. Both will be considered in the following sections.

The electromagnetic torque as a function of the flux linkages is obtained by substituting the stator currents in terms of the flux linkages and is derived as

$$T_e = \frac{3}{2} \frac{P}{2} \frac{1}{L_q} \left[\rho \lambda_{af} + (1-\rho) \lambda_{ds}^r \right] \lambda_{qs}^r = \frac{3}{2} \frac{P}{2} \left[\lambda_{ds}^r i_{qs}^r - \lambda_{qs}^r i_{ds}^r \right] \quad (3.77)$$

where the saliency ratio is defined as

$$\rho = \frac{L_q}{L_d} \quad (3.78)$$

The second part of the torque expression conveys a better understanding of the machine as the air gap torque is the resultant of the interaction between the d-axis flux linkages and q-axis current in the windings and vice versa. The negative sign associated with the product of the q-axis flux linkages and the d-axis current is because it produces a countertorque to that of the other torque component due to the d-axis flux linkages and the q-axis current.

3.9 EQUIVALENT CIRCUITS

The equivalent circuit of the PMSM can be derived from the stator equations and is shown in [Figure 3.8](#).

The equivalent circuits are

1. Dynamic stator q-axis equivalent circuit
2. Dynamic stator d-axis equivalent circuit
3. Zero sequence equivalent circuit

The equivalent circuits are useful in system studies, particularly with regard to faults.

The equivalent circuits can be modified to account for the core losses. The core losses are produced by the hysteresis and eddy current losses in the iron laminations. While these losses are commonly governed by the flux density, frequency of excitation, and lamination material characteristics, and lamination thickness in the case of eddy current losses only, it is noted that each of these variables affects the core loss component very differently. Further, there are losses on the pole face and harmonic losses generated in the windings and stator and rotor laminations. Such a loss model for each and everyone of the component may not be easily integrated into simple equivalent circuits. But a simple model to account for the core losses due to the fundamental excitation is possible by an equivalent resistance, even though other secondary losses such as pole face losses and harmonic losses are excluded in

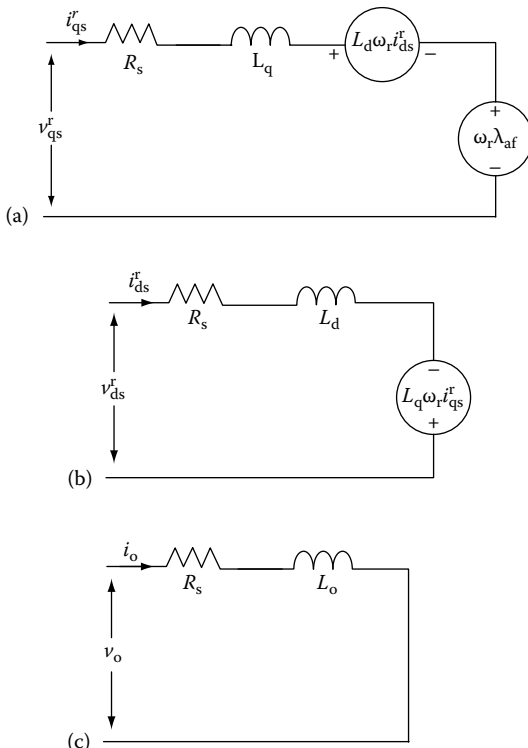


FIGURE 3.8 Dynamic equivalent circuits of PMSM neglecting core losses. (a) Dynamic stator q-axis equivalent circuit. (b) Dynamic stator d-axis equivalent circuit. (c) Zero sequence equivalent circuit.

such a model. The model then, is very useful in efficiency studies for optimal torque operation of the machine, and most importantly to determine the torque versus speed boundary for the optimal utilization and the safe operation of the machine. Relevant control strategies using the core loss-based equivalent circuit are given in Chapter 4. To consolidate the core losses as due to a single resistive element in the d and q equivalent circuits, it is assumed that the core losses are proportional to the square of the product of the frequency and flux. Such an assumption leads to the fact that the core losses are proportional to the induced emfs on each stator axis as the induced emfs are the result of the product of the frequency and flux and also, the core losses finally emerge as proportional to their product square. Therefore, the core losses are modeled with equivalent resistors across the stator q- and d-axes-induced emfs in the equivalent circuits. The core losses are of predominant concern during the steady-state operation and hence only steady-state equivalent circuits with core-loss modeling are shown in Figure 3.9. The inclusion of core losses in the dynamic operation is straightforward as seen from the dynamic equivalent circuits in Figure 3.8.

The insertion of the core loss resistors in the q- and d-axes equivalent circuits demonstrates that the currents consumed by them are lost for torque generation in

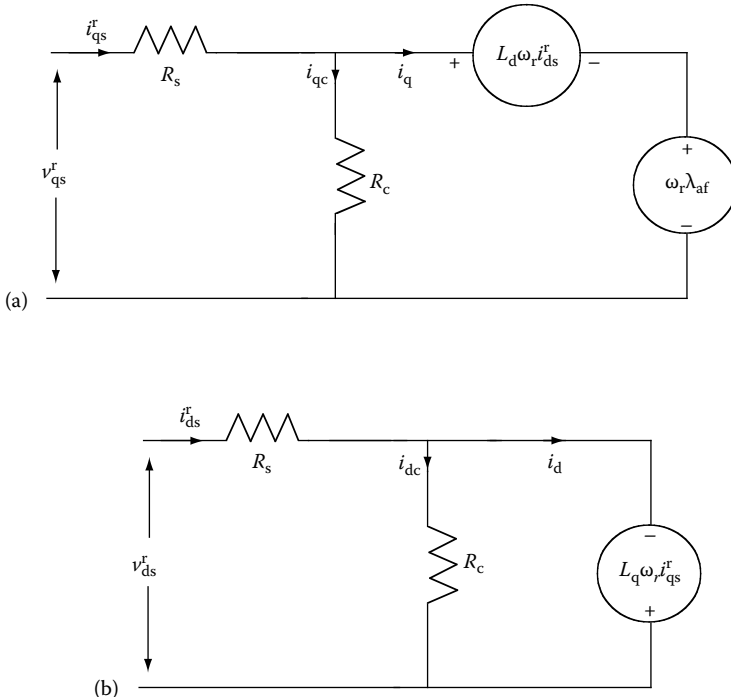


FIGURE 3.9 Steady-state equivalent circuits of PMSM with core losses. (a) Steady-state q-axis equivalent circuit and (b) Steady-state d-axis equivalent circuit.

the machine and is hence, a drain on the efficiency. More than that, the losses reduce the thermal capability of the machine. It is not uncommon in low hp machines to come across core losses that are as much as stator resistive losses at rated current. Therefore, a neglect of the core losses will lead to an optimistic efficiency prediction and also to an overrating of the machine by not considering the thermal derating that should be accounted for together with these additional losses.

Similarly, the block diagram of the PMSM can be derived in terms of the flux linkages and is shown in Figure 3.10. The electromagnetic torque is obtained in terms of the flux linkages or in terms of the product of flux linkages and the currents as shown in Equation 3.77. The currents can again be deduced from the flux linkages and they are not shown here for the sake of conceptual simplicity. The quadrature and direct axis stator time constant are given as τ_q and τ_d , respectively, and they are equal to L_q/R_s and L_d/R_s . The block diagram does not lend itself to mathematical computational simplicity as the q- and d-axes flux linkages are coupled. But they can be of some use in formulating control strategies as the signal paths are traceable to analyze visually and very elegantly the cause–effect relationships of a particular feedback or feedforward of a signal and its impact on the dynamic performance of the system. Such an approach by extension, to the space phasor model is formulated and powerfully exploited in induction motor drives to study the impact of the switching strategies, control structures, sensorless control algorithms, and for parameter sensitivity

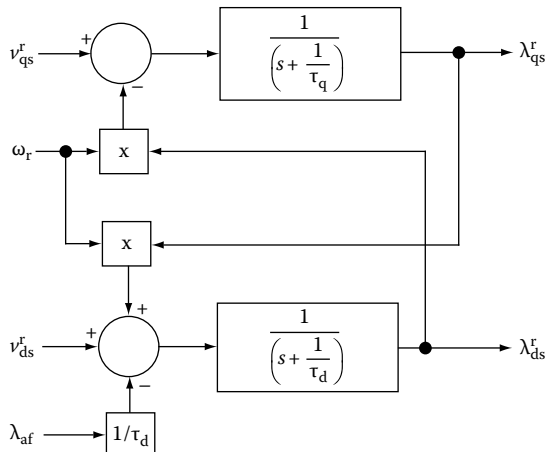


FIGURE 3.10 Block diagram of the PMSM.

compensation. Similarly a possibility exists with these block diagrams for the study of PMSM drives even though it is yet to emerge.

3.10 PER UNIT MODEL

The normalized model of the PMSM is derived by defining the base variables both in the abc and dqr frames. In the abc frames, let the rms values of the rated phase voltage and current form the base quantities, given as

$$\text{Base power} = P_b = 3V_{b3}I_{b3} \quad (3.79)$$

where V_{b3} and I_{b3} are the three-phase base voltage and current, respectively. Selecting the base quantities in the dqr frames denoted by V_b and I_b to be equal to the peak value of the phase voltage and current in abc frames results in

$$V_b = \sqrt{2}V_{b3} \quad (3.80)$$

$$I_b = \sqrt{2}I_{b3} \quad (3.81)$$

Hence, the base power is defined as

$$P_b = 3V_{b3}I_{b3} = 3 \frac{V_b}{\sqrt{2}} \frac{I_b}{\sqrt{2}} = \frac{3}{2} V_b I_b \quad (3.82)$$

The rotor reference frame model is chosen to illustrate the normalization process. To begin with consider the q-axis stator voltage, which is given in the following:

$$v_{qs}^r = (R_s + L_q p) i_{qs}^r + \omega_r (L_d i_{ds}^r + \lambda_{af}) \quad (3.83)$$

It is normalized by dividing it with the base voltage, V_b as

$$\frac{v_{qsn}^r}{V_b} = \frac{R_s}{V_b} i_{qs}^r + \frac{L_q}{V_b} p i_{qs}^r + \frac{\omega_r (L_d i_{ds}^r + \lambda_{af})}{V_b} \text{ (p.u.)} \quad (3.84)$$

Substituting base voltage in terms of base current, I_b , and base impedance, Z_b , or base speed and base flux linkages as

$$V_b = I_b Z_b = \omega_b \lambda_b = \omega_b L_b I_b \quad (\text{V}) \quad (3.85)$$

into Equation 3.84 yields

$$v_{qsn}^r = \left(\frac{R_s}{Z_b} \right) \left(\frac{i_{qs}^r}{I_b} \right) + \frac{1}{\omega_b} \left(\frac{L_q}{L_b} \right) p \left(\frac{i_{qr}^r}{I_b} \right) + \left(\frac{\omega_r}{\omega_b} \right) \left[\left(\frac{L_d}{L_b} \right) \left(\frac{i_{ds}^r}{I_b} \right) + \frac{\lambda_{af}}{\lambda_b} \right] \text{ (p.u.)} \quad (3.86)$$

Defining the normalized parameters and variables in the following manner:

$$R_{sn} = \frac{R_s}{Z_b} \text{ (p.u.)}, \quad L_{qn} = \frac{L_q}{L_b} \text{ (p.u.)}, \quad L_{dn} = \frac{L_d}{L_b} \text{ (p.u.)}, \quad \omega_m = \frac{\omega_r}{\omega_b} \text{ (p.u.)}$$

$$i_{qsn}^r = \frac{i_{qs}^r}{I_b} \text{ (p.u.)}, \quad i_{dsn}^r = \frac{i_{ds}^r}{I_b} \text{ (p.u.)}, \quad v_{qsn}^r = \frac{v_{qs}^r}{V_b} \text{ (p.u.)}, \quad v_{dsn}^r = \frac{v_{ds}^r}{V_b} \text{ (p.u.)} \quad (3.87)$$

and substituting Equation 3.87 in Equation 3.86, v_{qsn}^r is obtained as

$$v_{qsn}^r = \left(R_{sn} + \frac{L_{qn}}{\omega_b} p \right) i_{qsn}^r + \omega_m (L_{dn} i_{dsn}^r + \lambda_{afn}) \text{ (p.u.)} \quad (3.88)$$

Similarly, the d-axis stator voltage equation is normalized and given below:

$$v_{dsn}^r = -\omega_m L_{qn} i_{dsn}^r + \left(R_{sn} + \frac{L_{dn}}{\omega_b} p \right) i_{dsn}^r \text{ (p.u.)} \quad (3.89)$$

The electromagnetic torque has been derived as

$$T_e = \frac{3}{2} \frac{P}{2} \left[\lambda_{af} + (L_d - L_q) i_{ds}^r \right] i_{qs}^r \text{ (N} \cdot \text{m)} \quad (3.90)$$

Dividing this by the base torque normalizes the air gap torque. For normalization, a definition of the base torque is required and it is given as

$$T_b = \frac{P_b}{\frac{\omega_b}{P/2}} = \frac{P}{2} \frac{P_b}{\omega_b} = \frac{P}{2} \frac{3}{2} \frac{V_b I_b}{\omega_b} = \frac{P}{2} \frac{3}{2} \frac{\omega_b \lambda_b I_b}{\omega_b} = \frac{3}{2} \frac{P}{2} \lambda_b I_b \text{ (N·m)} \quad (3.91)$$

from which the normalized electromagnetic torque is obtained as

$$T_{en} = \frac{T_e}{T_b} = \left(\frac{i_{qs}^r}{I_b} \right) \left[\left(\frac{\lambda_{af}}{I_b} \right) - \left(\frac{i_{ds}^c}{I_b} \right) \left(\frac{L_d - L_q}{L_b} \right) \right] = i_{qs}^r \left[\lambda_{afn} - (L_{dn} - L_{qn}) i_{ds}^r \right] \text{ (p.u.)} \quad (3.92)$$

where

$$\lambda_{afn} = \frac{\lambda_{af}}{\lambda_b} \text{ (p.u.)} \quad (3.93)$$

The electromechanical dynamic equation is given by

$$T_e = J \frac{d\omega_m}{dt} + T_l + B\omega_m \quad (3.94)$$

where

ω_m is the mechanical rotor speed

J is the moment of inertia of the load and machine combined

B is the friction coefficient of the load and the machine, and T_l is the load torque

Normalizing this equation as

$$\begin{aligned} T_{en} &= \frac{T_e}{T_b} = \frac{J \frac{d\omega_m}{dt}}{\left(\frac{P_b \times P/2}{\omega_b} \right)} + \frac{T_l}{T_b} + \frac{B\omega_m}{\left(\frac{P/2 \times P_b}{\omega_b} \right)} = \frac{J \omega_b \omega_b}{(P/2)^2 P_b} \frac{d}{dt} \left(\frac{\omega_r}{\omega_b} \right) + T_{ln} + \frac{B \omega_b \omega_b \omega_r}{(P/2)^2 P_b \omega_b} \\ &= \frac{J \omega_b^2}{(P/2)^2 P_b} \frac{d\omega_m}{dt} + T_{ln} + \frac{B \omega_b^2}{(P/2)^2 P_b} \omega_m = 2H\omega_m + T_{ln} + B_n \omega_m \end{aligned} \quad (3.95)$$

where

$$H = \frac{1}{2} \frac{J \omega_b^2}{P_b (P/2)^2} \text{ (s)} \quad (3.96)$$

is known as the inertial constant and the normalized friction constant is

$$B_n = \frac{B \omega_b^2}{P_b (P/2)^2} \quad (3.97)$$

The normalized equations of the PMSM in rotor reference frames are given by Equations 3.88, 3.89, 3.92, and 3.95.

3.11 DYNAMIC SIMULATION

The dynamic simulation of the PMSM is explained in this section. The equations of the PMSM in rotor reference frames in normalized units are assembled and in a form that facilitates the computer solution as

$$p i_{qsn}^r = \omega_b \left(-\frac{R_{sn}}{L_{qn}} i_{qsn}^r - \frac{L_{dn}}{L_{qn}} \omega_m i_{dsn}^r - \frac{\lambda_{afn}}{L_{qn}} \omega_m + \frac{1}{L_{qn}} v_{qsn}^r \right) \quad (3.98)$$

$$p i_{dsn}^r = \omega_b \left(\frac{L_{qn}}{L_{dn}} \omega_m i_{qsn}^r - \frac{R_{sn}}{L_{dn}} i_{dsn}^r + \frac{1}{L_{dn}} v_{dsn}^r \right) \quad (3.99)$$

$$p \omega_m = \frac{1}{2H} \left(\lambda_{afn} i_{qsn}^r - (L_{dn} - L_{qn}) i_{dsn}^r i_{qsn}^r - B_n \omega_m - T_{en} \right) \quad (3.100)$$

$$p \theta_r = \omega_r = \omega_m \omega_b \quad (3.101)$$

The last equation is added to find the rotor position as it is of crucial importance in determining the voltage and current in each phase of the machine. The rotor position is in radians, and not in normalized units to enable the instantaneous current or voltage command generation as a function of time. It is seen that these system equations are nonlinear as, products of variables are involved. Therefore, the only way the system solution can be obtained is by a numerical solution. The solution of the system is then obtained by integrating the differential equations. The Runge–Kutta Gill method can be used for numerical integration or in the case illustrated in the MATLAB program, a simple solution by discretization can be obtained.

The inputs are q^r - and d^r -axes stator voltages, which are obtained from the abc stator voltages by the transformation of T_{abc} . The transformation requires a rotor position that is obtained at every step of the solution. Then the solution of the equation leads to the solution of the stator currents in the rotor reference frames, speed, and rotor position. The abc phase currents can be obtained from dq currents in rotor reference frames by using the inverse transformation matrix. From the dq stator currents, the electromagnetic torque is obtained for plotting. This is updated for every step of integration until the desired final time is reached in the iteration. The steps involved in the solution are shown in the flowchart given in [Figure 3.11](#).

Using the flowchart and machine parameters given in previous examples, the simulation of a direct line-starting of the PMSM is illustrated in the accompanying MATLAB program. The performance under the condition of simulation is shown in [Figure 3.12](#). There is no control imposed on the PMSM based on its rotor position in this simulation. Because of this, the stator currents attain high values with the attendant oscillation in air gap torque, resulting in a significant oscillation of the rotor. Such an operation is undesirable. For this simulation, the load torque is considered to be zero and the applied phase voltages are equal to the base voltage in magnitude

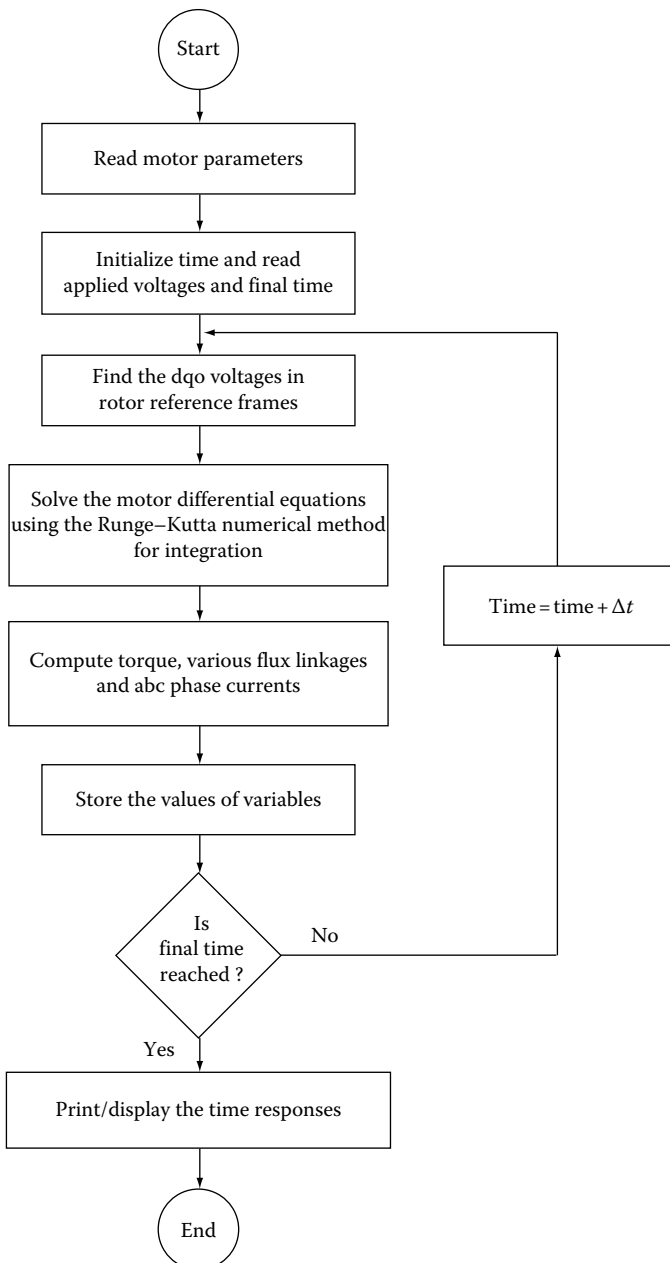


FIGURE 3.11 Flowchart for dynamic simulation of the PMSM.

and a set of balanced three-phase voltages is impressed at 60 Hz. The q- and d-axes stator voltages in the rotor reference frames are not constants but oscillatory in this example. It is because the rotor position derived from rotor speed is oscillatory. The oscillatory rotor position influences the stator currents in rotor reference frames because the transformation matrix is solely a function of rotor position.

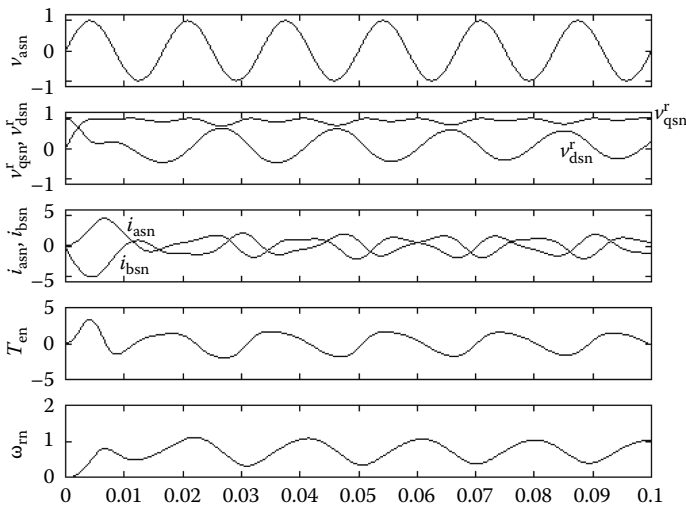


FIGURE 3.12 Dynamic simulation results in normalized units with line-start of the PMSM.

```
% Line start Dynamic simulation of the PMSM using per unit model.
%
% Pb - Base power, Tb- Base torque, Ib- Base current, P - Poles,
% lamaf- rotor flux linkages, Rs - stator resistance per phase,
% lq- q axis inductance, ld- d axis inductance, ro- saliency ratio
%
clear all;close all;
m=0;
lq=0.0125; ld=0.0057; ro=lq/ld;Rc=416;lamaf=0.123; Rs=1.2;
Pb=890;Tb=2.43;Ib=4.65;P=4;
ws=(2*pi*1800/60)*P/2; % Stator frequency, rad/sec
B=0.0005; % Friction coefficient of load and machine
J=0.0002; % Moment of inertia of load and machine
tln=0; % Load torque, p.u.
%Base values
Vb=Pb/(3*Ib); % Base voltage
zb=Vb/Ib; % Base impedance
lamb=lamaf; % Base flux linkages
lb=lamb/Ib; % Base inductance
wb=Vb/lamb; % Base speed
rsn=Rs/zb; % Normalized resistance
lqn=lq/lb; % Normalized q axis inductance
ldn=ld/lb; % Normalized d axis resistance
Bn= B*wb^2/(Pb*(P/2)^2); % Normalized friction coefficient
H=J*wb^2/(2*Pb*(P/2)^2); % Normalized inertia
lamafn=lamaf/lamb; % Normalized rotor flux linkages
% Actual base power is 890W for this machine.
% Initial conditions.
x1=0; % q axis current in rot. ref. frames, p.u.
x2=0; % d axis current in rot. ref. frames, p.u.
x3=0, % Rotor speed, p.u.
x4=0; % Instantaneous rotor position, rad
tp=2*pi/3;
```

```

n=1;
dt=0.0001; % Integration step interval, sec
for t=0:0.0001:0.1;
    wst=ws*t; % Stator phase angle;
    vabc= [sin(wst); sin(wst-tp); sin(wst+tp)]; % abc voltage vector
    % transformation to dq axis in the rotor
    T=2/3*[cos(x4) cos(x4-tp) cos(x4+tp)]; %abc to qdo change.
    sin(x4) sin(x4-tp) sin(x4+tp);
    0.5 0.5 0.5];
    vqdo=T*vabc; % qdo axes voltages in rot. ref.
    %q axis volt.eqn
    x1=x1+dt*wb*(-rsn/lqn*x1-x3*ldn/lqn*x2+1/lqn*(vqdo(1)-x3*lamafn));
    x2=x2+dt*wb*(x3*lqn/ldn*x1-rsn/ldn*x2+vqdo(2)/ldn); %d axis volt. eqn
    Ten=(lamafn-(ldn-lqn)*x2)*x1;% Electromagnetic torque
    x3=x3+dt*(Ten-Bn*x3-tln)/(2*H); % Rotor speed equation
    x4=x4+dt*x3*wb; % Rotor position equation
    %q axis volt.eqn
    %q axis volt.eqn
    iqgd=[x1;x2]; % qd stator currents in rotor ref. frames
    T1=[cos(x4) sin(x4); sin(x4) cos(x4)]; % Transformation from qd to abc
    currents
    cos(x4-tp) sin(x4-tp);
    cos(x4+tp) sin(x4+tp)];
    iabc=T1*iqgd; % abc current vector
    % Storing variables for plotting
    vas(n)=vabc(1); % a phase voltage
    vqs(n)=vqdo(1); % q axis stator voltage in rot. ref.
    vds(n)=vqdo(2); % d axis stator voltage in rot. ref.
    ias(n)=iabc(1); % a phase current
    ibs(n)=iabc(2); % b phase current
    Te(n)=Ten; % Torque
    speed(n)=x3; % Speed
    time(n)=t; % time
    n=n+1;
end
% Computation ends and plotting begins
subplot(5,1,1); % Five plots are produced
plot(time,vas,'k');
axis([0 0.1 -1.2 1.2]);set(gca,'xticklabel',[]);
subplot(5,1,2);
plot(time,vqs,'k',time,vds,'k');
axis([0 0.1 -1.2 1.2]);set(gca,'xticklabel',[]);
subplot(5,1,3)
plot(time,ias,'k',time,ibs,'k');
axis([0 0.1 -6 6]);set(gca,'xticklabel',[]);
subplot(5,1,4);
plot(time,Te,'k');
axis([0 0.1 -5 5]);set(gca,'xticklabel',[]);
subplot(5,1,5);
axis([0 0.1 0 1.2]);plot(time,speed,'k');

```

For a better operation of the PMSM, consider a simple closed loop control by which the rotor position is utilized to set phase a voltage as a sinusoid of rotor position and a fixed angle α . The b and c phase voltages are similarly derived. The angle α is known as the stator voltage phasor angle. More on this will be encountered in the

section on control strategies for PMSM drives. The magnitude of the phase voltages is given as a function of the rotor speed plus an offset voltage as

$$V_m = K_b \omega_r + 1 \text{ (V)} \quad (3.102)$$

where

ω_r is the rotor speed

K_b is the proportionality or emf constant

The offset voltage overcomes the stator resistance voltage drop to make it feasible to generate a current at the time of starting from standstill. Readers familiar with inverter driven induction motor drives may realize that the offset voltage serves the same purpose in the volt/Hertz control too. Assuming that the base voltage is V_b , the normalized phase voltage is written as

$$v_{asn} = \frac{V_m}{V_b} \sin(\omega_r t + \alpha) \text{ (p.u.)} \quad (3.103)$$

The load torque is maintained at zero but there is a friction torque in the drive system. These modifications can be introduced in the above MATLAB program in two lines and results can be obtained for various torque and other operating conditions. To get more insight into the operation of the machine, an analytical correlation to the simulation results are important and are left as exercise for the readers. The performance of the drive system under this condition in normalized units is shown in Figure 3.13.

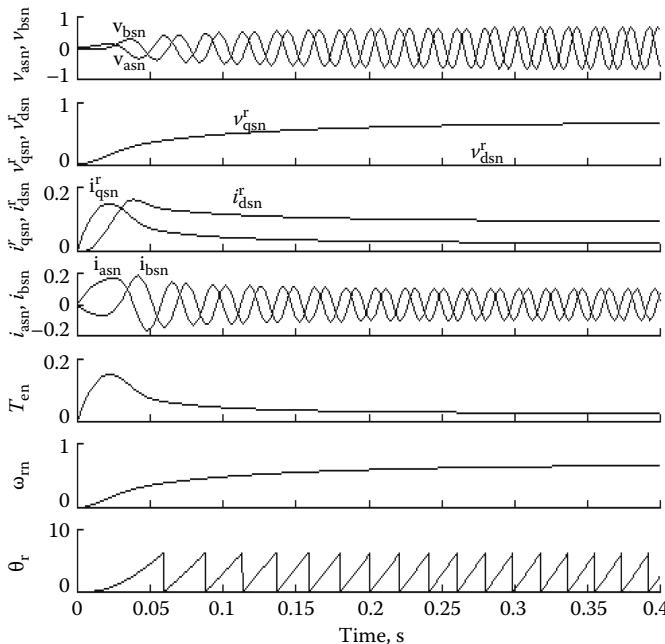


FIGURE 3.13 PMSM dynamic performance in normalized units with rotor position feedback with the voltage phasor leading the rotor flux linkages by 90 electrical degrees and voltage as a function of rotor speed.

The voltage rises in proportion to the speed. The angle between the rotor flux linkages and the voltages is maintained at 90° , i.e., $\alpha=90^\circ$. The air gap torque is nonoscillatory and decreases as the currents come down in magnitude due to the induced emfs rising with increasing speed. It is assumed that the voltage, and the frequency of the voltages and their phases can be programmed from the control signals. It is to be noted that very basic feedback control stabilizes this motor drive when compared to the previous case where there was no feedback control at all.

3.12 SMALL-SIGNAL EQUATIONS OF THE PMSM

3.12.1 DERIVATION

The electrical equations of the PMSM and the electromechanical subsystems given in Equations 3.98 through 3.101 combine to give the dynamic equations of the motor-load system. These dynamic equations are nonlinear as some of the terms are the products of two current variables or a current variable and a rotor speed. For a controller design with linear control system design techniques, the nonlinear dynamic equations cannot be directly used. They have to be linearized around an operating point using perturbation techniques. For small-signal inputs or disturbances, the linearized equations are valid. The ideal model for perturbation to get the linearized model is that one with steady-state operating state variables as dc values. This is possible only with the rotor reference frames model of the PMSM. The linearized equations are obtained as follows.

The voltages, currents, torque, stator frequency, and rotor speed in their steady states are designated by an additional subscript with an “o” in the variables and in capital letters, and the perturbed increments designated with a δ preceding the variables. Accordingly, the variables in the SI units after perturbation are

$$v_{qs}^r = V_{qso}^r + \delta v_{qs}^r \quad (3.104)$$

$$v_{ds}^r = V_{dso}^r + \delta v_{ds}^r \quad (3.105)$$

$$i_{qs}^r = I_{qso}^r + \delta i_{qs}^r \quad (3.106)$$

$$i_{ds}^r = I_{dso}^r + \delta i_{ds}^r \quad (3.107)$$

$$T_e = T_{eo} + \delta T_e \quad (3.108)$$

$$T_l = T_{lo} + \delta T_l \quad (3.109)$$

$$\omega_r = \omega_{ro} + \delta \omega_r \quad (3.110)$$

where

$$T_{eo} = \frac{3}{2} \frac{P}{2} (\lambda_{af} - (L_d - L_q) I_{dso}^r) I_{qso}^r \quad (3.111)$$

By substituting Equations 3.104 through 3.111 into the system equations and neglecting the second-order terms, and canceling the steady-state terms on the right- and left-hand sides of the equations, the small-signal dynamic equations are obtained. The small-signal equations are

$$\delta v_{qs}^r = (R_s + L_s p) \delta i_{qs}^r + \omega_{ro} L_d \delta i_{ds}^r + (L_d I_{dso}^r + \lambda_{af}) \delta \omega_r \quad (3.112)$$

$$\delta v_{ds}^r = -\omega_{ro} L_q \delta i_{qs}^r + (R_s + L_d p) \delta i_{ds}^r - L_q I_{qso}^r \delta \omega_r \quad (3.113)$$

$$Jp \delta \omega_r + B \delta \omega_r = \frac{P}{2} (\delta T_e - \delta T_i) \quad (3.114)$$

$$p \delta \theta_r = \delta \omega_r \quad (3.115)$$

$$\delta T_e = \frac{3}{2} \frac{P}{2} \left(\lambda_{af} \delta i_{qs}^r + (L_d - L_q) \{ I_{dso}^r \delta i_{qs}^r + I_{qso}^r \delta i_{ds}^r \} \right) \quad (3.116)$$

Combining Equations 3.112 through 3.116, and casting them in a state-space form gives

$$pX = AX + BU \quad (3.117)$$

where

$$X = [\delta i_{qs}^r \quad \delta i_{ds}^r \quad \delta \omega_r \quad \delta \theta_r]^t \quad (3.118)$$

$$U = [\delta v_{qs}^r \quad \delta v_{ds}^r \quad \delta T_i]^t \quad (3.119)$$

$$A = \begin{bmatrix} -\frac{R_s}{L_q} & -\frac{L_d}{L_q} \omega_{ro} & -(\lambda_{af} + L_d I_{dso}^r) & 0 \\ \frac{L_q}{L_d} \omega_{ro} & -\frac{R_s}{L_d} & \frac{L_q}{L_d} I_{qso}^r & 0 \\ k_1 \{\lambda_{af} + (L_d - L_q) I_{dso}^r\} & k_1 (L_d - L_q) I_{dso}^r & -\frac{B}{J} & 0 \\ 0 & 0 & 1 & 0 \end{bmatrix} \quad (3.120)$$

$$B = \begin{bmatrix} \frac{1}{L_q} & 0 & 0 \\ 0 & \frac{1}{L_d} & 0 \\ 0 & 0 & -\frac{P}{2J} \\ 0 & 0 & 0 \end{bmatrix} \quad (3.121)$$

$$k_l = \frac{3}{2} \left(\frac{P}{2} \right)^2 \frac{1}{J} \quad (3.122)$$

The output of interest can be a function of the state variables and inputs and it is expressed as

$$y = CX + DU \quad (3.123)$$

where C and D are now vectors of appropriate dimensions. The system and its output are described by Equations 3.117 and 3.123, respectively. For the sake of compactness in the formulation, the load torque, which is a disturbance, has been absorbed as an input.

3.13 EVALUATION OF CONTROL CHARACTERISTICS OF THE PMSM

The control characteristics of the PMSM consist of stability, and frequency and time responses. They require the evaluation of various transfer functions. Stability is evaluated by finding the eigenvalues of the system matrix A in Equation 3.119. It can be found using standard subroutines available in a software library. The evaluation of transfer functions, frequency, and time responses are available in control system simulation libraries. Simple algorithms to develop the above are given [1] in this section for online control implementations in the drive system.

3.13.1 TRANSFER FUNCTIONS AND FREQUENCY RESPONSES

Taking the Laplace transform of Equations 3.117 and 3.123 with the assumption of zero initial conditions gives

$$sX(s) = AX(s) + B_l u(s) \quad (3.124)$$

$$y(s) = CX(s) + Du(s) \quad (3.125)$$

where s is Laplace operator.

Manipulating Equations 3.120 and 3.121, the output is expressed as

$$y(s) = [C(sI - A)^{-1} B_l + D] u(s) \quad (3.126)$$

where I is an identity matrix of appropriate dimensions. Since the transfer function involves one input, the input matrix product is then written as

$$B_l u(s) = b_i u_i(s) \quad (3.127)$$

where b_i is the i th column vector of the B matrix and i corresponds to the element number in the input vector. Then, correspondingly,

$$Du(s) = d_i u_i(s) \quad (3.128)$$

and the resulting equations are

$$\begin{aligned} sX(s) &= AX(s) + b_i u_i(s) \\ y(s) &= CX(s) + d_i u_i(s) \end{aligned} \quad (3.129)$$

The evaluation of transfer functions is made simple if the canonical or phase variable form of the state equation given in Equation 3.117 is found. Assuming that it is effected by the following transformation:

$$X = T_p X_p \quad (3.130)$$

the state and output equations are transformed to

$$pX_p = A_p X_p + B_p u_i \quad (3.131)$$

$$y = C_p X_p + d_i u_i \quad (3.132)$$

where

$$A_p = T_p^{-1} A T_p \quad (3.133)$$

$$B_p = T_p^{-1} b_i \quad (3.134)$$

$$C_p = C T_p \quad (3.135)$$

These matrices and vectors are of the form

$$A_p = \begin{bmatrix} 0 & 1 & 0 \\ 0 & 0 & 1 \\ -m_1 & -m_2 & -m_3 \end{bmatrix} \quad (3.136)$$

$$B_p = [0 \quad 0 \quad 1]^t \quad (3.137)$$

$$C_p = [n_1 \quad n_2 \quad n_3] \quad (3.138)$$

And the transfer function by observation is written as

$$\frac{y(s)}{u_j(s)} = \frac{n_1 + n_2 s + n_3 s^2}{m_1 + m_2 s + m_3 s^2 + s^3} + d_i \quad (3.139)$$

The problem lies in finding the transformation matrix, T_p . An algorithm to construct T_p is given below:

$$\left. \begin{array}{l} T_p = [t_1 \quad t_2 \quad t_3] \\ t_3 = b_i \\ t_{3-k} = At_{3-k+1} + m_{3-k+1}b_i; \quad k = 1, 2 \end{array} \right\} \quad (3.140)$$

where t_1 , t_2 , and t_3 are the column vectors. The last equation needs the coefficients of the characteristic equation and is computed beforehand using the Leverrier algorithm. The Leverrier algorithm is given in the following:

$$\left. \begin{array}{l} m_3 = -\text{trace}(A); \quad H_3 = A + m_3 I \\ m_2 = -\frac{1}{2} \text{trace}(AH_3); \quad H_2 = AH_3 + m_4 I \\ m_1 = -\frac{1}{5} \text{trace}(AH_2) \end{array} \right\} \quad (3.141)$$

where the trace of a matrix is equal to the sum of its diagonal elements. The frequency response is evaluated from Equation 3.126 by substituting, $s = j\omega$ wherever s occurs. The magnitude and phase plots can be drawn over the desired frequency range for the evaluation of the control properties. The computation of time responses is considered next.

3.14 COMPUTATION OF TIME RESPONSES

If the state equation given in Equation 3.117 is transformed into the diagonal form:

$$X = T_d Z \quad (3.142)$$

then the transformed equations are

$$\dot{Z} = T_d^{-1} A T_d Z + T_d^{-1} B U = M Z + H U \quad (3.143)$$

where M is a diagonal matrix with distinct eigenvalues and

$$M = T_d^{-1} A T_d \quad (3.144)$$

$$H = T_d^{-1} B \quad (3.145)$$

solving z_1, \dots, z_n from Equation 3.145:

$$z_n(t) = \left(\sum_{j=1}^m H_{nj} u_j \right) \frac{(-1 + e^{\lambda_n t})}{\lambda_n} \quad (3.146)$$

where

λ_n is the n th eigenvalue

m is the number of inputs

Once vector Z is evaluated by Equation 3.142, the output y is obtained from the following:

$$y = CX + DU = CT_d Z + DU \quad (3.147)$$

With the help of standard software such as MATLAB, the above-mentioned steps need not be programmed as they are available with simple commands. An illustration of MATLAB's elementary capabilities is given in the following example. It needs to be mentioned that the capabilities of MATLAB are manifold when compared to what is illustrated in the problem (Figures 3.14 through 3.16).

Example 3.4

With the given machine data in Example 3.1, find the transfer function between the q-axis stator current and its voltage input in that axis in rotor reference frames, eigenvalues of the system, frequency response with Bode plot, root locus, and step response. The initial conditions are given and they are made use of in the

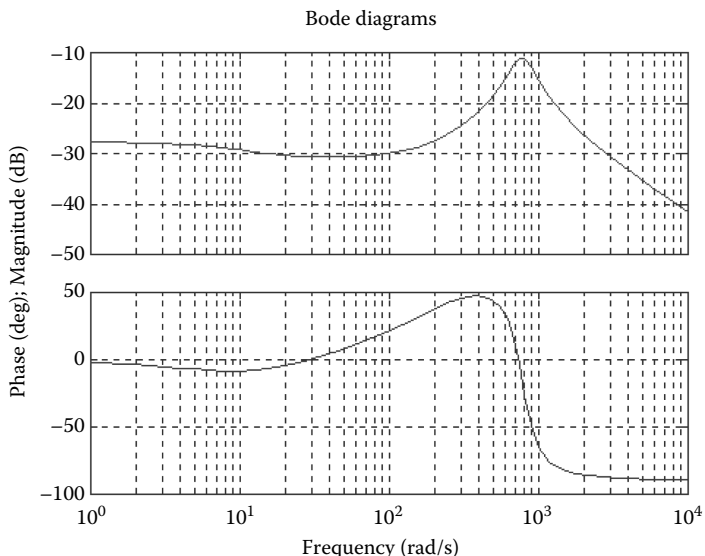


FIGURE 3.14 Bode plot.

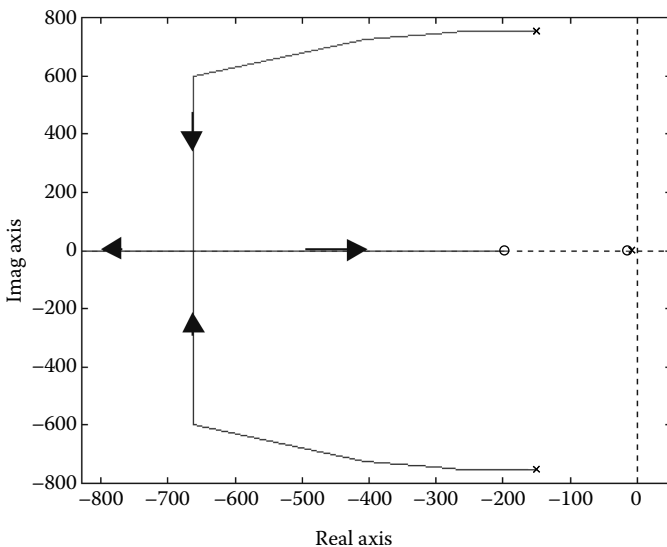


FIGURE 3.15 Root locus plot.

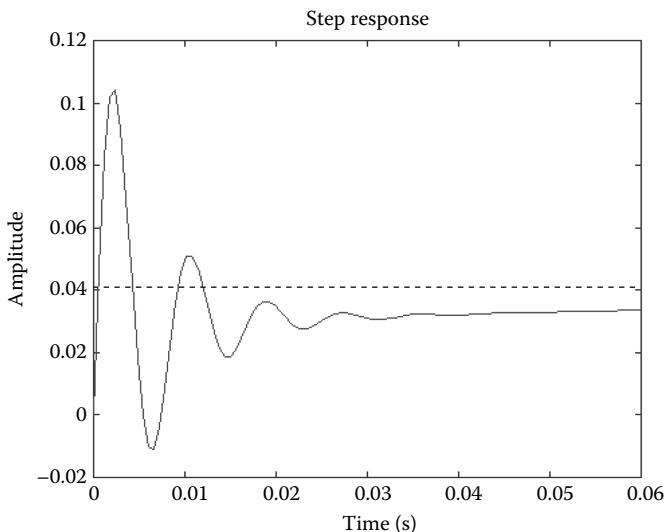


FIGURE 3.16 q-Axis stator current response in rotor reference frames for a step input in the q-axis stator voltage.

evaluation of small-signal system matrices derived and given in Equations 3.120 and 3.121.

Solution

The MATLAB program with very elementary commands to solve the problem is given with the outputs.

```

% To find transfer function, frequency response, root locus,
% and step response.
% Example problem.
%
close all;clear all;
%Data
rs=1.2, lq=0.012;ld=0.0057;lamaf=0.123;P=4;B=0.0001; J= 0.0005;
% Operating steady state values
wro=2*pi*120;Iqso=4; Idso=-2;
% System A matrix
k1=3/2*(P/2)^2/J;
A=[-rs/lq -(ld/lq)*wro -(lamaf+ld*Idso);
   wro*lq/ld -rs/ld (lq/ld)*Iqso;
   k1*(lamaf+(ld-lq)*Idso) k1*(ld-lq)*Iqso -B/J ];
B=[1/lq 0 0; 0 1/ld 0; 0 0 -P/(2*J)];
C= [1 0 0];
D= [0 0 0];
% The transfer function is between q axis stator current and q axis
stator
% voltage, which is the first input in the input vector.
IU=1; % Chosen input
% Find the transfer function
[num,den]=ss2tf(A,B,C,D,IU) % Numerator and denominator
G1=tf(num,den) % G1 is the transfer function
% Express the transfer function in the zero, pole and gain form
zpktf=zpk(G1) % G1 is zero,pole and gain form
% Eigenvalues of the system
K=eig(A) % Eigenvalues of the system
% Poles of the transfer function are also given by the following
command
K1=pole(G1) % Alternate way of finding them
% Frequency response with Bode plot
figure(1) % Frequency response plot
bode(G1);
%Root locus plot
figure(2) % Root locus plot
rlocus(G1);
% Step response
figure(3) % Step response plot of G1 for 0.06 s
step(G1,0.06);

num = 1.0e+005 *
      0          0.0008  0.1756  2.1572
den = 1.0e+006 *
      0.0000     0.0003  0.5923  5.2647
Transfer function:
83.33 s^2 + 1.756e004 s + 2.157e005
-----
s^3 + 310.7 s^2 + 5.923e005 s + 5.265e006
Zero/pole/gain:
83.3333 (s+197.6) (s+13.1)
-----
(s+8.929) (s^2 + 301.8s + 5.896e005)

```

```

K =                               (Eigenvalues)
 1.0e+002 *
 -1.5090+ 7.5291i
 -1.5090- 7.5291i
 -0.0893

K1 =                               (Poles)
 1.0e+002 *
 -1.5090+ 7.5291i
 -1.5090- 7.5291i
 -0.0893

```

3.15 SPACE PHASOR MODEL

3.15.1 PRINCIPLE

The stator flux linkages phasor is the resultant stator flux linkages found by taking the vector sum of the respective d and q components of the flux linkages. Note that the flux linkages phasor describes its spatial distribution. Instead of using two axes such as the d and q for a balanced polyphase machine, the flux linkage phasor can be thought of being produced by an equivalent single-phase stator winding. Such a representation has many advantages but only in symmetric machines such as the PMSM with surface mounted magnets: (1) the system of equations could be compact and reduced from two to one, (2) the system reduces to a single winding system such as the dc machine and hence the apparent similarity of it with the consequent control analogue to obtain a decoupled independent flux and torque control as in the dc machine, (3) a clear conceptualization of the dynamics of the machine as it is easier to visualize the interaction of one winding and the rotor magnet flux rather than two windings and the magnet rotor, resulting in an in-depth understanding of the dynamic processes, which are used in developing high-performance control strategies, and (4) an easier analytical solution of the dynamic transients of the machine as it involves only the solution of one differential equation with complex coefficients. Such an analytical solution improves the understanding of the machine behavior in terms of machine parameters leading to the formulation of the machine design requirements for variable speed applications. Such a space phasor model is derived in this section.

3.15.2 MODEL DERIVATION

The PMSM with surface-mount magnets is considered from this section onward. The rotor symmetry together with and assuming that the direct and quadrature axis winding inductances are equal to a value given as L_s give the stator voltage equations with very little change except substituting the q- and d-axes inductances with L_s . The voltage, current, and stator flux linkage phasors in the rotor reference frames as the result of their d- and q-axes components are defined as

$$v_s^r = v_{qs}^r - jv_{ds}^r \quad (3.148)$$

$$i_s^r = i_{qs}^r - ji_{ds}^r \quad (3.149)$$

$$\lambda_s^r = \lambda_{qs}^r - j\lambda_{ds}^r \quad (3.150)$$

Using this definition for the current and voltage phasor, the stator voltage phasor for the PMSM with surface mount magnets is derived as

$$v_s^r = (R_s + L_s p) i_s^r + j\omega_r \lambda_s^r \quad (3.151)$$

The q- and d-axes components of the flux linkages are defined as in the earlier and given below:

$$\lambda_{qs}^r = L_s i_{qs}^r \quad (3.152)$$

$$\lambda_{ds}^r = L_s i_{ds}^r + \lambda_{af} \quad (3.153)$$

These two are combined to get the flux linkages phasor from which the stator current phasor is derived as

$$i_s^r = \frac{\lambda_s^r + j\lambda_{af}}{L_s} \quad (3.154)$$

Substituting this into the voltage phasor equation and with the assumption that the variation in the rotor flux linkages with time is to be zero, which actually is the case in a PM motor, the resulting stator voltage phasor is

$$v_s^r = \left(p + \frac{1}{\tau_s} + j\omega_r \right) \lambda_s^r + j \frac{\lambda_{af}}{\tau_s} \quad (3.155)$$

It is then seen that the machine stator is represented by one complex equation with one complex time constant. The real part of the root of the system is given by the inverse stator time constant and the imaginary part of the root is given by the electrical rotor speed of the system. The first part contributes to the response term of exponential nature and the second part contributes to the phase. This part has come in because the model is in rotor reference frames obtained by the phase rotation added to the stationary reference frames model. The eigenvalue has a physical interpretation in this model because of the above explained facts. The block diagram of the PMSM in space phasors is derived from the stator voltage phasor equation (Equation 3.155) and shown in [Figure 3.17](#).

In the two stator windings model, the eigenvalues are given by the root of the space phasor model and its complex conjugate. Even though the eigen frequencies are different, i.e., one is positive and the other negative, note that the damping is preserved as the real terms are the same regardless of the model.

Importantly, a single eigenvalue and a single time constant powerfully evoke the similarity of this machine to the dc machine armature and its PM field to the field of the dc machine. Since the dynamics of the PM field is ignored as it is assumed to be

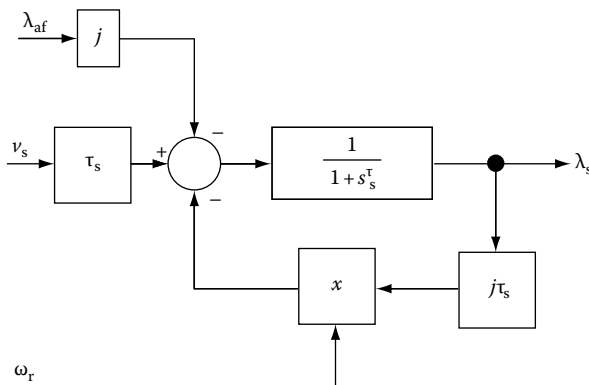


FIGURE 3.17 Space phasor model of the electrical part of the PMSM.

a constant, it does not enter into the picture except in the form of motional emf generated in the machine. Since the similarity to the dc machine is seen through the space phasor model, likewise the speed control similarity between the armature-controlled dc and the PMSM becomes evident. Therefore, a decoupled control of its mutual flux linkages and electromagnetic torque can be obtained in the PMSM also.

In the separately excited dc machine, both the armature and field currents are independently controlled through their windings. Keeping the field current constant, and then varying the armature current only, varies the electromagnetic torque. Thus, both the field flux and air gap torque are controlled without any coupling between the two windings and only with the magnitude control of the armature and field currents. The phase relationship between the main field and the armature field is spatially fixed by the commutator and brushes in the dc machine, thus performing the task of the inverter with this arrangement. In the case of the PMSM, the armature current may be thought of as the stator current phasor and the rotor field as the main field. The spatial relationship between them is maintained by moving the stator current phasor in synchronism with the rotor, thus keeping the phase between them a constant under constant load or a variable under dynamic condition. Therefore, the stator current phasor both in its magnitude and in phase has to be controlled to maintain the synchronism between its rotor field and its armature field. This is achieved through the inverter and its control. Most essentially, the position of the rotor field, i.e., absolute rotor position, must be known to enforce this control unlike in the case of the dc machine. Such a requirement of instantaneous rotor position places a higher cost burden even for basic operations of this motor drive unlike the dc and induction motor drives. The position can either be sensed with a sensor or estimated from the machine variables or measured using an additional injection of signals into the machine and presented in Chapter 8.

Example 3.5

Compute the stator flux linkages phasor and stator current phasor, and plot the stator flux linkages magnitude, current phasor magnitude, and air gap torque when

the speed is maintained constant at 3500 rpm and the applied voltage phasor is $j40V$.

Solution

The stator flux linkages phasor is obtained from the time domain solution of the voltage phasor equation, given in Equation 3.155, assuming that the applied voltage and rotor flux linkages are constant in magnitude as

$$\lambda_s^r = \frac{V(0 + j1) - j \frac{\lambda_{af}}{\tau_s}}{\frac{1}{\tau_s} + j\omega_r} \left[1 - e^{-\left(\frac{1}{\tau_s} + j\omega_r\right)t} \right] (\text{V}\cdot\text{s})$$

from which the stator current is derived and then the air gap torque is computed using the relationship given in Equation 3.151.

The MATLAB program is given in the following and the performance of the system is illustrated in Figures 3.18 through 3.20 depicting the loci of the stator flux linkages and the stator current, and the magnitudes of the stator current and flux linkages versus time, and finally the electromagnetic torque versus time, all in normalized units.

The MATLAB program to compute the transient response using space phasor model for Example 3.5 is given below.

```
% To compute the transient response of flux linkages for PMSM using
% the
% Space Phasor Model (SPM) of the machine for the example problem.
```

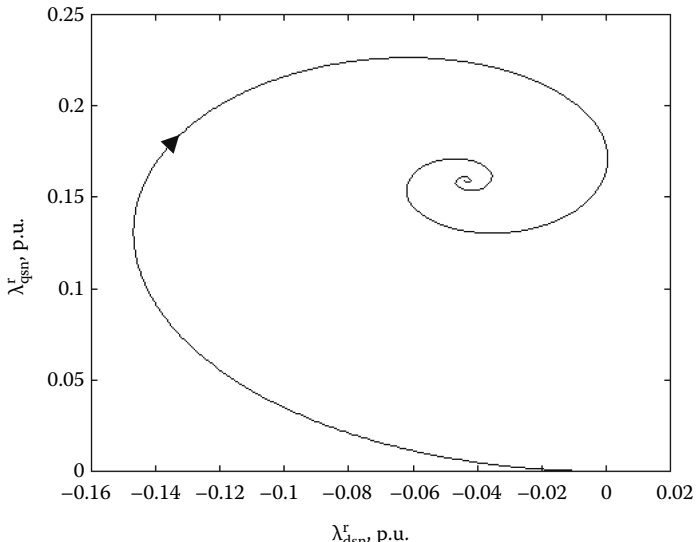


FIGURE 3.18 Trajectory of the stator flux linkages phasor for the voltage input when the machine speed is constant.

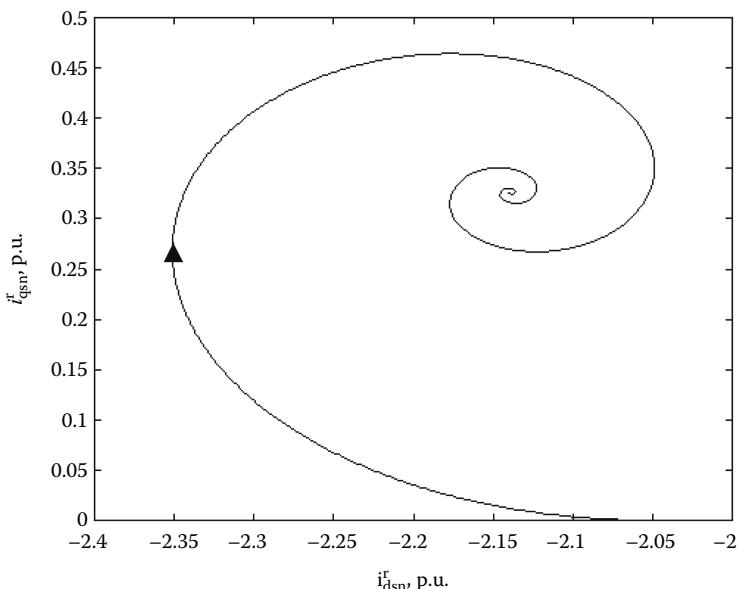


FIGURE 3.19 Trajectory of the current phasor under constant speed and a voltage input.

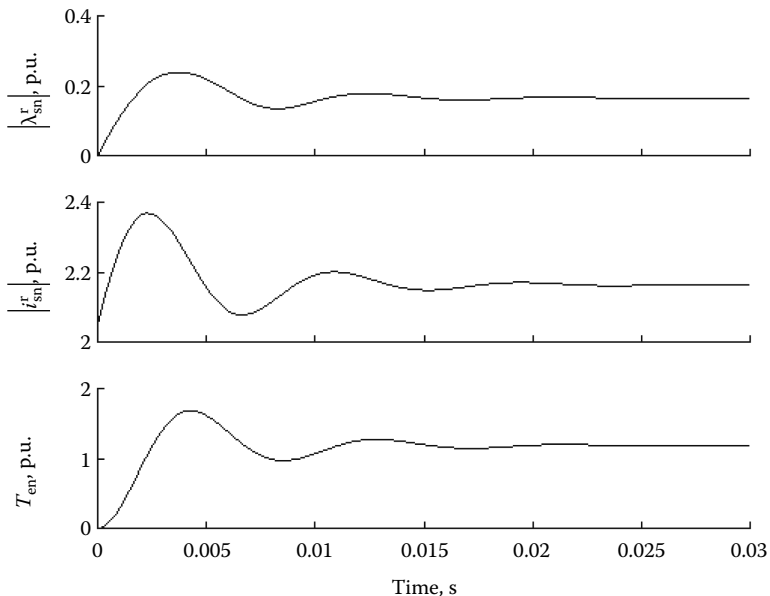


FIGURE 3.20 Magnitude of stator flux linkages and current phasors and air gap torque under constant speed and a voltage input.

```
close all; clear all;
% Input data
lamaf=0.123; % Rotor flux linkages
Rs=1.2; % Stator phase resistance
Ls=0.006; % Inductance
```

```

ts=Ls/Rs; % Stator time constant
P=4; % Number of poles
w=(2*pi*3500/60)*P/2; % Rotor speed in elec. rad/sec
V=40; % Stator voltage magnitude
a=0;b=1; % Stator phasor voltage components,
V(a+jb)
n=0; % Iteration number
% Base values
Ib=10; % Base current
lamb=lamaf; % Base flux linkages
wb = w; % Base speed, elec. rad/sec.
Pb=745.6; % Base power, W
Tb=Pb*(P/2)/wb % Base torque, N.m.
% Computation begins
for t = 0:0.00001:0.0299999 % Beginning of do loop for time
    n = n+1;
    lams = (V*(a+b*i)-lamaf*i/ts)*(1-exp((-1/ts-w*i)*t))/(1/ts+w*i); % Stator flux linkages phasor
    lamq(n)=real(lams)/lamb; % p.u. q axis stator flux linkages
    lamd(n)=-imag(lams)/lamb; % p.u. d axis stator flux linkages
    mag(n)=abs(lams)/lamb; % Magnitude of stator flux linkages,p.u.
    is(n)=(lams+lamaf*i)/Ls; % Stator current phasor,A
    te(n)=1.5*P*imag(conj(lams)*is(n))/Tb; % Air gap torque,p.u.
    isn(n)=abs(is(n))/Ib; % Stator current magnitude, p.u.
    time(n)=t; % time
end
% Computation ends and plotting begins
figure(1); % D axis vs. q axis stator flux linkages
figure(2); % D vs. q axis stator current
figure(3);
subplot(3,1,1) % Stator flux linkages phasor magnitude vs. time
plot(time,mag,'k'); set(gca,'xticklabel',[]);box off;
subplot(3,1,2) % Stator current phasor magnitude vs. time
plot(time,isn,'k'); set(gca,'xticklabel',[]);box off;
subplot(3,1,3) % Air gap torque vs. time
plot(time,te,'k');box off;

```

So far, there is no distinct advantage in computation in using the space phasor model as against the dq model since the solution of eigenvalues in the dq model involves only a second-order system, which is analytically achievable. The real merit will come in when the space phasor PMSM representation is taken and coupled to the load through the load equation as in the following. The electromagnetic torque is derived as

$$T_e = \frac{3}{2} \frac{P}{2} \text{Im}[\lambda_s^* i_s^r] \quad (3.156)$$

where Im indicates the imaginary part and the asterisk, the conjugate of that variable. Substituting this in the load equation and taking the Laplace transform of it gives

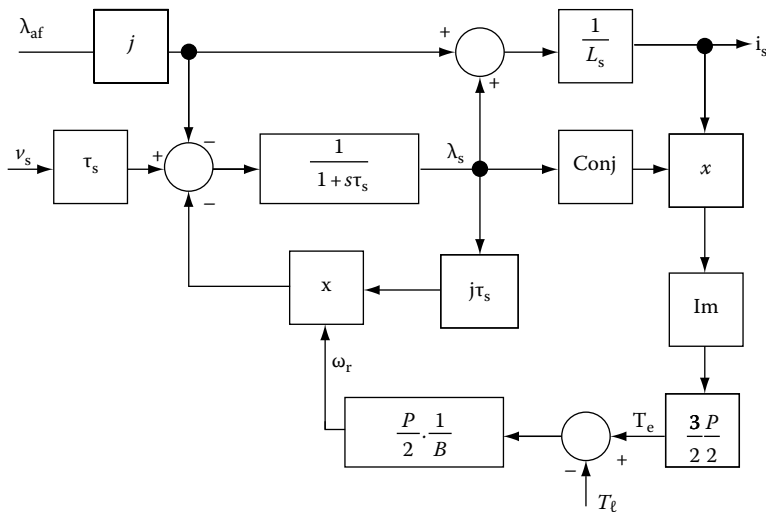


FIGURE 3.21 Space phasor model of the PMSM with load.

$$\omega_r(s) = \frac{1}{(1+s\tau_m)} \frac{P}{2} \frac{1}{B} \left[\frac{3}{2} \frac{P}{2} \text{Im}\{\lambda_s^* i_s^*\} - T_\ell \right] \quad (3.157)$$

After substituting it for the stator current phasor in this expression, the complete block diagram of the PMSM incorporating the load dynamics is shown in Figure 3.21. The signal flow from one to another point is very clear in this diagram with much less complexity than with the block diagram of the dq model. Because of this, it is quite straightforward to analyze control strategies, sensorless control schemes, and parameter sensitivity effects and their compensation schemes. Further, the small-signal eigenvalues of the total system are only two as against three in the dq model based block diagram. This has the distinct advantage of an analytic solution when compared to the numerical solution required with the dq model.

The interior PMSM with rotor saliency can be modeled in complex variables. Such a formulation is hard to reconcile with the space phasor definition. Hence the elegance and insight that comes with the space phasor representation is lost but the compact representation in complex variables will be achieved. That approach is not pursued any further in this chapter.

REFERENCES

Dynamic Models

1. R. Krishnan, *Electric Motor Drives*, Prentice Hall, Englewood Cliffs, NJ, 2001.
2. N. N. Hancock, *Matrix Analysis of Electrical Machinery*, Pergamon Press, The Macmillan Company, New York, 1964.
3. P. C. Krause, *Analysis of Electrical Machinery*, McGraw-Hill Book Company, New York, 1986.

4. P. K. Kovacs and E. Racz, *Transient Phenomena in Electrical Machines*, Elsevier Science Publishers, Amsterdam, 1984.
5. T. Sebastian, G. R. Slemon, and M. A. Rahman, Modelling of permanent magnet synchronous motors, *IEEE Transactions on Magnetics*, pp. 1069–1071, 1986.
6. P. Pillay and R. Krishnan, Development of digital models for a vector controlled permanent magnet synchronous motor drive, *Conference Record of the Industry Applications Society Annual Meeting (IEEE Cat. No. 88CH2565-0)*, pp. 476–482, 1988.
7. P. Pillay and R. Krishnan, Modeling, simulation, and analysis of permanent-magnet motor drives. I. The permanent-magnet synchronous motor drive, *IEEE Transactions on Industry Applications*, pp. 265–273, 1989.
8. R. Krishnan and G. H. Rim, Performance and design of a variable speed constant frequency power conversion scheme with a permanent magnet synchronous generator, *Conference Record of the IEEE Industry Applications Society Annual Meeting*, pp. 45–50, 1989.

Circuit Parameters and Equivalent Circuits

9. A. Consoli and G. Renna, Interior type permanent magnet synchronous motor analysis by equivalent circuits, *IEEE Transactions on Energy Conversion*, 4(4), 681–689, 1989.
10. A. Consoli and A. Raciti, Analysis of permanent magnet synchronous motors, *IEEE Transactions on Industry Applications*, 27(2), 350–354, 1991.
11. A. Consoli and A. Raciti, Experimental determination of equivalent circuit parameters for PM synchronous motors, *Electric Machines and Power Systems*, 20(3), 283–296, 1992.
12. E. C. Lovelace, T. M. Jahns, and J. H. Lang, A saturating lumped-parameter model for an interior PM synchronous machine, *IEEE Transactions on Industry Applications*, 38(3), 645–650, 2002.
13. B. Stumberger, G. Stumberger, D. Dolinar et al., Evaluation of saturation and cross-magnetization effects in interior permanent-magnet synchronous motor, *IEEE Transactions on Industry Applications*, 39(5), 1264–1271, 2003.

Loss Modeling

14. C. Mi, G. R. Slemon, and R. Bonert, Modeling of iron losses of permanent-magnet synchronous motors, *IEEE Transactions on Industry Applications*, 39(3), 734–742, 2003.
15. F. Giulii Capponi, R. Terrigi, and G. De Donato, A synchronous axial flux PM machine d,q axes model which takes into account iron losses, saturation and temperature effect on the windings and the permanent magnets, *International Symposium on Power Electronics, Electrical Drives, Automation and Motion, 2006. SPEEDAM 2006*, pp. 421–427, 2006.

Finite Element-Based Models

16. O. A. Mohammed, S. Ganu, N. Abed et al., High frequency PM synchronous motor model determined by FE analysis, *IEEE Transactions on Magnetics*, 42(4), 1291–1294, 2006.
17. O. A. Mohammed, S. Liu, and Z. Liu, FE-based physical phase variable model of PM synchronous machines with stator winding short circuit fault, *Sixth International Conference on Computational Electromagnetics CEM 200*, pp. 185–186, 2006.
18. K. Gyu-Hong, H. Jung-Pyo, K. Gyu-Tak et al., Improved parameter modeling of interior permanent magnet synchronous motor based on finite element analysis, *IEEE Transactions on Magnetics*, pp. 1867–1870, 2000.

4 Control Strategies for a Permanent Magnet Synchronous Machine

The freedom to change and control stator currents in a permanent magnet synchronous machine (PMSM), not only in magnitude and frequency, but also in phase, bestows a control equivalent to that of the separately excited dc machine control. The separation of control for torque and mutual flux from each other, termed decoupling or vector control, is presented in this chapter. Additional performance measures such as constant torque angle, unity power factor (UPF), control of angle between flux and current phasors, optimum torque per unit current, constant power loss, and maximum efficiency can be superposed over the vector control and are also described in this chapter. The control strategies are illustrated with steady-state characteristics and, relevant equations for performance prediction are derived and included.

A few references on general dynamic performance [1–5], dynamic simulation [6–12], various control strategies [13–26], direct torque control [27,28], computer programs for analysis [29,30], and application characteristics of PMSMs are given at the end of this chapter. Interested readers are encouraged to find additional recent publications on specific topics.

4.1 VECTOR CONTROL

Vector control, also known as decoupling or field orientated control, came into the field of ac drives research in the late 1960s and was developed prominently in the 1980s to meet the challenges of oscillating flux and torque responses in inverter fed induction and synchronous motor drives [5a]. The inexplicable dynamic behavior of large current transients and the resulting failure of inverters was a curse and barrier to the entry of inverter fed ac drives into the market. Compared to these ac drives, the separately excited dc motor drives were a picture of health with excellent dynamic control of flux and torque. The key to the dc motor drives, performance is its ability to independently control the flux and torque. The flux is controlled by the field current alone and this current may be termed for later use, as, flux-producing current. Keeping the field current constant at any time instant and hence the flux constant, the torque is controlled independently by the armature current alone, and then, this armature current may be seen as the torque-producing current. Controlling the field and armature current magnitudes as they are dc variables, the flux and electromagnetic torque are controlled precisely in a separately excited dc motor drive. Only if such separate and independent controls of flux and torque are feasible, will the problem of dynamic

control go away. The key to it then, lies in finding an equivalent flux-producing current and torque-producing current (i.e., the armature current) in ac machines leading to the control of the flux and torque channels in them. The key to that, for ac drives, came in two forms: (1) the machine modeling in space phasor form, which reduced a three-phase machine into a machine with one winding each on stator and rotor, thereby making it into an equivalent dc machine (explained in Chapter 3) and (2) the ability of the inverter to produce a current phasor with absolute control of its magnitude, frequency, and phase (given in Chapter 2). Both these features are exploited to make the PMSM drive system a high-performance drive system with independent control of its mutual flux and electromagnetic torque and are developed in the following section.

4.2 DERIVATION OF VECTOR CONTROL

The vector control separates the torque and flux channels in the machine through its stator excitation inputs. The vector control for PMSM is very similar to the vector control of induction motor drives. Many variations of the vector control but similar to that of an induction machine are possible. In this section, the vector control of the three-phase PMSM is derived from its dynamic model. Considering the currents as inputs, the three-phase currents are

$$i_{as} = i_s \sin(\omega_r t + \delta) \quad (4.1)$$

$$i_{bs} = i_s \sin\left(\omega_r t + \delta - \frac{2\pi}{3}\right) \quad (4.2)$$

$$i_{cs} = i_s \sin\left(\omega_r t + \delta + \frac{2\pi}{3}\right) \quad (4.3)$$

where

ω_r is the electrical rotor speed

δ is the angle between the rotor field and stator current phasor and known as the torque angle

From Chapter 2, the inverter control of the voltage/current phasor's magnitude, frequency, and phase has been learnt and from now on, it is assumed that the commanded phasor is ideally obtained through the inverter to derive the vector control. The rotor field travels at a speed of ω_r electrical rad/s which is equal to the rotor speed in electrical rad/s. The q- and d-axes stator currents in the rotor reference frames are obtained through the transformation matrix developed in Chapter 3 on the PMSM modeling given by

$$\begin{bmatrix} i_{qs}^r \\ i_{ds}^r \end{bmatrix} = \frac{2}{3} \begin{bmatrix} \cos \omega_r t & \cos\left(\omega_r t - \frac{2\pi}{3}\right) & \cos\left(\omega_r t + \frac{2\pi}{3}\right) \\ \sin \omega_r t & \sin\left(\omega_r t - \frac{2\pi}{3}\right) & \sin\left(\omega_r t + \frac{2\pi}{3}\right) \end{bmatrix} \begin{bmatrix} i_{as} \\ i_{bs} \\ i_{cs} \end{bmatrix} \quad (4.4)$$

Substituting Equations 4.1 through 4.3 into Equation 4.4, the stator currents in the rotor reference frames are obtained as

$$\begin{bmatrix} i_{qs}^r \\ i_{ds}^r \end{bmatrix} = i_s \begin{bmatrix} \sin \delta \\ \cos \delta \end{bmatrix} \quad (4.5)$$

That the q- and d-axes currents are constants in rotor reference frames is to be noted as, the torque angle δ is a constant for a given load torque. At this time, it is very useful to draw the phasor diagram, shown in Figure 4.1 [5a], of the machine from what is known and what could be assumed. The rotor flux and its linkages are on the d-axis of the machine, which is right on the rotor and rotating at the angular velocity of ω_r electrical rad/s measured from a stationary reference point (also termed as the stator reference frame) by its instantaneous position of θ_r radian, which can be obtained from the product of angular velocity and time, assuming that the initial rotor position is zero. The stator current phasor, which is the result of quadrature and direct axes currents in all reference frames (rotor reference frames are used predominantly in synchronous machines control), is supplied at an angular frequency of rotor electrical speed, i.e., ω_r electrical rad/s with a phase of δ radian from the rotor flux linkages phasor. The differential velocity between the current phasor and the rotor (i.e., rotating d-axis) is zero. But it has a phase difference of δ radian, which is a constant for a given torque and programmed into the stator currents. The resolution of the stator current phasor on the rotating direct and quadrature axes (known as rotor reference frames) gives i_{ds}^r and i_{qs}^r , respectively, and they correspond to the current components given by Equation 4.5. Note that they are constants for a given stator current phasor and torque angle. The stator current component along the rotor flux axis, i.e., along the rotating d-axis, can only produce a flux and hence can be appropriately named as the flux-producing component of stator current and denoted as i_f . This current only partially contributes to the d-axis flux and the remaining part of the rotor flux is contributed by the permanent magnets (PMs). The PM flux can be considered as produced by an equivalent current source as derived in Chapter 1. The stator

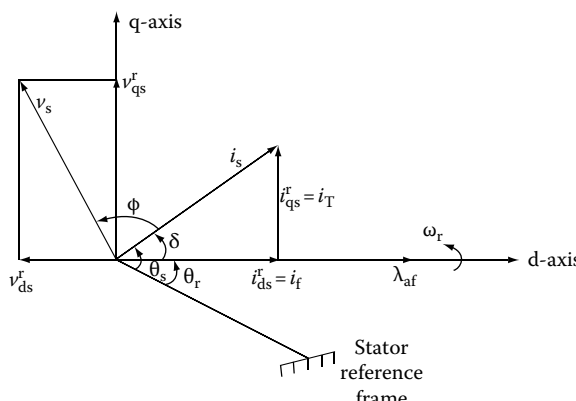


FIGURE 4.1 Phasor diagram of the PMSM. (From Krishnan, R., *Electric Motor Drives*, Figure 9.9, Prentice Hall, Upper Saddle River, NJ, 2001. With permission.)

component that is in quadrature to the rotor flux can produce a torque in interaction with the rotor flux and hence may be appropriately named as the torque-producing current, i_T , very similar to the armature current of the separately excited dc machine. They may then be represented in terms of the q- and d-axes stator currents as

$$i_{qs}^r = i_T \quad (4.6)$$

$$i_{ds}^r = i_r \quad (4.7)$$

In order to complete the phasor diagram, the voltage phasor can be assumed to be leading the stator current phasor by an angle, ϕ , whose cosine is the power factor of the machine, and which may be recalled from the fundamentals. Its components along the d- and q-axes are v_{ds}^r and v_{qs}^r , respectively, and they are shown in [Figure 4.1](#).

4.2.1 ELECTROMAGNETIC TORQUE

The electromagnetic torque expression from Chapter 3 is recalled and it is given by

$$T_e = \frac{3}{2} \cdot \frac{P}{2} \left[\lambda_{af} i_{qs}^r + (L_d - L_q) i_{qs}^r i_{ds}^r \right] \quad (\text{N}\cdot\text{m}) \quad (4.8)$$

For the moment, assuming that the stator flux current component is zero by making the torque angle, zero, i.e., $i_{ds}^r = 0$, we get the electromagnetic torque as

$$T_e = \frac{3}{2} \cdot \frac{P}{2} \lambda_{af} i_{qs}^r = K_1 \lambda_{af} i_s \quad (\text{N}\cdot\text{m}) \quad (4.9)$$

where

$$K_1 = \frac{3}{2} \cdot \frac{P}{2} \quad (4.10)$$

Note that the torque-producing component of the stator current phasor is equal to the stator current phasor magnitude itself, as, the torque angle becomes equal to 90° . Under this condition, the PMSM becomes exactly analogous to a separately excited dc machine as seen from the torque expression where, the torque is produced by the interaction of the rotor flux and stator current, whereas, in the dc machine, it is produced by the interaction of the stator flux and rotor (well-known as armature) current. The product $K_1 \lambda_{af}$ is the torque constant expressed in units of $\text{N}\cdot\text{m}/\text{A}$ for constant rotor flux linkages. This is not usually a constant as, the magnet rotor flux linkages are not a constant due to the sensitivity of magnets to temperature fluctuations in the rotor. More on this will be discussed in Chapter 7, on the parameter sensitivity of PMSM drive systems.

Substituting for the quadrature and direct axis stator currents in the rotor reference frames from Equation 4.5 in the torque expression, torque is expressed in terms of the stator current magnitude and the torque angle as

$$T_e = \frac{3}{2} \cdot \frac{P}{2} \left[\lambda_{af} i_s \sin \delta + \frac{1}{2} (L_d - L_q) i_s^2 \sin 2\delta \right] \text{ (N}\cdot\text{m)} \quad (4.11)$$

It is easy to recognize that the first part of the expression on the right-hand side denotes the synchronous torque produced by the interaction of the PM field and the stator current and the second term gives the torque due to a reluctance variation known as the reluctance torque. The role of these torque components in providing maximum torque was discussed in Chapter 3. This expression clearly demonstrates that the control variables stator current magnitude and the torque angle determine the electromagnetic torque provided, the machine inductances and rotor flux linkages are constant.

4.2.2 STATOR D- AND Q-AXIS CURRENTS IN STATOR REFERENCE FRAMES

Resolving the stator current phasor along the stator reference frames (which is the d-axis in that frame) and adding an axis quadrature to it (stator q-axis) but which is not shown in [Figure 4.1](#), the d- and q-axes stator reference frame currents can be directly derived as

$$\begin{bmatrix} i_{qs} \\ i_{ds} \end{bmatrix} = i_s \begin{bmatrix} \sin(\omega_r t + \delta) \\ \cos(\omega_r t + \delta) \end{bmatrix} \quad (4.12)$$

When they are transformed into a-, b-, and c-axes, the phase currents derived are the same as given in Equation 4.1. Superposing the abc phase axes on the phasor diagram, and then placing the projection of the stator current phasor onto them gives the instantaneous phase currents directly thereby eliminating the middle step through the d- and q-axes transformation and then from there to a-, b-, and c-axes transformation.

4.2.3 MUTUAL FLUX LINKAGES

The mutual flux linkages, which is in the air gap, is the result of the rotor flux linkages and the stator flux linkages. It is required in control to weaken the flux in the air gap similar to the flux-weakening operation performed in the separately excited dc motor. The rotor flux linkages are concentrated in the rotor d-axis (say, along the north pole of a two-pole PM rotor) and their quadrature axis component is zero. But the stator flux linkages have two nonzero components; one along its direct axis and the other along its quadrature axis and they are, $L_d i_{ds}$ and $L_q i_{qs}$, respectively, where L_d and L_q are direct and quadrature axes reactances, respectively. Then, these flux linkages combine with the rotor flux linkages along respective direct and quadrature

axes to give the result air gap or mutual flux linkages. The result of the mutual direct and quadrature flux linkages is obtained by their phasor sum the magnitude of which is given as

$$\lambda_m = \sqrt{\left(\lambda_{af} + L_d i_{ds}^r\right)^2 + \left(L_q i_{qs}^r\right)^2} \quad (\text{Wb-Turn}) \quad (4.13)$$

The phase of the mutual flux linkages is given by the arctan of the ratio between the quadrature to direct axis mutual flux linkages.

4.2.4 ROLE OF A TORQUE ANGLE IN MACHINE OPERATIONS

It is instructive to observe the machine performance under certain conditions from Equations 4.5, 4.11, and 4.13. If δ is greater than $\pi/2$, the flux-producing stator component of the current, i_{ds}^r , becomes negative. Hence, the resultant mutual flux linkages decrease. This is the key to flux-weakening in the PM synchronous motor drives. If δ is negative with respect to the rotor flux linkages phasor, the torque-producing stator current component is negative, resulting in a negative torque. For the direction of rotation assumed in the phasor diagram, which is positive, the positive torque monitors and, therefore, the negative torque generates (sometimes this mode of operation is referred to as the regenerating mode). During this time, the air gap power of the machine is negative, implying that the machine generates.

4.2.5 KEY RESULTS

The key results of this section form the backbone of the control of the PM synchronous motor drive and its various implementations. It is worth a summary for easy reference here.

1. Control of the phase, δ , (also named as torque angle), and the magnitude of the current phasor, i_s , achieved through the inverter the determines the torque and its control exclusively.
2. Control of the angular frequency of the current phasor determines the rotor speed, ω_r electrical rad/s.
3. The PM synchronous motor drive is shown to be analogous to the separately excited dc motor drive. It is achieved by finding the equivalent of the dc machine's field and armature currents, in the PMSMs, i_f and i_T , respectively. They are components of the stator current phasor and referred to as flux- and torque-producing components of stator current.
4. Independent control of the electromagnetic torque and the mutual flux is exercised through the torque- and flux-producing stator current components, similar to that of the case in the separately excited dc motor drive with its independent control of its armature and field currents.

4.3 DRIVE SYSTEM SCHEMATIC

The implementation of the vector-controlled PM synchronous motor is derived in this section based on the understanding gained in the previous section on vector control. Both the torque- and speed-controlled systems are illustrated below.

4.3.1 TORQUE-CONTROLLED DRIVE SYSTEM

Consider a PMSM drive with external inputs of torque and mutual flux linkages commands (known as references in control literature). They can be independent inputs as in the case of a torque-controlled motor drive in an electric propulsion application or can be part of a speed-controlled drive's dependent internal variable. Given the torque reference, T_e^* , the references for stator current, i_s^* , and torque angle, δ^* , are obtained from the known equations of torque and mutual flux linkages except that, reference variables are introduced instead of the real variables, and they are

$$T_e^* = \frac{3}{2} \cdot \frac{P}{2} \left[\lambda_{af} i_s^* \sin \delta^* + \frac{1}{2} (L_d - L_q) (i_s^*)^2 \sin 2\delta^* \right] \quad (\text{N} \cdot \text{m}) \quad (4.14)$$

$$\lambda_m^* = \sqrt{(\lambda_{af} + L_d i_s^* \cos \delta^*)^2 + (L_q i_s^* \sin \delta^*)^2} \quad (\text{Wb-Turn}) \quad (4.15)$$

Given the external inputs of torque and mutual flux linkages references, the stator current magnitude and torque angle references can be evaluated from Equations 4.14 and 4.15 assuming that the machine parameters are constants. The complexity involved in the solution of these equations is evident particularly for a PMSM with saliency. It requires some form of iterative solution with off-line computations and tables in the implementation. A surface-mounted PMSM, where the direct and quadrature inductances are equal, is illustrated for implementation here. Then the references for torque and mutual flux linkages are reduced to

$$T_e^* = \frac{3}{2} \cdot \frac{P}{2} [\lambda_{af} i_s^* \sin \delta^*] \quad (\text{N} \cdot \text{m}) \quad (4.16)$$

$$\begin{aligned} \lambda_m^* &= \sqrt{(\lambda_{af} + L_d i_s^* \cos \delta^*)^2 + (L_q i_s^* \sin \delta^*)^2} = \sqrt{(\lambda_{af} + L_d i_s^* \cos \delta^*)^2 + (L_d i_s^* \sin \delta^*)^2} \\ &= \sqrt{\lambda_{af}^2 + (L_d i_s^*)^2 + 2(\lambda_{af} L_d i_s^* \cos \delta^*)} \quad (\text{Wb-Turn}) \end{aligned} \quad (4.17)$$

Solution for torque angle reference is obtained analytically with the following steps:

Step 1: The flux-producing component of the stator current $i_s^* \cos \delta^*$ is solved from the second expression in Equation 4.17 by substituting $i_s^* \sin \delta^*$ from Equation 4.16 yielding

$$i_s^* \cos \delta^* = \frac{\left[\sqrt{(\lambda_m^*)^2 - L_d^2} \frac{(T_e^*)^2}{\left(\frac{3}{2} \frac{P}{2} \lambda_{af} \right)^2} \right] - \lambda_{af}}{L_d} \quad (4.18)$$

Step 2: The stator current reference is obtained from the final expression in Equation 4.17 by substituting $i_s^* \cos \delta^*$ from Equation 4.18 as

$$i_s^* = \frac{\sqrt{(\lambda_m^*)^2 - \lambda_{af}^2 - 2\lambda_{af}(i_s^* \cos \delta^*)}}{L_d} \quad (4.19)$$

The reference torque angle can be found from Equations 4.18 and 4.19. From the current and torque angle references, the flux- and torque-producing stator current components can be evaluated from Equation 4.5 adjusted for reference variables in place of real variables as

$$\begin{bmatrix} i_T^* \\ i_f^* \end{bmatrix} = i_s^* \begin{bmatrix} \sin \delta \\ \cos \delta \end{bmatrix} \quad (4.20)$$

Applying the transformation from rotor frame reference currents to abc currents, the phase current references are obtained as

$$\begin{bmatrix} i_{as}^* \\ i_{bs}^* \\ i_{cs}^* \end{bmatrix} = \begin{bmatrix} \cos \theta_r & \sin \theta_r \\ \cos \left(\theta_r - \frac{2\pi}{3} \right) & \sin \left(\theta_r - \frac{2\pi}{3} \right) \\ \cos \left(\theta_r + \frac{2\pi}{3} \right) & \sin \left(\theta_r + \frac{2\pi}{3} \right) \end{bmatrix} \begin{bmatrix} i_T^* \\ i_f^* \end{bmatrix} = i_s^* \begin{bmatrix} \sin(\theta_r + \delta^*) \\ \sin \left(\theta_r + \delta^* - \frac{2\pi}{3} \right) \\ \sin \left(\theta_r + \delta^* + \frac{2\pi}{3} \right) \end{bmatrix} \quad (4.21)$$

The phase current references can also be directly obtained by simply projecting the stator current phasor reference onto a-, b-, and c-axes from the phasor diagram 4.1. With this, the vector controller derivation is complete for the torque-controlled PMSM drive. A basic implementation schematic is shown in [Figure 4.2](#). The control schematic does not change for the salient pole varieties of the PM synchronous motor drive except for the equations to be derived from Equations 4.14 and 4.15 which are very similar to the surface-mounted PMSM illustrated in the earlier discussion for computing the references for stator current phasor magnitude and torque angle. The calculations can be made online or stored in tables computed off-line to save computational time. To accommodate parameter variations, multiple tables for each

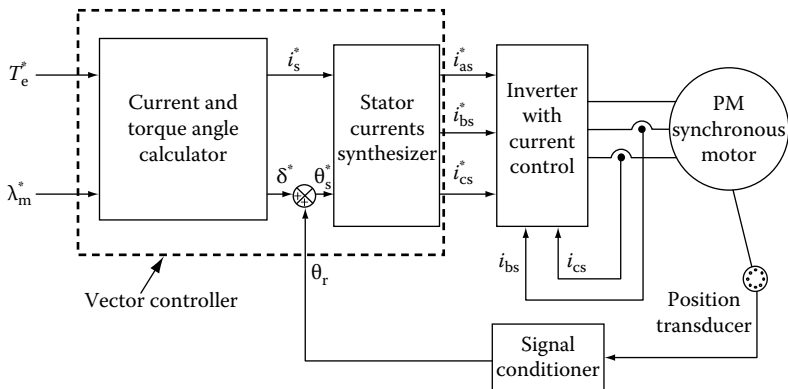


FIGURE 4.2 Schematic diagram of a vector-controlled PMSM torque drive.

variation can be saved and recalled during operation. The phase of the stator current phasor with respect to stationary reference frames is obtained by summing the rotor flux position and the torque angle as seen from the phasor diagram and given by

$$\theta_s^* = \theta_r + \delta^* = \omega_r t + \delta^* \quad (4.22)$$

Using Equations 4.21 and 4.22, the stator current references are synthesized in the second block of the vector controller. The process of acquiring the stator phase current commands from the torque and mutual flux linkages references is the heart of the vector controller and is shown in dotted lines. The system is current controlled as the torque and mutual flux linkages are directly controlled by currents. Therefore, the current control involves feedback current control and these details are not shown here. There are only two currents measured as the sum of the three-phase currents in a healthy three-phase three-wire system is zero and hence, the third-phase current can be reconstructed from the other two-phase currents alone. The error between the phase currents and their references is processed through, say, proportional and integral controllers to yield phase voltage references. They can be enforced in the inverter through hysteresis or pulse width modulation (PWM) or space vector modulation controls. Even though the details of the current control are not shown in the block diagram, its implementation through the inverter has been considered in Chapter 2. The algorithm for the hysteresis controller is illustrated here.

4.3.1.1 Hysteresis Current Controller

The current or hysteresis window, Δi , is preselected in the implementation and two variables are generated by summing and subtracting it from the stator phase current reference to generate the bounded envelope within which the stator phase current has to be maintained [11]. Based on that, and, the value of the stator phase current, the switching logic for the hysteresis phase current controller is given as

$$\text{If } (i_{\text{as}} - i_{\text{as}}^*) \text{ greater than or equal to } \Delta i, \text{ then, } v_{\text{ao}} = \frac{V_{\text{dc}}}{2}$$

If $(i_{as} - i_{as}^*)$ less than or equal to $-\Delta i$, then, $v_{ao} = -\frac{V_{dc}}{2}$

It may be recalled that v_{ao} is the midpoint voltage of the phase a's inverter leg. The implementation for other phases can be similarly made. From the midpoint voltages, the line voltages and phase voltages can be derived and, they then, can be transformed into d- and q-voltages in rotor reference frames as explained elsewhere for the dynamic simulation of the PMSM. The solution of machine equations gives the rotor reference frames d- and q-axes stator currents and which by inverse transformation leads to stator phase currents. Torque and mutual flux linkages are computed from the rotor reference frame currents.

4.3.2 SIMULATION AND RESULTS OF A TORQUE-CONTROLLED DRIVE SYSTEM

The speed of the machine is maintained at a constant speed, say, by a dynamometer and then, the torque reference is put on the motor drive. This is easy to test in a laboratory but it is not how a torque-controlled motor drive is put into practice. There usually is a speed control in one form or another in practice, such as, a human being closing the speed loop in the electric vehicle drives using a torque-controlled motor drive. A simpler drive with torque angle reference at 90° is chosen for illustration with the result that the entire stator current goes to produce electromagnetic torque and there is no flux-producing stator current component with the result that there is no flux weakening along the magnet axis. That does not mean there is no variation in the mutual flux linkages. It is there, because, the q-axis stator flux linkages due to the q-axis stator current component joins the rotor PM flux linkages. With an increasing stator current magnitude, an increase in mutual flux linkages can be seen. For faster computation, a numerical integration of machine differential equations is performed using Euler's integration method rather than the conventionally used fourth order Runge–Kutta integration method.

The simulation results for a torque drive, maintained at a speed of 0.5 p.u., is shown in [Figure 4.3](#) with a hysteresis controller in the current control loop. The current window is set at 0.1 p.u., rather a large value but very handy to illustrate the pulsations in torque. Because of the high current ripple on the q-axis current, the torque ripple is also high in proportion. The current controllers force the currents to follow their respective references with very little delay, a distinct advantage with the hysteresis current controller. It is seen that the mutual or air gap flux linkages grow with the stator current. The torque angle is controlled on an average to the desired value but their excursions from the reference value is primarily due to the deviation in the current from its reference determined by the current control quality in the inverter and machine parameters. The flux-producing component of the stator current is likewise, held at zero on an average for the same reason as explained for the torque angle performance. The plotted variables are in normalized units of p.u. except for the torque angle, which is in electrical degrees and time. The code in MATLAB® for the simulation is given below.

```
%PMSM SIMULATION Constant Angle
%HYSTERESIS CONTROLLER
%TORQUE DRIVE
```

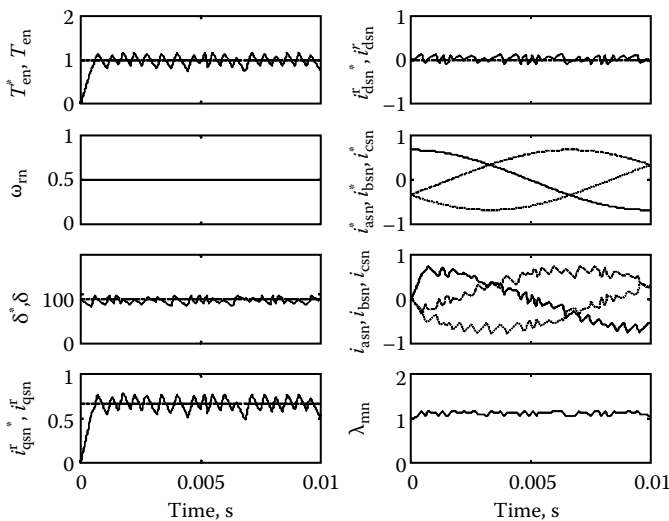


FIGURE 4.3 Dynamic performance of a torque-controlled drive with a hysteresis current controller.

```

clear all; close all;

%Machine Parameters
P=6; %Number of Poles
Rs=1.4; %Stator Resistance
Ld=0.0056; %d axis inductance
Lq=0.009; %q axis inductance
lamaf=.1546; %Rotor Flux linkage
B=0.01; %Friction Coefficient
J=0.006; %Moment of Inertia
vdc=285; %DC Link voltage
wr_ref=314.3; %Rated speed

%Base values
Tb=5.5631; %Base torque value
Ib=12; %Base current value
wb=628.6; %Base speed value
Vb=97.138; %Base voltage value
Lb=0.0129; %Base inductance value

%Converter and Controller Parameters
deli=0.1*Ib; %Current window
%Initial Parameters
theta_r=0; %Initial position
wr=wr_ref; %Initial speed
t=0; %Initial time
dt=1e-6; %Integration Time step

```

```

tfinal=.01;                      %Final time
if_ref=-1e-16;                   %Set d axis current
iqs=0;ids=0;                     %Initial conditions for currents
vqs=0;vds=0;                     %Initial conditions for voltages
n=1;
x=1;
signe=1;
ramp=-1;
ias=0;ibs=0;ics=0;t1=0;
vax1=0;vbx1=0;vcx1=0;
zia=0;zib=0;zic=0;

%Simulation Starts Here
while (t<tfinal),

    Te_ref=Tb;                  %Set required torque value
    %Set reference q axis current
    it_ref=Te_ref*(2/3)*(2/P)/((Ld-Lq)*if_ref+lamaf);
    %Set reference stator current and torque angle
    is_ref=sqrt(it_ref^2+if_ref^2);
    delta_ref=atan(it_ref/if_ref);
    if delta_ref<0,
        delta_ref=delta_ref+pi;
    end

    ias_ref=is_ref*sin(theta_r+delta_ref);
    ibs_ref=is_ref*sin(theta_r+delta_ref-2*pi/3);
    ics_ref=is_ref*sin(theta_r+delta_ref+2*pi/3);

    %Hysteresis Controller
    if (ias_ref-ias)>=deli,
        vao=vdc/2;
    end
    if (ias_ref-ias)<-deli,
        vao=-vdc/2;
    end

    if (ibs_ref-ibs)>=deli,
        vbo=vdc/2;
    end
    if (ibs_ref-ibs)<-deli,
        vbo=-vdc/2;
    end

    if (ics_ref-ics)>=deli,
        vco=vdc/2;
    end
    if (ics_ref-ics)<-deli,
        vco=-vdc/2;
    end

```

```

%Compute line voltages
vab=vao-vbo;
vbc=vbo-vco;
vca=vco-vao;
%Compute phase voltages
vas=(vab-vca)/3;
vbs=(vbc-vab)/3;
vcs=(vca-vbc)/3;
%q and d axes voltages
vqs=(2/3)*(cos(theta_r)*vas+cos(theta_r-2*pi/3)*vbs+cos(theta_r+2*pi/3)*vcs);
vds=(2/3)*(sin(theta_r)*vas+sin(theta_r-2*pi/3)*vbs+sin(theta_r+2*pi/3)*vcs);

%Machine equation
d_iqs=(vqs-Rs*iqs-wr*Ld*ids-wr*lamaf)*dt/Lq;
iqs=iqs+d_iqs;
d_ids=(vds+wr*Lq*iqs-Rs*ids)*dt/Ld;
ids=ids+d_ids;

%Calculate stator current and torque angle
is=sqrt(iqs^2+ids^2);
delta=atan(iqs/ids);
if delta<0,
    delta=delta+pi;
end

%Calculate torque
Te=(3/2)*(P/2)*iqs*( (Ld-Lq)*ids+lamaf) ;
wr=314.3;
%Calculate position
d_theta_r=wr*dt;
theta_r=theta_r+d_theta_r;

%Phase currents
ias=iqs*cos(theta_r)+ids*sin(theta_r);
ibs=iqs*cos(theta_r-2*pi/3)+ids*sin(theta_r-2*pi/3);
ics=-(ias+ibs);
t=t+dt;      %Increment time
%
%Plot variables after normalization
%
if x>16,
    t
    tn(n)=t;
    Teref(n)=Te_ref/Tb;
    it_refn(n)=it_ref/Ib;
    is_refn(n)=is_ref/Ib;
    ias_refn(n)=ias_ref/Ib;
    ibs_refn(n)=ibs_ref/Ib;

```

```

ics_refn(n)=ics_ref/Ib;
iasn(n)=ias/Ib;
ibsn(n)=ibs/Ib;
icsn(n)=ics/Ib;
iqsn(n)=iqs/Ib;
idsn(n)=ids/Ib;
isn(n)=is/Ib;
ifrefn(n)=if_ref/Ib;
delta_refn(n)=delta_ref;
deltan(n)=delta;
Ten(n)=Te/Tb;
wrn(n)=wr/wb;
lammn(n)=sqrt( (1+Ld*ids/(Ib*Lb) )^2+(Lq*iqs/(Ib*Lb) )^2 );
n=n+1;
x=1;
end
x=x+1;
end
figure(1);orient tall;
subplot(4,2,1)
plot(tn,Teref, 'k--',tn,Ten, 'k');axis([0 .01 0 2]);
set(gca,'xticklabel',[]);
subplot(4,2,3)
plot(tn,wrn, 'k');axis([0 .01 0 1]);
set(gca,'xticklabel',[]);
subplot(4,2,5)
plot(tn,delta_refn*180/pi, 'k--',tn,deltan*180/pi, 'k');
axis([0 .01 0 180]);
set(gca,'xticklabel',[]);
subplot(4,2,7)
plot(tn,it_refn, 'k--',tn,iqsn, 'k');axis([0 .01 0 1]);
subplot(4,2,2)
plot(tn,ifrefn, 'k--',tn,idsn, 'k');axis([0 .01 -1
1]);set(gca,'xticklabel',[])
subplot(4,2,4)
plot(tn,ias_refn, 'k',tn,ibsn_refn, 'k--',tn,ics_refn, 'k:');
axis([0 .01 -1 1]);set(gca,'xticklabel',[])
subplot(4,2,6)
plot(tn,iasn, 'k',tn,ibsn, 'k--',tn,icsn, 'k:');
axis([0 .01 -1 1]);set(gca,'xticklabel',[])
subplot(4,2,8)
plot(tn,lammn, 'k')
axis([0 .01 0 2]);

```

A torque-drive performance with sine triangle-based PWM controllers is shown in Figure 4.4 for identical operating conditions as that of the hysteresis controller. The implementation of the PWM current control is illustrated in the speed-controlled motor drive in the following sections and, therefore, it is not presented here. The PWM carrier frequency is 20kHz. The current ripples and hence, the

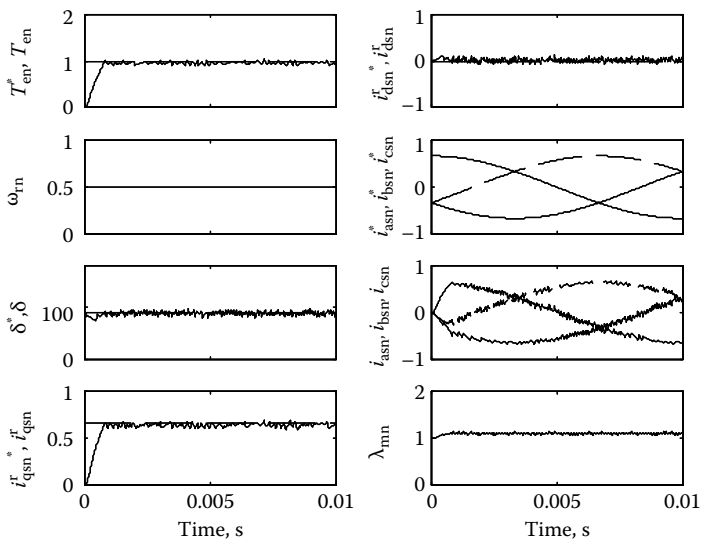


FIGURE 4.4 Dynamic performance of a torque-controlled drive with PWM current control.

torque pulsations are very small with high switching frequency when compared to a hysteresis control-based drive with a large hysteresis window. But, on an average, the drive variables, such as, the torque and air gap flux linkages, are identical in both the schemes. The difference in the performance is in the magnitudes of the current ripple and the torque pulsation.

4.3.3 SPEED-CONTROLLED DRIVE SYSTEM

A speed-controlled drive system is obtained, by taking the torque-controlled drive system shown in Figure 4.2 as the basic core and then, superimposing on it, an outer speed feedback control loop for regulation of rotor speed of the drive system and as shown in Figure 4.5. The speed error between the speed and its reference, given by $(\omega_r^* - \omega_r)$, is processed through a proportional plus integral (PI) type controller (hereafter known as the speed controller) to nullify the steady-state error in speed. The output of this speed controller constitutes the electromagnetic torque reference, T^* , because the speed error can be nulled and minimized only by increasing or decreasing the electromagnetic torque in the machine, depending on whether the speed error is positive or negative, respectively. For a fast response of the speed, a proportional integral derivative (PID) speed controller is appropriate.

The mutual flux linkages reference is generated by the demands of the rotor speed. As long as the line-to-line-induced emf magnitude does not exceed the dc supply voltage to the inverter, the ratio between the induced emf and stator frequency remains a constant, resulting in constant mutual flux and the maximum frequency, (known as base frequency), within this limit, gives a speed known as base speed. As soon as the frequency exceeds its base value, it results in the speed being driven beyond the

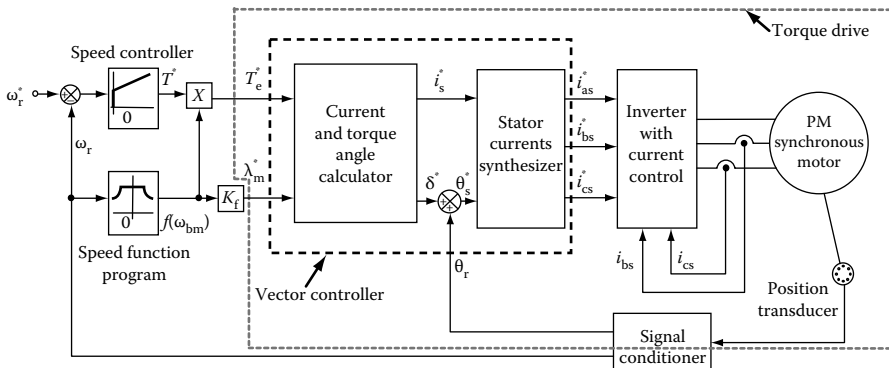


FIGURE 4.5 Speed-controlled PM synchronous motor drive.

base speed and consequently the induced emf starts exceeding the dc supply voltage magnitude. That makes the control of stator currents very difficult and thereby the control of the torque also. The drive control becomes sluggish in this region. In order to maintain the current control, as well as, to maintain the control over the induced emf magnitude, the mutual flux can be programmed to decrease in inverse proportion to the speed so that the induced emf is pegged to the level where it corresponds to base speed even though the speed is pushed beyond that. This operation is known as flux weakening and, accordingly, this mode of operation is named flux-weakening control. But torque cannot be expected to be maintained at the base level that corresponds to the base speed whose product gives the base air gap power and it can never be exceeded in a machine in steady state as it involves higher losses that will result in thermal run off, leading to machine failure. Further, it requires stator currents exceeding their base values in the machine. All these problems are addressed by reducing the torque, when the speed is beyond its base value, by programming it to decrease from its base value so that the air gap power produced is equal to the base power. That will also keep the stator current within its base value. This seemingly complex control can be simply implemented in the following two steps.

4.3.3.1 Mutual Flux Programming

A controller, which gives one p.u. up to base speed, and beyond speed, that gives an output inversely proportional to normalized speed, is created using a function generator to delineate the constant torque- and flux-weakening regions of operation of the motor drive. This output is termed $f(\omega_{bm})$ and is proportional to the mutual flux linkages reference. The constant of proportionality, K_f , is introduced here for that purpose. The function generator, $f(\omega_{bm})$, sets the reference for the resultant mutual flux linkages, involving a constant K_f . The output of the function generator being in p.u., the value of K_f is unity.

4.3.3.2 Torque Programming in the Flux-Weakening Region

This involves the reprogramming of the speed controller produced torque reference, T^* , as a function of the speed. Just as the mutual flux linkages are programmed to

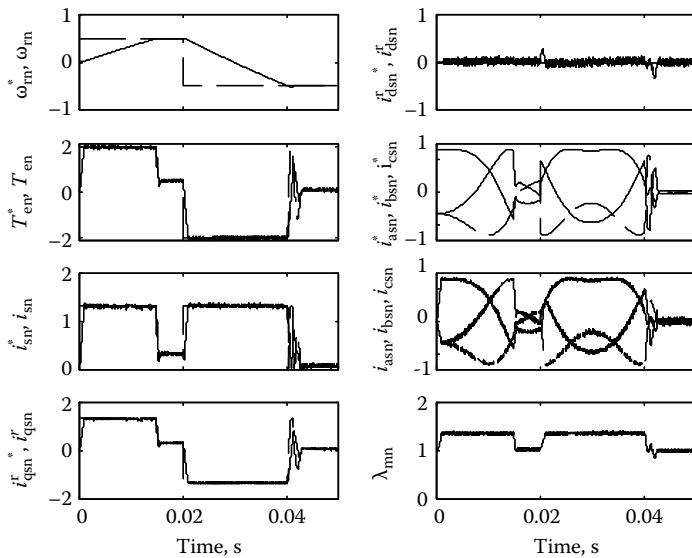


FIGURE 4.6 Performance of a four-quadrant speed-controlled drive with PWM current control.

be inversely proportional to the rotor speed, likewise, the output of the flux programmed controller can be used to adjust the torque reference T^* to yield a usable torque reference, T_e^* , in the vector controller by multiplying T^* and $f(\omega_{bm})$ as shown in Figure 4.6. The reason for this block is to adjust the torque-producing component of the stator current both, in the constant torque and constant power regions of operation. It is proved as follows.

The function generator operating on the speed has the following characteristics:

$$\left. \begin{aligned} f(\omega_{bm}) &= \frac{\omega_b}{\omega_r}; & \pm \omega_b < \omega_r < \pm \omega_{\max} \\ &= 1; & 0 < \omega_r < \pm \omega_b \end{aligned} \right\} \quad (4.23)$$

where ω_b is the base speed. The air gap power is given by

$$P_a = \omega_m T_e^* = \frac{\omega_r}{P/2} f(\omega_{bm}) T^* \quad (4.24)$$

Substituting the function from Equation 4.23 into Equation 4.24, the air gap power for the constant torque region is obtained as

$$P_a = \frac{\omega_r T^*}{P/2} = \omega_m T^* \quad (4.25)$$

This equation clearly indicates that the air gap power is proportional to speed when the torque is constant until the speed reaches its base value. Note that the torque reference from the speed controller, T^* , is a constant for a steady-state speed. This is not yet amended to yield the final electromagnetic torque reference, T_e^* , to the vector controller. For the constant power operation region, the air gap power is similarly obtained and given as

$$P_a = \frac{\omega_b T^*}{P/2} \quad (4.26)$$

The base speed ω_b and T^* are constant and hence the power output in the flux-weakening mode is maintained constant at base power. Hence, the constant torque and constant power modes of operation are implemented with this function generator block, as seen from Equations 4.25 and 4.26, respectively. Note that subtracting shaft losses from air gap power gives the shaft output power.

The speed-controlled motor drive system is the inner core of the position-controlled drive system. Superposition of a rotor position feedback control loop converts the speed-controlled motor drive system into a rotor position-controlled motor drive system. Such position-controlled motor drive systems can, for example, be found in machine tool servos. Interested readers can simulate such a drive by adding a few lines of simulation codes in the following section as an intellectual exercise.

4.3.4 SIMULATION AND RESULTS OF A SPEED-CONTROLLED DRIVE SYSTEM

The simulation given below in MATLAB, incorporates the torque-producing stator current reference derived from the torque reference. As for flux linkages, the reference is no longer kept as the mutual flux linkages, as discussed in the earlier section, but an easier way is taken by keeping the reference as the direct axis mutual flux linkages in rotor reference frames. That means, the mutual d-axis rotor flux linkages are the sum of the rotor magnet flux linkages and, the direct axis flux linkages of the flux-producing component of the stator current. In spite of these changes, the dynamic performance of the motor drive remains very good as is seen from the simulation results. Note that the reference mutual flux linkages is not implemented in this manner in practice.

The speed loop on the torque drive is closed and a four-quadrant operation is simulated with a load torque of 0.3 p.u. The results are shown in [Figure 4.6](#). A PI speed controller is in place for this drive. PWM current control is continued for this simulation. The machine is at a standstill at the start and, with a positive speed command, the torque reference is driven to a positive maximum, and is maintained there until the rotor speed matches the speed command. When the rotor speed is equal to the command speed, the torque reference comes down to match the load torque and the friction torque. The torque reference is driven to negative when the speed reference changes from 0.5 to -0.5 p.u. The rotor slows down to zero speed. Maintaining the negative torque forces the rotor to reverse direction and catch up with the speed reference, -0.5 p.u. As it coasts at -0.5 p.u., the electromagnetic torque is reduced slightly lower than the positive load torque of 0.3 p.u. because, the friction torque is negative, and, note that the sum of friction and load torques gives the air gap torque. The importance of the current loop

performance is evident in the need for sudden phase inversions in the phase currents during speed reversal. A sluggish performance by the current loop will adversely impact on the speed response both in response time and possibly in the speed oscillations.

The MATLAB code for the simulation is given below:

```
% PMSM SIMULATION Constant Torque Angle
% PWM CONTROLLER
% FOUR QUADRANT SPEED DRIVE

clear all;close all;

%Machine Parameters

P=6; %Number of Poles
Rs=1.4; %Stator Resistance
Ld=0.0056; %d axis inductance
Lq=0.009; %q axis inductance
lamaf=.1546; %Rotor Flux linkage
B=0.01; %Friction Coefficient
J=0.0012; %Moment of Inertia
vdc=285; %DC Link voltage
wr_ref=314.3; %Rated speed

%Converter and Controller Parameters

fc=20000;
Kpi=10;
Kp=2;
Ki=1;

%Converter and Controller Parameters

fc=20000; %PWM switching frequency
Kpi=10; %Proportional gain of current controller
Kp=2; %Proportional gain of speed controller
Ki=1; %Integral gain of speed controller

%Base values

Tb=5.5631; %Base torque value
Ib=12; %Base current value
wb=628.6; %Base speed value
Vb=97.138; %Base voltage value
Lb=0.0129; %Base inductance value

ias=0;ibs=0;ics=0;t1=0;
vax1=0;vbx1=0;vcx1=0;
y=0;

%Initial Parameters

theta_r=0; %Initial position
wr=0; %Initial speed
```

```

t=0;                                %Initial time
dt=1e-6;                             %Integration Time step
tfinal=.05;                           %Final time
if_ref=-1e-16;                        %Set d axis current to small negative value
iqs=0;ids=0;                          %Initialize q and d axes currents
vqs=0;vds=0;                          %Initialize q and d axes voltages
Tl=0.3*Tb;                            %Load torque value
n=1;
x=1;
signe=1;
ramp=-1;
ias=0;ibs=0;ics=0; %Initialize phase currents
t1=0;
vax1=0;vbx1=0;vcx1=0;
zia=0;zib=0;zic=0;

%Simulation Starts Here
while (t<tfinal),
    %Negative speed is commanded after 0.02s

    if t>0.02,
        wr_ref=-314.3;
    end

    wr_err=wr_ref-wr; %Speed Error
    y=y+wr_err*dt;     %Speed PI controller
    Te_ref=Kp*wr_err+Ki*y;

    %Limiter
    if Te_ref>2*Tb,
        Te_ref=2*Tb;
    end
    if Te_ref<-2*Tb,
        Te_ref=-2*Tb;
    end

    %Calculate reference currents

    it_ref=Te_ref*(2/3)*(2/P)/((Ld-Lq)*if_ref+lamaf);
    is_ref=sqrt(it_ref^2+if_ref^2);
    if it_ref>=0,
        delta_ref=pi/2;
    elseif it_ref<0,
        delta_ref=-pi/2;
    end

    %Calculate reference phase currents

    ias_ref=is_ref*sin(theta_r+delta_ref);
    ibs_ref=is_ref*sin(theta_r+delta_ref-2*pi/3);
    ics_ref=is_ref*sin(theta_r+delta_ref+2*pi/3);

```

```
%Calculate control voltages to be applied to PWM controller

vax=Kpi*(ias_ref-ias);
if vax>1,
    vax=1;
elseif vax<-1,
    vax=-1;
end
vbx=Kpi*(ibs_ref-ibs);
if vbx>1,
    vbx=1;
elseif vbx<-1,
    vbx=-1;
end
vcx=Kpi*(ics_ref-ics);
if vcx>1,
    vcx=1;
elseif vcx<-1,
    vcx=-1;
end

%Sample and hold

if t1>1/fc,
    vax1=vax;
    vbx1=vbx;
    vcx1=vcx;
    t1=0;
end

%PWM Controller

if vax1>=ramp,
    vao=vdc/2;
elseif vax1<ramp,
    vao=-vdc/2;
end
if vbx1>=ramp,
    vbo=vdc/2;
elseif vbx1<ramp,
    vbo=-vdc/2;
end

if vcx1>=ramp,
    vco=vdc/2;
elseif vcx1<ramp,
    vco=-vdc/2;
end

%Compute line voltages

vab=vao-vbo;
```

```

vbc=vbo-vco;
vca=vco-vao;

%Compute phase voltages

vas=(vab-vca)/3;
vbs=(vbc-vab)/3;
vcs=(vca-vbc)/3;
%q and d axes voltages in rotor reference frames
vqs=(2/3)*(cos(theta_r)*vas+cos(theta_r-2*pi/3)*vbs+cos(theta_r+2*pi/3)*vcs);
vds=(2/3)*(sin(theta_r)*vas+sin(theta_r-2*pi/3)*vbs+sin(theta_r+2*pi/3)*vcs);
%Machine equations to compute currents in rotor reference
frames, and torque angle, torque
d_iqs=(vqs-Rs*iqs-wr*Ld*iqs-wr*lamaf)*dt/Lq;
iqs=iqs+d_iqs;
d_ids=(vds+wr*Lq*iqs-Rs*ids)*dt/Ld;
ids=ids+d_ids;
is=sqrt(iqs^2+ids^2);
delta=atan(iqs/ids); % Torque angle
Te=(3/2)*(P/2)*iqs*(Ld-Lq)*ids+lamaf); %Calculate torque

%Calculate speed and position

d_wr=((P/2)*(Te-Tl)-B*wr)*dt/J;
wr=wr+d_wr;
d_theta_r=wr*dt;
theta_r=theta_r+d_theta_r;

%Phase currents

ias=iqs*cos(theta_r)+ids*sin(theta_r);
ibs=iqs*cos(theta_r-2*pi/3)+ids*sin(theta_r-2*pi/3);
ics=-(ias+ibs);

%PWM RAMP

ramp=signe*(2/(1/(2*fc)))*dt+ramp;
if ramp>1,
  signe=-1;
end
if ramp<-1,
  signe=1;
end

t=t+dt; %Increment time
t1=t1+dt;
%Plot variables
if x>16,
  t
  tn(n)=t;

```

```

Teref(n)=Te_ref/Tb;
it_ref(n)=it_ref/Ib;
if_ref(n)=if_ref/Ib;
is_ref(n)=is_ref/Ib;
ias_ref(n)=ias_ref/Ib;
ibs_ref(n)=ibs_ref/Ib;
ics_ref(n)=ics_ref/Ib;
iasn(n)=ias/Ib;
ibsn(n)=ibs/Ib;
icsn(n)=ics/Ib;
vasn(n)=vas/Vb;
vbsn(n)=vbs/Vb;
vcsn(n)=vcs/Vb;
iqsn(n)=iqs/Ib;
idsn(n)=ids/Ib;
isn(n)=is/Ib;
Ten(n)=Te/Tb;
wrn(n)=wr/wb;
wrrefn(n)=wr_ref/wb;
lammn(n)=sqrt( (1+Ld*ids/(Ib*Lb) )^2+(Lq*iqs/(Ib*Lb) )^2);
n=n+1;
x=1;
end
x=x+1;
end

% Plotting

figure(1);orient tall;
subplot(4,2,3)
plot(tn,Teref,'k--',tn,Ten,'k');axis([0 .05 -2.1 2.1]);
set(gca,'xticklabel',[]);
subplot(4,2,5)
plot(tn,is_refn,'k--',tn,isn,'k');axis([0 .05 0 2]);
set(gca,'xticklabel',[]);
subplot(4,2,1)
plot(tn,wrrefn,'k--',tn,wrn,'k');axis([0 .05 -1 1]);
set(gca,'xticklabel',[]);
subplot(4,2,7)
plot(tn,it_refn,'k--',tn,iqsn,'k');axis([0 .05 -2 2]);
subplot(4,2,2)
plot(tn,if_refn,'k--',tn,idsn,'k');axis([0 .05 -1 1]);
set(gca,'xticklabel',[]);
subplot(4,2,4)
plot(tn,ias_refn,'k',tn,ibs_refn,'k:',tn,ics_refn,'k--');
axis([0 .05 -1.5 1.5]);set(gca,'xticklabel',[]);
subplot(4,2,6)
plot(tn,iasn,'k',tn,ibsn,'k:',tn,icsn,'k--')
axis([0 .05 -1.5 1.5]);set(gca,'xticklabel',[]);
subplot(4,2,8)
plot(tn,lamnn,'k')
axis([0 .05 0 2]);

```

A flux-weakening operation is shown in the simulation results of Figure 4.7. Above 0.5 p.u., flux weakening is initiated using the algorithm given earlier. The d-axis current reference is reduced during flux weakening, resulting in a reduction of air gap flux linkages. The performance of the drive under this condition is identical to the earlier four quadrant performance. Note that during flux weakening, the torque command is reduced to maintain the constant air gap power. The following MATLAB code can be added in the simulation loop after the calculation of the reference torque:

```
if wr<wb/2,
    fwr=1;
end
if wr>wb/2,
    fwr=(wb/2)/wr;
```

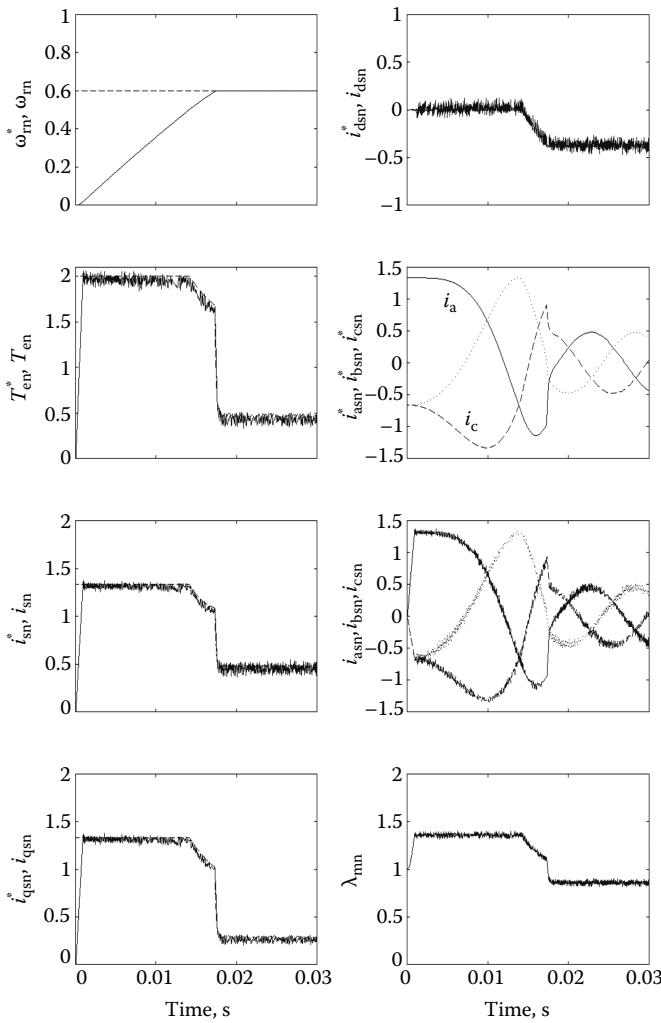


FIGURE 4.7 Speed-drive performance with flux-weakening control.

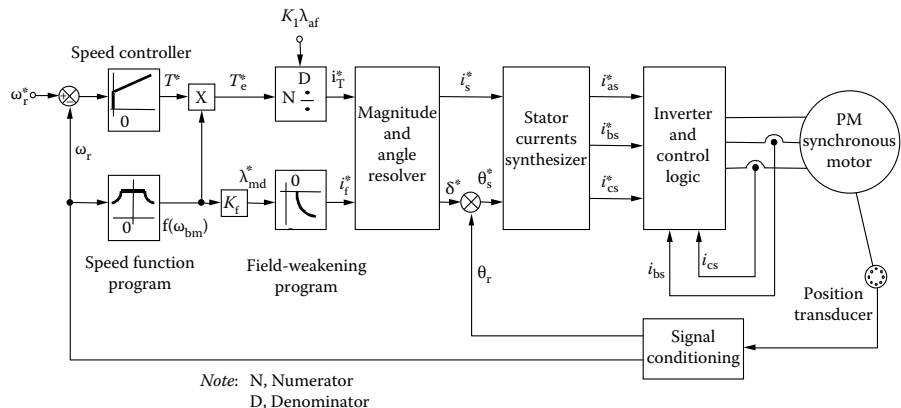


FIGURE 4.8 A simpler speed-controlled PM synchronous motor drive for simulation. (From Krishnan, R., *Electric Motor Drives*, Figure 9.10, Prentice Hall, Upper Saddle River, NJ, 2001. With permission.)

```

end
Te_refnew=Te_ref*fwr;
if_ref=(fwr-1)*lamaf/Ld;
it_ref=Te_refnew*(2/3)*(2/P)/((Ld-Lq)*if_ref+lamaf);

```

A speed-controlled surface-mounted PM synchronous motor drive system is shown [5a] in Figure 4.8. Recall that the surface-mounted-type PMSM has no reluctance variation between the quadrature and the direct axes. The result is that the reluctance torque does not exist in such a motor drive, leading to a simpler torque expression. The torque-producing current reference is obtained by dividing the torque reference by the product of the rotor magnet flux linkages and the constant term K_1 , that is, 1.5 times the pair of rotor poles for a three-phase machine. The torque is adjusted for flux weakening by multiplying the speed function generator output with the output of the speed controller. The flux weakening is similar to that discussed earlier and the flux-producing current can either be calculated or programmed in a table that can be stored in a read-only memory (ROM) for implementation and, the latter approach is shown in the block diagram. Note that, only the mutual direct axis flux linkages are controlled but not, the mutual flux linkages which is the result of the stator and magnet rotor flux linkages. This subtle difference has to be noted.

4.4 CONTROL STRATEGIES

Vector control proves and provides the decoupling between torque and flux channels in the PMSM. Such decoupling need not be the only performance requirement for a drive system. The performance measures can be a simpler control strategy, a UPF operation, a mutual flux linkages control, an optimum torque per unit current, a maximum efficiency control, and a maximum torque speed boundary control. These performance measures can be enforced by the stator current phase control and, in many cases also provide decoupling control of torque and flux [13–27].

Such performance measures are important in many applications. For example, a mutual air gap flux linkages control gives a smooth control over the entire torque speed region, with a seamless transition to flux weakening above the base speed. Similarly, a maximum efficiency control is of paramount importance in applications where energy saving and cost of electricity are critical home appliances, fans, pumps, hybrid electric and electric vehicle motor drives. This particular criterion is rapidly becoming one of the most overriding concerns in industrial and home applications with motor drives especially in the context of global energy and global warming crises.

The following additional control strategies are considered in further detail for the PMSM drive:

1. Constant torque angle control or zero direct axis current control
2. UPF control
3. Constant mutual air gap flux-linkages control
4. Angle control of air gap flux and current phasors
5. Optimum torque per ampere control
6. Constant loss based maximum torque speed boundary control
7. Minimum loss or maximum efficiency control

These control strategies are derived step by step and analyzed in the following and illustrated for the steady-state operation only.

4.4.1 CONSTANT ($\delta=90^\circ$) TORQUE ANGLE CONTROL

In this control [5a], the torque angle, δ , is maintained at 90° and hence, the field or direct axis current is brought to zero leaving only the torque or quadrature axis current in place. This is the mode of operation below the base speed, corresponding to the constant direct axis mutual flux linkages and, such a strategy is popular in many of the drive systems. The relevant equations of performance in this mode of operation are

$$T_e = \frac{3}{2} \cdot \frac{P}{2} \lambda_{af} \cdot i_{qs}^r = \frac{3}{2} \cdot \frac{P}{2} \lambda_{af} \cdot I_s \quad (\text{N}\cdot\text{m}) \quad (4.27)$$

where I_s is the magnitude of the stator current phasor. The torque per unit stator current is constant and given by

$$\frac{T_e}{I_s} = \frac{3}{2} \cdot \frac{P}{2} \lambda_{af} \quad (\text{N}\cdot\text{m}/\text{A}) \quad (4.28)$$

and the normalized electromagnetic torque is expressed as

$$T_{en} = \frac{T_e}{T_b} = \frac{\frac{3}{2} \cdot \frac{P}{2} \lambda_{af} \times I_s}{\frac{3}{2} \cdot \frac{P}{2} \lambda_{af} \times I_b} = I_{sn} \quad (\text{p.u.}) \quad (4.29)$$

indicating that torque equals the stator current in p.u., which gives the simplest control for implementation in the PMSM drives. Note that I_{sn} is the normalized stator current phasor magnitude. Relevant equations to determine the steady-state performance of the PMSM drive with this control strategy are derived in the following. The quadrature and direct axes stator voltages in rotor reference frames, in steady state, are

$$v_{qs}^r = (R_s + L_q p)I_s + \omega_r \lambda_{af} = R_s I_s + \omega_r \lambda_{af} \quad (\text{V}) \quad (4.30)$$

$$v_{ds}^r = -\omega_r L_q I_s \quad (\text{V}) \quad (4.31)$$

Note that the rate of change of currents is zero in the rotor reference frames as they are constants in the steady state. The magnitude of the stator voltage phasor is given by

$$V_s = \sqrt{(v_{qs}^r)^2 + (v_{ds}^r)^2} \quad (\text{V}) \quad (4.32)$$

and V_s in normalized units is obtained by combining Equations 4.29 through 4.31 as

$$V_{sn} = \frac{V_s}{V_b} = \frac{V_s}{\omega_b \lambda_{af}} = \sqrt{(\omega_m + R_{sn} I_{sn})^2 + (L_{qn} I_{sn} \omega_m)^2} \quad (\text{p.u.}) \quad (4.33)$$

From the phasor diagram shown in Figure 4.9 and the quadrature and direct axes stator voltages in the rotor reference frames, the power factor is obtained exploiting the fact that the quadrature stator current is in phase with the quadrature axis stator voltage, as

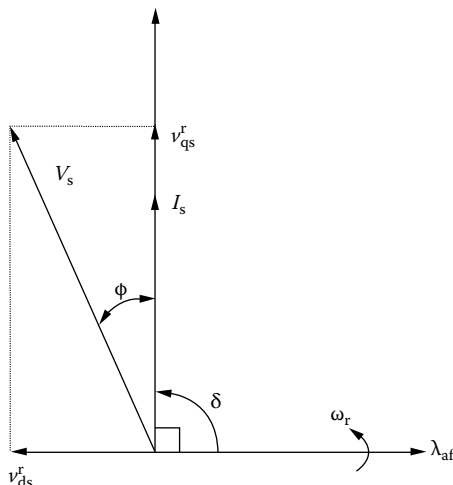


FIGURE 4.9 Constant torque angle control. (From Krishnan, R., *Electric Motor Drives*, Figure 9.11, Prentice Hall, Upper Saddle River, NJ, 2001. With permission.)

$$\cos\phi = \frac{v_{qs}^r}{V_s} = \frac{v_{qs}^r}{\sqrt{(v_{qs}^r)^2 + (v_{ds}^r)^2}} = \frac{1}{\sqrt{1 + \left(\frac{(L_{qn}I_{sn})^2}{1 + \frac{R_{sn}I_{sn}}{\omega_{rn}}} \right)^2}} \quad (4.34)$$

This equation implies that the power factor deteriorates with increasing rotor speed. The maximum rotor speed with this control strategy for a given stator current and, neglecting stator resistive drop, is obtained from the voltage magnitude expression 4.33 as follows:

$$\omega_{rn}(\max) \equiv \frac{V_{sn}(\max)}{\sqrt{1 + L_{qn}^2 I_{sn}^2}} \quad (4.35)$$

where $V_{sn(\max)}$ is obtained from the dc link voltage, V_{dc} , approximately as

$$V_{sn(\max)} = \frac{\sqrt{2} \times 0.45 V_{dc}}{V_b} \quad (4.36)$$

assuming that a six-step switching is performed in the inverter, neglecting device and cable voltage drops. It is realistic to consider a PWM-based inverter, in which case, the available voltage is further reduced by a factor of K_{dr} , usually in the range of 0.85 to 0.95 giving the voltage phasor as

$$V_{sn(\max)} \equiv \frac{0.636 K_{dr} V_{dc}}{V_b} \quad (4.37)$$

A PMSM with $R_{sn}=0.1729$ p.u., $L_b=0.0129$ H, $L_{qn}=0.6986$ p.u., $L_{dn}=0.4347$ p.u., $\omega_b=628.6$ rad/s, $V_b=97.138$ V, $I_b=12$ A is considered for the plotting of performance characteristics utilizing the constant torque angle control strategy and they are shown in Figure 4.10 for a 1 p.u. rotor speed. Note that the apparent power, i.e., volt-ampere (VA) is also plotted as a function of stator current to assess the VA rating required of the inverter and for the purpose of comparing various control strategies under discussion. The change in power factor from 1 to 0.859 over a 0 to 1 p.u. change in stator current is significant as this creates a need for a reactive VA, thus demanding a higher VA from the inverter.

The dc link voltage required to operate this PMSM at 1 p.u. speed and current is approximately estimated using Equation 4.37. Consider the derating factor to be 0.8 to allow for a margin of voltage for current control and, the V_{sn} required for this operating point is 1.365 p.u. From this the required dc link voltage is obtained as

$$V_{dc} = \frac{1.365}{0.636 \times 0.8} = 2.68 \text{ p.u.} = 2.68 \times 97.138 \text{ V} = 260.6 \text{ V}$$

If current control is not required and the six-step voltage source operation is resorted to in the inverter, the derating factor K_{dr} will go up to 0.92–0.95. This would generate peaky currents, resulting in higher copper losses in the machine

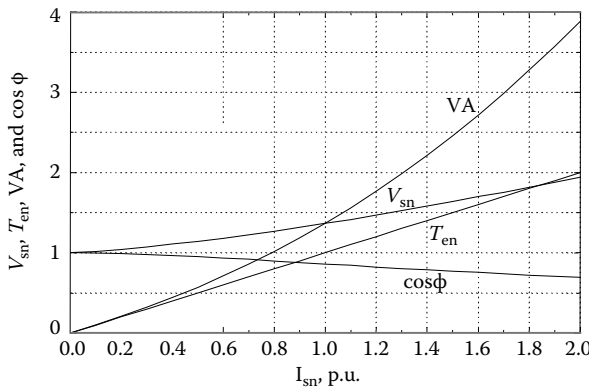


FIGURE 4.10 Performance characteristics for constant torque angle control. (From Krishnan, R., *Electric Motor Drives*, Figure 9.12, Prentice Hall, Upper Saddle River, NJ, 2001. With permission.)

in addition to the increased peak inverter current rating. But the six-step operation will contribute to a significant enhancement of the electromagnetic torque and the power output, particularly in the flux-weakening region. The maximum speed for this drive, neglecting stator resistive voltage drop using Equation 4.35 is 1.18 for 1 p.u. current.

That a weakening of mutual flux linkages is not possible with this control strategy is seen from the normalized mutual flux linkages expression given below:

$$\lambda_{mn} = \sqrt{1 + L_{qn}^2 I_{sn}^2} \quad (4.38)$$

The variation of mutual flux linkages can only vary from 1 p.u. to a point greater than that. But there is no way to reduce it below 1 p.u. so long as the torque angle is maintained at 90°, making the flux-producing current zero. Because of this fact, this control strategy is limited to servo drive applications requiring no flux-weakening operation. At higher air gap torques, the quadrature axis stator current increases proportionally, thus increasing the mutual flux linkages and hence, the stator voltage requirement.

Example 4.1

Draw the maximum torque versus speed envelope for the machine considered in this chapter using a constant torque angle control. The inverter current is restricted to a maximum of 2 p.u. and the voltage is limited to 1 p.u.

Solution

The stator voltage magnitude is

$$V_{sn} = \sqrt{(\omega_m + R_{sn} I_{sn})^2 + (\omega_m L_q I_{sn})^2} = 1 \text{ p.u.}$$

from which the stator current magnitude is derived as

$$I_{sn} = \frac{-\omega_m R_{sn} + \sqrt{\omega_m^2 R_{sn}^2 + (1 - \omega_m)^2 (\omega_m^2 L_{qn}^2 + R_{sn}^2)}}{\omega_m^2 L_{qn}^2 + R_{sn}^2}$$

In the numerator, only the positive sign is considered as I_{sn} has to be positive. The inverter current limit is incorporated by the following logic:

If $i_{sn} > 2$, $i_{sn} = 2$ p.u.

else, $i_{sn} = i_{sn}$

Since, the normalized torque is equal to the normalized stator current magnitude in this control strategy, the normalized current versus normalized speed gives the maximum torque versus speed envelope, as in Figure 4.11. The drive provides 2 p.u. torque only from 0 to 0.46 p.u. speed and 1 p.u. torque up to 0.7 p.u. Higher currents drastically reduce the maximum speed at which the constant torque is delivered.

4.4.2 UNITY POWER FACTOR CONTROL

A UPF control implies that the VA rating of the inverter is fully utilized for the real power input to the PMSM. The UPF control is enforced by controlling the torque angle as a function of the motor variables. The performance equations in this mode of operation are derived [5a] and given below.

The steady state quadrature and direct axes stator currents in the rotor reference frames are

$$I_{qs}^r = I_s \sin \delta \quad (4.39)$$

$$I_{ds}^r = I_s \cos \delta \quad (4.40)$$

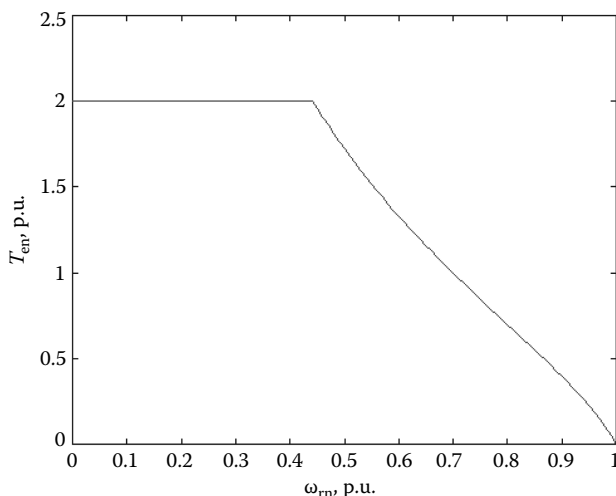


FIGURE 4.11 Normalized torque versus normalized speed.

and the normalized torque is obtained as

$$T_{\text{en}} = I_{\text{sn}} \left\{ I_{\text{sn}} \cdot \frac{L_{\text{dn}} - L_{\text{qn}}}{2} \cdot \sin 2\delta + \sin \delta \right\} \quad (\text{p.u.}) \quad (4.41)$$

The q- and d-axes normalized stator voltages are

$$v_{\text{qsn}}^{\text{r}} = \omega_{\text{m}} \left\{ 1 + L_{\text{dn}} I_{\text{sn}} \cos \delta + \frac{R_{\text{sn}} I_{\text{sn}}}{\omega_{\text{m}}} \cdot \sin \delta \right\} \quad (\text{p.u.}) \quad (4.42)$$

$$v_{\text{dsn}}^{\text{r}} = \omega_{\text{m}} I_{\text{sn}} \left\{ \frac{R_{\text{sn}}}{\omega_{\text{m}}} \cdot \cos \delta - L_{\text{qn}} \sin \delta \right\} \quad (\text{p.u.}) \quad (4.43)$$

from which the stator voltage phasor magnitude is obtained as

$$V_{\text{sn}} = \sqrt{(v_{\text{qsn}}^{\text{r}})^2 + (v_{\text{dsn}}^{\text{r}})^2} \quad (\text{p.u.}) \quad (4.44)$$

and the angle between the d-axis and the resultant voltage V_{sn} is

$$\tan(\delta + \phi) = \frac{v_{\text{qsn}}^{\text{r}}}{v_{\text{dsn}}^{\text{r}}} \quad (4.45)$$

Since the power factor angle has to be zero in this control,

$$\phi = 0 \quad (4.46)$$

it gives the following relationship for the torque angle,

$$\tan \delta = \frac{v_{\text{qsn}}^{\text{r}}}{v_{\text{dsn}}^{\text{r}}} \quad (4.47)$$

The substitution of Equations 4.42 and 4.43 into Equation 4.47 results in

$$\frac{\sin \delta}{\cos \delta} = \frac{1 + L_{\text{dn}} I_{\text{sn}} \cos \delta + \frac{R_{\text{sn}} I_{\text{sn}}}{\omega_{\text{m}}} \cdot \sin \delta}{\frac{R_{\text{sn}} I_{\text{sn}} \cos \delta}{\omega_{\text{m}}} - L_{\text{qn}} I_{\text{sn}} \sin \delta} \quad (4.48)$$

which on simplification gives

$$I_{\text{sn}} (L_{\text{qn}} \sin^2 \delta + L_{\text{dn}} \cos^2 \delta) = -\cos \delta \quad (4.49)$$

from which the torque angle is computed as

$$\delta = \cos^{-1} \left\{ \frac{-1 \pm \sqrt{1 - 4L_{qn}I_{sn}^2(L_{dn} - L_{qn})}}{2I_{sn}(L_{dn} - L_{qn})} \right\} \text{ (rad)} \quad (4.50)$$

Note that $(L_{dn} - L_{qn})$ is negative for the PMSM and the torque angle has to be greater than 90° . If the torque angle is less than 90° , it will result in an increase of mutual flux linkages contributing to a saturation in the machine, which is undesirable from the point of view of losses. Therefore, only a positive sign in Equation 4.50 will satisfy the requirement of $\delta > 90^\circ$. This expression provides the enforcement of the UPF control and, its implementation requires the motor phase current magnitude and motor parameters L_{qn} and L_{dn} . Note that the enforcing torque angle is independent of rotor speed.

For the same machine cited in the illustration of the constant torque angle control, the performance characteristics with the UPF control is shown in Figure 4.12. The normalized torque per unit normalized current is less than 1, indicating that this control strategy is not optimal in terms of torque generation and, its efficiency will be less due to the increased copper losses for the generation of the same torque. Its overall volt-ampere requirement is only 1.09 p.u. as against 1.355 p.u. for the constant torque angle control. The motor phasor voltage requirement is 1.098 p.u. against 1.365 p.u. for the constant torque angle control. This demonstrates that the reserve voltage availability with the UPF control would extend the constant torque region, resulting in a higher output of the PMSM drive. This feature is very desirable in many applications requiring extended speed range.

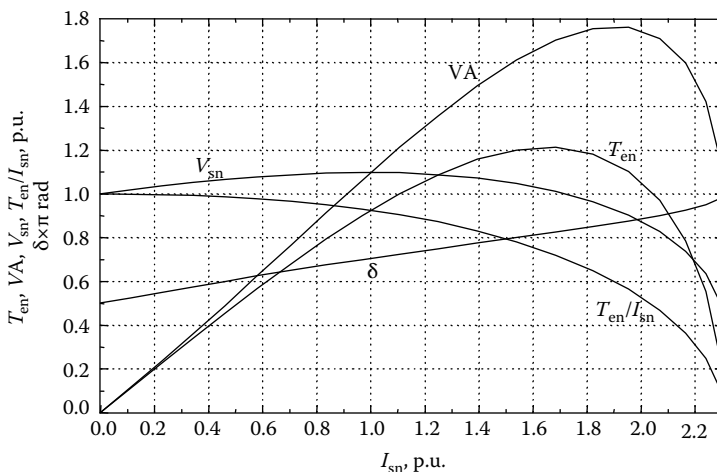


FIGURE 4.12 Performance characteristics for the UPF control. (From Krishnan, R., *Electric Motor Drives*, Figure 9.13, Prentice Hall, Upper Saddle River, NJ, 2001. With permission.)

Example 4.2

Draw the mutual flux linkages versus stator current magnitude for the UPF control strategy.

Solution

The torque angle is evaluated for each stator current magnitude from Equation 4.50 and then the mutual flux linkages is evaluated as

$$\lambda_{mn} = \sqrt{(1+L_{dn}I_{dn})^2 + (L_{qn}I_{qn})^2}$$

where

$$I_{dn} = I_{sn} \cos \delta$$

$$I_{qn} = I_{sn} \sin \delta$$

The mutual flux linkages versus stator current magnitude plot is shown in Figure 4.13. The maximum stator current is determined by the maximum direct axis stator current magnitude to nullify the stator flux linkages. It is derived as

$$I_{dn(max)} = -\frac{1}{L_{dn}} = -2.3 \text{ p.u.}$$

and

$$I_{sn(max)} = |I_{dn(max)}| = 2.3 \text{ p.u.}$$

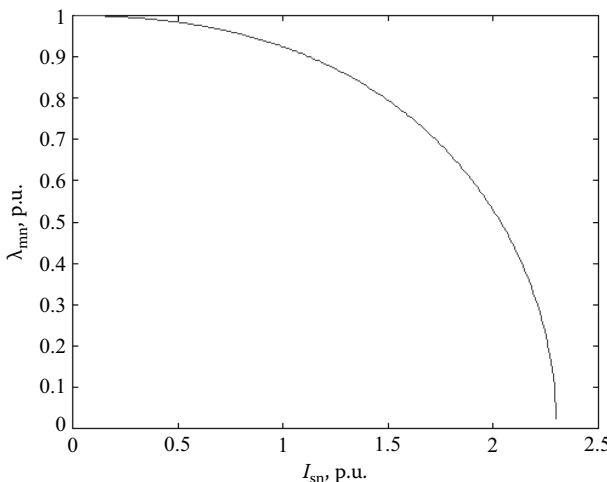


FIGURE 4.13 Mutual flux linkages versus stator current magnitude.

4.4.3 CONSTANT MUTUAL FLUX LINKAGES CONTROL

In this control strategy, the resultant flux linkages of the stator quadrature and direct axes and rotor, known as mutual flux linkages, is maintained at a constant [5a] and most usually at a value equal to the rotor flux linkages, λ_{af} . Its main advantage is that by limiting the mutual flux linkages, the stator voltage requirement is kept comparably low. In addition, varying mutual flux linkages provides a simple and straightforward flux weakening for operation at speeds higher than the base speed. Hence, the mutual flux linkages control is one of the powerful techniques useful in the entire speed range as against other schemes, which are limited to operations below the base speed only. The mutual flux linkages are expressed as follows:

$$\lambda_m = \sqrt{(\lambda_{af} + L_d I_{ds}^r)^2 + (L_q I_{qs}^r)^2} \quad (4.51)$$

and equating

$$\lambda_m = \lambda_{af} \quad (4.52)$$

and substituting the direct and quadrature axis currents in terms of the stator current phasor and torque angle in the above equations results in

$$I_s = -\frac{2\lambda_{af}}{L_d} \left[\frac{\cos \delta}{\cos^2 \delta + \rho^2 \sin^2 \delta} \right] \quad (4.53)$$

where the saliency ratio is given by

$$\rho = \frac{L_q}{L_d} \quad (4.54)$$

Two distinct cases arise here depending on the saliency ratio, ρ . For surface-mounted magnets, ρ is around unity, and for a buried or interior PM rotor construction, it could have values as high as 3. Much higher values have been achieved in special designs. These two cases are analyzed separately in the following.

Case (i): $\rho = 1$

This amounts to a value of torque angle, δ , derived using Equations 4.51 and 4.52 in conjunction with the fact that the saliency ratio is one to give

$$\delta = \cos^{-1} \left\{ \frac{-L_d I_s}{2\lambda_{af}} \right\} \quad (\text{rad}) \quad (4.55)$$

Note that the base voltage is defined as

$$V_b = \omega_b \lambda_{af} \quad (\text{V}) \quad (4.56)$$

and base impedance is

$$Z_b = \omega_b L_b = \frac{V_b}{I_b} \quad (\Omega) \quad (4.57)$$

Using these for normalization of the motor current given in Equation 4.53, the torque angle is derived as

$$\delta = \cos^{-1} \left\{ -\frac{L_d I_b \cdot I_s / I_b}{2\lambda_{af}} \right\} = \cos^{-1} \left\{ -\frac{I_{sn} L_{dn}}{2} \right\} \quad (\text{rad}) \quad (4.58)$$

Case (ii): $\rho \neq 1$

This yields the torque angle as

$$\delta = \cos^{-1} \left\{ \frac{1}{L_{dn} I_{sn} (1-\rho^2)} \pm \sqrt{\left\{ \frac{1}{L_{dn} (1-\rho^2) I_{sn}} \right\}^2 - \frac{1}{(1-\rho^2)}} \right\} \quad (\text{rad}) \quad (4.59)$$

The minimum of the two possible values of δ is chosen so that the demagnetizing current is small. Note also, that δ has to be greater than 90° . The other performance equations are as given in the previous section and so also, the machine parameters.

The performance characteristics are shown in Figure 4.14. The torque per ampere is slightly less than unity and the stator voltage phasor magnitude is approximately 1.17 p.u. and is less than required for a constant torque angle control, and the VA rating is also less for this control. The power factor is close to unity upto 1 p.u. stator current, indicating that this scheme is much closer to the UPF control than

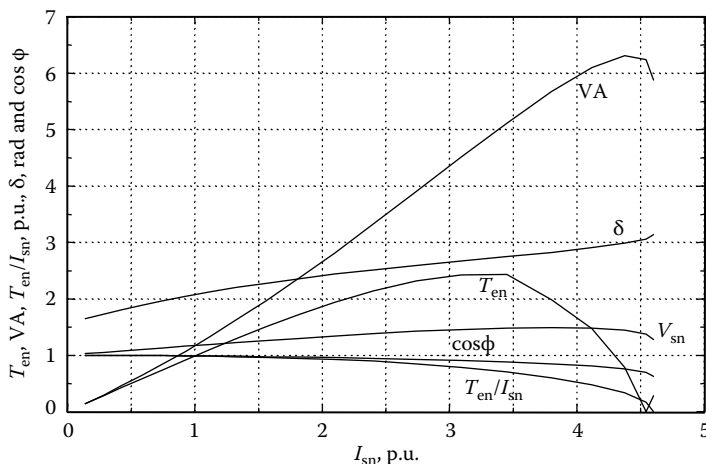


FIGURE 4.14 Performance characteristics for constant mutual flux linkages control. (From Krishnan, R., *Electric Motor Drives*, Figure 9.14, Prentice Hall, Upper Saddle River, NJ, 2001. With permission.)

to the constant torque angle control in this narrow range. Its torque per unit current decreases beyond 2 p.u. stator current but provides a significant torque over a greater current range when compared to the UPF control scheme.

4.4.4 ANGLE CONTROL OF AIR GAP FLUX AND CURRENT PHASORS

The air gap torque can be alternately derived as

$$T_e = \frac{3}{2} \frac{P}{2} \lambda_m i_s \sin \theta_{ms} \quad (4.60)$$

where θ_{ms} is the angle between the current and the air gap flux phasors. The relationship between the current and the mutual flux linkages in its direct and quadrature components and phasors are shown in Figure 4.15. The derivation of this key expression is given later. A control strategy can be synthesized to keep the flux current angle, θ_{ms} , at 90° . In that case, the control of this machine reduces to the control of a separately excited dc machine, in which, the torque is the product of the field flux linkages and the armature current. In the separately excited dc machine, the field flux can be maintained constant because the field current is individually controlled. But in the PMSM, the air gap flux, which is the result of the rotor and stator flux linkages, cannot be maintained constant for all currents while the angle between the air gap flux and the current phasors is maintained at 90° . Consequently, the torque constant varies as a function of the armature current in contrast to the separately excited dc machine, where the torque constant is kept constant by keeping the field current, a constant. Further, the implication of such a control can be examined in the following.

The induced emf phasor leads the air gap flux phasor by 90° . Controlling the current phasor to lead the air gap flux phasor by the same angle results in the coincidence of the induced emf and current phasors. If the stator resistance is neglected,

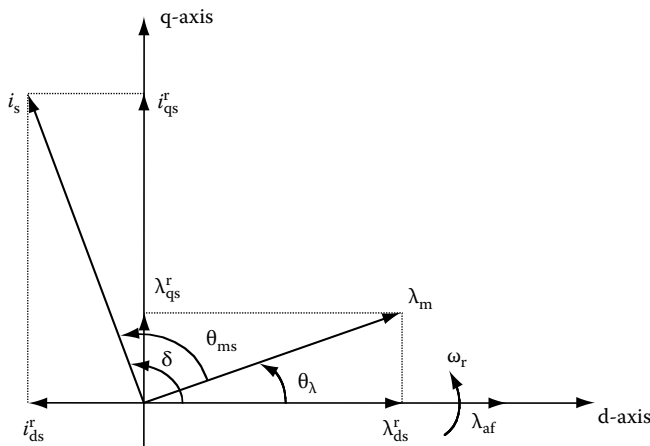


FIGURE 4.15 Phasor diagram of the PMSM showing the mutual flux linkages.

note that the stator terminal voltage is equal to the induced emf, and the relative phase between them is zero. Therefore, the angle between the current and voltage phasors is zero, resulting in the UPF operation of the PMSM drive.

The advantage of such a control is that it is very similar to the situation in a dc machine with regard to its field, where the field and the armature current have a perpendicular phase relationship. This enables the development of a simple control strategy even without a position sensor. As the air gap induced emf is leading the mutual flux by 90° , injecting the stator current phasor in phase with that will have the angle between the mutual flux and the stator current phasor leading at 90° . Then the placement of the current vector no longer requires the position sensor feedback if, the induced emf is available. Note that the induced emf signal is nonexistent at zero speed, and, finding it around that speed is very difficult given the measurement problems. But an estimation is possible which will allow this strategy to be used effectively for nonpositioning applications requiring no low-speed performance. Starting may be achieved by microstepping and other techniques that will be discussed later.

To understand this strategy, it is essential to derive the air gap torque in terms of the flux angle between the current and the mutual flux and the stator current and the mutual flux linkages magnitudes. From [Figure 4.9](#), the quadrature and direct axis stator currents and flux linkages in the rotor reference frames are obtained by geometric projections on the quadrature and direct axes as

$$\begin{aligned}\theta_{ms} &= \delta - \theta_\lambda \\ \lambda_{qs}^r &= \lambda_m \sin \theta_{ms} \\ \lambda_{ds}^r &= \lambda_m \cos \theta_{ms} \\ i_{qs}^r &= i_s \sin \delta \\ i_{ds}^r &= i_s \cos \delta\end{aligned}\tag{4.61}$$

where θ_λ is the angle between the mutual flux linkages and the magnet rotor flux linkages. Substitute these relationships into the torque expression, which on simplification gives

$$T_e = \frac{3}{2} \frac{P}{2} \left[\lambda_{af} i_{qs}^r + (L_d - L_q) i_{qs}^r i_{ds}^r \right] = \frac{3}{2} \frac{P}{2} \left[\lambda_{ds}^r i_{qs}^r - \lambda_{qs}^r i_{ds}^r \right] = \frac{3}{2} \frac{P}{2} \lambda_m i_s \sin \theta_{ms}\tag{4.62}$$

The flux angle and the torque angle are related by this flux current angle as

$$\delta = \theta_{ms} + \theta_\lambda = \frac{\pi}{2} + \theta_\lambda\tag{4.63}$$

from which the following relationship is developed:

$$\sin \delta = \cos \theta_\lambda\tag{4.64}$$

The torque angle and the flux angle can be substituted in terms of the direct and quadrature axis currents and flux linkages from Equation 4.61 to obtain a polynomial in the normalized d-axis current as

$$a(i_{\text{dsn}}^{\text{r}})^4 + b(i_{\text{dsn}}^{\text{r}})^3 + c(i_{\text{dsn}}^{\text{r}})^2 + d = 0 \quad (4.65)$$

where

$$a = L_{\text{qn}}^2 - L_{\text{dn}}^2; \quad b = -2L_{\text{dn}}; \quad c = -1 - 2L_{\text{qn}}^2 i_{\text{sn}}^2; \quad d = L_{\text{qn}}^2 i_{\text{sn}}^4 \quad (4.66)$$

Solving the polynomial equation, and finding the appropriate root of that, yields the normalized direct axis stator current, from which the quadrature axis stator current is found as the stator current phasor is known to start with the computation. Then, all other variables such as torque, flux linkages, torque angle, stator voltage magnitude for a given speed and volt ampere are computed. The MATLAB code for this computation is given below. The performance characteristics of this control strategy are shown in Figure 4.16. The characteristics very closely resemble that of the UPF control strategy as reasoned in the above. The striking feature is the low volt-ampere requirement for this operation as, the mutual flux linkages decrease with increasing current, limiting the stator voltage requirement.

```
% Program to compute the performance characteristics of the
% angle control of the flux and current phasors strategy .
% It is in normalized form.
clear all;close all;
```

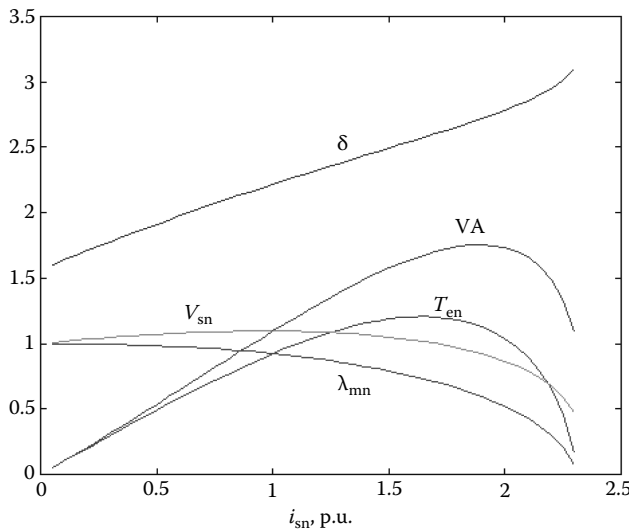


FIGURE 4.16 Performance characteristics of the angle control between the flux and current phasors.

```
% data

n=1;rsn=0.1729;
lqn=0.699; ldn=0.4367; ro=lqn/ldn;
a=(ro^2-1)*ldn^2;b=-2*ldn; % Polynomial coefficients

% computation starts

for isn=0.05::0.05:2.3, % Stator current magnitude
    c=-1-2*lqn^2*isn^2;d=lqn^2*isn^4; % Polynomial
    coefficients
    y=[a b c 0 d]; % Poly. coef. vector
    sols=roots(y) % Solution of the d axis
    current
    for t=1:4, % Roots are stored in matrix
        form
        sols1(n,t)=sols(t);
    end
    id(n)=sols1(n,3); % D axis current
    iq(n)=sqrt(isn^2-id(n)^2); % Q axis current
    del(n)=acos(id(n)/isn); % Torque angle
    ten(n)=iq(n)*(1+(1-ro)*ldn*id(n)); % Air gap torque
    lamda(n)=sqrt((1+ldn*id(n))^2+
        (lqn*iq(n))^2); % Mutual flux linkages
    tpuc(n)=ten(n)/isn; % Torque per unit current
    vs(n)=sqrt((rsn*id(n)-
        lqn*iq(n))^2+(1+rsn*iq(n)+ldn*id(n))^2); % Stator
    voltage magnitude
    va(n)=vs(n)*isn; % Volt ampere requirement
end

% Computation ends and plotting begins

plot(isn1,ten,isn1,del,isn1,lamda,isn1,vs,isn1,va) % Plotting of variables versus current
```

4.4.5 OPTIMUM TORQUE PER UNIT CURRENT CONTROL

A control strategy to maximize electromagnetic torque for a unit stator current is valuable from the optimum machine and, inverter utilization points of view [5a]. As in other control strategies, this control strategy is enforced with a torque angle control. The torque angle, for a given stator current magnitude, for this control strategy is derived as follows. The electromagnetic torque is

$$T_e = \frac{3}{2} \cdot \frac{P}{2} \left[\lambda_{af} i_s \sin \delta + \frac{1}{2} (L_d - L_q) i_s^2 \sin 2\delta \right] \quad (\text{N}\cdot\text{m}) \quad (4.67)$$

which in terms of normalized units is

$$T_{\text{en}} = i_{\text{sn}} \left[\sin \delta + \frac{1}{2} (L_{\text{dn}} - L_{\text{qn}}) i_{\text{sn}} \sin 2\delta \right] \quad (\text{p.u.}) \quad (4.68)$$

where the base torque is defined as

$$T_b = \frac{3}{2} \cdot \frac{P}{2} \lambda_{\text{af}} I_b \quad (\text{N} \cdot \text{m}) \quad (4.69)$$

The torque per unit stator current is given as

$$\left(\frac{T_{\text{en}}}{i_{\text{sn}}} \right) = \left[\sin \delta + \frac{1}{2} (L_{\text{dn}} - L_{\text{qn}}) i_{\text{sn}} \sin 2\delta \right] \quad (4.70)$$

Its maximum is found by differentiating with respect to δ and equating it to zero to obtain the condition for torque angle as

$$\delta = \cos^{-1} \left\{ -\frac{1}{4a_1 i_{\text{sn}}} + \sqrt{\left(\frac{1}{4a_1 i_{\text{sn}}} \right)^2 + \frac{1}{2}} \right\} \text{(rad)} \quad (4.71)$$

where

$$a_1 = (L_{\text{dn}} - L_{\text{qn}}) = L_{\text{dn}}(1 - \rho) \quad (4.72)$$

Only the positive sign in the argument is considered as, δ has to be greater than 90° to reduce the field in the air gap. To illustrate the superior performance of this control against constant torque angle control, the torque versus stator current is shown in Figure 4.17. It has 3.2% and 11.05% torque enhancement for 1 and 2 p.u. stator currents,

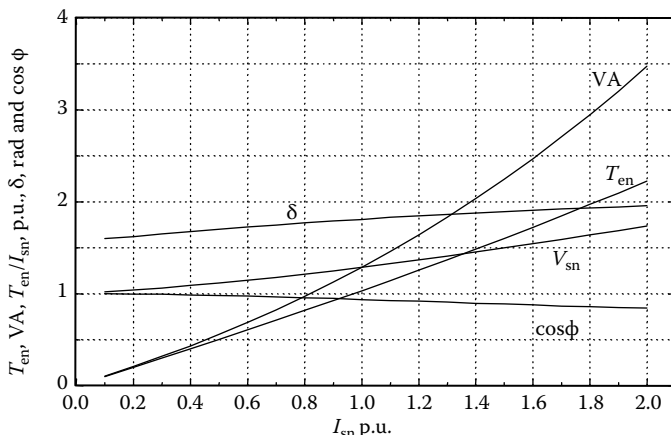


FIGURE 4.17 Maximum torque per unit stator current control performance. (From Krishnan, R., *Electric Motor Drives*, Figure 9.15, Prentice Hall, Upper Saddle River, NJ, 2001. With permission.)

respectively, when compared to the constant torque angle operation and, requires a stator voltage of 1.286 and 1.736 p.u., respectively. This is the penalty paid for using this control strategy in terms of the poor inverter utilization, which needs 3.472 p.u. the VA rating is at 2 p.u. stator current as against 2.8 p.u. for the constant mutual flux linkages control with a torque derating of 0.065 p.u. only. Note that, the torque enhancement could be nearly 100% for $\rho=3.5$ at 2 p.u. stator current and this control strategy is, in general, preferred for highly salient machines with $\rho>2$, and in the lower speed range.

The torque enhancement due to higher saliency ratios and maximum torque per unit stator current control is illustrated in Figures 4.18 and 4.19, respectively. Here the direct axis inductance is taken as the base inductance and the rotor flux linkages

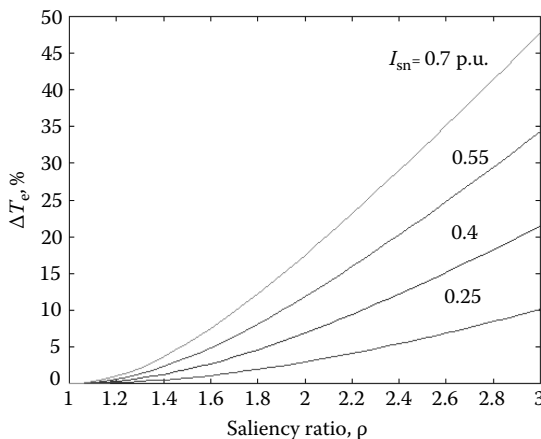


FIGURE 4.18 Torque increase versus saliency ratio for various currents.

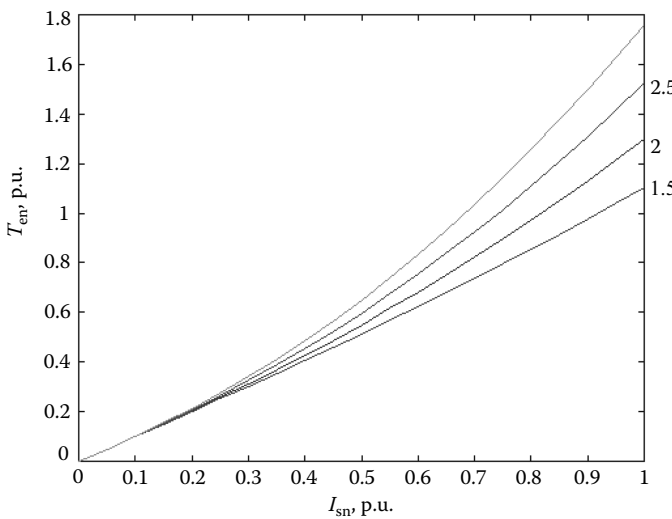


FIGURE 4.19 Normalized torque versus stator current for various saliency ratios.

are the base flux linkages. The rated current works out to be equal to 0.25 p.u. for the machine considered for illustration. Torque enhancement with higher saliency ratios is around a 10%–15% range for rated current, and considerably more for higher currents. From a steady-state operational point of view, torque enhancement is nominal and may not be a critical factor in choosing this strategy for many applications.

4.4.6 CONSTANT POWER LOSS CONTROL

The maximum torque versus speed envelope for the control strategies in the lower than base speed region is commonly found by limiting the stator current magnitude to the rated value. In the higher than base speed region, the shaft power is commonly limited to rated value. Current limiting restricts copper losses but not necessarily the core losses. Similarly, limiting the shaft power does not limit power losses directly. Limiting current and power to rated values, ignores the thermal robustness of the machine that requires the total losses be constrained to a permissible value. Rated current and power guarantee acceptable power losses only at rated speed. Therefore, these simplistic restrictions are only valid for motion control applications requiring operation at rated speed. Increasingly, at present, single speed-driven applications are being retrofitted or replaced with variable speed motor drives to increase process efficiency and operational flexibility. Also, for manufacturing cost optimization, the same machine designs are utilized in vastly different environmental conditions thus, necessitating control methods to maintain the thermal robustness of the machine while extracting the maximum torque over a wide speed range. The constant power loss-based operation provides the maximum torque versus speed envelope from these viewpoints.

A criterion to find the maximum operating envelope for wide speed range applications is based on the premise that the operational boundary of any machine is defined by the maximum permissible power loss for that machine. A comparison between the power loss-limited operational boundary and the current- and power-limited operational boundary reveals that the loss-based method results in a significant increase in permissible torque at lower than base (rated) speeds. Consequently, the dynamic response is enhanced below the base speed. It is also demonstrated that the conventional method of limiting current or power can lead to the generation of excessive power loss in the flux-weakening region.

An implementation strategy for this scheme is based on an outer power loss feedback control loop. The input to the system is the desired maximum power loss of the machine. The feedback loop limits the torque command such that, the power loss does not exceed the maximum set value at any operating point. This system is applicable to all types of motor drives for the full range of operation, and is independent of the choice of control strategy for the dynamic control of torque. This strategy can be integrated into all high-performance motor drives with very little modification in their control algorithms. A load duty cycle can be integrated into the system controller to maintain the effective total power loss by varying the power loss reference in the outer control loop as a function of the duty load cycle. Further, it is noted, that the underlying control algorithm lends itself to real-time implementation. The maximum permissible power loss of a machine must be chosen based on a preset temperature rise for the machine. Therefore, the allowable constant power losses may vary significantly depending on the operational environment, ambient temperature, and the cooling arrangement for the machine.

The following assumptions are made to give a conceptual and analytical insight and clarity:

1. All motor drive parameters are assumed to be constant.
2. Windage, friction, and inverter losses are ignored even though they can be integrated, depending on their significance.
3. A high bandwidth vector controller is utilized in the drive system, resulting in a negligible stator current error.
4. The rated current is defined as the current that generates rated torque using the zero direct axis current control strategy.
5. Base values used for normalization of the plots are chosen as the rated value of the variables.

Machine model with losses: A dq model for a PMSM in rotor reference frames in steady state with simplified loss representation is given in Figure 4.20, where, I_{qs}^r and I_{ds}^r are quadrature and direct axis stator currents, respectively, and V_{qs}^r and V_{ds}^r are quadrature and direct axis stator voltages, respectively. I_q and I_d are q- and d-axes torque-generating currents, respectively, and I_{qc} and I_{dc} are q- and d-axes core loss currents, respectively. R_s and R_c are stator and core loss resistors, respectively, and L_q and L_d are q- and d-axes self-inductances, respectively. λ_{af} is the magnet flux linkages, and ω_r is the rotor electrical speed.

Input stator currents and voltages are derived from the equivalent circuit model with losses as

$$\begin{bmatrix} I_{qs}^r \\ I_{ds}^r \end{bmatrix} = \begin{bmatrix} 1 & \frac{L_d \omega_r}{R_c} \\ -\frac{L_q \omega_r}{R_c} & 1 \end{bmatrix} \begin{bmatrix} I_q \\ I_d \end{bmatrix} + \begin{bmatrix} \frac{\lambda_{af} \omega_r}{R_c} \\ 0 \end{bmatrix} \quad (4.73)$$

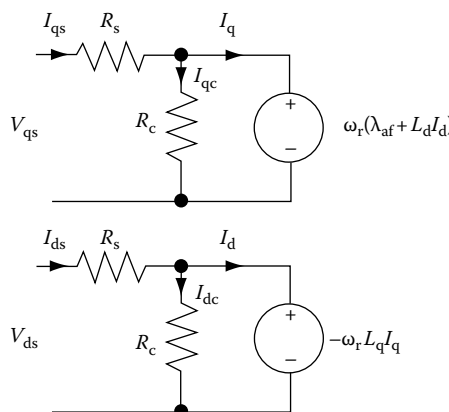


FIGURE 4.20 Machine model in rotor reference frames including stator and core loss resistances.

$$\begin{bmatrix} V_{qs}^r \\ V_{ds}^r \end{bmatrix} = \begin{bmatrix} R_s & \omega_r L_d \left(1 + \frac{R_s}{R_c}\right) \\ -\omega_r L_q \left(1 + \frac{R_s}{R_c}\right) & R_s \end{bmatrix} \begin{bmatrix} I_q \\ I_d \end{bmatrix} + \begin{bmatrix} \omega_r \lambda_{af} \left(1 + \frac{R_s}{R_c}\right) \\ 0 \end{bmatrix} \quad (4.74)$$

The torque, T_e , as a function of I_q and I_d is given below:

$$T_e = 0.75P(\lambda_{af}I_q + (L_d - L_q)I_dI_q) \quad (4.75)$$

where

T_e is torque

P is the number of rotor poles

The net core losses, P_c , for the machine is computed as follows [23]:

$$P_c = \frac{1.5\omega_r^2(L_qI_q)^2}{R_c} + \frac{1.5\omega_r^2(\lambda_{af} + L_dI_d)^2}{R_c} = \frac{1.5}{R_c}\omega_r^2\lambda_m^2 \quad (4.76)$$

where λ_m can be recognized as the mutual air gap flux linkages. Finally, the total power loss, P_l , including both copper and core losses, can be represented as

$$P_l = 1.5R_s(I_{qs}^2 + I_{ds}^2) + \frac{1.5}{R_c}\omega_r^2[(L_qI_q)^2 + (\lambda_{af} + L_dI_d)^2] \quad (4.77)$$

In the next subsection, the operational envelope, resulting from the application of the constant power loss control (CPLC) to a PMSM, is discussed.

Constant power loss control and comparison: The maximum permissible power loss, P_{lm} , depends on the desired temperature rise for the machine. P_{lm} can be chosen to be equal to the net losses at the rated torque and speed, assuming that the machine is running under exact operating conditions as defined in the manufacturer data sheets. At any given speed, the current phasor, which is the result of I_q and I_d , and its trajectory for maximum power loss is given by Equation 4.77 with P_l replaced by P_{lm} . This trajectory is a circle at zero speed and a semicircle at nonzero speeds. The operating point of a PMSM must always be on or inside the trajectory defined by Equation 4.77 for that speed, so that, the net losses do not exceed P_{lm} . At any given speed, the operating point on the constant power loss trajectory, which also results in maximum torque, defines the operational boundary at that speed. At this operating point, maximum torque is generated for the given power loss of P_{lm} . In the flux-weakening region, both voltage and power loss restrictions limit the maximum torque at any given speed. The following relationship is true for any stator current phasor operating point in the flux-weakening region, assuming that the voltage drop across the phase resistance is negligible:

$$V_{sm} = [(L_qI_q)^2 + (\lambda_{af} + L_dI_d)^2]^{0.5}\omega_r = \omega_r\lambda_m \quad (4.78)$$

where V_{sm} is either the maximum desired back emf or the fundamental component of the maximum voltage available to the phase. The latter applies to the six-step voltage

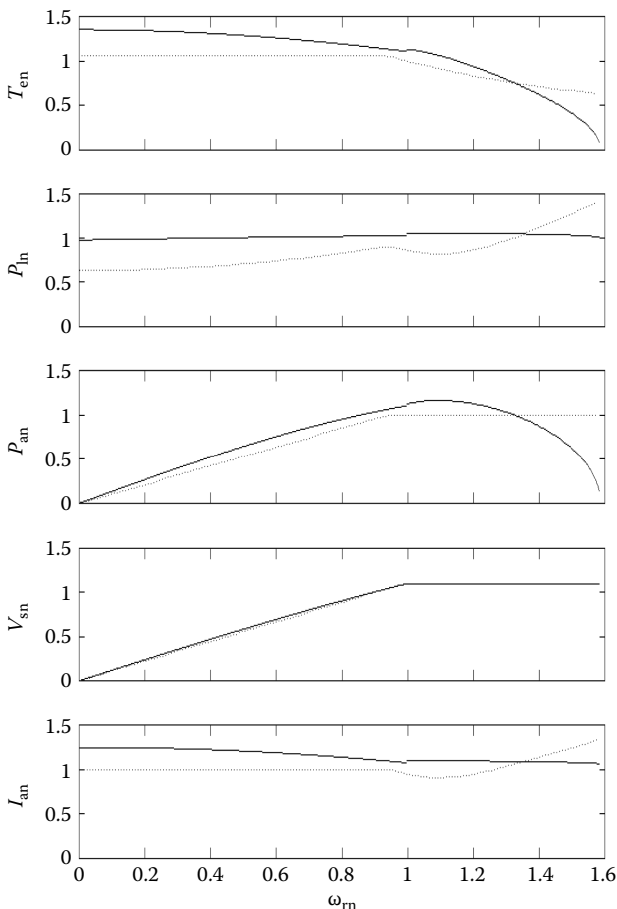


FIGURE 4.21 Normalized maximum torque, power loss, air gap power, voltage, and phase current for the CPLC scheme (solid lines) and for the scheme with current and power limited to rated values (dotted lines).

control strategy. At any given speed, the stator current phasor that results in a set power loss can be found by solving Equation 4.77. This operating point corresponds to the maximum permissible torque at the given speed in the flux-weakening region.

Figure 4.21 shows the maximum torque possible for the full range of speed for the motor drive. The power loss is limited to the rated value of 121 W at all operating points.

Operation below base speed: The base speed, ω_b , is defined as the speed beyond which the applied phase voltage must remain constant along the CPLC scheme boundary. In a lower than base speed operating region, torque is only limited by the power loss, while phase voltage is less than the maximum possible value, V_{sm} . This region of operation is shown in Figure 4.21 between 0 and 1 p.u. speed. Power loss, air gap power, phase voltage, and current along the CPLC scheme boundary are also shown in that figure, demonstrating that it is superior to the conventional control method.

Flux-weakening region: The portion in Figure 4.21 between 1 and 1.55 p.u. speed corresponds to the flux-weakening region of operation, where back emf is limited to 1.1 p.u. It is seen that the CPLC boundary drops at a faster rate in this region due to voltage restrictions. The maximum possible air gap power continues to rise beyond the rated speed up to approximately 1.15 p.u. speed. The operational boundary resulting from limiting current and power to rated values is also shown in Figure 4.21. It can be concluded from the example, that the application of the constant current and power operational envelope results in

1. Underutilization of the machine at lower than base speed
2. Generation of excessive power loss at higher than rated speeds unless, both power and current are limited to rated values in the flux-weakening region
3. Underutilization of the machine in some intervals of the flux-weakening region

Constant power loss control implementation: Figure 4.22 shows the block diagram for an implementation strategy of the CPLC scheme.

The wide speed-range linear torque controller is assumed to provide torque linearity over the full range of operating speed including the flux-weakening range. Any control strategy can be utilized in the torque controller block. The current controller takes the quadrature and direct axis stator current commands, (\dot{I}_{qs}^*) and (\dot{I}_{ds}^*) in rotor reference frames, as well as the rotor position, θ_r , as its inputs. The copper and core losses of the machine are estimated utilizing the currents and speed. All the required variables for power loss estimation are already available within most high-performance control systems. The estimated power loss is compared with the power loss reference, P_{lm}^* . The difference is processed through a proportional and integral (PI) controller. The output of the power loss controller determines the maximum permissible torque, T_{lim} . If the torque command is higher than the maximum limit then, the system automatically adjusts the torque to the maximum possible value, T_{lim} . However, if the torque command is less than the maximum possible torque at a given speed then, the final torque command is unaltered. The same absolute

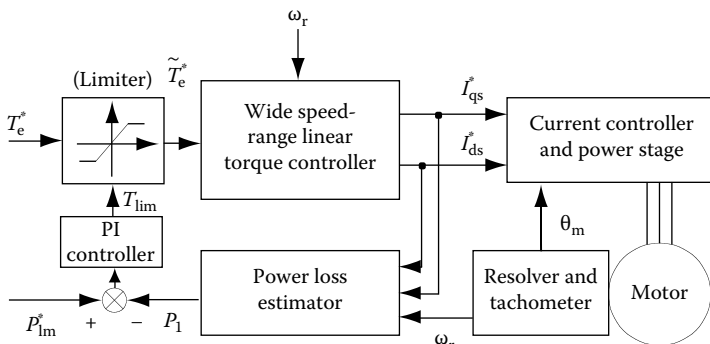


FIGURE 4.22 Implementation strategy for the constant power loss controller.

value of the torque limit is applied to both positive and negative torque commands. The salient features of this implementation strategy are summarized below:

1. Off-line calculation of the maximum torque versus speed envelope is not necessary.
2. Maximum power loss can be adjusted by an operator or by a process demand.
3. The system is independent of the control strategy used in the torque block.
4. All machine parameters required for implementing this control strategy are already available in most high-performance controllers.
5. The implementation lends itself to real-time implementation.

The control scheme impacts the inverter drive due to a higher current acceptance at speeds lower than that of the base speed and parameter sensitivity effects. They are discussed below.

Higher current operation at lower than base speed: It is seen from [Figure 4.21](#) that the CPLC provides a 39% higher torque at zero speed when compared to the maximum torque possible with rated current. This requires 25% more than rated current in the low-speed region only. It is to be noted that this additional current requirement does not result in a proportional increase in the price of the drive. This is mainly due to the fact that the voltage requirements of both control strategies are similar. Therefore, the power switches have to be upgraded only for current and not for a higher voltage.

Parameter dependency: The scheme is dependent on the machine parameters L_d , L_q , and λ_{af} . L_d does not vary significantly. L_q varies as a result of magnetic saturation, but can be estimated accurately as a function of phase current. An accurate estimation of λ_{af} requires more complex algorithms. Any implementation strategy for the CPLC is by nature parameter dependent. This is the case with all model-based control strategies.

4.4.7 MAXIMUM EFFICIENCY CONTROL

A control strategy, minimizing the total electrical losses at all operating points, is a good candidate in many applications where a maximum efficiency operation is required. Such applications can be found predominantly in heating ventilation and air conditioning, and home appliances such as washers, dryers, freezers, refrigerators and battery-operated hand tools, lawn mowers, garden tools, and vacuum cleaners. In all other high-performance applications, maximization of efficiency enables higher thermal robustness and hence, a longer life for the machine insulation, resulting in a high operational reliability of the motor drive system.

Maximum torque per unit current strategy only minimizes stator resistive losses but does not optimize the core losses and hence, the combined electrical losses. This was explained in the section on constant power loss control strategy. The CPLC strategy derives the maximum torque speed operational envelope for a fixed electrical power loss. If the minimum power input for each and every operating point is found and implemented, then it leads to a minimization of power losses and hence to a maximization of the efficiency. Consider the operation of a PMSM whose data

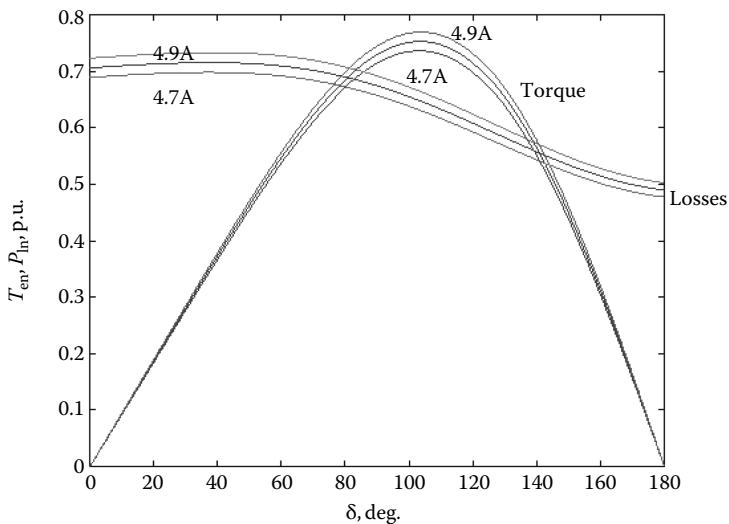


FIGURE 4.23 Normalized air gap torque and electrical power losses versus torque angle for 4.7, 4.8, and 4.9A stator currents.

is given in Example 3.1. Its torque versus torque angle characteristics for varying currents is shown in Figure 4.23. The total losses, normalized to its rated losses are also shown the same figure. In order to understand distinctly that the maximum torque per unit current operating point is not optimal from the losses and hence, the efficiency performance index, the figure for the torque angle from 90° to 115° is expanded and shown in Figure 4.24. Consider the desired operating point to be the

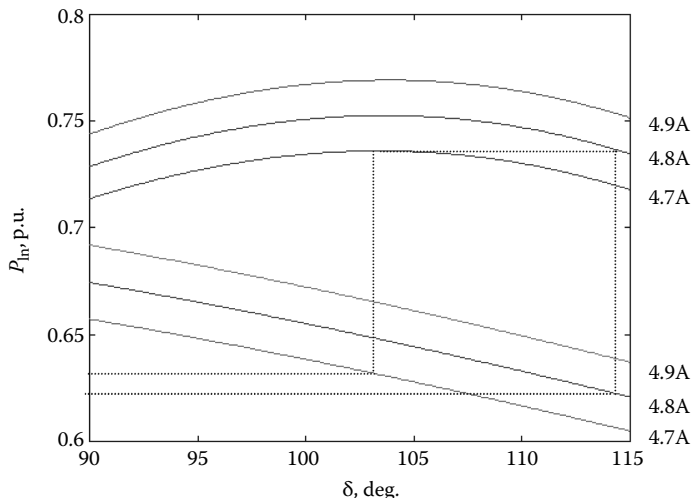


FIGURE 4.24 Expanded characteristics between 90° and 115° of torque angle from the previous figure.

maximum torque for 4.7A stator current operation. Then the operating torque angle is 103.5° . The same torque can be obtained operating on the 4.8A stator current phasor characteristic also, but with a torque angle of 114.5° as shown by extending the dotted line from the maximum torque point on the 4.7A stator current phasor characteristic. The corresponding total power losses are lower when operating with a 4.8A stator current phasor as compared to the 4.7A stator current phasor operation. The torque per unit current is high for a 4.7A operation as against the 4.8A operation. Even though this is graphically demonstrated for an incremental change in the stator current, it becomes obvious that for higher currents such as 4.9 or 5A, the losses are even smaller when compared to the 4.7 or 4.8A stator current operations. This analysis has ignored the additional losses such as conduction losses incurred in the inverter due to a higher current flow. That these losses are smaller than that of the incremental electrical power losses of the machine is a reasonable assumption. If they are significant, they can be incorporated into the loss versus torque angle plot to find the minimum loss operating point.

The reason why the losses decrease with increasing stator current and torque angle is that the core losses decrease as the mutual flux linkages decrease even though the stator resistive losses increase slightly. With an increasing torque angle, the direct axis stator current increases and hence the direct axis flux linkages decrease. Even if the quadrature axis current stays the same or increases, thus maintaining or increasing the same quadrature axis flux linkages, the direct axis mutual flux decreases invariably, depending on the direct axis stator current. These have the cumulative effect of reducing the mutual flux linkages. As the core losses are proportional to the mutual flux linkages, its reduction leads to an overall decrease in the electrical power losses. In a salient pole PMSM, the quadrature axis stator current need not increase to maintain the same torque before and after the torque angle change. One of the advantages of this control strategy is that it is applicable to machines even with a saliency ratio of one and, saliency does not significantly alter the benefits of this control scheme.

Although the concept is simple, it is not feasible to have a simple algorithm for implementing this strategy online. The minimum loss for every operating point is computed off-line and then could be loaded into tables for efficient use in the implementation. This approach seems to be the most feasible at present. Similar to fuzzy control techniques adapted in induction motor loss minimization, an equivalent approach is feasible for the PMSM drive. The incorporation of the maximum efficiency control is shown schematically in Figure 4.25.

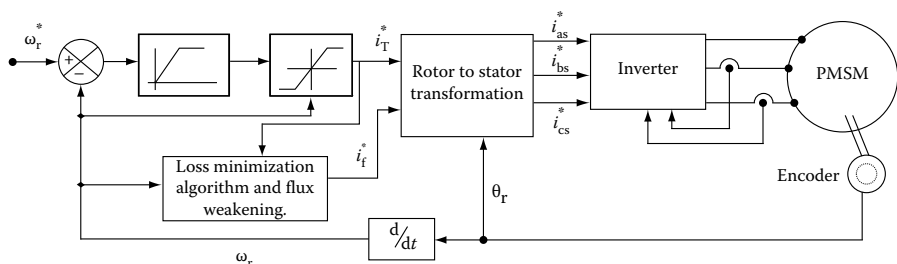


FIGURE 4.25 Loss minimization control schematic for the PMSM drive system.

REFERENCES

Dynamic Performance

1. K. J. Binns and M. A. Jabbar, Dynamic performance of a permanent-magnet synchronous motor, *Conference on Small Electrical Machines*, pp. 78–81, 1976.
2. H. Grotstollen, G. Pfaff, A. Weschta, et al., Design and dynamic behaviour of a permanent-magnet synchronous servo-motor with rare-earth-cobalt magnets, *International Conference on Electrical Machines*, pp. 320–329, 1980.
3. M. E. Abdelaziz, Dynamic braking of permanent magnet synchronous motors, *Proceedings of the International Conference on Electrical Machines*, pp. 587–590, 1984.
4. T. Himei, S. Funabiki, Y. Agari et al., Analysis of voltage source inverter-fed permanent magnet synchronous motor taking account of converter performance, *IEEE Transactions on Industry Applications*, IA-21(1), 279–284, 1985.
5. S. Bolognani and G. S. Buja, Dynamic characteristics of a PWM voltage source inverter-fed PM brushless motor drive under field orientation, *Electric Energy Conference 1987, an International Conference on Electrical Machines and Drives*, pp. 91–95, 1987.
- 5a. R. Krishnan, *Electric Motor Drives*, Prentice Hall, Upper Saddle River, NJ, 2001.

Dynamic Simulation

6. T. W. Nehl, F. A. Fouad, N. A. Demerdash et al., Dynamic simulation of radially oriented permanent magnet type electronically operated synchronous machines with parameters obtained from finite element field solutions, *IEEE Transactions on Industry Applications*, IA-18(2), 172–182, 1982.
7. P. Pillay and R. Krishnan, Development of digital models for a vector controlled permanent magnet synchronous motor drive, *Conference Record, IEEE Industry Applications Society Annual Meeting (IEEE Cat. No. 88CH2565-0)*, pp. 476–482, 1988.
8. R. Krishnan and G. H. Rim, Design and operation of an adjustable power factor sinusoidal convertor for variable speed constant frequency generation with permanent magnet synchronous machine, *Conference Record, IEEE Industry Applications Society Annual Meeting (Cat. No. 89CH2792-0)*, pp. 835–842, 1989.
9. S. Morimoto, Y. Takeda, and T. Hirasa, Current phase control methods for permanent magnet synchronous motors, *IEEE Transactions on Power Electronics*, 5(2), 133–139, 1989.
10. F. Parasiliti and M. Tursini, Modelling and simulation of a buried permanent magnet synchronous motor drive, *3rd European Conference on Power Electronics and Application*, pp. 201–206, 1989.
11. P. Pillay and R. Krishnan, Modeling, simulation, and analysis of permanent-magnet motor drives. I. The permanent-magnet synchronous motor drive, *IEEE Transactions on Industry Applications*, pp. 265–273, 1989.
12. P. Pillay and R. Krishnan, Control characteristics and speed controller design for a high performance permanent magnet synchronous motor drive, *IEEE Transactions on Power Electronics*, 5(2), 151–159, 1990.

Control Strategies

13. S. Morimoto, Y. Takeda, K. Hatanaka et al., Design and control system of inverter-driven permanent magnet synchronous motors for high torque operation, *IEEE Transactions on Industry Applications*, 29(6), 1150–1155, 1993.
14. S. R. Macminn and T. M. Jahns, Control techniques for improved high-speed performance of interior PM synchronous motor drives, *IEEE Transactions on Industry Applications*, 27(5), 997–1004, 1991.
15. R. Krishnan, Control and operation of PM synchronous motor drives in the field-weakening region, *IEEE IECON Proceedings (Industrial Electronics Conference)*, pp. 745–750, 1993.

16. S. Morimoto, T. Ueno, M. Sanada et al., Effects and compensation of magnetic saturation in permanent magnet synchronous motor drives, *Conference Record of the IEEE Twenty-Eighth IAS Annual Meeting (Cat. No. 93CH3366-2)*, pp. 59–64, 1993.
17. S. Morimoto, Y. Tong, Y. Takeda, et al., Loss minimization control of permanent magnet synchronous motor drives, *IEEE Transactions on Industrial Electronics*, 41(5), 511–516, 1994.
18. Y. Tong, S. Morimoto, Y. Takeda et al., Maximum efficiency control for permanent magnet synchronous motors, *Proceedings IEEE International Conference on Industrial Electronics, Control and Instrumentation (Cat. No. 91CH2976-9)*, pp. 283–288, 1991.
19. T. M. Jahns, G. B. Kliman, and T. W. Neumann, Interior permanent-magnet synchronous motors for adjustable-speed drives, *IEEE Transactions on Industry Applications*, IA-22(4), 738–747, 1986.
20. T. Senju, T. Shimabukuro, and K. Uezato, Vector control of synchronous permanent magnet motors including stator iron loss, *Transactions of the Institute of Electrical Engineers of Japan, Part D*, 114-D(12), 1300–1301, 1994.
21. S. Vaez-Zadeh, Variable flux control of permanent magnet synchronous motor drives for constant torque operation, *IEEE Transactions on Power Electronics*, 16(4), 527–534, 2001.
22. R. Monajemy and R. Krishnan, Implementation strategies for concurrent flux weakening and torque control of the PM synchronous motor, *Conference Record of the IEEE Industry Applications Conference (Cat. No. 95CH35862)*, pp. 238–245, 1995.
23. R. Monajemy and R. Krishnan, Control and dynamics of constant-power-loss-based operation of permanent-magnet synchronous motor drive system, *IEEE Transactions on Industrial Electronics*, 48(4), 839–844, 2001.
24. J. Faiz and S. H. Mohseni-Zonoozi, A novel technique for estimation and control of stator flux of a salient-pole PMSM in DTC method based on MTPF, *IEEE Transactions on Industrial Electronics*, 50(2), 262–271, 2003.
25. Q. Liu, A. M. Khambadkone, and M. A. Jabbar, Direct flux control of interior permanent magnet synchronous motor drives for wide-speed operation, *Fifth International Conference on Power Electronics and Drive Systems (IEEE Cat. No. 03TH8688)*, pp. 1680–1685, 2003.
26. A. M. Llor, J. M. Retif, X. Lin-Shi et al., Direct stator flux linkage control technique for a permanent magnet synchronous machine, *IEEE 34th Annual Power Electronics Specialists Conference, Conference Proceedings (Cat. No. 03CH37427)*, pp. 246–250, 2003.

Direct Torque Control

27. F. Minghua and X. Longya, A sensorless direct torque control technique for permanent magnet synchronous motors, *Conference Record of the IEEE Industry Applications Conference. Thirty-Forth IAS Annual Meeting (Cat. No. 99CH36370)*, pp. 159–164, 1999.
28. D. Sun, W. Fang, and Y. He, Study on the direct torque control of permanent magnet synchronous motor drives, *Proceedings of the Fifth International Conference on Electrical Machines and Systems (IEEE Cat. No. 01EX501)*, pp. 571–574, 2001.

Computer Programs

29. P. Pillay and M. Wu, A computer program to predict the performance of permanent magnet synchronous motor drives, *Proceedings. IEEE SOUTHEASTCON (Cat. No. 92CH3094-0)*, pp. 517–522, 1992.
30. R. Krishnan, R. A. Bedingfield, A. S. Bharadwaj and P. Ramakrishna, Design and development of a user-friendly PC-based CAE software for the analysis of torque/speed/position controlled PM brushless DC motor drive system dynamics, *IEEE-IAS Annual Meeting, Conference Record*, pp. 1388–1394, Oct. 1991.

Application Characteristics

31. A. Fratta and A. Vagati, Synchronous vs. DC brushless servomotor: the machine behaviour, *IEEE Symposium on Electrical Drive*, Cagliari, Italy, pp. 53–60, 1987.
32. P. Pillay and R. Krishnan, Application characteristics of permanent magnet synchronous and brushless DC motors for servo drives, *IEEE Transactions on Industry Applications*, 27(5), 986–996, 1991.
33. S. Morimoto, K. Hatanaka, Y. Tong, et al., High performance servo drive system of salient pole permanent magnet synchronous motor, *Conference Record, IEEE Industry Applications Society Annual Meeting (Cat. No. 91CH3077-5)*, pp. 463–468, 1991.

5 Flux-Weakening Operation

Due to the upper limit placed on the available dc link voltage and current ratings of a given inverter, the motor input voltage and current ratings are limited. The voltage and current limits impact the maximum speed with rated torque capability and the maximum torque producing capability of the motor drive system, respectively. It is required and desirable to produce the rated power with the highest attainable speed for many applications such as electric vehicles, people carriers in airport lobbies, forklifts, machine tool spindle drives, etc. Corresponding to the maximum dc link voltage and hence the maximum input machine voltage and rated torque, the machine attains a speed known as the rated (base) speed. Above this speed, the induced emf will exceed the maximum input voltage, making the flow of current into machine phases impractical. To overcome this situation, the induced emf is constrained to be less than the applied voltage by weakening the air gap flux linkages. The flux weakening is made to be inversely proportional to the stator frequency so that the induced emf is a constant and will not increase with the increasing speed.

This chapter considers the operation of the permanent magnet synchronous motor drives when they are constrained to be within the permissible envelope of the maximum inverter voltage and current to produce the rated power and to provide this with the highest attainable rotor speed. The rated torque is intended for steady-state operation and multiple times that is preferred for fast accelerations and decelerations during transient operation. Effective torque delivery during flux-weakening operation with high transient capability is preferable. High-performance current control can overcome the saturation of the current loop that creates significant harmonic content in the stator currents, resulting in higher torque ripples and higher losses. Usually this involves a certain amount of voltage being set aside for current control only. That margin of voltage required for current control can be alternatively used to support higher speed for a given stator flux linkage and hence the output power. A basic operation of the inverter, viz., six-step operation provides the maximum voltage to the machine where the current can only be influenced by the instantaneous angle control of the voltage phasor with respect to the rotor magnet flux linkages. Such an operation with its merits and demerits is also considered in this chapter.

There is no accepted classification of flux-weakening control schemes for permanent magnet synchronous motor drives in the literature. But one such classification can help in formal understanding of the subject matter and it is accordingly presented here. All the flux-weakening control schemes are based either on machine model and parameters or free of model and machine parameters, thus forming two categories of flux-weakening control, shown in [Figure 5.1](#). The first category has the advantage of

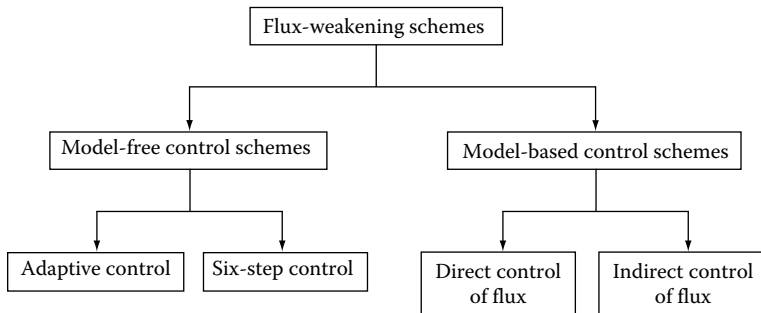


FIGURE 5.1 Classification of flux-weakening control schemes.

precision control so long as the parameter sensitivity does not come into picture, while the latter category endows an implementation simplicity, leading to easier tuning of the controller. Each category is further differentiated. The model-based controller is based on two approaches: (1) Indirect control scheme—highly computation-based flux-weakening controller as the air gap flux is controlled not directly but only indirectly by taking into account all the time the current and torque constraints but the scheme never explicitly considers the air gap flux control. It is highly parameter dependent. (2) Direct control scheme—It is similar to flux-weakening controller in dc motor drives where the air gap flux is directly controlled by commanding it as an input. It is dependent on some machine parameters. Because of direct air gap flux control, the transition from constant torque to constant power mode of operation is straightforward unlike in the indirect controller where two different controllers are required, one for each mode of operation. The model-free controllers, in turn, are classified into two subcategories: (1) Adaptive control scheme—the controller adapts to flux-weakening mode when the voltage required is more than the inverter can deliver and is independent of any other command signal. (2) Six-step control scheme—the inverter is switched into six-step voltage (SSV) mode. The control is exercised through the voltage phasor positioning and has no direct control of air gap flux with the result that the controller supplies maximum available voltage to the machine with control being exercised only by one variable, which is the voltage phasor position. These schemes are described in this chapter.

Some references on aspects of flux weakening and its control [1–19], speed control [20–22], loss minimizing strategies [23–26], and related machine issues [27–33] are given at the end of the chapter for further reading.

5.1 MAXIMUM SPEED

To understand the scope of the flux weakening of the PMSM drive, it is essential to determine the maximum speed. The maximum speed for a given set of stator voltages and currents is obtained analytically for the purpose of design calculations. The maximum operating speed with zero torque is calculated [14a] from the steady-state stator voltage equations as follows. The normalized stator equations in the rotor reference frames are given as

$$\begin{aligned} v_{qsn}^r &= (R_{sn} + L_{qn} p) i_{qsn}^r + \omega_m (L_{dn} i_{dsn}^r + 1) \\ v_{dsn}^r &= -\omega_m L_{qn} i_{qsn}^r + (R_{sn} + L_{dn} p) i_{dsn}^r \end{aligned} \quad (5.1)$$

where the abc to qd transformation valid for voltages, currents, and flux linkages is used to obtain the voltages in rotor reference frames as

$$\begin{bmatrix} v_{qsn}^r \\ v_{dsn}^r \end{bmatrix} = \frac{2}{3} \begin{bmatrix} \cos \theta_r & \cos \left(\theta_r - \frac{2\pi}{3} \right) & \cos \left(\theta_r + \frac{2\pi}{3} \right) \\ \sin \theta_r & \sin \left(\theta_r - \frac{2\pi}{3} \right) & \sin \left(\theta_r + \frac{2\pi}{3} \right) \end{bmatrix} \begin{bmatrix} V_{asn} \\ V_{bsn} \\ V_{csn} \end{bmatrix} \quad (5.2)$$

The steady-state stator voltage equations are obtained by putting the derivative of the current variables to zero in Equation 5.1 as

$$\begin{aligned} v_{qsn}^r &= R_{sn} i_{qsn}^r + \omega_m (L_{dn} i_{dsn}^r + 1) \\ v_{dsn}^r &= -\omega_m L_{qn} i_{qsn}^r + R_{sn} i_{dsn}^r \end{aligned} \quad (5.3)$$

The maximum speed is attained by letting the air gap flux reduce drastically and all the stator current is utilized for that purpose only. That means the q-axis current is set to zero, i.e., $i_{qsn}^r = 0$. The stator voltage phasor then is given as

$$v_{sn}^2 = v_{dsn}^r + v_{qsn}^r = \omega_m^2 (1 + L_{dn} i_{dsn}^r)^2 + R_{sn}^2 (i_{dsn}^r)^2 \quad (5.4)$$

from which the maximum speed for a given stator current magnitude of i_{dsn}^r is

$$\omega_m(\max) = \frac{\sqrt{v_{sn}^2 - R_{sn}^2 i_{dsn}^r}}{(1 + L_{dn} i_{dsn}^r)} \quad (5.5)$$

Note that the denominator of Equation 5.5 has to be positive, giving the condition that the maximum stator current to be applied to counter the magnet flux linkages is

$$i_{dsn}^r(\max) < -\frac{1}{L_{dn}} \quad (5.6)$$

5.2 FLUX-WEAKENING ALGORITHM

Considering the steady state and by neglecting the resistive terms, the voltage phasor [14a] is written as

$$v_{sn}^2 = \omega_m^2 \left\{ (1 + L_{dn} i_{dsn}^r)^2 + (L_{qn} i_{qsn}^r)^2 \right\} (\text{p.u.}) \quad (5.7)$$

where the voltage phasor, v_{sn} , is defined as

$$v_{sn} = \sqrt{\left(v_{qsn}^r\right)^2 + \left(v_{dsn}^r\right)^2} \text{ (p.u.)} \quad (5.8)$$

The quadrature current i_{qsn}^r can be written in terms of the stator current phasor and stator direct-axis current as

$$i_{qsn}^r = \sqrt{i_{sn}^2 - i_{dsn}^r} \text{ (p.u.)} \quad (5.9)$$

Substituting Equation 5.7 into Equation 5.8, the following equation relating the stator voltage phasor magnitude in terms of the stator current phasor, stator direct-axis current and rotor speed is obtained:

$$v_{sn}^2 = \omega_m^2 \left\{ L_{qn}^2 (i_{sn}^2 - i_{dsn}^r) + (1 + L_{dn} i_{dsn}^r)^2 \right\} \text{ (p.u.)} \quad (5.10)$$

Note that the voltage phasor and current phasor, v_{sn} and i_{sn} , respectively, correspond to the maximum values that could be obtained from the inverter operation. Hence for the field-weakening operation, these are considered to be constant based on the assumption that the inverter input dc voltage remains constant. This leads to the appreciation that the equation contains only two variables ω_m and i_{dsn}^r . Therefore given one of these two variables, the other could be computed analytically. This is the key to the control and operation of the PMSM drive in the flux-weakening region. Further, Equation 5.10 is written in terms of i_{dsn}^r and ω_m as

$$v_{sn} = \omega_m \sqrt{\left\{ a \left(i_{dsn}^r\right)^2 + b i_{dsn}^r + c \right\}} \text{ (p.u.)} \quad (5.11)$$

where the constants are

$$a = L_{dn}^2 - L_{qn}^2 \quad (5.12)$$

$$b = 2L_{dn} \quad (5.13)$$

$$c = 1 + L_{qn}^2 i_{sn}^2 \quad (5.14)$$

Assuming the rotor speed is available for feedback control and using Equations 5.10 through 5.13, the d-axis stator current is found, which would automatically satisfy the constraints of maximum stator current, i_{sn} and stator voltage, v_{sn} . From the stator current magnitude and the d-axis stator current using Equation 5.19, the maximum permitted q-axis stator current could be calculated. The d- and q-axes

stator currents then determine the stator phase currents using the inverse transformation as

$$\begin{bmatrix} i_{asn} \\ i_{bsn} \\ i_{csn} \end{bmatrix} = \begin{bmatrix} \cos \theta_r & \sin \theta_r \\ \cos\left(\theta_r - \frac{2\pi}{3}\right) & \sin\left(\theta_r - \frac{2\pi}{3}\right) \\ \cos\left(\theta_r + \frac{2\pi}{3}\right) & \sin\left(\theta_r + \frac{2\pi}{3}\right) \end{bmatrix} \begin{bmatrix} i_{qsn}^r \\ i_{dsn}^r \end{bmatrix} \quad (5.15)$$

Combining equations $i_{qsn}^r = i_{sn} \sin \delta$ and $i_{qsn}^r = i_{sn} \cos \delta$ with Equation 5.15, the normalized stator phase currents are obtained by the following relationship:

$$\begin{bmatrix} i_{asn} \\ i_{bsn} \\ i_{csn} \end{bmatrix} = \begin{bmatrix} \sin(\theta_r + \delta) \\ \sin\left(\theta_r + \delta - \frac{2\pi}{3}\right) \\ \sin\left(\theta_r + \delta + \frac{2\pi}{3}\right) \end{bmatrix} i_{sn} \quad (5.16)$$

and the torque angle is obtained as

$$\delta = \tan^{-1} \left(\frac{i_{qsn}^r}{i_{dsn}^r} \right) \quad (5.17)$$

Note that the calculated q-axis stator current together with d-axis stator current determines the torque, T_{ef} , that could be produced, and it is then used to modify the torque command, T_{ec} , generated from the speed error, in a drive system. If the torque request, T_{ec} , is more than T_{ef} , the torque calculated by the flux-weakening module, then the final torque request is made equal to that of the calculated one. If T_{ec} is less than T_{ef} , then the final torque command is maintained at T_{ec} . The final torque request arrived at by a logic-based determination between the two is denoted as T_e^* . From T_e^* , the required q-axis current in the machine could be calculated from the torque equation and i_{dsn}^r request as

$$i_{qsn}^r = \frac{T_e^*}{1 + (L_{dn} - L_{qn})i_{dsn}^r} \text{ (p.u.)} \quad (5.18)$$

Although the above relationships were derived based on the steady-state performance, it is to be noted that some voltage reserve is set aside for dynamic control of

currents. With smaller voltage reserve, the current loops will become sluggish and beyond their limit points, they will no longer control the current, thus making the applied voltages to be six step, leading to higher harmonic content in the currents.

5.2.1 INDIRECT CONTROL SCHEME

An indirect control scheme for the PMSM drive in both the regions of constant torque and flux weakening could be formulated with the derivations and understanding provided in the previous section. The scheme does not request a specific air gap flux request directly in its controller but implements the flux weakening in an indirect manner. It is achieved by only considering the rotor speed request, and accordingly the d-axis current for that speed is computed. This, together with the stator q-axis current that is allowed within the maximum allowable stator current magnitude, determines the torque generation and indirectly the air gap flux. Schematically the control scheme [14a] is shown in Figure 5.2. Assuming a speed-controlled drive system, the torque command T_{ec} is generated by the speed error. Depending on the mode of operation, the torque command is processed by block 1 or 2. Block 1 corresponds to the constant torque mode controller whereas block 2 corresponds to the flux-weakening mode controller. These blocks are explained in the subsequent paragraphs. The outputs of the controllers are stator current magnitude command and the torque angle command. They, together with the electrical rotor position, provide the phase current commands through the stator reference transformation block. Then the resulting stator current commands in stator reference frames are enforced with an inverter by current feedback control, with any one of the current control schemes available. Various current control schemes are discussed in Chapter 6. For a simple illustration here, pulse width modulation for the current control is chosen. The rotor position and rotor speed are assumed to be obtained with an encoder and a signal conditioner, respectively.

5.2.2 CONSTANT TORQUE MODE CONTROLLER

The block 1 contains the constant torque mode controller with maximum torque per ampere [14a] as explained in Chapter 4. The torque versus stator current magnitude

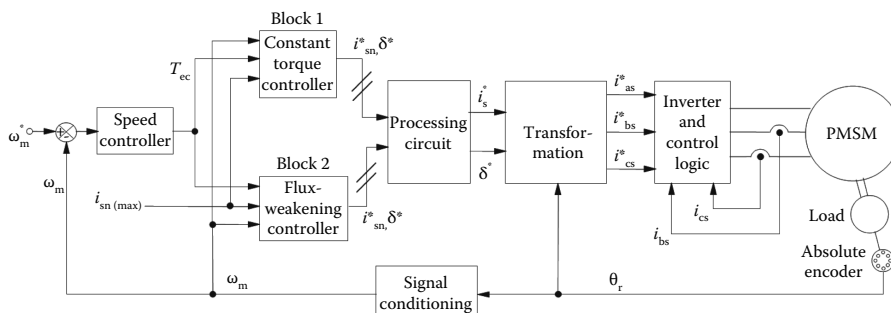


FIGURE 5.2 Schematic of the PMSM drive control strategy. (From Krishnan, R., *Electric Motor Drives*, Figure 9.16, Prentice Hall, Upper Saddle River, NJ, 2001. With permission.)

and torque angle are computed using Equations 4.68 and 4.71. Note that for easier computation, the stator current magnitude is varied and the torque angle and the torque are evaluated. For implementation, note that the inverse is needed, i.e., given the torque request, the stator current magnitude and torque angle are to be made available. This could be accomplished by curve fitting the characteristics for online computation or programming it in memory for retrieval and use. The characteristics of stator current magnitude and torque angle versus torque are shown in Figure 5.3. These characteristics, for the drive system under illustration, are curve fitted by the following expressions with minimum error:

$$i_{\text{sn}} = 0.01 + 0.954T_{\text{en}} - 0.189T_{\text{en}}^2 + 0.02T_{\text{en}}^3 \quad (5.19)$$

$$\delta = 1.62 + 0.715T_{\text{en}} - 0.3T_{\text{en}}^2 + 0.04T_{\text{en}}^3 \quad (5.20)$$

Algorithm and procedure for obtaining a curve fit may be obtained from a standard textbook on numerical analysis. The detailed schematic of the torque mode controller, then takes the form shown in Figure 5.4. Equations 5.19 and 5.20 can be realized in the form of tables to realize the block 1. The speed signal determines the mode of operation of the drive system. In the torque control mode, if the rotor speed is less than the base speed, then it enables the block 1 in the form of onward transmission of the torque command signal, T_{cc} . This torque signal is limited by the maximum torque that could be generated with the maximum permissible stator current phasor magnitude, which may be a variable depending on the drive being in steady state or in intermittent peak operation. Then the resulting torque signal provides the stator current magnitude and torque angle commands from the memory that may have characteristics given in Equations 5.19 and 5.20. For regenerative action, note that the torque angle is multiplied by the sign of the torque request to meet the bidirectional torque requirement.

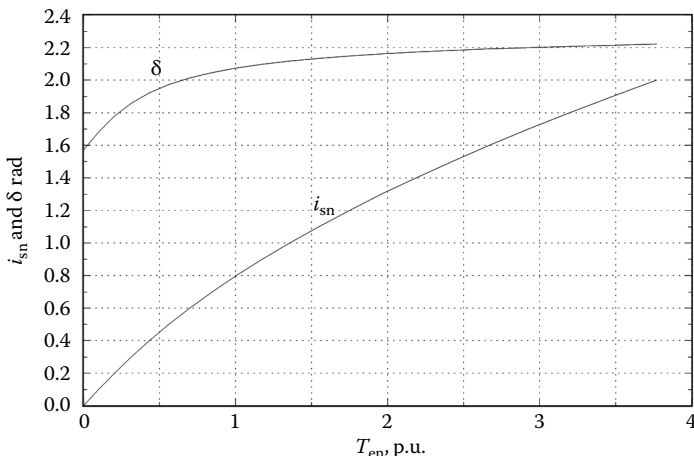


FIGURE 5.3 Stator current magnitude and torque angle versus electromagnetic torque. (From Krishnan, R., *Electric Motor Drives*, Figure 9.17, Prentice Hall, Upper Saddle River, NJ, 2001. With permission.)

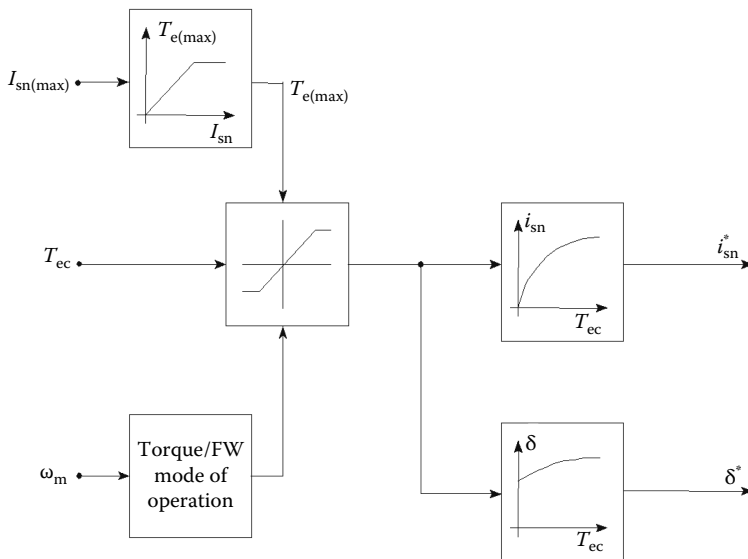


FIGURE 5.4 Schematic of constant torque mode controller. (From Krishnan, R., *Electric Motor Drives*, Figure 9.18, Prentice Hall, Upper Saddle River, NJ, 2001. With permission.)

5.2.3 FLUX-WEAKENING CONTROLLER

From Section 5.2, the flux-weakening controller emerges [14a], which could be schematically captured as shown in Figure 5.5. The inputs to this module are three variables, viz., the torque request, rotor speed, and maximum permissible stator current. The module's outputs are the stator current magnitude request and the torque angle request.

The rotor speed determines the d-axis stator current request through Equation 5.11 in a slightly modified form as

$$i_{dsn}^r = \frac{-b + \sqrt{\left\{ b^2 - 4a \left(c - \frac{v_{sn}^2}{\omega_m} \right) \right\}}}{2a} \quad (5.21)$$

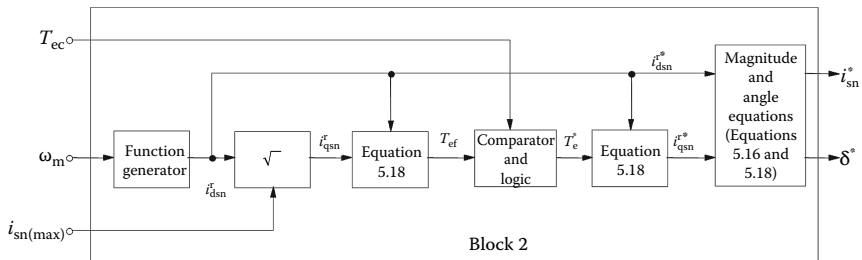


FIGURE 5.5 Schematic realization of the flux-weakening controller. (From Krishnan, R., *Electric Motor Drives*, Figure 9.19, Prentice Hall, Upper Saddle River, NJ, 2001. With permission.)

where a , b , and c are given in Equations 5.12 through 5.14. Note that constant c is dependent on the maximum stator current limit. It could be either programmed or captured in a tabular form for retrieval and use in the feedback control computations. The d-axis current request indicated with an asterisk in [Figure 5.5](#), along with the maximum stator current, determines the permissible quadrature-axis current, i_{qsn}^r . This q-axis current reference with the d-axis current determines the maximum electromagnetic torque allowed, T_{ef} , within maximum voltage and current constraints. It is then compared with the torque request T_{ec} , generated by the speed error. Then the following logic is evaluated to find the torque command input to compute the command q-axis current:

$$\begin{aligned} T_{ec} > T_{ef}, \quad &\text{then } T_e^* = T_{ef} \\ T_{ec} < T_{ef}, \quad &\text{then } T_e^* = T_{ec} \end{aligned} \quad (5.22)$$

This logic submodule adjusts the torque request depending on the load and maximum capability of the motor drive system as a function of the rotor speed. From this final torque request, T_e^* , the stator q-axis current is computed using Equation 5.18. The direct and quadrature axes stator current requests are then used to calculate the stator current phasor magnitude and torque angle requests. The torque mode or flux-weakening controller module is chosen based on the rotor speed being lower and higher than its base value, respectively.

5.2.4 SYSTEM PERFORMANCE

The drive system performance with the strategy incorporating both the optimized constant torque mode and flux-weakening controllers is modeled and simulated to evaluate its performance. The PWM frequency of the inverter is set at 5 kHz. The dc link voltage is 280 V and the load torque is zero. To prove the operation in the four-quadrant operation, a step speed command from 7 to -7 p.u. is given and various machine and control variables are viewed at. The machine variables of interest are the torque and speed. Likewise the control variables such as torque request and speed command are monitored. The simulation results are shown in [Figure 5.6](#). The torque command follows the maximum trajectory as a function of speed and the actual torque very closely follows its command. The power trajectory is maintained at its set maximum in the flux-weakening mode and the drive speed envelope is smooth during the entire speed of operation. Note that the base speed is 1 p.u. and beyond it, flux weakening is exercised in the drive system.

Example 5.1

A PMSM has the following parameters, $R_{sn}=0.173$ p.u., $L_{dn}=0.435$ p.u., $L_{qn}=0.699$ p.u., $V_{sn}=1.45$ p.u., $I_{sn}=1$ p.u. Find (i) the maximum speed with and without neglecting stator resistances and (ii) the steady-state characteristics in the flux-weakening region.

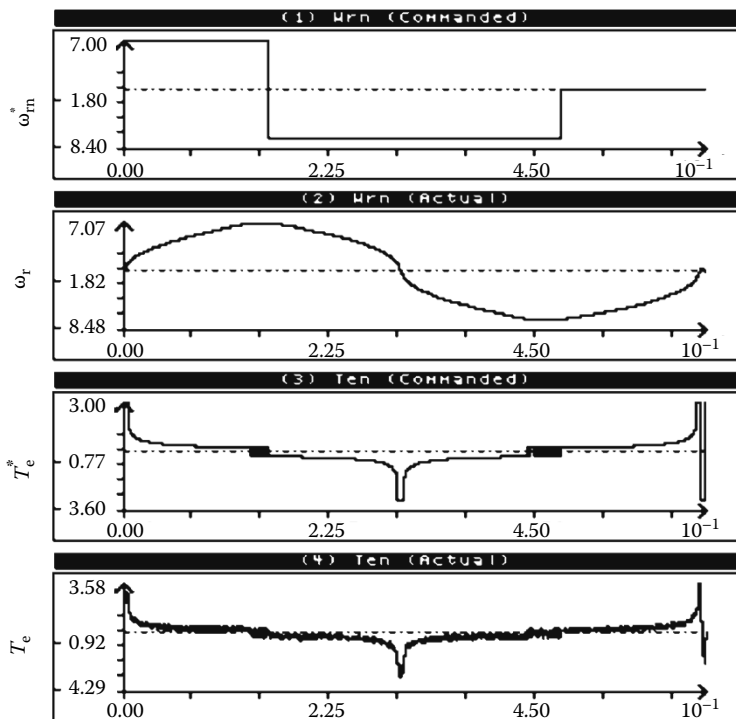


FIGURE 5.6 Simulation results. (From Krishnan, R., *Electric Motor Drives*, Figure 9.20, Prentice Hall, Upper Saddle River, NJ, 2001. With permission.)

Solution

Part (i): Maximum speed

$$\text{Maximum speed} = \frac{\sqrt{V_{sn}^2 - (R_{sn}I_{sn})^2}}{(1 + L_{dn}I_{dsn}^r)} \text{ (p.u.)}$$

Note that $I_{dsn}^r = -I_{sn}$, hence

$$\begin{aligned}\omega_m(\max) &= \frac{\sqrt{1.45^2 - 0.173^2}}{1 - 0.435} \text{ (p.u.)} \\ &= 2.547 \text{ p.u.}\end{aligned}$$

Neglecting stator resistance, the maximum speed of the PMSM is given by

$$\begin{aligned}\omega_m(\max) &= \frac{V_{sn}}{(1 - L_{dn}I_{sn})} \\ &= \frac{1.45}{1 - 0.435} \\ &= 2.565 \text{ p.u.}\end{aligned}$$

The effect of the stator resistance is usually negligible in the maximum speed prediction but not for small machines because they have larger stator resistances compared to large machines.

Part (ii): Steady-state performance computation in the flux-weakening operation:

The steady-state flux-weakening performance is computed from the following steps.

For computing I_{dsn}^r during field weakening when $I_{qsn}^r \neq 0$, the effect of resistive drops is in general as much as $I_{sn}R_{sn}$ approximately and hence reduce V_{sn} approximately to 1.25 p.u.

With $V_{sn} = 1.25$ p.u., compute I_{dsn}^r from

$$V_{sn} = \omega_{rn} \sqrt{aI_{dsn}^{r^2} + bI_{dsn}^r + c}$$

for each value of increasing ω_{rn} . Select the smaller of the roots for I_{dsn}^r to give the d-axis current. With that d-axis current, compute I_{qsn}^r with I_{sn} set at 1 p.u.

Compute v_{qsn}^r , v_{dsn}^r , and V_{sn} to check if it is equal to or is less than the original assigned value of 1.45 p.u. Otherwise, go to step 2 to give a smaller value of V_{sn} .

Compute voltage phasor angle, current phasor angle, hence power factor angle, torque and power output, all in p.u.

The performance characteristics are plotted and shown in Figure 5.7.

Example 5.2

The parameters of a star-connected, six-pole, 1.5 kW, 9.2 A, 1500 rpm, 9.55 N m, three-phase PMSM are given below:

$R_s = 0.513 \Omega$, $L_d = 4.74 \text{ mH}$, $L_q = 9.51 \text{ mH}$, $B = 9.36 \times 10^{-4} \text{ N m/(rad/s)}$, $J = 0.01 \text{ kg m}^2$, emf constant = 0.0669 V/rpm , Inverter input voltage = 285 V.

Determine the maximum speed of the PMSM drive system.

Without exceeding the stator rated current and inverter input voltage, find the maximum speed at which the rated power is delivered.

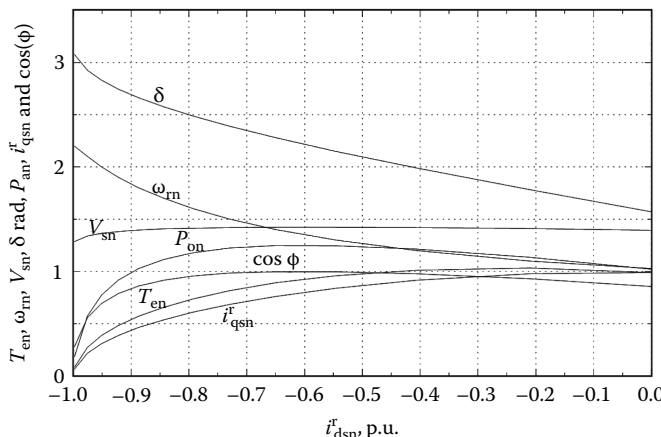


FIGURE 5.7 Performance characteristics of the PMSM in the flux-weakening region. (From Krishnan, R., *Electric Motor Drives*, Figure 9.21, Prentice Hall, Upper Saddle River, NJ, 2001. With permission.)

The stator resistive voltage drop may be ignored in the calculation for (ii) and the maximum stator phase peak voltage obtained through inverter is 55% of the dc link voltage.

Solution

The base values are calculated as follows.

$$I_b = 9.2 \text{ A}, P_b = 1500 \text{ W}, T_b = 9.55 \text{ N m.}$$

$$\text{Base voltage, } V_b = \frac{P_b}{3I_b} = \frac{1500}{3 \times 9.2} = 54.35 \text{ V}$$

$$\text{Base speed, } \omega_b = \frac{P_b}{T_b} = \frac{1500}{9.55} = 157.068 \text{ rad/s}$$

$$\text{Base impedance, } Z_b = \frac{V_b}{I_b} = \frac{54.35}{9.2} = 5.91 \Omega$$

$$\text{Base inductance, } L_b = \frac{Z_b}{\omega_b} = \frac{5.91}{157.07} = 37.6 \text{ mH}$$

$$\text{Normalized stator resistance, } R_{sn} = \frac{R_s}{Z_b} = \frac{0.513}{5.91} = 0.868 \text{ p.u.}$$

Stator phasor voltage, V_s is equal to the peak value of the stator phase voltage, and it is calculated from the given information:

$$V_s = 0.55V_{dc} = 0.55(285) = 156.75$$

$$\text{Its normalized value, } V_{sn} = \frac{V_s}{V_b} = \frac{156.75}{54.35} = 2.884 \text{ p.u.}$$

$$\text{Normalized direct-axis inductance, } L_{dn} = \frac{L_d}{L_b} = \frac{4.74 \text{ mH}}{37.6} = 0.126 \text{ p.u.}$$

$$\text{Normalized quadrature-axis inductance, } L_{qn} = \frac{L_q}{L_b} = \frac{9.51 \text{ mH}}{37.6} = 0.2529 \text{ p.u.}$$

The maximum speed is obtained as

$$\omega_{m(\max)} = \frac{\sqrt{V_{sn}^2 - R_{sn}^2(i_{dsn}^r)^2}}{1 + L_{dn}i_{dsn}^r} = 3.2986 \text{ p.u.}$$

when the d-axis current is set at -1 p.u.

To find the speed at which the constant air gap power is delivered without exceeding the stator current and voltage constraints, the air gap power in terms of these variables and machine parameters is found as follows:

The normalized air gap power is derived as

$$P_{an} = \frac{P_a}{P_b} = \frac{\omega_m T_e}{\omega_b T_b} = \omega_{mn} T_{en}$$

Substituting in air gap power for the torque and speed in terms of the voltage and mutual flux linkages, which, in turn, in terms of the currents and machine parameters gives

$$P_{an} = I_{qsn}^r [1 + (L_{dn} - L_{qn}) I_{dsn}^r] \frac{V_{sn}}{\sqrt{L_{qn}^2 (I_{sn}^2 - \{I_{dsn}^r\}^2) + (1 + L_{dn} I_{dsn}^r)^2}}$$

Note that the stator current and voltage phasor magnitudes are constants and hence this equation is only a function of the d-axis current variable. Squaring both sides of the equation and rearranging the equation results in a fourth-order polynomial in d-axis stator current as

$$a(I_{dsn}^r)^4 + b(I_{dsn}^r)^3 + c(I_{dsn}^r)^2 + dI_{dsn}^r + e = 0$$

where

$$\begin{aligned} a &= -V_{sn}^2 (L_{dn}^2 - L_{qn}^2) \\ b &= -2(L_{dn} - L_{qn}) V_{sn}^2 \\ c &= -V_{sn}^2 + I_{sn}^2 (L_{dn} - L_{qn})^2 - P_{an}^2 (L_{dn}^2 - L_{qn}^2) \\ d &= -2L_{dn} P_{an}^2 + 2(L_{dn} - L_{qn}) V_{sn}^2 I_{sn}^2 \\ e &= V_{sn}^2 I_{sn}^2 - P_{an}^2 (1 + L_{qn}^2 I_{sn}^2) \end{aligned}$$

Then solving for the d-axis current with the following constrained values:

$V_{sn} = 2.884$ p.u., $I_{sn} = 1$ p.u., and $P_{sn} = 1$ p.u.
gives the d-axis current as -0.9567 p.u. from which the q-axis current is found as 0.2911 p.u., yielding a torque of 0.3265 p.u. at the 3.268 p.u. speed.

5.3 DIRECT FLUX WEAKENING

An alternative flux-weakening control strategy is based on directly controlling the mutual flux linkages [14a], which is inversely proportional to electrical rotor speed. This is very much similar to controlling the field flux of a separately excited dc machine. The mutual flux linkages, under the assumption that the rotor magnet flux linkages constitute the base flux linkages, is defined as

$$\lambda_{mn} = \sqrt{(L_{dn} i_{dsn} + 1)^2 + (L_{qn} i_{qsn})^2} \text{ (p.u.)} \quad (5.23)$$

Neglecting the stator resistance voltage drops, the stator voltage phasor is given in terms of the mutual flux linkages and electrical rotor speed by using Equation 5.7 as

$$v_{sn} = \omega_m \lambda_{mn} \text{ (p.u.)} \quad (5.24)$$

This implies that during flux weakening, when the dc link voltage and hence the stator voltage phasor magnitude is constant, the mutual flux linkages have to be decreased inversely proportional to the rotor electrical speed. Such a control is straightforward and simple in the high-speed operational region compared to other schemes in the literature. To implement this, the independent references to be commanded are the mutual flux linkages and electromagnetic torque. To incorporate any control strategy such as the maximum torque per unit stator current, constant air gap flux linkages, unity power factor, or constant torque angle below the base speed region, the corresponding mutual flux linkages are calculated and preprogrammed in the mutual flux linkages controller. As for the region above the base speed, the mutual flux linkages are made to be inversely proportional to the rotor electrical speed to work within the limited dc link voltage. The machine will be operated within its maximum torque capability for a given mutual flux linkages command. It is enforced by finding the maximum permissible electromagnetic torque for the commanded mutual flux linkages and keeping the machine operation within it.

5.3.1 MAXIMUM PERMISSIBLE TORQUE LIMIT

The maximum electromagnetic torque for a given mutual flux linkage is found as follows. The torque in terms of motor parameters, mutual flux linkages, and d-axis stator current is given by

$$T_{en} = \frac{(L_{dn} - L_{qn})i_{dsn}^r + 1}{L_{qn}} \sqrt{\lambda_{mn}^2 - (1 + L_{dn}i_{dsn}^r)^2} \quad (5.25)$$

Differentiating this with respect to the d-axis stator current and equating it to zero, the condition for maximum permissible electromagnetic torque for a given mutual flux linkage is found. Substituting this condition for the d-axis stator current in Equation 5.25 yields the maximum permissible electromagnetic torque for the given mutual flux linkages.

[Figure 5.8](#) shows such a relationship for $L_{qn} = 0.699$ and $L_{dn} = 0.434$. It can be seen that for the given system parameters the $T_{enn}^*(\lambda_{mn}^*)$, the relationship is nearly linear. This means that a simple first- or second-order polynomial can be used to implement this relationship. In general, the function $T_{enn}^*(\lambda_{mn}^*)$ can be computed off line for the appropriate range of λ_{mn}^* , and subsequently incorporated into the system as a simple lookup table.

5.3.2 SPEED CONTROL SCHEME

The mutual flux linkage weakening and torque controls are incorporated in a speed control system [14a] as shown in [Figure 5.9](#). T_{ecn}^* is the output of the speed PI controller. The command processor weakens T_{ecn}^* inversely proportional to speed when the speed is higher than 1 p.u. to limit the machine's power. Note that the torque

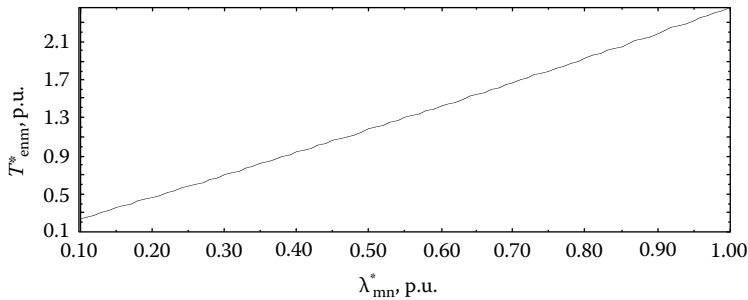


FIGURE 5.8 Maximum permissible torque command as a function of flux command. (From Krishnan, R., *Electric Motor Drives*, Figure 9.22, Prentice Hall, Upper Saddle River, NJ, 2001. With permission.)

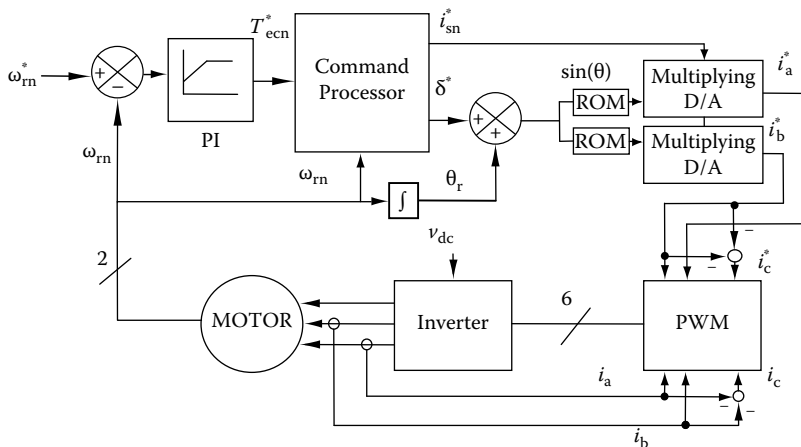


FIGURE 5.9 The speed control system with mutual flux linkage based controller. (From Krishnan, R., *Electric Motor Drives*, Figure 9.23, Prentice Hall, Upper Saddle River, NJ, 2001. With permission.)

command is limited to its maximum permissible value, which depends on the mutual flux linkage command. The command processor also generates the mutual flux linkage command. The mutual flux weakening operation begins at base speed, which may be less than or equal to 1 p.u. The outcome, T_{en}^* , along with the commanded mutual flux linkage, λ_{mn}^* , are provided to the current and angle resolver to generate the appropriate commands for the stator current, i_{sn}^* , and its angle, δ^* . The angle δ^* is added to the rotor's absolute angle to provide the desired current angle with respect to the stator's reference frame. The $\{i_{sn}^*, \delta^*\}$ pair is itself a command input to a PWM current controller. Figure 5.10 shows the operations performed by the command processor.

5.3.3 IMPLEMENTATION STRATEGY

In this section, an implementation strategy for online computation of $\{i_{sn}^*, \delta^*\}$ from $\{T_{en}^*, \lambda_{mn}^*\}$ is discussed. The strategy follows the general format as given below:

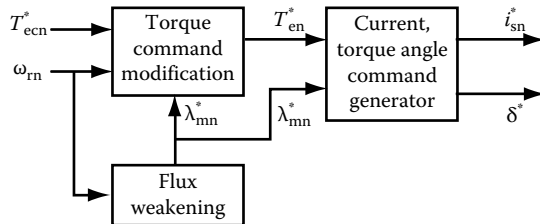


FIGURE 5.10 The command processor.

$$i_{\text{sn}}^* = \Omega(T_{\text{en}}^*, \lambda_{\text{mn}}^*) \quad (5.26)$$

$$\delta^* = \Lambda(T_{\text{en}}^*, \lambda_{\text{mn}}^*) \quad (5.27)$$

A method for realizing the functions $\Omega(\cdot, \cdot)$ and $\Lambda(\cdot, \cdot)$ are presented. It is based on lookup tables. The method is illustrated through an example using the model parameters of a PMSM. These values are $L_{\text{dn}} = 0.434$ p.u., $L_{\text{qn}} = 0.699$ p.u., and $R_{\text{sn}} = 0.1729$ p.u. The base values are $V_b = 97.138$ V, $I_b = 12$ A, $L_b = 0.0129$ H, and $\omega_b = 628.6$ rad/s.

5.3.3.1 Lookup Tables Realization

Equations 5.26 and 5.27 can be realized using separate three-dimensional lookup tables. These lookup tables are generated off-line by numerically solving system equations. Two of the independent axes of each table are assigned to T_{en}^* and λ_{mn}^* , respectively. On the third dimension, i_{sn}^* or δ^* is stored for access. The lookup tables need only provide the data for positive torque commands. For negative torque commands, the respective angle from the table must be applied with negative sign. λ_{mn}^* is limited to values between 0 and 1 since the only interest is in weakening the mutual flux linkage. The numerical solution to the system variables, for the following range of normalized mutual flux linkage command,

$$0.2 \leq \lambda_{\text{mn}}^* \leq 1 \text{ (p.u.)}$$

and for the motor parameters given earlier, yields the viable ranges for the other three variables as

$$0 \leq T_{\text{en}}^* \leq 2.44 \text{ (p.u.)}$$

$$0 \leq i_{\text{sn}} \leq 3.3 \text{ (p.u.)}$$

$$1.57 \leq \delta \leq 3.14 \text{ (rad.)}$$

Figures 5.11 and 5.12 depict the three-dimensional tables for this system. The variables are digitized under the following constraints:

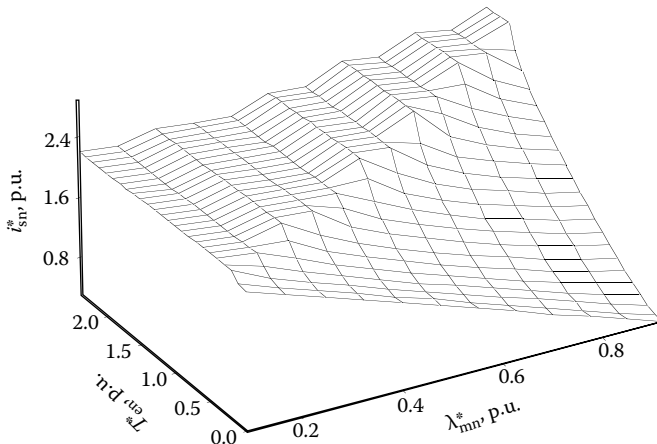


FIGURE 5.11 Current command as a function of torque and mutual flux linkage commands. (From Krishnan, R., *Electric Motor Drives*, Figure 9.25, Prentice Hall, Upper Saddle River, NJ, 2001. With permission.)

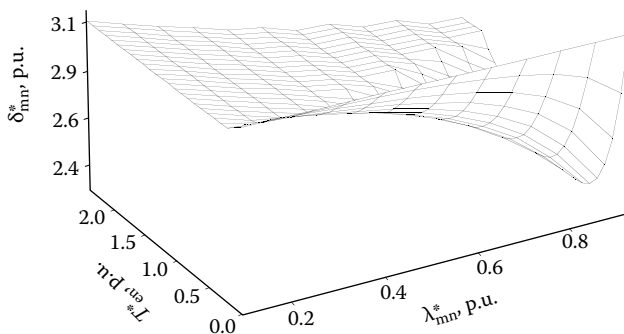


FIGURE 5.12 Angle command as a function of the torque and mutual flux linkage commands. (From Krishnan, R., *Electric Motor Drives*, Figure 9.26, Prentice Hall, Upper Saddle River, NJ, 2001. With permission.)

$$T_{enm}^*; 9 \text{ bits}; \lambda_{mn}^*; 7 \text{ bits}; i_{sn}^* \text{ and } \delta^*; 8 \text{ bits each}$$

Once the torque command reaches its maximum permissible value, the current and angle commands are frozen. The fact that each graph has two distinct areas is due to this limitation. In each graph, the border between these two surfaces appears to be a straight line, which can be attributed to the fact that the $T_{enm}^*(\lambda_{mn}^*)$ relationship is nearly linear. The $T_{enm}^*(\lambda_{mn}^*)$ relationship suggests that for the given parameters, the relationship can adequately be approximated with a first or at most a second-order polynomial. Thus, any of the following two polynomials can be used for the on line calculation of T_{enm}^* from λ_{mn}^* in this example.

$$T_{enm}^* = 0.21\lambda_{mn}^{*2} + 2.23\lambda_{mn}^* + 0.0059$$

or much simply as

$$T_{\text{enm}}^* = 2.44\lambda_{\text{mn}}^*$$

The polynomials are both derived using the least squares fit method.

5.3.4 SYSTEM PERFORMANCE

Using these tables, an accurate enforcement of the commanded torque and the commanded mutual flux linkage is achieved. As a result, the voltage requirement is closely maintained at a maximum level of 1 p.u. Figure 5.13 shows the simulation results for a

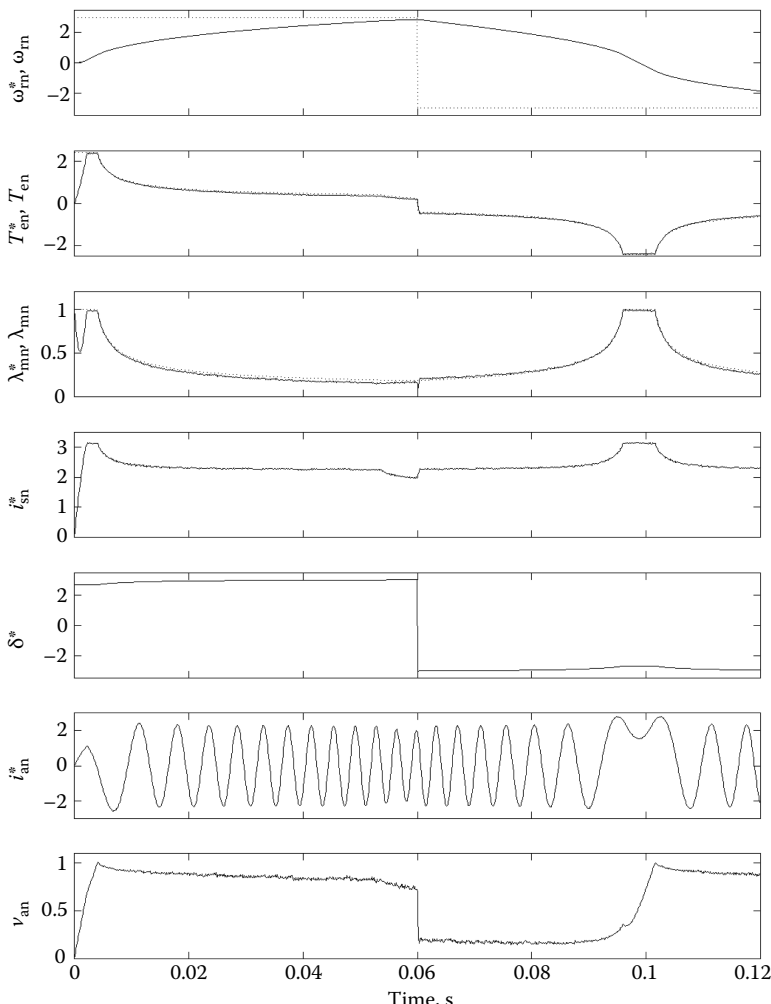


FIGURE 5.13 Simulation results for a ± 3 p.u. step speed command. (From Krishnan, R., *Electric Motor Drives*, Figure 9.27, Prentice Hall, Upper Saddle River, NJ, 2001. With permission.)

speed control system that uses the two tables for a speed-controlled operation with +3 and -3 p.u. speed commands. The dotted lines represent commanded values and the solid lines represent actual values. The PWM inverter is operating at 20 kHz switching frequency and the current error is amplified by a factor of 200. The stator resistance is taken into account in the simulation, and therefore, the mutual flux weakening is initiated at a speed of $.53\text{ p.u.}$ instead of 1 p.u. As a result, the voltage requirement is successfully limited to 1 p.u. Due to the limited bandwidth of the current controller, the ability of the system to enforce desired currents decreases as speed increases. As a consequence, the mutual flux linkage error increases with speed. Note that memory chips are required to store the relatively large look-up tables. Each table has 2^{16} entries. Therefore, each table requires 64 kilobytes of storage capacity.

The table lookup approach provides a high level of accuracy in terms of enforcing the torque and mutual flux linkage commands. Using the lookup table method meets the specified voltage requirements of the drive system, thereby satisfying a key factor in the drive operation. The system is also relatively fast since implementing it mainly involves reading data from a memory chip, and the performance of minimal calculations. However, implementing this system requires a considerable amount of digital memory. For the example considered, 128 kilobytes of read-only memory (ROM) is required to store the tables.

5.4 PARAMETER SENSITIVITY

Parameter variations are a major source of error in model-based motor controllers such as the one discussed. The effect of the variations of three of the PMSM parameters, namely stator resistance, q-axis inductance, and rotor flux linkages, on the input voltage requirement of the simulated example is briefly discussed in this section.

5.4.1 STATOR RESISTANCE VARIATION

The stator resistance may vary in the range of approximately one to two times its nominal value. As the rotor resistance increases, the input voltage requirement also increases. Figure 5.14 shows the effect of a stator resistance increase of 100% on the voltage requirements of the simulated system.

If maintaining a 1 p.u. input voltage is the main objective, the solution is to initiate the mutual flux weakening operation at lower speeds. Note that as the mutual flux

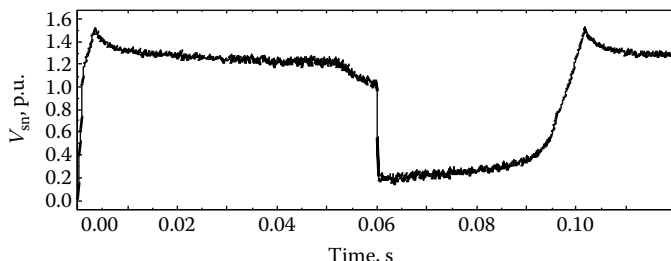


FIGURE 5.14 Input voltage requirement with double the stator resistance. (From Krishnan, R., *Electric Motor Drives*, Figure 9.28, Prentice Hall, Upper Saddle River, NJ, 2001. With permission.)

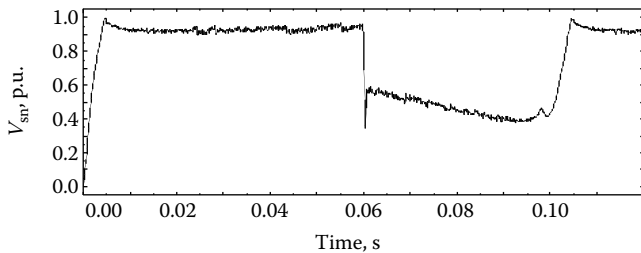


FIGURE 5.15 Input stator phasor voltage requirement when λ_{af} decreases by 20% from its nominal value. (From Krishnan, R., *Electric Motor Drives*, Figure 9.29, Prentice Hall, Upper Saddle River, NJ, 2001. With permission.)

linkage is further weakened, the maximum permissible torque also decreases. This, in turn, increases the response time of the motor.

5.4.2 ROTOR FLUX LINKAGE VARIATION

The rotor flux linkage of a PMSM may decrease as much as 20% depending on the magnet used. Figure 5.15 shows the effect of a 20% reduction of λ_{af} on the simulated example. It can be seen that the overall voltage requirement is higher than the case when the rotor flux linkage is at its nominal value (see Figure 5.3). Under identical torque requirements, as the rotor flux linkage decreases, the current requirements increase, and therefore, the input voltage requirements increase.

5.4.3 Q-AXIS INDUCTANCE VARIATION

The q-axis self inductance, L_q , may vary in the range of approximately 0.8–1.1 times its nominal value. Figures 5.16 and 5.17 show the effect of L_q variations on the input voltage requirement.

Decreasing L_q does not require voltage less than 1 p.u. The increase of L_q over its nominal value results in higher voltage requirements. The voltage requirement exceeds the 1 p.u. threshold at some instances. This indicates that a good reserve margin in the dc link voltage has to be given considering the parameter variations

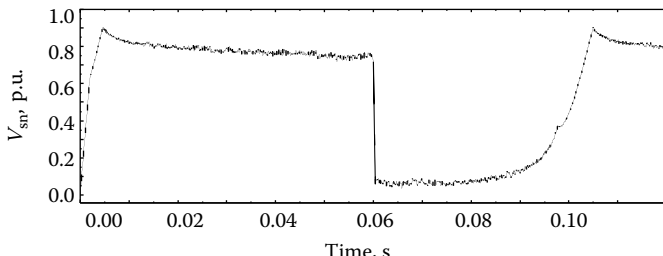


FIGURE 5.16 Input voltage requirement for a 20% reduction in L_q . (From Krishnan, R., *Electric Motor Drives*, Figure 9.30, Prentice Hall, Upper Saddle River, NJ, 2001. With permission.)

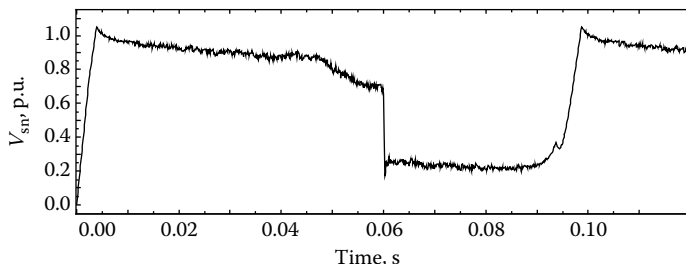


FIGURE 5.17 Input voltage requirement for a 10% increase in L_q . (From Krishnan, R., *Electric Motor Drives*, Figure 9.31, Prentice Hall, Upper Saddle River, NJ, 2001. With permission.)

that are bound to affect the performance. The extreme cases only need to be taken into account in the design process. Alternatively, the effect of parameter variations can be compensated for by estimating the respective parameter and subsequently entering it into the system as a new input variable to modify the current and angle commands appropriately.

5.5 MODEL-FREE (PARAMETER-INSENSITIVE) FLUX-WEAKENING METHOD

Methods discussed so far are machine model based. Parameter sensitivity degrades the performance of the drive system in both the steady state and dynamic operations. Model-free flux-weakening strategies overcome this shortcoming but they are invariably accompanied by sluggish and poor tracking performance. One method of model free flux weakening is discussed in this section.

The principle behind this scheme is that when reference voltage command exceeds a set value, it indicates that the drive requests for a higher voltage than that available from the dc link voltage of the inverter. At that instance, the only way that the motor drive can operate within the set voltage maximum is by injecting a demagnetizing current (d-axis stator current), causing a reduction in the q-axis-induced emf and therefore a reduction in the q-axis input voltage. Although the q-axis stator voltage is decreased, the d-axis voltage is increased to generate a d-axis current, thus resulting in partial shifting of the q-axis voltage to the d-axis voltage. The resultant of the q- and d-axes stator voltages is the stator voltage phasor that has to be within the set maximum value. Therefore, a balancing act is done to keep the operation within the set voltage of the stator voltage. It is accomplished by taking the stator voltage phasor error to determine the d-axis current to reduce the q-axis current and hence the magnitude of the stator q axis voltage. But another cardinal rule of flux weakening is not to let the magnitude of stator current to exceed its set value. To incorporate this constraint, the d-axis stator current reference, in turn, sets the q-axis stator current reference.

The implementation of the scheme is shown in [Figure 5.18](#) and explained in the following. The q- and d-axes currents and their references are compared to their respective measured currents. The current errors are then amplified through proportional plus integral controllers to develop the q- and d-axes voltage references. The references are in rotor reference frames and they are converted into stator reference

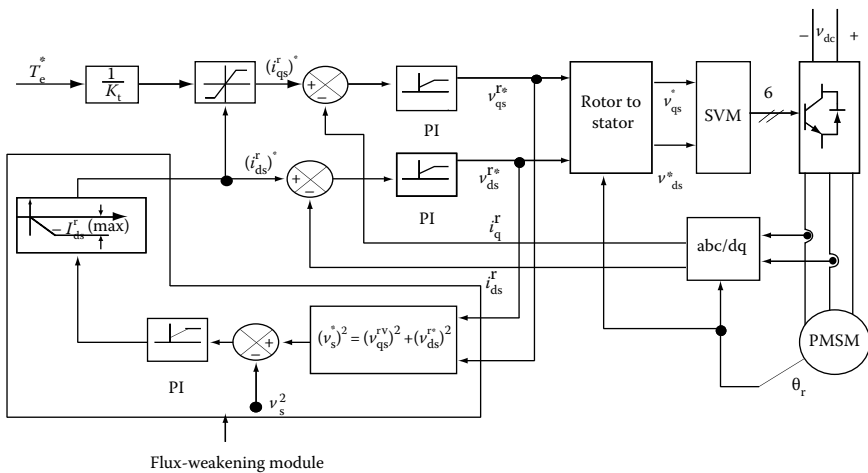


FIGURE 5.18 Parameter insensitive flux-weakening controller.

frames for implementation with space vector modulation or any other modulation scheme of the inverter.

Instead of measuring the voltages in the machine, the d- and q-axes voltage references in the rotor reference frames are considered to be equal to their q- and d-axes machine voltages. The corollary of this assumption is that there is no need for voltage transducers in the implementation. The resultant phasor voltage magnitude is compared with the set value. The set value changes depending on the inverter mode of operation, viz., six-step or sinusoidal voltage operation. The set value then is given for these modes as

$$\begin{aligned} v_s &= 0.577V_{dc} \quad \text{for sine wave operation} \\ &= 0.637V_{dc} \quad \text{for six-step operation} \end{aligned}$$

The error between the negative of the stator voltage and its request is amplified through a proportional plus integral controller. The positive error signal is only considered as that is when the request exceeds the available set voltage magnitude. The signal then is used to generate the d-axis current reference with a maximum set limit. Note that it has to be negative in polarity. The generation of the d-axis current can be proportional in magnitude to the amplified error or can be a function of other variables to maximize torque production. The d-axis current is another input to the q-axis current generator to keep the current phasor within its limit.

The sluggishness in response arises from the inaccurate conversion of error stator voltage phasor to the flux current by a simple proportional constant. It has been proven earlier that such a simple proportional relationship between them does not exist and therefore this implementation leads to an imprecise d-axis current request, resulting in a coupling of the d- and q-axes flux channels in the machine. Differently programming this control block will eliminate the shortcoming.

5.6 SIX-STEP VOLTAGE AND CONSTANT BACK EMF CONTROL STRATEGIES FOR PMSM

Most high-performance applications require instantaneous control over torque and fast response at speeds lower than the base speed. However, only a limited number of applications require the same level of control over torque at speeds higher than the base speed or in the flux-weakening region. Either six-step voltage (SSV) or constant back emf (CBE) control strategies can be applied to a PMSM in the flux-weakening region. In the CBE control strategy, the back emf is limited to a desired value such that a constant voltage margin is preserved throughout the flux-weakening region. This margin allows the system to retain dynamic control over current and high-torque responses in the flux-weakening region. In this region, both back emf and instantaneous torque are controlled by coordinating the current phasor's magnitude and angle with respect to the rotor. This type of control is only suitable for a limited spectrum of high-performance applications. In the SSV control strategy, the maximum possible voltage is always applied to the phases. Average torque is controlled by varying the angle of voltage phasor with respect to the rotor magnetic field.

In this section, the two control strategies are compared in terms of maximum torque versus speed envelope, current requirements, base speed, current and torque ripple, and implementation complexity. The maximum torque versus speed envelope for both control strategies is found by limiting the power losses of the machine to a desired level. By setting this criterion, the motor always operates within a safe thermal boundary. The SSV control strategy is shown to provide a significantly larger maximum torque versus speed envelope for constant power losses or any other criteria that may include constant power, maximum torque per unit stator current, unity power factor, etc. A larger operational envelope translates into a wider speed range as well. The fundamental component of current is shown to be constant in the flux weakening region based on the constant power loss criterion. The fundamental component of current in the case of SSV control strategy is shown to be lower in magnitude than that of the CBE control strategy. It is also shown that the application of the SSV control strategy results in a wider range of control below base speed before flux weakening needs to be initiated. Analytical derivations of the maximum current requirement in the flux-weakening region and maximum speed in each case are provided. The current ripple for the CBE control strategy results from PWM current control. The PWM current ripple has a relatively small peak-to-peak magnitude and high frequency. Therefore, the impact of this ripple can be ignored as compared to the six-step ripple, resulting from the application of the SSV control strategy. The frequency of six-step current and torque ripples under the SSV control strategy is six times the frequency of the phase current. A procedure for deriving the instantaneous phase current and torque waveforms in steady state under the SSV control strategy is introduced. It is shown that the magnitude of the current and torque ripples arising out of SSV inputs are relatively low. The relatively low magnitude of ripple can be attributed to the fact that in PMSM, the phase self-inductance limits the current ripple. This is not the case with induction motors where the ripple is only limited by leakage inductances. At higher than base speed, the frequency of the torque ripple is relatively high with no significant adverse

effects on the speed. The SSV and CBE control strategies are also compared as far as complexity of implementation is concerned. It is shown that the SSV control strategy is simpler to implement as it requires only position information contrary to the CBE control strategy, which requires, in addition, information on two phase currents. This increases the sensor requirements for CBE strategy compared to the SSV strategy.

The comparison of surface mount PM (SMPM) and interior PM (IPM) synchronous machine performance in the flux-weakening region is of interest as the IPMs have been installed as the final arbiter in this region of operation for sometime in research. While considering the criterion of torque, it may be so but not when considering the air gap power is proven in this chapter. This may have some bearing in applications as well as in the perception of the capability of these machines. A type of SMPM with salient stator poles has come to the fore as described in Chapter 1 that has superior to IPSMs in flux-weakening region of operation is worth noting at this stage.

5.6.1 CONSTANT BACK EMF CONTROL STRATEGY

The CBE control strategy is discussed here. The operational envelope and current requirements of the system are studied.

5.6.1.1 The Basics

The model with losses given in Section 4.2.7 is considered for illustration here. In this mode, the d- and q-axes current commands, i_q and i_d , respectively, are coordinated to achieve a desired CBE as well as torque linearity. Currents i_q and i_d need to satisfy Equations 5.28 and 5.29 at a given speed, ω_r , and for a desired back emf, E_m , and a desired torque, T_e :

$$\left(\frac{E_m}{\omega_r} \right)^2 = (\lambda_{af} + L_d i_d)^2 + (L_q i_q)^2 \quad (5.28)$$

$$T_e = 0.75P(\lambda_{af} i_q + (L_d - L_q) i_q i_d) \quad (5.29)$$

where

P is the number of poles

λ_{af} is the magnet flux linkages

L_q and L_d are the q- and d-axes inductances, respectively

Equation 5.28 ensures that the back emf remains constant at a desired value E_m . Equation 5.29 ensures torque linearity. Note that in the flux-weakening region each of the two current commands is a function of both speed and torque commands as described below:

$$i_q = \Lambda(T_e, \omega_r) \quad (5.30)$$

$$i_d = \Gamma(T_e, \omega_r) \quad (5.31)$$

where Λ and Γ represent the relationship as described by Equations 5.28 and 5.29. The implementation of these equations can be performed in software or using a programmable ROM as discussed earlier.

5.6.1.2 Maximum Current in the Flux-Weakening Region

The maximum current in a machine in steady state is determined by the designed maximum permissible power losses. The electrical power losses in a machine are copper and core losses. Equation 5.32 provides a simplified estimation of the net power losses of a PMSM:

$$P_l = 1.5R_s I_s^2 + \frac{1.5}{R_c} \omega_r^2 \lambda_m^2 \quad (5.32)$$

where

P_l is the total electrical power losses of the motor

R_s is the stator phase resistance

R_c is the per phase equivalent core loss resistance

I_s is the phase current

λ_m is the air gap flux linkage as described below

$$\lambda_m = [(\lambda_{af} + L_d I_d)^2 + (L_q I_q)^2]^{0.5} \quad (5.33)$$

The second term on the right-hand side of Equation 5.32 represents the core losses of the motor.

The product of speed and air gap flux linkages is equal to the desired CBE in the flux-weakening region. On the other hand, the maximum permissible torque at a given speed happens when the power losses are equal to the maximum permissible power losses, P_{lm} . P_{lm} is assumed to be a constant for the full range of operating speed. Therefore, it can be concluded from Equation 5.32 that

$$P_{lm} = 1.5R_s(I_{sm})^2 + 1.5\frac{E_m^2}{R_c} \quad (5.34)$$

where I_{sm} is the value of current along the operational boundary. It is noted that the core losses are constant in the flux-weakening region as the induced emf is kept constant. Therefore, for constant power losses, the phase current magnitude is also a constant and this is inferred from Equation 5.34, which defines the current requirement in the flux-weakening region as a function of maximum permissible power losses and desired back emf for the CBE control strategy.

5.6.1.3 Operational Boundary

The maximum possible torque at a given speed in the flux-weakening region is the torque that results in maximum permissible power losses. The current phasor at which maximum torque is produced while both back emf and power losses are at maximum level must satisfy the following equations:

$$\left(\frac{E_m}{\omega_r}\right)^2 = (\lambda_{af} + L_d I_{dm})^2 + (L_q I_{qm})^2 \quad (5.35)$$

$$I_{sm}^2 = I_{dm}^2 + I_{qm}^2 = \frac{P_{lm}}{1.5R_s} - \frac{E_m^2}{R_c R_s} \quad (5.36)$$

where the current phasor is the resultant of q- and d-axes currents I_{qm} and I_{dm} , respectively. Inserting I_{qm} and I_{dm} into the torque Equation 5.29 gives the maximum permissible torque at speed ω_r . Therefore, the operational envelope can be described as

$$T_e = \Phi(\omega_r) \quad (5.37)$$

where Φ represents the concurrent solution of Equations 5.36 and 5.37 at a given speed.

5.6.1.4 Maximum Speed in the Flux-Weakening Region

At maximum speed, torque is zero. At this point maximum possible current is used to counter the rotor magnet flux linkages, and I_q is zero. Therefore, it can be concluded that the maximum speed is given as

$$\omega_{rm} = \frac{E_m}{\lambda_{af} - L_d I_{sm}} = \frac{E_m}{\left(\lambda_{af} - L_d \left(\frac{P_{lm}}{1.5R_s} - \frac{E_m^2}{R_c R_s} \right)^{0.5} \right)} \quad (5.38)$$

where ω_{rm} is the maximum speed. Note that this equation is used to compute the maximum speed under CBE strategy as well as under SSV control strategy. The maximum permissible induced emf is used in the numerator for the CBE strategy and the maximum available voltage phasor is used in the numerator instead of the maximum set induced emf in this equation for the SSV control strategy. This makes it obvious that the speed range is higher for the six-step control strategy with very little control over the current waveform.

5.6.2 Six-Step Voltage Control Strategy

An alternative to the CBE control strategy is to apply the full bus voltage to the motor in the flux-weakening region. In this case, the phase voltage is quasinsinusoidal with six steps such as the one shown in Figure 5.22. The maximum fundamental voltage available from the inverter is at six-step operation as discussed in Chapter 2. It is accompanied by the disadvantage of high fifth and seventh harmonic voltages contributing to respective harmonic currents in the stator phases. These harmonic currents interact with the rotor magnetic field to produce torque pulsations at six times the fundamental frequency. The fifth harmonic current induced magnetic field is rotating in opposite direction to rotor magnetic field at five times the synchronous

speed whereas the seventh harmonic current-induced magnetic field is travelling in the same direction as the rotor magnetic field. The net velocity difference between the fifth stator and rotor fundamental and seventh stator and rotor fundamental magnetic fields is at six times the synchronous speed with the result that the torque pulsation is at sixth harmonic frequency due to the fifth and seventh harmonic currents. Its magnitude can be as high as 20%–25% of the rated torque. Similarly the interaction of fifth and seventh harmonic rotor magnetic field on the fundamental stator currents produce a sixth harmonic torque pulsation that is additive to the previously discussed torque pulsation component, thus increasing the magnitude of the resulting sixth harmonic torque pulsation. Similarly, there is a family of torque pulsations that are at multiples of sixth harmonic frequency present in the machine but their magnitudes are negligible compared to the sixth harmonic torque. In spite of this higher sixth harmonic torque pulsation magnitude, its effect on speed is negligible for speeds greater than base speed because of filtering effect of mechanical impedance at higher speeds, i.e., higher frequencies. Therefore, maximum fundamental voltage availability and negligible effects of torque pulsations on speed performance make SSV control for flux-weakening operation acceptable in many applications. Torque in this control strategy is controlled by varying the angle of the voltage phasor with respect to the rotor field. The magnitude of the maximum voltage phasor is determined solely by the dc bus voltage. The basis, operation, and control of flux-weakening using the SSV control are discussed in this section.

5.6.2.1 Fundamental Analysis

The average torque produced in SSV mode can be calculated from the fundamental component of the six-step input voltage. The peak of the fundamental component of voltage available to the motor phase for a three-phase star-connected motor with a full bridge power stage is described as

$$V_m = \left(\frac{2}{\pi} \right) V_{dc} \quad (5.39)$$

where V_{dc} is the bus voltage. Therefore, the fundamental components of q- and d-axes voltages in the rotor reference frame, V_{qs}^r and V_{ds}^r , can be expressed as

$$V_{qs}^r = V_m \sin(\alpha) \quad (5.40)$$

$$V_{ds}^r = V_m \cos(\alpha) \quad (5.41)$$

where α is the angle of the voltage phasor with reference to the rotor d-axis. The voltage drop across the stator resistance is negligible since this voltage drop is small relative to phase voltage in the flux-weakening region. Therefore, V_{qs}^r and V_{ds}^r in steady state can be described as

$$V_{qs}^r = \omega_r (\lambda_{af} + L_d I_d) \quad (5.42)$$

$$V_{ds}^r = -\omega_r L_q I_q \quad (5.43)$$

The axes currents can be derived from Equations 5.40 through 5.43 and inserted in Equation 5.29 to provide the relationship between torque and the angle of voltage phasor as given below:

$$T_e = 0.75P \left(\frac{-V_m}{\omega_r L_d} \right) \left[\lambda_{af} \cos(\alpha) + \frac{(L_d - L_q)V_m}{2\omega_r L_q} \sin(2\alpha) \right] \quad (5.44)$$

The torque expression has some similarities to dc motor and ac induction motor drives. It deserves the following observations:

1. In a phase-controlled dc motor, if α is considered the triggering delay angle, the torque is proportional to the cosine of this angle. In the PMSM drive considering only the synchronous torque, which is the first part of the Equation 5.44, on the right-hand side, the similarity between the phase controlled dc and PMSM drive is striking.
2. Considering that the voltage and frequency are variables and voltage phasor angle a constant, then the torque is proportional to the ratio between the stator voltage magnitude and frequency. That is similar to the volt/Hz control strategy of the induction motor drives. Volts/Hz ratio is usually kept a constant in induction motor drives in the constant torque operational region. Keeping that a constant is not possible in PMSM as it will induce large currents and hence it is varied for torque control.

These observations indicate that the voltage phasor controlled operation is similar to other motor drives and therefore similarly viable control strategies of other drives in this mode of operation are applicable to the PMSM drive. The air gap torque versus voltage phase angle characteristic, derived from Equation 5.44, is shown in [Figure 5.19](#). Note that the synchronous and reluctance torque components are also shown to indicate their relative importance in the overall air gap torque production. Note that the motoring torque is produced in the 90° – 270° region and in contrast to the current controlled PMSM drives operating from 0° to 180° torque angle.

Equation 5.44 can be used to calculate α as a two-dimensional function of ω_r and desired torque, T_e , as given below:

$$\alpha = K(T_e, \omega_r) \quad (5.45)$$

where the function K is described in Equation 5.44. The implementation of such an equation can be performed in software or using a programmable memory chip.

As far as the fundamental components are concerned the CBE and SSV control strategies can be evaluated using the same basic equations such as Equations 5.28 and 5.29 and Equation 5.34. The only difference is that the peak voltage available to

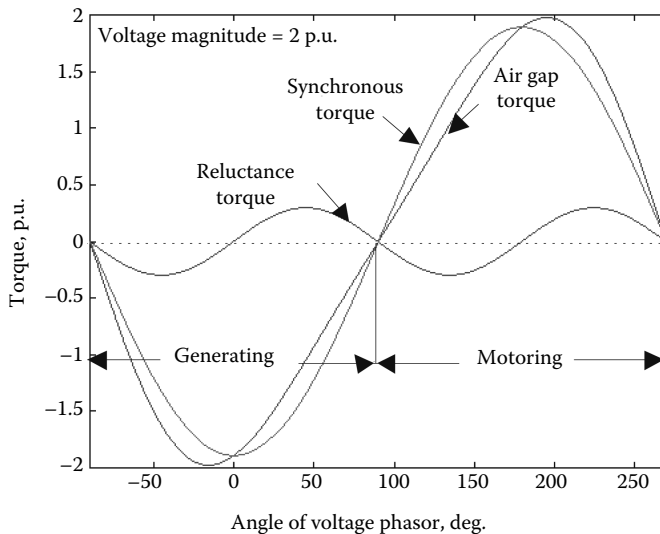


FIGURE 5.19 Air gap torque versus voltage phase angle characteristics.

the phase is different in each case. For the CBE control strategy the peak voltage is E_m , and for the SSV control strategy the peak voltage is V_m given by Equation 5.39.

5.6.2.2 Steady-State Current in SSV Mode

In the SSV mode v_{qs} , v_{bs} , and v_{cs} are balanced SSV. In steady state, the q- and d-axis voltages, v_{qs}^r and v_{ds}^r , respectively, are periodic with a period of $\pi/3$ electrical radians. Accordingly, the q- and d-axis currents are also periodic with the same period. i_{qs}^r and i_{ds}^r are both continuous variables. However qd voltages are not necessarily continuous variables. These conditions, along with the fact that currents and voltages are all periodic, are exploited to derive the steady-state instantaneous currents in one electrical cycle. The subscript “n” denotes that the respective variable is normalized using rated values. In this simulation, the voltage phasor angle α is chosen to be 115° and speed is 1500 r/m, the results are shown in Figure 5.20.

5.6.2.3 Operational Boundary for the SSV Control Strategy

The maximum torque at a given speed under the SSV control strategy can be found by observing the fundamental components of phase voltages and currents. The only difference between the CBE and the SSV strategies is that the maximum desired back emf, E_m , is replaced by V_m as defined in Equation 5.39. Therefore, the fundamental value of current under the SSV control strategy is

$$I_{sm} = \left(\frac{P_{lm}}{1.5R_s} - \frac{V_m^2}{R_c R_s} \right)^{0.5} \quad (5.46)$$

The maximum permissible torque can be found by replacing E_m with V_m , and using the maximum permissible current.

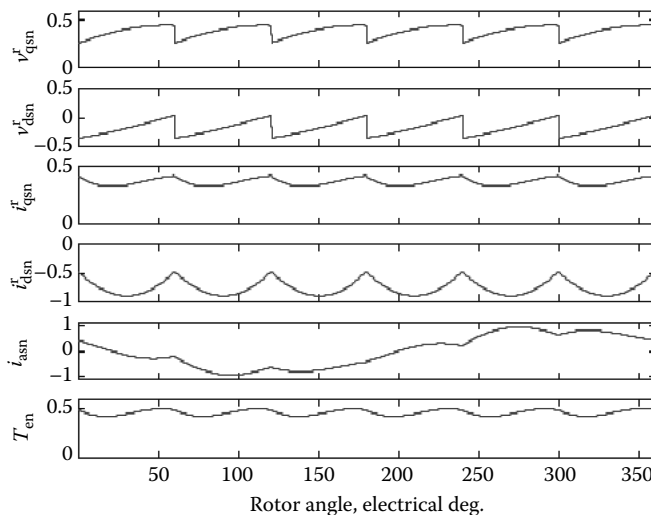


FIGURE 5.20 Normalized motor variables in steady state for a SSV input versus rotor angle.

5.6.2.4 Comparison

The SSV and CBE control strategies are compared for operational speed versus torque boundary and torque ripple in this section. This is to facilitate the process of choosing the most suitable control strategy for a particular application.

Operational boundary: Figure 5.21 shows the operational boundary for the CBE control strategy with $E_m = 0.8$ p.u. The operational boundary for the SSV control strategy is also shown. It is seen that the operational boundary for the SSV control strategy is significantly larger than that of the CBE control strategy. The starting speed for each control strategy is the base speed for the respective control strategy. A comparison of the two control strategies as far as the base speed is discussed next.

Torque ripple: The torque ripple, resulting from the application of the CBE control strategy, is caused by PWM current control system. The impact of this torque ripple on system performance is negligible as compared to the torque ripple inherent to the SSV control strategy. The dominant torque ripple inherent to the SSV control strategy is caused by the sixth harmonic input voltages, resulting in sixth harmonic current and sixth harmonic torque pulsations.

Figure 5.21 shows the peak to peak torque pulsation as a percentage of torque command along the maximum torque versus speed envelope for the SSV control strategy. The absolute peak to peak value of the torque pulsation is also shown. It is seen that the peak to peak torque pulsation remains within 8%–16% of the average torque along the operational boundary. The impact of this torque pulsation on speed is minimal as its frequency is relatively high in the higher than base speed operating region.

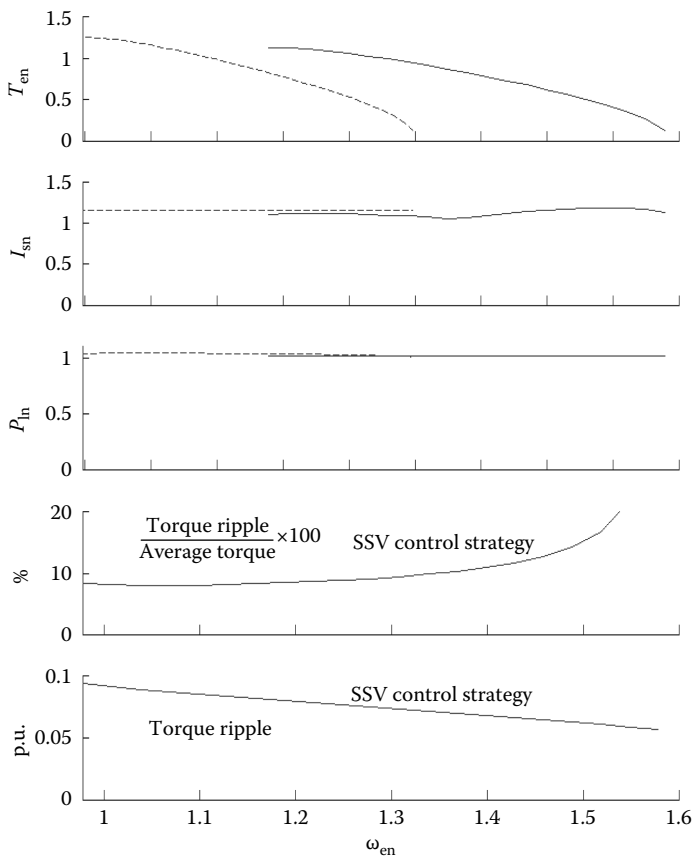


FIGURE 5.21 Maximum torque, peak current, power losses, torque ripple as a percentage of average torque, and peak torque ripple for SSV (solid lines) and CBE (dashed lines, $E_m = 0.8$ p.u.) control strategies.

5.7 DIRECT STEADY-STATE EVALUATION

The steady state has been calculated so far using the fundamental of the input voltages only. The steady-state performance for the actual input voltages including harmonics is necessary to select the rating of the converter–inverter switches and computation of losses and derating of the PMSM. The steady state then is calculated by (1) using steady-state harmonic equivalent circuits and summing the responses, (2) directly by matching the boundary conditions, and (3) running the dynamic simulation until it reaches steady state and then considering one cycle to find the average value of torque. The harmonic equivalent circuit approach has the conceptual advantage of simplicity but carries the disadvantage of accuracy being limited by the number of harmonics considered in the input voltages. The direct steady-state evaluation and the dynamic simulation approaches overcome this disadvantage but

is limited due to the requirement of a computer for solution. Further the direct steady-state evaluation requires very small number of steps in achieving the result and therefore it is preferred in practice. This method is derived and discussed in the section that follows.

The direct method exploits the symmetry of input voltages and currents in the steady state. As they are symmetric over a given interval, in this case 60° , their boundaries are matched to extract an elegant solution.

5.7.1 INPUT VOLTAGES

The input phase voltages are the six-stepped waveforms shown in Figure 5.22. Using the transformation, the d- and q-stator voltages in rotor reference frames are

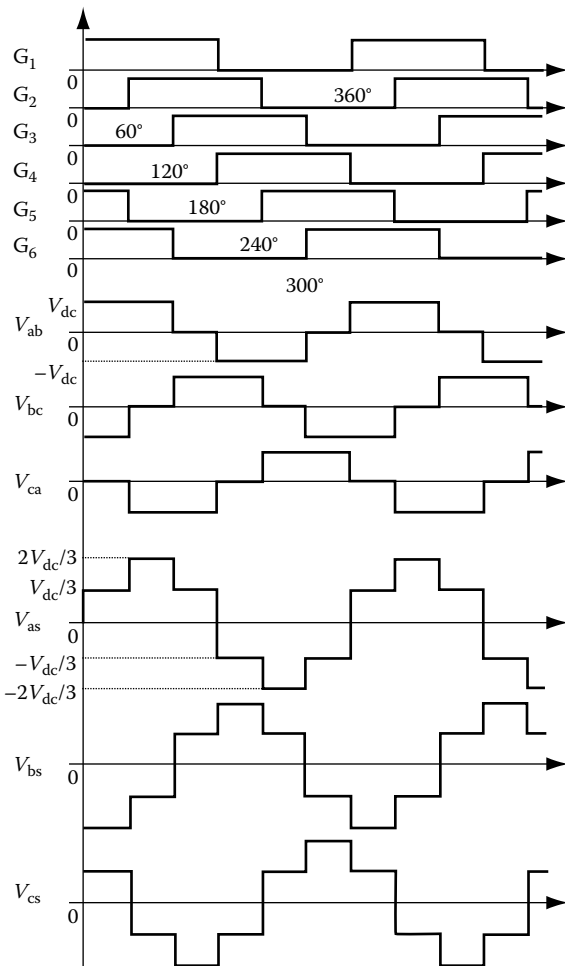


FIGURE 5.22 Inverter gate (base) signals and line and phase voltage waveforms.

For the interval one, $0 \leq \theta_r \leq \pi/3$ the d- and q-axes voltages are

$$v_{qsI}^r(\theta_r) = \frac{2}{3} V_{dc} \cos\left(\theta_r + \frac{\pi}{3}\right) \quad (5.47)$$

$$v_{dsI}^r(\theta_r) = \frac{2}{3} V_{dc} \sin\left(\theta_r + \frac{\pi}{3}\right) \quad (5.48)$$

where

$$\theta_r = \omega_r t \quad (5.49)$$

For the interval two, $\frac{\pi}{3} \leq \theta_r \leq \frac{2\pi}{3}$, the voltages are

$$v_{qsII}^r(\theta_r) = \frac{2}{3} V_{dc} \cos(\theta_r) \quad (5.50)$$

$$v_{dsII}^r(\theta_r) = \frac{2}{3} V_{dc} \sin(\theta_r) \quad (5.51)$$

But Equations 5.50 and 5.51 can be written as

$$v_{qsII}^r(\theta_r) = \frac{2}{3} V_{dc} \cos\left(\theta_r + \frac{\pi}{3} - \frac{\pi}{3}\right) \quad (5.52)$$

$$v_{dsII}^r(\theta_r) = \frac{2}{3} V_{dc} \sin\left(\theta_r + \frac{\pi}{3} - \frac{\pi}{3}\right) \quad (5.53)$$

Equations 5.52 and 5.53 signify that q- and d-axes voltages are similar for each 60° and they are periodic. They are shown in [Figure 5.23](#). The symmetry of these voltages is exploited to find directly the steady state. Note that this voltage representation considers the actual waveforms of the inverter, i.e., the fundamental and higher order harmonics included.

The voltage phasor, which is the resultant of the q- and d-axes voltages, is positioned at angle of α and this is with respect to the rotor. The positioning of this voltage phasor at any angle is made feasible by the inverter with its logic and gating control. Then this voltage phasor angle has to be incorporated in the voltages that are derived in the above. The q- and d-axes voltages can be then written as

$$v_{qsI}^r = \frac{2}{3} V_{dc} \cos\left(\theta_r + \frac{\pi}{3} - \alpha\right) \quad (5.54)$$

$$v_{dsI}^r = \frac{2}{3} V_{dc} \sin\left(\theta_r + \frac{\pi}{3} - \alpha\right) \quad (5.55)$$

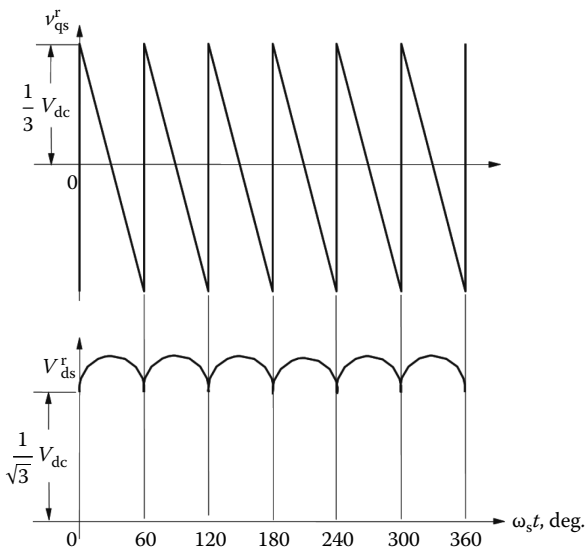


FIGURE 5.23 The q- and d-axes voltages in the synchronous reference frames.

And their average values are

$$v_{qs}^r = \frac{2}{3}V_{dc} \sin(\alpha) \quad (5.56)$$

$$v_{ds}^r = \frac{2}{3}V_{dc} \cos(\alpha) \quad (5.57)$$

These average voltages on the rotor reference frames are nothing but the reflection of the peak fundamental component of the abc phase voltages.

It has been demonstrated that the input q- and d-axes voltages are periodic for every 60 electrical degrees. Hence for a linear system, which is the case when speed is constant in the PMSM, the response must also be periodic. That is, the stator currents will also be periodic. The next step is to assemble the machine equations in the state space form. To find the steady state, the inputs to the machine may be considered to consist of the stator input voltages and the induced emf on the q-axis. As the system is linear in the steady state, the property of superposition can be used to find the response due to each of these component inputs and then add them to obtain the total response of the system. Such an approach is taken here. The response due to the stator input voltages is found by boundary matching technique.

5.7.2 MACHINE EQUATIONS IN STATE SPACE FORM

The PMSM equations in rotating rotor reference frames are written in state variable form as

$$\dot{X}_1 = A_1 X_1 + B_1 U_1 + B_1 e \quad (5.58)$$

where

$$X_1 = [i_{qs}^r \quad i_{ds}^r]^t \quad (5.59)$$

$$A_1 = Q^{-1} P_1 \quad (5.60)$$

$$B_1 = Q^{-1} \quad (5.61)$$

$$U_1 = [v_{qs}^r \quad v_{ds}^r]^t \quad (5.62)$$

$$e = [\omega_r \lambda_{af} \quad 0] \quad (5.63)$$

$$Q = \begin{bmatrix} L_q & 0 \\ 0 & L_d \end{bmatrix} \quad (5.64)$$

$$P_1 = \begin{bmatrix} -R_s - \omega_s L_d \\ \omega_s L_q - R_s \end{bmatrix} \quad (5.65)$$

From Equations 5.54 and 5.55, the voltages are written in state space form as

$$\begin{bmatrix} p v_{qs}^r \\ p v_{ds}^r \end{bmatrix} = \begin{bmatrix} 0 & -\omega_r \\ \omega_r & 0 \end{bmatrix} \begin{bmatrix} v_{qs}^r \\ v_{ds}^r \end{bmatrix} \quad (5.66)$$

Considering only that part without rotor flux-induced emf in the q-axis, Equations 5.58 and 5.59 are combined to give

$$\begin{bmatrix} \dot{X}_1 \\ \dot{X}_2 \end{bmatrix} = \begin{bmatrix} A_1 & B_1 \\ 0 & S \end{bmatrix} \begin{bmatrix} X_1 \\ X_2 \end{bmatrix} \quad (5.67)$$

where

$$X_2 = [v_{qs}^r \quad v_{ds}^r]^t \quad (5.68)$$

$$S = \begin{bmatrix} 0 & -\omega_r \\ \omega_r & 0 \end{bmatrix} \quad (5.69)$$

and matrices A_1 and B_1 are of compatible dimensions. Equation 5.67 in a compact form is expressed as

$$\dot{X} = AX \quad (5.70)$$

where

$$X = [X_1 \quad X_2]^t \quad (5.71)$$

$$A = \begin{bmatrix} A_1 & B_1 \\ 0 & S \end{bmatrix} \quad (5.72)$$

5.7.3 BOUNDARY MATCHING CONDITION AND SOLUTION

The solution of Equation 5.70 is written as

$$X(t) = e^{At} X(0) \quad (5.73)$$

where the initial steady-state vector $X(0)$ is to be evaluated to compute $X(t)$ and the electromagnetic torque. It is found by the fact that the state vector has periodic symmetry and hence

$$X\left(\frac{\pi}{3\omega_s}\right) = S_1 X(0) \quad (5.74)$$

where S_1 is evaluated later. The boundary condition for the currents are

$$X_1\left(\frac{\pi}{3\omega_s}\right) = X_1(0) \quad (5.75)$$

The boundary matching condition for the voltage vector is obtained by expanding Equations 5.52 and 5.53 and substituting Equations 5.47 and 5.48 into them. The direct-axis voltage is

$$\begin{aligned} v_{qsII}^r(\theta_r) &= \frac{2}{3} V_{dc} \cos\left(\theta_r + \frac{\pi}{3} - \frac{\pi}{3}\right) \\ &= \frac{2}{3} V_{dc} \left\{ \cos\left(\theta_r + \frac{\pi}{3}\right) \cos \frac{\pi}{3} + \sin\left(\theta_r + \frac{\pi}{3}\right) \sin \frac{\pi}{3} \right\} \\ &= \frac{1}{2} v_{qsI}^r(\theta_s) + \frac{\sqrt{3}}{2} v_{dsI}^r(\theta_s) \end{aligned} \quad (5.76)$$

Similarly,

$$v_{dsII}^r = \frac{1}{2} v_{dsI}^r - \frac{\sqrt{3}}{2} v_{qsl}^r \quad (5.77)$$

Hence

$$X_2 \left(\frac{\pi}{3\omega_s} \right) = \begin{bmatrix} \frac{1}{2} & \frac{\sqrt{3}}{2} \\ -\frac{\sqrt{3}}{2} & \frac{1}{2} \end{bmatrix} X_2(0) = S_2 X_2(0) \quad (5.78)$$

where

$$S_2 = \begin{bmatrix} \frac{1}{2} & \frac{\sqrt{3}}{2} \\ -\frac{\sqrt{3}}{2} & \frac{1}{2} \end{bmatrix} \quad (5.79)$$

S_1 is obtained from Equations 5.75 and 5.78 as

$$S_1 = \begin{bmatrix} I & 0 \\ 0 & S_2 \end{bmatrix} \quad (5.80)$$

where I is a 2×2 identity matrix.

Substituting Equation 5.74 into Equation 5.73:

$$X \left(\frac{\pi}{3\omega_s} \right) = S_1 X(0) = e^{A(\pi/3\omega_s)} X(0) \quad (5.81)$$

Hence

$$\left[S_1 - e^{A(\pi/3\omega_s)} \right] X(0) = 0 \quad (5.82)$$

or

$$WX(0) = 0 \quad (5.83)$$

where

$$\begin{aligned} W &= \left[S_1 - e^{A(\pi/3\omega_s)} \right] \\ &= \begin{bmatrix} W_1 & W_2 \\ W_3 & W_4 \end{bmatrix} \end{aligned} \quad (5.84)$$

where

W_1 is 2×2 matrix

W_2 is 2×2 matrix

W_3 is 2×2 matrix

W_4 is 2×2 matrix

It can be proved that W_3 is a null matrix. Only expanding the upper row in Equation 5.83, gives the following relationship:

$$W_1 X_1(0) + W_2 X_2(0) = 0 \quad (5.85)$$

from which the steady-state current vector $X_1(0)$ is obtained as

$$X_1(0) = -W_1^{-1} W_2 X_2(0) \quad (5.86)$$

Having evaluated the initial current vector, it could be used to evaluate currents for one full cycle and the electromagnetic torque. A set of steady-state waveforms is shown in Figure 5.20. The peaking of the current is significant to determine the peak rating of the devices in the inverter. Note that this approach is suitable for steady-state calculation of six-stepped voltage inputs irrespective of the control strategy used. The electromagnetic torque has a dominant sixth harmonic torque ripple in the six-stepped voltage-fed PMSM drive. The steady-state response due to the induced emf by the rotor flux linkages is found as follows. As the induced emf is a constant at a given speed, its response in the machine has to also be a constant in steady state. Hence the d- and q-axes current derivatives are zero. With that the steady-state currents are

$$\begin{bmatrix} I_{qse}^r \\ I_{dse}^r \end{bmatrix} = \begin{bmatrix} -\frac{\omega_r \lambda_{af} R_s}{R_s^2 + \omega_r^2 L_d L_q} \\ -\frac{\omega_r^2 L_d L_q}{R_s^2 + \omega_r^2 L_d L_q} \end{bmatrix} \quad (5.87)$$

Then the complete response is given by

$$i_{qs}^r = X(1) + I_{qse}^r \quad (5.88)$$

$$i_{ds}^r = X(2) + I_{dse}^r \quad (5.89)$$

where the vector X is the initial vector $X_1(0)$ obtained from the boundary matching condition technique.

5.7.4 MATLAB® PROGRAM

A MATLAB program to compute the direct steady state is given below.

```
% Program to find the direct steady of PMSM with six step
input voltages
%
close all; clear all;
% Data
lq=0.0127;ld=0.0055;rs=1.2;P=4;wr=P/2*2*pi*1500/60;lamaf=0.123;
Tb=2.4;Ib=6.5;Vb=85; % Base values
tp=2*pi/3;
vdc=57;vd1=vdc/3; vd2=2*vd1; % Dc link voltage
alf=115; % Stator phase angle, deg.
alfa=alf*pi/180; % Stator phase angle, rad.
del=1/(rs^2+wr^2*ld*lq);
% Steady state currents due to induced emf
iqso=-wr*lamaf*rs*del;
idso=-wr^2*lq*lamaf*del;
% Machine system matrix
B=[-rs/lq -wr*ld/lq;
   wr*lq/ld -rs/ld];
C=[1/lq 0;
   0 1/ld];
% Voltage generating matrix
D=[0 -wr;
   wr 0];
% Null matrix
Z=[0 0;
   0 0];
%
A=[B C;
   Z D];
%
S3=[0.5 sqrt(3)/2;
   -sqrt(3)/2 0.5];
S2=[1 0;
   0 1];
S1=[S2 Z;
   Z S3];
%
W=S1-expm(A*pi/(3*wr)); % W matrix
W1=W(1:2,1:2); % Partitioning of W matrix
W2=W(1:2,3:4);
W4=W(3:4,3:4);
W3=W(3:4,1:2);
%
X2Z=vd2*[cos(-alfa+pi/3); % Initial steady state voltage
vector
```

```

    sin(-alfa+pi/3)];
X1Z=-(W1^-1)*W2*X2Z;           % Initial steady state current
                                % vector
% Initial steady state vector
XZ=[X1Z;
     X2Z];
% Computation of steady state currents and torque in p.u.
for pos=1:1:300;               % Position do loop, 1/5th of a
                                % degree
posrad=pos/5*pi/180;          % Position in radians
t=posrad/wr;                  % Time
X=expm(A*t)*XZ;              % Computation of response
iqs(pos)=(X(1)+iqso)/Ib;      % q axis stator current
ids(pos)=(X(2)+idso)/Ib;      % D axis stator current
Te(pos)=.75*P*(lamaf+(ld-lq)*ids(pos)*Ib)
*iqs(pos)*Ib/Tb;             % Air gap torque
ias(pos)=(cos(posrad)*iqs(pos)
+sin(posrad)*ids(pos));        % A phase current
vas(pos)=(cos(posrad)*X(3)+sin(posrad)*X(4))/Vb;
                                % A phase voltage
vqs(pos)=X(3)/Vb;            % Q axis stator voltage
vds(pos)=X(4)/Vb;            % D axis stator voltage
time(pos)=pos/5;              % Rotor position in deg.
end
for pos=301:1:1800;            % Iteration for the rest of the cycle
posrad=pos/5*pi/180;
iqs(pos)=iqs(pos-300);
ids(pos)=ids(pos-300);
Te(pos)=.75*P*(lamaf+(ld-lq)*ids(pos)*Ib)*iqs(pos)*Ib/Tb;
ias(pos)=(cos(posrad)*iqs(pos)+sin(posrad)*ids(pos));
time(pos)=pos/5;
vqs(pos)=vqs(pos-300);
vds(pos)=vds(pos-300);
vas(pos)=(cos(posrad)*vqs(pos)+sin(posrad)*vds(pos));
end
% Computation ends
% Plotting
figure(3);orient tall;
subplot(6,1,1)
plot(time,vqs);ylabel('v_{qsn}');set(gca,'xticklabel',[]);
subplot(6,1,2)
plot(time,vds);ylabel('v_{dsn}');set(gca,'xticklabel',[]);
subplot(6,1,3)
plot(time,iqs);ylabel('i_{qsn}');set(gca,'xticklabel',[]);
subplot(6,1,4);
plot(time,ids);ylabel('i_{dsn}');set(gca,'xticklabel',[]);
subplot(6,1,5);
plot(time,ias);ylabel('i_{asn}');set(gca,'xticklabel',[]);

```

5.8 FLUX WEAKENING IN SMPM AND IPM SYNCHRONOUS MACHINES

Flux weakening in relationship to surface mount (SMPM) and interior permanent magnet synchronous machines (IPSM) requires some elaboration. The conventional wisdom is that IPSM are superior to SMPM for flux-weakening operation. That has to be examined in some depth so that the flux-weakening capabilities of these machines can be understood. Such a treatment is presented here. For their comparison, a new set of base values are required so that comparison is not clouded by a large number of parameters. Further, the derivations are made using the fundamental relationships in the steady state.

5.8.1 FLUX-WEAKENING EQUATIONS IN NEW BASE

To derive fundamental characteristics in terms of the stator current and voltage phasors and machine saliency so as to clearly see its role in flux-weakening operation and thereby compare it with that of the surface mount machine with a saliency of one, the following base values are defined:

$$\lambda_b = \lambda_{af} = L_b I_b = L_d I_b \quad (5.90)$$

Ignoring stator resistance voltage drops, the base change reduces the voltage phasor from Equation 5.4 to the following as

$$v_{sn}^2 = v_{dsn}^r + v_{qsn}^r = \omega_m^2 \left[(1 + i_{dsn}^r)^2 + \rho^2 i_{qsn}^r \right] \text{ (p.u.)} \quad (5.91)$$

This equation gives the speed only as a function of voltage phasor, stator current components, and saliency ρ is defined as the ratio between the quadrature to direct-axis inductances. The SMPM machine is modeled for a saliency of one in this general equation relating speed to other machine variables and all other rotors with magnets either partially or fully imbedded are modeled with a saliency greater than one and are hereafter referred to as interior permanent magnet (IPM) machines.

The normalized electrical rotor speed of the PMSM is given by

$$\omega_m = \frac{v_{sn}}{\sqrt{(1 + i_{dsn}^r)^2 + \rho^2 i_{qsn}^r}} \text{ (p.u.)} \quad (5.92)$$

The normalized speed of the SMPM is obtained from this equation by equating the saliency to one and for the IPM it is obtained with saliency values higher than unity. The ratio between the SMPM and IPM machine normalized speeds for equal voltage and current conditions is

$$\omega_{si} = \frac{\text{SMPM speed}}{\text{IPM speed}} = \sqrt{\frac{(1+i_{dsn}^r)^2 + \rho^2 i_{qsn}^r}{(1+i_{dsn}^r)^2 + i_{qsn}^r}} = \sqrt{\frac{(1+i_{dsn}^r)^2 + \rho^2(i_{sn}^2 - i_{dsn}^r)^2}{(1+i_{dsn}^r)^2 + (i_{sn}^2 - i_{dsn}^r)^2}} \quad (5.93)$$

The normalized air gap torque of the PMSM is given by

$$T_{en} = i_{qsn}^r \left[1 + (1-\rho)i_{dsn}^r \right] \text{ (p.u.)} \quad (5.94)$$

The torque ratio between the SMPM and IPM machines can then be derived as

$$T_{si} = \frac{\text{SMPM air gap torque}}{\text{IPM air gap torque}} = \frac{1}{1 + (1-\rho)i_{dsn}^r} \quad (5.95)$$

By substituting for saliency of unity for SMPM machine and nonunity values for the IPM machine, in both the normalized speed and air gap torque expressions, their respective speeds and air gap torques are evaluated and hence their air gap power by taking the product of their respective torque and speed. Then the ratio between their air gap powers can be obtained by dividing the SMPM's to IPM's air gap power.

Accordingly, the air gap power ratio between the SMPM and IPM air gap powers follows as

$$P_{si} = \frac{\text{SMPM air gap power}}{\text{IPM air gap power}} = \frac{1}{1 + (1-\rho)i_{dsn}^r} \sqrt{\frac{(1+i_{dsn}^r)^2 + \rho^2(i_{sn}^2 - i_{dsn}^r)^2}{(1+i_{dsn}^r)^2 + (i_{sn}^2 - i_{dsn}^r)^2}} \quad (5.96)$$

Then the variables of interest can be viewed as air gap torque ratio, speed ratio, and air gap power ratio between the SMPM and IPM machines. Also the air gap powers for both the machines are also included and they are all plotted for stator current phasors of 0.25, 0.5, and 1 p.u. for various saliencies of 1, 3, 5, and 7 given in [Figure 5.24](#). Note that the base values of the current are, in general but not always, multiple times the rated current in the machine because of the choice of the base inductance in this treatment. For example, consider the following machine parameters:

$$\lambda_{af} = 0.0858 \text{ V s, rated current, } I_r = 7.07 \text{ A (peak), } L_d = 3.74 \text{ mH, } L_q = 11.04 \text{ mH}$$

$$\text{Base current, } I_b = \frac{\lambda_{af}}{L_d} = \frac{0.0858}{0.00374} = 22.94 \text{ A}$$

$$\text{Normalized rated current, } I_m = \frac{I_r}{I_b} = \frac{7.07}{22.94} = 0.308 \text{ p.u.}$$

Likewise, the normalized rated currents are found for various sample machines taken from various publications and shown in [Table 5.1](#). It is found that the normalized rated currents with respect to the defined base current are more in the vicinity

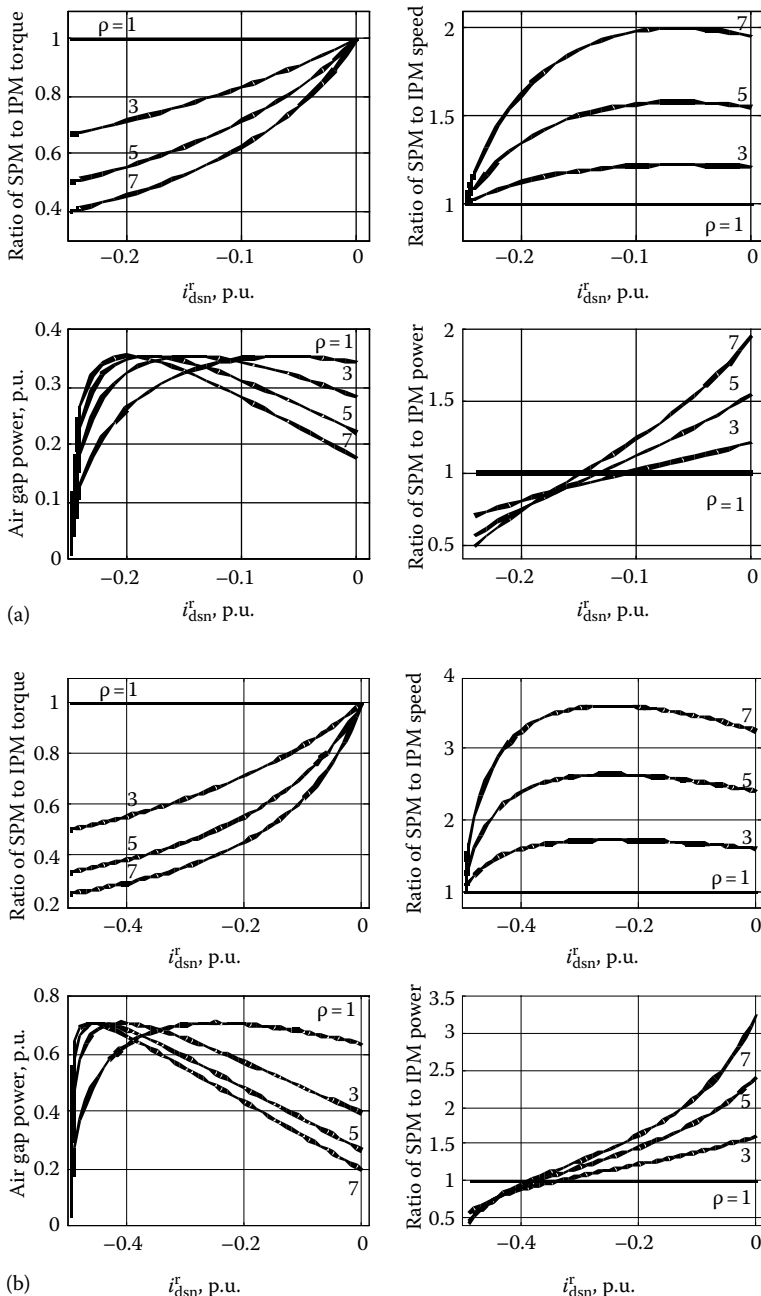
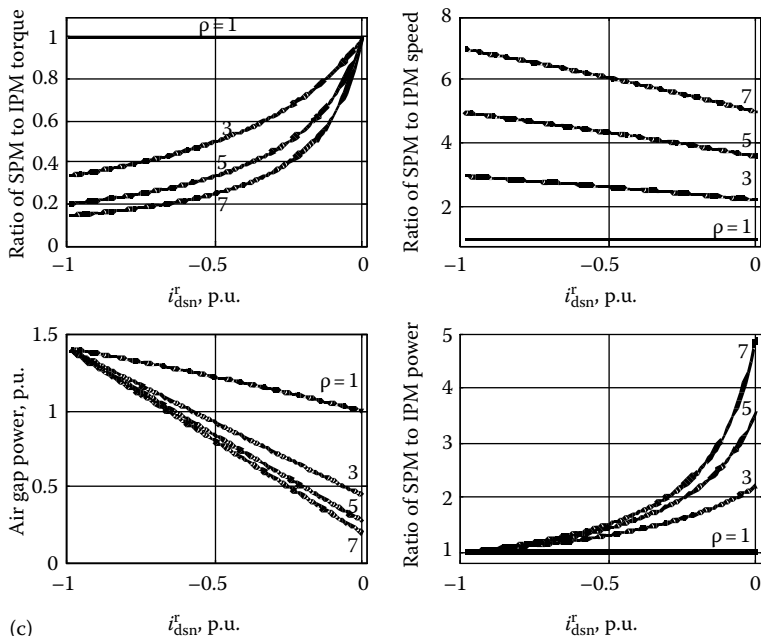


FIGURE 5.24 Influence of saliency in PMSMs for various stator current magnitudes.
 (a) $i_{sn} = 0.25$ p.u., (b) $i_{sn} = 0.5$ p.u., and (c) $i_{sn} = 1$ p.u.

**FIGURE 5.24 (continued)****TABLE 5.1****Sample PMSM Ratings, Parameters and Their Normalized Rated Currents**

Power (kW)	I_r , A (rms)	L_d (mH)	L_q (mH)	ρ	λ_{af} (V s)	I_b (A)	(p.u.)
1.5	5	3.74	11.04	2.95	0.0858	22.94	0.308
50	160	0.23	0.56	2.43	0.104	452.2	0.50
0.89	6.6	5.7	12.5	2.19	0.122	21.4	0.436
52.19	315	0.1104	0.2459	2.227	0.05658	512.5	0.869
	2.65	44.8	102.7	2.29	0.533	11.89	0.315
	300	0.1	0.3	3	0.01226	122.6	3.46
	5	8.72	8.72	1	0.1077	12.3	0.575
	3	42.44	42.44	1	0.311	7.328	0.579
	5.9	5	5	1	0.1	20	0.417
	2.4	34	150	4.41	0.215	6.32	0.536
11	58.6	0.49	0.49	1	0.1473	300.6	0.275

of 0.4 p.u. but they do not exceed 3.5. With that in view, the results shown in figures have to be interpreted.

Three ranges of normalized stator d-axis current are considered and they cover the entire flux-weakening operation of the motor drive. If the direct-axis current

exceeds 1 p.u., then the magnet flux linkages become negative and around this region many permanent magnets are permanently demagnetized or close to being demagnetized. Therefore, usually operation beyond zero direct-axis flux linkages is not recommended, thus limiting the d-axis stator current to 1 p.u. operation with the new base current definition. The performance in the three regions of d-axis current operation is discussed in the following. In these ranges, the maximum stator current magnitude is assumed to be 0.25, 0.5, and 1.0 p.u., respectively, with the result that the q-axis current is the phasor difference of the stator current phasor and the d-axis stator current given by

$$i_{qsn}^r = \sqrt{i_{sn}^2 - (i_{dsn}^r)^2}$$

This relationship is strictly enforced in finding the performance characteristics. It is because the rated current is usually the maximum operating current in steady state and not be allowed to exceed for thermal reason.

1. Maximum stator current of 0.25 p.u.: The performance characteristics for this range are shown in [Figure 5.24a](#). As the saliency increases, the operational speed of the SMPM is more advantageous over a larger range of d-axis stator current operation but not necessarily in torque. The net effect is the power output, which is not dramatically affected by saliency. There is a decided advantage for the IPM beyond 0.1 p.u. d-axis stator current operation and that too as the saliency increases, which is pushed even higher with the result that the SMPM provides better air gap power performance below that range. There is no decisive advantage for IPM in comparison to SMPM in this range of stator current operation.
2. Maximum stator current of 0.5 p.u.: Only for a small range of d axis current operation around and beyond -0.4 p.u., IPM has an advantage whereas below that value, the SMPM is capable of higher air gap power. SMPM is more advantageous than an IPM over most of the operational range is clearly seen from the performance characteristics given in [Figure 5.24b](#).
3. Maximum stator current of 1 p.u.: In this range of operation, the SMPM is superior to IPM in its entire range is shown by the characteristics in [Figure 5.24c](#). The advantage of IPM's torque capability is countered by the SMPM's speed capability with the result that the latter is dominant in air gap power performance in the entire range.

Only looking at air gap torque, IPM is better all the time compared to SMPM machines. When the speed range availability for the same voltage is considered, the SMPM is better compared to IPM machines. But when the most important index of air gap power is considered, the SMPM is better in almost all the ranges compared to IPM. The natural question is what happens when the q-axis current is kept constant while the d-axis current is varied. To a large extent, the range of benefit for IPM improves but it does not completely perform superior to the SMPM machines can be proved.

The generalized results prove that there is no advantage for IPM over SMPM in flux-weakening operation when the air gap power is considered the primary factor. It is recalled from electric motor drives primers that in the flux-weakening region, the dominant requirement is to hold the air gap power at the rated value or as close to it as possible without exceeding the set current of rated current in steady state and everything else is relegated to lower priority.

REFERENCES

Flux Weakening Control

1. T. M. Jahns, Flux-weakening regime operation of an interior permanent-magnet synchronous motor drive, *IEEE Transactions on Industry Applications*, IA-23(4), 681–689, 1987.
2. S. R. Macminn and T. M. Jahns, Control techniques for improved high-speed performance of interior PM synchronous motor drives, *IEEE Transactions on Industry Applications*, 27(5), 997–1004, 1991.
3. R. Krishnan, Control and operation of PM synchronous motor drives in the field-weakening region, *IEEE IECON Proceedings (Industrial Electronics Conference)*, pp. 745–750, 1993.
4. S. Morimoto, T. Ueno, M. Sanada et al., Variable speed drive system of interior permanent magnet synchronous motors for constant power operation, *Conference Record, Power Conversion Conference, Yokohama, Japan (Cat. No. 93TH0406-9)*, pp. 402–407, 1993.
5. R. Monajemy and R. Krishnan, Implementation strategies for concurrent flux weakening and torque control of the PM synchronous motor, *Conference Record, IEEE Industry Applications Conference (Cat. No. 95CH35862)*, pp. 238–245, 1995.
6. R. Monajemy and R. Krishnan, Performance comparison for six-step voltage and constant back EMF control strategies for PMSM, *Conference Record, IEEE Industry Applications Conference (Cat. No. 99CH36370)*, pp. 165–172, 1995.
7. C. C. Chan, J. Z. Jiang, W. Xia et al., Novel wide range speed control of permanent magnet brushless motor drives, *IEEE Transactions on Power Electronics*, 10(5), 539–546, 1995.
8. J.-H. Song and S.-K. Sul, Torque maximizing control of permanent magnet synchronous motor under voltage and current limitations of PWM inverter, *Conference Proceedings—IEEE Applied Power Electronics Conference and Exposition—APEC*, pp. 758–763, 1996.
9. Z. Zeng, E. Zhou, and D. T. W. Liang, New flux weakening control algorithm for interior permanent magnet synchronous motors, *IECON Proceedings (Industrial Electronics Conference)*, vol. 2, pp. 1183–1186, 1996.
10. Z. Zhaohui, E. Zhou, and D. T. W. Liang, A new flux weakening control algorithm for interior permanent magnet synchronous motors, *Proceedings, IEEE IECON 22nd International Conference on Industrial Electronics, Control, and Instrumentation (Cat. No. 96CH35830)*, pp. 1183–1186, 1996.
11. N. Bianchi, S. Bolognani, and M. Zigliotto, Analysis of PM synchronous motor drive failures during flux weakening operation, *PESC Record—IEEE Annual Power Electronics Specialists Conference*, pp. 1542–1548, 1996.
12. J. Bonet-Madurga and A. Diez-Gonzalez, Control system for high speed operation of the permanent magnet synchronous motor, *International Power Electronics Congress—CIEP*, pp. 63–66, 1996.

13. D. S. Maric, S. Hiti, C. C. Stancu, et al., Two flux weakening schemes for surface-mounted permanent-magnet synchronous drives—design and transient response considerations, *IEEE International Symposium on Industrial Electronics*, vol. 2, pp. 673–678, 1999.
14. J.-J. Chen and K.-P. Chin, Automatic flux-weakening control of permanent magnet synchronous motors using a reduced-order controller, *IEEE Transactions on Power Electronics*, 15(5), 881–890, 2000.
- 14a. R. Krishnan, *Electric Motor Drives*, Prentice Hall, Upper Saddle River, NJ, 2001.
15. K. Yamamoto, K. Shinohara, and H. Makishima, Comparison between flux weakening and PWM inverter with voltage booster for permanent magnet synchronous motor drive, *Proceedings of the Power Conversion Conference, Osaka, Japan (Cat. No. 02TH8579)*, pp. 161–166, 2002.
16. Y. F. Shi, Z. Q. Zhu, Y. S. Chen, et al., Investigation of flux-weakening performance and current oscillation of permanent magnet brushless ac drives, *Conference Proceedings—4th International Power Electronics and Motion Control Conference*, pp. 1257–1262, 2004.
17. T. Yamakawa, S. Wakao, K. Kondo, et al., A new flux weakening operation of interior permanent magnet synchronous motors for railway vehicle traction, *IEEE 11th European Conference on Power Electronics and Applications*, p. 6, 2005.
18. K. Tae-suk and S. Seung-Ki, A novel flux weakening algorithm for surface mounted permanent magnet synchronous machines with infinite constant power speed ratio, *Proceedings of the International Conference on Electrical Machines and Systems*, pp. 440–445, 2007.
19. Y. Young-Doo, L. Wook-Jin, and S. Seung-Ki, Flux weakening control for high saliency interior permanent magnet synchronous machine without any tables, *European Conference on Power Electronics and Applications*, pp. 1350–1356, 2007.

Speed Control

20. K. Jang-Mok and S. Seung-Ki, Speed control of interior permanent magnet synchronous motor drive for the flux weakening operation, *IEEE Transactions on Industry Applications*, 33(1), 43–48, 1997.
21. J.-M. Kim and S.-K. Sul, Speed control of interior permanent magnet synchronous motor drive for the flux weakening operation, *IEEE Transactions on Industry Applications*, 33(1), 43–48, 1997.
22. Y. S. Kim, Y. K. Choi, and J. H. Lee, Speed-sensorless vector control for permanent-magnet synchronous motors based on instantaneous reactive power in the wide-speed region, *IEE Proceedings—Electric Power Applications*, 152(5), 1343–1349, 2005.

Loss Minimizing Strategies

23. R. Monajemy and R. Krishnan, Control and dynamics of constant-power-loss-based operation of permanent-magnet synchronous motor drive system, *IEEE Transactions on Industrial Electronics*, 48(4), 839–844, 2001.
24. J.-J. Chen and K.-P. Chin, Minimum copper loss flux-weakening control of surface mounted permanent magnet synchronous motors, *IEEE Transactions on Power Electronics*, 18(4), 929–936, 2003.
25. J. S. Lawler, J. Bailey, and J. McKeever, Minimum current magnitude control of surface PM synchronous machines during constant power operation, *IEEE Power Electronics Letters*, 3(2), 53–56, 2005.

26. K. Yamazaki and Y. Seto, Iron loss analysis of interior permanent magnet synchronous motors variation of main loss factors due to driving condition, *International Electric Machines and Drives Conference (IEEE Cat. No. 05EX1023C)*, pp. 1633–1638, 2005.

Machine-Related Issues

27. J. C. Teixeira, C. Chillet, and J. P. Yonnet, Structure comparison of buried permanent magnet synchronous motors for flux weakening operation, *Sixth International Conference on Electrical Machines and Drives (Conf. Publ. No. 376)*, pp. 365–370, 1993.
28. D. M. Ionel, M. J. Balchin, J. F. Eastham, et al., Finite element analysis of brushless DC motors for flux weakening operation, *IEEE Transactions on Magnetics*, 32(5 pt 2), 5040–5042, 1996.
29. D. M. Ionel, J. F. Eastham, T. J. E. Miller, et al., Design considerations for permanent magnet synchronous motors for flux weakening applications, *IEE Proceedings: Electric Power Applications*, 145(5), 435–440, 1998.
30. Z. Q. Zhu, Y. S. Chen, and D. Howe, Iron loss in permanent-magnet brushless AC machines under maximum torque per ampere and flux weakening control, *IEEE Transactions on Magnetics*, 38(5), 3285–3287, 2002.
31. A. M. El-Refaie and T. M. Jahns, Comparison of synchronous PM machine types for wide constant-power speed range operation, *Conference Record—IAS Annual Meeting (IEEE Industry Applications Society)*, pp. 1015–1022, 2005.
32. C. H. Chen and M. Y. Cheng, Design of a multispeed winding for a brushless DC motor and its sensorless control, *IEE Proceedings: Electric Power Applications*, 153(6), 834–841, 2006.
33. A. M. El-Refaie and T. M. Jahns, Impact of winding layer number and magnet type on synchronous surface PM machines designed for wide constant-power speed range operation, *IEEE Transactions on Energy Conversion*, 23(1), 53–60, 2008.

6 Design of Current and Speed Controllers

The design of current and speed controllers is usually based on linear control system techniques such as the Bode plot or the root locus or by using standard optimum functions such as the symmetric optimum. The design of the current controller, which usually is a proportional integral (PI) type, can be achieved by considering the self-inductances and the stator resistances of the machine for each phase of the machine. Such an approach has the disadvantage of ignoring the variation of inductance as a function of the rotor position such as in the interior PMSM. While such current controllers are sufficient for many applications, they may be insufficient for high-performance applications. In such cases, a fully model-based current controller is required and such a controller design is derived in this chapter. First, a decoupling current controller in rotor reference frames and then its version in stator reference frames are derived. A deadbeat controller and a predictive form of current controller that give very high and dynamic responses are also derived and presented in this chapter.

Once the current controller is designed, the outer closed loop of speed can be considered. The performance of the speed control loop is highly dependent on the inner current control loop and therefore the highest priority must be placed on the current controller design. The design of the speed controller becomes tedious if the system's nonlinearity is considered. Simplification leads to a linear system and it is used in the synthesis of the speed controller. A symmetric optimum approach is pursued in this section, but any other frequency response or time-domain linear control technique will also facilitate this process.

A small number of references is given on aspects of speed control [1] and current control [2–23], and their controller design. It can be seen from the literature that the development of equivalence between PMSMs, and, for that matter ac machines, in general, and separately excited dc machines in its modeling and control aspects led to the use of similar techniques of current and speed control and their controller designs. In implementation, the dc machine current control is simpler as it is only based on the magnitude whereas ac machines require magnitude, frequency, and phase controls. Note that the decoupling or vector control of ac machines in select reference frames, such as synchronous reference frames for induction motor drives and rotor reference frames for permanent magnet synchronous motor drives, is based on q- and d-axes currents being dc variables. The current control techniques based on such an understanding are predominant in ac drives and permanent magnet synchronous machines; being in the family of ac machines, they share all the techniques of that group.

6.1 CURRENT CONTROLLER

The design of the current controller for PMSM drives becomes crucial in high-performance applications. The design procedure to synthesize and implement current controllers is very similar to the high-performance current controllers in induction motor drives. The current controllers are implemented in stationary or rotor reference frames. The choice of reference frames affects the outcome in terms of the phase error between current references and machine currents. Before moving on to further details, the process of the current control in the PMSM is first examined [5] to gain an understanding of the interaction of the machine, the inverter, and the current controller. Consider the gain of the inverter to be K_r and its time constant to be T_r , which is equal to half of the time period of the PWM carrier frequency. If the desired performance of the current control loop is to resemble a first-order lag system given by

$$\frac{\dot{i}_{ds}^r}{i_{ds}^{r*}} = \frac{K_i}{1 + sT_i} \quad (6.1)$$

where

K_i is the feedback gain of the current sensor

T_i is the desired lag

i_{ds}^r and i_{ds}^{r*} are the d-axis winding currents in rotor reference frames and their references, respectively

Note that the references are indicated by an asterisk in the superscript of the variable i_{ds}^r

Then a similar relationship also holds for the q-axis current and its reference in the rotor reference frames. Equation 6.1 can be put in different forms such as

$$\frac{di_{qs}^r}{dt} = \frac{1}{T_i K_i} \left\{ i_{qs}^{r*} - K_i i_{qs}^r \right\} \quad (6.2)$$

and for the q-axis control,

$$\frac{di_{qs}^r}{dt} = \frac{1}{T_i K_i} \left\{ i_{qs}^{r*} - K_i i_{qs}^r \right\} \quad (6.3)$$

Then the machine equations can be considered by first applying these relationships to the q-axis stator voltage equation:

$$\begin{aligned} v_{qs}^{r*} &= \frac{v_{qs}^r}{K_r} = \frac{(R_s + L_q p) i_{qs}^r + \omega_r (\lambda_{af} + L_d i_{ds}^r)}{K_r} \\ &= \frac{R_s i_{qs}^r + \frac{L_q}{T_i K_i} \left\{ i_{qs}^{r*} - K_i i_{qs}^r \right\} + \omega_r (\lambda_{af} + L_d i_{ds}^r)}{K_r} \end{aligned} \quad (6.4)$$

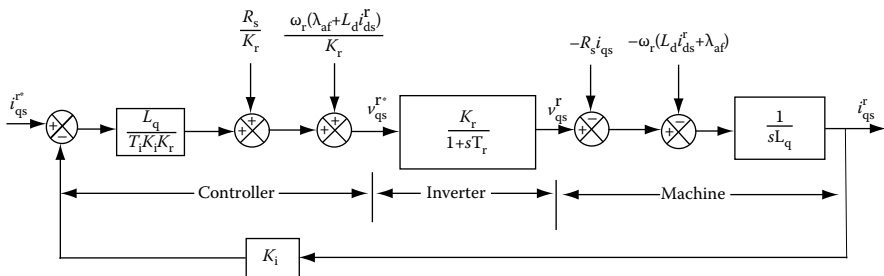


FIGURE 6.1 Block diagram of current control loop in q-axis in rotor reference frames.

The d-axis voltage command expression is similarly derived. The current error, say, in the q-axis stator, multiplied by its amplification factor $L_q/T_i K_r$, is then added with a resistive drop and induced emfs due to d-axis and rotor flux linkages to yield the q-axis voltage command; v_{qs}^{r*} . It is processed through the inverter to obtain the input q-axis stator voltage, v_{qs}^r . Using the machine equation, it is seen that the machine produces the q-axis current, which is then fed back for comparison with its reference as shown in Figure 6.1. The d-axis current control loop black diagram can be similarly derived.

If the compensating terms such as the resistive voltage drop and the induced emfs are equal to their actual values in the machine, then the responses of the current loops will be a first order lag as described in Equations 6.2 and 6.3. Therefore the current controller is a proportional controller with a gain of $L_q/T_i K_r$. In this case, it is assumed that the inverter lag is very small or negligible. Similarly, for the d-axis, the current controller gain is derived as $L_d/T_i K_r$.

On account of parameter sensitivity and instrumentation errors, perfect compensation of resistive voltage drops and induced emf terms are not ideally achieved. The errors due to such phenomena are overcome by the closed loop current control, as their effects are rather secondary.

6.1.1 ROTOR REFERENCE FRAME CURRENT CONTROLLERS

The implementation of the current controllers in rotor reference frames is shown in Figure 6.2. The abc phase currents are transformed to rotor reference frames using the rotor position. The speed signal together with the d- and q-axes stator currents in rotor reference frames are fed to the decoupling current controller along with the current errors. This block has been explained above and shown in Figure 6.1. The output of the decoupling current controller block gives the dq-axes stator voltage references that are then transformed to the abc phase voltage commands using the rotor-to-stationary reference frames matrix. The abc phase voltage commands are pulse-width modulated to obtain control signals for the inverter gates. This completes the implementation of the current controlled PMSM drive.

An important fact to note in this scheme is that the dq current errors are dc and not sinusoidal ac signals. Hence, the processing circuit is not hampered by bandwidth considerations and there is no phase error between the currents and their references

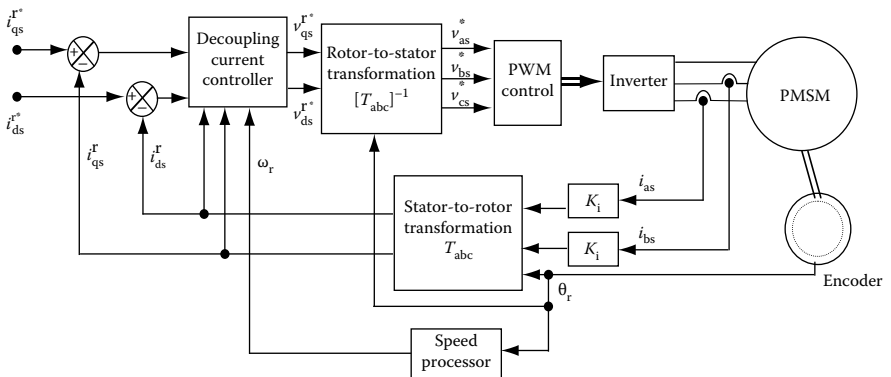


FIGURE 6.2 Current controlled PMSM drive schematic in rotor reference frames.

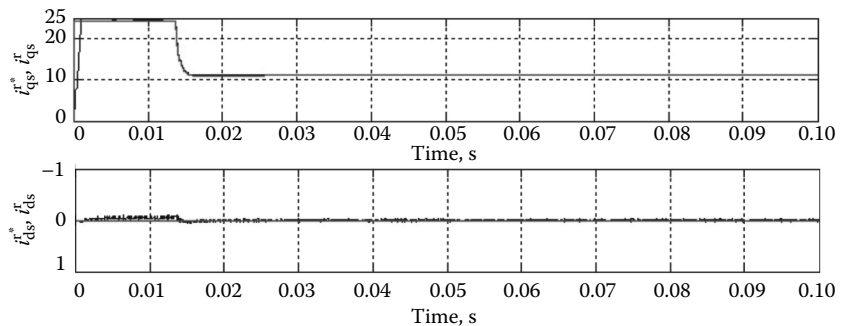


FIGURE 6.3 Current response from the PMSM drive with rotor reference frames synchronous control.

injected in this scheme. Figure 6.3 shows the results of a PMSM drive simulation with rotor reference frames synchronous with current control. The q-axis current has a delay but follows the reference with no error in the steady state. The command d-axis current of zero value is replicated in performance with very negligible deviations initially and then closely later on. Current error is reduced to zero with this control structure, which decouples both d- and q-axes currents.

6.1.2 STATOR REFERENCE FRAMES CURRENT CONTROLLER

There is no analogous rotor reference frames current controller in the stationary reference frames because the inductances are functions of a rotor position in the interior PMSM. A single current controller in the stator reference frames can be synthesized from the qd-axes rotor reference frames currents by transforming them into abc phase currents using the rotor-to-stationary reference frames transformation matrix. The abc phase current references are compared to the respective phase currents and their errors are processed through PI controllers. The output of these

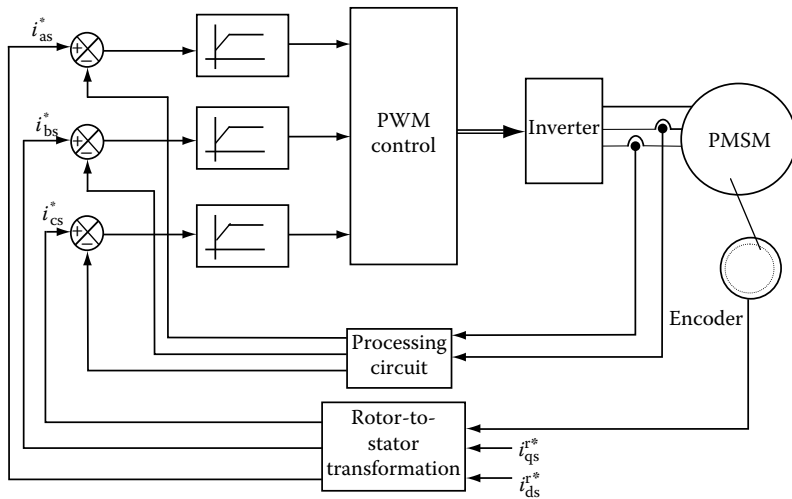


FIGURE 6.4 Current controlled PMSM drive with stator reference frames implementation.

current controllers is pulse-width modulated to produce the inverter logic signals. The block diagram for this scheme is shown in Figure 6.4.

The primary advantage of this scheme is that it requires low part count and it is simple and straightforward to implement. The disadvantage stems from the current errors, which are sinusoidal ac signals whose frequency is proportional to the speed of the motor drive and hence vary over a wide range. It imposes a large bandwidth requirement on the error processing and current controller circuits. Further, it results in phase errors between the currents and their references, primarily due to the delay introduced by the inverter. In the frequency domain, the current reference is given by

$$i_{as}^* = i_{as} (1 + j\omega_r T_r) \quad (6.5)$$

where, ω_r is the electrical rotational frequency of the rotor. For example, the phase errors for the practical stator frequency and the PWM frequency are shown in Table 6.1 where $T_r = 1/2f_c$.

TABLE 6.1
Phase Errors for Various Carrier and Stator Frequencies

f_c (kHz)	Phase Error (Deg)			
	$f_s = 10$ Hz	$f_s = 25$ Hz	$f_s = 50$ Hz	$f_s = 100$ Hz
5	0.359	0.899	1.799	3.595
10	0.179	0.499	0.899	1.799
20	0.0899	0.225	0.449	0.899

Significant phase errors result particularly at low carrier frequencies and high stator frequencies, and have an adverse impact on the torque and speed responses of the drive system. This lag can be compensated for in the dq-axes current references in the rotor reference frames itself before they are transformed to the abc phase current references. This is much easier than compensating for the phase error in stationary reference frames as the circuits are bandwidth limited. In rotor reference frames, the compensation term for phase error is the product of ω_r and T_r , and, is only a dc term. It is derived below.

The compensation on i_{as}^* has to be $(1 + sT_r)$ to advance the phase and hence cancels it in the plant. This is the same for b and c phase references. If i_{as}^* is sinusoidal and is given by

$$i_{as}^* = I_m \sin(\omega_r t + \delta) \quad (6.6)$$

then the compensated a phase current reference is

$$i_{asc}^* = (1 + pT_r) i_{as}^* = I_m \{ \sin(\omega_r t + \delta) + \omega_r T_r \cos(\omega_r t + \delta) \} \quad (6.7)$$

The compensated phase currents for b and c phases are similarly derived. They are phase shifted from a phase by $2\pi/3$ and $4\pi/3$. These compensated phase current references are applied to the transformation to the dq-axes in rotor frames to obtain

$$i_{qsc}^{r*} = i_{qs}^{r*} + \omega_r T_r i_{ds}^{r*} \quad (6.8)$$

$$i_{dsc}^{r*} = i_{ds}^{r*} - \omega_r T_r i_{qs}^{r*} \quad (6.9)$$

where the terms with the product $\omega_r T_r$ are added after multiplying them with the other axis currents. Here, in rotor frames, the compensation is simple and unaffected by the bandwidth considerations. But multiplications are required for implementation and the part count may increase with the present scheme. The implementation for phase error compensation is shown in [Figure 6.5](#). After the compensated current references in the dq-axes are obtained, the implementation uses the schematic shown in [Figure 6.4](#). Note that Figure 6.4 is altered by opening the uncompensated dq current references and placing the phase error compensation circuit therein. Its outputs are taken for transformation to obtain the abc phase current commands, which are now phase error compensated.

All the current controllers discussed hitherto have assumed that compensation for dead time, device voltage drop, and voltage drops associated with parameter variations in stator resistance, rotor flux linkages, and stator inductances have been incorporated. If the compensation is not exact, then the steady-state errors between the stator currents and their references will come into existence. The distortions caused in the stator current by inexact compensation lead to a significant reduction in air gap torque capability and an increase in copper losses [17]. An inner stator flux linkage control loop is used to obtain good current control in the cited reference.

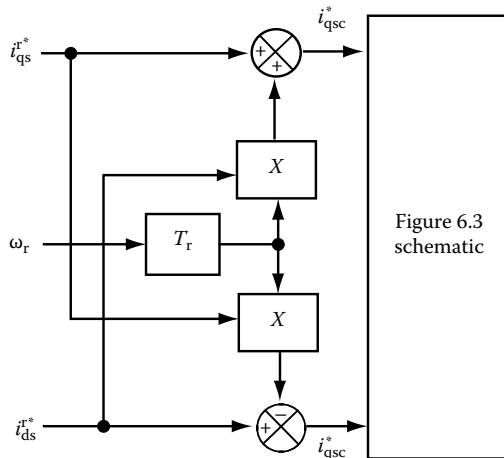


FIGURE 6.5 Phase error compensation for stator reference frames current controller.

6.1.3 DEADBEAT CURRENT CONTROLLERS

6.1.3.1 Deadbeat Controller

Another rotor reference frames controller for high-performance current control is the deadbeat current controller. This current controller minimizes the current error to zero in the smallest number of sampling intervals and as a result achieves high bandwidths. The controller is derived from the discrete model of the PMSM in the rotor reference frames. The current controller from sampled variables, according to [14,16] is

$$v_{qs}^{r*}(k+1) = R_s i_{qs}^r(k) + L_q \frac{[i_{qs}^{r*}(k) - i_{qs}^r(k)]}{T_s} + \omega_r [L_d i_{ds}^r(k) + \lambda_{af}] + e_{hq}(k) \quad (6.10)$$

$$v_{ds}^{r*}(k+1) = R_s i_{ds}^r(k) + L_d \frac{[i_{ds}^{r*}(k) - i_{ds}^r(k)]}{T_s} - \omega_r L_q i_{qs}^r(k) + e_{hd}(k) \quad (6.11)$$

where

k denotes the sample

v_{qs}^{r*} , v_{ds}^{r*} are the d- and q-axes voltage commands for the next sampling instant

T_s is the sampling period

Variables e_{hq} and e_{hd} are the nonfundamental harmonic components of the induced emf

The variables are included because, in spite of the machine design, there will be some residue attributable to manufacturing tolerances and human errors in the manufacture of the machine.

They can be obtained from the harmonic mutual flux linkages in the d- and q-axes as

$$e_{hq}(k) = \omega_r \frac{d\lambda_{afhq}(\theta_r)}{d\theta_r} \quad (6.12)$$

$$e_{hd}(k) = \omega_r \frac{d\lambda_{afhd}(\theta_r)}{d\theta_r} \quad (6.13)$$

If current error is zero, note that

$$v_{qs}^{r^*}(k+1) = v_{qs}^{r^*}(k) \quad (6.14)$$

$$v_{ds}^{r^*}(k+1) = v_{ds}^{r^*}(k) \quad (6.15)$$

A delay of one sampling period results in a persistent oscillation of current response. The deadbeat controller is not robust enough to withstand deviations from the PMSM parameters which leads to the magnification of the persistent oscillation in the current response. In order to reduce the oscillations due to delay, predicting the current at the instant where control is applied, yields better results. A controller based on this principle is known as a predictive current controller.

6.1.3.2 Predictive Deadbeat Controller

The predicted current at the next sampling instant is

$$\hat{i}_{qs}^r(k+1) = i_{qs}^r(k) + \frac{T_s}{L_q} \left[v_{qs}^r(k) - R_s i_{qs}^r(k) - \omega_r L_d i_{ds}^r(k) - \omega_r \lambda_{af} - e_{hq}(k) \right] \quad (6.16)$$

$$\hat{i}_{ds}^r(k+1) = i_{ds}^r(k) + \frac{T_s}{L_d} \left[v_{ds}^r(k) - R_s i_{ds}^r(k) + \omega_r L_q i_{qs}^r(k) - e_{hd}(k) \right] \quad (6.17)$$

where $\hat{\cdot}$ denotes the estimated value, and, $v_{qs}^r(k)$ and $v_{ds}^r(k)$ are the exact inverter output voltages. Equations 6.16 and 6.17 can be substituted for $i_{qs}^r(k)$ and $i_{ds}^r(k)$ in Equations 6.10 and 6.11 respectively, yielding the predictive current controller:

$$v_{qs}^{r^*}(k+1) = R_s \hat{i}_{qs}^r(k+1) + L_q \frac{\left[i_{qs}^{r^*}(k) - \hat{i}_{qs}^r(k+1) \right]}{T_s} + \omega_r L_q \hat{i}_{ds}^r(k+1) + \omega_r \lambda_{af} + e_{hq} (\theta_r + \omega_r T_s) \quad (6.18)$$

$$v_{ds}^*(k+1) = R_s \hat{i}_{ds}^r(k+1) + L_q \left[\frac{\hat{i}_{ds}^r(k) - \hat{i}_{ds}^r(k+1)}{T_s} \right] - \omega_r L_q \hat{i}_{qs}^r(k+1) + e_{hd}(k+1) \quad (6.19)$$

Equations 6.18 and 6.19 give the predictive deadbeat current controller.

Figure 6.6 shows the current response from a PMSM drive simulated with the deadbeat current controller given by Equations 6.18 and 6.19. As expected, there is a delay initially, in the q-axis current response but thereafter, it tracks its command giving a fast transient response. The d-axis current response has deviations but they are very small in comparison to the q-axis command of 60 A initially. However, these deviations are within a few hundred milliamperes and hence, negligible in its effects. Figure 6.7 shows the enlarged but sampled version of Figure 6.6 for the predictive deadbeat controller operation.

Errors in prediction also arise from (1) dead time errors in the inverter and their compensation, (2) imprecise harmonic voltage compensation, (3) imprecise estimation of inverter output voltage due to fluctuations in the ac supply voltage to the rectifier or controlled rectifier and partly to the load disturbances, (4) restricted voltage vector of

$$v_{s(\max)} = \frac{\pi}{2\sqrt{3} \sin \left[\arg(v_s) - (n-1)\frac{\pi}{3} + \frac{\pi}{3} \right]} \quad (6.20)$$

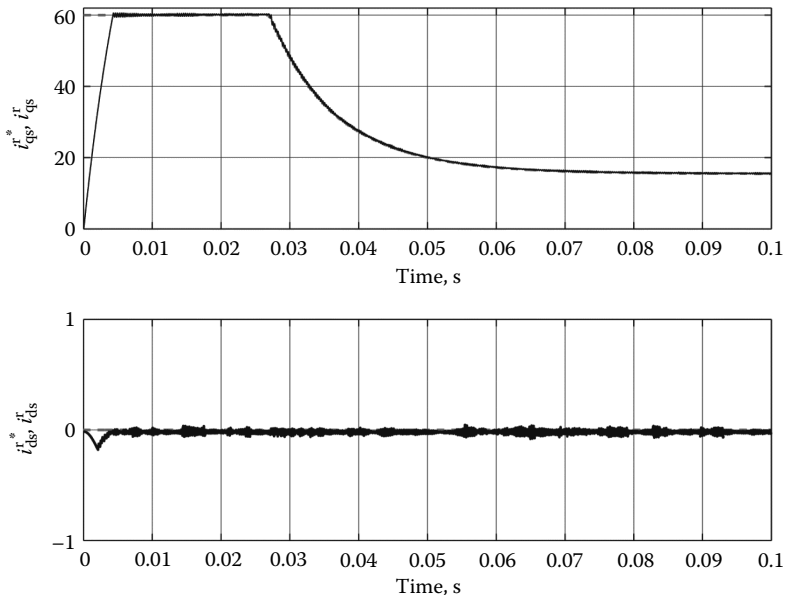


FIGURE 6.6 Current response from simulation with predictive deadbeat controller.

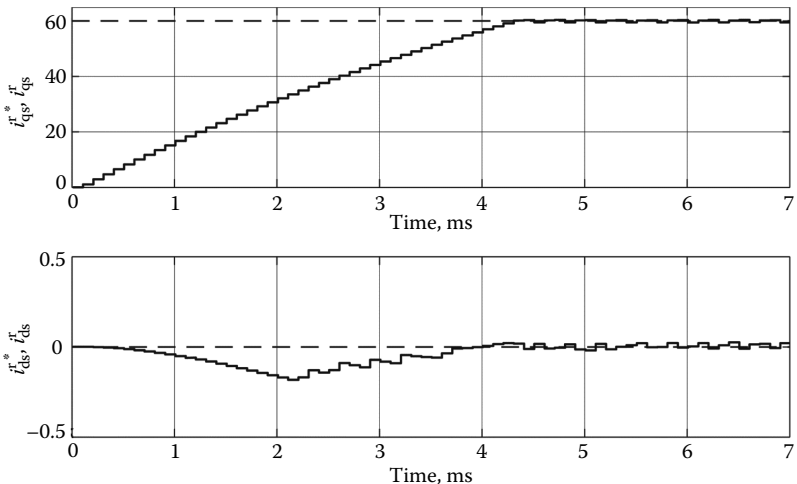


FIGURE 6.7 Zoomed in widow of the sampled current from [Figure 6.6](#).

where $n = 1, 2, \dots, 6$ is the respective edge of the hexagon, and (5) change in the rotor position between the sampling instances which requires the induced emf to be advanced by this angle as given below:

$$e_{hq}(k) = f_q \left\{ \theta_r(k) + \frac{\omega T_s}{2} \right\} \quad (6.21)$$

$$e_{hd}(k) = f_d \left\{ \theta_r(k) + \frac{\omega T_s}{2} \right\} \quad (6.22)$$

$$e_{hq}(k+1) = e_{hq} \left\{ k + \frac{3}{2} \omega T_s \right\} \quad (6.23)$$

6.1.3.3 Improved Predictive Deadbeat Controller

Signal variables are accurate at only sampling intervals and change dynamically between sampling intervals. These changes are high for step commands, resulting in large prediction errors. In this case, average system variables can be used for prediction in a sampling interval that would lead to an improved current predictive controller. This improved current predictor is

$$\hat{i}_{qs}^r(k+1) = i_{qs}^r(k) + \frac{T_s}{L_q} \left[v_{qs}^r(k) - R_s \bar{i}_{qs}^r(k) - \omega_r L_d \bar{i}_{ds}^r(k) - \omega_r \lambda_{af} - \bar{e}_{hq}(k) \right] \quad (6.24)$$

$$\hat{i}_{ds}^r(k+1) = i_{ds}^r(k) + \frac{T_s}{L_d} \left[v_{ds}^r(k) - R_s \bar{i}_{ds}^r(k) + \omega_r L_q \bar{i}_{qs}^r(k) - \bar{e}_{hd}(k) \right] \quad (6.25)$$

where “—” denotes the average system values.

Then the improved predictive deadbeat current controller is given as

$$\begin{aligned} v_{qs}^{r^*}(k+1) = & R_s \hat{i}_{qs}^r(k+1) + L_q \frac{\hat{i}_{qs}^{r^*}(k) - \hat{i}_{qs}^r(k+1)}{T_s} \\ & + \omega_r \left[L_d \hat{i}_{ds}^r(k+1) + \lambda_{af}(k+1.5\omega_r T_s) \right] + e_{hq}(k+1.5\omega_r T_s) \quad (6.26) \end{aligned}$$

$$\begin{aligned} v_{ds}^{r^*}(k+1) = & R_s \hat{i}_{ds}^r(k+1) + L_d \left\{ \frac{\hat{i}_{ds}^{r^*}(k) - \hat{i}_{ds}^r(k+1)}{T_s} \right\} \\ & - \omega_r L_q \hat{i}_{qs}^r(k+1) + e_{hd}(k+1.5\omega_r T_s) \quad (6.27) \end{aligned}$$

where

$$\hat{i}_{qs}^r(k+1) = \frac{\hat{i}_{qs}^r(k+1) + \hat{i}_{qs}^{r^*}(k+1)}{2} \quad (6.28)$$

$$\hat{i}_{ds}^r(k+1) = \frac{\hat{i}_{ds}^r(k+1) + \hat{i}_{ds}^{r^*}(k+1)}{2} \quad (6.29)$$

Wherever it is not possible to predict the future value of a variable, it may be safely assumed to be equal to its command value at the sampling instant under consideration. The controllers developed here have been based on such an assumption.

The number of computations increases in the current controller as it progresses from deadbeat to predictive to improved predictive controllers.

6.2 SPEED CONTROLLER

The design of the speed controller is important from the point of view of imparting desired transient and steady-state characteristics to the speed-controlled PMSM drive system. A proportional plus integral controller is sufficient for many industrial applications and hence, it is considered in this section. Selection of the gain and time constants for such a controller using the symmetric optimum principle is straightforward if, the d-axis stator current is assumed to be zero. In the presence of the d-axis stator current, the d- and q-current channels are cross-coupled and the model is nonlinear due to the torque term.

With the assumption that $\hat{i}_{ds}^r = 0$, the system becomes linear and resembles a separately excited dc motor with constant excitation. From then on, the block diagram derivation, current loop approximation, speed loop approximation, and the derivation speed controller using symmetric optimum becomes identical to that of dc and vector-controlled induction motor drive speed controller design procedures [17a].

6.2.1 DERIVATION OF BLOCK DIAGRAM

The motor q-axis voltage equation with the d-axis current being zero becomes

$$v_{qs}^r = (R_s + L_q p) i_{qs}^r + \omega_r \lambda_{af} \quad (6.30)$$

and the electromechanical equation is

$$\frac{P}{2} (T_e - T_\ell) = J p \omega_r + B_l \omega_r \quad (6.31)$$

where the electromagnetic torque is given by

$$T_e = \frac{3}{2} \cdot \frac{P}{2} \lambda_{af} i_{qs}^r \quad (6.32)$$

and if the load is assumed to be frictional, then,

$$T_\ell = B_\ell \omega_m \quad (6.33)$$

which on substitution gives the electromechanical equation as

$$(Jp + B_l) \omega_r = \left\{ \frac{3}{2} \left(\frac{P}{2} \right)^2 \cdot \lambda_{af} \right\} i_{qs}^r = K_t \cdot i_{qs}^r \quad (6.34)$$

where

$$B_l = \frac{P}{2} B_\ell + B_l \quad (6.35)$$

$$K_t = \frac{3}{2} \left(\frac{P}{2} \right)^2 \cdot \lambda_{af} \quad (6.36)$$

Equations 6.30 and 6.34, when combined into a block diagram with the current and speed feedback loops added, are shown in [Figure 6.8](#).

The inverter is modeled as a gain with a time lag by

$$G_r(s) = \frac{K_r}{1 + s T_r} \quad (6.37)$$

where

$$\left. \begin{aligned} K_r &= 0.65 \frac{V_{dc}}{V_{cm}} \\ T_r &= \frac{1}{2f_c} \end{aligned} \right\} \quad (6.38)$$

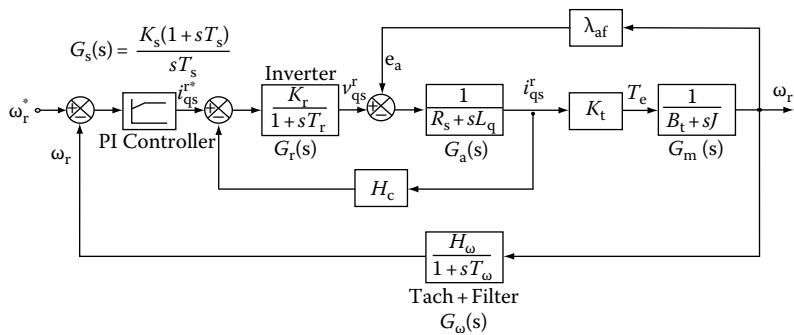


FIGURE 6.8 Block diagram of the speed-controlled PMSM drive. (From Krishnan, R., *Electric Motor Drives*, Figure 9.32, Prentice Hall, Upper Saddle River, NJ, 2001. With permission.)

where

V_{dc} is the dc link voltage input to the inverter

V_{cm} is the maximum control voltage

f_c is the switching (carrier) frequency of the inverter

The induced emf due to rotor flux linkages, e_a , is

$$e_a = \lambda_{af} \omega_r \text{ (V)} \quad (6.39)$$

6.2.2 SIMPLIFIED CURRENT LOOP TRANSFER FUNCTION

The induced emf loop crosses the q-axis current loop and it could be simplified by moving the pick-off point for the induced emf loop from speed to current output point. This gives the current loop transfer function from [Figure 6.9](#) as

$$\frac{i_{qs}^r(s)}{i_{qs}^*(s)} = \frac{K_r K_a (1+sT_m)}{H_c K_a K_r (1+sT_m) + (1+sT_r) \{K_a K_b + (1+sT_a)(1+sT_m)\}} \quad (6.40)$$

where

$$K_a = \frac{1}{R_s}; T_a = \frac{L_q}{R_s}; K_m = \frac{1}{B_t}; T_m = \frac{J}{B_t}; K_b = K_t K_m \lambda_{af} \quad (6.41)$$

The following approximations are valid near the vicinity of crossover frequency:

$$1 + sT_r \approx 1 \quad (6.42)$$

$$1 + sT_m \approx sT_m \quad (6.43)$$

$$(1 + sT_a)(1 + sT_r) \approx 1 + s(T_a + T_r) \approx 1 + sT_{ar} \quad (6.44)$$

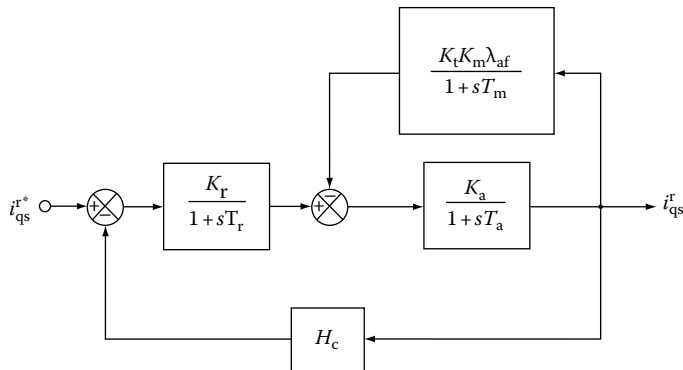


FIGURE 6.9 Current controller. (From Krishnan, R., *Electric Motor Drives*, Figure 9.33, Prentice Hall, Upper Saddle River, NJ, 2001. With permission.)

where

$$T_{ar} = T_a + T_r \quad (6.45)$$

with this the current loop transfer function is approximated as

$$\frac{i_{qs}^r(s)}{i_{qs}^{r*}(s)} \approx \frac{(K_a K_r T_m) s}{K_a K_b + (T_m + K_a K_r T_m H_c) s + (T_m T_{ar}) s^2}$$

$$\approx \left(\frac{T_m K_r}{K_b} \right) \frac{s}{(1 + sT_1)(1 + sT_2)} \quad (6.46)$$

It is found that $T_1 < T_2 < T_m$ and hence, on further approximation that, $(1 + sT_2) \approx sT_2$. The approximate current loop transfer function is then given by

$$\frac{i_{qs}^r(s)}{i_{qs}^{r*}(s)} \approx \frac{K_i}{(1 + sT_i)} \quad (6.47)$$

where

$$K_i = \frac{T_m K_r}{T_2 K_b} \quad (6.48)$$

$$T_i = T_1 \quad (6.49)$$

This simplified current loop transfer function is substituted in the design of the speed controller as follows.

6.2.3 SPEED CONTROLLER

The speed loop with the simplified current loop is shown in Figure 6.10.

Near the vicinity of the crossover frequency, the following approximations are valid:

$$(1+sT_m) \cong sT_m \quad (6.50)$$

$$(1+sT_i)(1+sT_\omega) \cong 1+sT_{\omega i} \quad (6.51)$$

$$1+sT_\omega \cong 1 \quad (6.52)$$

where

$$T_{\omega i} = T_\omega + T_i \quad (6.53)$$

The speed loop transfer function with approximations is given by

$$GH(s) \cong \frac{K_i K_m K_t H_\omega}{T_m} \cdot \frac{K_s}{T_s} \cdot \frac{(1+sT_s)}{s^2(1+sT_{\omega i})} \quad (6.54)$$

from which the closed loop speed transfer function is obtained as

$$\frac{\omega_r(s)}{\omega_r^*(s)} \cong \frac{1}{H_\omega} \left\{ \frac{K_g \frac{K_s}{T_s} (1+sT_s)}{s^3 T_{\omega i} + s^2 + K_g \frac{K_s}{T_s} (1+sT_s)} \right\} \quad (6.55)$$

where

$$K_g = \frac{K_i K_m K_t H_\omega}{T_m} \quad (6.56)$$

Equating this transfer function to a symmetric optimum function with a damping ratio of 0.707 gives the closed loop speed transfer function as

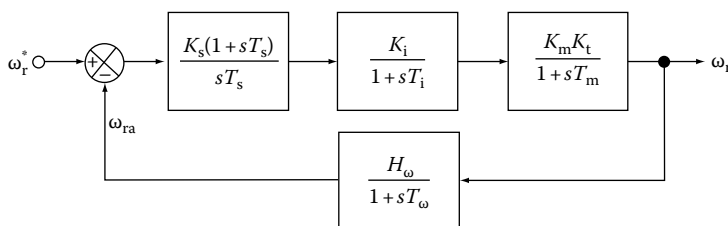


FIGURE 6.10 Simplified speed control loop. (From Krishnan, R., *Electric Motor Drives*, Figure 9.34, Prentice Hall, Upper Saddle River, NJ, 2001. With permission.)

$$\frac{\omega_r(s)}{\omega_r^*(s)} \cong \frac{1}{H_\omega} \cdot \frac{(1+sT_s)}{1+(T_s)s + \left(\frac{3}{8}T_s^2\right)s^2 + \left(\frac{1}{16}T_s^3\right)s^3} \quad (6.57)$$

Equating the coefficients of Equations 6.55 and 6.57 and solving the constants, yields the time and gain constants of the speed controller as

$$T_s = 6T_{\omega i} \quad (6.58)$$

$$K_s = \frac{4}{9K_g T_{\omega i}} \quad (6.59)$$

Hence, the proportional gain, K_{ps} , and integral gain, K_{is} , of the speed controller are derived as

$$K_{ps} = K_s = \frac{4}{9K_g T_{\omega i}} \quad (6.60)$$

$$K_{is} = \frac{K_s}{T_s} = \frac{1}{27K_g T_{\omega i}^2} \quad (6.61)$$

The validity of various approximations is verified through a worked example.

Example 6.1

The PMSM drive system parameters are

$$\begin{aligned} R_s &= 1.4 \Omega, & L_d &= 0.0056 H, & L_q &= 0.009 H, & \lambda_{af} &= 0.1546 \text{ Wb-Turn}, \\ B_t &= 0.01 \text{ N}\cdot\text{m/rad/s}, & J &= 0.006 \text{ kg m}^2, & P &= 6, & f_c &= 2 \text{ kHz}, & V_{cm} &= 10 \text{ V}, \\ H_\omega &= 0.05 \text{ V/V}, & H_c &= 0.8 \text{ V/A}, & V_{dc} &= 285 \text{ V}. \end{aligned}$$

Design a symmetric optimum-based speed controller and verify the validity of assumptions made in its derivation. The damping ratio required is 0.707.

Solution

$$\text{Inverter: Gain, } K_r = 0.65 \frac{V_{dc}}{V_{cm}} = 18.525 \text{ V/V.}$$

$$\text{Time constant, } T_r = \frac{1}{2f_c} = 0.00025 \text{ s}$$

$$G_r(s) = \frac{K_r}{1+sT_r} = \frac{18.525}{(1+0.00025s)}$$

Motor (electrical): Gain, $K_a = 1/R_s = 0.7143$; Time constant, $T_a = L_q/R_s = 0.0064\text{ s}$

$$G_a(s) = \frac{K_a}{1+sT_a} = \frac{0.7143}{(1+0.0064s)}$$

Induced emf loop: Torque constant, $K_t = \frac{3}{2} \left(\frac{P}{2}\right)^2 \cdot \lambda_{af} = 2.087 \text{ N}\cdot\text{m/A}$

Mechanical gain, $K_m = \frac{1}{B_t} = 100 \text{ rad/s/N}\cdot\text{m}$

$$G_b(s) = \frac{K_t K_m \lambda_{af}}{(1+sT_m)} = \frac{32.26}{(1+0.6s)}$$

where the mechanical time constant is

$$T_m = \frac{J}{B_t} = 0.6 \text{ s}$$

Motor (mechanical): $G_m(s) = \frac{K_m K_t}{(1+sT_m)} = \frac{208.7}{(1+0.6s)}$

Equivalent electrical time constants of the motor: Solve the roots of $as^2 + bs + c = 0$.

where

$$a = T_m T_{ar}$$

$$b = T_m + K_a K_r T_m H_c$$

$$c = K_a K_b$$

where

$$K_b = K_t K_m \lambda_{af} = 32.26$$

Then the inverse of the roots will give T_1 and T_2 as

$$T_1 = 0.0005775, \text{ s}$$

$$T_2 = 0.301, \text{ s}$$

Simplified current loop transfer function: $G_{is}(s) = \frac{K_i}{1+sT_i}$

$$T_i = T_l = 0.0005775 \text{ (s)}$$

$$K_i = \frac{T_m K_r}{T_2 K_b} = 1.1443$$

Exact current loop transfer function: $G_i(s) = \frac{G_r(s) \cdot G_a(s) / [1 + G_a(s) \cdot G_b(s)]}{1 + H_c \cdot G_a(s) \cdot G(s) / [1 + G_a(s) \cdot G_b(s)]}$

Speed controller:

$$K_g = K_i K_m K_t \frac{H_\omega}{T_m} = 19.90$$

$$T_{\omega i} = T_\omega + T_i = 0.0025775 \text{ (s)}$$

$$T_s = 6T_{\omega i} = 0.0155 \text{ (s)}$$

$$K_s = \frac{4}{9K_g T_{\omega i}} = 8.6638$$

Simplified speed loop transfer function: $G_{ss}(s) \equiv \frac{1}{H_\omega} \left\{ \frac{K_g \frac{K_s}{T_s} (1+sT_s)}{s^3(T_{\omega i}) + s^2 + K_g \frac{K_s}{T_s} (1+sT_s)} \right\}$

Exact speed loop transfer function: $G_{se}(s) = \frac{G_m(s) \cdot G_i(s) \cdot G_s(s)}{1 + G_\omega(s) \cdot G_m(s) \cdot G_i(s) \cdot G_s(s)}$

where

$$G_s(s) = \frac{K_s}{T_s} \cdot \frac{(1+sT_s)}{s} = (560.2) \frac{(1+0.0155s)}{s}$$

$$G_\omega(s) = \frac{H_\omega}{1+sT_\omega} = \frac{0.05}{(1+0.002s)}$$

6.2.3.1 Smoothing

Smoothing is achieved by canceling the zero, $(1 + sT_s)$, with a pole inserted in the series with the speed reference. Note that it leaves the final speed loop transfer function with only poles. The smoothing can also be thought of as the soft start controller employed in almost all of the drive systems in practice.

All these transfer function gains and phases are plotted in Figures 6.11 through 6.13 [17a]. In the frequency regions of interest, note that the approximations hold good both in magnitude and phase in spite of the reduction of the fifth-order system to an equivalent third-order system in the case of the speed loop and the third- to first-order reduction in the current loop.

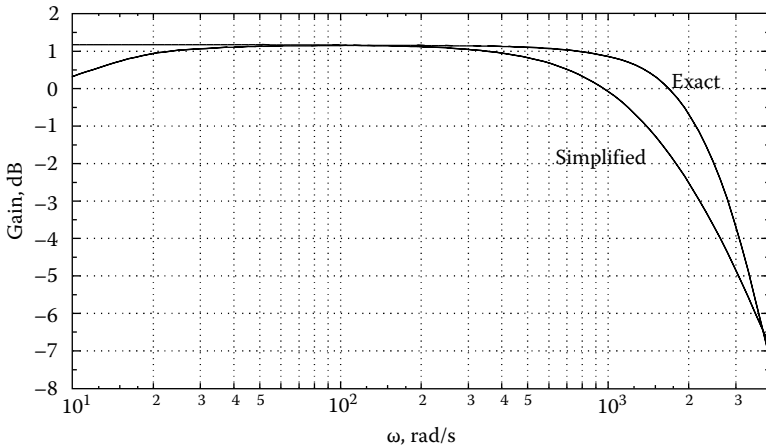


FIGURE 6.11 Exact and simplified current loop gain plots. (From Krishnan, R., *Electric Motor Drives*, Figure 9.35, Prentice Hall, Upper Saddle River, NJ, 2001. With permission.)

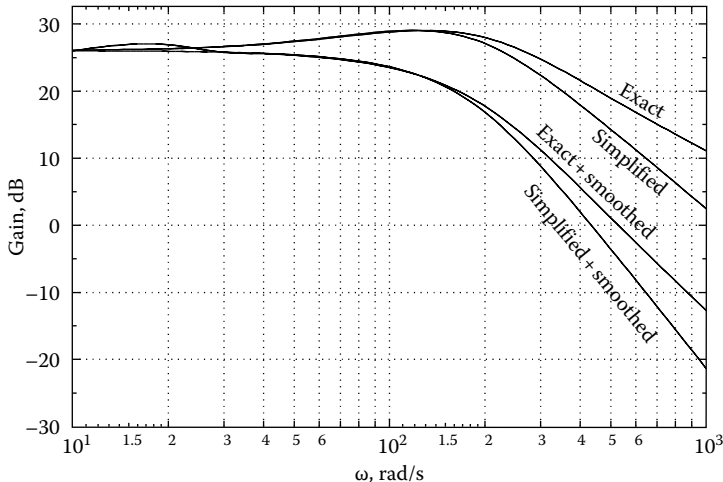


FIGURE 6.12 Gain plots of various speed loop transfer functions. (From Krishnan, R., *Electric Motor Drives*, Figure 9.36, Prentice Hall, Upper Saddle River, NJ, 2001. With permission.)

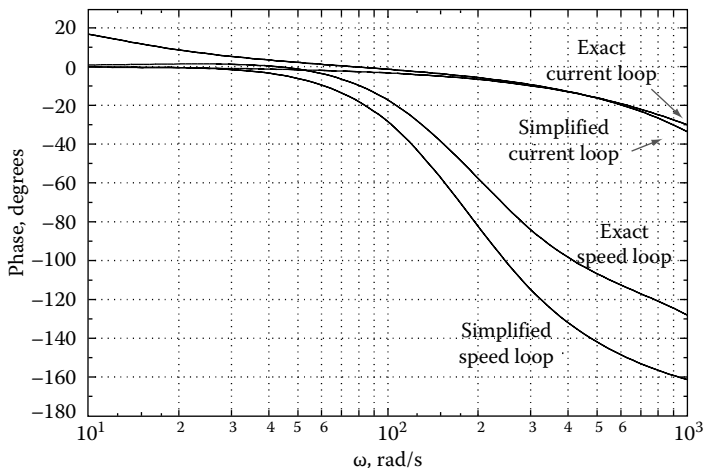


FIGURE 6.13 Phase plots of exact and simplified current and speed loop transfer functions. (From Krishnan, R., *Electric Motor Drives*, Figure 9.37, Prentice Hall, Upper Saddle River, NJ, 2001. With permission.)

REFERENCES

1. P. Pillay and R. Krishnan, Control characteristics and speed controller design for a high performance permanent magnet synchronous motor drive, *Conference Record, 18th Annual IEEE Power Electronics Specialists Conference* (Cat. No. 87CH2459-6), pp. 598–606, 1987.
2. P. Freere and P. Pillay, Design and evaluation of current controllers for PMSM drives, *Conference Record, IEEE Industrial Electronics Society* (Cat. No. 90CH2841-5), pp. 1193–1198, 1990.
3. T. Rekioua, M. Meibody-Tabar, F. M. Sargos et al., Modelling and digital simulation of two current control methods for a permanent magnet synchronous motor supplied by PWM-VSI, *4th European Conference on Power Electronics and Applications*, pp. 457–462, 1991.
4. J. Holtz and E. Bube, Field-oriented asynchronous pulse-width modulation for high-performance AC machine drives operating at low switching frequency, *IEEE Transactions on Industry Applications*, 27(3), 574–581, 1991.
5. K. Thiagarajah, Study on converters and control techniques for high performance permanent magnet synchronous motor drives, PhD thesis, Chapter 5, Indian Institute of Science, Bangalore, 1992.
6. Y. Baudon, D. Jouye, and J.-P. Ferrieux, Current control of permanent magnet synchronous machines. Experimental and simulation study, *IEEE Transactions on Power Electronics*, 7(3), 560–567, 1992.
7. H. Bouzekri, F. Meibody Tabar, B. Davat, et al., Influence of current observers on the performances of a PMSM supplied by hysteresis current controlled VSI, *Fifth European Conference on Power Electronics and Applications* (Conf. Publ. No. 377), pp. 359–362, 1993.
8. C. Attaianese, A. Del Pizzo, A. Perfetto, et al., Predictive VSI current controllers in PM brushless and induction motor drives, *International Conference on Electrical Machines*, pp. 195–198, 1994.

9. J. F. Moynihan, M. G. Egan, and J. M. D. Murphy, Application of state observers in current regulated PM synchronous drives, *Conference Record, IEEE Industrial Electronics Society*, pp. 20–25, 1994.
10. J. Holtz and B. Beyer, Fast current trajectory tracking control based on synchronous optimal pulsewidth modulation, *IEEE Transactions on Industry Applications*, 31(5), 1110–1120, 1995.
11. S. Brock, A novel space vector based current controller for PWM inverter-fed permanent magnet synchronous motor, *International Conference on Electrical Drives and Power Electronics*, pp. 442–447, 1996.
12. J.-W. Choi and S.-K. Sul, Design of fast-response current controller using d-q axis cross coupling: Application to permanent magnet synchronous motor drive, *IEEE Transactions on Industrial Electronics*, 45(3), 522–524, 1998.
13. M. F. Rahman, L. Zhong, and L. Khiang Wee, A direct torque-controlled interior permanent magnet synchronous motor drive incorporating field weakening, *IEEE Transactions on Industry Applications*, 34(6), 1246–1253, 1998.
14. L. Springob and J. Holtz, High-bandwidth current control for torque-ripple compensation in PM synchronous machines, *IEEE Transactions on Industrial Electronics*, 45(5), 713–721, 1998.
15. A. M. Khambadkone and J. Holtz, Fast current control for low harmonic distortion at low switching frequency, *IEEE Transactions on Industrial Electronics*, 45(5), 745–751, 1998.
16. J. O. Krah and J. Holtz, High-performance current regulation and efficient PWM implementation for low-inductance servo motors, *IEEE Transactions on Industry Applications*, 35(5), 1039–1049, 1999.
17. J. A. Haylock, B. C. McCrow, A. G. Jack, and D. J. Atkinson, Enhanced current control of high speed pm machine drives through the use of flux controllers, *IEEE Trans. Ind. Appl.*, 35(5), 1030–1038, Sept./Oct. 1999.
18. R. Krishnan, *Electric Motor Drives*, Prentice Hall, Upper Saddle River, NJ, 2001.
19. F. Briz, M. W. Degner, and R. D. Lorenz, Analysis and design of current regulators using complex vectors, *IEEE Transactions on Industry Applications*, 36(3), 817–825, May/June 2000.
20. H. Takami, Design of an optimal servo-controller for current control in a permanent magnet synchronous motor, *IEE Proceedings: Control Theory and Applications*, 149(6), 564–572, 2002.
21. J. Holtz, Q. Juntao, J. Pontt, et al., Design of fast and robust current regulators for high-power drives based on complex state variables, *IEEE Transactions on Industry Applications*, 40(5), 1388–1397, 2004.
22. A. Moussi, A. Terki, and G. Asher, Hysteresis current control of a permanent magnet brushless DC motor PV pumping system, *International Solar Energy Conference*, pp 523–528, 2005.
23. S. Lerduomsak, S. Doki, and S. Okuma, A novel current control system for PMSM considering effects from inverter in overmodulation range, *International Conference on Power Electronics and Drive Systems (PEDS '07)*, pp. 794–800, 2007.
24. J. Holtz and N. Oikonomou, Estimation of the fundamental current in low-switching-frequency high dynamic medium-voltage drives, *IEEE Transactions on Industry Applications*, 44(5), 1597–1605, 2008.

7 Parameter Sensitivity and Compensation

7.1 INTRODUCTION

Temperature variation changes the stator resistance and flux remanence in the permanent magnets. The sensitivity of residual flux density in magnets for 100°C rise in temperature in ferrite, neodymium, and samarium cobalt magnets are -19%, -12%, and -3%, respectively, from their nominal values. The effect due to the loss of magnetism with temperature variations is predominant compared to the effect of stator resistance variations on the performance of the drive system [1]. Furthermore the stator resistance sensitivity is overcome in current-regulated drives due to the nature of closed loop control. The current control has no impact on the drive system due to temperature sensitivity of the magnets. A closed loop speed-controlled drive system will minimize the effects due to temperature sensitivity of the magnets. To have an understanding of this operation, consider that the drive system is running in steady state and the magnet flux density has decreased in a step fashion, which is not usually the case but taken up here as an extreme case for easier illustration. The torque will decrease instantaneously as the current magnitude command is a constant in steady state. With the decrease in the torque, the rotor will slow down, resulting in higher speed error, higher torque command, and hence higher current command. The torque then will rise and hence the rotor speed and this cycle of events will go on depending on the dynamics of the system until the system reaches steady state again. In the wake of such a disturbance in the magnet flux linkages, the drive system will encounter an electromagnetic torque oscillation as explained and that may not be very desirable in high-performance drives.

Saturation will usually affect the quadrature axis inductance than the direct axis inductance. It is due to the fact that the direct axis with its magnets presents a very high reluctance path as the magnets have a relative permeability comparable to that of air. Whereas in the quadrature axis, the reluctance is lower as most of the flux path is through the iron.

Defining the temperature variation efforts by α and saturation effects by β , relationships between the torque to its reference and mutual flux linkages to its reference are derived with the speed loop open for the PMSM drive [2,3]. It is further assumed that the drive has inner current loops and the actual currents equal their references.

7.1.1 RATIO OF TORQUE TO ITS REFERENCE

It is derived [6] as follows:

$$\frac{T_e}{T_e^*} = \frac{\alpha \lambda_{af}^* i_{qs}^{r*} + (L_d - \beta L_q) i_{ds}^{r*} i_{qs}^{r*}}{\lambda_{af}^* i_{qs}^{r*} + (L_d - L_q) i_{ds}^{r*} i_{qs}^{r*}} = \frac{\alpha \lambda_{af}^* + L_d (1 - \beta \rho) i_{ds}^{r*}}{\lambda_{af}^* + L_d (1 - \rho) i_{ds}^{r*}} \quad (7.1)$$

Note that the ratio of torque to its reference is independent of the q-axis stator current. Dividing the numerator and denominator by the base flux linkages, $L_b I_b$, the torque to its reference is derived as

$$\frac{T_e}{T_e^*} = \frac{\alpha \lambda_{afn} + (1 - \beta \rho) L_{dn} i_{dsn}^r}{\lambda_{afn} + (1 - \rho) L_{dn} i_{dsn}^r} \quad (7.2)$$

where the normalized rotor flux linkages is given as

$$\lambda_{afn} = \frac{\lambda_{af}}{L_b I_b} = \frac{\lambda_{af}}{\lambda_b} \quad (\text{p.u.}) \quad (7.3)$$

Note that

$$i_{dsn}^r = \left(i_{dn}^r \right)^* \quad (7.4)$$

For the same machine details used in all the previous illustrations, the ratio of torque to its reference plotted against α is shown in [Figure 7.1](#) for various values of β ranging from 80% to 100% of the nominal value of L_q . Note that $i_{dn}^r = -1$ p.u., $\rho = 1.607$, $L_{dn} = 0.435$ p.u. α is varied from 0.7 to 1 with lower values of α for increased rotor temperature and the value of 1 corresponding to the operation at ambient temperature with no derating of magnet flux. Increasing temperature reduces the output torque for the same stator current and saturation further decreases it from the nominal value.

Note that when torque angle is set at $\pi/2$, $i_{dsn}^r = 0$, the torque to its reference equals α . Then it becomes independent of saturation. This is contrary to the performance of an indirect vector-controlled induction motor.

For the machine under consideration, [Figure 7.2](#) shows the relationship between reference and actual torque for a variation in the flux linkage λ_{af} . It is clearly seen that a 15% variation in flux linkage causes a 14.2% variation in torque when the control scheme used is the maximum torque per ampere scheme. Because of the large variations in the torque due to variations in rotor flux and its negative impact on the response of the system, it is important to compensate for such sensitivity. It was also found that 15% variations in q- and d-axes inductances caused variations in torque of only 2.21% and 1.38%, respectively, which can be considered negligible.

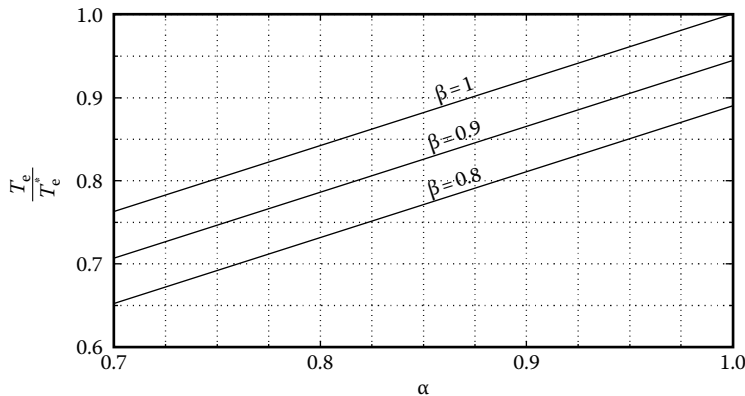


FIGURE 7.1 Ratio of electromagnetic torque to its command for various saturation levels with speed loop open. (From Krishnan, R., *Electric Motor Drives*, Figure 9.41, Prentice Hall, Upper Saddle River, NJ, 2001. With permission.)

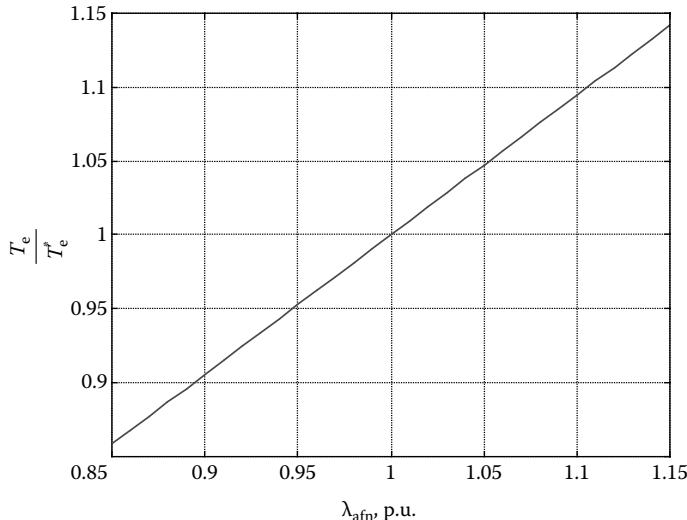


FIGURE 7.2 Variation of electromagnetic torque with variation in flux linkage. (From Krishnan, R., *Electric Motor Drives*, Figure 9.42, Prentice Hall, Upper Saddle River, NJ, 2001. With permission.)

7.1.2 RATIO OF MUTUAL FLUX LINKAGES TO ITS REFERENCE

It is derived [6] as

$$\frac{\lambda_m}{\lambda_m^*} = \frac{\sqrt{(\alpha \lambda_{afn} + L_{dn} i_{dsn}^r)^2 + (\beta L_{qn} i_{qsn}^r)^2}}{\sqrt{(\lambda_{afn} + L_{dn} i_{dsn}^r)^2 + (L_{qn} i_{qsn}^r)^2}} = \frac{\sqrt{(\alpha \lambda_{afn} + L_{dn} i_{dsn}^r)^2 + (\beta \rho L_{dn} i_{qsn}^r)^2}}{\sqrt{(\lambda_{afn} + L_{dn} i_{dsn}^r)^2 + (\rho L_{dn} i_{qsn}^r)^2}} \quad (7.5)$$

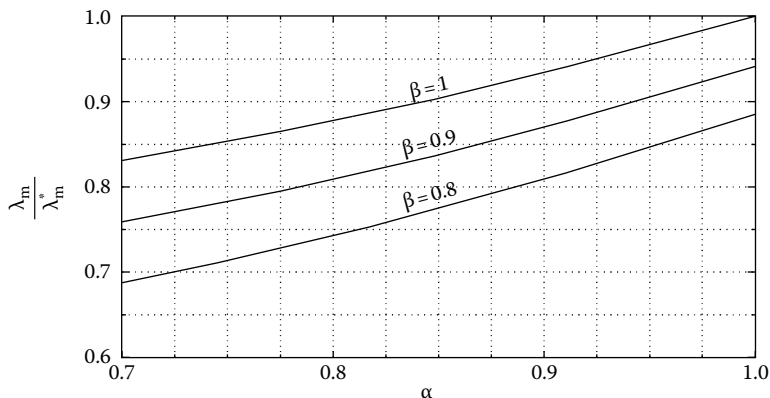


FIGURE 7.3 Ratio of mutual flux linkages to its reference value for various saturation levels with speed loop open.

where ρ is the saliency factor given by the ratio between the quadrature and direct axis inductances. For the same values considered in previous illustration, the ratio of mutual flux linkages to its reference versus α for various β values is shown in Figure 7.3. They follow the trend of the torque to its reference versus α characteristics except that they are not linear anymore.

Temperature and saturation variations produce a nonlinear torque and mutual flux linkages amplifier of the PMSM drive with the consequence that the motor drive is not suitable for precision torque and speed control applications. The changes in the parameter variations could be detected and compensated similar to the methods described in vector-controlled induction motor drives. Two such methods are given in the following sections.

7.2 PARAMETER COMPENSATION THROUGH AIR GAP POWER FEEDBACK CONTROL

Air gap power is a clear indicator of the actual power into the machine and hence in the variations in rotor flux linkages and saturation in the q-axis of the PMSM [6]. Air gap power is computed from the input power of the machine by subtracting the stator resistance losses. If this air gap power is filtered to remove the switching ripple due to stator currents and the transient magnetic energy, then it is a dc signal for a given operating point. This is denoted as

$$P_a = P_i - \frac{3}{2} \left\{ (i_{qs}^r)^2 + (i_{ds}^r)^2 \right\} R_s \quad (7.6)$$

where input power, P_i , is

$$P_i = \frac{3}{2} \left\{ v_{qs}^r i_{qs}^r + v_{ds}^r i_{ds}^r \right\} = v_{as} i_{as} + v_{bs} i_{bs} + v_{cs} i_{cs} \quad (7.7)$$

Note that variations in the machine rotor flux linkages are embodied in the q-axis voltage and saturation effects in the form of L_q variation are contained in the d-axis voltage. Hence air gap power indicates the effects of major parameter variations including that of R_s . The closure of air gap power feedback control requires the determination of reference air gap power.

The reference air gap power is obtained from the reference or actual speed and torque reference in the drive system as

$$P_a^* = \frac{\omega_r T_e^*}{(P/2)} \quad (7.8)$$

The error between the reference and computed/measured air gap power is amplified, and limited to provide a q-axis stator current correction signal to compensate for the parameter variations as shown in Figure 7.4. This signal denoted as Δi_{qs}^* is summed with the calculated q-axis current, $(i_{qsc}^r)^*$, to provide the compensated q-axis current reference, $(i_{qs}^r)^*$ [4].

The working of this feedback loop is explained as follows. Assuming a reduction in the rotor flux linkages from its nominal value, it is deduced that q-axis voltage will be reduced and hence a reduction in the measured/computed air gap power, P_a , sets in. This will result in a positive and a larger Δi_{qs}^r thus increasing the stator q-axis current, resulting in increasing air gap power to equal its reference, P_a^* . Similar reasoning would show that compensation for saturation effects also is achieved with this control strategy.

7.2.1 ALGORITHM

The correction signal is denoted as Δi_{qs}^r and is given by

$$\Delta i_{qs}^{r*} = K_p(P_a^* - P_a) + K_i \int (P_a^* - P_a) \quad (7.9)$$

where K_p and K_i are the proportional and integral gains of the speed controller. When the torque angle is 90° , the q-axis current command in rotor reference frame is obtained as

$$i_{qs}^{r*} = \frac{T_e^*}{\frac{3}{2} \frac{P}{2} \lambda_{af}^*} \quad (7.10)$$

The reference torque component of the current is now given by

$$i_T^* = i_{qs}^{r*} + \Delta i_{qs}^{r*} \quad (7.11)$$

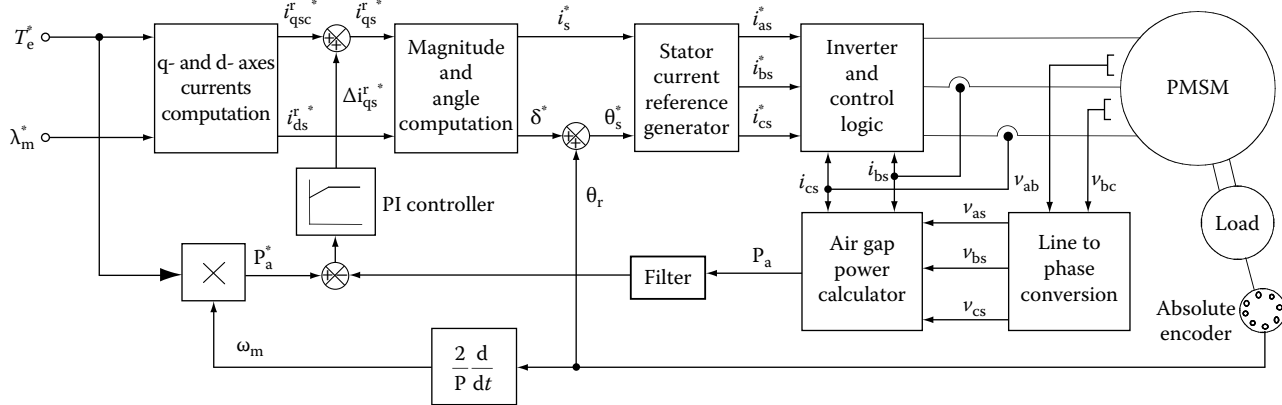


FIGURE 7.4 Parameter compensation of PMSM drive with air gap power feedback control. (From Krishnan, R., *Electric Motor Drives*, Figure 9.43, Prentice Hall, Upper Saddle River, NJ, 2001. With permission.)

from which the magnitude of reference stator current is obtained as follows:

$$i_s^* = \sqrt{i_T^{*2} + i_f^{*2}} \quad (7.12)$$

The flux-producing component of the stator current command, i_f^* , is zero for $\delta = 90^\circ$ but it is nonzero for δ other than 90° . i_f^* is nonzero when flux weakening is resorted to and incorporated later in this section.

The phase angle of the reference stator current is given by

$$\theta_s^* = \delta^* + \theta_r \quad (7.13)$$

where the torque angle is calculated as

$$\delta^* = a \tan\left(\frac{i_T^*}{i_f^*}\right) \quad (7.14)$$

The reference stator phase currents can be generated from i_s^* and θ_s^* using the transformation equations as

$$i_{as}^* = i_s^* \sin(\theta_s^*) \quad (7.15)$$

$$i_{bs}^* = i_s^* \sin\left(\theta_s^* - \frac{2\pi}{3}\right) \quad (7.16)$$

$$i_{cs}^* = i_s^* \sin\left(\theta_s^* + \frac{2\pi}{3}\right) \quad (7.17)$$

The reference currents are fed to the inverter in this particular case using a hysteresis controller, which makes the actual motor currents follow the commanded values at all times. Current feedback is required for the hysteresis controller to achieve this. A description of the hysteresis current controller can be obtained in Chapter 2. The reference phase currents are compared to the actual line currents by the hysteresis controller, which in turn controls the switching of the inverter and hence controls the average phase voltages supplied to the PMSM. To operate above the rated speed, flux weakening is applied. The block labeled as q- and d-axes currents in Figure 7.4 is elaborated in Figure 7.5 using a simple flux-weakening control strategy. In Figure 7.5, the block labeled as FW for flux-weakening unit has the following output:

$$f(\omega_r) = \begin{cases} \frac{\omega_b}{\omega_r}; & \omega_b < \omega_r < \omega_{max} \\ 1; & 0 < \omega_r < \omega_b \end{cases} \quad (7.18)$$

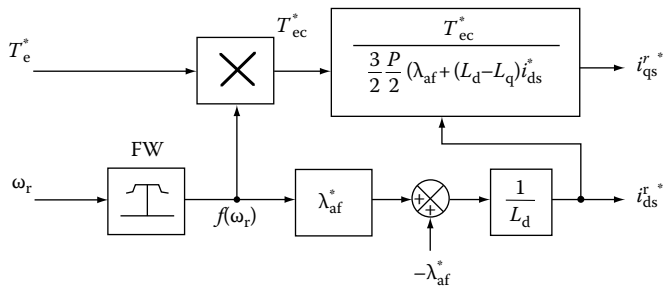


FIGURE 7.5 Schematic of the q- and d-axes command current generator of Figure 7.4. (From Krishnan, R., *Electric Motor Drives*, Figure 9.44, Prentice Hall, Upper Saddle River, NJ, 2001. With permission.)

If the speed is less than the rated speed, the output of block FW is 1 and hence $i_f^* = 0$. If the speed is greater than the rated speed, the flux-weakening component of the stator current is

$$i_f^* = \frac{(f(\omega_r) - 1)\lambda_{af}^*}{L_d} \quad (7.19)$$

Note that $i_f^* < 0$ for flux weakening. The q-axis reference current i_{qs}^{r*} , is obtained as follows:

$$T_{ec}^* = T_e^* \cdot f(\omega_r) \quad (7.20)$$

$$i_{qs}^{r*} = \frac{T_{ec}^*}{\frac{3}{2} \frac{P}{2} [\lambda_{af}^* + (L_d - L_q) i_{ds}^*]} \quad (7.21)$$

This completes the algorithm for the q- and d-axes command current generator blocks shown in Figure 7.4.

7.2.2 PERFORMANCE

Dynamic simulation results of the drive system with parameter compensation shown in Figure 7.4 are presented in this section.

Torque drive performance: Figure 7.6 shows the simulations for a step change of rotor flux linkages in the uncompensated and compensated torque drive systems. The system starts at nominal rotor flux linkages and after $t = 0.02$ s, λ_{af} is changed to 85% of its nominal value and the corresponding effects are studied. It is observed that in the uncompensated system, since $\Delta i_{qs}^{r*} = 0$, i_s^* does not change, thereby reflecting no changes in phase currents due to this step change in rotor flux linkages. Therefore, a decrease in the value of electromagnetic torque from its reference value is seen resulting in a corresponding decrease in the actual air

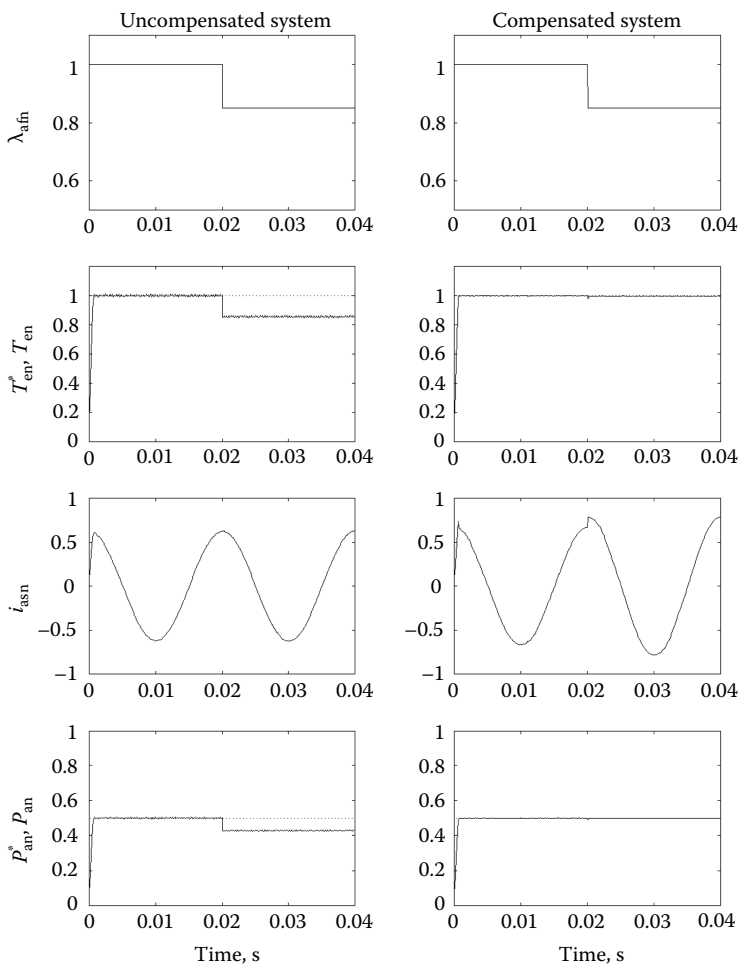


FIGURE 7.6 Simulation results of the constant torque angle-controlled torque drive system with and without parameter compensation when a step change in the rotor flux linkages is applied. (From Krishnan, R., *Electric Motor Drives*, Figure 9.45, Prentice Hall, Upper Saddle River, NJ, 2001. With permission.)

gap power. In the compensated system, it is noticed that torque rises to match its reference after initially dropping to a lower value. A corresponding rise in the value of i_{as} , the phase a current is seen. In this torque drive system, the rotor speed is maintained at 0.5 p.u., which is the rated speed for the machine under consideration.

Speed-controlled drive performance: The second set of simulations is for a speed-controlled drive system with a step change in its speed from 0 to 0.5 p.u. applied initially and then a step change of load torque T_l from 0 to 1.65 p.u. is applied when the speed equals its command. Finally λ_{af} is changed from nominal to 0.85 times the nominal value. The results for both the uncompensated and compensated

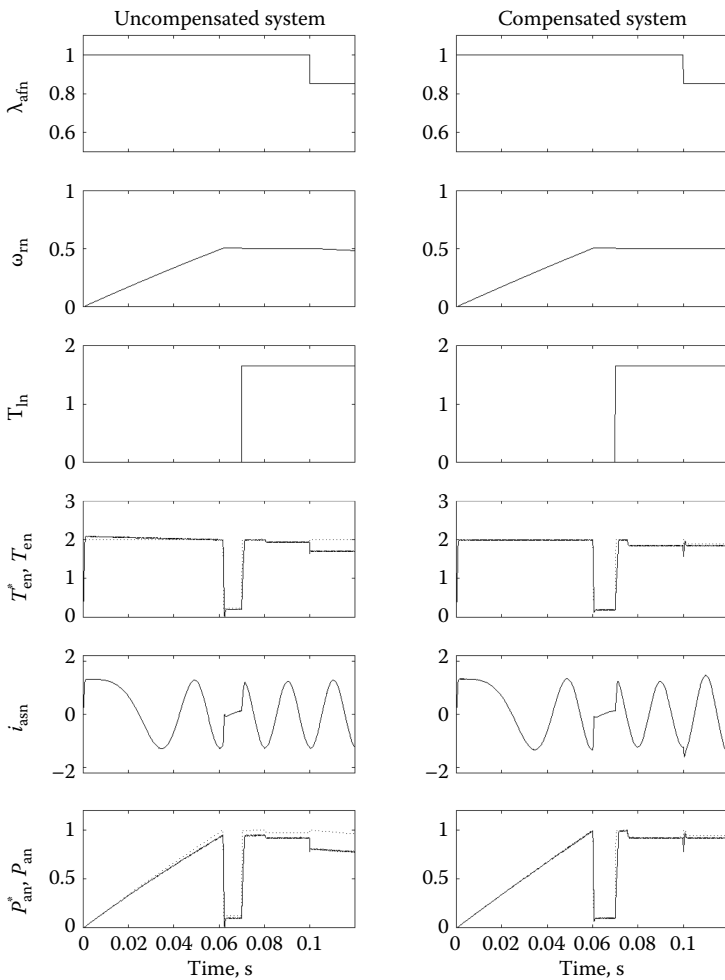


FIGURE 7.7 Simulation results of the speed-controlled drive system with constant torque angle for a step change in λ_{afn} . (From Krishnan, R., *Electric Motor Drives*, Figure 9.46, Prentice Hall, Upper Saddle River, NJ, 2001. With permission.)

speed controlled drive systems are shown in Figure 7.7. The reference torque T_e^* is limited to 2 p.u. In the uncompensated system, the change in rotor flux linkages causes a reduction in torque and hence in the speed momentarily. This increases the torque reference through the action of the outer speed feedback loop, resulting in an increase in the air gap power reference as shown by dotted lines. The q-axis stator current increases to meet the load torque, resulting in the speed being maintained equal to its reference in steady state. In the compensated system, the torque reference and air gap power reference do not change but the stator q-axis current is increased until it delivers the torque equal to its reference. The resulting compensation has the advantage that it does not change torque reference and hence will not lead to a speed drop as in the uncompensated system. For example, consider

the torque reference is altered by the speed feedback loop in the uncompensated system from 2 to 2.5 p.u. and the torque limiter has a maximum of only 2 p.u. This means that the stator q-axis current will be generated only for 2 p.u. torque reference, producing less than 2 p.u. torque for a reduction in rotor flux linkages. If load torque is 2 p.u., then the speed will have to be reduced, whereas this is not the case in compensated system is obvious.

Flux-weakening drive performance: The third set of simulations are for the speed-controlled drive system operating in the flux-weakening region. The condition for the simulation is to have a step change of λ_{af} from nominal to 0.85 times the nominal value with the drive system operating in the flux-weakening mode. The simulation results are shown in Figure 7.8. The flux-weakening process is

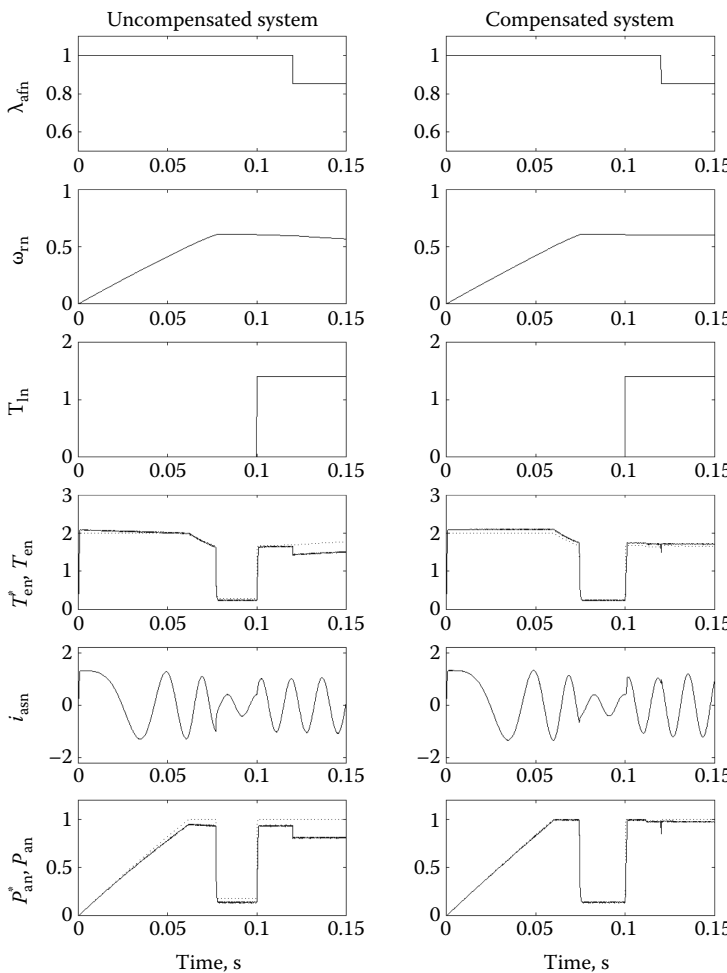


FIGURE 7.8 Simulation results of a speed-controlled drive system operating in the flux-weakening mode with a step change in λ_{af} . (From Krishnan, R., *Electric Motor Drives*, Figure 9.47, Prentice Hall, Upper Saddle River, NJ, 2001. With permission.)

initiated in this drive when the speed is greater than 0.5 p.u., where the reference torque T_e^* and hence the actual torque start falling as expected till the commanded speed is reached. When a step change is applied to λ_{af} , a rise in reference torque is observed but the actual torque does not rise to match the reference torque due to a drop in rotor flux linkages. The compensated system, however, shows a perfect matching of the torque and its reference due to almost instantaneous compensation.

Effect of quadrature axis inductance variation: The final set of simulations show the step change of L_q from nominal to 0.85 times the nominal value in Figure 7.9 including the operation in the flux-weakening mode. The variation of L_q would

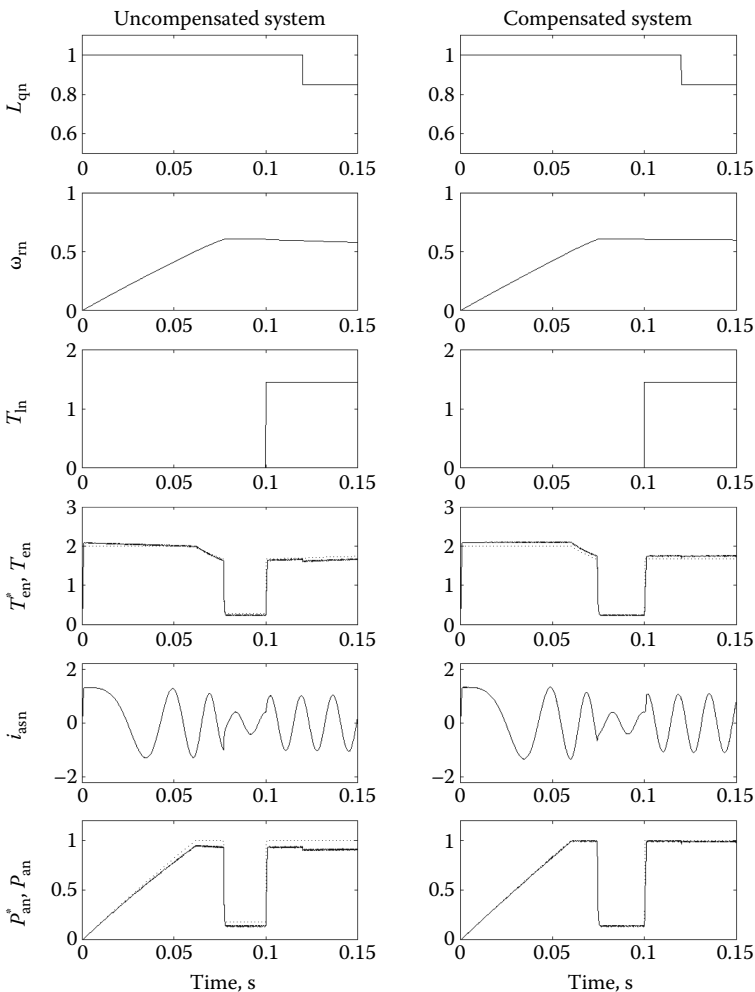


FIGURE 7.9 Simulation results of the effect of variation of L_q on the speed-controlled drive system including the operation in the flux-weakening mode. (From Krishnan, R., *Electric Motor Drives*, Figure 9.48, Prentice Hall, Upper Saddle River, NJ, 2001. With permission.)

not have any effect on a constant torque angle-controlled system where $\delta = 90^\circ$, because the controller parameters and the output torque is not dependent on the quadrature axis inductance. But it does affect a system in the flux-weakening mode as both the controller parameters and torque output are dependent on the quadrature axis inductance. The compensated system however corrects for changes in L_q as shown in [Figure 7.8](#). The effects are similar to the case where λ_{af} changes.

Effect of stator resistance variation: Since the air gap power calculator is dependent on the stator resistance, which changes with temperature, simulations for a step change of stator resistance are necessary to verify the adequacy of the air gap power compensation scheme to neutralize the variations in stator resistance. The effects were seen to be negligible on the compensated system. The stator resistance variations can also be compensated by direct temperature measurement. The quadrature axis inductance variations can be compensated by monitoring the q-axis current magnitude. No direct monitoring of the rotor magnets or its temperature is possible to compensate for rotor flux linkages variation. Hence schemes such as the air gap power feedback control are necessary to overcome the parameter sensitivity of the rotor flux linkages variation and the same then could be used to compensate for other motor parameter variations.

7.3 PARAMETER COMPENSATION BY REACTIVE POWER FEEDBACK CONTROL

A parameter compensation scheme using reactive power feedback control is examined in this section. Reactive power can be calculated in PMSM drives since it reflects change in the rotor flux linkage accurately while not having the detrimental effect of instrumenting the value of stator resistance in the controller. Then this reactive power can be used to compensate for the variation in torque induced by changes in the rotor flux linkages [5]. The advantage of the reactive power feedback is that it is not dependent on the stator resistance like the air gap power feedback control scheme but has the disadvantage of requiring a field component of current for its control. Except for the constant torque angle method, where flux component of stator current is zero, note that all other control methods require the flux component of the stator current. Invariably, for high-performance PMSM controllers requiring operation at unity power factor or maximum efficiency or constant air gap flux or maximum torque per unit current, maximum torque per unit loss produces the field component part of the stator current to enforce the stated performance indices. Therefore the requirement of the field component of current in the course of operation of the drive does not preclude the use of the reactive power feedback control scheme. The reactive power-based compensation scheme is incorporated in the dynamic model of the PMSM drive and verified for step and ramp changes in the rotor flux of a torque-controlled PMSM drive. Simulation results demonstrate the viability of this method of parameter compensation. The contrast between this scheme and the method based on air gap power feedback control is also included.

7.3.1 PRINCIPLE OF THE REACTIVE POWER FEEDBACK COMPENSATION SCHEME

Assuming that the currents follow their references with zero time lag and no amplitude error and L_d and L_q are constants, the reference reactive power Q^* in steady state is derived as

$$\begin{aligned} Q^* &= v_{ds}^r * i_{qs}^r - v_{qs}^r * i_{ds}^r \\ &= -\omega_r (L_d (i_{ds}^r)^2 + L_q (i_{qs}^r)^2) - \omega_r \lambda_{af}^* i_{ds}^r \end{aligned} \quad (7.22)$$

It should be noted that the steady-state value of the reference reactive power is considered here instead of the dynamic value since it is difficult to instrument the time derivative of currents. The calculated reactive power, Q , is filtered by passing it through a first-order filter to obtain the filtered value of the reactive power, Q_f . Assuming that L_q and L_d do not change, the change in reactive power in steady state is obtained as

$$\begin{aligned} \Delta Q = Q^* - Q_f &= -\omega_r (L_d (i_{ds}^r)^2 + L_q (i_{qs}^r)^2) - \omega_r \lambda_{af}^* i_{ds}^r \\ &\quad - (-\omega_r (L_d i_{ds}^r)^2 + L_q i_{qs}^r)^2 - \omega_r \lambda_{af} i_{ds}^r) \\ &= -\omega_r i_{ds}^r (\lambda_{af}^* - \lambda_{af}) = -\omega_r i_{ds}^r \Delta \lambda_{af} \end{aligned} \quad (7.23)$$

The change in flux linkage in steady state is then obtained as

$$\Delta \lambda_{af} = -\frac{\Delta Q}{\omega_r i_{ds}^r} = -\frac{\Delta Q}{\omega_r i_s^* \cos(\delta^*)} \quad (7.24)$$

The compensating feedback ΔC is computed from Equation 7.24 as

$$\Delta C = \frac{\lambda_{af}^*}{\lambda_{af}^* - \Delta \lambda_{af}} \quad (7.25)$$

The compensated torque is given by

$$T_{ec}^* = T_e^* \Delta C \quad (7.26)$$

While the illustration of the procedure is given in terms of steady-state performance, the dynamic reactive power is used in the control scheme. Since the steady-state reference reactive power and the instantaneous reactive power are compared to obtain the compensating feedback, there is a small error in the ΔC due to transients. It can be proven that it is negligible.

7.3.2 DRIVE SCHEMATIC

The schematic of the drive system is shown in Figure 7.10. The machine, position sensor, reactive power feedback, reactive power controller, and inverter constitute the PMSM drive system. All the reference values are denoted with an asterisk in the

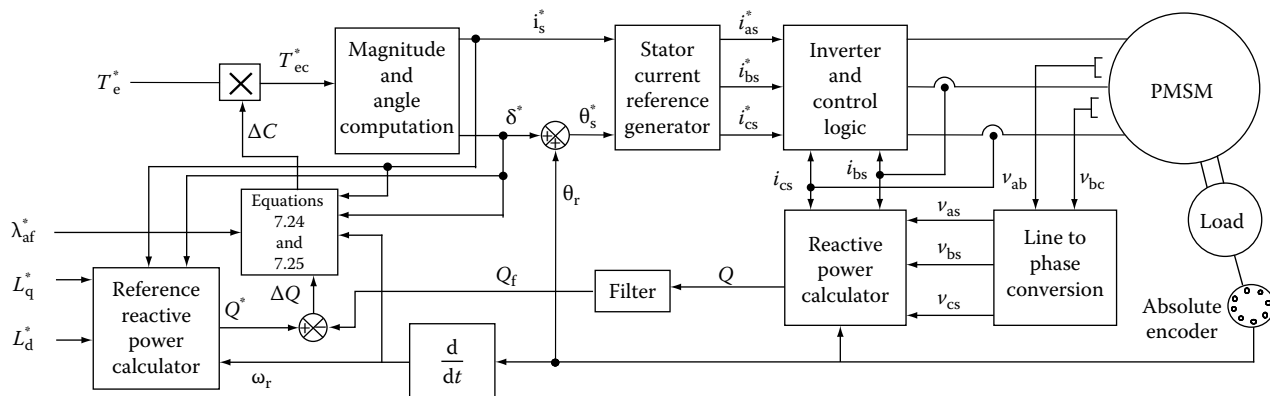


FIGURE 7.10 Schematic of the proposed parameter compensated PMSM drive system. (From Krishnan, R. and Vijayraghavan, P., *Proc. IEEE Int. Symp. Indus. Electron.*, 2, 661, 1999. With permission.)

diagram. In the maximum torque per unit current strategy, the reference torque T_e^* is multiplied with the compensating feedback and the product T_{ec}^* generates the stator current reference i_{sn}^* and the torque angle δ^* by means of a table. All other control blocks are the same as for any other PMSM drive and described in the Section 7.3.

7.3.3 SIMULATION RESULTS

A dynamic simulation is developed for the system delivering rated torque for step and ramp changes in the rotor flux linkage λ_{af} . A comparison is also made with the air gap power feedback scheme in terms of the effect of varying stator resistance. Reference variables are indicated by dotted lines and all simulations are conducted at rated speed.

Figure 7.11 shows the simulation for a step change in rotor flux linkages of an uncompensated and Figure 7.12 shows the results for a compensated torque drive

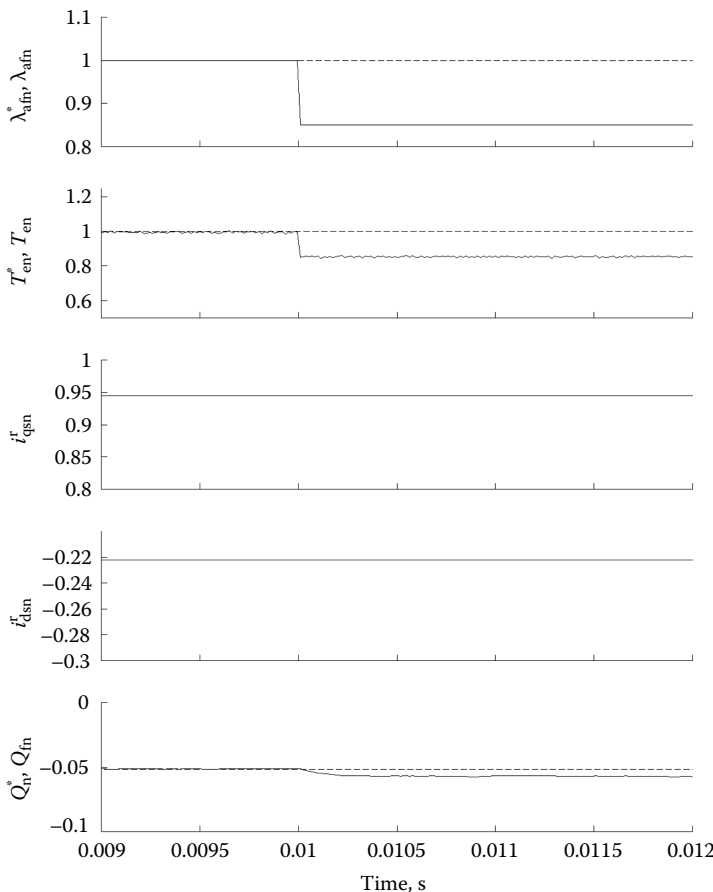


FIGURE 7.11 Normalized responses (in p.u.) for a step change in flux linkage without compensation. (From Krishnan, R. and Vijayraghavan, P., *Proc. IEEE Int. Symp. Indus. Electron.*, 2, 661, 1999. With permission.)

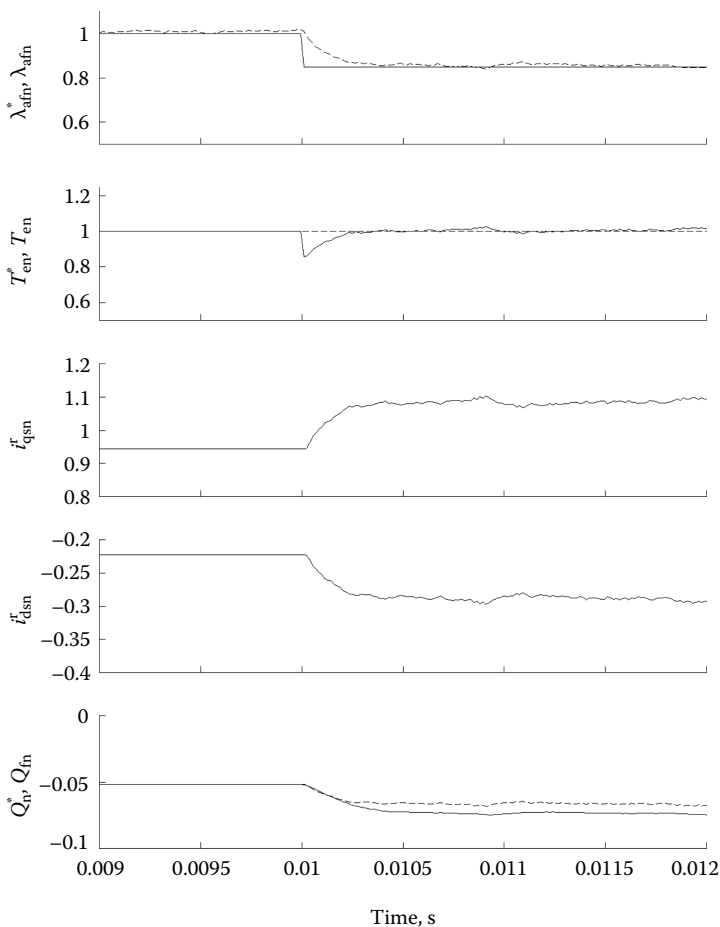


FIGURE 7.12 Normalized responses (in p.u.) for a step change in flux linkage with compensation. (From Krishnan, R. and Vijayraghavan, P., *Proc. IEEE Int. Symp. Indus. Electron.*, 2, 661, 1999. With permission.)

system. The system runs at a nominal value of λ_{af} for 0.01 s and is changed to 85% of its nominal value after 0.01 s. The uncompensated system shows that the reference or estimated value of rotor flux linkage does not change and hence there is a 15% reduction in developed torque when the rotor flux linkage is changed. The compensated system shows that when the rotor flux linkage is changed, the estimated or reference rotor flux linkage also changes to track the actual value. This causes an increase in T_{ec}^* , resulting in a change in i_{qs}^* and i_{ds}^* , thus increasing the stator current references. It results in an increase in actual stator currents in the machine and hence an increase in the torque developed in the machine. It is observed that the reference and actual reactive powers do not match exactly. This is due to the fact that the compensation is aimed at air gap torque but not on the reactive power itself in the machine with the specific control strategy chosen in the illustration and also the controller has no integral part.

Figures 7.13 and 7.14 show a more realistic ramp change in rotor flux linkages of an uncompensated and compensated torque drive system. The system runs at a nominal value of λ_{af} for 0.01 s and is changed linearly to 85% of its nominal value after 0.01 s. The uncompensated system shows a linear reduction in developed torque when the rotor flux linkage is changed. The compensated system shows that when the rotor flux linkages change, the estimated or reference rotor flux linkage also changes to match the electromagnetic torque to its reference.

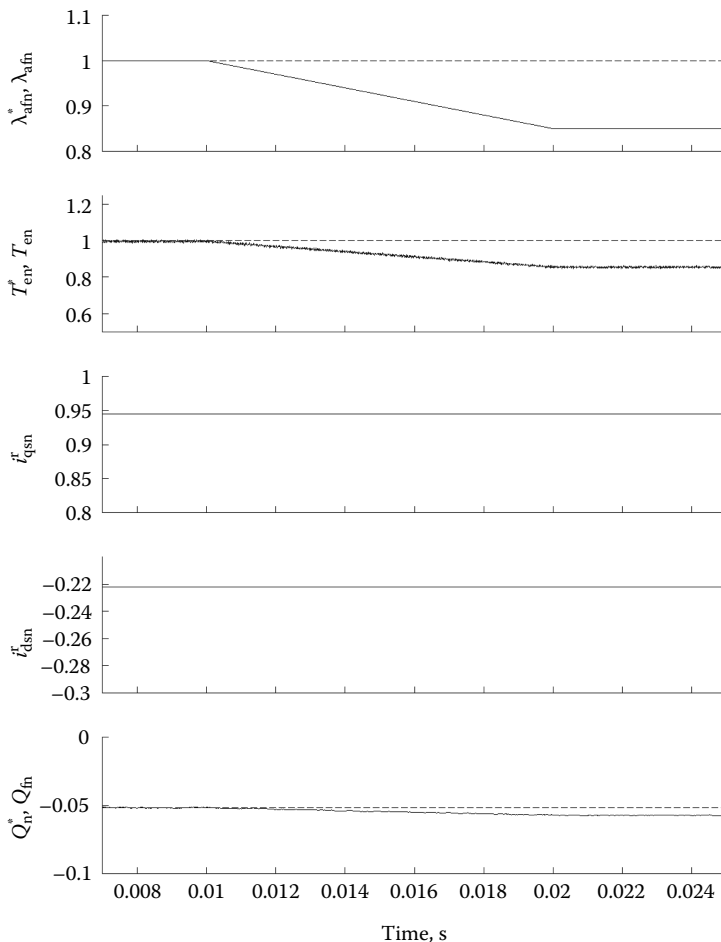


FIGURE 7.13 Normalized responses (in p.u.) for a ramp change in flux linkage without compensation. (From Krishnan, R. and Vijayraghavan, P., *Proc. IEEE Int. Symp. Indus. Electron.*, 2, 661, 1999. With permission.)

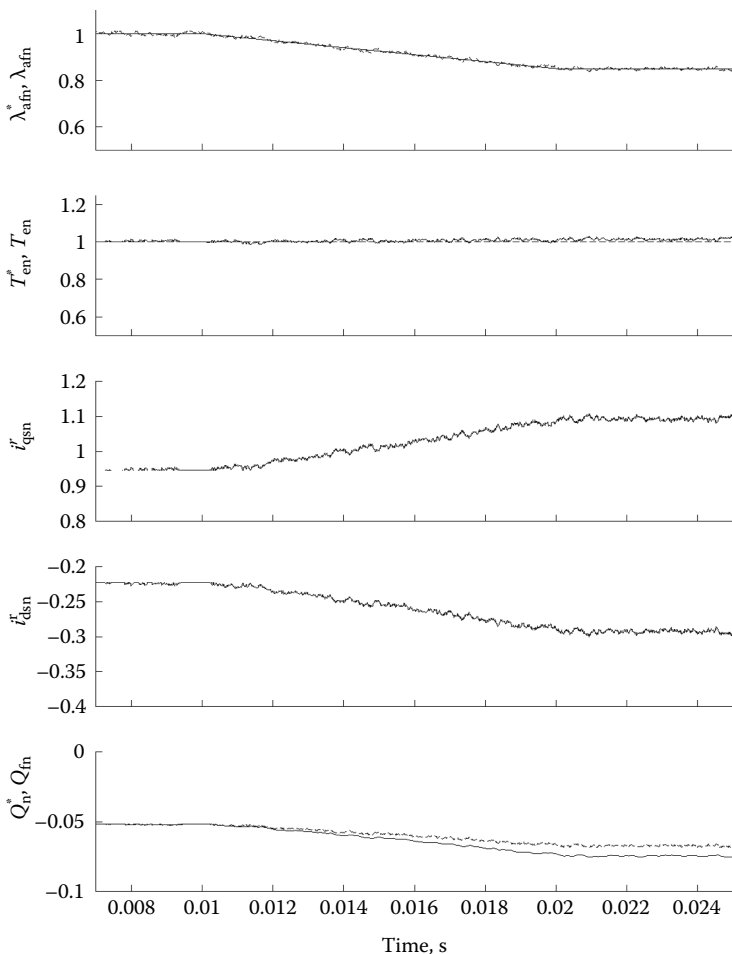


FIGURE 7.14 Normalized responses (in p.u.) for a ramp change in flux linkage with compensation. (From Krishnan, R. and Vijayraghavan, P., *Proc. IEEE Int. Symp. Indus. Electron.*, 2, 661, 1999. With permission.)

7.3.4 COMPARISON WITH AIR GAP POWER FEEDBACK SCHEME

Figure 7.15 shows the effect of varying the stator resistance on the compensated system. It is observed that there is no change in reference and developed torque. The compensation scheme is independent of the stator resistance and hence changing stator resistance does not affect the scheme. This is not so in the air gap power feedback scheme, which is dependent on the value of stator resistance and variation of stator resistance causes variations in developed torque. Figure 7.16

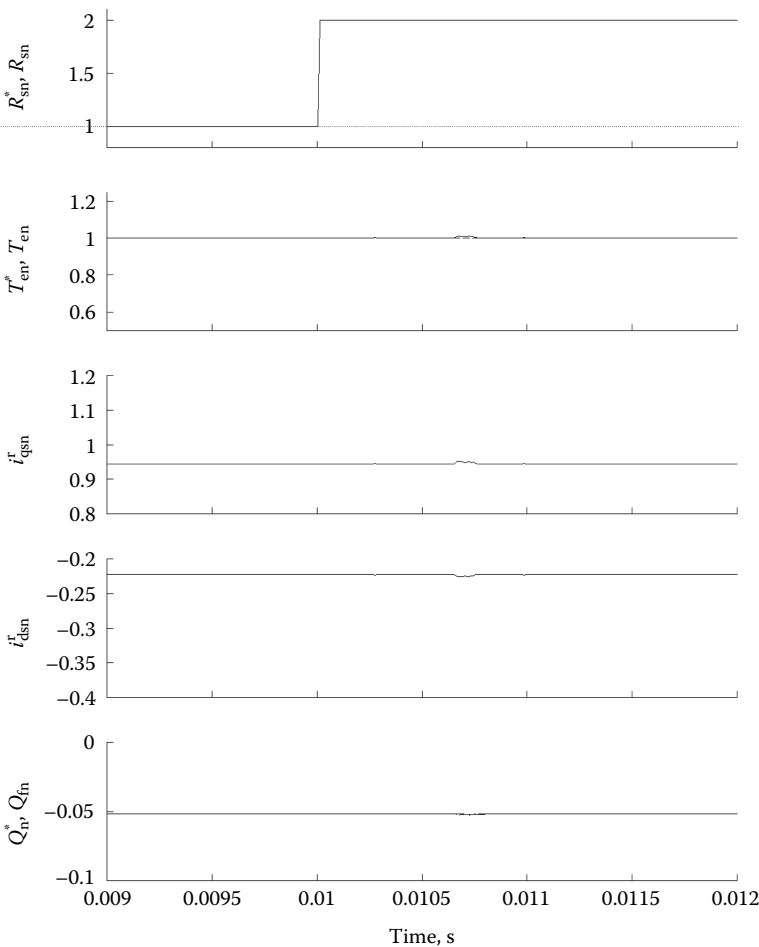


FIGURE 7.15 Normalized responses (in p.u.) for a step change in stator resistance with compensation. (From Krishnan, R. and Vijayraghavan, P., *Proc. IEEE Int. Symp. Indus. Electron.*, 2, 661, 1999. With permission.)

shows the effect of varying the stator resistance on the air gap power feedback compensated system. It is observed that when the stator resistance is changed and is different from the reference value, the compensation scheme does not work, thereby showing a drop in the developed torque. The compensation scheme is dependent on the stator resistance and hence changing stator resistance affects the scheme.

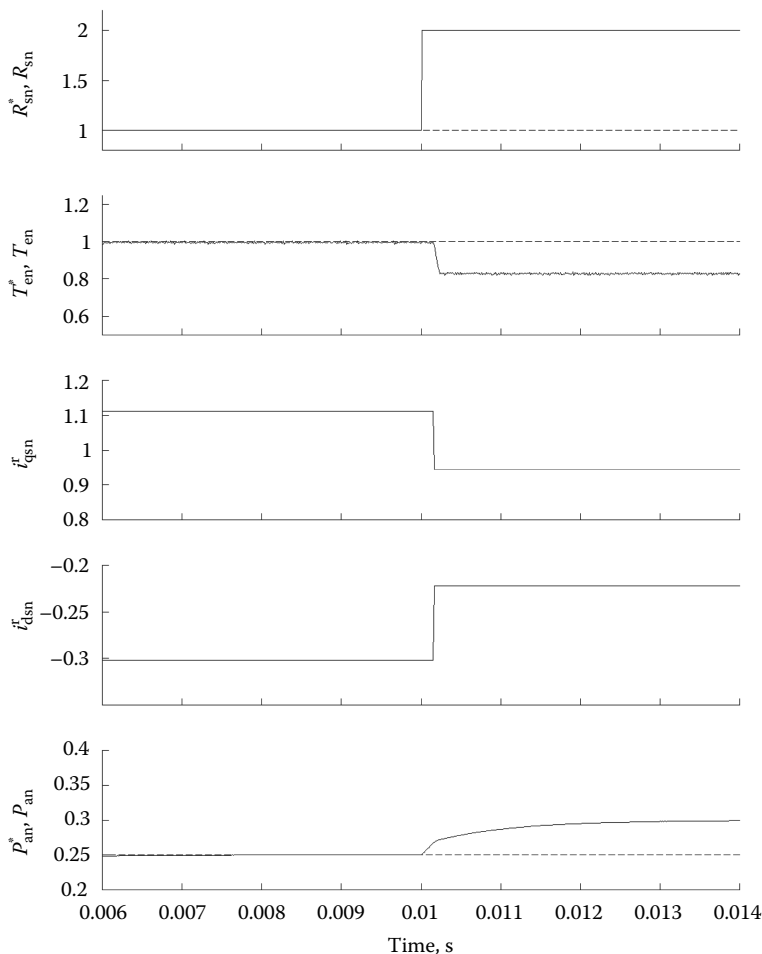


FIGURE 7.16 Normalized responses (in p.u.) for a step change in stator resistance with air gap power feedback compensation. (From Krishnan, R. and Vijayraghavan, P., *Proc. IEEE Int. Symp. Indus. Electron.*, 2, 661, 1999. With permission.)

REFERENCES

1. R. Krishnan, Selection criteria for servo motor drives, *IEEE Transactions on Industry Applications*, IA-23(2), 270–275, 1987.
2. R. Krishnan and P. Pillay, Parameter sensitivity in vector controlled AC motor drives, *Conference Record, IEEE International Conference on Industrial Electronics, Control, and Instrumentation (Cat. No. CH2484-4)*, pp. 212–218, 1987.
3. R. Krishnan and A. S. Bharadwaj, A review of parameter sensitivity and adaptation in indirect vector controlled induction motor drive systems, *IEEE Transactions on Power Electronics*, 6(4), 695–703, 1991.

4. R. Krishnan and P. Vijayraghavan, Parameter compensation of permanent magnet synchronous machines through airgap power feedback, *Conference Record, IEEE International Conference on Industrial Electronics, Control, and Instrumentation (Cat. No. 95CH35868)*, pp. 411–416, 1995.
5. R. Krishnan and P. Vijayraghavan, Fast estimation and compensation of rotor flux linkage in permanent magnet synchronous machines, *Proceedings of the IEEE International Symposium on Industrial Electronics (Cat. No. 99TH8465)*, pp. 661–666, 1999.
6. R. Krishnan, *Electric Motor Drives*, Prentice Hall, Upper Saddle River, NJ, 2001.

8 Rotor Position Estimation and Position Sensorless Control

The PMSM drive requires two current sensors and a rotor position sensor for the implementation of any control strategy discussed in Chapter 4. The rotor position is sensed with an optical encoder or a resolver for high-performance applications. The position sensors cost as much as a low-power motor, thus making the total system cost very noncompetitive compared to other types of motor drives. As for the current sensors, they are not as expensive as the rotor position sensor and note that other types of drives also require their use in feedback control. Hence, the control and operation of PMSM drive without a rotor position sensor would enhance its applicability to many other cost-sensitive applications and to provide a backup control in sensor-based drives during sensor failures. Four methods of rotor position sensorless control strategy are discussed in this chapter. They are (1) current model adaptive scheme where only currents and their differences with previous values are utilized to estimate the rotor position, (2) sensing by external signal injection and under this category are schemes using revolving voltage signal injection, flux linkage injection in rotating q-axis, and alternating voltage phasor injection, (3) current model-based injection scheme, and (4) using only PWM carrier components. Only limited schemes are treated in this chapter and this does not justify the entire research results that are in this domain. Readers are encouraged to review the references for a good coverage.

Some references that describe a general summary on sensorless control of ac machines [1–3], and also present various sensorless control techniques using observers/estimators [4–11], Klamann filter approach [12–15], induced emf [16–22], PWM or space vector modulation signals [23–28], and signal injection [29–41] are provided. Machine related issues [42–45] to provide good estimation basis for control schemes and other approaches to sensorless control schemes [46–53] are included in the references.

8.1 CURRENT MODEL ADAPTIVE SCHEME

The basis for this control strategy is that the error between the measured currents and the calculated currents from the machine model gives the difference between the assumed rotor speed and the actual rotor speed of the motor drive [23a]. Nulling current error results in the synchronous operation of the motor drive. It is achieved through the process of estimating rotor position from the current error. The relevant algorithm for rotor position sensorless control is developed below [11].

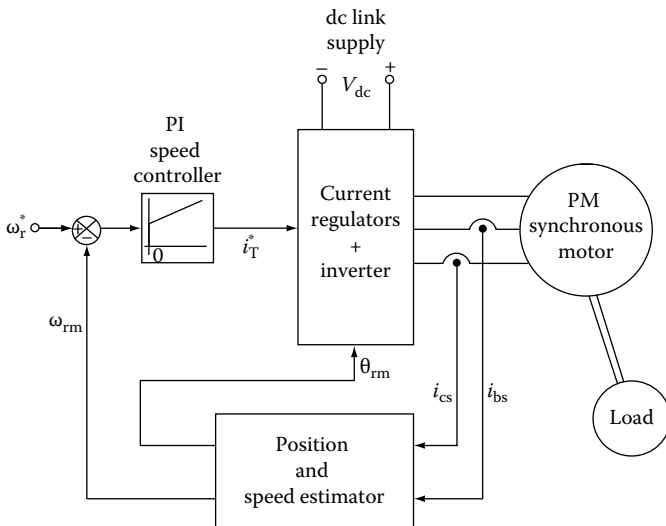


FIGURE 8.1 Control schematic diagram of the sensorless PMSM drive. (From Krishnan, R., *Electric Motor Drives*, Figure 9.38, Prentice Hall, Upper Saddle River, NJ, 2001. With permission.)

The following assumptions are made to develop this control algorithm.

1. Motor parameters and rotor PM flux are constant.
2. Induced emfs in the machine are sinusoidal.
3. The drive operates in the constant torque region and flux-weakening operation is not considered.

The basic control schematic diagram is shown in Figure 8.1. Two-phase currents constitute the inputs to the electrical rotor position and speed estimator. The error between the reference speed, ω_r^* , and the estimated rotor speed, ω_{rm} , is amplified and limited to provide the torque-producing component of the stator current, i_T^* , which is the q-axis stator current in the rotor reference frames. The estimated rotor position together with i_T^* provide the stator current commands, which are enforced by a three-phase inverter, feeding the PMSM. The position and speed estimator is derived from the machine equations.

Consider that the machine is running at a speed, ω_r , whereas the model starts with an assumed rotor speed, ω_{rm} . This is shown in the phasor diagram given in Figure 8.2. The assumed rotor position θ_{rm} lags behind the actual rotor position θ_r by $\delta\theta$ radians. They are related to the actual and assumed or model speed as

$$\theta_r = \int \omega_r dt \quad (8.1)$$

$$\theta_{rm} = \int \omega_{rm} dt \quad (8.2)$$

$$\delta\theta = \theta_r - \theta_{rm} = \int (\omega_r - \omega_{rm}) dt \quad (8.3)$$

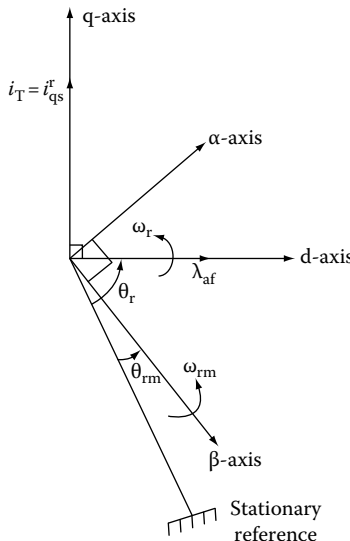


FIGURE 8.2 Phasor diagram corresponding to an error between the actual and assumed rotor positions. (From Krishnan, R., *Electric Motor Drives*, Figure 9.39, Prentice Hall, Upper Saddle River, NJ, 2001. With permission.)

The machine model is utilized to compute the stator currents and note it is carried out in reference frames at an assumed rotor speed. That implies that the reference frames are α - and β -axes and not d - and q -axes, which are the usual rotor reference frames. Therefore the machine equations in the assumed rotor speed reference frames are

$$\begin{bmatrix} pi_{\alpha m} \\ pi_{\beta m} \end{bmatrix} = \begin{bmatrix} -\frac{R_s}{L_q} & -\omega_{rm} \frac{L_d}{L_q} \\ \omega_{rm} \frac{L_q}{L_d} & -\frac{R_s}{L_d} \end{bmatrix} \begin{bmatrix} i_{\alpha m} \\ i_{\beta m} \end{bmatrix} + \begin{bmatrix} -\frac{\omega_{rm} \lambda_{af}}{L_q} \\ 0 \end{bmatrix} + \begin{bmatrix} \frac{v_\alpha}{L_q} \\ \frac{v_\beta}{L_d} \end{bmatrix} \quad (8.4)$$

To the same reference frames, the actual machine equations are written from the d - and q -axes as

$$\begin{bmatrix} pi_\alpha \\ pi_\beta \end{bmatrix} = \begin{bmatrix} -\frac{R_s}{L_q} & -\omega_{rm} \frac{L_d}{L_q} \\ \omega_{rm} \frac{L_q}{L_d} & -\frac{R_s}{L_d} \end{bmatrix} \begin{bmatrix} i_\alpha \\ i_\beta \end{bmatrix} + \begin{bmatrix} -\frac{\omega_r \lambda_{af}}{L_q} \cos \delta\theta \\ \frac{\omega_r \lambda_{af}}{L_d} \sin \delta\theta \end{bmatrix} + \begin{bmatrix} \frac{v_\alpha}{L_q} \\ \frac{v_\beta}{L_d} \end{bmatrix} \quad (8.5)$$

The variables without the second subscript indicate that they are actual machine variables whereas the machine model (or estimated) variables end with subscript m .

The actual machine equations are derived on the understanding that α - β -axes are the considered reference axes and hence the rotor flux linkages have components on them from the d-axis given as a function of the error in rotor position, $\delta\theta$. It is assumed that the entire rotor field is aligned on the d-axis.

Discretizing the two sets of model and actual current equations, respectively, as

$$\begin{bmatrix} i_{\alpha m}(kT) \\ i_{\beta m}(kT) \end{bmatrix} = \begin{bmatrix} i_{\alpha m}(k-1)T \\ i_{\beta m}(k-1)T \end{bmatrix} + \begin{bmatrix} pi_{\alpha m}(k-1)T \\ pi_{\beta m}(k-1)T \end{bmatrix} T \quad (8.6)$$

$$\begin{bmatrix} i_{\alpha}(kT) \\ i_{\beta}(kT) \end{bmatrix} = \begin{bmatrix} i_{\alpha}(k-1)T \\ i_{\beta}(k-1)T \end{bmatrix} + \begin{bmatrix} pi_{\alpha}(k-1)T \\ pi_{\beta}(k-1)T \end{bmatrix} T \quad (8.7)$$

where

T is the sampling time

k is the present sampling instant

p is the time derivative operator

Substituting for the derivative terms in terms of the currents, induced emfs, and input voltages from Equations 8.4 and 8.5 into Equations 8.6 and 8.7 and finding their respective current errors yields the following:

$$\begin{bmatrix} \delta i_{\alpha}(kT) \\ \delta i_{\beta}(kT) \end{bmatrix} = \begin{bmatrix} i_{\alpha}(kT) - i_{\alpha m}(kT) \\ i_{\beta}(kT) - i_{\beta m}(kT) \end{bmatrix} = T \begin{bmatrix} -\frac{\lambda_{af}}{L_q}(\omega_r \cos \delta\theta - \omega_{rm}) \\ \frac{\omega_r \lambda_{af}}{L_d} \sin \delta\theta \end{bmatrix} \quad (8.8)$$

A number of assumptions have been made to derive (Equation 8.8) and they are the following: (1) The difference between the model and actual currents when multiplied by T becomes negligible. (2) The sampling time is very small compared to the electrical and mechanical time constants of the drive system.

If $\delta\theta$ is small, then the following approximations are valid for use in interpreting the above results:

$$\sin \delta\theta \approx \delta\theta \quad (8.9)$$

$$\cos \delta\theta \approx 1 \quad (8.10)$$

Hence on substituting these into error currents results in

$$\delta i_{\alpha}(kT) = -\frac{\lambda_{af}}{L_q} T(-\omega_{rm} + \omega_r) \quad (8.11)$$

$$\delta i_{\beta}(kT) = \omega_r \frac{\lambda_{af}}{L_d} \delta\theta \quad (8.12)$$

from which the actual rotor speed is obtained as

$$\omega_r = -\frac{L_q}{\lambda_{af}} \frac{1}{T} \delta i_\alpha(kT) + \omega_{rm} \quad (8.13)$$

and the error in estimated rotor position is

$$\delta\theta = \frac{L_d}{\lambda_{af}} \frac{1}{T} \frac{\delta i_\beta(kT)}{\omega_r} \quad (8.14)$$

Substitution for the rotor speed in the error rotor position equation gives $\delta\theta$ as

$$\delta\theta = \frac{\left(\frac{L_d}{T\lambda_{af}} \right) \delta i_\beta(kT)}{\left[\omega_{rm} - \frac{L_q}{T\lambda_{af}} \delta i_\alpha(kT) \right]} \quad (8.15)$$

Note that $\delta\theta$, ω_{rm} , and ω_r are for the sampling instant of kT also. They have to be evaluated for each sampling instant to follow the rotor position closely. The rotor position then is

$$\theta_r = \theta_{rm} + \delta\theta \quad (8.16)$$

which becomes the estimate for θ_{rm} in the next sampling interval for feeding into the controller to compute stator current commands. Filters are required to smooth ripples in the current errors due to switching of the voltages in the machine. The realization of the position and speed estimator is shown in block diagram form in Figure 8.3.

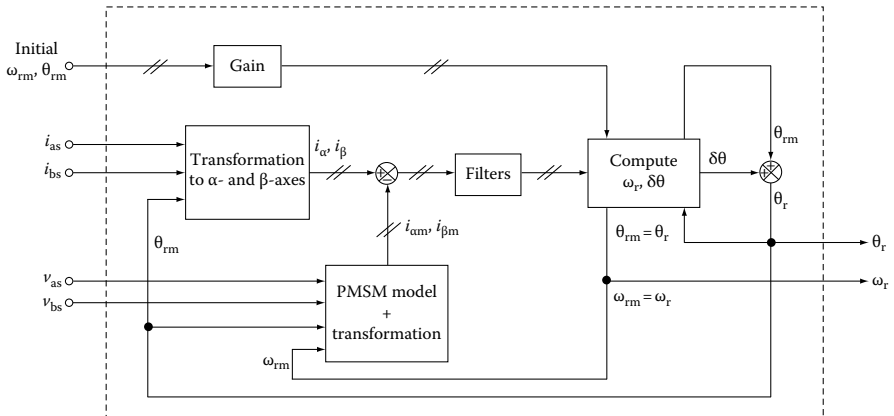


FIGURE 8.3 Block diagram realization of electrical rotor position and speed estimation. (From Krishnan, R., *Electric Motor Drives*, Figure 9.40, Prentice Hall, Upper Saddle River, NJ, 2001. With permission.)

Starting from standstill is achieved by bringing the rotor to a particular position by energizing the stator phases accordingly. Alternatively, a sequence of pulse pattern is issued to the inverter, which would enable the motor to achieve a significantly small rotor speed to start the estimation. During this time, the estimator is kept inactive and brought into the control process by switching off the starting process. The input of initial values of speed and rotor position serves to help the transition process from initial starting to estimation process for continued operation and control. Low-speed operation continues to be a challenge using this technique.

A number of other methods exist to estimate the rotor position. The induced emf of the stator phases could be estimated from the measured stator currents and voltages. This method has the problem of finding the position at zero speed as there are no phase induced emfs at that point and at low speeds, induced emfs would be difficult to estimate accurately due to their small magnitude. Hence this method has to incorporate initial starting process as discussed above.

8.2 SENSING BY EXTERNAL SIGNAL INJECTION

Ideally rotor position can be obtained from stator self-inductances. The reluctance variation between, say q- and d-axes, in the machine occurs when the magnets have a pole arc less than 180 electrical degrees regardless of the methods of magnet placement in the rotor. This variation in the reluctance can be measured by noninvasive measurement techniques and then they can be used to extract the rotor position information. This reluctance variation is prominent in the machine with high saliency. Even the surface magnet machines exhibit a 10% variation in their reluctance between the d- and q-axes. References contain research papers discussing alternative methods of estimating rotor position. Only a very limited number of methods are chosen for inclusion in this text. They are a good sample of existing schemes and by no means cover all the categories that exist in publications. To a large extent, only fundamentals and their illustrations with some schemes are given. It is believed that this will prepare the readers to a better understanding of the basics of signal injection in rotor position sensing so that they can on their own venture into research publications.

8.2.1 REVOLVING VOLTAGE PHASOR INJECTION SCHEME

The basic scheme in signal injection is to apply three-phase voltages at a signal frequency that is different from the fundamental frequency in the machine. Sometimes it is referred to as revolving voltage phasor injection scheme because a balanced three-phase voltage regardless of frequency can be seen as a voltage phasor that is revolving at the injected frequency. The voltage phasor is the vector summation of direct (d) and quadrature (q) axes voltages, which in return are derived from the three-phase (abc) voltages. Chapter 3 contains all these definitions and derivations and readers starting with this chapter are encouraged to refer to Chapter 3. When such balanced voltages are applied, they will produce a set of three-phase currents in addition to the already existing three-phase fundamental currents in the machine. These currents result in flux linkages that only depend on leakage paths as do the high-frequency currents. As the revolving voltage phasor interacts with a machine rotating at rotor

angular frequency of ω_i (also known as electrical rotor speed), the resulting currents in the stator due to injected signals will be modulated by the difference in angular frequencies of the injected signals and rotor speed and by q- and d-axes leakage inductances. When these currents are recovered in the stator reference frame, which is the only frame that they can be measured, then the currents have frequency components that are at injected frequency and a component that is the difference between twice the rotor frequency and injected frequency. The latter components are useful to extract the rotor position by means of observer. Detailed derivation of the scheme is attempted in the following.

The injected voltages at a frequency ω_i are given by

$$\begin{aligned} v_{asi} &= V_i \sin(\omega_i t) = V_i \sin \theta_i \\ v_{bsi} &= V_i \sin\left(\omega_i t - \frac{2\pi}{3}\right) = V_i \sin\left(\theta_i - \frac{2\pi}{3}\right) \\ v_{csi} &= V_i \sin\left(\omega_i t + \frac{2\pi}{3}\right) = V_i \sin\left(\theta_i + \frac{2\pi}{3}\right) \end{aligned} \quad (8.17)$$

where $\theta_i = \omega_i t$. These voltages are transformed into q- and d-axes as

$$\begin{aligned} v_{qsi} &= v_{asi} = V_i \sin(\omega_i t) = V_i \sin \theta_i \\ v_{dsi} &= \frac{1}{\sqrt{3}}(v_{csi} - v_{bsi}) = V_i \cos(\omega_i t) = V_i \cos \theta_i \end{aligned} \quad (8.18)$$

Note these are in the stator or stationary reference frames. These voltages are added to the fundamental voltage commands, which then are finally enforced in the inverter. The currents produced by these injected signal voltages can be easily derived from the rotor reference frame relationships by equating the injected signal voltages to leakage inductive voltage drops in the same frame. Then these currents are obtained in stator frames by appropriate transformation. Therefore, three steps are involved here to obtain the currents due to injected signal voltages in stator reference frames and they are as follows:

1. Transformation of the stator injected voltages from stator reference frames to rotor reference frames
2. Solution of the currents at injected signal frequency in rotor reference frames by using the relationship between the rotor reference frame voltages and rotor reference frame currents linked by the leakage inductances in q- and d-axes
3. Transformation of these rotor reference frame currents at injected signal frequency into stator reference frames that could be measured in the system

The derivations for all the three steps are given in the following. The rotor reference frame variables are denoted with a superscript r and stator reference

frames do not have this superscript. The rotor reference frame-based q- and d-axes voltages are

$$\begin{bmatrix} v_{qsi}^r \\ v_{dsi}^r \end{bmatrix} = \begin{bmatrix} \cos \theta_r & -\sin \theta_r \\ \sin \theta_r & \cos \theta_r \end{bmatrix} \begin{bmatrix} v_{qsi} \\ v_{dsi} \end{bmatrix} = V_i \begin{bmatrix} \sin(\theta_i - \theta_r) \\ \cos(\theta_i - \theta_r) \end{bmatrix} \quad (8.19)$$

where θ_r is the rotor position, which is related to rotor speed and equals $\omega_r t$ where t is time in seconds. It is seen that the injected voltages in the rotor reference frames are modulated by the rotor position. But these voltages are not measurable except in stator reference frames and, therefore, to make use of the information content embedded in them, their effects on the machine currents have to be evaluated. The relationship between the injected voltages and resulting currents is set by the leakage inductances in the q- and d-axes in rotor reference frames where the relationship is most simple and elegant. These applied stator voltages derived in rotor reference frames are equal to voltage drop across these leakage inductances. This step is achieved by ignoring the voltage drop across the stator resistances and given as

$$\begin{bmatrix} v_{qsi}^r \\ v_{dsi}^r \end{bmatrix} = \begin{bmatrix} L_{q1} & 0 \\ 0 & L_{d1} \end{bmatrix} \begin{bmatrix} pi_{qsi}^r \\ pi_{dsi}^r \end{bmatrix} = V_i \begin{bmatrix} \sin(\theta_i - \theta_r) \\ \cos(\theta_i - \theta_r) \end{bmatrix} \quad (8.20)$$

where

L_{q1} is q-axis leakage inductance

L_{d1} is the d-axis leakage inductance

p is the derivative operator d/dt

From this relationship, the stator signal currents can be evaluated but they are in the rotor reference frames and, therefore, cannot be directly measured. Then the information content in the stator currents that are in the stator reference frames, which are measurable for analysis and used in position sensing, is only considered. The relevant signal currents in the rotor reference frames are

$$\begin{bmatrix} i_{qsi}^r \\ i_{dsi}^r \end{bmatrix} = \frac{V_i}{(\omega_i - \omega_r)L_{d1}L_{q1}} \begin{bmatrix} -L_{d1} \cos(\theta_i - \theta_r) \\ L_{q1} \sin(\theta_i - \theta_r) \end{bmatrix} \quad (8.21)$$

They then are transformed into stator frames as

$$\begin{bmatrix} i_{qsi} \\ i_{dsi} \end{bmatrix} = \begin{bmatrix} \cos \theta_r & \sin \theta_r \\ -\sin \theta_r & \cos \theta_r \end{bmatrix} \begin{bmatrix} i_{qsi}^r \\ i_{dsi}^r \end{bmatrix} = \frac{V_i}{(\omega_i - \omega_r)L_{d1}L_{q1}} \begin{bmatrix} -L_{d1} \cos \theta_r \cos(\theta_i - \theta_r) + L_{q1} \sin \theta_r \sin(\theta_i - \theta_r) \\ L_{d1} \sin \theta_r \cos(\theta_i - \theta_r) + L_{q1} \cos \theta_r \sin(\theta_i - \theta_r) \end{bmatrix} \quad (8.22)$$

The q- and d-axes stator currents due to the injected signals in the exponential form are obtained as

$$i_{qsi} = \frac{V_i}{4(\omega_i - \omega_r)L_{dl}L_{ql}} \left[\{ae^{j\theta_i} - be^{j(\theta_i - 2\theta_r)}\} + \{ae^{-j\theta_i} - be^{-j(\theta_i - 2\theta_r)}\} \right] \quad (8.23)$$

$$i_{dsi} = \frac{V_i}{j4(\omega_i - \omega_r)L_{dl}L_{ql}} \left[\{ae^{j\theta_i} + be^{j(\theta_i - 2\theta_r)}\} - \{ae^{-j\theta_i} + be^{-j(\theta_i - 2\theta_r)}\} \right] \quad (8.24)$$

where

$$\begin{aligned} a &= L_{dl} + L_{ql} \\ b &= L_{ql} - L_{dl} \end{aligned} \quad (8.25)$$

The current phasor at injected signal frequency can be defined and derived from the above q- and d-current components as

$$i_{si} = i_{dsi} + ji_{qsi} = i_{qsi} = -j \frac{V_i}{2(\omega_i - \omega_r)L_{dl}L_{ql}} \left[ae^{j\theta_i} - be^{-j(\theta_i - 2\theta_r)} \right] \quad (8.26)$$

The stator current has positive and negative sequence components of injected signal frequency and they can be separated, respectively, as

$$\begin{aligned} i_{ip} &= -j \frac{V_i}{4(\omega_i - \omega_r)L_{dl}L_{ql}} ae^{j\theta_i} \\ i_{in} &= j \frac{-V_i}{4(\omega_i - \omega_r)L_{dl}L_{ql}} be^{-j(\theta_i - 2\theta_r)} \end{aligned} \quad (8.27)$$

where i_{ip} and i_{in} are positive and negative sequence current components, respectively, of the d-axis stator current due to injected signal voltages. Consider the positive sequence component of current. It has no information on the rotor position. The negative sequence component rotates at a frequency which is the difference between the injected signal and twice that of the rotor frequency and here lies the information on the rotor position. The rotor position from the negative sequence component could be extracted by many techniques. Note that the stator currents consist of two components. One is the power-producing component of stator frequency corresponding to rotational frequency and the other is the high-frequency component due to signal injection. In order to extract the signal due to injection, it needs to be separated from the power-producing component frequency and that is achieved via a bandpass filter. Then this signal itself consists of two component parts, i.e., the positive and negative sequence components of the injected frequency. The negative sequence component can be transformed to a frame rotating at the injected signal frequency resulting in

$$i_{in} = j \frac{-V_i}{4(\omega_i - \omega_r)L_{dl}L_{ql}} b e^{j2\theta_r} \quad (8.28)$$

from which the rotor position can be extracted using an observer. More information on bandpass filtering and observer is given in the following section.

The fundamental problem with this approach is that absolute position is being sought and this makes undue demands on the observer, which in turn becomes difficult to realize. Therefore, schemes have been developed to extract the difference between the actual and estimated rotor position and to null the difference through an observer known as tracking observer. Here the absolute rotor position is not being tracked and in its place only the error rotor position is tracked. Then the updating rotor position is the sum of the past estimated rotor position and the error rotor position obtained through the tracking observer. Observers are better at tracking the errors than they are in tracking the absolute value of the variable itself. The following few methods explore this alternative approach.

8.2.2 FLUX LINKAGE INJECTION IN ROTATING Q-AXIS

Consider a perfectly decoupled system. In this case, the control of q- and d-axes currents and hence the respective flux linkages can be varied without affecting one another. It implies that a variation of q-axis current has no effect on d-axis. By the same understanding, if a high-frequency current is injected into q-axis, and if a corresponding frequency current is detected in the d-axis, then the decoupling is not perfect. To achieve this, the estimated rotor position is varied in the controller until it becomes zero by forcing the estimated rotor position to the actual rotor position.

To implement such a sensing strategy, the injected signal is a high-frequency sinusoid in the estimated rotor reference frames. That is transformed into stationary reference frames using the estimated rotor position. Let the estimated rotor position be θ_{re} . When these voltages are applied to the machine, there is a response to the input very much similar to modulation of a signal, which in this case is the fundamental current-producing torque and power in the machine. The response to the input injected signal will also be the same as the input signal frequency as the system is linear during a fundamental period of the signal. It will be further amplitude modulated by the differential frequency of the power and injected signal. It can be proved that

$$i_{dsi}^e = I_2 \sin(\omega_i t) \cdot \sin[2(\theta_r - \theta_{re})] \quad (8.29)$$

where ω_i is the angular frequency of the injected signal. Then the response signal is demodulated to get a signal whose magnitude is proportional to $\sin[2(\theta_r - \theta_{re})]$. This error signal is fed to an observer to update the velocity and rotor position estimate so as to force the error to zero. This is shown in [Figure 8.4](#). The signals that are injected into the stator are fed as inputs into the controller, which computes the required voltages to be applied at that frequency. The signals are then modulated with the power

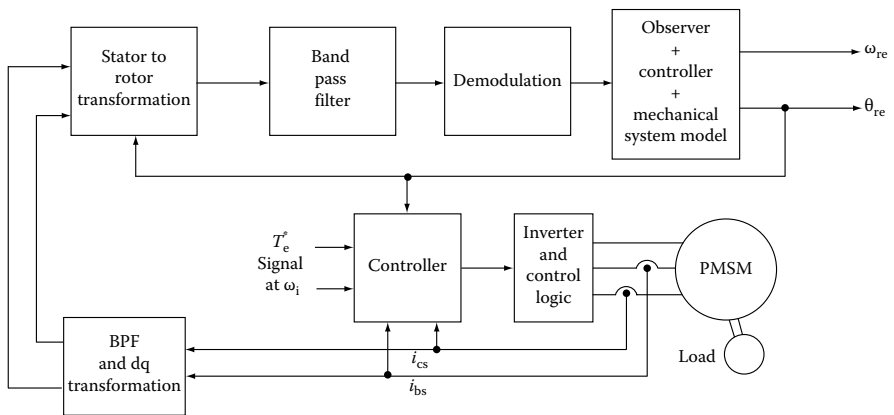


FIGURE 8.4 Sensing with signal injection.

signal references. The injection signal frequency has to be different from the PWM frequency. There are three frequencies in the machine, the fundamental frequency, carrier frequency, and injected frequency. For a small machine drive (<5 hp), the fundamental frequency may be in the range of 0–300 Hz, the carrier (PWM) frequency is 12–20 kHz, and injected frequency is in the order of 1–2 kHz.

8.2.2.1 Algorithm

In order to understand the algorithm for this technique, various reference frames that are essential to realization are shown in Figure 8.5. The stator and rotor reference frames are conventional and are well defined in Chapter 3. The rotor reference q- and d-

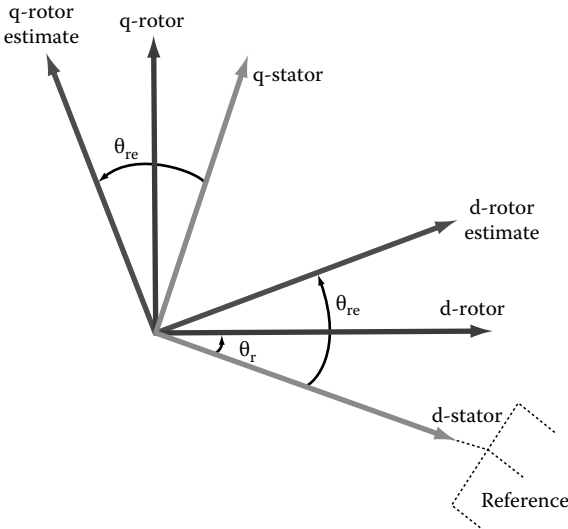


FIGURE 8.5 Various reference frames.

d-axes, which constitute the rotor reference frames, are away from the corresponding stator q- and d-axes by the rotor position and these axes constitute the stator reference frames. The stator reference frames are stationary and are therefore shown to be fixed to a point. The rotor reference frames move at the speed of ω_r electrical rad/s. As there is no rotor position sensor in this scheme, these q- and d-axes are not known. Only an estimate of these axes is made in the scheme and, therefore, represented with an error to the actual rotor reference frames. These q- and d-rotor estimate axes constitute the estimated rotor reference frames. Their position with respect to corresponding to stator reference frames is given by θ_{re} electrical radian. If variables are known on one set of axes (reference frames), their counterparts on another set of axes (reference frames) can be obtained by taking the geometric projections as done in Chapter 3.

The d- and q-axes flux linkages in rotor reference frames are given from Chapter 3 as

$$\begin{bmatrix} \lambda_{qs}^r \\ \lambda_{ds}^r \end{bmatrix} = \begin{bmatrix} L_q & 0 \\ 0 & L_d \end{bmatrix} \begin{bmatrix} i_{qs}^r \\ i_{ds}^r \end{bmatrix} + \begin{bmatrix} 0 \\ \lambda_{af} \end{bmatrix} \quad (8.30)$$

and voltage equations neglecting resistive voltage drops as

$$\begin{bmatrix} v_{qs}^r \\ v_{ds}^r \end{bmatrix} = \begin{bmatrix} p & \omega_r \\ -\omega_r & p \end{bmatrix} \begin{bmatrix} \lambda_{qs}^r \\ \lambda_{ds}^r \end{bmatrix} \quad (8.31)$$

where p is the derivative operator d/dt . Let the injected flux linkages in q phase in estimated rotor reference frames be a sinusoid and the injected d-axis flux linkages is zero and they are given as

$$\lambda_{qsi}^e = V_{si} \sin(\omega_i t) \quad (8.32)$$

$$\lambda_{dsi}^e = 0 \quad (8.33)$$

Then using Equation 8.31, the voltages required to produce the desired flux linkages for injection in q- and d-axes are derived as

$$\begin{bmatrix} v_{qsi}^e \\ v_{dsi}^e \end{bmatrix} = \left[\frac{d}{dt} \right] \lambda_{qsi}^e = \begin{bmatrix} 1 \\ -\frac{\omega_r}{\omega_i} \end{bmatrix} V_i \sin(\omega_i t) \quad (8.34)$$

in the estimated position reference frames. This step is essential as flux linkages cannot be injected directly but they can be generated only through the voltages and they are inputs that are available for control through the inverter. Once these voltages are injected, the desired flux linkages calculated in the estimated rotor reference frames are induced in the machine. These flux linkages are a function of the machine inductances and stator currents. Therefore from these flux linkages, the stator currents can

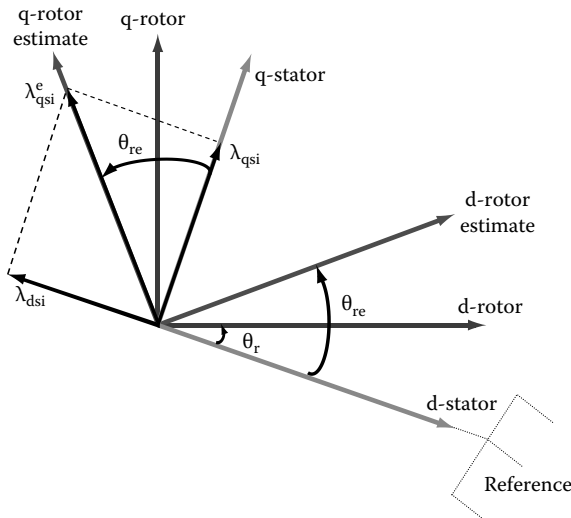


FIGURE 8.6 Projection of flux linkages from estimated rotor reference to stator frames.

be deduced. But these stator currents have to be on stator reference frames because that is the frame in which they can be directly measured. In order to get the currents in the stator reference frames, the stator flux linkages are first converted into the stator reference frames from the estimated rotor reference frames and then the stator flux linkages and current relationships can be used to obtain the stator currents. The steps involved are given in the following.

The injected flux linkages in the stator reference frames are derived by projecting the rotor reference frames based flux linkages on the stator qd-axes as shown in Figure 8.6.

And they are given as

$$\begin{bmatrix} \lambda_{qsi} \\ \lambda_{dsi} \end{bmatrix} = \begin{bmatrix} \cos(\theta_{re}) & -\sin(\theta_{re}) \\ \sin(\theta_{re}) & \cos(\theta_{re}) \end{bmatrix} \begin{bmatrix} \lambda_{qsi}^e \\ \lambda_{dsi}^e \end{bmatrix} \quad (8.35)$$

From the equations given in Chapter 3, the stator flux linkages, in terms of the stator inductances, rotor position, and stator currents in stator reference frames are derived as

$$\begin{bmatrix} \lambda_{qsi} \\ \lambda_{dsi} \end{bmatrix} = \begin{bmatrix} L_1 + L_2 \cos(2\theta_r) & -L_2 \sin(2\theta_r) \\ -L_2 \sin(2\theta_r) & L_1 - L_2 \cos(2\theta_r) \end{bmatrix} \begin{bmatrix} i_{qsi} \\ i_{dsi} \end{bmatrix} \quad (8.36)$$

where

$$L_1 = \frac{L_q + L_d}{2} \quad (8.37)$$

$$L_2 = \frac{L_q - L_d}{2} \quad (8.38)$$

Then the signal frequency of the stator currents in stationary reference frames are obtained using Equations 8.35 and 8.36 as

$$\begin{bmatrix} i_{qsi} \\ i_{dsi} \end{bmatrix} = \sin(\omega_i t) \begin{bmatrix} I_1 \cos \theta_{re} - I_2 \cos[2(\theta_r - \theta_{re})] \\ -I_1 \sin \theta_{re} + I_2 \sin[2(\theta_r - \theta_{re})] \end{bmatrix} \quad (8.39)$$

The d-axis error current resulting from signal injection is obtained by transforming it to estimated rotor position reference frames as

$$i_{dsi}^e = i_{qsi} \sin(\theta_{re}) + i_{dsi} \cos(\theta_{re}) \quad (8.40)$$

and that turns out to be

$$i_{dsi}^e = I_2 \sin(\omega_i t) \left[\sin\{2(\theta_r - \theta_{re})\} \right] \quad (8.41)$$

where

$$I_1 = \frac{V_i}{\omega_i} \frac{L_1}{L_1^2 - L_2^2}; \quad I_2 = \frac{V_i}{\omega_i} \frac{L_2}{L_1^2 - L_2^2} \quad (8.42)$$

The d-axis current in the estimated rotor reference frames is given in Equation 8.41. It is a signal at injected frequency and amplitude modulated by the position error. The position error is defined as the difference between the actual and estimated rotor positions. To extract the position error from this signal, it can be demodulated and processed to obtain an estimate of the rotor position. This is considered next.

8.2.2.2 Demodulation

Demodulation is the process of recovering the modulating signal from the injected signal. It is refreshed here in principle as follows. Let the signal to be recovered here be $\sin(2[\theta_r - \theta_{re}])$ that is with the high-frequency signal $I_2 \sin(\omega_i t)$. Let the bandpass filtered signal then be written as

$$i_{dsi}^e = y(t)x(t) \quad (8.43)$$

where

$$\begin{aligned} x(t) &= \sin[2(\theta_r - \theta_{re})] \\ y(t) &= I_2 \sin(\omega_i t) \end{aligned} \quad (8.44)$$

Multiply the bandpass filter signal with $\sin(\omega_i t)$ and the resulting signal is written as

$$\begin{aligned} e_r &= i_{dsi}^e \sin(\omega_i t) = y(t)x(t)\sin(\omega_i t) \\ &= x(t)I_2 \left[\frac{1 - \cos(2\omega_i t)}{2} \right] \end{aligned} \quad (8.45)$$

This signal then can be low-pass filtered to remove the second harmonic of the injected signal leaving only the desired error term. From this, it is seen that the demodulation process yields the position error signal, given as $x(t)I_2$. This is a dc signal provided that the position error is a constant. Otherwise, it is a slowly varying signal and for that reason it is treated most of the times as a constant. The demodulation process described gives a simplistic approach while many other forms of demodulation can be found in standard textbooks on communication. The demodulated signal also contains the current term I_2 , which is dependent on the q- and d-axes inductances. In case of varying stator currents for varying loads, saturation will affect the q- and d-axes inductances, more in the former than in the latter, resulting in a steady-state error of the demodulated signal even when the rotor position error is zero. It can be corrected provided the inductance values are instrumented for varying stator currents. This makes the scheme indirectly dependent on machine saturation influencing the inductance parameters.

8.2.2.3 Observer

When the rotor position error signal is obtained after demodulation, it is used as an input to an observer to find the estimated rotor position and estimated rotor speed. The position error signal is amplified through a proportional, integral, and derivative (PID) controller whose respective gains are K_2 , K_3 , and K_1 . The controller output forms the input to the mechanical system of the machine and load comprising of an inertia and friction. The output of the mechanical system is the estimated rotor speed and on integration, this yields estimated rotor position. The controller and observer realizations are shown in Figure 8.7. The derivative output of the controller

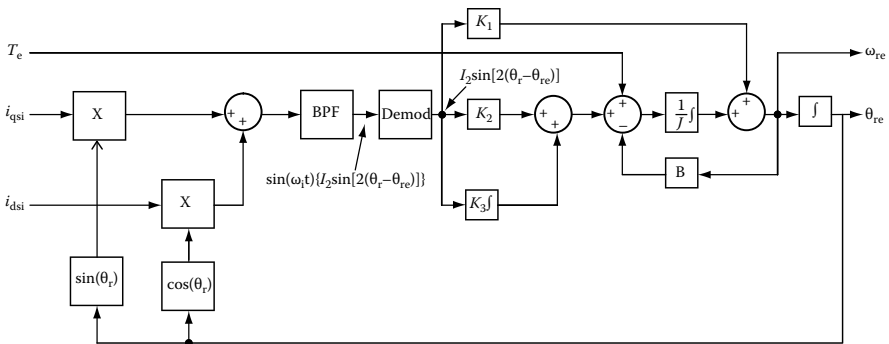


FIGURE 8.7 Controller and observer implementation starting with injected currents in stator frames.

is constructed without taking it through the stage of differentiation because this input has to go through the integration stage of the mechanical system. Therefore combining the two stages, the derivative part of the controller output is constructed directly from the position error signal multiplied by the derivative gain. The advantage is that this derivative equivalent signal is processed in the observer without requiring a differentiator to construct this signal. Then this signal is added past the mechanical integrator. The equivalence becomes obvious when the output from derivative gain block is moved ahead to the summer at the input of the mechanical system. In that case, the gain of the derivative block becomes sK_1J where s is the Laplace operator. When this is processed through the integrator with gain of $1/J$, the final signal is K_1 times the position error signal itself. This clearly demonstrates that the signal added past the mechanical integrator is nothing but the derivative controller output signal. The sum of the derivative gain times the position error signal and the output of the mechanical integrator gives the estimated rotor speed. For faster dynamics, torque signal is inserted at the input of the mechanical system.

8.2.2.4 Implementation

The overall implementation of the system is shown as a schematic ([Figure 8.8](#)). The vector controller gives the current command in rotor reference frames and those currents are used to compare with the measured stator currents transformed in estimated rotor reference frames and their respective errors are processed with conventional proportional and integral current controllers or any of the current controllers described in Chapter 6. The outputs of the current controllers are the q- and d-voltage commands in the rotor reference frames. To them are added the injected q- and d-axes voltages to create the rotor flux linkages in the estimated q-axis to provide the final q- and d-axes voltage commands in the estimated rotor reference frames. These final voltage commands are transformed into stator reference frames using the estimated rotor position. They then can be enforced in the inverter with either PWM or space vector modulation techniques.

[Figure 8.9](#) shows the simulation results in normalized units for dynamic performances of the speed-controlled drive system implementing the position estimation scheme using injected signals. Speed command of 0.5 p.u. is imposed at standstill, hence producing the maximum torque while the rotor is accelerating its speed. The error signal serves as the input to the speed observer that guarantees position convergence as the error is driven to zero. The observer uses the same mechanical system model as the motor. Speed estimation is based on the mechanical torque equation.

[Figure 8.10](#) compares the actual and estimated rotor positions showing the tracking ability of the position estimator when the motor is running at (a) 3000 rpm and (b) 5000 rpm. There is no appreciable difference in position tracking, regardless of speed as long as the rotor speed is not very low. In the case of an abrupt speed command or load change, the observer may not be able to track the actual rotor speed effectively, thus degrading the accuracy of position estimation. Therefore, to guarantee the desired tracking performance at various speed and load conditions, the information about load torque is needed to compensate this load-dependent error.

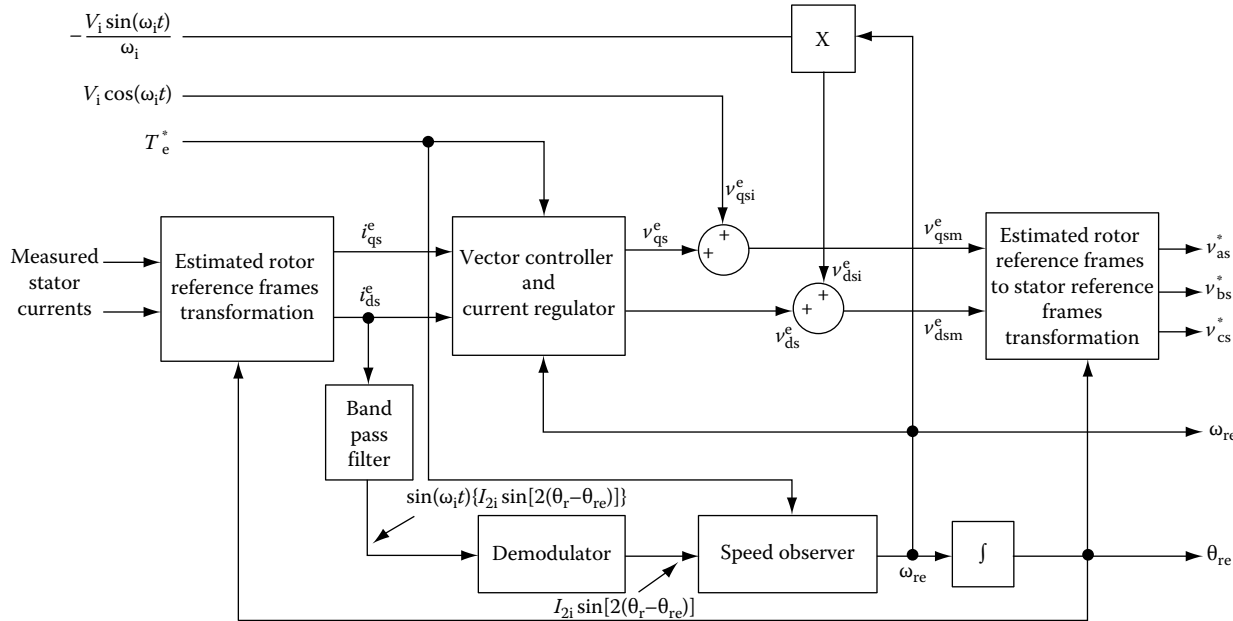


FIGURE 8.8 Overall schematic of the rotor position estimator.

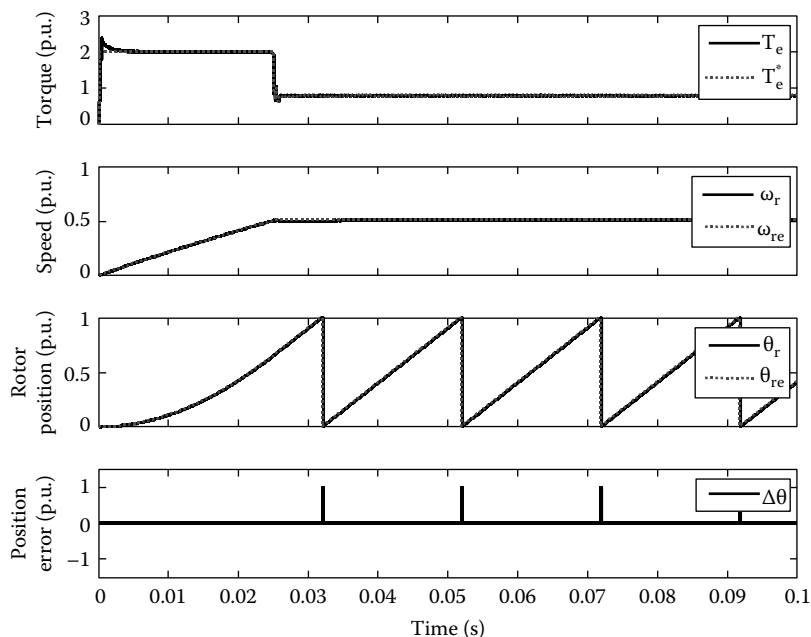


FIGURE 8.9 Dynamic response of a speed-controlled sensorless drive system (T_e ; torque; T_e^* ; torque command; ω_r ; actual rotor speed; ω_{re} ; estimated rotor position; θ_r ; actual rotor position; θ_{re} ; estimated rotor position; $\Delta\theta$; position error).

8.2.2.5 Merits and Demerits of the Scheme

The scheme has the following merits:

1. Independent of speed and hence could be used for standstill position estimation
2. Independent of current magnitude
3. Only dependent on the position error and therefore insensitive to current magnitude
4. Provides a wide range of operational speed

The scheme has the following demerits:

1. Load-dependent error requires compensation as saturation is dependent on stator current, which in turn affects the value of inductances and hence the estimation of current responses for injected signals.
2. Signal-to-noise ratio is poor in this scheme.
3. Accuracy is dependent on saliency of the machine and that makes it impossible to use in machines with very low saliency such as surface-mount PMSMs.
4. Observer and load modeling are required for successful working of the scheme. Load modeling is inherently fraught with difficulties and uncertainties.

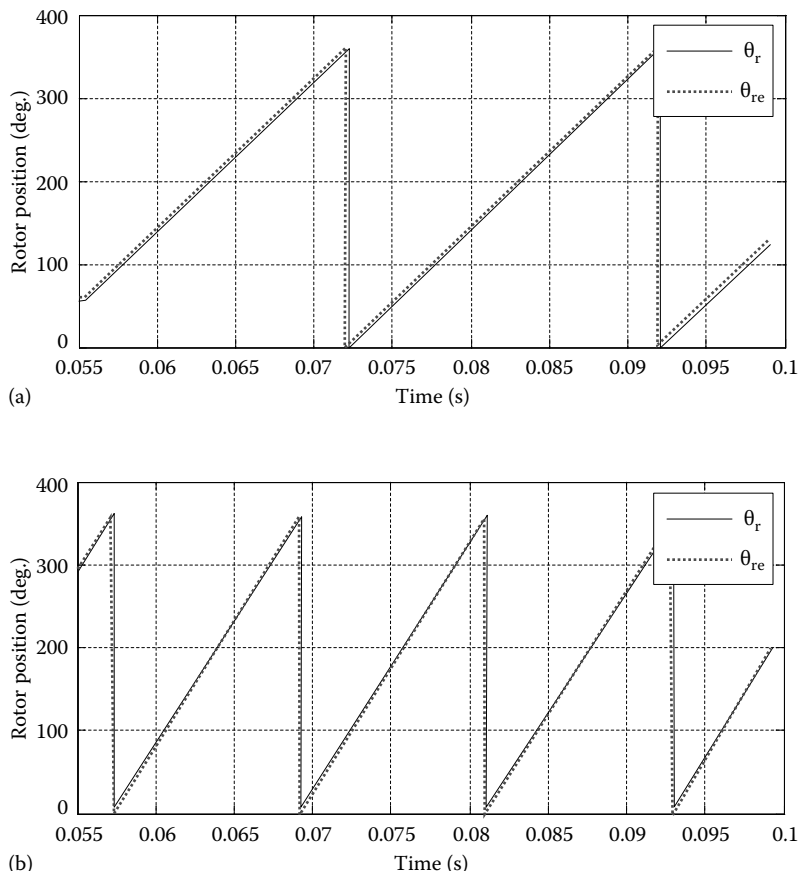


FIGURE 8.10 Actual and estimated rotor positions at steady state operation. θ_r ; actual rotor position (solid); θ_{re} ; estimated rotor position (dotted). (a) Steady-state operation at 3000 rpm and (b) steady-state operation at 5000 rpm.

5. Tuning to be carried out individually for every load and drive setup. That is an expensive process.
6. Considerable torque ripple, as much as 2% or more of the rated value, due to injected current is generated in this scheme. This is undesirable in high-performance positioning applications but usually acceptable in many variable speed drive systems.

It must be noted that this has been an evolving scheme and many of these disadvantages have been already eliminated with further work. Various new developments by Holtz and his colleagues [34,40,41] that have delivered a high-precision position-controlled PMSM drives with no position sensor is recognized here. A brief description of their algorithm and its key features are outlined in the following. Interested readers are referred to many of their publications given in the references.

8.2.3 ALTERNATING VOLTAGE PHASOR INJECTION

Saliency in the PMSM is inherent in interior type of machines due to the isotropy of the rotor magnets. In surface-mount magnet machines, this saliency effect is very small and in that case, position estimation techniques are not able to perform satisfactorily. Realizing that saliency is induced also by saturation, it can be effectively exploited for position estimation. In such a case, even surface-mount PMSMs can have a reliable position estimation and control. Such a scheme is discussed in this section. An alternating voltage signal, v_i^a is injected at a frequency ω_i in the estimated rotor or anisotropic axis, which is almost at the rotor speed. In the rotor reference frames, this voltage signal transformed into that axis is equal to the product of leakage inductances (L_{dl} and L_{ql}) and rate of change in current. Note that the leakage inductances are for high frequency and are aligned with the anisotropic frames. This current phasor, i_{si}^a , due to the injected voltage, can then be transformed into stator reference frames, i_{si}^s , which has positive and negative sequence components at $(\omega_i + \omega_a)$ and $(\omega_i - \omega_a + 2\omega_r)$. Transforming the positive sequence component into a reference frame rotating at $-(\omega_i + \omega_a)$, the real part of the positive sequence current due to injected voltage is found to be proportional to the rotor position error (the difference between the actual rotor position and anisotropic or injected reference frames or axis). Rotor position is tracked by driving this error to zero to obtain the final position. The current produced in the q-axis winding due to signal injection is not significant and negligible and hence torque due to it and losses are negligible. This is the heart of the scheme and its algorithm is given in the following.

8.2.3.1 Sensorless Algorithm

Consider a voltage vector being injected into the machine at signal injection frequency of ω_i with a magnitude of V_i :

$$V_{si}^a = V_i \cos(\omega_i t) \quad (8.46)$$

This may be seen on the stator reference frames as

$$V_{si}^s = V_{si}^a e^{j\omega_a t} = V_i (\cos \omega_i t) e^{j\omega_a t} \quad (8.47)$$

This decomposes into the rotor reference frames as

$$V_{si}^r = V_{si}^s e^{-j\omega_r t} = \frac{V_i}{2} \left[e^{j(\omega_i - \omega_r)t} + e^{-j(\omega_i + \omega_r)t} \right] = V_{dsi}^r + j V_{qsi}^r \quad (8.48)$$

Note that the real and imaginary parts correspond to the q- and d-axes voltages in the rotor reference frames which equal voltage drops across the respective leakage inductances of the q- and d-axes given by

$$\begin{bmatrix} v_{qsi}^r \\ v_{dsi}^r \end{bmatrix} = \begin{bmatrix} L_{ql} & 0 \\ 0 & L_{dl} \end{bmatrix} \begin{bmatrix} p i_{qsi}^r \\ p i_{dsi}^r \end{bmatrix} \quad (8.49)$$

where p is the derivative operator d/dt . The rotor currents due to the signal injection can be solved and are obtained as

$$i_{\text{qsi}}^r = \frac{V_i}{L_{\text{qI}}\omega_i} \sin(\omega_i t) \sin(\overline{\omega_a - \omega_r} t) \quad (8.50)$$

$$i_{\text{dsi}}^r = \frac{V_i}{\omega_i L_{\text{dl}}} \sin(\omega_i t) \cos(\overline{\omega_a - \omega_r} t) \quad (8.51)$$

which can then be transformed into stator reference frames by the following as

$$\begin{bmatrix} i_{\text{qsi}}^s \\ i_{\text{dsi}}^s \end{bmatrix} = \begin{bmatrix} \cos \theta_r & \sin \theta_r \\ -\sin \theta_r & \cos \theta_r \end{bmatrix} \begin{bmatrix} i_{\text{qsi}}^r \\ i_{\text{dsi}}^r \end{bmatrix} \quad (8.52)$$

The various frames and the variables on the axes are similar to [Figure 8.6](#). Realizing that the stator current vector is

$$\begin{aligned} i_{\text{si}}^s &= i_{\text{dsi}}^s + j i_{\text{qsi}}^s = \frac{V_i}{2\omega_i L_{\text{ql}} L_{\text{dl}}} \left[a \{ \cos \omega_a t + j \sin \omega_a t \} + \right. \\ &\quad \left. b \{ \cos(\omega_a - 2\omega_r)t - j \sin(\omega_a - 2\omega_r)t \} \right] \\ &= \frac{V_i}{j4\omega_i L_{\text{ql}} L_{\text{dl}}} \left[a \{ e^{j(\omega_a + \omega_i)t} \} + b \{ e^{j(\omega_i - \omega_a + 2\omega_r)t} \} \right. \\ &\quad \left. - a \{ e^{j(\omega_a - \omega_i)t} \} - b \{ e^{j(2\omega_r - \omega_a - \omega_i)t} \} \right] \\ &= i_{\text{sp}}^s + i_{\text{sn}}^s \end{aligned} \quad (8.53)$$

where $a = L_{\text{ql}} + L_{\text{dl}}$ and $b = L_{\text{ql}} - L_{\text{dl}}$.

The positive sequence and negative sequence currents in the stator frames are identified as

$$i_{\text{sp}}^s = \frac{V_i}{j4\omega_i L_{\text{ql}} L_{\text{dl}}} \left\{ a e^{j(\omega_a + \omega_i)t} + b e^{j(\omega_i - \omega_a + 2\omega_r)t} \right\} \quad (8.54)$$

$$i_{\text{sn}}^s = \frac{V_i}{j4\omega_i L_{\text{ql}} L_{\text{dl}}} \left\{ -a e^{j(\omega_a - \omega_i)t} - b e^{j(2\omega_r - \omega_a - \omega_i)t} \right\} \quad (8.55)$$

The rotor position information can be tapped by transforming the positive sequence current in the stator to a reference frames rotating at the sum of the injection frequency and anisotropic frame velocity, i.e., $(\omega_i + \omega_a)$ and given by

$$\begin{aligned}
 i_{\text{sp}}^{(\omega_i + \omega_a)} &= \frac{V_i}{j4\omega_i L_{\text{ql}} L_{\text{dl}}} i_{\text{sp}}^s e^{-j(\omega_i + \omega_a)t} = \frac{V_i}{j4\omega_i L_{\text{ql}} L_{\text{dl}}} \left\{ a + b e^{j(2\omega_r - 2\omega_a)t} \right\} \\
 &= \frac{V_i}{j4\omega_i L_{\text{ql}} L_{\text{dl}}} \left\{ a + b \cos 2(\omega_r - \omega_a)t + j b \sin 2(\omega_r - \omega_a)t \right\} \quad (8.56)
 \end{aligned}$$

For small values of $(\omega_r - \omega_a)$, the real part of the positive sequence current amounts to

$$\text{Re}[i_{\text{sp}}^{(\omega_i + \omega_a)}] \approx \frac{V_i}{4\omega_i L_{\text{ql}} L_{\text{dl}}} \{2b\Delta\theta\} \quad (8.57)$$

where

$$\Delta\theta = \theta_r - \theta_a = (\omega_r - \omega_a)t \quad (8.58)$$

The real part of the positive sequence current in the new frames is directly proportional to the error in rotor position, which can be reduced to zero by using a tracking observer. The tracking error signal is robust against noise and measurement errors.

8.2.3.2 Implementation

The implementation of the scheme is shown in schematic form in Figure 8.11. The stator current is filtered to pass only the frequency of injected signal by transforming it into anisotropic frames, which acts like a bandpass filter and it is filtered with another bandpass so that only signal of estimated rotor or anisotropic frequency is considered. It is then transformed into injected frequency frame by angle θ_i , which is nothing but $\omega_i t$ and is then processed for finding the real part of the vector. The outcome is the signal given in Equation 8.57. A PI controller processes this signal to feed into an oscillator so that the position error signal is converted into the estimated field angle, θ_a . The loop is closed and the newer estimated position is updated for each current vector sampling with the result that the error is quickly reduced to zero.

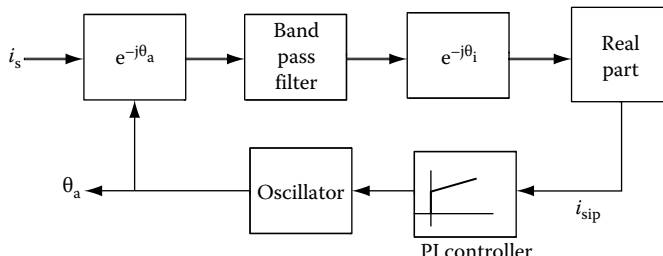


FIGURE 8.11 Schematic implementation of the signal processing of the sensorless scheme with alternating voltage injection.

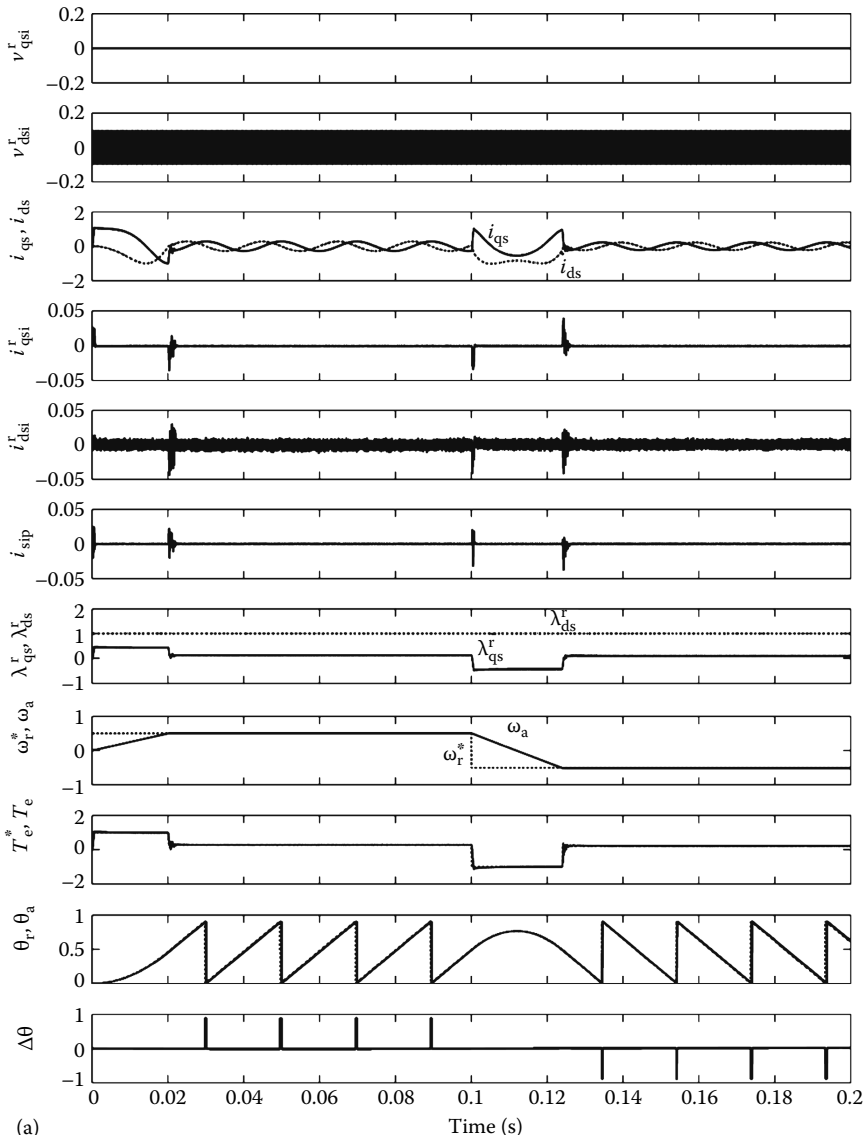
Note that the rotor angle error is tracked here but not the rotor angle itself and because of this, the resolution of the high-frequency current is not critical. Also $\Delta\theta$ is an incremental variable that changes slowly with respect to sampling frequency and therefore it can be accurately tracked. It is parameter insensitive as it is not calculated but narrowed by a tracking observer. The injection signal-based excitation is aligned with the rotor field and hence has almost no effect on torque production. It leads to almost no torque ripple due to signal injection and hence the scheme is suitable for high-performance motor drives.

A sample simulation result of the scheme is shown in [Figure 8.12a](#) and [b](#). [Figure 8.12b](#) is only an expanded version of a small interval from [Figure 8.12a](#) so that some of the variables can be minutely viewed. The motor drive is given a speed command that covers both directions of rotation and in that process the drive is forced into a four-quadrant operation. The variables in normalized units are presented and the rotor position is normalized with respect to 2π . The additional subscript of n is omitted here because of compact packaging of the plots. A signal voltage is injected in the d-axis of the estimated rotor (anisotropic) frame at a select frequency whereas its counterpart in q-axis is zero. Various variables follow pretty much their characteristic vector controlled pattern. Note that the d-axis current in rotor frames is at injected frequency whereas the q-axis current is almost nonexistent except at transitions of the sharp air gap torque variations. Note that the magnitudes of these currents are in a few to tens of mA, challenging the control engineer in its precise acquisition. The extraction is made more complicated by its presence in a noisy environment with the switching of the inverter having the fundamental frequency currents with orders of magnitude higher than the signal currents at injected frequency and the pulse width modulation frequency currents also exceeding or equaling the injected frequency signal currents. The performance of the drive is the same as the scheme with the rotor position sensor in its control. The scheme is not affected by the variation of the motor mechanical constants and hence their variation in one way or another does not affect the performance of this scheme. That is one of the advantages of this scheme compared to some other schemes.

Problems facing this scheme are

1. The scheme performs well as long as the ratio between the injected signal frequency and stator fundamental frequency is high. This means the performance is good at low speeds but not at high speeds. Increasing the injection signal frequency is not an option as it may start overlapping with the switching frequency of the inverter. This problem is common for all schemes with signal injection.
2. Voltage distortion caused by the inverter nonlinearity, which is induced by inverter delay, and dead time are common to all schemes. They may be compensated by various techniques discussed in Chapter 2. To overcome this problem of distortion in the voltage signal apart from compensation of the dead time and delay, injection signal phase angle has been proposed, which needs to be maintained at 0.5π radian. This eliminates the q-axis high-frequency current, making only the d-axis high-frequency current present in the system.

This scheme has been demonstrated with closed loop position control using the estimated rotor position for feedback and its performance with a 10 bits rotor position resolution has been very good. Further, this is also the first scheme to demonstrate such robust positioning capability as seen from publications.



(a)

FIGURE 8.12 Simulation results of the alternating voltage phasor injection sensorless scheme shown in normalized variables: (a) for one cycle of four quadrant operation and (b) for a small interval of time with expanded time axis scale.

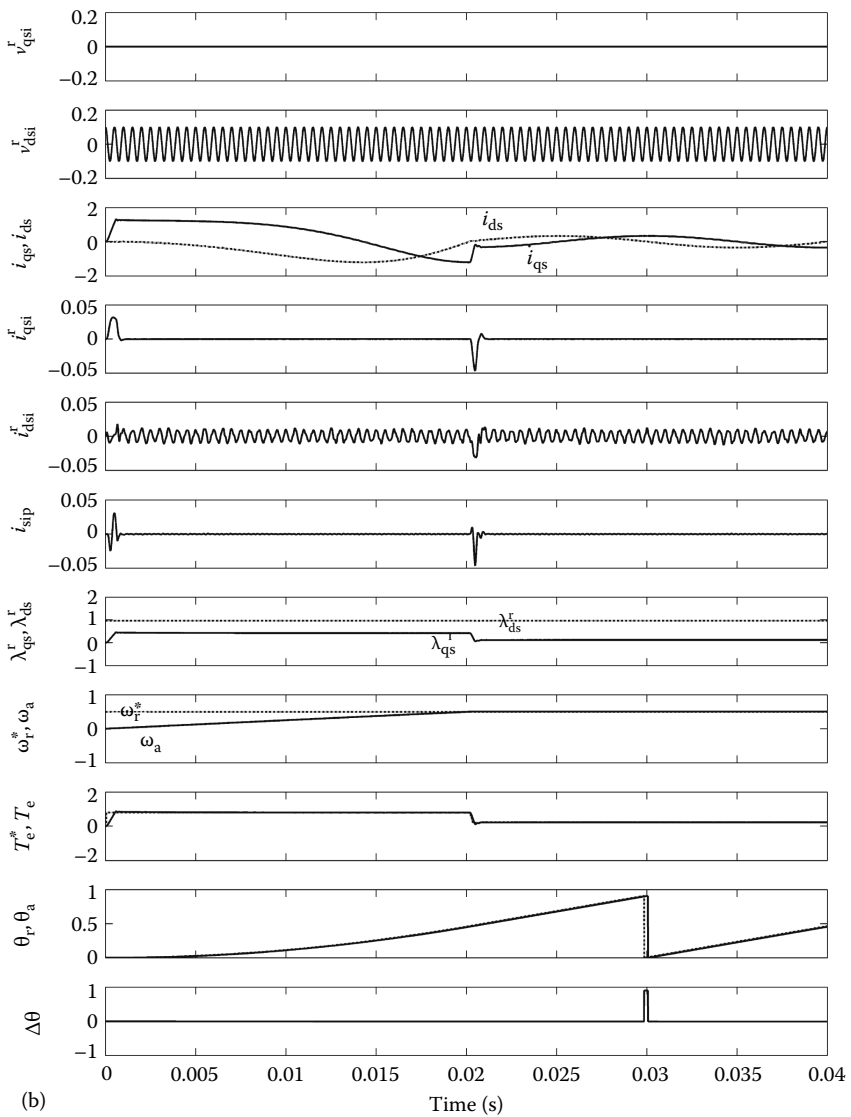


FIGURE 8.12 (continued)

8.3 CURRENT MODEL-BASED INJECTION SCHEME

A model-based injection scheme uses an external voltage signal similar to the previous schemes. A voltage signal injection into the d-axis winding with an ac square waveform of equal duration produces ramp like rising and falling current with very little deviation in the q-axis current. The incremental current is estimated but never measured and processed. This is the heart of this scheme.

This incremental current is related to the estimated position error as explained in Section 8.1. Since the d-axis current is perturbed, its effect on air gap torque is not significant with the result that torque ripple is minimized and measurable magnitude can be applied without undue concern for acoustic noise produced by torque perturbations. The performance of this scheme even at zero speed under load is very good with errors not exceeding 5° under both steady state and dynamic conditions.

8.4 POSITION ESTIMATION USING PWM CARRIER COMPONENTS

Position estimation using PWM carrier component scheme uses the saliency of the machine as the two previous schemes but does not require an extra signal injection. This is a distinct advantage. It exploits the harmonic voltages inherent in the PWM voltage source inverter outputs and their harmonic current responses. Separating the harmonics from the fundamental is done elegantly by this method. The harmonic voltages and currents, assuming negligible harmonic resistive voltage drops and harmonic induced emfs, are related as

$$v_h = L \frac{di_h}{dt} \quad (8.59)$$

where

v_h and i_h are vectors containing the q- and d-axes voltages and currents
 L is the inductance matrix in stationary reference frames given by

$$L = \begin{bmatrix} L_1 + L_2 \cos 2\theta_r & -L_2 \sin 2\theta_r \\ -L_2 \sin 2\theta_r & L_1 - L_2 \cos 2\theta_r \end{bmatrix} \quad (8.60)$$

If the harmonic voltages and currents are known, then the inductance matrix is computed from which the rotor position is obtained as

$$\theta_r = \frac{1}{2} \tan^{-1} \left[-\frac{L_{12} + L_{21}}{L_{11} - L_{22}} \right] \quad (8.61)$$

Consider switching in a PWM cycle as shown in Figure 8.13. The basis for extraction of harmonic voltages and currents are provided with this figure.

8.4.1 HARMONIC VOLTAGE AND CURRENT VECTORS

The inverter has eight switching voltage state vectors and denoted as V_k , $k=1, 2, \dots, 8$. The average voltage phasor is given by

$$e = \sum d_k V_k \quad (8.62)$$

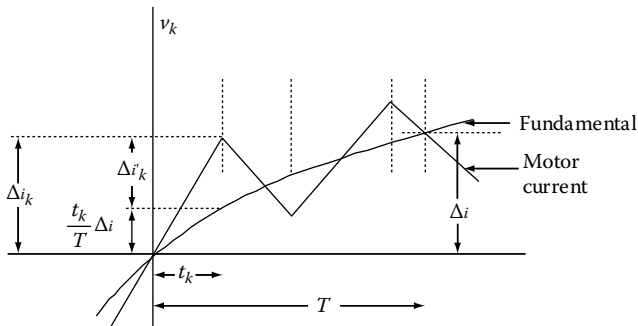


FIGURE 8.13 Current waveform during a PWM cycle.

where d_k is the duty cycle of the k th switching state voltage vector and $d_k = t_k/T$. The harmonic voltage vector is obtained by

$$v_{hk} = V_k - e \quad (8.63)$$

From the current waveforms, the current variation for the modulation period is obtained as

$$\Delta i = \sum \Delta i_k, k = 1, 2, \dots, 8 \quad (8.64)$$

Assuming that in one modulation cycle, the fundamental current change is linear, the harmonic current is derived from the figure as

$$i_{hk} = \Delta i_k - d_k \Delta i \quad (8.65)$$

8.4.2 ROTOR POSITION ESTIMATION

The harmonic currents and voltages for discrete intervals of time are related by

$$L_i = V_{hk} t_k \quad (8.66)$$

and for one modulation period written as

$$L \begin{bmatrix} i_{h1} & i_{h2}, \dots, i_{h8} \end{bmatrix} = \begin{bmatrix} V_{h1} t_1 & V_{h2} t_2, \dots, V_{h8} t_8 \end{bmatrix} \quad (8.67)$$

from which the inductance matrix is obtained by the following operation using left pseudoinverse operator:

$$L^t = \left[I_{hk} \right]^{ps} \begin{bmatrix} V_{hk} t_k \end{bmatrix} \quad (8.68)$$

where the superscript ps indicates a pseudoinverse operation. The pseudoinverse operator performs the following function:

$$[i_{hk}]^{\text{ps}} = [(i_{hk})^t (i_{hk})]^{-1} [i_{hk}]^t = \begin{bmatrix} \sum i_{hkq}^2 & \sum i_{hkq} i_{hkd} \\ \sum i_{hkq} i_{hkd} & \sum i_{hkd}^2 \end{bmatrix} \quad (8.69)$$

Note the additional subscripts q and d indicate the q- and d-axes currents in the stationary reference frames. Also, the following relationships are important for the computation of the average voltage vector:

$$e = \sum d_k V_k \quad (8.70)$$

$$\sum d_k = 1 \quad (8.71)$$

Since an inverse of the matrix is involved, the current vectors have to be linearly independent. It is assured in this scheme by providing with redundant voltage vectors in a modulation period. The redundant vectors ensure the harmonic voltage vector moves around the switching voltage vector hexagon in every other switching. There is symmetry also in this modification of switching with redundant voltage vectors.

8.4.3 PERFORMANCE

The scheme performs very well at zero speed also and has been shown to provide positioning performance and a fairly fast response. The advantage of this scheme is that it does not use any coordinate transformation in estimation like other schemes. But it does require a large amount of algebraic computations. The schematic of the drive scheme is shown in Figure 8.14.

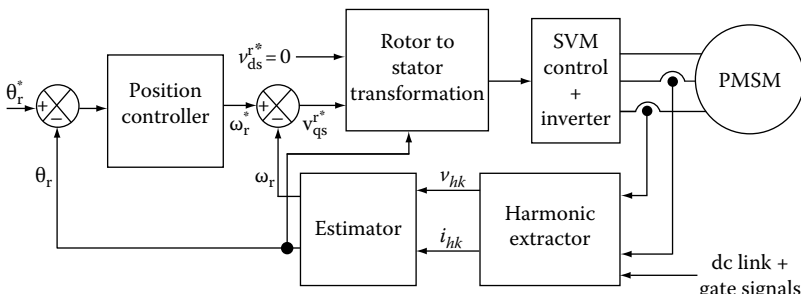


FIGURE 8.14 Implementation of PWM harmonics-based sensorless drive.

REFERENCES

General Summary on Sensorless Control of ac Machines

1. J. Holtz, State of the art of controlled AC drives without speed sensor, *Proceedings of 1995 International Conference on Power Electronics and Drive Systems (Cat. No. 95TH8025)*, pp. 1–6, 1995.
2. J. Holtz, Developments in sensorless AC drive technology, *Sixth International Conference on Power Electronics and Drive Systems (IEEE Cat. No. 05TH8824C)*, pp. 9–16, 2005.
3. J. Holtz, Sensorless control of induction motor drives, *Proceedings of the IEEE*, 90(8), 1359–1394, 2002.

Observer/Estimator-Based

4. M. Schroedl, An improved position estimator for sensorless controlled permanent magnet synchronous motors, *4th European Conference on Power Electronics and Applications*, pp. 418–423, 1991.
5. M. Schroedl, Sensorless control of permanent magnet synchronous motors, *Electric Machines and Power Systems*, 22(2), 173–185, 1994.
6. S. Shinnaka, New “mirror-phase vector control” for sensorless drive of permanent-magnet synchronous motor with pole saliency, *IEEE Transactions on Industry Applications*, 40(2), 599–606, 2004.
7. S. Shinnaka, New “D-state-observer”-based vector control for sensorless drive of permanent-magnet synchronous motors, *IEEE Transactions on Industry Applications*, 41(3), 825–833, 2005.
8. S. Shinnaka, New sensorless vector control using minimum-order flux state observer in a stationary reference frame for permanent-magnet synchronous motors, *IEEE Transactions on Industrial Electronics*, 53(2), 388–398, 2006.
9. S. Shiinaka, A new speed-varying ellipse voltage injection method for sensorless drive of permanent-magnet synchronous motors with pole saliency—new PLL method using high-frequency current component multiplied signal, *IEEE Transactions on Industry Applications*, 44(3), 777–788, 2008.
10. M. Hasegawa, S. Yoshioka, and K. Matsui, Position estimation of permanent magnet synchronous motor using un-known input observer, *International Conference on Power Electronics and Drive Systems (PEDS '07)*, pp. 816–821, 2007.
11. R. Mizutani, T. Takeshita, and N. Matsui, Current model-based sensorless drives of salient-pole PMSM at low speed and standstill, *IEEE Transactions on Industry Applications*, 34(4), 841–846, 1998.

Kalman Filter Approach

12. S. Bolognani, R. Oboe, and M. Zigliotto, Sensorless full-digital PMSM drive with EKF estimation of speed and rotor position, *IEEE Transactions on Industrial Electronics*, 46(1), 184–191, 1999.
13. G. Terorde, K. Hameyer, and R. Belmans, Sensorless control of a permanent magnet synchronous motor for PV-powered water pump systems using the extended Kalman filter, *IEEE Conference Publication*, no. 468, pp. 366–370, 1999.
14. M. Boussak, Digital signal processor based sensorless speed control of a permanent magnet synchronous motor drive using extended Kalman filter, *EPE Journal (European Power Electronics and Drives Journal)*, 11(3), 7–15, 2001.
15. S. Bolognani, L. Tubiana, and M. Zigliotto, Extended Kalman filter tuning in sensorless PMSM drives, *IEEE Transactions on Industry Applications*, 39(6), 1741–1747, 2003.

EMF-Based

16. R. Wu and G. R. Slemon, A permanent magnet motor drive without a shaft sensor, *IEEE Transactions on Industry Applications*, 27(5), 1005–1011, 1991.
17. S. Morimoto, K. Kawamoto, M. Sanada et al., Sensorless control strategy for salient-pole PMSM based on extended EMF in rotating reference frame, *IEEE Transactions on Industry Applications*, 38(4), 1054–1061, 2002.
18. B. Nahid-Mobarakeh, F. Meibody-Tabar, and F. M. Sargos, Back EMF estimation-based sensorless control of PMSM: robustness with respect to measurement errors and inverter irregularities, *IEEE Transactions on Industry Applications*, 43(2), 485–494, 2007.
19. C. Zhiqian, M. Tomita, S. Doki et al., An extended electromotive force model for sensorless control of interior permanent-magnet synchronous motors, *IEEE Transactions on Industrial Electronics*, 50(2), 288–295, 2003.
20. M. Tursini, R. Petrella, and A. Scafati, Speed and position estimation for PM synchronous motor with back-EMF observer, *Conference Record, IEEE Industry Applications Annual Meeting (IEEE Cat. No. 05CH37695)*, pp. 2083–2090, 2005.
21. H. Rasmussen and P. Vadstrup, A novel back EMF observer for sensorless control of interior permanent magnet synchronous motors, *IEEE Industrial Electronics Conference (IEEE Cat. No. 05CH37699)*, pp. 1528–1531, 2005.
22. P. Kshirsagar, R. P. Burgos, A. Lidozzi et al., Implementation and sensorless vector-control design and tuning strategy for SMPM machines in fan-type applications, *Conference Record of the 2006 IEEE Industry Applications Conference Forty-First IAS Annual Meeting (IEEE Cat. No. 06CH37801)*, vol. 4, pp. 2062–2069, 2006.

PWM/SVM Signal-Based

23. S. Ogasawara and H. Akagi, Implementation and position control performance of a position-sensorless IPM motor drive system based on magnetic saliency, *IEEE Transactions on Industry Applications*, 34(4), 806–812, July/Aug. 1998.
- 23a. R. Krishnan, *Electric Motor Drives*, Prentice Hall, Upper Saddle River, NJ, 2001.
24. T. M. Wolbank and J. Machl, A modified PWM scheme in order to obtain spatial information of AC machines without mechanical sensors, *Proceedings of the IEEE Applied Power Electronics Conference*, Dallas, TX, pp. 310–315, 2002.
25. V. Petrovic, A. M. Stankovic, and V. Blasko, Position estimation in salient PM synchronous motors based on PWM excitation transients, *IEEE Transactions on Industry Applications*, 39(3), 835–843, 2003.
26. G. Qiang, G. M. Asher, M. Sumner, et al., Position estimation of AC machines over a wide frequency range based on space vector PWM excitation, *IEEE Transactions on Industry Applications*, 43(4), 1001–1011, 2007.
27. R. Raute, C. Caruana, J. Cilia, et al., A zero speed operation sensorless PMSM drive without additional test signal injection, *European Conference on Power Electronics and Applications*, pp. 1–10, 2007.
28. Q. Gao, G. M. Asher, and M. Sumner, Zero speed position estimation of a matrix converter fed AC PM machine using PWM excitation, *13th International Power Electronics and Motion Control Conference*, pp. 2261–2268, 2008.

Signal Injection

29. M. J. Corley and R. D. Lorenz, Rotor position and velocity estimation for a salient-pole permanent magnet synchronous machine at standstill and high speeds, *IEEE Transactions on Industry Applications*, 34(4), 784–789, 1998.
30. W. Limei and R. D. Lorenz, Rotor position estimation for permanent magnet synchronous motor using saliency-tracking self-sensing method, *Conference Record IEEE Industry Applications Conference (Cat. No. 00CH37129)*, pp. 445–450, 2000.

31. L. Wang, Q. Guo, and R. D. Lorenz, Sensorless control of permanent magnet synchronous motor, *Proceedings, Third International Power Electronics and Motion Control Conference (IEEE Cat. No. 00EX435)*, pp. 186–190, 2000.
32. F. Briz, M. W. Degner, A. Diez et al., Measuring, modeling, and decoupling of saturation-induced saliences in carrier-signal injection-based sensorless AC drives, *IEEE Transactions on Industry Applications*, 37(5), 1356–1364, 2001.
33. C. Silva, G. M. Asher, and M. Sumner, Influence of dead-time compensation on rotor position estimation in surface mounted PM machines using HF voltage injection, *Proceedings of the Power Conversion Conference-Osaka, Japan, (Cat. No. 02TH8579)*, pp. 1279–1284, 2002.
34. M. Linke, R. Kennel, and J. Holtz, Sensorless position control of permanent magnet synchronous machines without limitation at zero speed, *IEEE Industrial Electronics Conference (Cat. No. 02CH37363)*, pp. 674–679, 2002.
35. B.-H. Bae, S.-K. Sul, J.-H. Kwon, et al., Implementation of sensorless vector control for super-high-speed PMSM of turbo-compressor, *IEEE Transactions on Industry Applications*, 39(3), 811–818, 2003.
36. J. Holtz and P. Hangwen, Acquisition of rotor anisotropy signals in sensorless position control systems, *IEEE Transactions on Industry Applications*, 40(5), 1379–1387, 2004.
37. A. Arias, G. Asher, M. Sumner, et al., High frequency voltage injection for the sensorless control of permanent magnet synchronous motors using matrix converters, *IEEE Industrial Electronics Conference (IEEE Cat. No. 04CH37609)*, pp. 969–974, 2004.
38. Y.-S. Jeong, R. D. Lorenz, T. M. Jahns et al., Initial rotor position estimation of an interior permanent-magnet synchronous machine using carrier-frequency injection methods, *IEEE Transactions on Industry Applications*, 41(1), 38–45, 2005.
39. C. S. Staines, C. Caruana, N. Teske et al., Sensorless speed, position and torque control using AC machine saliencies, *International Electric Machines and Drives Conference (IEEE Cat. No. 05EX1023C)*, pp. 1392–1399, 2005.
40. J. Holtz, Initial rotor polarity detection and sensorless control of PM synchronous machines, *Conference Record, IEEE Industry Applications (IEEE Cat. No. 06CH37801)*, pp. 2040–2047, 2006.
41. J. Holtz, Acquisition of position error and magnet polarity for sensorless control of PM synchronous machines, *IEEE Transactions on Industry Applications*, 44(4), 1172–1180, 2008.

Machine-Related Issues

42. N. Bianchi, and S. Bolognani, Influence of rotor geometry of an IPM motor on sensorless control feasibility, *IEEE Transactions on Industry Applications*, 43(1), 87–96, 2007.
43. N. Imai, S. Morimoto, M. Sanada, et al., Influence of magnetic saturation on sensorless control for interior permanent-magnet synchronous motors with concentrated windings, *IEEE Transactions on Industry Applications*, 42(5), 1193–1200, 2006.
44. N. Imai, S. Morimoto, M. Sanada, et al., Influence of rotor configuration on sensorless control for permanent-magnet synchronous motors, *IEEE Transactions on Industry Applications*, 44(1), 93–100, 2008.
45. N. Bianchi, S. Bolognani, J. Ji-Hoon, et al., Comparison of PM motor structures and sensorless control techniques for zero-speed rotor position detection, *IEEE Transactions on Power Electronics*, 22(6), 2466–2475, 2007.

Other Approaches

46. T. Song, M. F. Rahman, K. W. Lim, et al., A singular perturbation approach to sensorless control of a permanent magnet synchronous motor drive, *IEEE Transactions on Energy Conversion*, 14(4), 1359–1365, 1999.

47. A. Consoli, G. Scarella, and A. Testa, Industry application of zero-speed sensorless control techniques for PM synchronous motors, *IEEE Transactions on Industry Applications*, 37(2), 513–521, 2001.
48. D. Howe, J. X. Shen, and Z. Q. Zhu, Improved speed estimation in sensorless PM brushless AC drives, *IEEE Transactions on Industry Applications*, 38(4), 1072–1080, 2002.
49. F. Blaabjerg, J. K. Pedersen, P. Thogersen, et al., A sensorless, stable V/f control method for permanent-magnet synchronous motor drives, *IEEE Transactions on Industry Applications*, 39(3), 783–791, 2003.
50. T. Preuber, Sensorless INFORM-control of permanent magnet synchronous machines, *EPE Journal*, 13(3), 19–21, 2003.
51. Y. S. Kim, Y. K. Choi, and J. H. Lee, Speed-sensorless vector control for permanent-magnet synchronous motors based on instantaneous reactive power in the wide-speed region, *IEE Proceedings-Electric Power Applications*, 152(5), 1343–1349, 2005.
52. S. Ichikawa, M. Tomita, S. Doki, et al., Sensorless control of permanent-magnet synchronous motors using online parameter identification based on system identification theory, *IEEE Transactions on Industrial Electronics*, 53(2), 363–372, 2006.
53. S. Jul-Ki, L. Jong-Kun, and L. Dong-Choon, Sensorless speed control of nonsalient permanent-magnet synchronous motor using rotor-position-tracking PI controller, *IEEE Transactions on Industrial Electronics*, 53(2), 399–405, 2006.

Part III

Permanent Magnet Brushless DC Machines and Their Control

9 PM Brushless DC Machine

PMSMs having the trapezoidal-induced emf are known as the PM brushless dc machines (PMBDCM). The advantage of such a machine in comparison to that of the PMSM has been discussed in Chapter 1. The main reason for the popularity of these machines over its counterpart is because of its control simplicity. To initiate the onset and commutation of current in the phase of a machine, the beginning and end of the constant flat portion of the induced emf have to be tracked. That amounts to only six discrete positions for a three-phase machine in each of the electrical cycle. These signals could easily be generated using three Hall sensors displaced from each other by 120 electrical degrees. The Hall sensors are mounted facing a small magnet wheel fixed to the rotor having the same number of poles as in the rotor of the PMBDCM or the extra magnet wheel may be dispensed with by extending the rotor beyond the stack length of the stator and use the rotor magnets to provide the position information. Such an arrangement tracks the absolute position of the rotor magnets and hence the shape and position of the induced emfs in all the machine phases. In contrast to the PMSM, which requires continuous and instantaneous absolute rotor position, the PMBDCM position feedback requirement is much simpler as it requires only six discrete absolute positions for a three-phase machine, resulting in a major cost saving in the feedback sensor. Further the control involves significant vector operations in the PMSM drive whereas such operations are not required for operation of the PMBDCM drive.

The dynamic modeling of PM brushless dc motor with its control scheme is considered in this chapter. Simulation and analysis follow dynamic modeling. A sample MATLAB® code for dynamic simulation is given for illustration of dynamic drive performance of the system. Some references on modeling and control [1–20], simulation [21–25], and performance and improvement [26–33] of the motor drive system are included.

9.1 MODELING OF PM BRUSHLESS DC MOTOR

The flux distribution in PM brushless dc motor is trapezoidal and therefore the d-q rotor reference frames model developed for the PM synchronous motor is not applicable. Given the nonsinusoidal flux distribution, it is prudent to derive a model of the PMBDCM in phase variables. The derivation of this model is based [17a] on the assumptions that the induced currents in the rotor due to stator harmonic fields are neglected and iron and stray losses are also neglected. Damper windings are not usually a part of the PMBDCM and damping is provided by the inverter control. The motor is considered to have three phases even though for any number of phases the derivation procedure is valid.

The coupled circuit equations of the stator windings in terms of motor electrical constants are

$$\begin{bmatrix} v_{as} \\ v_{bs} \\ v_{cs} \end{bmatrix} = \begin{bmatrix} R_s & 0 & 0 \\ 0 & R_s & 0 \\ 0 & 0 & R_s \end{bmatrix} \begin{bmatrix} i_{as} \\ i_{bs} \\ i_{cs} \end{bmatrix} + p \begin{bmatrix} L_{aa} & L_{ab} & L_{ac} \\ L_{ba} & L_{bb} & L_{bc} \\ L_{ca} & L_{cb} & L_{cc} \end{bmatrix} \begin{bmatrix} i_a \\ i_b \\ i_c \end{bmatrix} + \begin{bmatrix} e_{as} \\ e_{bs} \\ e_{cs} \end{bmatrix} \quad (9.1)$$

where R_s is the stator resistance per phase and it is assumed to be equal for all three phases. The induced emfs e_{as} , e_{bs} , and e_{cs} are all assumed to be trapezoidal. E_p is the peak value derived as

$$E_p = (Blv)N = N(Blr\omega_m) = N\phi_a\omega_m = \lambda_p\omega_m \quad (9.2)$$

where

N is the number of conductors in series per phase

v is the velocity, m/s

l is the length of the conductor, m

r is the radius of the rotor bore, m

ω_m is the angular velocity, rad/s

B is the flux density of the field in which the conductors are placed

This flux density is solely due to the rotor magnets. The product (Blr), which is ϕ_a , has the dimensions of flux and is directly proportional to the air gap flux, ϕ_g , as

$$\phi_a = Blr = \frac{1}{\pi} B \pi l r = \frac{1}{\pi} \phi_g \quad (9.3)$$

Note that the product of flux and number of conductors in series has the dimension of flux linkages and denoted by λ_p . Since this is only proportional to phase a flux linkages by a factor of $1/\pi$, it is hereafter referred to as modified flux linkages.

If there is no change in the rotor reluctance with angle, and assuming symmetric three phases, the self-inductances of all phases are equal and the mutual inductance between phases are equal to one another and they are denoted as

$$L_{aa} = L_{bb} = L_{cc} = L \quad \text{and} \quad L_{ab} = L_{ba} = L_{ac} = L_{ca} = L_{bc} = L_{cb} = M, H \quad (9.4)$$

Substituting Equations 9.3 and 9.4 in Equation 9.1, the PMBDCM model is obtained as

$$\begin{bmatrix} v_{as} \\ v_{bs} \\ v_{cs} \end{bmatrix} = R_s \begin{bmatrix} 1 & 0 & 0 \\ 0 & 1 & 0 \\ 0 & 0 & 1 \end{bmatrix} \begin{bmatrix} i_{as} \\ i_{bs} \\ i_{cs} \end{bmatrix} + \begin{bmatrix} L & M & M \\ M & L & M \\ M & M & L \end{bmatrix} p \begin{bmatrix} i_a \\ i_b \\ i_c \end{bmatrix} + \begin{bmatrix} e_{as} \\ e_{bs} \\ e_{cs} \end{bmatrix} \quad (9.5)$$

The stator phase currents are constrained to be balanced, i.e., $i_{as} + i_{bs} + i_{cs} = 0$, which leads to the simplification of inductance matrix in the model as

$$\begin{bmatrix} v_{as} \\ v_{bs} \\ v_{cs} \end{bmatrix} = \begin{bmatrix} R_s & 0 & 0 \\ 0 & R_s & 0 \\ 0 & 0 & R_s \end{bmatrix} \begin{bmatrix} i_{as} \\ i_{bs} \\ i_{cs} \end{bmatrix} + \begin{bmatrix} (L-M) & 0 & 0 \\ 0 & (L-M) & 0 \\ 0 & 0 & (L-M) \end{bmatrix} p \begin{bmatrix} i_a \\ i_b \\ i_c \end{bmatrix} + \begin{bmatrix} e_{as} \\ e_{bs} \\ e_{cs} \end{bmatrix} \quad (9.6)$$

It is observed that the phase voltage equation is identical to that of the armature voltage equation of a dc machine. Resemblance to a dc machine and having no brushes and commutator are the reasons behind the machine being called a PM brushless dc machine in industrial circles.

The electromagnetic torque is given by

$$T_e = [e_{as}i_{as} + e_{bs}i_{bs} + e_{cs}i_{cs}] \frac{1}{\omega_m} \text{ (N} \cdot \text{m)} \quad (9.7)$$

The instantaneous-induced emfs can be written as

$$e_{as} = f_{as}(\theta_r)\lambda_p\omega_m \quad (9.8)$$

$$e_{bs} = f_{bs}(\theta_r)\lambda_p\omega_m \quad (9.9)$$

$$e_{cs} = f_{cs}(\theta_r)\lambda_p\omega_m \quad (9.10)$$

where the functions $f_{as}(\theta_r)$, $f_{bs}(\theta_r)$, and $f_{cs}(\theta_r)$ have the same shape as e_{as} , e_{bs} , and e_{cs} with a maximum magnitude of ± 1 . The induced emfs do not have sharp corners as shown in trapezoidal functions but have rounded edges. It is because the emfs are the derivatives of the flux linkages and the flux linkages are continuous functions and fringing also makes the flux density functions smooth with no abrupt edges. The electromagnetic torque can be written as

$$T_e = \lambda_p [f_{as}(\theta_r)i_{as} + f_{bs}(\theta_r)i_{bs} + f_{cs}(\theta_r)i_{cs}] \text{ (N} \cdot \text{m)} \quad (9.11)$$

The equation of motion for a simple system with inertia J , friction coefficient B , and load torque T_l is

$$J \frac{d\omega_m}{dt} + B\omega_m = (T_e - T_l) \quad (9.12)$$

and electrical rotor speed and position are related by

$$\frac{d\theta_r}{dt} = \frac{P}{2}\omega_m \quad (9.13)$$

where

P is the number of poles

ω_m is the rotor speed in mechanical rad/s

θ_r is the rotor position in rad

Combining all the relevant equations, the system is cast in state space form as

$$\dot{x} = Ax + Bu \quad (9.14)$$

where

$$x = [i_{as} \ i_{bs} \ i_{cs} \ \omega_m \ \theta_r]^t \quad (9.15)$$

$$A = \begin{bmatrix} -\frac{R_s}{L_l} & 0 & 0 & -\frac{\lambda_p}{L_l} f_{as}(\theta_r) & 0 \\ 0 & -\frac{R_s}{L_l} & 0 & -\frac{\lambda_p}{L_l} f_{bs}(\theta_r) & 0 \\ 0 & 0 & -\frac{R_s}{L_l} & -\frac{\lambda_p}{L_l} f_{cs}(\theta_r) & 0 \\ \frac{\lambda_p}{J} f_{as}(\theta_r) & \frac{\lambda_p}{J} f_{bs}(\theta_r) & \frac{\lambda_p}{J} f_{cs}(\theta_r) & -B/J & 0 \\ 0 & 0 & 0 & \frac{P}{2} & 0 \end{bmatrix} \quad (9.16)$$

$$B = \begin{bmatrix} \frac{1}{L_l} & 0 & 0 & 0 \\ 0 & \frac{1}{L_l} & 0 & 0 \\ 0 & 0 & \frac{1}{L_l} & 0 \\ 0 & 0 & 0 & -\frac{1}{J} \\ 0 & 0 & 0 & 0 \end{bmatrix} \quad (9.17)$$

$$L_l = L - M \quad (9.18)$$

$$u = [v_{as} \ v_{bs} \ v_{cs} \ T_l]^t \quad (9.19)$$

The state variable θ_r , rotor position, is required so as to have the functions $f_{as}(\theta_r)$, $f_{bs}(\theta_r)$, and $f_{cs}(\theta_r)$, which can be realized from a stored table. This completes the modeling of the PMBDCM.

9.2 NORMALIZED SYSTEM EQUATIONS

The equations of the PMBDCM can be normalized using base voltage V_b , base current I_b , base flux linkages λ_b , base power P_b , and base frequency ω_b . Considering only phase a for normalization, it is achieved as follows [17a]:

$$v_{\text{asn}} = \frac{v_{\text{as}}}{V_b} = \frac{1}{V_b} \left[Ri_{\text{as}} + (L - M)p i_{\text{as}} + \lambda_p \omega_m f_{\text{as}}(\theta_r) \right] \quad (9.20)$$

but the base voltage can be written as

$$V_b = I_b \cdot Z_b = \lambda_b \cdot \omega_b \quad (9.21)$$

Substituting this in the voltage equation, the phase a normalized voltage expression is obtained as

$$v_{\text{asn}} = R_{\text{an}} i_{\text{asn}} + (X_{\text{Ln}} - X_{\text{Mn}}) \frac{P}{\omega_b} i_{\text{asn}} + \lambda_n \omega_{\text{mn}} f_{\text{as}}(\theta_r) \quad (9.22)$$

where

$$R_{\text{an}} = \frac{R}{Z_b} \quad (\text{p.u.}) \quad (9.23)$$

$$X_{\text{Ln}} = \frac{\omega_b L}{Z_b} \quad (\text{p.u.}) \quad (9.24)$$

$$X_{\text{Mn}} = \frac{\omega_b M}{Z_b} \quad (\text{p.u.}) \quad (9.25)$$

$$\lambda_n = \frac{\lambda_p}{\lambda_b} \quad (\text{p.u.}) \quad (9.26)$$

$$\omega_{\text{mn}} = \frac{\omega_m}{\omega_b} \quad (\text{p.u.}) \quad (9.27)$$

$$T_{\text{eb}} = 2\lambda_b I_b \quad (\text{N} \cdot \text{m}) \quad (9.28)$$

$$Z_b = \frac{V_b}{I_b} \quad (\Omega) \quad (9.29)$$

Similarly the other two-phase equations can be derived. The electromechanical equation is derived as

$$T_e = T_l + B\omega_m + J \frac{d\omega_m}{dt} \quad (9.30)$$

and in normalized form the electromagnetic torque is given as

$$T_{\text{en}} = \frac{T_e}{T_b} = T_{\text{en}} + B_n \omega_{\text{mn}} + 2H_p \omega_{\text{mn}} \quad (9.31)$$

where

$$T_{\text{en}} = \frac{T_e}{T_b} \quad (\text{p.u.}) \quad (9.32)$$

$$B_n = \frac{B\omega_b^2}{P_b} \quad (\text{p.u.}) \quad (9.33)$$

$$H = \frac{1}{2} \frac{J\omega_b^2}{P_b (P/2)^2} \quad (\text{s}) \quad (9.34)$$

The electromagnetic torque in terms of the flux linkages and motor currents is derived as

$$T_e = \frac{e_{as}i_{as} + e_{bs}i_{bs} + e_{cs}i_{cs}}{\omega_m} = \lambda_p [i_{as}f_{as}(\theta_r) + i_{bs}f_{bs}(\theta_r) + i_{cs}f_{cs}(\theta_r)] \quad (9.35)$$

and in normalized units it is given as

$$T_{\text{en}} = \frac{1}{2} \lambda_n [i_{asn}f_{as}(\theta_r) + i_{bsn}f_{bs}(\theta_r) + i_{csn}f_{cs}(\theta_r)] \quad (\text{p.u.}) \quad (9.36)$$

9.3 THE PMBDCM DRIVE SCHEME

For constant torque operation below the base speed, this drive requires information on six discrete positions. They correspond to every 60 electrical degrees for energizing the three stator phases.

The control of this drive system was briefly discussed in Section 1.4.5. It is strongly recommended to review it with reference to Figure 1.35 before reading this section.

The flux weakening is slightly different for this motor and is discussed later. The control scheme for the PMBDM drive is simple and is shown in Figure 9.1. The resolver gives absolute rotor position and it is converted into rotor speed through the signal processor. The rotor speed is compared to its reference and the rotor speed error is amplified through the speed controller. The output of the speed controller provides the reference torque, T_e^* . The current magnitude command, I_p^* , is obtained from the torque expression as

$$T_e^* = \lambda_p [f_{as}(\theta_r)i_{as}^* + f_{bs}(\theta_r)i_{bs}^* + f_{cs}(\theta_r)i_{cs}^*] \quad (9.37)$$

As only two machine phases conduct current at any time with the two phases being in series for a full wave inverter operation, the phase currents are equal in magnitude but opposite in sign. The rotor position-dependent functions have the same signs as the stator phase currents in the motoring mode and have opposite signs to

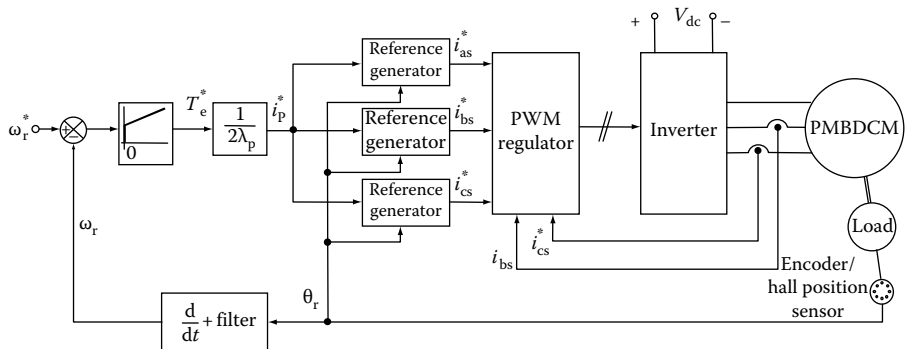


FIGURE 9.1 Speed-controlled PMBDM drive scheme without flux weakening. (From Krishnan, R., *Electric Motor Drives*, Figure 9.49, Prentice Hall, Upper Saddle River, NJ, 2001. With permission.)

the currents in regeneration. The result of such sign relationships is the simplification of torque command as

$$T_e^* = 2\lambda_p I_p^* \quad (9.38)$$

The stator current command is derived from Equation 9.37 as

$$I_p^* = \frac{T_e^*}{2\lambda_p} \quad (9.39)$$

The individual stator phase current commands are generated from the current magnitude command and absolute rotor position. These current commands are amplified through the inverter by comparing them with their respective currents in the stator phases. Only two phase currents are necessary in the balanced three-phase system to obtain the third phase current since the sum of all the three phase currents is zero.

The current errors are amplified and used with pulse width modulation or hysteresis logic to produce the switching logic signals for the inverter switches, as explained in Chapter 2.

9.4 DYNAMIC SIMULATION

The simulation results for a step speed reference input of 0–1 p.u. are shown in Figure 9.2 for the PWM current controllers. The rotor is at standstill at time zero. With the onset of speed reference, the speed error and torque reference attain a maximum value, which is limited to 2.0 p.u. in this case. The current is made to follow the reference by the current controller. Because of this, the electromagnetic torque follows its reference very closely. The torque ripples are due to current ripples produced by the switching. The PWM control considered in this case is operating at 4 kHz and the current controller has an amplification of 100. Also

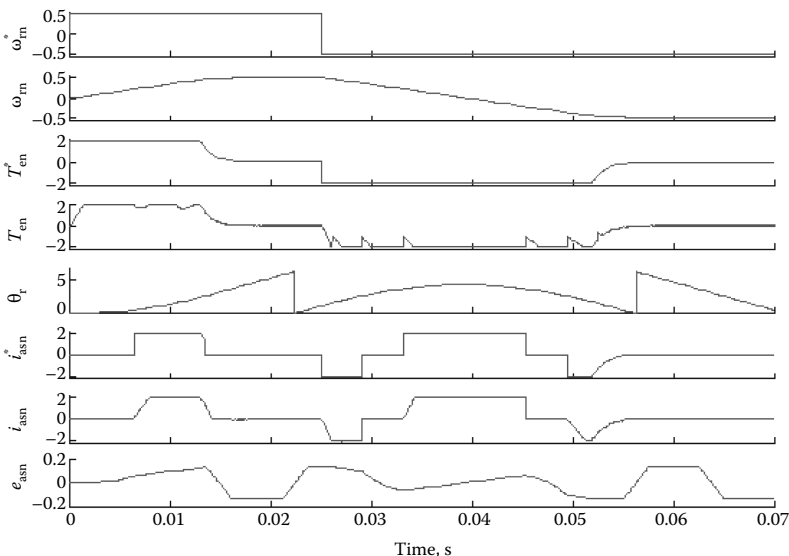


FIGURE 9.2 PMBDC speed drive with full-wave converter.

the MATLAB codes for the simulation of the speed-controlled drive systems are given below. The torque drive can be simulated by setting the actual speed to be constant and setting a reference constant torque value.

```
%*****
% PMBDC speed control using pwm current controller
% 12-10-98 by B.S. Lee and R. Krishnan
%*****

clear all;close all;
global phase rs ls_lm vas vbs vcs eas ebs ecs
global inertia b_fric pole te tl

% PMBDC motor parameter
% p_hp[HP], rs[Ohm], ls[H], lm[H]
% kb[V/rad/sec(elec)], lamda_p[V/rad/sec(mech), N-m/A]
% inertia[Kg-m&cap;2], b_fric[N-m/rad/sec]

rs = 0.7; ls_lm = 5.21e-3; inertia = 0.00022; b_fric = 0;
p_hp = 1; pole = 4; vdc = 160; kb = 0.05238; lamda_p =
kb*(pole/2);
ip_rate = 8.5; te_rate = 1.7809; wbase_rpm = 4000;

% base values
pbase = p_hp*746;
vbase = vdc;
ibase = ip_rate;
```

```
tbase = te_rate;
wbase = wbase_rpm*(pi/30)*(pole/2);

% setting the initial conditions

% initial stator current
ias = 0; ibs = 0; ics = 0;

% rotor speed and position
wrthr = zeros(2,1);
wr = wrthr(1,1);
thr = wrthr(2,1);

% old initial position
thr_old = thr;
wr_cmd = 0; % speed command
kp_w = 0.1; ki_w = 0.001; % pi speed controller gains

% wr_intg = integrator, _cmd = after limit, _star = before
% limit
wr_intg = 0; te_cmd = 0; te_star = 0;

% torque limit => up to 2 [p.u.]
te_lim_p = 2*te_rate; te_lim_n = -2*te_rate;

tl = 0; % load torque
kp_i = 100; % p current controller gain

% controller output
vasc = 0; vbsc = 0; vcsc = 0;

% triangular wave frequency and peak voltage
ftr = 4000; vtr_r = 10;

% voltage command limit
vc_lim_p = 9; vc_lim_n = -9;

% initial time, time increment, and final time

tt = 0; dt = 10e-6; tf = 0.07001;

% variables for plotting

count = 0;
no_int = 0;
no_ds = fix(tf/dt/(no_int+1));
p_vabcs = zeros(no_ds,3);
p_fabcs = zeros(no_ds,3);
```

```

p_eabcs = zeros(no_ds,3);
p_isc = zeros(no_ds,4);
p_iabcs = zeros(no_ds,3);
p_torq = zeros(no_ds,5);
p_wrthr = zeros(no_ds,4);
p_t = zeros(no_ds,1);

% solving the dynamics of motor

iter = 0;
iter1 = 0;

while (tt<=tf)

    % speed command
    if ((tt>0)&(tt<=0.025))
        wr_cmd = 0.5*wbase;
    elseif ((tt>0.025)&(tt<=0.07))
        wr_cmd = -0.5*wbase;
    end

    % compute torque command using pi with anti-windup reset
    wr_err = wr_cmd-wr;

    wr_intg = wr_intg+ki_w*(wr_err+te_cmd-te_star)*dt;
    te_star = wr_intg+kp_w*wr_err;

    if (te_star>=te_lim_p)
        te_cmd = te_lim_p;
    elseif (te_star<=te_lim_n)
        te_cmd = te_lim_n;
    else
        te_cmd = te_star;
    end

    % compute peak current command
    ip_cmd = te_cmd/(2*lamda_p);

    % conversion of the unit of thr : rad => deg
    thr_deg = thr*180/pi;

    % adjust the range of th_deg (0<=th_deg<=360)
    while ( (thr_deg<0) | (thr_deg>360) )
        if (thr_deg<0)
            thr_deg = thr_deg+360;
        elseif (thr_deg>360)
            thr_deg = thr_deg-360;
        end
    end
end

```

```
% phase current command according to the rotor position
if (((thr_deg>=0)&(thr_deg<30))|((thr_deg>=330)&(thr_
deg<=360)))
    mode = 1;
    ias_cmd = 0;
    ibs_cmd = -ip_cmd;
    ics_cmd = ip_cmd;
elseif ((thr_deg>=30)&(thr_deg<90))
    mode = 2;
    ias_cmd = ip_cmd;
    ibs_cmd = -ip_cmd;
    ics_cmd = 0;
elseif ((thr_deg>=90)&(thr_deg<150))
    mode = 3;
    ias_cmd = ip_cmd;
    ibs_cmd = 0;
    ics_cmd = -ip_cmd;
elseif ((thr_deg>=150)&(thr_deg<210))
    mode = 4;
    ias_cmd = 0;
    ibs_cmd = ip_cmd;
    ics_cmd = -ip_cmd;
elseif ((thr_deg>=210)&(thr_deg<270))
    mode = 5;
    ias_cmd = -ip_cmd;
    ibs_cmd = ip_cmd;
    ics_cmd = 0;
elseif ((thr_deg>=270)&(thr_deg<330))
    mode = 6;
    ias_cmd = -ip_cmd;
    ibs_cmd = 0;
    ics_cmd = ip_cmd;
end

% fas(thr): rotor position dependent function
if ((thr_deg>=0)&(thr_deg<30))
    fas_thr = thr_deg/30;
elseif ((thr_deg>=30)&(thr_deg<150) )
    fas_thr = 1;
elseif ((thr_deg>=150)&(thr_deg<210) )
    fas_thr = -thr_deg/30+6;
elseif ((thr_deg>=210)&(thr_deg<330) )
    fas_thr = -1;
elseif ((thr_deg>=330)&(thr_deg<=360) )
    fas_thr = thr_deg/30-12;
end

% fbs(thr): rotor position dependent function
if ((thr_deg>=0)&(thr_deg<90) )
    fbs_thr = -1;
```

```

elseif ((thr_deg>=90)&(thr_deg<150))
  fbs_thr = thr_deg/30-4;
elseif ((thr_deg>=150)&(thr_deg<270))
  fbs_thr = 1;
elseif ((thr_deg>=270)&(thr_deg<330))
  fbs_thr = -thr_deg/30+10;
elseif ((thr_deg>=330)&(thr_deg<=360))
  fbs_thr = -1;
end

% fcs(thr): rotor position dependent function
if ((thr_deg>=0)&(thr_deg<30))
  fcs_thr = 1;
elseif ((thr_deg>=30)&(thr_deg<90))
  fcs_thr = -thr_deg/30+2;
elseif ((thr_deg>=90)&(thr_deg<210))
  fcs_thr = -1;
elseif ((thr_deg>=210)&(thr_deg<270))
  fcs_thr = thr_deg/30-8;
elseif ((thr_deg>=270)&(thr_deg<=360))
  fcs_thr = 1;
end

% compute back emf
eas = fas_thr*kb*wr;
ebs = fbs_thr*kb*wr;
ecs = fcs_thr*kb*wr;

% triangular carrier wave
vtr = rem(4*ftr*vtr_r*tt,4*vtr_r);

if (vtr<vtr_r)
  vtr = vtr;
elseif (vtr<(3*vtr_r) )
  vtr = 2*vtr_r-vtr;
else
  vtr = vtr-4*vtr_r;
end

% compute position difference
del_thr = thr-thr_old;
thr_old = thr;

% compute A phase control voltage : p control or
freewheeling
if ((mode~=1)&(mode~=4))
  ias_det = 1;
  vasc = kp_i*(ias_cmd-ias);
  if (vasc>vc_lim_p)
    vasc = vc_lim_p;

```

```
elseif (vasc<vc_lim_n)
    vasc = vc_lim_n;
end
if (vasc>=vtr)
    vas = vdc/2;
else
    vas = -vdc/2;
end
elseif (((del_thr<0)&(mode==1)) | ((del_thr>=0)&(mode==4)))
if (ias<=0)
    ias_det = 0;
    ias = 0;
    vas = eas;
else
    ias_det = 1;
    vas = -vdc/2;
end
elseif (((del_thr>=0)&(mode==1)) | ((del_thr<0)&(mode==4)))
if (ias>=0)
    ias_det = 0;
    ias = 0;
    vas = eas;
else
    ias_det = 1;
    vas = vdc/2;
end
end

% compute B phase control voltage : p control or
freewheeling
if ((mode~=3)&(mode~=6))
    ibs_det = 1;
    vbsc = kp_i*(ibs_cmd-ibs);
    if (vbsc>vc_lim_p)
        vbsc = vc_lim_p;
    elseif (vbsc<vc_lim_n)
        vbsc = vc_lim_n;
    end
    if (vbsc>=vtr)
        vbs = vdc/2;
    else
        vbs = -vdc/2;
    end
elseif (((del_thr<0)&(mode==3)) | ((del_thr>=0)&(mode==6)))
if (ibs<=0)
    ibs_det = 0; ibs = 0; vbs = ebs;
else
    ibs_det = 1;
    vbs = -vdc/2;
end
```

```

elseif (((del_thr>=0)&(mode==3)) | ((del_thr<0)&(mode==6)))
if (ibs>=0)
    ibs_det = 0; ibs = 0; vbs = ebs;
else
    ibs_det = 1;
    vbs = vdc/2;
end
end

% compute C phase control voltage : p control or
freewheeling
if ((mode~=5)&(mode~=2))
    ics_det = 1;
    vcsc = kp_i*(ics_cmd-ics);
    if (vcsc>vc_lim_p)
        vcsc = vc_lim_p;
    elseif (vcsc<vc_lim_n)
        vcsc = vc_lim_n;
    end
    if (vcsc>=vtr)
        vcs = vdc/2;
    else
        vcs = -vdc/2;
    end
elseif (((del_thr<0)&(mode==5)) | ((del_thr>=0)&(mode==2)))
if (ics<=0)
    ics_det = 0;
    ics = 0;
    vcs = ecs;
else
    ics_det = 1;
    vcs = -vdc/2;
end
elseif (((del_thr>=0)&(mode==5)) | ((del_thr<0)&(mode==2)))
if (ics>=0)
    ics_det = 0;
    ics = 0;
    vcs = ecs;
else
    ics_det = 1;
    vcs = vdc/2;
end
end

% runge-kutta 4th order method to find ias
if (ias_det==1)
    phase = 1;
    grad_1 = seq_iabcs(tt,ias);
    grad_2 = seq_iabcs(tt+dt/2,ias+dt*grad_1/2);

```

```

grad_3 = seq_iabcs(tt+dt/2,ias+dt*grad_2/2);
grad_4 = seq_iabcs(tt+dt,ias+dt*grad_3);
ias = ias+(grad_1+2*grad_2+2*grad_3+grad_4)*dt/6;
end
% runge-kutta 4th order method to find ibs
if (ibs_det==1)
    phase = 2;
    grad_1 = seq_iabcs(tt,ibs);
    grad_2 = seq_iabcs(tt+dt/2,ibs+dt*grad_1/2);
    grad_3 = seq_iabcs(tt+dt/2,ibs+dt*grad_2/2);
    grad_4 = seq_iabcs(tt+dt,ibs+dt*grad_3);
    ibs = ibs+(grad_1+2*grad_2+2*grad_3+grad_4)*dt/6;
end
% runge-kutta 4th order method to find ics
if (ics_det==1)
    phase = 3;
    grad_1 = seq_iabcs(tt,ics);
    grad_2 = seq_iabcs(tt+dt/2,ics+dt*grad_1/2);
    grad_3 = seq_iabcs(tt+dt/2,ics+dt*grad_2/2);
    grad_4 = seq_iabcs(tt+dt,ics+dt*grad_3);
    ics = ics+(grad_1+2*grad_2+2*grad_3+grad_4)*dt/6;
end

% compute electromagnetic torque
tas = (pole/2)*kb*fas_thr*ias;
tbs = (pole/2)*kb*fbs_thr*ibs;
tcs = (pole/2)*kb*fcs_thr*ics;
te = tas+tbs+tcs;

% runge-kutta 4th order method to find [wr thr]
slope_1 = seq_wrthr(tt,wrthr);
slope_2 = seq_wrthr(tt+dt/2,wrthr+dt*slope_1/2);
slope_3 = seq_wrthr(tt+dt/2,wrthr+dt*slope_2/2);
slope_4 = seq_wrthr(tt+dt,wrthr+dt*slope_3);
wrthr = wrthr+(slope_1+2*slope_2+2*slope_3+slope_4)*dt/6;

wr = wrthr(1,1);
thr = wrthr(2,1);

% save some variables
if (iter==no_int)
    iter = 0;
    count = count+1;
    p_vabcs(count,:) = [vas vbs vcs];
    p_fabcs(count,:) = [fas_thr fbs_thr fcs_thr];
    p_eabcs(count,:) = [eas ebs ecs];
    p_isc(count,:) = [ias_cmd ibs_cmd ics_cmd ip_cmd];
    p_iabcs(count,:) = [ias ibs ics];
    p_torq(count,:) = [te_cmd te tas tbs tcs];

```

```

p_wrthr(count,:) = [wr thr thr_deg wr_cmd];
p_t(count,:) = tt;

else
    iter = iter+1;
end

if (iter1==1000)
    iter1 = 0; tt
else
    iter1 = iter1+1;
end

% time is increased by dt
tt = tt+dt;
end

% plot the graph
subplot(8,1,1); plot(p_t,p_wrthr(:,4)/wbase); ylabel('omega_r_n
&cap;');
grid off; box off; axis([0 tf -0.6 0.6])
set(gca,'XTick',0:0.01:0.07); set(gca,'XTickLabel',{})
subplot(8,1,2); plot(p_t,p_wrthr(:,1)/wbase);
ylabel('omega_r_n'); grid off; box off; axis([0 tf -0.6
0.6])
set(gca,'XTick',0:0.01:0.07); set(gca,'XTickLabel',{})
subplot(8,1,3); plot(p_t,p_torque(:,1)/tbase);
ylabel('T_e_n&cap;');
grid off; box off; axis([0 tf
-2.2 2.2])
set(gca,'XTick',0:0.01:0.07); set(gca,'XTickLabel',{})
subplot(8,1,4); plot(p_t,p_torque(:,2)/tbase); ylabel('T_e_n');
grid off; box off; axis([0 tf -2.2 2.2])
set(gca,'XTick',0:0.01:0.07); set(gca,'XTickLabel',{})
subplot(8,1,5); plot(p_t,p_wrthr(:,3)*pi/180); ylabel('theta_
r');
grid off; box off; axis([0 tf 0 7])
set(gca,'XTick',0:0.01:0.07); set(gca,'XTickLabel',{})
subplot(8,1,6); plot(p_t,p_isc(:,1)/
ibase); ylabel('i_a_s_n&cap;');
grid off; box off; axis([0
tf -2.2 2.2])
set(gca,'XTick',0:0.01:0.07); set(gca,'XTickLabel',{})
subplot(8,1,7); plot(p_t,p_iabcs(:,1)/ibase);
ylabel('i_a_s_n'); grid off; box off; axis([0 tf -2.2 2.2])
set(gca,'XTick',0:0.01:0.07); set(gca,'XTickLabel',{})
subplot(8,1,8); plot(p_t,p_eabcs(:,1)/vbase);
ylabel('e_a_s_n'); grid off; box off; axis([0 tf -0.2 0.2])
set(gca,'XTick',0:0.01:0.07); set(gca,'XTickLabel',{})
set(gca,'XTickLabel',{ '0', '0.01', '0.02', '0.03', '0.04', '0.05', '0.06', '0.07' });
xlabel('Time, sec')

```

REFERENCES

Modeling and Control

1. R. Hanitsch and A. Meyna, Digital control for brushless DC motors, *Elektrotechnische Zeitschrift ETZ A*, 97(4), 204–211, 1976.
2. N. A. Demerdash and T. W. Nehl, Dynamic modeling of brushless DC motor-power conditioner unit for electromechanical actuator application, *IEEE Power Electronics Specialists Conference*, pp. 333–343, 1979.
3. D. B. Rezine and M. Lajoie-Mazenc, Modelling of a brushless DC motor with solid parts involving eddy currents, *Conference Record of the IEEE Industry Applications Society*, pp. 488–493, 1983.
4. S. Bolognani and G. S. Buja, Modeling and dynamic characteristics of a permanent magnet brushless DC motor drive with current inverter, *Proceedings of the IASTED International Symposium Robotics and Automation*, pp. 197–201, 1985.
5. P. F. Muir and C. P. Neuman, Pulsewidth modulation control of brushless DC motors for robotic applications, *IEEE Transactions on Industrial Electronics*, IE-32(3), 222–229, 1985.
6. T. M. Hijazi and N. A. Demerdash, Computer-aided modeling and experimental verification of the performance of power conditioner operated permanent magnet brushless DC motors including rotor damping effects, *IEEE Transactions on Energy Conversion*, 3(3), 714–721, 1988.
7. G. Carrara, D. Casini, A. Landi, et al., Brushless DC servomotor switching strategies, *Proceedings of the Seventeenth IASTED International Symposium. Simulation and Modelling*, pp. 183–186, 1989.
8. J. S. Mayer and O. Wasynczuk, Analysis and modeling of a single-phase brushless DC motor drive system, *IEEE Transactions on Energy Conversion*, 4(3), 473–479, 1989.
9. P. Pillay and R. Krishnan, Modeling, simulation, and analysis of permanent-magnet motor drives. II. The brushless DC motor drive, *IEEE Transactions on Industry Applications*, pp. 274–279, 1989.
10. R. Krishnan and G.-H. Rim, Modeling, simulation, and analysis of variable-speed constant frequency power conversion scheme with a permanent magnet brushless dc generator, *IEEE Transactions on Industrial Electronics*, 37(4), 291–296, 1990.
11. S. D. Sudhoff and P. C. Krause, Average-value model of the brushless DC 120 deg inverter system, *IEEE Transactions on Energy Conversion*, 5(3), 553–557, 1990.
12. T. S. Low, K. J. Tseng, T. H. Lee, et al., Strategy for the instantaneous torque control of permanent-magnet brushless DC drives, *IEE Proceedings B (Electric Power Applications)*, 137(6), 355–363, 1990.
13. N. Hemati and M. C. Leu, A complete model characterization of brushless DC motors, *IEEE Transactions on Industry Applications*, 28(1), 172–180, 1992.
14. M. A. Alhamadi and N. A. Demerdash, Modeling and experimental verification of the performance of a skew mounted permanent magnet brushless DC motor drive with parameters computed from 3D-FE magnetic field solutions, *IEEE Transactions on Energy Conversion*, 9(1), 26–35, 1994.
15. S. -J. Kang and S. -K. Sul, Direct torque control of brushless DC motor with nonideal trapezoidal back EMF, *IEEE Transactions on Power Electronics*, 10(6), 796–802, 1995.
16. K. A. Corzine, S. D. Sudhoff, and H. J. Hegner, Analysis of a current-regulated brushless DC drive, *IEEE Transactions on Energy Conversion*, 10(3), 438–445, 1995.
17. P. L. Chapman, S. D. Sudhoff, and C. A. Whitcomb, Multiple reference frame analysis of non-sinusoidal brushless DC drives, *IEEE Transactions on Energy Conversion*, 14(3), 440–446, 1999.
- 17a. R. Krishnan, *Electric Motor Drives*, Prentice Hall, Upper Saddle River, NJ, 2001.

18. M. A. Jabbar, P. Hla Nu, L. Zhejie, et al., Modeling and numerical simulation of a brushless permanent-magnet DC motor in dynamic conditions by time-stepping technique, *IEEE Transactions on Industry Applications*, 40(3), 763–770, 2004.
19. L. Yong, Z. Q. Zhu, and D. Howe, Direct torque control of brushless DC drives with reduced torque ripple, *IEEE Transactions on Industry Applications*, 41(2), 599–608, 2005.
20. F. Rodriguez and A. Emadi, A novel digital control technique for brushless DC motor drives, *IEEE Transactions on Industrial Electronics*, 54(5), 2365–2373, 2007.

Simulation

21. T. W. Nehl, F. A. Fouad, N. A. Demerdash, et al., Dynamic simulation of radially oriented permanent magnet type electronically operated synchronous machines with parameters obtained from finite element field solutions, *IEEE Transactions on Industry Applications*, IA-18(2), 172–182, 1982.
22. A. Boglietti, M. Chiampi, and D. Chiarabaglio, Computer aided analysis of a DC brushless motor by means of a finite element technique, *Fourth International Conference on Electrical Machines and Drives (Conf. Publ. no. 310)*, pp. 38–42, 1989.
23. R. Krishnan, R. A. Bedingfield, A. S. Bharadwaj et al., Design and development of a user-friendly PC-based CAE software for the analysis of torque/speed/position controlled PM brushless DC motor drive system dynamics, *Conference Record, IEEE Industry Applications Society Annual Meeting (Cat. No. 91CH3077-5)*, pp. 1388–1394, 1991.
24. S. K. Safi, P. P. Acarnley, and A. G. Jack, Analysis and simulation of the high-speed torque performance of brushless DC motor drives, *IEE Proceedings: Electric Power Applications*, 142(3), 191–200, 1995.
25. G. K. Miti and A. C. Renfrew, Analysis, simulation and microprocessor implementation of a current profiling scheme for field-weakening applications and torque ripple control in brushless dc motors, *IEE Conference Publication*, no. 468, pp. 361–365, 1999.

Performance and Improvement

26. N. A. Demerdash, R. H. Miller, T. W. Nehl, et al., Comparison between features and performance characteristics of fifteen HP samarium cobalt and ferrite based brushless DC motors operated by same power conditioner, *IEEE Transactions on Power Apparatus and Systems*, PAS-102(1), 104–112, 1983.
27. P. Pillay and R. Krishnan, Investigation into the torque behavior of a brushless dc motor drive, *Conference Record—IEEE Industry Applications Society Annual Meeting*, pp. 201–208, 1988.
28. A. Fratta and A. Vagati, Synchronous vs. DC brushless servomotor: the machine behaviour, *IEEE Symposium on Electrical Drive, Cagliari, Italy*, pp. 53–60, 1987.
29. G. Henneberger, Dynamic behaviour and current control methods of brushless DC motors with different rotor designs, *3rd European Conference on Power Electronics and Applications*, pp. 1531–1536, 1989.
30. P. Pillay and R. Krishnan, Application characteristics of permanent magnet synchronous and brushless DC motors for servo drives, *IEEE Transactions on Industry Applications*, 27(5), 986–996, 1991.
31. C. S. Berendsen, G. Champenois, and A. Bolopion, Commutation strategies for brushless DC motors: influence on instant torque, *IEEE Transactions on Power Electronics*, 8(2), 231–236, 1993.
32. C. C. Chan, W. Xia, J. Z. Jiang, et al., Permanent magnet brushless drives, *IEEE Industry Applications Magazine*, 4(6), 16–22, 1998.
33. G. H. Jang and M. G. Kim, Optimal commutation of a BLDC motor by utilizing the symmetric terminal voltage, *IEEE Transactions on Magnetics*, 42(10), 3473–3475, 2006.

10 Commutation Torque Ripple and Phase Advancing

PM brushless dc machines with ideal trapezoidal induced emfs fed with rectangular currents of electrical 120° duration have a constant torque with no torque ripples. Deviation from ideal conditions introduces torque ripples [1–4] and mainly there are two kinds:

1. Current initiation and turn off in machine phases deviate from desired constant magnitude current commands produce commutation torques that are very significant in magnitude
2. Switching harmonics in the inverter output voltages generate harmonic currents which in turn result in switching harmonic torques

There are other kinds due to magnets and their assembly asymmetries, air gap eccentricity and cogging, to mention a few. The commutation torque is analyzed in this chapter for possible deviations in flux distribution and current commutation for given machine parameters and analytical results [3] are derived.

Flux weakening in PM brushless dc machines [5–8] is somewhat similar to that in the PMSMs by advancing the onset of currents. It is initiated when the machine-induced emf is equal or exceeds the maximum available machine phase voltage from the inverter output. In this mode, note that there is no instantaneous current control since current control is saturated as the induced emf of the machine phase exceeds or equals the maximum applied phase voltage from the inverter output. Then the only option is to have voltage control by advancing the onset of voltage when the induced emf is lower than the applied voltage. That happens when the trapezoidal induced emf is rising and falling from its flat or constant maximum value region. Then the current onset is advanced, resulting in phase advancing of the current. Here again analytical results are derived for conceptual understanding and for use in applications. Steady state predictions come from considering fundamental of the input currents of ideal trapezoidal waveforms and flux density distribution. But in reality the currents are responses to applied voltages and therefore they need to be evaluated to obtain the torque and should not be assumed, particularly in phase advancing mode. That requires dynamic model of the PMBDC machine and drive with provision to program desired voltage inputs so as to study the machine performance in the form of its instantaneous torque and currents for any set speed. The model of the motor drive to accomplish this is presented in this chapter. Note that the torque ripples are required to evaluate the suitability of a motor drive in specific applications and hence the need for its computation for all conditions including that of the current phase advancing mode.

10.1 COMMUTATION TORQUE RIPPLE

The desired current waveform is rectangular and 120° wide in each half cycle for the PM brushless dc motors (PMBDCM) drive. Due to the leakage inductance, L_l , the stator currents take a finite time to rise and fall, thus distorting the ideal rectangular waveforms into trapezoidal shapes. The effect of this is the torque ripple generated at the current transitions. For a three-phase machine, there will be six torque ripples for every 360 electrical degrees as there are six current transitions. They will also reduce the average torque if the conduction time is maintained at electrical 120° whereby the constant current region is reduced below electrical 120° . The consequences of a set of practical currents on the performance of the PMBDCM drive can be analyzed using Fourier series approach as follows. The torque expressions below are given [3a] considering only a two-pole machine and for P-pole machine, the expressions have to be multiplied by the pole pairs.

The phase current is generalized and shown in Figure 10.1. The phase a current can be resolved into Fourier series as

$$i_{as}(\theta_r) = \frac{4I_p}{\pi(\theta_2 - \theta_1)} \left[(\sin \theta_2 - \sin \theta_1) \sin \theta_r + \frac{1}{3^2} (\sin 3\theta_2 - \sin 3\theta_1) \sin 3\theta_r + \dots \right] \quad (10.1)$$

Similarly the Fourier series of the flux linkages of phase a assuming a trapezoidal waveform and constant for $(\pi - 2h)$ electrical degrees in each half cycle is

$$\lambda_{af}(\theta_r) = \frac{4\lambda_p}{\pi h} \left[\sinh \sin \theta_r + \frac{1}{3^2} (\sin 3h \sin 3\theta_r) + \frac{1}{5^2} (\sin 5h \sin 5\theta_r) + \dots \right] \quad (10.2)$$

where λ_p is the peak value of the modified flux linkages and the flux linkage waveform is shown in Figure 10.2. Similarly the phase b and phase c currents and their modified flux linkages can be derived.

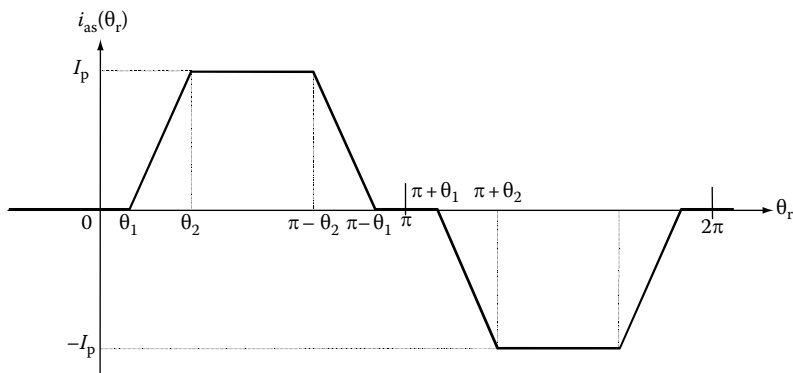


FIGURE 10.1 General phase current waveform of the PMBDCM. (From Krishnan, R., *Electric Motor Drives*, Figure 9.51, Prentice Hall, Upper Saddle River, NJ, 2001. With permission.)

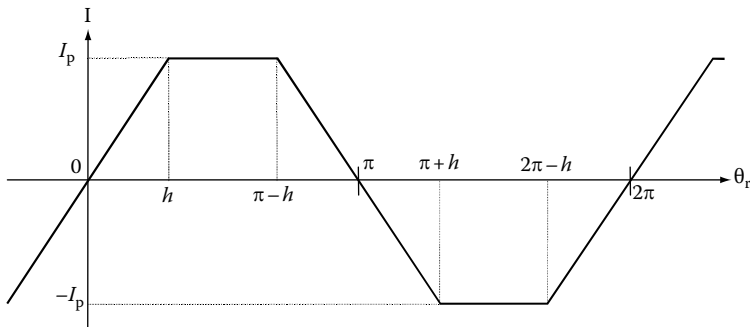


FIGURE 10.2 The rotor flux linkage waveform. (From Krishnan, R., *Electric Motor Drives*, Figure 9.52, Prentice Hall, Upper Saddle River, NJ, 2001. With permission.)

The fundamental electromagnetic torque is computed by considering the product of fundamental terms in the phase air gap flux linkages and respective stator phasor currents for a two-pole machine as

$$T_{e1} = \lambda_{af1}(\theta_r)i_{as1}(\theta_r) + \lambda_{bf1}(\theta_r)i_{bs1}(\theta_r) + \lambda_{cf1}(\theta_r)i_{cs1}(\theta_r), \text{ N} \cdot \text{m} \quad (10.3)$$

Substituting the fundamental terms and expanding the expressions yields

$$\begin{aligned} T_{e1} = & \frac{16I_p\lambda_p}{\pi^2 h(\theta_2 - \theta_1)} \left[\sinh(\sin\theta_2 - \sin\theta_1)\sin^2\theta_r \right. \\ & + \sinh(\sin\theta_2 - \sin\theta_1)\sin^2(\theta_r - 2\pi/3) \\ & \left. + \sinh(\sin\theta_2 - \sin\theta_1)\sin^2(\theta_r + 2\pi/3) \right] \end{aligned} \quad (10.4)$$

For $h = \pi/6$ the electromagnetic torque for three phases is evaluated as

$$\begin{aligned} T_{e1} = & [I_p\lambda_p] \left\{ \frac{48}{\pi^3(\theta_2 - \theta_1)} (\sin\theta_2 - \sin\theta_1) \right\} \left[\frac{3}{2} \right] \\ = & 2.3193 \left[\frac{\sin\theta_2 - \sin\theta_1}{\theta_2 - \theta_1} \right] [I_p\lambda_p], \text{ N} \cdot \text{m} \end{aligned} \quad (10.5)$$

The normalized fundamental torque in p.u. as a function of θ_2 for θ_1 and h equal to 30° is shown in Figure 10.3, for 1 p.u. current. This shows that the increasing rise time of the current decreases the fundamental torque. At higher speeds, for the same rise time of the current, note that θ_2 increases and hence there will be a greater reduction in the fundamental torque of the motor drive.

For a rectangular current of electrical 120° duration, the fundamental torque is

$$T_{e1} = 2.011 I_p\lambda_p \quad (10.6)$$

which closely approximates the available torque calculated in Chapter 1.

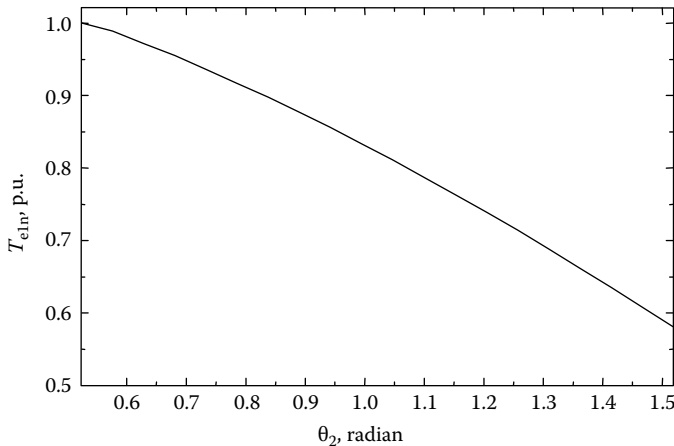


FIGURE 10.3 The fundamental torque as a function of θ_2 for $\theta_1=0.524$ rad and $h=0.524$ rad for $I_p=1$ p.u. (From Krishnan, R., *Electric Motor Drives*, Figure 9.53, Prentice Hall, Upper Saddle River, NJ, 2001. With permission.)

The commutation torque is at six times the fundamental frequency. It can be seen as the result of the sum of the fundamental rotor flux linkages interacting with the fifth and seventh current harmonics and the fundamental of the current interacting with the fifth and seventh harmonic rotor flux linkages. It is derived as follows:

$$\begin{aligned}
 T_{e6} &= \frac{4\lambda_p I_p}{\pi(\theta_2 - \theta_1)} \left[(\sin \theta_2 - \sin \theta_1) \left\{ -\frac{1}{5^2} (\sin 5h) + \frac{1}{7^2} (\sin 7h) \right\} \right] \frac{4}{\pi h} \\
 &\quad + \frac{4}{\pi h} \cdot \frac{4}{\pi(\theta_2 - \theta_1)} \left[\sinh \left\{ -\frac{1}{5^2} (\sin 5\theta_2 - \sin 5\theta_1) + \frac{1}{7^2} (\sin 7\theta_2 - \sin 7\theta_1) \right\} \right] \\
 &= \frac{16\lambda_p I_p}{\pi^2 h(\theta_2 - \theta_1)} \left[(\sin \theta_2 - \sin \theta_1) \left\{ -\frac{1}{5^2} \sin 5h + \frac{1}{7^2} \sin 7h \right\} \right. \\
 &\quad \left. + \sinh \left\{ -\frac{1}{5^2} (\sin 5\theta_2 - \sin 5\theta_1) + \frac{1}{7^2} (\sin 7\theta_2 - \sin 7\theta_1) \right\} \right] \quad (10.7)
 \end{aligned}$$

In general, the harmonic torque of frequency m times the fundamental is given by

$$\begin{aligned}
 T_{em} &= \frac{16\lambda_p I_p}{\pi^2 h(\theta_2 - \theta_1)} \left[(\sin \theta_2 - \sin \theta_1) \left\{ -\frac{1}{(m-1)^2} \sin m-1h + \frac{1}{(m+1)^2} \sin m+1h \right\} \right. \\
 &\quad \left. + \sinh \left\{ -\frac{1}{(m-1)^2} (\sin m-1\theta_2 - \sin m-1\theta_1) + \frac{1}{(m+1)^2} (\sin m+1\theta_2 - \sin m+1\theta_1) \right\} \right] \\
 &\quad m = 6, 12, 18, 24, \dots \quad (10.8)
 \end{aligned}$$

TABLE 10.1**Sixth Harmonic Torque for Various θ_2 with $\theta_1 = 30^\circ$**

Harmonic Number		Sixth Harmonic Torque Component					
Rotor Flux Linkages	Stator Current	$\theta_2 = 32.5^\circ$	35°	37.5°	40°	45°	50°
1	5	0.424	0.439	0.447	0.448	0.428	0.383
1	7	-0.258	-0.221	-0.178	-0.132	-0.037	-0.044
5	1	-0.079	-0.078	-0.077	-0.076	-0.075	-0.071
7	1	-0.041	-0.040	-0.039	-0.039	-0.037	-0.036
Total	T_{e6n}	0.047	0.101	0.153	0.202	0.280	0.320

TABLE 10.2**Twelfth Harmonic Torque for $\theta_1 = 30^\circ = h$**

Harmonic Number		12th Harmonic Torque Component					
Rotor Flux Linkages	Stator Current	$\theta_2 = 32.5^\circ$	35°	37.5°	40°	45°	50°
1	11	-0.201	-0.203	-0.190	-0.163	-0.088	-0.018
1	13	0.122	0.078	0.031	-0.012	-0.063	-0.057
11	1	0.016	0.016	0.016	0.016	0.015	0.015
13	1	0.012	0.012	0.011	0.011	0.011	0.010
Total	T_{el2n}	-0.051	-0.097	-0.131	-0.149	-0.126	-0.05

Note that this is for one phase only. The negative sign attributed to the fifth harmonic rotor flux linkage and current is due to the fact that they are revolving against the fundamental rotor flux linkage and current and hence their torque contributions are considered negative. The detailed calculations for the 6th and 12th harmonic torques are given in Tables 10.1 and 10.2, respectively.

The harmonic torques are normalized on the basis of the fundamental torque for a perfect rectangular current. It is rational from the point of view of application considerations. Hence the normalized harmonic torques combined for all three phases are

$$\begin{aligned}
 T_{emn} &= \frac{3T_{em}}{T_{el}} = \frac{24}{\pi^2 h(\theta_2 - \theta_1)} \left[(\sin \theta_2 - \sin \theta_1) \left\{ -\frac{1}{(m-1)^2} \sin m - lh + \frac{1}{(m+1)^2} \sin m + lh \right\} \right. \\
 &\quad \left. + \sinh \left\{ -\frac{1}{(m-1)^2} (\sin m - lh - \sin m - l\theta_1) \right\} \right] , \text{ p.u.} \quad \text{for } m = 6, 12, 18, \dots
 \end{aligned} \tag{10.9}$$

10.2 PHASE ADVANCING

The magnitude of the induced emfs increases with increasing speed. When the magnitude of the line-to-line induced emf comes closer to the magnitude of dc link voltage, it will not be possible to maintain the currents at desired level. Then the currents can be advanced [3a] in phase so that the line-to-line induced emfs are lower than the dc link voltage facilitating the establishment of the desired current magnitude.

During the intervals that the line-to-line induced emf becomes greater than the dc link voltage, the current cannot flow from the dc link to the motor windings. The energy stored in the leakage inductance (L_M) prior to that instant will keep the current circulating in the windings through the freewheeling diodes of the inverter. During this interval, the currents will decrease. This translates into a reduction of torque. If the speed is increased beyond rated value, then the power output can be maintained at rated value for a small range of speed even with decreasing torque production. Note that this mode of operation is usually attempted for a very small speed range. The phase advancing effect is quantified as follows.

Considering an ideal current with 120° constancy and an ideal flux linkage waveform, they can be resolved into harmonic components and written as

$$i_{as}(\theta_r) = \frac{4\sqrt{3}I_p}{2\pi} \left[\sin \theta_r + \frac{1}{5} \sin 5\theta_r + \dots \right] \quad (10.10)$$

$$\lambda_{afl}(\theta_r) = \frac{24\lambda_p}{\pi^2} \left[\frac{1}{2} \sin \theta_r + \frac{1}{9} \sin 3\theta_r + \frac{1}{2} \cdot \frac{1}{25} \sin 5\theta_r + \dots \right] \quad (10.11)$$

Advancing the current by an angle θ_a can be represented as

$$i_{as}(\theta_r + \theta_a) = \frac{4\sqrt{3}}{2\pi} I_p \left[\sin(\theta_r + \theta_a) + \frac{1}{5} \sin \{5(\theta_a + \theta_r)\} + \dots \right] \quad (10.12)$$

Similarly expressions for other phase currents $i_{bs}(\theta_r + \theta_a)$ and $i_{cs}(\theta_r + \theta_a)$ can be written. Substituting these into the torque expression, the fundamental torque is obtained as

$$\begin{aligned} T_{el} &= \lambda_{afl}(\theta_r)i_{as1}(\theta_r + \theta_a) + \lambda_{bfl}(\theta_r)i_{bs1}(\theta_r + \theta_a) + \lambda_{cfl}(\theta_r)i_{cs1}(\theta_r + \theta_a) \\ &= \frac{96\sqrt{3}}{4\pi^3} \lambda_p I_p [\sin \theta_r \sin(\theta_r + \theta_a) + \sin(\theta_r - 2\pi/3) \sin(\theta_r - 2\pi/3 + \theta_a) \\ &\quad + \sin(\theta_r + 2\pi/3) \sin(\theta_r + 2\pi/3 + \theta_a)] \\ &= 2.0085 \lambda_p I_p \cos \theta_a \end{aligned} \quad (10.13)$$

For speeds less than rated value, the advance angle is zero and giving the fundamental torque as

$$\therefore T_{e1} = 2.0085\lambda_p I_p = T_{er} \quad (10.14)$$

where T_{er} is the rated value of the electromagnetic torque. For speeds higher than rated value, the phase advance angle, θ_a , is nonzero. Then the torque can be represented in terms of the rated value and advance angle from Equations 10.12 and 10.13 as

$$T_{e1} = T_{er} \cos \theta_a \quad (10.15)$$

Assuming that the base flux linkages is equal to λ_p and the base current is I_b , then the torque in normalized unit is

$$T_{en1} = I_{pn} \cos \theta_a \quad (10.16)$$

where I_{pn} is the normalized peak current in a machine phase. It is to be noted that these expressions are valid only for ideal current waveforms and in practical situation, they will deviate from the ideal considerably. The phase advancing of currents not only decreases the available torque but also drastically increases the harmonic torque. For the current advance in one phase, initially the air gap flux linkages are not a constant but a ramp. The result of their interaction is a ramp-shaped torque giving way to significant pulsating torque component. Their quantification can be achieved by following a similar procedure given in the commutation torque ripple section.

10.3 DYNAMIC MODELING

The dynamic model is necessary to study both the steady state and transients of the motor drive system and particularly for flux-weakening operation. The instantaneous currents are crucial for loss computation and electromagnetic torque is of importance in evaluating the drive system performance. While torque ripple at speeds beyond nominal speed may not be of significance in industrial and appliance drive systems, it becomes a significant factor in many appliances, fans, airborne and marine applications due to its impact on structural vibrations and acoustic noise. In order to accommodate the performance computation with voltage control during flux-weakening operation as well with a pulsed voltage operation, the drive system equations are derived for an open loop control of the flux weakening of this motor drive system. The closed loop speed control operation is simple as it involves only the speed control loop with no inner current control loop in place. The inner current loop is of no consequence as the current control is saturated at speeds beyond base speed and hence may be ignored. In such a case, the output of the speed error is amplified to yield a torque reference, which could be converted into an appropriate advance

angle for the applied voltage to the phases. The advance angles may be derived either from steady-state analysis given in the previous section or from the analysis that will be made using the dynamic system equations derived in this section.

10.3.1 MACHINE EQUATIONS

A three-phase PM brushless machine connected to an inverter with a fictitious midpoint in its dc supply is shown in Figure 10.4. Then the electrical period is divided into six 60° durations called modes and for each of them the phase currents are assumed to have a certain polarity and also the voltages between the supply dc midpoint and the midpoint of the inverter phases are identified. From the latter, the line voltages to the machine are derived and then they serve as the inputs in to the system equations. This procedure [5,7] is given below. Letters s, c, and e correspond to a phase current that it is starting, continuing to flow, and ending depending on whether that phase has just been initiated to conduct current, left undisturbed to conduct continuously, turned off or commutated, respectively. The induced emfs per phase are denoted by e_{as} , e_{bs} , and e_{cs} for phases a, b, and c, respectively.

Consider mode 1 where $30^\circ \leq \theta \leq 90^\circ$ and phase c is being commutated, phase a is being initiated and phase b is undisturbed to conduct with the result that the voltages between the midpoint dc supply source and inverter midpoint are derived as

$$\text{If } i_a > 0, v_{a0} = \frac{v_{dc}}{2} \text{ and } v_{b0} = \frac{v_{dc}}{2} \quad (10.17)$$

$$v_{c0} = -\frac{v_{dc}}{2} \text{ until } i_c \text{ goes to zero}$$

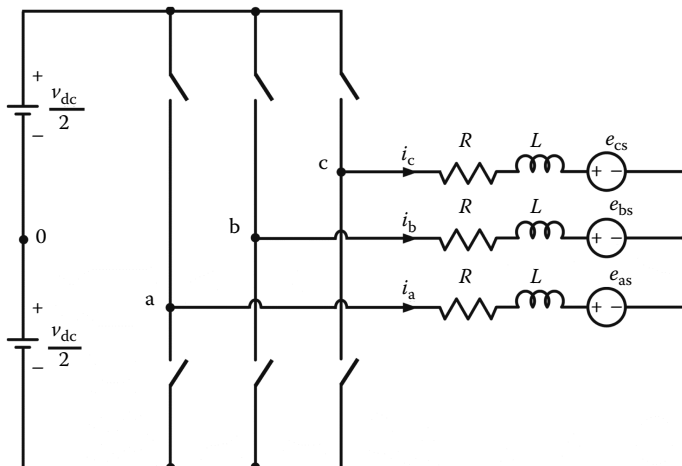


FIGURE 10.4 Schematic of a three phase PM brushless dc machine connected to an inverter.

$$\therefore v_{ab} = v_{dc}$$

$$i_a = -i_b$$

The symbols (+) and (-) indicate currents that they are positive and negative, respectively. Similarly other modes of operation can be derived and given in [Table 10.3](#).

The dynamic machine equations can be derived from the midpoint voltages and the conduction angles. Mode 1 is shown in [Figure 10.5](#) and the corresponding system equations are in the following:

Mode 1: $30^\circ \leq \theta \leq 90^\circ$

Consider the phase equations from the previous chapter and subtracting phase b voltage equation from phase a voltage equation gives the first equation in terms of the ab line voltage and likewise subtracting phase b voltage equation from phase c voltage equation gives the second equation in terms of the cb line voltage as

$$v_{ab} = R_s [i_a - i_b] + Lp [i_a - i_b] + e_{ab} \quad (10.18)$$

$$v_{cb} = R_s [i_c - i_b] + Lp [i_c - i_b] + e_{cb} \quad (10.19)$$

where the line to line induced emf between a and b phases is given by $e_{ab} = e_{as} - e_{bs}$ and likewise other line to line induced emfs are defined.

Noting that the sum of the three phase currents is zero, the phase c current is derived as

$$i_c = -(i_a + i_b) \quad (10.20)$$

Substituting phase c current in terms of the phase a and b currents in the previous equations lead to

$$\begin{bmatrix} v_{ab} \\ v_{cb} \end{bmatrix} = R_s \begin{bmatrix} 1 & -1 \\ -1 & -2 \end{bmatrix} \begin{bmatrix} i_a \\ i_b \end{bmatrix} + Lp \begin{bmatrix} 1 & -1 \\ -1 & -2 \end{bmatrix} \begin{bmatrix} i_a \\ i_b \end{bmatrix} + \begin{bmatrix} e_{ab} \\ e_{cb} \end{bmatrix} \quad (10.21)$$

The derived equations can be cast in the state space form as

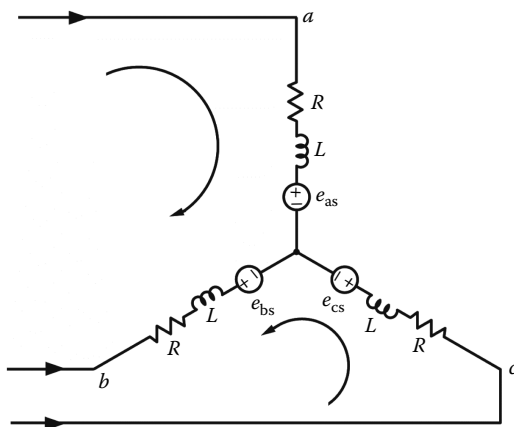
$$\therefore p \begin{bmatrix} i_a \\ i_b \end{bmatrix} = -\frac{R_s}{L} \begin{bmatrix} i_a \\ i_b \end{bmatrix} - \frac{1}{3L} \begin{bmatrix} -2 & 1 \\ 1 & 1 \end{bmatrix} \begin{bmatrix} v_{ab} - e_{ab} \\ v_{cb} - e_{cb} \end{bmatrix} \quad (10.22)$$

$$= -\frac{R_s}{L} \begin{bmatrix} i_a \\ i_b \end{bmatrix} - \frac{1}{3L} \begin{bmatrix} -2(v_{ab} - e_{ab}) + (v_{cb} - e_{cb}) \\ (v_{ab} - e_{ab}) + (v_{cb} - e_{cb}) \end{bmatrix} \quad (10.23)$$

TABLE 10.3
The Complete Modes of the PM Brushless dc Motor Drive System

θ, deg	i_a	i_b	i_c	v_{a0}	v_{b0}	v_{c0}	Conducting Phases
30–90	s (+)	c (–)	e (+)	$\frac{v_{dc}}{2}$	$-\frac{v_{dc}}{2}$	$-\frac{v_{dc}}{2}$ until $i_c \Rightarrow 0 (\theta = \theta_c)$	Until $30 + \theta_c \Rightarrow 3 \text{ ph}$ $\Rightarrow a, b, c [ac, b]$ After $30 + \theta_c \Rightarrow 2 \text{ ph}$ $\Rightarrow a, b$
90–150	c (+)	e (–)	s (–)	$\frac{v_{dc}}{2}$	$+\frac{v_{dc}}{2}$ until $i_b \Rightarrow 0 (\theta = \theta_c)$	$-\frac{v_{dc}}{2}$	3 ph $\Rightarrow a, b, c [a, bc]$ 2 ph $\Rightarrow a, c$
150–210	e (+)	s (+)	c (–)	$-\frac{v_{dc}}{2}$ until $i_a \Rightarrow 0 (\theta = \theta_c)$	$\frac{v_{dc}}{2}$	$-\frac{v_{dc}}{2}$	3 ph $\Rightarrow a, b, c [ab, c]$ 2 ph $\Rightarrow b, c$
210–270	s (–)	c (+)	e (–)	$-\frac{v_{dc}}{2}$	$\frac{v_{dc}}{2}$	$+\frac{v_{dc}}{2}$ until $i_c \Rightarrow 0 (\theta = \theta_c)$	3 ph $\Rightarrow a, b, c [b, ca]$ 2 ph $\Rightarrow b, a$
270–330	c (–)	e (+)	s (+)	$-\frac{v_{dc}}{2}$	$-\frac{v_{dc}}{2}$ until $i_b \Rightarrow 0 (\theta = \theta_b)$	$\frac{v_{dc}}{2}$	3 ph $\Rightarrow a, b, c [cb, a]$ 2 ph $\Rightarrow c, a$
330–30	e (–)	s (–)	c (+)	$+\frac{v_{dc}}{2}$ until $i_a \Rightarrow 0 (\theta = \theta_a)$	$-\frac{v_{dc}}{2}$	$\frac{v_{dc}}{2}$	3 ph $\Rightarrow a, b, c [c, ab]$ 2 ph $\Rightarrow c, b$

c → continuing; s → starting; e → ending; + → positive current; – → negative current.

**FIGURE 10.5** Mode 1.

Note that there are only two differential equations to be solved and this is true in all the six modes. Accordingly, the variables can be generically named for each mode as in the following so that the solution of two differential equations can go on for all modes with the input variables and resulting output variables can be gleaned from their modes.

$$\text{Let } v_{12} \Rightarrow v_{ab} \quad i_a \Rightarrow i_1 \quad (10.24)$$

$$v_{23} \Rightarrow v_{cb} \quad i_c \Rightarrow i_2 \quad (10.25)$$

Similarly for all other modes from 2 to 6 the machine state and equations are derived and given below. Only the bare equations, conditions, and figures are given for brevity.

Mode 2: $90^\circ \leq \theta \leq 150^\circ$

$$i_a \rightarrow c$$

$$i_b \downarrow e \quad (-) \quad \frac{sc}{ac} \quad \frac{ec}{bc}$$

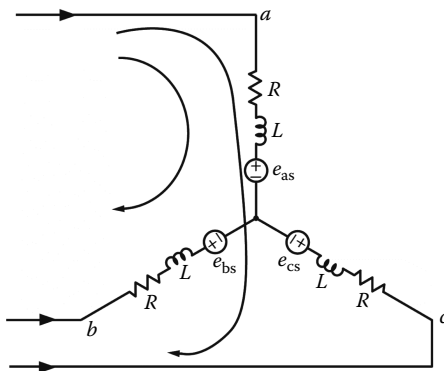
$$i_c \uparrow s \quad (-)$$

The mode 2 operation of the drive system in circuit schematic is shown in [Figure 10.6](#).

$$v_{ac} = R_s [i_a - i_c] + L p [i_a - i_c] + e_{ac} \quad (10.26)$$

$$v_{bc} = R_s [i_b - i_c] + L p [i_b - i_c] + e_{bc} \quad (10.27)$$

$$i_b = -(i_a + i_c)$$

**FIGURE 10.6** Mode 2.

$$\begin{bmatrix} v_{ac} \\ v_{bc} \end{bmatrix} = R_s \begin{bmatrix} 1 & -1 \\ -1 & -2 \end{bmatrix} \begin{bmatrix} i_a \\ i_c \end{bmatrix} + L p \begin{bmatrix} 1 & -1 \\ -1 & -2 \end{bmatrix} \begin{bmatrix} i_a \\ i_b \end{bmatrix} + \begin{bmatrix} e_{ab} \\ e_{bc} \end{bmatrix} \quad (10.28)$$

$$p \begin{bmatrix} i_a \\ i_c \end{bmatrix} = -\frac{R_s}{L} \begin{bmatrix} i_a \\ i_c \end{bmatrix} - \frac{1}{3L} \begin{bmatrix} -2 & 1 \\ 1 & 1 \end{bmatrix} \begin{bmatrix} v_{ab} - e_{ab} \\ v_{bc} - e_{bc} \end{bmatrix} \quad (10.29)$$

Let

$$v_{12} = v_{ac}, \quad i_a \Rightarrow i_1 \quad (10.30)$$

$$v_{23} = v_{bc}, \quad i_c \Rightarrow i_2 \quad (10.31)$$

Mode 3: $150^\circ \leq \theta \leq 210^\circ$

$$i_a \downarrow e$$

$$i_b \uparrow s \quad \frac{sc}{ac} \quad \frac{ec}{bc}$$

$$i_c \rightarrow c(-)$$

$$v_{ac} = R_s [i_a - i_c] + L p [i_a - i_c] + e_{ac} \quad (10.32)$$

$$v_{bc} = R_s [i_b - i_c] + L p [i_b - i_c] + e_{bc} \quad (10.33)$$

$$i_a = -(i_b + i_c) \quad (10.34)$$

$$P \begin{bmatrix} i_b \\ i_c \end{bmatrix} = -\frac{R_s}{L} \begin{bmatrix} i_b \\ i_c \end{bmatrix} - \frac{1}{3L} \begin{bmatrix} -2 & 1 \\ 1 & 1 \end{bmatrix} \begin{bmatrix} v_{bc} & -e_{bc} \\ v_{ac} & -e_{ac} \end{bmatrix} \quad (10.35)$$

$$v_{12} = v_{bc}, \quad i_b \Rightarrow i_1 \quad (10.36)$$

$$v_{23} = v_{ac}, \quad i_c \Rightarrow i_2 \quad (10.37)$$

Mode 4: $210^\circ \leq \theta \leq 270^\circ$

$$\begin{array}{ccc} s & c & e \\ & & \\ a & b & c \end{array} \quad \begin{array}{cc} \frac{sc}{ac} & \frac{ec}{bc} \end{array}$$

The mode 4 operation of the drive system in circuit schematic is shown in Figure 10.7.

$$v_{ab} = R_s [i_a - i_b] + L p [i_a - i_b] + e_{ab} \quad (10.38)$$

$$v_{cb} = R_s [i_c - i_b] + L p [i_c - i_b] + e_{cb} \quad (10.39)$$

$$i_c = -(i_a + i_b) \quad (10.40)$$

$$\begin{bmatrix} v_{ab} \\ v_{cb} \end{bmatrix} = R_s \begin{bmatrix} 1 & -1 \\ -1 & -2 \end{bmatrix} \begin{bmatrix} i_a \\ i_b \end{bmatrix} + L p \begin{bmatrix} 1 & -1 \\ -1 & -2 \end{bmatrix} \begin{bmatrix} i_a \\ i_b \end{bmatrix} + \begin{bmatrix} e_{ab} \\ e_{cb} \end{bmatrix} \quad (10.41)$$

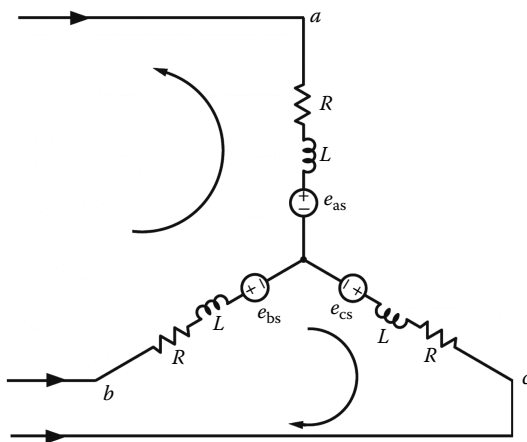


FIGURE 10.7 Mode 4.

$$p \begin{bmatrix} i_a \\ i_b \end{bmatrix} = -\frac{R_s}{L} \begin{bmatrix} i_a \\ i_b \end{bmatrix} - \frac{1}{3L} \begin{bmatrix} -2 & 1 \\ 1 & 1 \end{bmatrix} \begin{bmatrix} v_{ab} - e_{ab} \\ v_{cb} - e_{cb} \end{bmatrix} \quad (10.42)$$

Note that $i_a \Rightarrow -ve$, $i_b \Rightarrow +ve$

Mode 5: $270^\circ \leq \theta \leq 330^\circ$

$$\begin{array}{ccc|cc} s & c & e & \frac{sc}{ca} & \frac{ec}{ba} \\ i_a & i_b & i_c & & \end{array}$$

$$v_{ca} = R_s [i_c - i_a] + Lp [i_c - i_a] + e_{ca} \quad (10.43)$$

$$v_{ba} = R_s [i_b - i_a] + Lp [i_b - i_a] + e_{ba} \quad (10.44)$$

$$\begin{bmatrix} v_{ca} \\ v_{ba} \end{bmatrix} = R_s \begin{bmatrix} 1 & -1 \\ -1 & -2 \end{bmatrix} \begin{bmatrix} i_c \\ i_a \end{bmatrix} + Lp \begin{bmatrix} 1 & -1 \\ -1 & -2 \end{bmatrix} \begin{bmatrix} i_c \\ i_a \end{bmatrix} + \begin{bmatrix} e_{ca} \\ e_{ba} \end{bmatrix} \quad (10.45)$$

$$p \begin{bmatrix} i_c \\ i_a \end{bmatrix} = -\frac{R_s}{L} \begin{bmatrix} i_c \\ i_a \end{bmatrix} - \frac{1}{3L} \begin{bmatrix} -2 & 1 \\ 1 & 1 \end{bmatrix} \begin{bmatrix} v_{ca} - e_{ca} \\ v_{ba} - e_{ba} \end{bmatrix} \quad (10.46)$$

Let,

$$v_{12} = v_{ca}, \quad i_c = i_1 \quad (10.47)$$

$$v_{23} = v_{ba}, \quad i_a = i_2 \quad (10.48)$$

Mode 6: $330^\circ \leq \theta \leq 30^\circ$

$$\begin{array}{ccc|cc} a & b & c & \frac{sc}{bc} & \frac{ec}{ac} \\ e & s & c & & \\ (-) & (-) & (+) & & \end{array}$$

$$v_{bc} = R_s [i_b - i_c] + Lp [i_b - i_c] + e_{bc} \quad (10.49)$$

$$v_{ac} = R_s [i_a - i_c] + Lp [i_a - i_c] + e_{ac} \quad (10.50)$$

$$\begin{bmatrix} v_{bc} \\ v_{ac} \end{bmatrix} = R_s \begin{bmatrix} 1 & -1 \\ -1 & -2 \end{bmatrix} \begin{bmatrix} i_b \\ i_c \end{bmatrix} + Lp \begin{bmatrix} 1 & -1 \\ -1 & -2 \end{bmatrix} \begin{bmatrix} i_b \\ i_c \end{bmatrix} + \begin{bmatrix} e_{bc} \\ e_{ac} \end{bmatrix} \quad (10.51)$$

$$p \begin{bmatrix} i_b \\ i_c \end{bmatrix} = -\frac{R_s}{L} \begin{bmatrix} i_b \\ i_c \end{bmatrix} - \frac{1}{3L} \begin{bmatrix} -2 & 1 \\ 1 & 1 \end{bmatrix} \begin{bmatrix} v_{bc} - e_{bc} \\ v_{ac} - e_{ac} \end{bmatrix} \quad (10.52)$$

$$v_{12} = v_{bc} \quad i_b = i_1 \quad (10.53)$$

$$v_{23} = v_{ac} \quad i_c = i_2 \quad (10.54)$$

The addition of mechanical load dynamics, in the form of a differential equation, completes the motor drive system modeling. To illustrate the simulation results, consider phase a input voltage with an advance angle of θ_a with respect to its induced emf, where it becomes the maximum value from its zero crossing as shown in Figure 10.8. A typical phase a current waveform for positive half wave is also provided in this figure. For example, the advance angle is set to 30° for which the applied phase midpoint inverter voltages are evaluated and given in Figure 10.9.

The simulation results are presented below to illustrate the varied operation of the PM brushless dc motor drive with advancing the voltage and only steady states are considered. An advance angle of 0° is applied at rated (base) speed and the responses

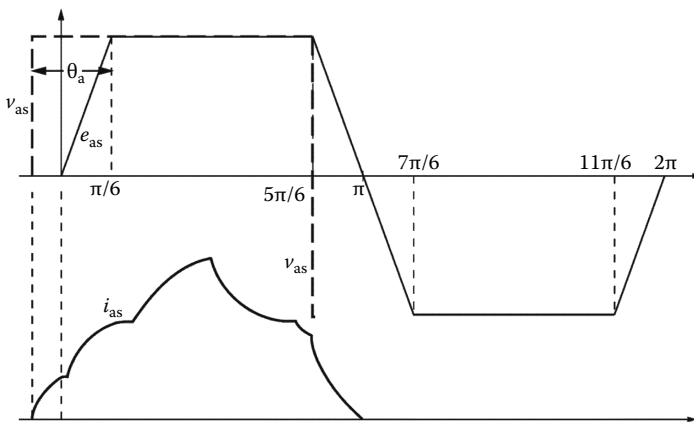


FIGURE 10.8 Illustration of advance phase a voltage application and resulting current.

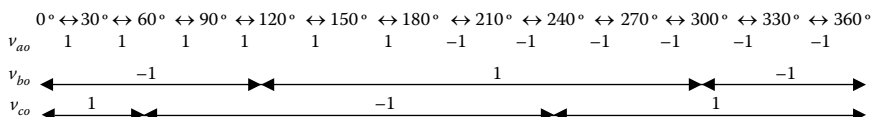


FIGURE 10.9 Applied midpoint inverter phase voltages to the machine.

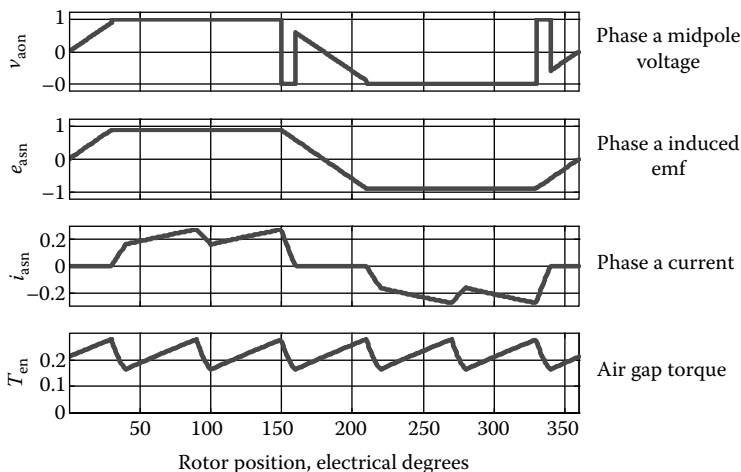


FIGURE 10.10 Applied midpoint inverter phase voltages to the machine.

are shown in Figure 10.10. The applied phase a inverter midpoint voltage during its zero current intervals reflects the phase a induced emf and that is why the ramp-like voltage pulses appear in its waveform. The diode conduction during phase commutation is displayed by negative voltage pulse during the positive current turnoff and likewise by the positive voltage pulse during the negative current turn off. The phase current is quasinsinoidal and the air gap torque has the dominant sixth harmonic ripple component as expected. All variables are normalized.

When the advance angle for the applied midpoint inverter phase a voltage is set at 30° at rated speed, it yields 0.5572 p.u. torque shown in Figure 10.11. That the torque is approximately 2.5 times the torque that was produced with an advance angle of 0° in the previous example is to be noted. The torque enhancement is because the applied voltage was greater than the induced emf all through the duration which led to higher current magnitude, resulting in higher torque generation. This mode of operation is beneficial near the base speed operation to boost the torque output. This example also clearly demonstrates the benefit of advancing the voltage onset to the phases. Even though the current is more sinusoidal than in the previous case, it does not lead to lower torque ripple. It is so because the induced emf is trapezoidal and not even remotely close to a sinusoid.

Consider the previous example but with one slight variation of the condition that the induced emf magnitude equals the midpoint inverter voltage. The onset of current is enabled by the advance angle of 30° during which the applied voltage exceeds the induced emf. Once the current is initiated, it hovers around that value because of the stored inductive energy in its windings ending up with almost a quasinsinoidal current but with a longer period of zero current dwell, shown in Figure 10.12. The current magnitude is severely limited resulting in much lower current value compared to the case where the induced emf is less than the applied voltage shown in Figure 10.11. In comparison with zero advance angle case shown in Figure 10.9, the current is more sinusoidal and the torque is higher when the applied voltage is advanced with respect to the induced emf. Thus the advancement of voltage placement results in higher torque and better torque waveform with slightly reduced ripple.

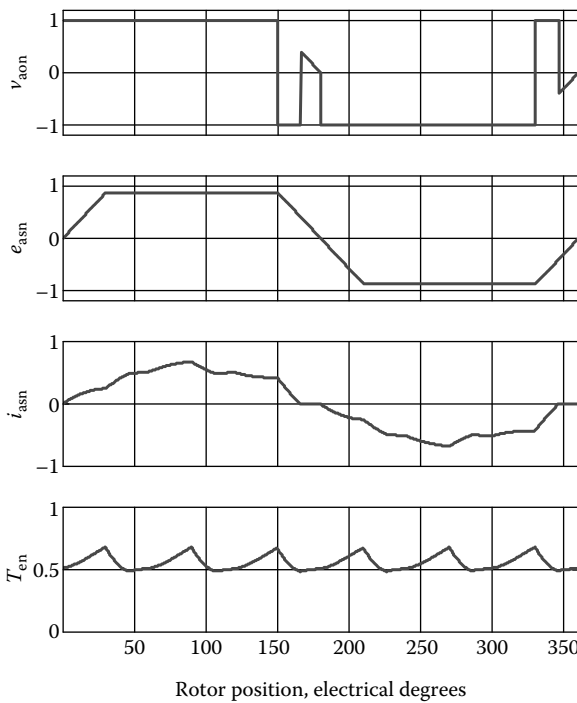


FIGURE 10.11 Steady-state performance at rated speed {speed 1 p.u., $V_{dc} = 100$ V (2 p.u.), $T_{e(av)} = 0.557$ p.u.}.

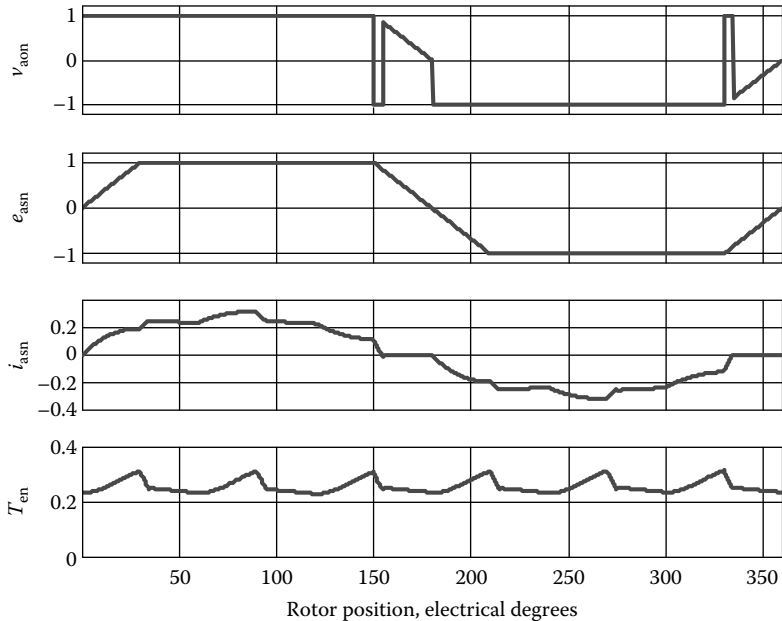


FIGURE 10.12 Performance for 30° advance at rated speed, 2 p.u. source voltage with a resultant air gap torque of 0.2579 p.u.

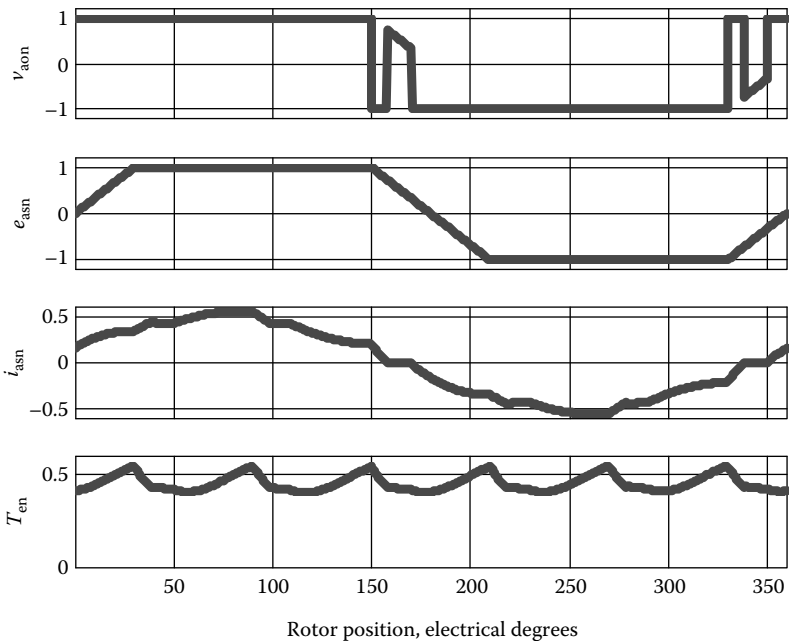


FIGURE 10.13 Applied and induced emfs are of same magnitude here, rated speed, T_e (ave) = 0.455 p.u. (whereas without advancing, the average torque will be zero is to be noted), advance angle of 40°.

Then the natural question arises whether further advance of the applied voltage will result in enhanced torque and as expected from analytical expressions in the previous section. Such a case is illustrated with advance angle of 40° in Figure 10.13 at rated speed and with the same dc bus and the magnitude of the applied voltage and induced emf matches. The torque has increased to 0.455 p.u. That is almost 50% more than that is obtained in the 30° advance case. Further the current is quasi-sinusoidal as against rectangular with the result that the current harmonics are minimized along with its losses. Normalized steady-state waveforms of applied midpole voltage, induced emf, and current in phase a at rated speed with an advance angle 40° are shown in Figure 10.14 for clarity.

So far, the midpoint inverter phase voltage inputs are displayed but they are not the same as the phase voltages in the machine. Figure 10.15 shows the example illustrated previously with phase voltage waveform. The applied phase voltage has induced emf appearing on it whenever its phase current is zero and note that the phase voltage is very different from the midpoint inverter phase voltage.

When midpoint voltage is applied to spread completely over the induced emf duration with their magnitudes matched, it results in very poor current and very small torque generation as shown in Figure 10.16. This mode of operation is not useful at base speed.

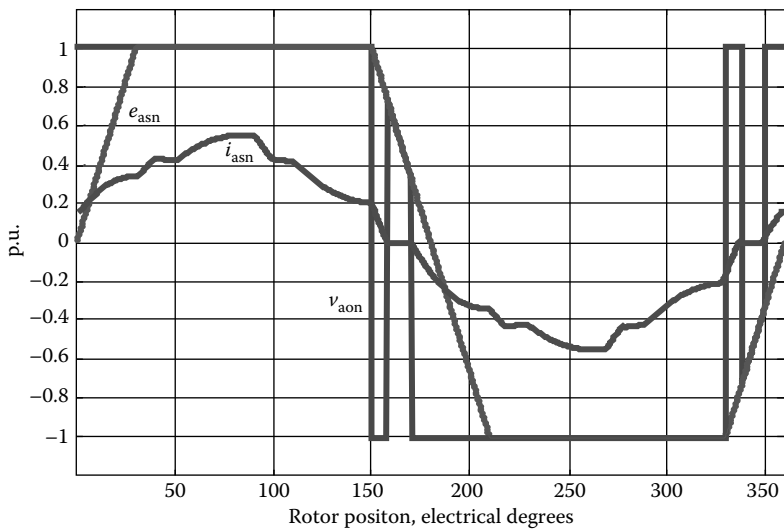


FIGURE 10.14 Performance for advance angle 40° at rated speed.

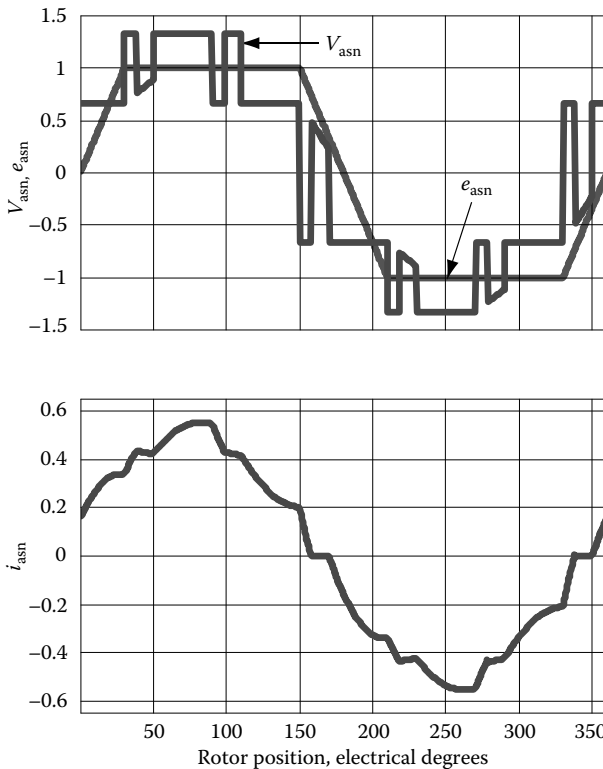


FIGURE 10.15 The amplified performance waveforms at an advance angle of 40° at rated speed.

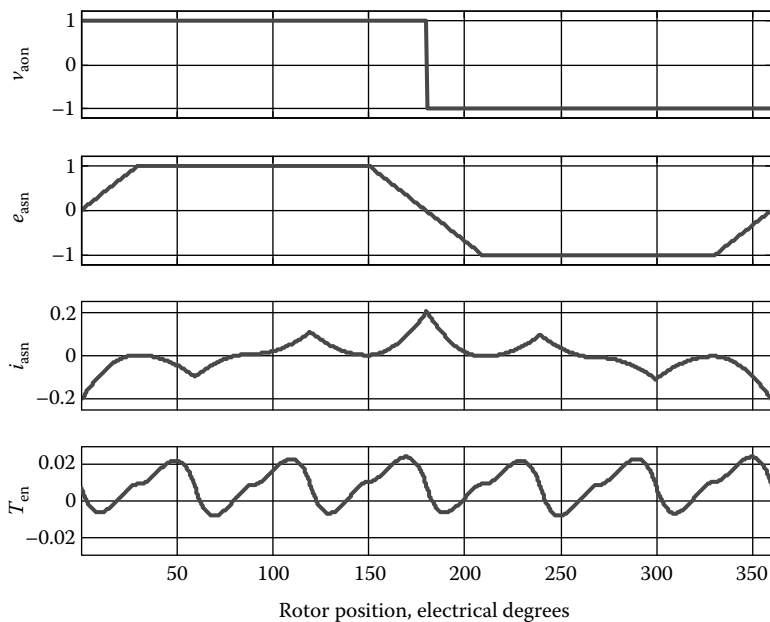


FIGURE 10.16 Performance at full 180° conduction near rated speed.

REFERENCES

Commutation Torque Ripple

1. H. R. Bolton and R. A. Ashen, Influence of motor design and feed-current waveform on torque ripple in brushless DC drives, *IEE Proceedings B (Electric Power Applications)*, 131(3), 82–90, 1984.
2. P. Pillay and R. Krishnan, Investigation into the torque behavior of a brushless dc motor drive, *Conference Record—IEEE Industry Applications Society Annual Meeting*, pp. 201–208, 1988.
3. R. Carlson, M. Lajoie-Mazenc, and J. C. S. Fagundes, Analysis of torque ripple due to phase commutation in brushless DC machines, *IEEE Transactions on Industry Applications*, 28(3), 632–638, 1992.
- 3a. R. Krishnan, *Electric Motor Drives*, Prentice Hall, Upper Saddle River, NJ, 2001.
4. M. Dai, A. Keyhani, and T. Sebastian, Torque ripple analysis of a PM brushless dc motor using finite element method, *IEEE Transactions on Energy Conversion*, 19(1), 40–45, 2004.

Flux Weakening

5. A. Fratta and A. Vagati, DC brushless servomotor: optimizing the commutation performances, *Conference Record of the IEEE Industry Applications Society Annual Meeting (Cat. No. 86CH2272-3)*, pp. 169–175, 1986.
6. G. Schaefer, Field weakening of brushless permanent magnet servomotors with rectangular current, *4th European Conference on Power Electronics and Applications*, pp. 429–434, 1991.

7. A. Fratta, A. Vagati, and F. Villata, Extending the voltage saturated performance of a DC brushless drive, *4th European Conference on Power Electronics and Applications*, pp. 134–138, 1991.
8. G. K. Miti, A. C. Renfrew, and B. J. Chalmers, Field-weakening regime for brushless DC motors based on instantaneous power theory, *IEE Proceedings: Electric Power Applications*, 148(3), 265–271, 2001.

11 Half-Wave PMBDCM Drives

A number of converter topologies emerges if the PMBDCM is operated in the half-wave mode, i.e., each phase is operated for electrical 120° , say, with positive current only, instead of an alternating current with electrical 120° conduction in each half cycle in a three-phase machine, which is known as the full-wave operational mode. This full-wave operation has been described earlier in previous chapters. This mode of operation provides very limited opportunities for innovation in the inverter topology and six-switch full-bridge topology has stayed on as the most optimal topology thus far. Cost minimization of the PMBDCM is of immense interest to the industry at present due to the opening up of a large number of applications to variable speed operation. Such applications are to be found in the HVACs, fans, pumps, washers, dryers, tread mills and other exercise equipments, wheel chairs, people's carriers in the airport lobbies, golf carts, freezers, refrigerators, automotives, handtools, and small process drives with velocity control for packaging, bottling, and food process applications. Due to the high-volume nature of these applications, cost minimization is of paramount importance not only to save materials and labor (and possibly due to parts reduction to enhance the reliability of the product) but also for the fact that without such a cost minimization, many of these applications with variable speed drives may not be realized, almost certainly in the present and probably in the future.

Although the cost of the motor and controller with single chips has been optimized, the only other subsystem available for optimization is the power converter. The half-wave operation is a major asset in this aspect as many power converter topologies are possible with minimum number of switches. Such a reduction in the number of power devices has an impact on the reduction in logic power supplies, heatsink volume, packaging size, enclosure size, and hence the overall cost of the drive system. Four power topologies for half-wave operation of the PMBDCM drive [1] are presented and discussed in this chapter. That does not preclude other converter topologies for such an operation and readers are encouraged to find them in the literature.

11.1 SPLIT SUPPLY CONVERTER TOPOLOGY

The power converter topology with a single switch per phase and minimum number of diodes in the rectifying section ideal for fractional horse power (fhp) PMBDC motor drives [1,3] is shown in [Figure 11.1](#). This topology is similar to the split voltage single switch per phase topology for the switched reluctance motor drive except that in switched reluctance motor drives, it is advocated usually for machines with even number of phases. Due to the unidirectional current handling capability of the

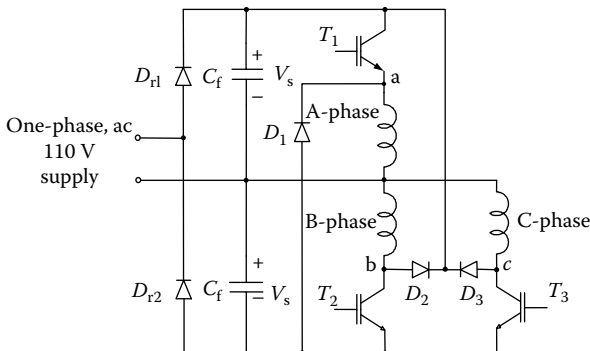


FIGURE 11.1 Split supply converter topology. (From Krishnan, R., *Electric Motor Drives*, Figure 9.54, Prentice Hall, Upper Saddle River, NJ, 2001. With permission.)

converter, which is ideal for switched reluctance motor drives, a restriction in the form of half-wave operation is imposed in the PMBDC motor drive with this converter. While such a restriction results in the underutilization of the motor, it leads to other advantages and very welcome features.

Using bifilar windings for the machine, the emitters of the power switches can be tied together and connected to the negative of the dc link voltage. This simplifies the gate circuitry and further can do away with the split supply and hence one power capacitor in the dc link. But the bifilar windings would have the leakage inductances due to the nonideal coupling of the bifilar windings, resulting in high switching turn-off voltages. The bifilar windings, in addition, also take up the slot volume, thus decreasing the area for the main winding, resulting in lower power and torque densities. Before a discussion of merits and demerits of the split supply converter topology is considered, it is instructive to see the operational modes of this converter with the PMBDC motor drive.

11.1.1 OPERATION OF THE PMBDC MOTOR WITH THE SPLIT SUPPLY CONVERTER

Consider the four-quadrant operation of the PMBDC motor with the half-wave converter with a restriction of unidirectional current capability. The operation would be taken on a quadrant-by-quadrant basis.

The first-quadrant operation is shown in Figure 11.2 where the phase sequence is maintained abc with the current injected into the windings when their respective induced emfs experience flat region and for electrical 120°.

Assuming that phase A operation is followed, for example, switch T_1 is turned on at the instant when the stator A phase-induced emf is 30° from its positive zero crossover point. Turn on of the switch T_1 results in the application of voltage V_s to phase winding A, assuming that the switches are ideal. If the phase current exceeds the reference current for that phase, the switch T_1 is turned off depending on the chosen switching strategy such as PWM or hysteresis.

During the turn off of T_1 , the phase current is routed through the diode D_1 , A phase winding and the bottom capacitor in the dc link, resulting in a voltage of $-V_s$ applied to the phase A winding. The negative voltage application to the phase reduces the current

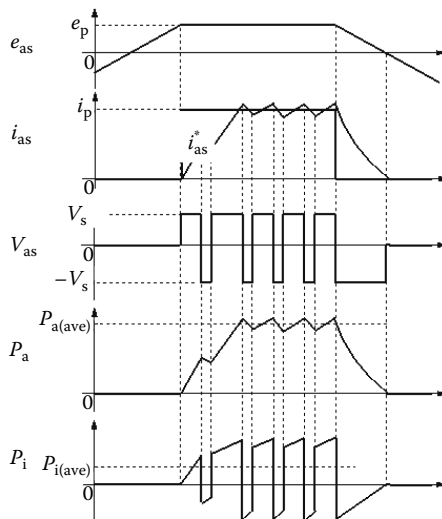


FIGURE 11.2 First-quadrant operation. (From Krishnan, R., *Electric Motor Drives*, Figure 9.55, Prentice Hall, Upper Saddle River, NJ, 2001. With permission.)

swiftly by transferring energy from machine phase to the dc link. Thus the current is controlled between desired limits in the machine phase with only one switch operation. When phase A has to be commutated, note that the switch T_1 is permanently turned off. The average power flow from the dc link source to the machine winding is positive, indicating that the machine is in motoring mode, i.e., first quadrant. Air gap power P_a and instantaneous input power P_i are shown in Figure 11.2, indicating the same.

To brake when the motor drive is in the forward direction of motion, the electromagnetic torque has to be reversed from positive to negative polarity, thereby the drive system will be in the fourth quadrant. Since the current cannot be reversed in this converter, the only alternative to get into this mode is to delay the onset of current in machine phases until their induced emfs have negative polarity and 30° from their negative zero crossover point, as shown in Figure 11.3. This results in negative torque and air gap power in the machine with the consequence that the drive system is in the fourth quadrant. The current control is very much similar to that of the technique described in the first quadrant.

The third-quadrant operation is reverse motoring, which is obtained by changing the phase sequence to acb to obtain the reversal of rotation of direction. Other than that, this mode is very much similar to the first quadrant. Similar is the second-quadrant operation to the fourth quadrant but in the reverse rotational direction. For the sake of brevity, these two quadrants of operation are not considered in detail even though they are dealt with in the modeling, simulation, and analysis later.

11.1.2 OPERATIONAL MODES OF THE CONVERTER

The operational modes of the converter are obtained from the above discussion and summarized in Table 11.1. Current conduction in one phase, which usually is the

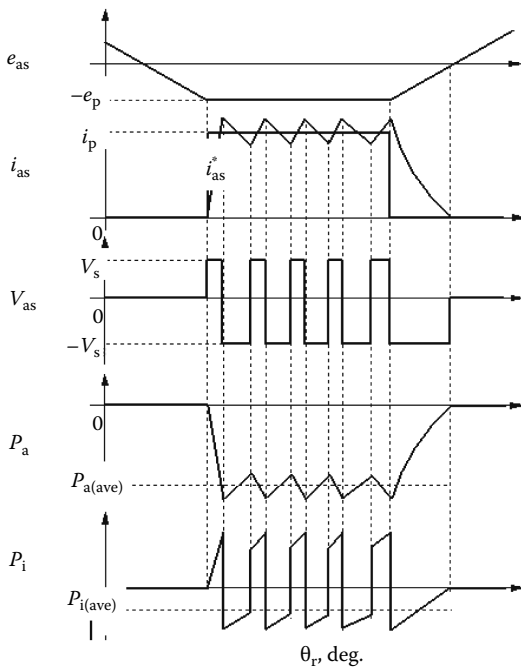


FIGURE 11.3 Fourth-quadrant operation. (From Krishnan, R., *Electric Motor Drives*, Figure 9.56, Prentice Hall, Upper Saddle River, NJ, 2001. With permission.)

TABLE 11.1
Modes of the Converter

Mode	T_1	T_2	D_1	D_2	i_{as}	i_{bs}	V_{as}	V_{bs}
1	On	Off	Off	Off	>0	0	V_s	0
2	Off	Off	On	Off	>0	0	$-V_s$	0
3	Off	On	On	Off	>0	>0	$-V_s$	V_s
4	Off	Off	On	On	>0	>0	$-V_s$	$-V_s$

Source: Krishnan, R., *Electric Motor Drives*, Table 9.3, Prentice Hall, Upper Saddle River, NJ, 2001. With permission.

case during most of the operational time, and conduction in two phases, which occur during the commutation of one phase and energization of the incoming phase, are considered here. Operational modes for phases A and B are identified and they are applicable to any two phases of the machine.

The distinct difference between the full-wave inverter modes and the proposed converter modes is that the proposed converter applies either a positive or a negative voltage across the phase winding when there is a current in it. This has the drawback of higher energy circulation in machine phases, resulting in a small reduction in efficiency and creating torque ripples higher than that of the full-wave inverter-based PMBDC system, which could result in higher acoustic noise in this drive system.

11.1.3 MERITS AND DEMERITS OF THE PMBDC DRIVE WITH THE SPLIT SUPPLY CONVERTER

The PMBDC motor drive with the proposed converter topology has the following advantages:

1. One switch and one diode per phase halves the power stage requirement of the switches and diodes compared to that of the full-wave inverter topology, resulting in low cost and high compactness in packaging.
2. Reduced gating driver circuits and logic power supplies lead to cost reduction and high compactness in packaging.
3. Full four-quadrant operational capability with the attendant possibility for high-performance applications such as in small process drives. Note that the regenerative brake is to be added, which is common even for the full-wave inverter topology.
4. High reliability due to the switch being always in series with the machine phase winding, thus preventing a shoot-through fault.
5. Possible to operate with one switch or phase winding failures whereas it is not possible under these conditions in the PMBDC drive with full-wave inverter. This is an important and an attractive feature for applications such as wheelchair drives and some process drives.
6. Lower conduction losses due to one switch and diode per phase as compared to two switches and two diodes being in operation for the full-wave inverter fed PMBDC motor drive, resulting in half the losses compared to the full-wave drive with the current being the same in both the drives. Further the turn-on losses are reduced by the higher machine inductance in the PMBDC motor for operation with the proposed converter topology as this allows for a soft turn-on of the power devices.
7. This topology allows for sensing of the induced emf across the machine phases by looking at the switch voltage during their turn-off intervals and mechanical or optical sensorless operation becomes possible using these signals to generate the control signals. Note that two-phase switches have the common return, thus doing away with isolation requirement for the transducer signal and also the fact that two-phase voltages are sufficient for generation of the control signals for a three-phase PMBDC motor drive.

The disadvantages of this are as follows:

1. Poorer utilization of the motor due to the half-wave operation. The torque density in terms of the torque per unit stator copper losses is lower in the half-wave-controlled machine by nearly 30% compared to the full-wave-controlled machine.
2. Extra power capacitor is required in the dc link due to split supply.
3. Larger self-inductance for this PMBDC motor results in large electrical time constant, leading to a slow response in current and hence in the torque compared to the full-wave inverter-fed PMBDC motor drive.
4. The commutation torque ripple frequency is halved in the proposed drive compared to that of the full-wave inverter drive. The commutation torque

ripple can be attenuated as in the full-wave inverter drive by coordinating the current in the rising phase with the outgoing phase winding current to yield a constant torque during the phase commutation.

Because of these disadvantages, this topology may not be useful and appropriate for integral hp drive systems.

11.1.4 DESIGN CONSIDERATIONS FOR THE PMBDC MOTOR

This section contains the design considerations of the PMBDC motor required to use with all the half-wave converter topologies. Wherever possible, all these important factors are contrasted with that of the H-bridge inverter (full-wave)-operated PMBDC motor. For the sake of comparison, the full-wave-operated motor is considered as the base.

The following relationships are made on the basis of equal copper volume in the slot of the PMBDC motor. The subscripts 1 and b correspond to the motor with the proposed converter and the motor with the full-wave converter, respectively.

The ratio of the induced emfs are

$$\frac{e_1}{e_b} = \left(\frac{k_1}{k_b} \right) \left(\frac{\omega_1}{\omega_b} \right) \quad (11.1)$$

where

k is the emf constant

ω is the rotor electrical speed

The air gap power ratio is given by

$$\frac{P_1}{P_b} = \frac{1}{2} \left(\frac{k_1}{k_b} \right) \left(\frac{\omega_1}{\omega_b} \right) \left(\frac{I_1}{I_b} \right) \quad (11.2)$$

where I is the current in the winding. The ratio of emf constants in terms of the number of turns per phase and conductor cross sections is

$$\frac{k_1}{k_b} = \frac{N_1}{N_b} = \frac{a_b}{a_1} \quad (11.3)$$

where

N denotes the number of turns/phase

a is the area of cross section of the conductor in general

The ratio of the copper losses is given as

$$\frac{P_{c1}}{P_{cb}} = \frac{1}{2} \left[\frac{I_1 N_1}{I_b N_b} \right]^2 = 2 \left[\frac{T_{el}}{T_{eb}} \right]^2 \quad (11.4)$$

where T_e corresponds to electromagnetic torque in general. The ratio of the stator resistances is

$$\frac{R_1}{R_b} = \frac{a_b N_1}{a_l N_b} = \left[\frac{N_1}{N_b} \right]^2 \quad (11.5)$$

From these relationships, it is possible to find the number of turns per phase, electromagnetic torque, induced emf, air gap power, and stator copper losses in the PMBDC motor for the proposed converter topology, depending on the choice of criterion such as equality of torque, equality of copper losses, and equality of air gap power.

As only one phase of the motor is producing the torque as against two phases in the conventional H-bridge-controlled PMBDC motor, the motor for use with the half-wave converter topology has to meet the following design considerations to provide the same output power within the same thermal capability. Assuming that the current has to be equal to that of the H-bridge inverter-driven PMBDC motor, then the torque constant of this motor has to be twice that of the H-bridge inverter-driven PMBDC motor. This is made possible by increasing the number of turns to twice the number of turns of the H-bridge inverter-driven PMBDC motor. Note that twice the number of turns, for the same wire size, doubles the resistance per phase of the H-bridge-driven PMBDC motor in the half-wave converter-driven motor. The copper losses are the same for both the drive systems as the stator currents are maintained equal to one another. If the copper volume has to be equal in both cases and note that half-wave machines will have four times the resistance (for twice the number of turns). This is not acceptable in practice, as it doubles the resistive losses.

Another alternative is to view the motor to double the speed of the operation of the motor driven by H-bridge inverter, with the same number of turns in both the machines and thus providing equal power at two different speeds. But the half-wave converter-driven motor would have only half the torque of that of the H-bridge-driven motor is to be noted. Given these options, the half-wave converter drive has to be applied fully understanding the application of the motor drive system.

A comparison of PMBDC machines for use with half-wave and full-wave inverter is made here. The basis of the comparison is restricted to equal stator phase currents and equal dc link voltage. Then three distinct options emerge as follows:

1. Unequal copper losses, equal volume of copper and hence copper fill, and equal maximum speeds.
2. Equal copper losses, equal volume of copper and hence copper fill, and unequal maximum speeds.
3. Equal copper losses, unequal volume of copper and hence unequal copper fill factors but such an option increases volume of the copper and possibly stator lamination size, resulting in a large machine size. This option also needs to be considered in applications where the size is not very critical and reliability is of high concern.

TABLE 11.2
Comparison of the PMBDC Machine Variables Based on the Half-Wave and the Full-Wave Inverter
Ratio between the C-Dump Based and That of the Full-Wave Inverter-Based

PMBDC Machine Variables	$N = 2N_b$ (i)	$N_1 = \sqrt{2}N_b$ (ii)	$N_1 = N_b, a_1 = a_b$ (iii)
Conductor area ratios	$\frac{1}{2}$	$\frac{1}{2}$	1
Maximum speed ratio	1	1.414	1
Electromagnetic torque ratio	1	0.707	1
Resistance ratio	4	2	2
Stator copper losses ratio	2	1	1
Size and cost ratio	1	1	>1

Based on the design derivations in Section 11.2.3, a comparison of the machine variables such as speed, torque, stator phase resistance, and total stator copper losses is tabulated in Table 11.2 for the options given in the above.

From the table, it is seen that the option 1 has the certain drawbacks of having twice the copper losses for half-wave controlled PMBDC machine compared to that of the full-wave inverter-based PMBDC machine. This drawback could be interpreted as the result of moving the switch conduction and switching losses from the converter to the machine. It is easier to cool the fractional horsepower machines without significant additional resources as the thermal mass and surface area per unit output watt is higher in fhp machines compared to the integral hp machines. Therefore the half-wave converter drives may be ideally suitable in fhp sizes. Further the increase in cost to handle the thermal effects of higher copper losses in the machine has to be viewed from the overall perspective of the total cost of the motor drive system. Option 2 is very preferable to inherently exploit the full dc link voltage in the half-wave converter-based PMBDCM drive as compared to its counterpart and therefore to achieve a higher speed. Such a characteristic may be possible to exploit in many pump and fan drive applications, thus making the half-wave controlled PMBDCM drive an attractive technical solution. If the route through option 2 is taken for comparison, a number of choices come into play and they are not discussed here for lack of space. Option 3 may be the least desirable *prima facie*, but has to be viewed in terms of the overall cost of the PMBDC motor drive system to assess its suitability for a given application.

11.1.5 IMPACT OF THE MOTOR INDUCTANCE ON THE DYNAMIC PERFORMANCE

From the machine equations, it is seen that the self-inductance of the phase winding plays a crucial role in the dynamics of the current loop and hence in the torque generation.

In the case of the full-wave-operated PMBDC machine, the electrical time constant is given by

$$\tau_{\text{fw}} = \frac{L_s - M}{R_s} \quad (11.6)$$

where M is the mutual inductance.

Consider a PMBDCM with twice the number of turns per phase as compared to the full-wave-operated machine, for operation with the half-wave converter and its self-inductance in terms of L_s is equal to $4L_s$ and its resistance for equal copper losses is $2R_s$, thus giving its electrical time constant as

$$\tau_{\text{hw}} = \frac{4L_s}{2R_s} = \frac{2L_s}{R_s} \quad (11.7)$$

To find the ratio between these two time constants, it is necessary to express M in terms of L_s from which

$$\frac{\tau_{\text{hw}}}{\tau_{\text{fw}}} = \frac{2L_s}{L_s - M} = \frac{2L_s}{L_s(1 - k_m)} = \frac{2}{1 - k_m} \quad (11.8)$$

where

$$M = k_m L_s \quad (11.9)$$

And k_m is used to evaluate the ratio of the time constants and given in Table 11.3 for a PMBDCM with twice, $\sqrt{2}$ and equal to the turns per phase of the full-wave-operated PMBDCM denoted by N_b . From the table, it is seen that the equivalent PMBDCM for operation with C-dump converter has the same electrical time constant compared to the full-wave PMBDCM drive, thus making the proposed drive suitable for very high-performance applications.

11.1.6 WINDING CONNECTIONS

The motor windings have to be connected as shown in Figure 11.4 for connection to the split supply converter as opposed to the half-wave converter connection with

TABLE 11.3
Ratio of Electrical Time Constants for Various Designs of the PMBDC

Stator Slots per Pole per Phase	Ratio of Mutual to Self-Inductance, k_m	Ratio of Time Constants $\tau_{\text{hw}}/\tau_{\text{fw}}$ for Turn per Phase		
		$2N_b$	$\sqrt{2}N_b$	N_b
1	0.333	1.500	1.050	0.750
2	0.400	1.428	1.010	0.714
3	0.415	1.413	0.999	0.706

Source: Krishnan, R., *Electric Motor Drives*, Table 9.6, Prentice Hall, Upper Saddle River, NJ, 2001. With permission.

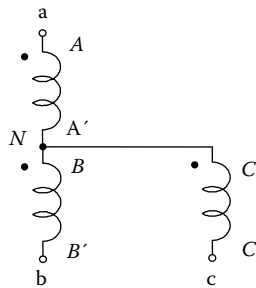


FIGURE 11.4 New machine winding connections for the half-wave converter topology. (From Krishnan, R., *Electric Motor Drives*, Figure 9.57, Prentice Hall, Upper Saddle River, NJ, 2001. With permission.)

all the phase wires forming the neutral have the same polarity for each winding. These connections will not create any additional manufacturing or design burden thus having no impact on the cost.

11.1.7 DRIVE SYSTEM DESCRIPTION

The speed-controlled PMBDCM drive system schematic is shown in Figure 11.5. The feedback signals available for control are the phase currents, discrete rotor position signals from the Hall sensors to generate the gating instances for the phase switches, and rotor speed signal from a tachogenerator or from the position signals itself. The inner current loops enforce current commands and the outer speed loop enforces the speed command. The speed signal is passed through a filter and the resulting modified speed signal is compared with the speed reference to produce the speed error signal. The torque command signal is obtained from the speed error signal through a speed controller that is a proportional plus integral (PI) type. The current magnitude reference is derived from the torque reference by a divider circuit and the phase current commands are generated in combination with respective Hall position sensor signals through a steering circuit. The gating signals are generated for each phase switch by obtaining the phase current errors and processing these errors with PI current controllers and then combining them with carrier frequency to generate the PWM signals.

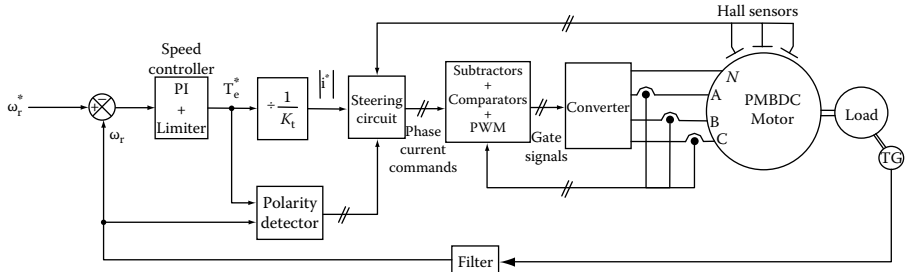


FIGURE 11.5 Schematic of the speed-controlled PMBDC motor drive system. (From Krishnan, R., *Electric Motor Drives*, Figure 9.58, Prentice Hall, Upper Saddle River, NJ, 2001. With permission.)

11.1.8 MODELING, SIMULATION, AND ANALYSIS OF THE PMBDC DRIVE SYSTEM

The various subsystems shown in Figure 11.5 are taken up for modeling, simulation, and analysis in this section.

11.1.8.1 Modeling of the PMBDCM with Converter Modes

PMBDCM model in abc phase variables is used in this simulation. Further an ideal model with zero conduction voltage drop and zero switching times is utilized in this simulation for the switches and diodes. The operational modes determine whether one phase or two phases conduct at a given time and accordingly the system equations emerge. To model when only phase A is conducting, the system equation is given by

$$R_s i_{as} + L_s p i_{as} + e_{as} = V_s \quad (11.10)$$

where

R_s is the stator phase resistance

L_s is the self-inductance of a phase

e_{as} is a phase-induced emf

p is the derivative operator

V_s is the dc link voltage of the top half

The induced emf is given by

$$e_{as} = K_b f_{as}(\theta) \omega_r V \quad (11.11)$$

where

f_{as} is a unit function generator to correspond to the trapezoidal-induced emf of the PMBDCM as a function of θ_r , which is the rotor electrical position

K_b is the emf constant

ω_r is the rotor electrical speed

f_{as} is given by

$$\begin{aligned} f_{as}(\theta_r) &= (\theta_r) \frac{6}{\pi}, & 0 < \theta_r < \frac{\pi}{6} \\ &= 1, & \frac{\pi}{6} < \theta_r < \frac{5\pi}{6} \\ &= (\pi - \theta_r) \frac{6}{\pi}, & \frac{5\pi}{6} < \theta_r < \frac{7\pi}{6} \\ &= -1, & \frac{7\pi}{6} < \theta_r < \frac{11\pi}{6} \\ &= (\theta_r - 2\pi) \frac{6}{\pi}, & \frac{11\pi}{6} < \theta_r < 2\pi \end{aligned} \quad (11.12)$$

For mode 3, when the phase a is being commutated and phase b is energized, the following equations apply:

$$R_s i_{as} + L_s p i_{as} + M p i_{bs} + e_{as} = -V_s \quad (11.13)$$

$$R_s i_{bs} + L_s p i_{bs} + M p i_{as} + e_{bs} = V_s \quad (11.14)$$

where the subscript b corresponds to respective phase b variables and parameters defined above. The f_{bs} is similar to f_{as} but phase displaced by electrical 120° . Similarly, the equations for other modes may be derived from Equations 11.10 through 11.14.

The electromechanical equation with the load is given by

$$J \frac{d\omega_m}{dt} + B\omega_m = T_e - T_l \quad (11.15)$$

where

J is the moment of inertia

B is the friction coefficient

T_l is the load torque

T_e is the electromagnetic torque given by

$$T_e = K_t \{ f_{as}(\theta) i_{as} + f_{bs}(\theta) i_{bs} + f_{cs}(\theta) i_{cs} \}, \text{ N}\cdot\text{m} \quad (11.16)$$

where K_t is the torque constant in N m/A unit given by $\lambda_p(P/2)$. To compute the torque, the rotor position is required to evaluate the emf functions. The rotor position is derived for simulation from the following equation:

$$p\theta_r = \omega_r \quad (11.17)$$

11.1.8.2 Modeling of the Speed Controller

The speed controller is modeled as a PI type as

$$G_s(s) = K_{ps} + \frac{K_{is}}{s} \quad (11.18)$$

where s is Laplace operator and from this equation, the torque and current references may be derived. This equation is written in time domain for simulation.

The state diagram of the speed controller with the limiter on its output to restrict it within maximum permissible torque commands is seen in [Figure 11.6](#). The relevant equations for the torque command, output of the PI speed controller, and the state relationships are

$$\dot{x} = K_{is} (\omega_r^* - \omega_r) \quad (11.19)$$

$$y_1 = \left\{ K_{ps} (\omega_r^* - \omega_r) + K_{is} \right\} \quad (11.20)$$

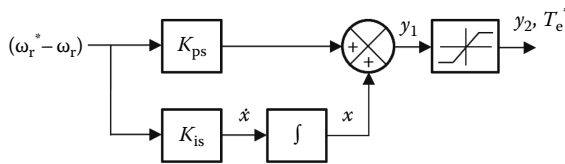


FIGURE 11.6 Schematic of the speed-controlled PMBDC motor drive system.

$$T_e^* = y_1; \quad -T_{em} \leq y_1 \leq +T_{em} \quad (11.21)$$

where $\pm T_{em}$ is the maximum positive and negative permitted for the command, respectively.

11.1.8.3 Steering Circuit

The steering circuit consists of three inputs, one of which is the current magnitude reference, and the other two are polarity signals of the rotor speed and torque reference denoted as $|i^*|$, ω_{rp} , T_{ep} , respectively. Depending on the polarity of the rotor speed and torque reference, the quadrant of operation and the phase sequence are determined as given in Table 11.4.

Depending on the quadrant of operation and the position of the rotor which determines induced emfs in the machine phases and hence the emf functions, the phase current commands are determined as follows:

Quadrant I	Quadrant IV
$f_{as}(\theta_r) \geq 1, i_{as}^* = i^* $	$f_{as}(\theta_r) \leq -1, i_{as}^* = i^* $
$f_{bs}(\theta_r) \geq 1, i_{bs}^* = i^* $	$f_{bs}(\theta_r) \leq -1, i_{bs}^* = i^* $
$f_{cs}(\theta_r) \geq 1, i_{cs}^* = i^* $	$f_{cs}(\theta_r) \leq -1, i_{cs}^* = i^* $

(11.22)

Similarly for the third and fourth quadrants, the phase current commands are derived. This completes the modeling of the steering circuit.

TABLE 11.4
Operational Quadrant Relationships

ω_{rp}	T_{ep}	Quadrant	Phase Sequence
≥ 0	≥ 0	I	abc
≥ 0	< 0	IV	abc
< 0	≥ 0	II	acb
< 0	< 0	III	acb

Source: Krishnan, R., *Electric Motor Drives*, Table 9.7, Prentice Hall, Upper Saddle River, NJ, 2001. With permission.

11.1.8.4 Current Loop Modeling

For phase A, the current loop model including the PWM is derived in the following but the same algorithm is applicable to all other phases is to be noted. The current error, say for phase A, i_{aer} , which is the difference between the current reference and actual current, is amplified and processed through a PI controller very much similar to that of the speed controller. The output of the current controller is limited to its maximum value given as i_{max} . The duty cycle of the switch for one period of the PWM cycle is then given by

$$\begin{aligned} d &= \frac{i_{aer}}{i_{max}}, & i_{aer} > 0 \\ &= 0, & i_{aer} < 0 \end{aligned} \quad (11.23)$$

The on time of the switch, T_{on} , is given by

$$T_{on} = dT_c = \frac{d}{f_c} \quad (11.24)$$

where

f_c is the carrier frequency of the PWM

T_c is the period of the PWM cycle

Note that the current loop is entered to update the on time of the switch only once in a PWM cycle. The off-time for the phase switches is obtained from the difference between T_c and T_{on} .

11.1.8.5 Simulation and Analysis

The parameters of the PMBDC drive system for dynamic simulation are given below:

PMBDCM Drive System Parameters

Poles = 4	hp = 0.5	
$R_s = 0.7 \Omega/\text{ph}$	$L = 2.72 \text{ mH}$	$M = 1.5 \text{ mH}$
$K_b = 0.5128 \text{ V}/(\text{rad/s})$ (Mech.)	$K_t = 0.049 \text{ N m/A}$	
$J = 0.0002 \text{ kg m/s}^2$	$B = 0.002 \text{ N m./rad/s}$	
$V_{s1} = V_{s2} = V_s = 160 \text{ V};$	$f_c = 2 \text{ kHz};$	Speed (base) = 4000 rpm
Current (base) = 17.35 A, V(base) = 40 V, Torque (base) = 0.89 N m.		
Torque(max) = 2*Torque(base); $I_{max} = 2^*\text{Current (base)}$		
Speed Controller: Proportional gain $K_{ps} = 20$, Integral gain $K_{is} = 1$		
Current Controllers: Proportional gain $K_{pi} = 50$, Integral gain $K_{ii} = 5$		

A fully four-quadrant operation is simulated by giving a two-directional step speed reference of rated value. The key responses of the actual speed, torque reference, actual torque, phase A current and its reference, phase B current, and rotor

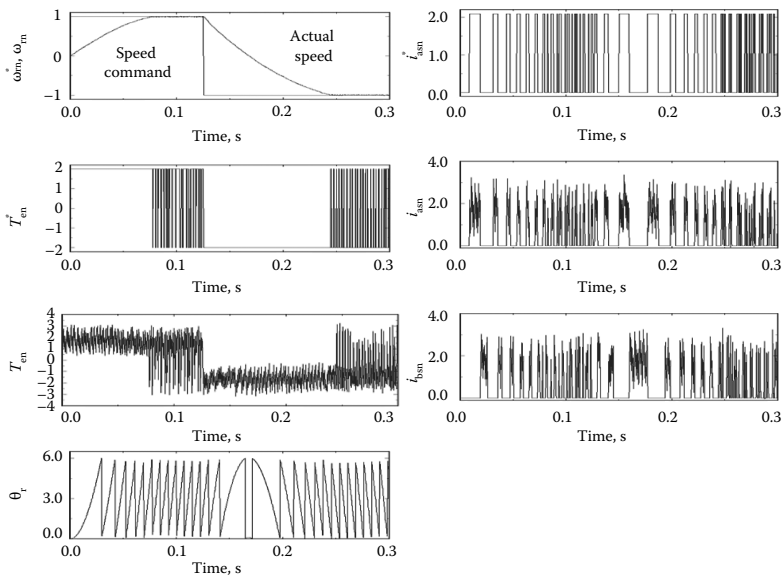


FIGURE 11.7 Dynamic simulation results of a four-quadrant PMBDC motor with the split supply converter topology. (From Krishnan, R., *Electric Motor Drives*, Figure 9.59, Prentice Hall, Upper Saddle River, NJ, 2001. With permission.)

position are shown in Figure 11.7 together with the speed reference, all in normalized units. While no steps have been taken to optimize the speed and current controllers, it becomes clear from the simulation results that the drive system is distinctly capable of four-quadrant operation. Further, it shows that the current response is fast enough for consideration of this drive in high-performance applications. This is to be further explored by evaluating the current commutation angle because the dynamics of commutation is slightly different from that of the full-wave inverter-fed PMBDCM drive system due to the different time constants and the effects of mutual coupling.

11.1.8.6 Current Commutation Angle

The current commutation angle for the above-stated reason is evaluated in this section. Equation 11.12 describes the phase A during current commutation. Neglecting the resistive voltage drop, and assuming that the phase B current rises linearly with respect to time for the sake of simplicity and a closed form solution to the commutation time is obtained. The condition used in the solution of the equation is that by the time the current in phase A is commutated, i.e., t_c , from I_p to zero, the current in phase B is at I_p . This stratagem relieves the solution of an otherwise transcendental equation. The current commutation time is given by

$$t_c = \frac{-b - \sqrt{b^2 - 4ac}}{2a} \quad (11.25)$$

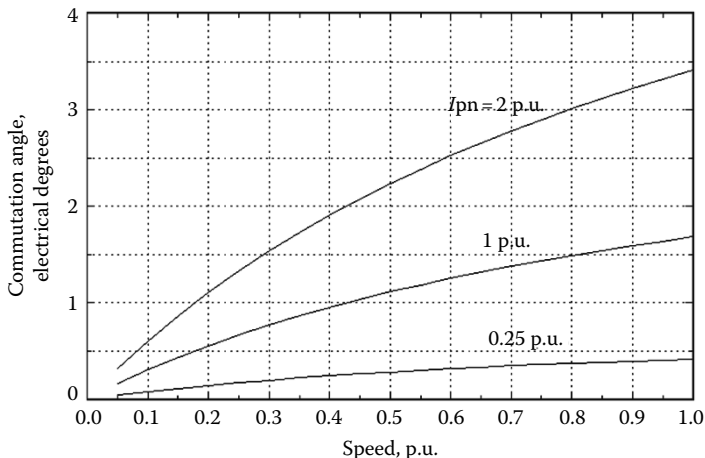


FIGURE 11.8 Commutation angle of the current in electrical degrees versus normalized rotor speed in p.u. as a function of stator current.

where

$$a = \frac{E_p}{2LT_1}; \quad b = -\frac{MI_p + 2E_p + 2V_s}{2L}; \quad c = I_p \quad (11.26)$$

where T_1 is equal to the time duration corresponding to the electrical 30° for the given rotor speed. The commutation angle is obtained by multiplying the commutation time with the rotor speed, which is assumed constant during commutation. The commutation angle versus normalized speed as a function of normalized phase currents of 0.25, 1, and 2 p.u. are shown in Figure 11.8. The commutation angle is less than 3.5° even for 2 p.u. current and 1 p.u. speed. It can be inferred that the commutation time is very small and constituting only a fraction of the phase conduction period. This will not cause appreciable increase in the rms current rating of the devices, thereby increasing the heatsink volume.

11.1.8.7 Comparison of the Half-Wave and Full-Wave Inverter-Based PMBDC Drives

Consider the average duty cycle of the switch during a phase conduction as h for deriving a comparison between the half-wave and the full-wave inverter-based PMBDCM drive system given in Table 11.5. Even though the Volt Ampere (VA) rating of the converters is the same, note that fewer devices with higher voltages usually cost less with the additional advantages of lower conduction and switching losses in the split supply converter topology. The comparison does not consider the regenerative brake circuit, which is required for both but with different VA ratings.

TABLE 11.5
Comparison of the Half-Wave Converter with the Full-Wave Converter-Based PMBDC System

Aspects	Split-Supply Converter-Based PMBDC	Full-Wave Converter-Based PMBDC
Number of power switches (all phases)	3	6
Number of diodes	3	6
Switch voltage (min.)	$2V_s$	V_s
Switch current (peak)	I_p	I_p
Switch current (rms)	$I_p/\sqrt{3}$	$I_p/\sqrt{3}$
Motor ph. current (rms)	$I_p/\sqrt{3}$	$\sqrt{2}I_p/\sqrt{3}$
Number of capacitors	2	1
Capacitor voltage	V_p	V_p
Min. number of diodes in the front-end rectifier	2	4
Number of logic power supplies for isolated operation (min.)	2	4
Number of gate drivers	3	6
Switch conduction losses	$hv_{sw}I_p^a$	$2hv_{sw}I_p$
Diode conduction losses	$(1-h)v_dI_p$	$2(1-h)v_dI_p$
VA rating (peak)	$6V_sI_p$	$6V_sI_p$
VA rating (rms)	$2\sqrt{3}V_sI_p$	$2\sqrt{3}V_sI_p$

Source: Krishnan, R., *Electric Motor Drives*, Table 9.8, Prentice Hall, Upper Saddle River, NJ, 2001.
With permission.

^aThis current may be higher because of circulation energy.

11.2 C-DUMP TOPOLOGY

The half-wave converter topology including split phase supply with one switch per phase has the disadvantage of utilizing only half of the maximum available dc link voltage. This could be changed if topologies with more than one switch per phase but less than two switches per phase are resorted to. Such topologies have been developed for switched reluctance motor drives with considerable success. One such topology is the C-dump converter with $n+1$ switches for a n -phase machine [4]. The C-dump topology is shown in Figure 11.9 for a three-phase machine. The principle of operation, and analysis and design of such a converter topology for a four-quadrant PMBDCM drive system is presented in this section. Design considerations for the PMBDCM to work with the C-dump power converter based on power and torque equality with full-wave-operated PMBDCM are developed. A comparison of the C-dump and full-wave PMBDCM drives is derived to highlight key advantages and disadvantages of the C-dump-operated PMBDCM drive system.

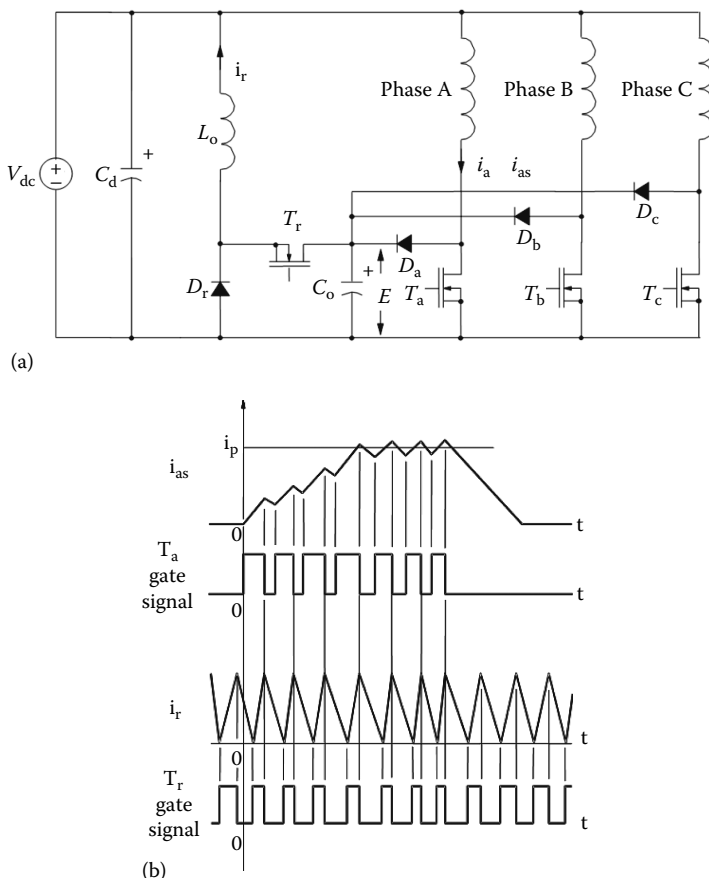


FIGURE 11.9 C-dump converter topology and key waveforms: (a) C-dump topology. (From Krishnan, R., *Electric Motor Drives*, Figure 9.60, Prentice Hall, Upper Saddle River, NJ, 2001. With permission.); (b) relationships between gate signals and currents.

11.2.1 PRINCIPLE OF OPERATION OF THE C-DUMP PMBDC DRIVE SYSTEM

The C-dump converter for a three-phase system shown in Figure 11.9 is considered. It has four power switches and four power diodes with one of each for each phase winding and one set for energy recovery from the capacitor, C_o . Since the phase has only one switch, the current in it could only be unidirectional and hence it is very much similar to the half-wave converter-driven PMBDCM in operation. The motoring (I-quadrant) and regenerative (IV-quadrant) control of the C-dump-based PMBDC are briefly described in the following.

11.2.1.1 Motoring Operation

Assume that the direction of the motor is clockwise, which may be considered positive with the phase sequence of abc of the motor phase windings for this discussion. The motoring operation is initiated when the phase voltage is in the flat

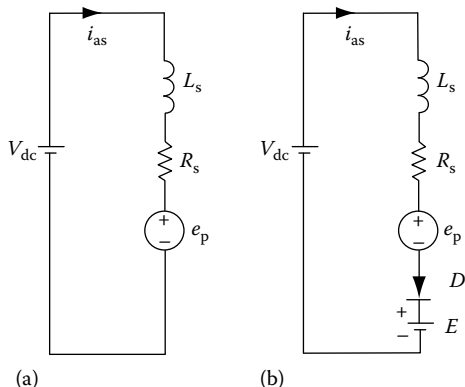


FIGURE 11.10 First-quadrant motoring operation with phase A of the PMBDC drive: (a) switch T_a on; (b) switch T_a off with continuous current in phase A. (From Krishnan, R., *Electric Motor Drives*, Figure 9.61, Prentice Hall, Upper Saddle River, NJ, 2001. With permission.)

region, i.e., at constant magnitude for a fixed speed and with the duration of electrical 120° degrees. The phase A is energized when the phase current is commanded by turning on switch T_a and the equivalent circuit is shown in Figure 11.10a. When the current error is negative, switch T_a is turned off and the current in the phase A winding is routed through the diode D_a to the energy recovery capacitor, C_o shown in Figure 11.10b. During this time, a negative voltage to the magnitude of $(E - V_{dc})$ is applied across the machine winding, thus reducing the current and bringing the current error to positive. The average air gap power and the input power are positive, giving a positive electromagnetic torque, thus indicating the operation is firmly in the first quadrant of the torque versus speed region.

Similar is the motoring operation in the counterclockwise (reverse) direction of rotation of the motor, excepting that the phase sequence will be acb in the energization of the motor phase windings. That corresponds to the III-quadrant of the torque speed characteristics.

11.2.1.2 Regenerative Operation

Whenever the energy has to be transferred from load to the supply, the PMBDCM is to be operated as a generator, i.e., by generating a negative torque in the machine as against the positive torque for the motoring operation. It is usual to provide a current of opposite polarity to that of the induced emf in the full-wave converter-operated PMBDCM to generate a negative torque. It is not feasible in this C-dump-operated PMBDCM due to its unidirectional current feature for the positive half-cycle of the induced emfs. Then the only alternative is to exploit the negative cycles of the induced emf where only positive currents are required to obtain the negative torque. Such an operation for phase A involves the turn on of T_a during negative constant emf period and when the error current becomes negative turning off T_a enabling the conduction of D_a , resulting in the energy transfer from the machine phase a to the energy recovery capacitor. These operations are shown in Figure 11.11a and b. Note that the air gap power and the average input power to the phase A are negative, indicating that the

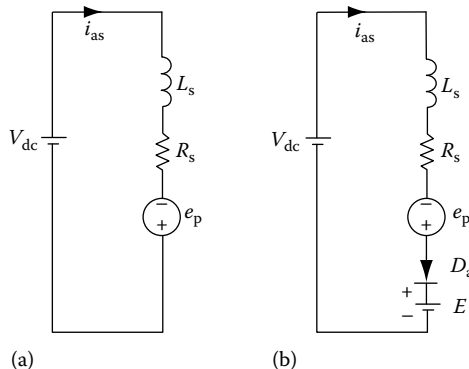


FIGURE 11.11 Operational mode and waveforms of variables for the IV-quadrant regenerative operation of PMBDC drive system: (a) T_a on; (b) T_a off. (From Krishnan, R., *Electric Motor Drives*, Figure 9.62, Prentice Hall, Upper Saddle River, NJ, 2001. With permission.)

power has been transferred from the machine to the energy recovery capacitor, C_o . The energy from C_o is recovered by a step-down chopper using switch T_r and diode D_r shown in Figure 11.9. Note that this regenerative operation corresponds to the IV-quadrant for a phase sequence of abc and similar is the regenerative operation for reverse rotational direction of the PMBDCM corresponding to the II-quadrant.

11.2.2 ANALYSIS OF THE C-DUMP PMBDCM DRIVE

The analysis of the drive system with the C-dump topology is presented in this section. Effort is primarily made to obtain the maximum speed of the motor in terms of the duty cycle of the phase switches and the energy transferred to the energy recovery capacitor and hence an estimate of the power to be handled by the recovery chopper for a given motor rating. It is assumed that the commutation pulses are available through Hall sensors or encoders or resolvers.

11.2.2.1 Maximum Speed

Consider the machine voltage equation in steady state for rated stator current given by I_b and it is given as follows:

$$V_{as} = R_s I_b + K_b \omega_r, \text{ V} \quad (11.27)$$

and the electrical rotor speed is obtained from this as

$$\omega_r = \frac{V_{as} - R_s I_b}{K_b}, \text{ rad/s} \quad (11.28)$$

For faster current loop performance and hence torque and speed responses, it is necessary to set aside some voltage, which is a fraction of the rated stator voltage given as $k_a V_{as}$, where k_a is a fraction. Including this factor, the rotor speed is modified to

$$\omega_r = \frac{1}{K_b} \left[V_{as} (1 - k_a) - R_s I_b \right] \quad (11.29)$$

If an average duty cycle of the phase switches is denoted as h , then the stator phase voltage in terms of the dc link voltage is written as

$$V_{as} = h V_{dc} \quad (11.30)$$

which when combined with the rotor speed equation and normalization yields the normalized rotor speed as

$$\omega_{rn} = h (1 - k_a) V_{dcn} - R_{sn}, \text{ p.u.} \quad (11.31)$$

where the additional subscript n denotes the normalized values of the variables and parameters. Typically, k_a is in the range of 0.2–0.4 and h is varied from nearly 0–1. This relationship explicitly gives speed in terms of the duty cycle, dc link voltage, stator resistance, and dynamic voltage reserve. This expression allows the determination of range of h variation for the desired variation of speed range. Determination of h is crucial to the evaluation of average energy recovery current and hence in the rating of that circuit.

11.2.2.2 Peak Recovery Current

The energy transferred to the energy storage capacitor, C_o , during the turn-off intervals of phase switches has to be recovered through the energy recovery circuit if losses are neglected. The average duty cycle of energy transfer from the dc link and machine phase into capacitor C_o is $(1-h)$. Assuming that this stored energy is recovered through the chopper in a duty cycle of h , as this is essential to keep the separation of energy storage and recovery circuits, the powers can be equated as

$$E(1-h)I_p = EhI_r \quad (11.32)$$

where I_r is the peak recovery current through chopper and could be written as

$$I_r = \frac{1-h}{h} I_p \quad (11.33)$$

As h increases, note that the energy recovered through chopper reduces as I_r goes down, which in turn reduces the volt-ampere rating of the energy recovery chopper circuit.

11.2.2.3 Energy Recovery Capacitor

The minimum voltage on this capacitor, C_o , is given by,

$$E(\min) = V_{dc} + E_p + \Delta E \quad (11.34)$$

where

E_p is the maximum induced voltage at maximum speed

ΔE is the voltage magnitude to be provided for in design to prevent the conduction of diodes D_a , D_b , and D_c during the negative half-cycles of the induced emf generation in the machine

11.2.2.4 Energy Recovery Chopper

The voltage rating is equal to E but its current rating is based on the power transfer from the energy recovery capacitor to the dc link. It is based on the speed of operation and load, which is a function of the duty cycle of the phase switch. The inductor L_o is rated based on the switching frequency of the chopper.

11.2.3 COMPARISON WITH FULL-WAVE INVERTER-CONTROLLED PMBDCM DRIVE

This section would compare the C-dump topology-based PMBDC with that of the H-bridge inverter-fed PMBDC motor drive system from the points of view of number of switches, passive components, their ratings, number of logic power supplies for gate drives, number of gate drives for isolated drive systems, converter losses, thermal management, and packaging requirements.

Some salient aspects and their comparison are given in [Table 11.6](#). The average duty cycle of the phase switches is h and k_1 denotes the fraction of voltage for safety margin in the operation of the drive. Let k_2 be the fraction to give the regeneration brake current and

$$k_3 = \frac{E}{V_{dc}} \quad (11.35)$$

This leads to the ratio of the VA rating as

$$\frac{VA_{cd}}{VA_{fw}} = \left[\frac{k_3}{1 + k_1} \right]^{3 + \frac{1-h}{h}} \frac{1-h}{6+k_2} \quad (11.36)$$

For nominal values of $k_1 = 0.1$ and $k_2 = 0.25$, the relationship between the ratio of VA rating versus the average duty cycle, h , for various values of k_3 ranging from 1.25 to 2 is shown in [Figure 11.12](#). The breakeven point for equal VA rating is shown with bold lines. Note that the duty cycle h is proportional to the normalized speed.

The converter switch losses are smaller for $h > 0.5$ in the case of the C-dump and the diode losses are half of the full-wave converter. This reduction in losses translates into heatsink and thermal management reduction by the same measure, resulting in a sizable reduction in packaging size. Further it is helped by the requirement of smaller number of logic power supplies, snubbers, and gate drivers.

TABLE 11.6
Comparison of the C-Dump and Full-Wave Based PMBDC Drive

Aspects	C-Dump Based PMBDC	Full-Wave Based PMBDC
Number of switch devices	4	7 (including regenerative brake)
Number of diodes	4	7
Switch voltage	E	V_{dc}
Switch peak current	I_p	I_p
RMS switch current	$\frac{I_p}{\sqrt{3}}$	$\frac{I_p}{\sqrt{3}}$
Motor phase rms current	$\frac{I_p}{\sqrt{3}}$	$\sqrt{\frac{2}{3}} I_p$
Power capacitors	2	1
Capacitor voltages	V_{dc} and E	V_{dc}
Number of logic power supplies(minimum)	2	4
Inductor	1	0
Number of gate drivers	4	7
Turn off snubbers (if needed)	0	6
Switch losses	$v_{sw} I_p \left[h + \frac{1-h}{h} \right]$	$2hv_{sw} I_p$
Diode losses	$v_d I_p (1 - h)$	$2v_d I_p (1 - h)$
Total peak switch VA rating	$EI_p \left[3 + \frac{1-h}{h} \right]$	$6v_{dc} (1 + k_1) I_p$ $+ v_{dc} (1 + k_1) I_p k_2$

Source: Lee, B.S. and Krishnan, R., *Proc. IEEE Int. Symp. Indus. Electron.*, 2, 689, 1999. With permission.

The comparison on features such as reliability of the converter, fault-tolerance, i.e., its operational capability with one or more phases of the machine or converter disabled has to be made. In every one of these, the C-dump-based PMBDCM drive is inherently superior to that of the full-wave inverter-based PMBDCM drive is obvious.

11.2.4 MODELING, SIMULATION, AND DYNAMIC PERFORMANCE

From earlier discussion, four distinct modes of operation can be identified for the proposed drive system. These modes, along with their dynamic modeling and system simulation, are given in this section.

11.2.4.1 Modeling

Only phase A is considered and the voltage drop on the devices and also the resistance of the energy recovery inductance are ignored. The drive system considered for modeling has the C-dump converter. For each mode the system equations are derived.

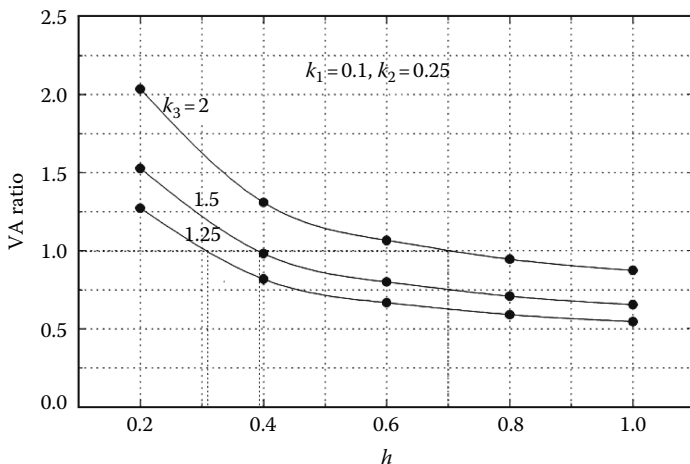


FIGURE 11.12 VA ratio versus average duty cycle for various values of energy recovery capacitor voltages. (From Krishnan, R., *Electric Motor Drives*, Figure 9.63, Prentice Hall, Upper Saddle River, NJ, 2001. With permission.)

Mode (i): Current buildup in phase A with T_a on and T_r off is given by

$$V_{dc} = R_s i_{as} + L_s p i_{as} + e_{as}, \text{ V} \quad (11.37)$$

The energy recovery action is represented by

$$L_0 p i_r = -V_{dc}, \text{ V (if } i_r > 0\text{)} \quad (11.38)$$

Mode (ii): Reverse phase voltage with T_a off and T_r off is given by the following equations:

$$V_{dc} = R_s i_{as} + L_s p i_{as} + e_{as} + E, \text{ V} \quad (11.39)$$

where E is the dump capacitor voltage given by

$$E = E_0 + \frac{1}{C_0} \int i_{as} dt, \text{ V} \quad (11.40)$$

The energy recovery operation is characterized during this time as

$$L_0 p i_r = -V_{dc}, \text{ V (if } i_r > 0\text{)} \quad (11.41)$$

where E_0 is the initial condition for the dump capacitor.

Mode (iii): Energy recovery when both T_a and T_r are on is given by the following equations:

$$V_{dc} = R_s i_{as} + L_s p i_{as} + e_{as}, \text{ V} \quad (11.42)$$

$$L_0 p i_r = E - V_{dc}, \text{V} \quad (11.43)$$

$$E = E_0 - \frac{1}{C_0} \int i_r dt, \text{V} \quad (11.44)$$

Mode (iv): Phase A is being de-energized while phase B is being energized with T_a and T_r off, T_b on and characterized by the following equations:

$$V_{dc} = R_s i_{as} + L_s p i_{as} + L_m p i_{bs} + e_{as} + E, \text{V} \quad (11.45)$$

$$V_{dc} = R_s i_{bs} + L_s p i_{bs} + L_m p i_{as} + e_{bs}, \text{V} \quad (11.46)$$

$$E = E_0 + \frac{1}{C_0} \int i_{as} dt, \text{V} \quad (11.47)$$

$$L_0 p i_r = -V_{dc}, \text{V} (\text{if } i_r > 0) \quad (11.48)$$

Note that the phase currents and i_r are always positive due to the converter configuration.

11.2.4.2 System Performance

The simulation takes the same drive system parameters as given for the split supply converter-operated drive system. The target value for the C-dump capacitor voltage is set to 175 V. The C-dump capacitor is initially charged to 100 V, which is the magnitude of the supply voltage. Figure 11.13 shows the commanded speed (ω_r^*), actual speed (ω_p), induced phase emf of phase a, phase a current, air gap torque, and the voltage of the C-dump capacitor for the simulated speed loop with a speed command of ± 1000 r/min.

The dump capacitor is charged to its target value of 175 V in less than 0.05 s. This voltage is then maintained in the proximity of 175 V. The transition from -1000 to $+1000$ r/min takes 0.9 s. As long as the commanded and actual speed are significantly different, the current command is at its maximum value of 20 A. Once the desired speed is achieved, the current drops to 8 A in order to support the motor load of $0.48 \text{ N}\cdot\text{m}$. While the direction of rotation and the sign of the air gap torque are different, the load torque acts in unison with the air gap torque to decelerate the rotor. This results in faster deceleration of the rotor. The situation is different during acceleration when the load opposes the air gap torque, resulting in slower acceleration than the deceleration.

11.3 VARIABLE dc LINK CONVERTER TOPOLOGY

One of the converter topologies with the advantage of varying the dc voltage input to the machine but with lower switch voltage not exceeding that of the dc source has other significant advantages also. They will be described in the succeeding discussion. Such a circuit is shown in Figure 11.14. In addition, this power

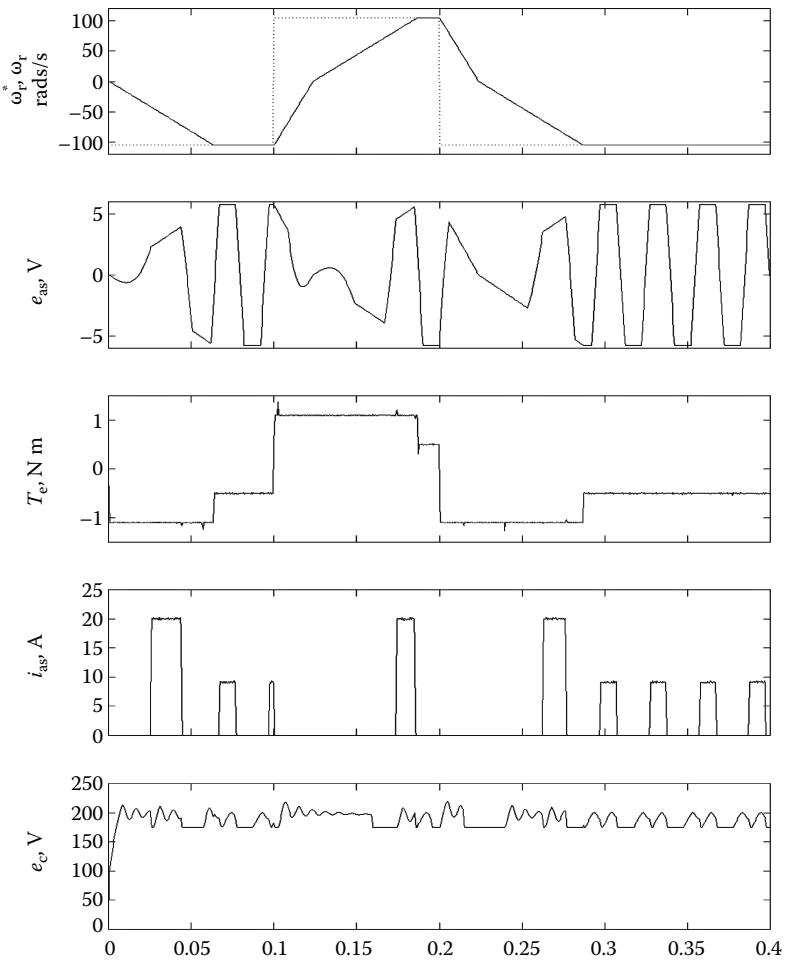


FIGURE 11.13 Dynamic simulation results. (From Krishnan, R., *Electric Motor Drives*, Figure 9.64, Prentice Hall, Upper Saddle River, NJ, 2001. With permission.)

converter topology has the advantages of the C-dump and split supply converter topologies.

11.3.1 PRINCIPLE OF OPERATION

The converter circuit for a three-phase output has four switches and diodes [5] with the additional capacitor and inductor for its operation. The converter has two stages. The first stage is the chopper, which allows the variation of the input voltage to the machine. Switch T, diode D, inductor L, and capacitor C form a step-down chopper power stage. The input voltage applied to the phases V_i is regulated by the operation of the chopper switch T. The inductor L and the capacitor C reduce the ripple content of the voltage V_i .

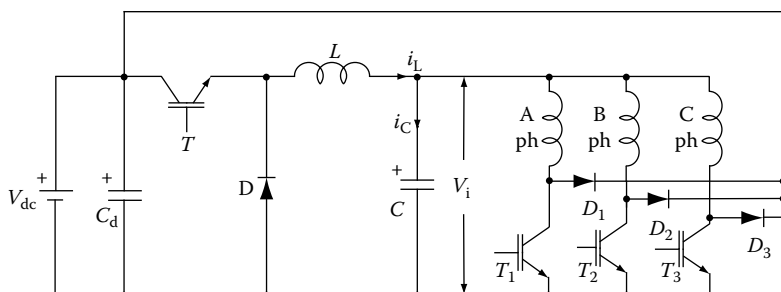


FIGURE 11.14 Variable dc link converter topology for PMBDC drives. (From Krishnan, R., *Electric Motor Drives*, Figure 9.65, Prentice Hall, Upper Saddle River, NJ, 2001. With permission.)

The second stage of the converter is the machine side converter for handling the energy from the dc link to the machine and from the machine to the source. The chopper switch can be coordinated with the phase switches to regulate the current without having to switch the phase windings at PWM carrier frequency. Because of the coordination option between the chopper switch and the phase switches, many modes of operation are possible in this drive system. The motoring (I-quadrant) and regenerative (IV-quadrant) control of the PMBDCM are briefly described with this converter.

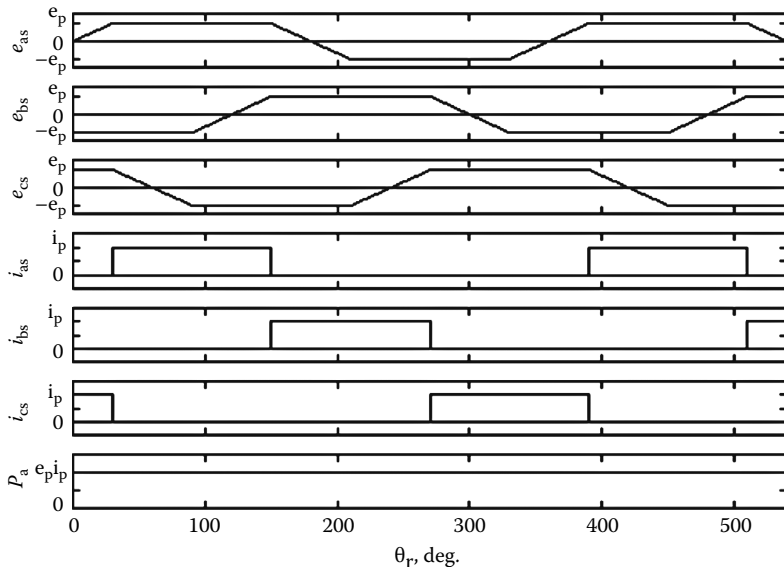


FIGURE 11.15 Voltage, current and airgap power waveforms of the half-wave converter-based PMBDCM.

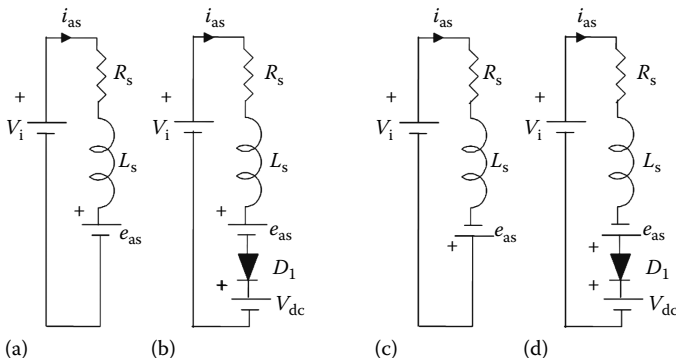


FIGURE 11.16 Operation of variable dc link current-based PMBDC drive. (a) I-Quadrant motoring operation with phase a of the PMBDCM drive, switch T_1 on. (b) I-Quadrant motor-ing operation with phase a of the PMBDC drive, switch T_1 off with continuous current in phase A. (c) IV-Quadrant regenerative operation with phase a of the PMBDCM drive, switch T_1 on. (d) IV-quadrant regenerative operation with phase a of the PMBDCM drive, switch T_1 off with continuous current in phase A.

11.3.2 MOTORING

Assume the direction of the motor is clockwise, which may be considered as positive with a phase sequence of abc of motor phase windings. The motoring operation is initiated when the phase voltage is constant positive for a fixed speed and with the duration of electrical 120° as shown in Figure 11.15. Phase a is energized when the switch T_1 is turned on and the equivalent circuit is shown in Figure 11.16a. To regulate current, T_1 is turned off, which initiates routing of the current through the freewheeling diode D_1 , source voltage V_{dc} , and capacitor C , applying a voltage of $(V_i - V_{dc})$ across the machine phases as shown in Figure 11.16b.

The motoring operation is similar in the reverse direction, except that the phase energization sequence will be acb in the motor phase windings. This corresponds to quadrant III operation.

11.3.2.1 Regenerative Operation

To transfer energy from the load to the source, the PMBDCM has to be operated as a generator, i.e., by providing negative torque to the machine. Negative torque is achieved by turning on T_1 during the negative constant emf period. The equivalent circuits during on time and off time of switch T_1 are shown in Figure 11.16c and d, respectively.

Based on the rotor position information and the polarity of the torque command, i^* , the appropriate machine phase is turned on. The phase switch is turned on and modulated only if the current in the phase increases beyond a current window over the reference current by hysteresis control. Normally due to precise control of the machine input voltage through the chopper switch T , the phase switch is rarely modulated to regulate the phase current. The phase switch is turned off only during commutation of the phase.

11.3.3 SYSTEM PERFORMANCE

Consider the drive system configuration as shown in Figure 9.1. Both the torque and speed-controlled drive systems are simulated and results are given below. When considering a torque drive, note that the speed loop is opened in the control schematic.

11.3.3.1 Torque Drive Performance

Figure 11.17 shows the simulation results of a torque drive system performance, i.e., a system operating with only inner current loops. The machine is operating at 50% of the rated speed. The reference torque T_e^* is set at 1 p.u. by setting i^* to 1 p.u. The phase currents i_{as} , i_{bs} , i_{cs} are seen to reach the same value as the reference current i^* in the machine. It can be observed that the actual torque developed in the machine T_e has dips when there are transitions from one phase to another. Coordinating the currents in the incoming and outgoing phases can solve this problem. After 0.035 s, the commanded torque is switched from 1 to -1 p.u. while the speed remains the same, i.e., to make the system operate in the IV-quadrant. It can be observed that the voltage applied to the machine phases is about 0.5 p.u. as it is sufficient. It is unlike in other converter topologies where a voltage switching between 0 and 1 p.u. is normally applied to the machine phases. Because of reducing the dc link voltage as a function of the mechanical speed, the switching losses are reduced apart from losses resulting from lower current ripple.

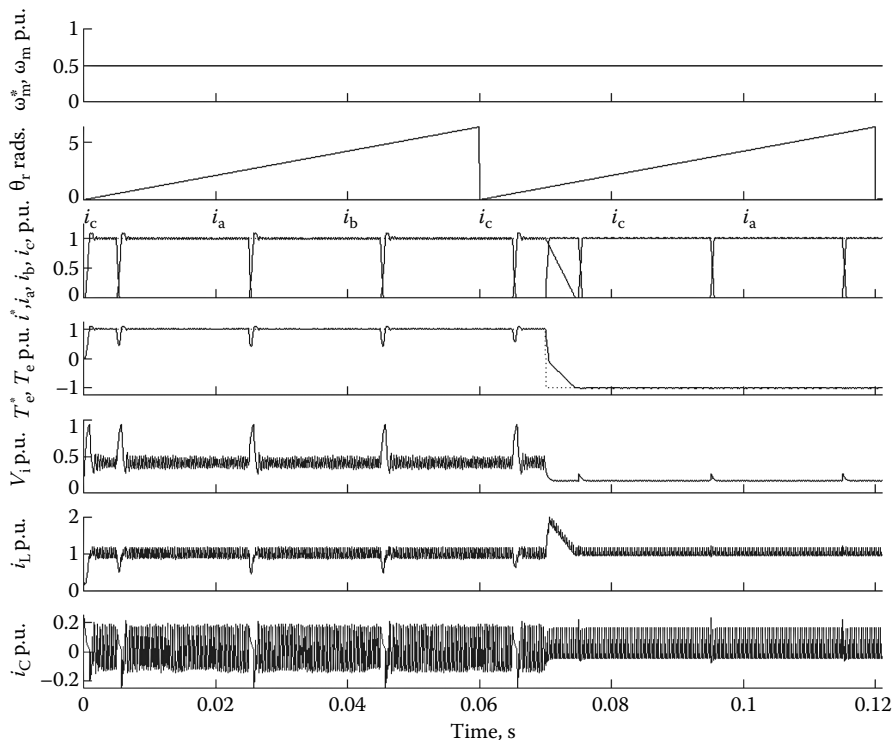


FIGURE 11.17 Torque drive performance.

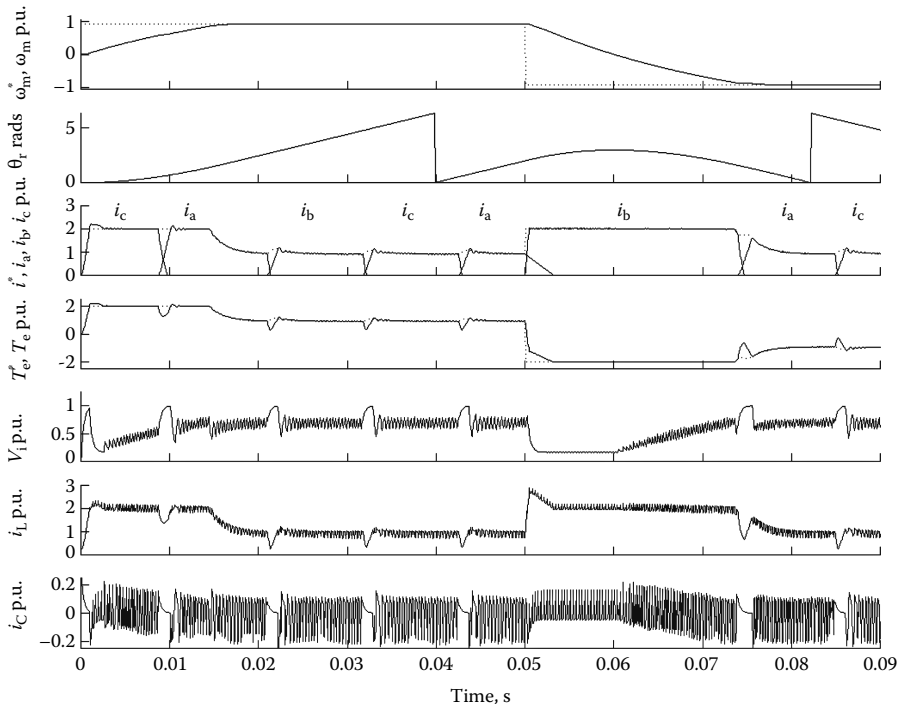


FIGURE 11.18 Speed-controlled drive system performance.

11.3.3.2 Speed-Controlled Drive Performance

Figure 11.18 shows the simulation of a speed-controlled system operating in both forward and reverse directions. The current and torque are limited to 2 p.u. The current in the machine phases is unidirectional but the torque developed by the machine is bidirectional. The input voltage to the phases V_i is varied based on the speed. The current through the chopper inductor i_L has a high ripple content but the currents in the machine phases have very little ripple. The reduction in the ripple is due to machine inductances and additionally because no subsequent switching occurs in the machine phases.

11.3.4 MERITS AND DEMERITS

The merits of the converter topology are listed below:

1. Only four switches and diodes required for four-quadrant operation with a three-phase PMBDCM.
2. Reduced gating driver circuits and logic power supplies.
3. Full four-quadrant operational capability.
4. Reduced possibility of shoot-through fault, as switch is in series with the machine phase winding.
5. Possible to operate with one switch failure or one phase-winding failure.
6. Lower phase switch losses.

7. High-frequency ripple in steady state operation can be considerably lower than that of the fixed dc link-based converters and this is a distinct advantage with the high-performance drive systems. Unlike the C-dump converter, this converter has no circulating energy resulting in better efficiency and very low torque ripple.
8. The power switches have a voltage rating equal to that of the source voltage, which is much lower than that of the C-dump and single switch per phase converter.

The topology has the demerits associated with any half-wave converter topology such as poorer utilization of the machine and a larger electrical time constant. In addition, this converter has two-stage power conversion, resulting in a slightly lower efficiency compared to single stage power converter topologies.

11.4 VARIABLE VOLTAGE CONVERTER TOPOLOGY WITH BUCK-BOOST FRONT-END

A variant of more than one but less than two switches per phase converter topology is another alternative converter topology for PMBDCM drives. Such a circuit has been proposed for switched reluctance motor drives and has attractive features for the PMBDC motor drives. This converter topology has a buck-boost front-end converter and a machine side converter. The machine side dc link voltage can be varied from zero to twice the dc source voltage through the step-down and step-up operation of buck-boost front-end chopper power stage. In low-speed operation range, small machine dc link voltage is sufficient for the phase current control due to low back emf generated. For this reason, lower switching ripple and hence lower torque ripple can be obtained by step-down operation of the buck-boost front-end converter. In high-speed operation, the motor back emf generated can not exceed approximately 60%–80% of the dc source voltage in PMBDC motor drives with the conventional converter topology in order to have current control. But this converter topology extends the operating speed range through the step-up operation of buck-boost front-end power stage and hence a substantial increase in the output power.

The principle of operation, merits, and demerits of the proposed topology for PMBDC motor drives, modeling, simulation, and analysis of the motor drive system, comparison of the proposed converter topology rating with that of the full-wave H-bridge converter topology, and required machine modifications for the proposed converter topology are presented in this section.

11.4.1 CONVERTER CIRCUIT

The power converter circuit with four switches and diodes [6] is shown in [Figure 11.19](#). There is only one switch per machine phase and the switch is connected in series with the phase winding. Therefore there is no shoot-through fault in this converter and the current in it is unidirectional and similar to half-wave-converter-driven PMBDC motor in operation. The switch T_c , diode D_c , inductor L , and output capacitor C form the buck-boost front-end power stage. The machine dc link voltage V_i can be varied from zero to greater, say, two times, than the dc source voltage V_{dc} to obtain the

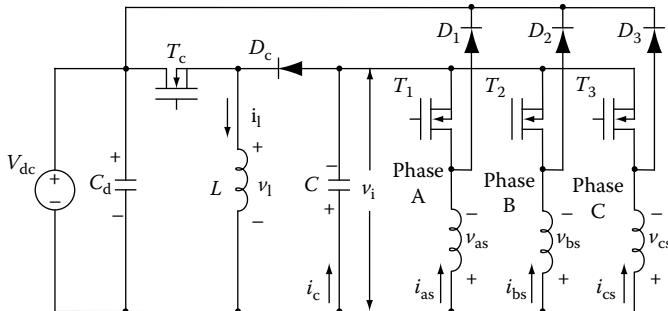


FIGURE 11.19 Proposed converter topology for PMBDC motor drives. (From Lee, B.S. and Krishnan, R., *Proc. IEEE Int. Symp. Indus. Electron.*, 2, 689, 1999. With permission.)

desirable input voltage to the machine windings. Further this stage provides the isolation required for faster commutation of the current with the constant source voltage V_{dc} . The energization mode is initiated by turning on the phase switch, say T_1 , which applies the voltage V_i to the machine phase A. To regulate the current in the winding, switch T_1 is turned off, which initiates the routing of the current through the freewheeling diode D_1 , the dc source voltage V_{dc} , and phase A winding regardless of on or off condition of the chopper switch T_c . This would apply a fixed negative dc source voltage V_{dc} across the machine phase winding. The energy in the output capacitor C will be able to cater to the oncoming phase, say B, during the time that the switch T_c is turned off. In this manner, the independence between various machine phases is maintained.

11.4.2 OPERATIONAL MODES AND MODELING OF THE PMBDC MOTOR DRIVE SYSTEM

Various operational modes of the circuit are derived by isolating the modes of the machine phase switches and diodes and the buck-boost chopper front-end power stage, which when combined provides all the modes of operation. This stratagem works very well in determining the modes of this converter circuit and they are assembled in [Table 11.7](#), assuming that phase A is in the active region of operation and there are no other freewheeling phases. Note that the first four modes are the distinct conduction modes and the latter five modes are accompanied by the existence of freewheeling current for that phase. Therefore, modes 1–4 are sufficient to fully understand the operation and hence to find analytical relationships between the converter and machine variables for the design of the converter. The state space modeling of the four distinct main modes is described in the following by using five state variables given by inductor current and machine dc link voltage of buck-boost front-end converter, and three-stator phase currents.

(i) Mode I: T_c on, T_1 on

The dc source voltage V_{dc} is supplying the magnetizing energy to the inductor of buck-boost front-end converter and the machine dc link voltage V_i is applied to the phase A winding to inject the current through the output capacitor C . The inductor

TABLE 11.7
Modes of Operation

Mode	T_c	D_c	i_l	T_i	D_i	i_{as}
I	On	Off	>0	On	Off	>0
II	Off	On	>0	On	Off	>0
III	On	Off	>0	Off	On	>0
IV	Off	On	>0	Off	On	>0
V	Off	Off	0	On	Off	>0
VI	On	Off	>0	Off	Off	0
VII	Off	Off	0	Off	On	>0
VIII	Off	On	>0	Off	Off	0
IX	Off	Off	0	Off	Off	0

Source: Lee, B.S. and Krishnan, R., *Proc. IEEE Int. Symp. Indus. Electron.*, 2, 689, 1999. With permission.

current, machine dc link voltage, and phase A current during this mode can be expressed as

$$\frac{di_l}{dt} = \frac{V_{dc}}{L}, \quad i_l \geq 0, \quad v_l = V_{dc} \quad (11.49)$$

$$\frac{dv_i}{dt} = -\frac{i_{as}}{C}, \quad i_c = -i_{as} \quad (11.50)$$

$$\frac{di_{as}}{dt} = \frac{1}{L_s} (v_i - R_s i_{as} - e_{as}), \quad i_{as} \geq 0, \quad v_{as} = v_i \quad (11.51)$$

To obtain the waveforms of state variables, Equations 11.49 through 11.51 are solved together with the appropriate boundary conditions. It is instructive to find Laplace transform of each state variables as a function of back emf and only the Laplace transform of phase A current is given below:

$$I_{as}(s) = \frac{-sE_{as}(s)}{L_s s^2 + R_s s + 1/C} \quad (11.52)$$

This mode has familiar second-order system characteristics and the natural frequency of oscillation and damping ratio are expressed, respectively, as

$$\omega_n = 1/\sqrt{L_s C} \quad (11.53)$$

$$\zeta = (R_s/2)\sqrt{C/L_s} \quad (11.54)$$

Similarly, for modes II, III, and IV, the relevant equations can be derived. Freewheeling of one or two phases can be modeled as

$$\begin{bmatrix} \frac{di_{as}}{dt} \\ \frac{di_{bs}}{dt} \end{bmatrix} = \begin{bmatrix} L_s & M \\ M & L_s \end{bmatrix}^{-1} \begin{bmatrix} v_{as} - R_s i_{as} - e_{as} \\ v_{bs} - R_s i_{bs} - e_{bs} \end{bmatrix}, \quad \begin{aligned} v_{as} &= v_i(T_1 = \text{on}) \text{ or} \\ v_{as} &= -V_{dc}(T_1 = \text{off}) \\ v_{bs} &= -V_{dc} \end{aligned} \quad (11.55)$$

$$\begin{bmatrix} \frac{di_{as}}{dt} \\ \frac{di_{bs}}{dt} \\ \frac{di_{cs}}{dt} \end{bmatrix} = \begin{bmatrix} L_s & M & M \\ M & L_s & M \\ M & M & L_s \end{bmatrix}^{-1} \begin{bmatrix} v_{as} - R_s i_{as} - e_{as} \\ v_{bs} - R_s i_{bs} - e_{bs} \\ v_{cs} - R_s i_{cs} - e_{cs} \end{bmatrix}, \quad \begin{aligned} v_{as} &= v_i(T_1 = \text{on}), \text{ or} \\ v_{as} &= -V_{dc}(T_1 = \text{off}) \\ v_{bs} &= -V_{dc} \\ v_{cs} &= -V_{dc} \end{aligned} \quad (11.56)$$

11.4.3 MERITS AND DEMERITS

The PMBDC motor drive with this converter topology has the following advantages:

1. Only four switches and diodes are required for the full four-quadrant operation, resulting in low cost and high compactness in packaging.
2. Independent phase current control is guaranteed.
3. The commutation voltage is fixed and equals the negative dc source voltage. This will reduce the phase current rapidly to zero, giving rise to a faster current response.
4. The minimum logic power supplies requirement is achieved due to the fact that the machine phase switches all have the same common.
5. The machine dc link voltage V_i can be varied from 0 to $2V_{dc}$ (say) to provide faster rise of current in machine phases and hence faster dynamic response and as well as to minimize the switchings.
6. Lower switching ripple and hence lower torque ripple can be obtained by using lower machine dc link voltage in low speed operation range when the back emf is very low.
7. In high-speed operation range, the motor back emf generated can not exceed approximately 0.6–0.8 p.u. of the fixed dc source voltage in PMBDC motor drives with the conventional converter topology because of requiring a voltage margin to control the phase current against the back emf. This reserve voltage for the phase current control amounts to 0.2–0.4 p.u. of the dc source voltage. But this converter topology can extend the operating speed range with higher machine dc link voltage V_i through the step-up operation of buck-boost front-end power stage with full dynamic current control. This will result in higher output power. **Table 11.8** shows the comparison of the output power capacity of the PMBDC motor and other machine variables between the buck-boost-based converter and the full-wave converter on the basis of equal copper losses, equal copper volume, and hence equal

TABLE 11.8**Comparison of the PMBDC Machine Variables Based on the Buck-Boost and the Full-Wave Converters**

Aspects	Buck-Boost Converter-Based PMBDC	Full-Wave Converter-Based PMBDC
Number of turns per phase	$\sqrt{2}N_b$	N_b
Conductor cross section area	$a_b/\sqrt{2}$	a_b
Phase winding resistance	$2R_b$	R_b
Phase winding self inductance	$2L_b$	L_b
Phase winding mutual inductance	$2M_b$	M_b
Electromagnetic torque	$T_{eb}/\sqrt{2}$	T_{eb}
Maximum speed for constant dc link voltage	$\sqrt{2}\omega_{mp}$	ω_{mb}
Output power for constant dc link voltage	P_b	P_b
Maximum speed for variable dc link voltage	$\sqrt{2}\omega_{mp} + \Delta\omega_m, \Delta\omega_m = \Delta V_r / (2K_b), \Delta V_r = 0.3V_{dc}$	—
Output power for variable dc link voltage	$P_b + \Delta P, \Delta P = \Delta\omega_m T_{eb}/\sqrt{2}$	—

Source: Lee, B.S. and Krishnan, R., *Proc. IEEE Int. Symp. Indus. Electron.*, 2, 689, 1999. With permission.

copper fill in the slot of the PMBDC motor. The subscript b corresponds to the motor with the full-wave converter, and buck-boost-converter-based PMBDC motor variables are on the basis of that value.

In Table 11.8, the reserve voltage ΔV_r for the phase current control is obtained as

$$\Delta V_r = 0.3V_{dc} \quad (11.57)$$

This voltage is applied to the two-phase windings connected in series in the full-wave converter-based PMBDC motor drives. On the contrary, this voltage is applied to one-phase winding in buck-boost-converter-based PMBDC motor drives, thereby the incremental mechanical operating speed range can be derived as

$$\Delta\omega_m = \frac{\Delta V_r/2}{K_b} \quad (11.58)$$

Finally, the increased output power can be expressed as

$$\Delta P = \Delta\omega_m \frac{T_{eb}}{\sqrt{2}} = \frac{\Delta V_r T_{eb}}{2\sqrt{2}K_b} \quad (11.59)$$

Note that this advantage is not achievable with any other converter other than this converter.

8. Machine phase winding is always connected in series with a phase switch, thereby achieving high reliability with no shoot-through fault.
9. Possible to operate with one switch or one phase winding failures.
10. Sensorless operation is made easier with the phase switches having a common.

The disadvantages are as follows:

1. Poorer utilization of the motor.
2. High volt-ampere ratings of the switches.
3. The buck-boost chopper circuit has to be rated for the PMBDC motor power rating, which may preclude its use in integral horsepower drives thus making it suitable only for fractional hp drive systems.
4. Due to the additional stage of power processing in the front-end buck-boost converter, the overall system efficiency of the PMBDC motor drive system is lower than that of the other schemes without the front-end converter stage.
5. Discontinuous current flows in C_d and C . It results in high ripple current rating of C_d and C .
6. Coordinated control of machine side and buck-boost converters is required.

11.4.4 COMPARISON WITH FULL-WAVE INVERTER DRIVE

This variable voltage converter-based PMBDC motor is compared with that of H-bridge full-wave-converter-based PMBDC motor drive system, assuming that the average duty cycle of the phase switch during phase conduction is h_1 and the average duty cycle of the common switch is h_2 . Some salient aspects and their comparison are given in [Table 11.9](#). Even though the VA rating of the proposed converter is higher than the H-bridge full-wave converter, note that this converter has fewer devices with higher voltage rating, which usually cost less and further has the additional advantages of lower conduction and switching losses.

11.4.5 DESIGN OF THE INDUCTOR AND OUTPUT CAPACITOR IN THE BUCK-BOOST FRONT-END

The inductor is rated based on the ripple current rating, which allows for the minimum energy storage to enable faster charging of the output capacitor. The minimum inductance can be obtained on the principle that the average voltage of the inductor is zero and given by

TABLE 11.9
Comparison with the Full-Wave Converter-Based PMBDC Drive System

Aspects	Buck-Boost Converter-Based PMBDC Motor	Full-Wave Converter-Based PMBDC Motor
Number of power switches	4	6
Number of power diodes	4	6
Minimum switch voltage	$V_{dc} + V_i$	V_{dc}
Peak phase switch current	I_p	I_p
RMS phase switch current	$I_p/\sqrt{3}$	$I_p/\sqrt{3}$
RMS common switch current	I_p	—
RMS motor phase current	$I_p/\sqrt{3}$	$(\sqrt{2/3})I_p$
Number of capacitors	2	1
dc source voltage	V_{dc}	V_{dc}
Machine dc link voltage	V_i	—
Minimum number of logic power supplies for isolated operation	2	4
Inductor	1	0
Number of gate drivers	4	6
Average switch conduction losses	$(h_1 + h_2)V_{sw} I_p$	$2 h_1 V_{sw} I_p$
Average diode conduction losses	$(2 - h_1 - h_2)V_d I_p$	$2(1 - h_1)V_d I_p$
Average switch VA rating	$4(V_{dc} + v_i)I_p$	$6V_{dc} I_p$
RMS switch VA rating	$(1 + \sqrt{3})(V_{dc} + v_i)I_p$	$2\sqrt{3}V_{dc} I_p$

Source: Lee, B.S. and Krishnan, R., Proc. IEEE Int. Symp. Indus. Electron., 2, 689, 1999. With permission.

$$L_{min} = \frac{hV_{dc}}{f_c \Delta i_l} \quad (11.60)$$

where

h is the average duty cycle

V_{dc} is the dc source voltage

f_c is the switching frequency

Δi_l is the maximum inductor ripple current

Similarly, the minimum output capacitance is derived on the principle that the average current of the output capacitor is zero and is given by

$$C_{min} = \frac{hI_p}{f_c \Delta v_i} \quad (11.61)$$

where

I_p is the peak phase current

f_c is the switching frequency

Δv_i is the maximum capacitor ripple voltage

11.4.6 CONTROL STRATEGIES AND PERFORMANCE

There are three control strategies for PMBDC motor drives based on the use of common switch T_c of the front-end power stage and they are discussed in this section. The following machine parameters are chosen for the simulation: 1 HP, Y Connection, 4 Poles, 4000RPM, $R_s = 0.7 \Omega$, $L_s = 3.908 \text{ mH}$, $M = -1.3015 \text{ mH}$, $K_b = 0.1048 \text{ V/(rad/s, mech)}$, $T_{e,\text{rated}} = 1.7809 \text{ N m}$, $I_{\text{rated}} = 8.5 \text{ A}$, $J = 0.00022 \text{ kg m}^2$, $B = 0 \text{ N m/(rad/s)}$. ac supply: 115 V, 60Hz, 1 phase.

11.4.6.1 Strategy I—Open Loop Voltage Control

The common switch T_c controls the machine dc link voltage V_i in an open loop manner with the fixed duty ratio and hence there is no feedback of the machine dc link voltage to close the control loop. The duty ratio for regulating the common switch of the buck-boost front-end converter is obtained as a linear function of the speed command, and it is very much similar to the constant voltage per unit frequency or volts/Hertz control method in induction motor. The phase current is controlled by the phase switches with the chosen switching strategies, such as PWM or hysteresis.

Figure 11.20 shows the schematic of the PMBDC motor drive scheme with the open loop voltage control strategy. The available feedback signals for control are the three phase currents, discrete rotor position signals from the pulse generator (PG) to generate the commutation pulses for the phase switches, and rotor speed signal from the position signal. The common switch and phase switches are controlled separately. The signal from PG is processed through the digital pulse-counting circuits and the resulting modified speed signal is compared with the speed reference to produce the speed error. The torque command signal is obtained from the speed error signal through a PI controller and limiter. The corresponding phase current command is generated using three inputs, that is, phase current magnitude reference, discrete rotor position signal, and the polarity of the phase current command. The gating signals for the phase switches are obtained from the phase current error signal using hysteresis controller.

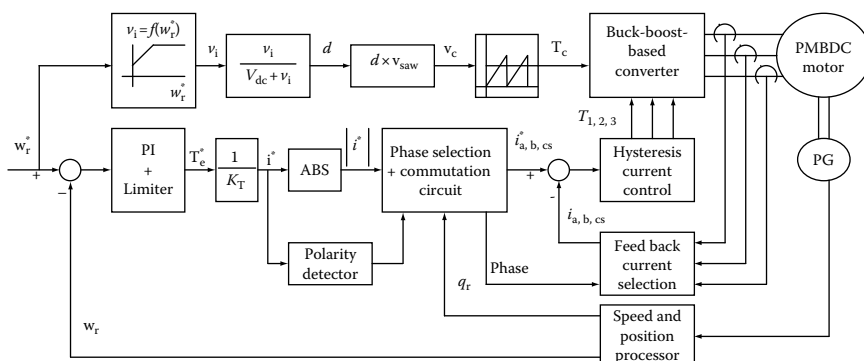


FIGURE 11.20 Schematic of the PMBDC motor speed control system. (From Lee, B.S. and Krishnan, R., *Proc. IEEE Int. Symp. Indus. Electron.*, 2, 689, 1999. With permission.)

Figure 11.21 shows the simulation of PMBDC motor torque drive system at 1 p.u. at the rated rotor speed. The inductor and output capacitor values used in the simulation are 0.6 mH and 130 μ F, respectively, and derived based on equations derived earlier. One p.u. torque command and hence the rated current command is initially applied and switched to -1 p.u. after 0.01 s so that both the first-quadrant motoring and the fourth-quadrant regenerative operation can be observed. The responses of the torque and its reference, speed, phase currents, and their reference, inductor current, output capacitor current, and machine dc link voltage are presented by using normalized unit. The phase currents follow the reference current of the machine and the machine dc link voltage is maintained at 1 p.u. It is noticed that the torque in the machine has dips at the instants of phase commutation.

Figure 11.22 shows the simulation of PMBDC motor torque drive system at 1.3 p.u. rotor speed and one advantage of increasing the operating speed range and hence the output power of the machine is verified. The actual torque and phase currents are tracking the references very well due to the higher machine dc link voltage provided by the buck-boost converter control.

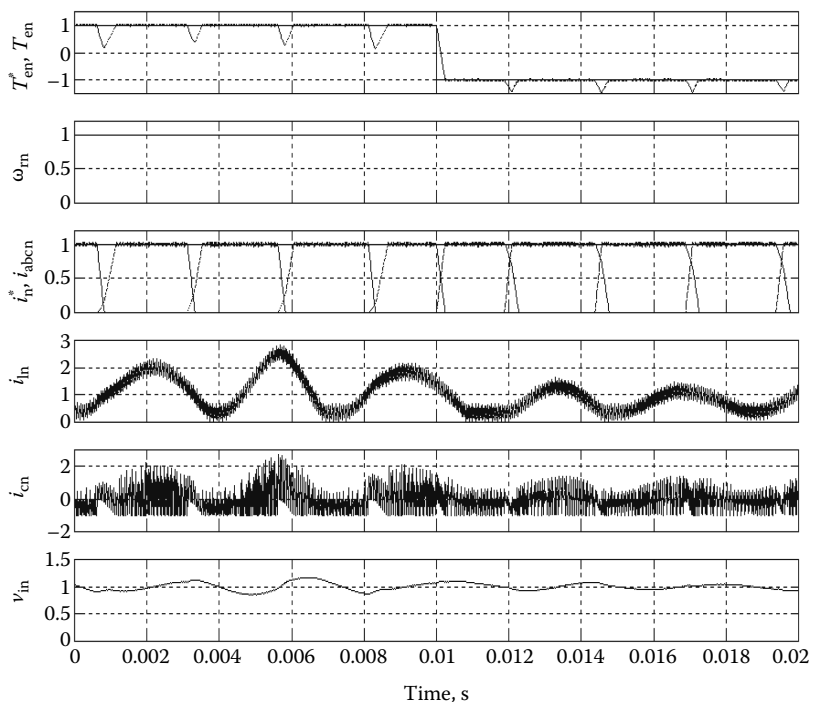


FIGURE 11.21 Dynamic simulation of PMBDC motor torque drive system at base rotor speed using strategy I. (From Lee, B.S. and Krishnan, R., *Proc. IEEE Int. Symp. Indus. Electron.*, 2, 689, 1999. With permission.)

11.4.6.2 Strategy II—Closed Loop Voltage Control

The machine dc link voltage control and phase current control in this strategy are basically same as those of strategy I, except that the common switch T_c is controlled by using the machine dc link voltage error between the reference and actual value. The machine dc link voltage error is processed through a PI controller and limiter to yield the duty-control voltage command. This control voltage is merged with saw-tooth carrier wave to generate the required PWM signal, which is the duty ratio of the main switch of buck-boost front-end converter.

The schematic of the PMBDC motor drive system with this strategy can easily be obtained by modifying Figure 11.20 based on the description of the above and it is not shown here. Figures 11.23 and 11.24 show the simulations of PMBDC motor torque drive system at 1 and 1.3 p.u. rotor speed, respectively. Similar current control performance to that of the strategy I is observed.

11.4.6.3 Strategy III—Direct Phase Current Control

The phase switch is continuously on for the corresponding phase conduction cycle, that is, electrical 120°. The common switch T_c directly controls the phase current using the current error between the reference and actual phase current. The current error is

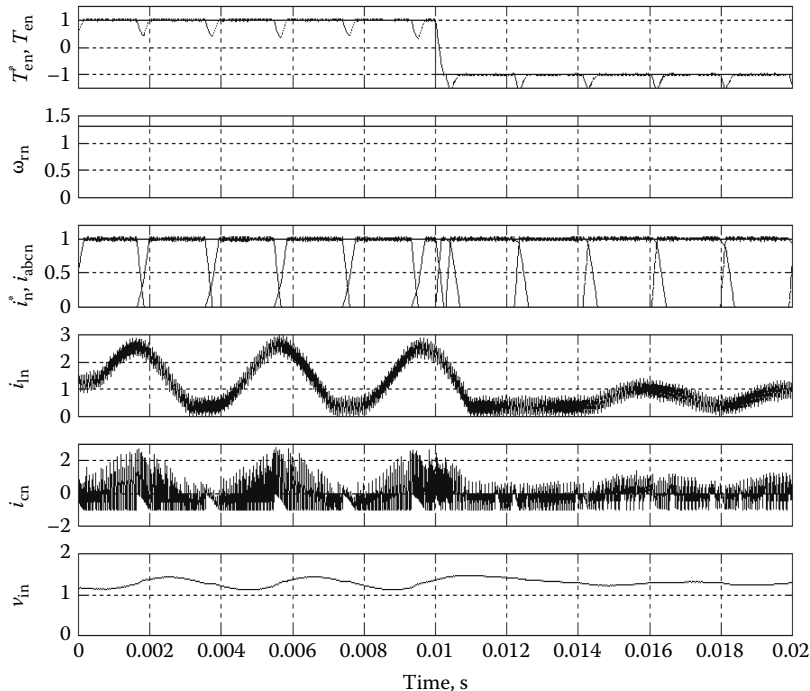


FIGURE 11.22 Dynamic simulation of PMBDC motor torque drive system at 1.3 p.u. rotor speed using strategy I. (From Lee, B.S. and Krishnan, R., *Proc. IEEE Int. Symp. Indus. Electron.*, 2, 689, 1999. With permission.)

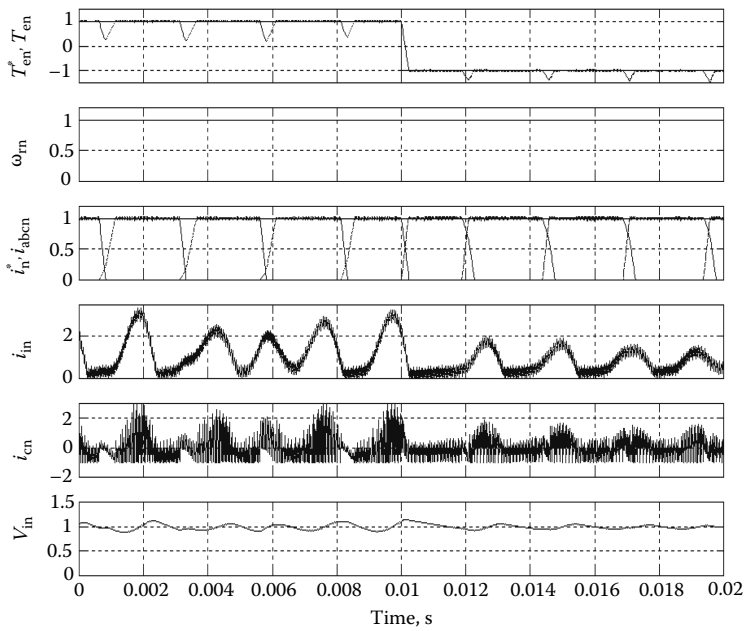


FIGURE 11.23 Dynamic simulation of torque-controlled PMBDC motor drive system at base rotor speed using strategy II. (From Lee, B.S. and Krishnan, R., *Proc. IEEE Int. Symp. Indus. Electron.*, 2, 689, 1999. With permission.)

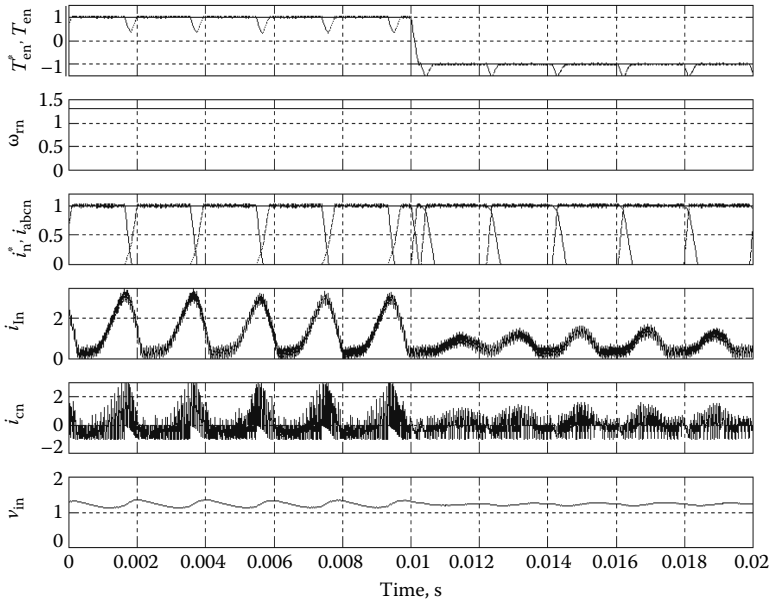


FIGURE 11.24 Dynamic simulation of PMBDC motor torque drive system at 1.3 p.u. rotor speed using strategy II.

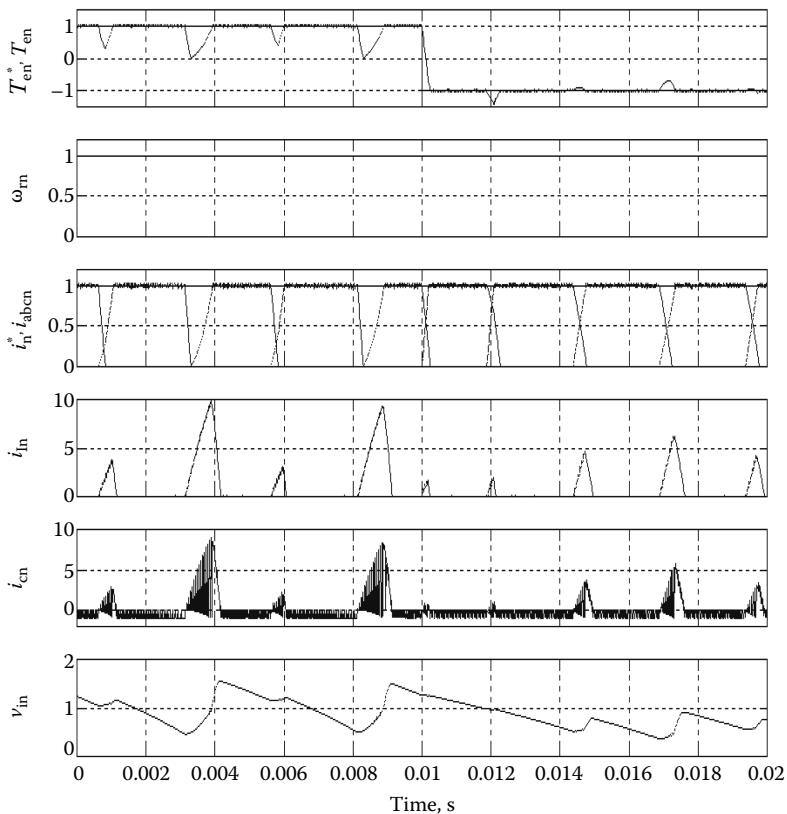


FIGURE 11.25 Dynamic simulation of PMBDC motor torque drive system at 1.3 p.u. rotor speed using strategy III.

processed through a PI controller and limiter to yield the reference voltage command for sawtooth carrier wave and hence the duty ratio of the common switch.

Figure 11.25 shows the simulation of PMBDC motor torque drive system at 1 p.u. rotor speed. Phase current is tracking the reference but very large discontinuous currents in the inductor and output capacitor of buck-boost front-end converter are observed. The machine dc link voltage is highly fluctuating. For this reason, this strategy is not desirable for PMBDC motor drive systems with this power converter.

REFERENCES

1. R. Krishnan, *Electric Motor Drives*, Prentice Hall, Englewood Cliffs, NJ, 2001.
2. R. Krishnan, S. Lee, and R. Monajemy, Modeling, dynamic simulation and analysis of a C-dump brushless DC motor drive, *Conference Record, IEEE Applied Power Electronics Conference and Exposition, (Cat. No. 96CH35871)*, pp. 745–750, 1996.
3. R. Krishnan, Novel single-switch-per-phase converter topology for four-quadrant PM brushless DC motor drive, *IEEE Transactions on Industry Applications*, 33(5), 1154–1161, 1997.

4. R. Krishnan and S. Lee, PM brushless DC motor drive with a new power-converter topology, *IEEE Transactions on Industry Applications*, 33(4), 973–982, 1997.
5. R. Krishnan and P. Vijayraghavan, New power converter topology for PM brushless dc motor drives, *Conference Record, IEEE Industrial Electronics Conference*, pp. 709–714, 1998.
6. B.-S. Lee and R. Krishnan, Variable voltage converter topology for permanent-magnet brushless DC motor drives using buck-boost front-end power stage, *IEEE International Symposium on Industrial Electronics*, vol. 2, pp. 689–694, 1999.
7. B. Zhou, Y. Fu, X.-h. Mu, et al., Design on the c-dump converter used in brushless DC motors, *Proceedings of the CSEE*, 20(4), 72–76, 2000.
8. A. Consoli, S. De Caro, A. Testa, et al., Unipolar converter for DC brushless motor drives, *9th European Conference on Power Electronics and Applications (EPE)*, p. 9, 2001.
9. L. Hao, H. A. Toliyat, and S. M. Madani, A low-cost four-switch BLDC motor drive with active power factor correction, *Conference Record, IEEE Industrial Electronics Conference*, pp. 579–584, 2002.
10. B.-K. Lee, T.-H. Kim, and M. Ehsani, On the feasibility of four-switch three-phase BLDC motor drives for low cost commercial applications: Topology and control, *IEEE Transactions on Power Electronics*, 18(1), part I, 164–172, 2003.
11. T. Gopalarathnam and H. A. Toliyat, A new topology for unipolar brushless dc motor drive with high power factor, *IEEE Transactions on Power Electronics*, 18(6), 1397–1404, 2003.

12 Design of Current and Speed Controllers

The basic speed-controlled drive given in Chapter 10 is considered for the design of the current and speed controllers in this chapter. The design procedure is developed step by step in deriving the subsystem transfer functions and assembling the open current and speed loop transfer functions. The proportional plus integral (PI) controller design has not been mentioned in Chapter 6 and it is presented here in detail. Most of the industrial drive systems have PI controllers in their feedback control of current and speed and their tuning process is company specific in the industry and most of the companies share the information with the public as well as the clients. From the point of the prevalence of the PI controllers in the motor drives industry, it is useful to get acquainted with them. Some references on current [1–8] and speed [9–14] controllers are given for further reading. Some aspects of the procedure are similar to controller design for PMSM drives.

12.1 TRANSFER FUNCTION OF MACHINE AND LOAD

The design of current and speed controllers is simple and straightforward in PMBDCM drives because of the fact that this machine is very similar to a dc machine [1]. The similarity holds when only two phases are conducting during the interval where the rotor flux linkages are constant as seen from these phases and all the phases are electrically symmetric and balanced. During two-phase conduction, the inverter output voltage, v_{is} , is applied to the two phases having an impedance of

$$Z = 2 \{R_s + s(L - M)\} = R_a + sL_a \quad (12.1)$$

where

$$R_a = 2R_s \quad (12.2)$$

$$L_a = 2(L - M) \quad (12.3)$$

And the voltage equation for the stator is given by

$$v_{is} = (R_a + sL_a)i_{as} + e_{as} - e_{cs} \quad (12.4)$$

where the last two terms are the induced emfs in phases a and c, respectively. But the induced emfs in phases a and c are equal and opposite during the regular operation of the drive scheme and given as

$$e_{as} = -e_{cs} = \lambda_p \omega_m \quad (12.5)$$

which on substitution gives the stator voltage equation as

$$v_{is} = (R_a + sL_a)i_{as} + 2\lambda_p \omega_m = (R_a + sL_a)i_{as} + K_b \omega_m \quad (12.6)$$

where the emf constant for both the phases is combined into one constant as

$$K_b = 2\lambda_p, \text{ V/rad/s} \quad (12.7)$$

The machine with an inner current control loop is shown in Figure 12.1. Note that the electromagnetic torque for two phases combined is given by

$$T_e = 2\lambda_p i_{as} = K_b i_{as}, \text{ N} \cdot \text{m} \quad (12.8)$$

The machine contains an inner loop due to the induced emf. It is not physically seen as it is magnetically coupled. The inner current loop will cross this back emf loop, creating a complexity in the development of the model. The interactions of these loops can be decoupled by suitably redrawing the block diagram. The development of such a block diagram for the machine is shown in Figure 12.2, step by step. The load is assumed to be proportional to speed:

$$T_l = B_l \omega_m \quad (12.9)$$

If it is not proportional to the speed as some of the loads are, then the load torque is truly a disturbance. In that case it is incorporated in the block diagram suitably but ignored in the controller design for most of the applications. Note that the controller's principal role is to minimize the effects of disturbance while following the varying speed and current commands with a specified damping and speed of response. To decouple the inner current loop from the machine inherent induced emf

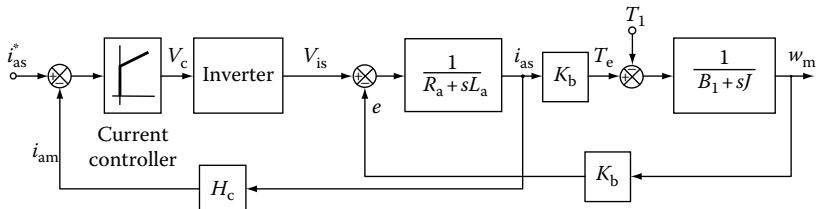


FIGURE 12.1 PMBDC and current control loop.

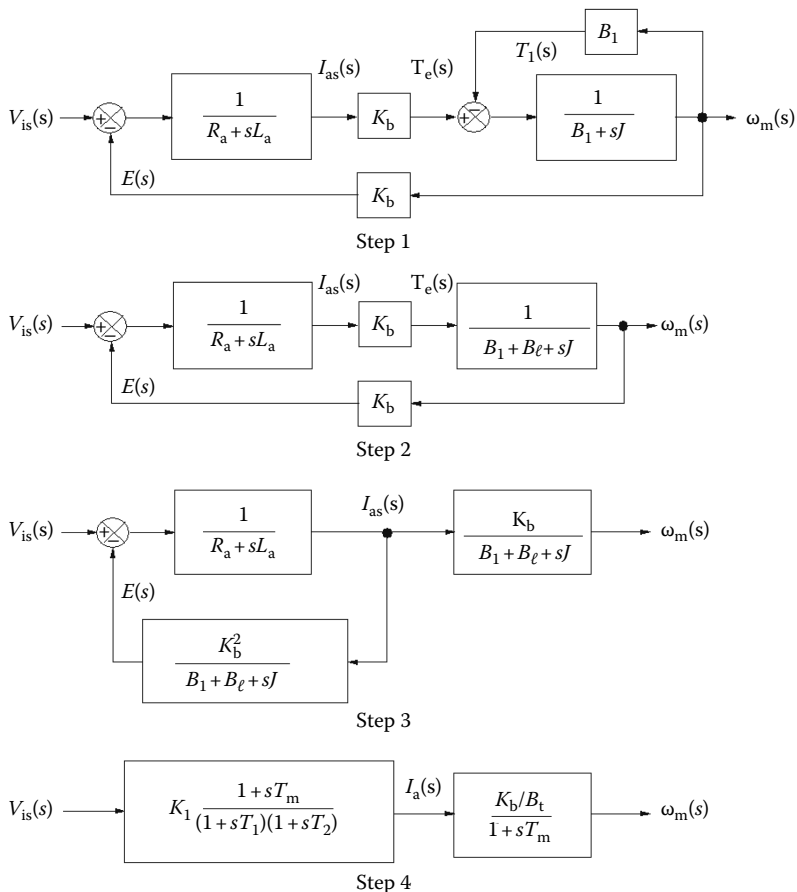


FIGURE 12.2 Step by step derivation of a dc motor.

loop, it is necessary to split the transfer function between the speed and voltage into two cascade transfer functions, between speed and phase current and between phase current and input voltage and represented as

$$\frac{\omega_m(s)}{V_{is}(s)} = \frac{\omega_m(s)}{I_{as}(s)} \cdot \frac{I_{as}(s)}{V_{is}(s)} \quad (12.10)$$

where

$$\frac{\omega_m(s)}{I_{as}(s)} = \frac{K_b}{B_t(1+sT_m)} \quad (12.11)$$

$$\frac{I_{as}(s)}{V_{is}(s)} = K_1 \frac{1+sT_m}{(1+sT_1)(1+sT_2)} \quad (12.12)$$

$$T_m = \frac{J}{B_t} \quad (12.13)$$

$$B_t = B_l + B_\ell \quad (12.14)$$

$$-\frac{1}{T_1}, -\frac{1}{T_2} = -\frac{1}{2} \left[\frac{B_t}{J} + \frac{R_a}{L_a} \right] \pm \sqrt{\frac{1}{4} \left(\frac{B_t}{J} + \frac{R_a}{L_a} \right)^2 - \left(\frac{K_b^2 + R_a B_t}{J L_a} \right)} \quad (12.15)$$

$$K_1 = \frac{B_t}{K_b^2 + R_a B_t} \quad (12.16)$$

12.2 INVERTER TRANSFER FUNCTION

The inverter is represented as a first-order lag with a gain given by

$$G_r(s) = \frac{V_{is}(s)}{v_c(s)} = \frac{K_r}{1 + sT_r} \quad (12.17)$$

The delay time T_r and gain K_r are evaluated in Chapter 6 but here must account for line to line output voltage.

12.3 TRANSFER FUNCTIONS OF CURRENT AND SPEED CONTROLLERS

The current and speed controllers are of proportional integral type. They are represented as

$$G_c(s) = \frac{K_c(1 + sT_c)}{sT_c} \quad (12.18)$$

$$G_s(s) = \frac{K_s(1 + sT_s)}{sT_s} \quad (12.19)$$

where the subscripts “c” and “s” correspond to the current and speed controllers, respectively. K and T correspond to the gain and time constants of the controllers.

12.4 CURRENT FEEDBACK

The gain of the current feedback is H_c . No significant filtering is required in most of the cases. In case of filtering requirement, a low-pass filter may be included in the analysis. Even then, the time constant of the filter may not be greater than a millisecond and is in the order of a few PWM sampling times.

12.5 SPEED FEEDBACK

Most of the high-performance systems use a dc tachogenerator and the filter required is low-pass with a time constant of 1–10 ms or less. The transfer function of the speed feedback filter is

$$G_\omega(s) = \frac{K_\omega}{1 + sT_\omega} \quad (12.20)$$

where

K_ω is the gain

T_ω is the time constant

12.6 DESIGN OF CONTROLLERS

The overall closed loop system is shown in Figure 12.3. It is seen that the current loop does not contain the inner induced emf loop because of the modification derived in previous section. The design of control loops starts from the innermost, i.e., fastest loop to the slowest loop, which in this case is the outer speed loop. The reason to proceed from the inner to the outer loop in the design process is that the gain and time constants of one controller is solved at a time instead of solving for the gain and time constants of all the controllers simultaneously. Not only is that logical but also has a practical implication. Note that every motor drive need not be speed-controlled but may be torque controlled such as for a traction application. In that case, the current loop is essential and exists whether the speed loop is going to be closed or not. Additionally, the performance of the outer loop is dependent on the inner loop and therefore the tuning of the inner loop has to precede the design and tuning of the outer loop. That way, the dynamics of the inner loop could be simplified and the impact of the outer loop could be minimized on its performance. The designs of these loops and their controllers are considered in this section.

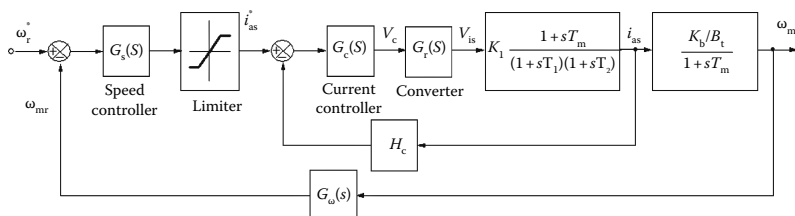


FIGURE 12.3 Block diagram of the motor drive.

12.6.1 CURRENT CONTROLLER

The current control loop is shown in Figure 12.4. The loop gain function is

$$GH_i(s) = \left\{ \frac{K_l K_c K_r H_c}{T_c} \right\} \cdot \frac{(1+sT_c)(1+sT_m)}{s(1+sT_1)(1+sT_2)(1+sT_r)} \quad (12.21)$$

This is a fourth-order system and simplification is necessary to synthesize a controller without resorting to computer. Noting that T_m is in the order of a second and in the vicinity of the gain crossover frequency, the following approximation is valid:

$$(1+sT_m) \cong sT_m \quad (12.22)$$

which reduces the loop gain function to

$$GH_i(s) \cong \frac{K(1+sT_c)}{(1+sT_1)(1+sT_2)(1+sT_r)} \quad (12.23)$$

where

$$K = \frac{K_l K_c K_r H_c T_m}{T_c} \quad (12.24)$$

The time constants in the denominator are seen to have the relationship

$$T_r < T_2 < T_1 \quad (12.25)$$

Equation 12.23 can be reduced to second order to facilitate a simple controller synthesis by judiciously selecting

$$T_c = T_2 \quad (12.26)$$

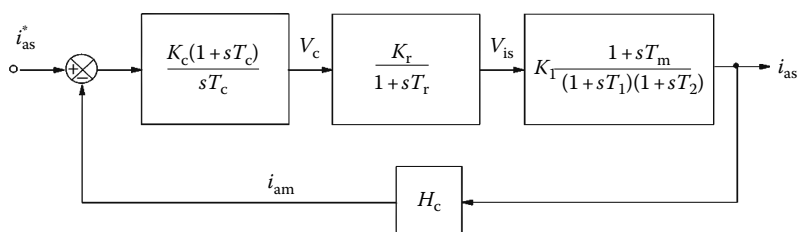


FIGURE 12.4 Current control loop.

Then the loop gain function is

$$GH_i(s) \equiv \frac{K}{(1+sT_l)(1+sT_r)} \quad (12.27)$$

The characteristic equation or denominator of the transfer function between the armature current and its command is

$$(1+sT_l)(1+sT_r)+K \quad (12.28)$$

This equation is expressed in the standard form as

$$T_l T_r \left\{ s^2 + s \left(\frac{T_l + T_r}{T_l T_r} \right) + \frac{K+1}{T_l T_r} \right\} \quad (12.29)$$

from which the natural frequency and damping ratio are obtained as

$$\omega_n^2 = \frac{K+1}{T_l T_r} \quad (12.30)$$

$$\zeta = \frac{\left(\frac{T_l + T_r}{T_l T_r} \right)}{2 \sqrt{\frac{K+1}{T_l T_r}}} \quad (12.31)$$

where ω_n and ζ are the natural frequency and damping ratio, respectively. For good dynamic performance, it is an accepted practice to have a damping ratio of 0.707. Hence equating the damping ratio to 0.707 in Equation 12.31:

$$K+1 = \frac{\left(\frac{T_l + T_r}{T_l T_r} \right)^2}{\left(\frac{2}{T_l T_r} \right)} \quad (12.32)$$

Realizing that

$$K \gg 1 \quad (12.33)$$

$$T_l \gg T_r \quad (12.34)$$

K is approximated as

$$K \approx \frac{T_l^2}{2T_l T_r} \approx \frac{T_l}{2T_r} \quad (12.35)$$

Equating Equations 12.24 through 12.35, the current controller gain is evaluated as

$$K_c = \frac{1}{2} \cdot \frac{T_l T_c}{T_r} \cdot \left(\frac{1}{K_l K_r H_c T_m} \right) \quad (12.36)$$

12.6.2 FIRST-ORDER APPROXIMATION OF INNER CURRENT LOOP

To design the speed loop, the second-order model of the current loop is replaced with an approximate first-order model. This helps to reduce the order of the overall speed loop gain function. The current loop is approximated by adding the time delay in the converter block to T_1 of the motor and due to the cancellation of one motor pole with a zero of the current controller, the resulting current loop is shown in Figure 12.5. The transfer function of the current and its commanded value is

$$\frac{I_{as}(s)}{I_{as}^*(s)} = \frac{\frac{K_c K_r T_l T_m}{T_c} \cdot \frac{1}{(1+sT_3)}}{1 + \frac{K_l K_c K_r H_c T_m}{T_c} \cdot \frac{1}{(1+sT_3)}} \quad (12.37)$$

where $T_3 = T_1 + T_r$. The transfer function may be simply arranged as

$$\frac{I_{as}(s)}{I_{as}^*(s)} = \frac{K_i}{(1+sT_i)} \quad (12.38)$$

where

$$T_i = \frac{T_3}{1 + K_{fi}} \quad (12.39)$$

$$K_i = \frac{K_{fi}}{H_c} \cdot \frac{1}{1 + K_{fi}} \quad (12.40)$$

$$K_{fi} = \frac{K_c K_r K_l T_m H_c}{T_c} \quad (12.41)$$

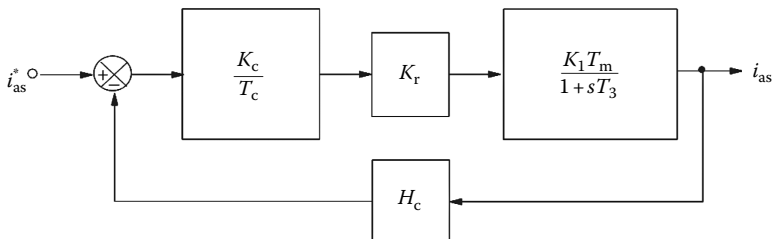


FIGURE 12.5 Simplified current control loop.

The resulting model of the current loop is a first-order system, suitable for use in the design of speed loop. The gain and delay of the current loop can also be found experimentally in a motor drive system. That would be more accurate for the speed controller design.

12.6.3 SPEED CONTROLLER

The speed controller design can be based on any linear control system technique. One method of optimizing the performance using symmetric optimum technique is considered here. The following is derived from Ref. [1], which is a well-known technique in Europe but not very popular in other parts of the world. The advantages of the symmetric optimum method are described near the end of this section.

The speed loop with the first-order approximation of the current control loop is shown in Figure 12.6. The loop gain function is

$$GH_s(s) = \left\{ \frac{K_s K_i K_b H_\omega}{B_i T_s} \right\} \cdot \frac{(1+sT_s)}{s(1+sT_i)(1+sT_m)(1+sT_\omega)} \quad (12.42)$$

This is a fourth-order system. To reduce the order of the system for analytical design of the speed controller, approximation is resorted to. In the vicinity of the gain cross-over frequency, the following is valid:

$$(1+sT_m) \approx sT_m \quad (12.43)$$

The next approximation is to build the equivalent time delay of the speed feedback filter and current loop. Their sum is very much less than the integrator time constant, T_s , and hence the equivalent time delay, T_4 , can be considered the sum of the two delays, T_i and T_ω . This step is very much similar to the equivalent time delay introduced in the simplification of the current loop transfer function. Hence the approximate loop gain function of the speed loop is

$$GH_s(s) \approx K_2 \frac{K_s}{T_s} \frac{1+sT_s}{s^2(1+sT_4)} \quad (12.44)$$

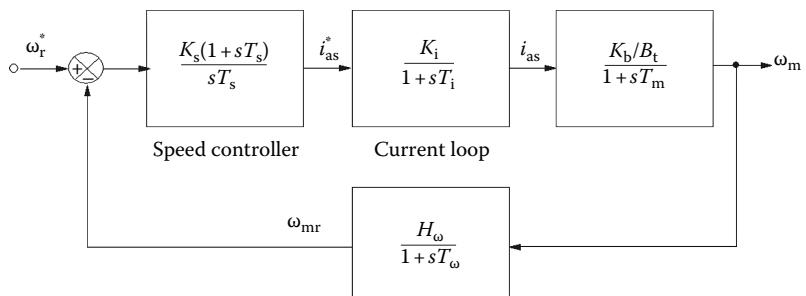


FIGURE 12.6 Representation of the outer speed loop in the dc motor drive.

where

$$T_4 = T_i + T_o \quad (12.45)$$

$$K_2 = \frac{K_i K_b H_\omega}{B_t T_m} \quad (12.46)$$

The closed loop transfer function of the speed to its command is

$$\frac{\omega_m(s)}{\omega_r^*(s)} = \frac{1}{H_\omega} \left[\frac{\frac{K_2 K_s}{T_s} (1 + sT_s)}{s^3 T_4 + s^2 + s K_2 K_s + \frac{K_2 K_s}{T_s}} \right] = \frac{1}{H_\omega} \frac{a_0 + a_1 s}{a_0 + a_1 s + a_2 s^2 + a_3 s^3} \quad (12.47)$$

where

$$a_0 = K_2 K_s / T_s \quad (12.48)$$

$$a_1 = K_2 K_s \quad (12.49)$$

$$a_2 = 1 \quad (12.50)$$

$$a_3 = T_4 \quad (12.51)$$

This transfer function is optimized to have a wider bandwidth and a magnitude of one over a wide frequency range by looking at its frequency response. Its magnitude is given by

$$\left| \frac{\omega_m(j\omega)}{\omega_r^*(j\omega)} \right| = \frac{1}{H_\omega} \sqrt{\frac{a_0^2 + \omega^2 a_1^2}{\{a_0^2 + \omega^2(a_1^2 - 2a_0 a_2) + \omega^4(a_2^2 - 2a_1 a_3) + \omega^6 a_3^2\}}} \quad (12.52)$$

This is optimized by making the coefficients of ω^2 and ω^4 to zero which yields the following conditions:

$$a_1^2 = 2a_0 a_2 \quad (12.53)$$

$$a_2^2 = 2a_1 a_3 \quad (12.54)$$

Substituting these conditions in terms of the motor and controller parameters given in Equations 12.48 through 12.51:

$$T_s^2 = \frac{2T_s}{K_s K_2} \quad (12.55)$$

resulting in

$$T_s K_s = \frac{2}{K_2} \quad (12.56)$$

Similarly,

$$\frac{T_s^2}{K_s^2 K_2^2} = \frac{2 T_s^2 T_4}{K_s K_2} \quad (12.57)$$

which after simplification gives the speed controller gain as

$$K_s = \frac{1}{2 K_2 T_4} \quad (12.58)$$

Substituting Equation 12.58 into Equation 12.56 gives the time constant of the speed controller as

$$T_s = 4 T_4 \quad (12.59)$$

Substituting for K_s and T_s into Equation 12.47 gives the closed loop transfer function of the speed to its command as

$$\frac{\omega_m(s)}{\omega_r^*(s)} = \frac{1}{H_o} \left[\frac{1 + 4T_4 s}{1 + 4T_4 s + 8T_4^2 s^2 + 8T_4^3 s^3} \right] \quad (12.60)$$

It is easy to prove that for the open loop gain function, the corner points are $1/4T_4$ and $1/T_4$ with the gain crossover frequency of $1/2T_4$. In the vicinity of the gain crossover frequency the slope of the magnitude response is -20 dB/decade , which is the most desirable characteristic for good dynamic behavior. Because of its symmetry at the gain crossover frequency, this transfer function is known as a symmetric optimum function. Further this transfer function has the following features:

1. Approximate time constant of the system is $4T_4$.
2. The step response is given by

$$\omega_r(t) = \frac{1}{H_o} \left(1 - e^{-t/2T_4} - 2e^{-t/4T_4} \cos(\sqrt{3}t/4T_4) \right) \quad (12.61)$$

with a rise time of $3.1T_4$, maximum overshoot of 43.4% and a settling time of $16.5T_4$.

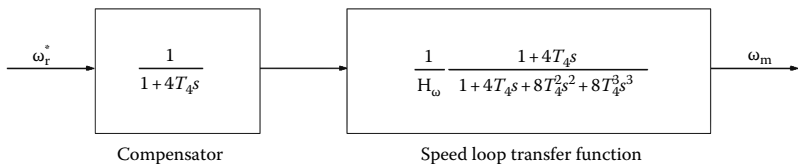


FIGURE 12.7 Smoothing of the overshoot with a compensator.

3. Since the overshoot is high, it can be reduced by compensating for its cause, i.e., the zero by a pole in the speed command path as shown in the Figure 12.7. The resulting transfer function of the speed to its command is

$$\frac{\omega_m(s)}{\omega_r^*(s)} = \frac{1}{H_\omega} \left[\frac{1}{1+4T_4s+8T_4^2s^2+8T_4^3s^3} \right] \quad (12.62)$$

whose step response is

$$\omega_r(t) = \frac{1}{H_\omega} \left(1 - e^{-t/2T_4} - \frac{2}{\sqrt{3}} e^{-t/4T_4} \sin \left(\sqrt{3}t/4T_4 \right) \right) \quad (12.63)$$

with a rise time of $7.6T_4$, maximum overshoot of 8.1%, and a settling time of $13.3T_4$. Even though the rise time has increased, the overshoot has been reduced to approximately 20% of its previous value and the settling time has come down by 19%.

4. The poles of the closed loop transfer function are

$$s = -\frac{1}{2T_4}; -\frac{1}{4T_4} \pm j \frac{\sqrt{3}}{4T_4} \quad (12.64)$$

As the real part of the poles are negative and as there are no repeated poles at the origin, the system is asymptotically stable. Hence in the symmetric optimum design, the system stability is guaranteed and in general, there is no need to check for it in the design process.

5. Symmetric optimum eliminates the effects due to the disturbance very rapidly compared to other optimum techniques employed in practical systems such as linear and modulus optimum, etc. This approach indicates one of the possible methods to synthesize the speed controller. The judicious choice of approximation based on the physical constants of the motor, converter and transducer gains and time delays is to be emphasized here.

The speed loop transfer function is expressed in terms of T_4 is significant in that it clearly links the dynamic performance to the speed feedback and current loop time constants. A faster current loop with a smaller speed filter time constant accelerates

the speed response is evident from this. Expressing T_4 in terms of the motor, converter, and transducer gains and time delays using Equations 12.39 and 12.40:

$$T_4 = T_i + T_\omega = \frac{T_3}{1 + K_{fi}} + T_\omega = \frac{T_1 + T_r}{1 + K_{fi}} + T_\omega \quad (12.65)$$

Since $K_{fi} \gg 1$, T_4 is found approximately after substituting for K_{fi} from Equation 12.41 in terms of gains and time delays as

$$T_4 \approx \frac{(T_1 + T_r)T_2}{T_m} \cdot \frac{1}{K_1 K_c K_r H_c} + T_\omega \quad (12.66)$$

This clearly shows the influence of the subsystem parameters on the system dynamics. A clear understanding of this would help the proper selection of the subsystems to obtain the required dynamic performance of the speed-controlled motor drive system. Further this derivation demonstrates that the system behavior to a large degree depends on the subsystem parameters rather than on the current and speed controller parameters or on the sophistication of their design.

REFERENCES

Current Controller

1. R. Krishnan, *Electric Motor Drives*, Prentice Hall, Englewood Cliffs, NJ, 2001.
2. C. Attaianese, A. Del Pizzo, A. Perfetto, et al., Predictive VSI current controllers in PM brushless and induction motor drives, *International Conference on Electrical Machines*, pp. 195–198, 1994.
3. K. A. Corzine, S. D. Sudhoff, and H. J. Hegner, Analysis of a current-regulated brushless DC drive, *IEEE Transactions on Energy Conversion*, 10(3), 438–445, 1995.
4. J. Faiz, M. R. Azizian, and M. Aboulghasemian-Azami, Simulation and analysis of brushless DC motor drives using hysteresis, ramp comparison and predictive current control techniques, *Simulation Practice and Theory*, 3(6), 347–363, 1996.
5. J. Chen and P.-C. Tang, Sliding mode current control scheme for PWM brushless dc motor drives, *IEEE Transactions on Power Electronics*, 14(3), 541–551, 1999.
6. J. W. Dixon and I. A. Leal, Current control strategy for brushless dc motors based on a common dc signal, *IEEE Transactions on Power Electronics*, 17(2), 232–240, 2002.
7. M. F. Rahman, K. S. Low, and K. W. Lim, Approaches to the control of torque and current in a brushless DC drive, *Sixth International Conference on Electrical Machines and Drives (Conf. Publ. No. 376)*, pp. 594–599, 1993.
8. A. Moussi, A. Terki, and G. Asher, Hysteresis current control of a permanent magnet brushless DC motor PV pumping system, *International Solar Energy Conference*, pp. 523–528, 2005.

Speed Controller

9. P. Crnosija, Z. Ban, and R. Krishnan, Application of model reference adaptive control with signal adaptation to PM brushless DC motor drives, *Proceedings, IEEE International Symposium on Industrial Electronics (Cat. No. 02TH8608C)*, pp. 689–694, 2002.

10. P. Crnosija, Z. Ban, and R. Krishnan, Overshoot controlled servo system synthesis using bode plot and its application to PM brushless DC motor drive, *Proceedings, International Workshop on Advanced Motion Control. Proceedings (Cat. No. 02TH8623)*, pp. 188–193, 2002.
11. P. Crnosija, T. Bjazic, and R. Krishnan, Optimization of PM brushless DC motor drive, *Conference Record, IEEE International Conference on Industrial Technology (IEEE Cat. No. 03TH8685)*, pp. 566–569, 2003.
12. P. Crnosija, R. Krishnan, and T. Bjazic, Transient performance based design optimization of PM brushless DC motor drive speed controller, *Proceedings, IEEE International Symposium on Industrial Electronics (IEEE Cat. No. 05TH8778)*, pp. 881–886, 2005.
13. P. Crnosija, T. Bjazic, R. Krishnan, et al., Robustness of PM brushless DC motor drive adaptive controller with reference model and signal adaptation algorithm, *IEEE International Symposium on Industrial Electronics*, pp. 16–21, 2006.
14. P. Crnosija, R. Krishnan, and T. Bjazic, Optimization of PM brushless DC motor drive speed controller using modification of Ziegler-Nichols methods based on Bode plots, *IEEE International Power Electronics and Motion Control Conference (IEEE Cat. No. 06EX1282)*, pp 343–348, 2006.

13 Sensorless Control of PMBDCM Drive

The drive system is dependent on the position and current sensors for control. Elimination of both the sensors is desirable in many applications, particularly in the low-cost but high-volume applications from the cost and compact packaging points of view. Between the two sensors, the current sensor is easier to accommodate in the electronics part of the system whereas the position sensor requires a considerable labor and spatial volume in the motor for its mounting. That makes it all the more important to do without the position sensor for the control of the PMBDCM drive system.

This chapter describes current sensing methods without external sensors, such as Hall effect current sensors. Sensorless methods of current commutation instances of phase windings are described by borrowing from [1]. Further material is added in regard to evolving methods and developments in recent times [19] including the artificial intelligence based technique [4]. For further reading, references [1–25] are given at the end of the chapter.

13.1 CURRENT SENSING

At least two-phase currents are required for the current control of a three-phase machine. The phase currents can be sensed from the dc link current and hence one sensor is sufficient for current control of the machine. The current sensors are relatively expensive if galvanic isolation is required. If isolation is not necessary, then the currents can be sensed inexpensively with precision resistors by measuring the voltage drops across them. The latter solution is used widely in low-cost motor drives. Sensor resistors have to share common with the control processor so that sensing current signal can be tied to it to minimize additional hardware elements. The control processor will have its common mostly connected to the negative rail of the dc bus that is supplying the inverter in such low-cost systems. In that case, note that the gate signals emerging from the control processor have to be isolated for feeding to the gates/bases of the top controllable devices in the inverter, particularly for systems operating at voltages higher than the automotive voltages of 12 V. Precautions such as this have to be taken to use the measured voltage across resistive sensors to evaluate the currents and their use in control circuits of the drive system. Another approach is to use the MOSFET devices with inbuilt current sensing capability to measure the currents. Alternatively, the MOSFET device itself serves as a sensing resistor during its conduction as it is a resistance. The accuracy of using the drain source voltage drop to estimate currents is fraught with inaccuracies due to temperature effect and for precise current control, the feedback from this voltage drop is not

a viable method. Hall effect current sensors are ideal for sensing the currents with galvanic isolation. At this stage, it is very near impossible to do away with current feedbacks for the control of the PMBDCM to deliver high performance.

If precise torque and speed control is not required, current feedback control and hence current sensing can be dispensed with. Then a simple duty cycle-based open loop PWM voltage controller is sufficient. However, the steering of the current to the appropriate machine phases requires the rotor position information. A number of methods have come into practice to estimate the rotor position without an externally mounted sensor [1–26]. The method of using only duty cycle control without regard to current control has the drawback of not being able to respond to load torque variations unless there is an outer speed feedback control. Consider a load variation and that will slow down the motor, thereby decreasing the induced emf leading to an increase in the stator phase currents for given fixed duty cycles. This is acceptable in motor drives where only torque is commanded. That can be made proportional to the duty cycle of voltage. Because of the lower thermal time constant of the inverter devices as compared to the motor, it is important that current control in one form or other is exercised with or without current feedback control. One way to achieve that is to combine the inverter devices' sensing of the collector emitter voltage and using it to shut them down when the current through it exceeds a set limit. The shutdown signal need not come from the control processor but can be hardware based by integrating this signal in base drive circuit itself as is done in many gating circuits. In motor drives where speed control is required, the duty cycle of the voltage has to be made a function of the speed regulation part. That can be achieved with an outer speed feedback control. Then again the issue of speed sensing or speed estimation becomes important to close the speed feedback control loop. If estimated speed is made use of in this scheme, this control system is truly a sensorless control system. Combined with a current limiting control, this system becomes robust.

13.2 POSITION ESTIMATION

Position can be sensed by Hall sensors overlooking a magnet wheel mounted on the shaft of the rotor extension with the magnets. This will provide just sufficient commutation signals, i.e., six per electrical cycle for a three-phase machine. Such low discrete pulse count is not suitable for high-performance applications. Optical encoders and resolvers can provide the rotor position with high resolution but they are expensive. Further, they require extensive mounting arrangements. High-volume applications demand that they be dispensed with due to the cost and manufacturing burdens. Many methods are possible to estimate the commutation signals and they are described briefly in the following:

1. *Estimation using machine model:* The induced emf can be sensed from the machine model using the applied currents and voltages and machine parameters of resistance, self-inductance, and mutual inductance. The advantage of this method is that an isolated signal can be extracted as the

input variables of currents and voltages are themselves isolated signals. The voltages can be extracted from the base or gate drive signals and the dc link voltage. The variations in the dc link voltage can be estimated from the dc link filter parameters and the dc link current. Parameter sensitivity, particularly that of the stator resistance, will introduce an error in the induced emf estimation, resulting in inaccurate commutation signals to the inverter.

2. *Induced emf from sensing coils:* Sensing coils in the machine can be installed inexpensively to obtain the induced emf signals. The advantages of this method are that the signals are fairly clean, parameter insensitive, and galvanically isolated. The disadvantages are in the manufacturing process and additional wire harness from the machine. The latter, for example, is not acceptable in refrigerator compressor motor drives due to the hermetic sealing requirements.
3. *Sensing emfs from inactive phases:* One of the most commonly used methods for acquiring position information is to monitor the induced emf of the machine phases when they are not being energized. Note that a machine phase is inactive for 33.33% of the time and only two phases conduct at any given time. During that time, the induced emf appears across the machine winding, which can be sensed. The induced emf of the phase yields the information on zero crossing and as well when the emf reaches the constant region, indicating when that phase has to be energized. The polarity of the induced emf determines the appropriate polarity of the current to be injected into that machine phase. Instead of waiting for the constant region of the induced emf for energizing a machine phase, the induced emf on integration from its zero crossing will attain a particular value corresponding to 30° from the zero crossing instant. The integrator output corresponding to 30° from the positive zero crossing may be termed the threshold value used in energizing a phase. This threshold is independent of the rotor speed as shown below.

Assuming a trapezoidal induced emf whose peak is E_p at the rotor electrical speed of ω_b , the slope of the rising portion of the induced emf for any speed ω_s is given by dividing the peak value of the voltage at that speed by the time interval corresponding to electrical 30° . Then the instantaneous value of the induced emf during its rising instant is given by

$$e_{as}(t) = \frac{\left(\frac{E_p}{\omega_b}\right)\omega_s t}{(\pi/6\omega_s)} \quad (13.1)$$

which on integration from 0 to $\pi/6\omega_s$, yields the sensor output voltage, V_{vs} as

$$V_{vs} = \int_0^{\pi/6\omega_s} e_{as}(t) dt = \frac{\pi}{12} \frac{E_p}{\omega_b} \quad (13.2)$$

It may be accordingly proven that this algorithm also works for machines with sinusoidal induced emf even though the sensor output voltage will be different. Note that the sensor output voltage is a constant and independent of the motor parameters and its magnitude is always the same for any operating speed of the machine. The only thing that may adversely affect the sensor output voltage is the induced emf peak decreasing with partial loss of the rotor flux due to temperature sensitivity of the rotor magnets. This will clearly introduce errors in that energization may not be exactly at electrical 30° from the zero crossing as desired. Optimal utilization of the machine may not be possible in this condition unless other corrective measures are taken.

4. *Third harmonic-induced emf:* An alternative method is to detect the third harmonic induced emf in the machine windings and use them to generate the control signals. A three-phase star-connected four wire system will allow the collection of the third harmonic-induced emf and this can be inexpensively instrumented with four resistors.

5. *Method based on artificial intelligent control:* Intelligent controllers such as neural network [5] or fuzzy controllers can extract the rotor position and or the commutation positions from the machine variables such as current and flux linkages. They are only techniques to extract the information when fed from variables in which rotor position information or commutation instances are latent. These techniques are inherently adaptive in that the learning of the controller continues to get refined in the course of time. With the current processor speeds, it becomes quite practical to code these controllers for applications. The major disadvantage of these controllers is that the training required for the neural network controller before it can be implemented. It can be accommodated with off line training.

All the methods that rely on the induced emf have the disadvantage in that at standstill, the position information is not available, as there is no induced emf at zero speed. Even at very low speeds, the induced emf may not be easily detectable. Therefore, a method to generate the control signals at and around zero speed has to be incorporated for successful starting of the machine to a speed at which the induced emf methods can come in to reliably generate the position information. Therefore, a starting procedure at standstill is required. This procedure can consist of two steps, which are explained below.

Step (i): Exciting one or two phases, the rotor may be aligned to a predetermined rotor position. This way, the starting position is known and hence correct starting control signals are generated. When the rotor starts moving at slow speed, the induced emf is small that it cannot be used for generating the commutation pulses until the rotor speed reaches a certain level. This fact necessitates a second step to complete the starting process.

Step (ii): Once the rotor starts moving, the stator phases are energized at a slowly varying frequency keeping the stator currents constant. The rate of frequency variation is kept low so that synchronism is maintained and can be controlled modestly

if the load is known a priori. If not, the stator frequency is altered by trial and error until it reaches the minimum speed at which the induced emfs are of sufficient magnitude to render themselves useful for control. This constitutes the second step in the starting process. The problem with this approach is that this is not precise and some jitter and vibrations can be felt during the starting which may not be significant in many applications. In many cases, step (i) is skipped and only step (ii) is used for starting the machine.

Single chip solution: Many single chip solutions for controlling the PM brushless dc motor drives are available in the market for operation with both the rotor position sensor and sensorless based schemes described above including the starting strategies. They are very popular in the low voltage ranges of 12–48 V which covers a wide range of applications. Caution must be exercised when higher voltage ranges are considered for the motor drive as switching noise interference with the control circuit becomes significant and robust performance of the control scheme is desired under these circumstances. Products with custom built controllers that are primarily controlled by digital signal or other type of microprocessors are prevalent at higher voltage ranges.

The method based on saliency using the techniques of signal injection described in Chapter 8 for PMSMs for finding the inductance and through it the rotor position is another technique that needs to be examined for application in the PM brushless machines. It will not help in the case of the PM brushless machines as the PMs are surface mounted and the difference between the quadrature and direct axis inductances is negligible. Note also that the signal injections used for finding the inductances require rotating vector at injected frequency superposed with the fundamental phasor. The fundamental phasor does not consist of a set of smooth sinusoid voltages or currents in the PM brushless dc machine and that makes this technique inapplicable to a large degree.

REFERENCES

1. R. Krishnan, *Electric Motor Drives*, Prentice Hall, Englewood Cliffs, NJ, 2001.
2. R. Krishnan and R. Ghosh, Starting algorithm and performance of a PM DC brushless motor drive system with no position sensor, *Conference Record, IEEE Power Electronics Specialists Conference (Cat. No. 89CH2721-9)*, pp. 815–812, 1987.
3. S. Ogasawara and H. Akagi, An approach to position sensorless drive for brushless DC motors, *IEEE Transactions on Industry Applications*, 27(5), 928–933, 1991.
4. L. Cardoletti, A. Cassat, and M. Jufer, Sensorless position and speed control of a brushless DC motor from start-up to nominal speed, *EPE Journal*, 2(1), 25–26, 1992.
5. F. Huang and D. Tien, Neural network approach to position sensorless control of brushless DC motors, *Conference Record, IEEE Industrial Electronics Conference*, vol. 2, pp. 1167–1170, 1996.
6. N. Matsui, Sensorless PM brushless DC motor drives, *IEEE Transactions on Industrial Electronics*, 43(2), 300–308, 1996.
7. N. Kasa and H. Watanabe, Sensorless position control system by salient-pole brushless DC motor, *Conference Record, IEEE Industrial Electronics Conference*, vol. 2, pp. 931–936, 1997.
8. M. Tomita, T. Senju, S. Doki, et al., New sensorless control for brushless DC motors using disturbance observers and adaptive velocity estimations, *IEEE Transactions on Industrial Electronics*, 45(2), 274–282, 1998.

9. N. Ertugrul and P. P. Acarnley, Indirect rotor position sensing in real time for brushless permanent magnet motor drives, *IEEE Transactions on Power Electronics*, 13(4), 608–616, 1998.
10. J. Doo-Hee and H. In-Joong, Low-cost sensorless control of brushless DC motors using a frequency-independent phase shifter, *IEEE Transactions on Power Electronics*, 15(4), 744–752, 2000.
11. G. H. Jang, J. H. Park, and J. H. Chang, Position detection and start-up algorithm of a rotor in a sensorless BLDC motor utilising inductance variation, *IEE Proceedings: Electric Power Applications*, 149(20), 137–142, 2002.
12. J. Shao, D. Nolan, M. Teissier et al., A novel microcontroller-based sensorless brushless DC (BLDC) motor drive for automotive fuel pumps, *IEEE Transactions on Industry Applications*, 39(6), 1734–1740, 2003.
13. K.-Y. Cheng and Y.-Y. Tzou, Design of a sensorless commutation IC for BLDC motors, *IEEE Transactions on Power Electronics*, 18(6), 1365–1375, 2003.
14. G.-J. Su and J. W. McKeever, Low-cost sensorless control of brushless DC motors with improved speed range, *IEEE Transactions on Power Electronics*, 19(2), 296–302, 2004.
15. T.-H. Kim and M. Ehsani, Sensorless control of the BLDC motors from near-zero to high speeds, *IEEE Transactions on Power Electronics*, 19(6), 1635–1645, 2004.
16. J. X. Shen, Z. Q. Zhu, and D. Howe, Sensorless flux-weakening control of permanent-magnet brushless machines using third harmonic back EMF, *IEEE Transactions on Industry Applications*, 40(6), 1629–1636, 2004.
17. Z. Genfu, W. Zhigan, and Y. Jianping, Improved sensorless brushless DC motor drive, *Conference Record, IEEE Annual Power Electronics Specialists Conference*, pp. 1353–1357, 2005.
18. M. Naidu, T. W. Nehl, S. Gopalakrishnan, et al., Keeping cool while saving space and money: A semi-integrated, sensorless PM brushless drive for a 42-V automotive HVAC compressor, *IEEE Industry Applications Magazine*, 11(4), 20–28, 2005.
19. P. P. Acarnley and J. F. Watson, Review of position-sensorless operation of brushless permanent-magnet machines, *IEEE Transactions on Industrial Electronics*, 53(2), 352–362, 2006.
20. W.-J. Lee and S.-K. Sul, A new starting method of BLDC motors without position sensor, *IEEE Transactions on Industry Applications*, 42(6), 1532–1538, 2006.
21. J. Shao, An improved microcontroller-based sensorless brushless DC (BLDC) motor drive for automotive applications, *IEEE Transactions on Industry Applications*, 42(5), 1216–1221, 2006.
22. C.-H. Chen and M.-Y. Cheng, A new cost effective sensorless commutation method for brushless dc motors without phase shift circuit and neutral voltage, *IEEE Transactions on Power Electronics*, 22(2), 644–653, 2007.
23. C. Cheng-Hu and C. Ming-Yang, A new cost effective sensorless commutation method for brushless DC motors without phase shift circuit and neutral voltage, *IEEE Transactions on Power Electronics*, 22(2), 644–653, 2007.
24. L. Cheng-Tsung, H. Chung-Wen, and L. Chih-Wen, Position sensorless control for four-switch three-phase brushless DC motor drives, *IEEE Transactions on Power Electronics*, 23(1), pp. 438–444, 2008.
25. K.-W. Lee, D.-K. Kim, B.-T. Kim et al., A novel starting method of the surface permanent-magnet BLDC motors without position sensor for reciprocating compressor, *IEEE Transactions on Industry Applications*, 44(1), 85–92, 2008.

14 Special Issues

A number of important areas of research and development have arisen in the wake of the success of the PM brushless drives in applications. The problems facing the second generation motor drives are common to all the ac motor drives. Therefore, the following list is not exclusive to PM brushless motor drives:

1. Torque smoothing for reducing the commutation torque pulsation
2. Minimization of parameter sensitivity effects
3. Faults and their diagnosis to improve the operational reliability of the motor drive
4. Vibration and noise and their minimization

A brief introduction to these issues is given in this chapter and interested readers are urged to seek out the references in the literature.

14.1 TORQUE SMOOTHING

It is not possible to generate ideal rectangular currents due to the time delay inherent in the machine. Therefore the currents become more or less trapezoidal, which produces a large commutation torque ripple as much as 10%–15% of the rated torque as shown in Chapter 10. Further, the induced emfs are not exact trapezoids due to significant slot harmonics. They in turn will generate harmonic ripple torques, resulting in poorer torque performance. The induced emfs are further affected by the type of winding that is chosen for cost effectiveness in manufacturing, which causes a greater deviation from the ideal waveforms. The cumulative effect of all these imperfections leads to a drive with uneven torque over an electrical cycle of its operation. That makes the drive highly unsuitable for high-performance applications. To overcome these disadvantages, methods based on current shaping to counter the ill effects of the flux distribution are successful.

To overcome the unevenness in the flux density distribution, this distribution is measured or computed and accordingly the current is adjusted continuously to generate a constant torque. To counter the commutation torque pulsation, the incoming phase and outgoing phase currents are coordinated in such a manner that the sum of the torque produced by the two phases is maintained constant. All of the algorithms require a set of fast acting current control loops to shape the current with no deviation either in magnitude or phase from their references. Similar techniques have been widely used in nonlinear systems such as variable speed controlled switched reluctance machines. Various techniques to minimize commutation torque ripple in PM brushless dc motor drives are given in references [1–11].

14.2 PARAMETER SENSITIVITY OF THE PMBDCM DRIVE

Machine parameters affect the performance [12] of the motor drive system. Temperature significantly changes the motor parameters. The motor parameters that are sensitive to variations in temperature are stator resistances and rotor magnets. The use of inner current loops overcomes the effect of stator resistance variations. The use of speed control loop counters the rotor flux linkages variation. In that process, the linearity of the torque to its reference may be lost. In order to preserve the torque linearity in the drive system, methods similar to the air gap power feedback control discussed in Chapter 7 have to be resorted to. The inductance variation is a function of saturation and hence the exciting current. Therefore, it is easy to counter the effects of saturation if the excitation current is measured and made available.

14.3 FAULTS AND THEIR DIAGNOSIS

The use of PM brushless motor drives in critical applications such as aerospace, medicine, and defense necessitates that a high amount of reliability be guaranteed for their operation under normal as well abnormal operating conditions such as faults in the machine, inverter, and controller. Recent research is starting to address the issues concerning faults and their diagnosis [13–18]. The development is steered toward methods to recognize faults when they occur in any subsystem of the motor drive and their diagnosis to determine whether ameliorative measures are available on hand to overcome or mitigate them. If they are not available, then the ultimate option is to shut down the motor drive very smoothly with least damage to the system. This is only one aspect of the studies. But the need to estimate the readiness of the system for a given period of time given the history of operation is another important area that is emerging. The outcome is to develop periodical maintenance schedules including replacement schedules of the motor drives before catastrophic faults can happen in the system that is in place. In some applications, operation of the motor drives at reduced power levels may be acceptable. In such cases, it is important to determine whether the machine with a specified fault can deliver such power and for how long without failing completely. To mention a few, faults can be due to any one or a combination of the following: short circuit in machine windings within themselves such as turn to turn fault or between windings, between a winding and earth, between phase terminals, open circuit of the windings, magnet degradations, open circuit and short circuit of the inverter controllable switches, and sensor failures. Scenarios emerge for each and every one of them with specific measures to cope with them.

14.4 VIBRATION AND NOISE

Very low cost applications such as automotive accessory motor drives that are under the hood of the vehicles have stringent noise requirements to meet. They are intended to decrease the audible noise to levels far below that of the traffic. In order to reduce the noise, stator vibrations have to be reduced. They in turn are

related to mechanical modes and their frequencies. If the force frequencies happen to be very close to the modal frequencies, then the noise is exacerbated. The force that matter most in the vibration of the machine body is the radial force and they are contributed by the normal and tangential flux densities. Uneven air gaps, bearing and rotor eccentricities, slot openings, and machining tolerances contribute to the normal forces that may not be balanced leading to vibrations also. Altogether, they all contribute to audible noise. Their characterization and measures to mitigate them are of importance in many applications. Some references on this subtopic are given in Chapter 1.

REFERENCES

Torque Ripple and Its Smoothing

1. H. R. Bolton and R. A. Ashen, Influence of motor design and feed-current waveform on torque ripple in brushless DC drives, *IEE Proceedings B (Electric Power Applications)*, 131(3), 82–90, 1984.
2. H. Le-Huy, R. Perret, and R. Feuillet, Minimization of torque ripple in brushless DC motor drives, *IEEE Transactions on Industry Applications*, IA-22(4), 748–755, 1986.
3. J. Y. Hung and Z. Ding, Design of currents to reduce torque ripple in brushless permanent magnet motors, *IEE Proceedings B (Electric Power Applications)*, 140(4), 260–266, 1993.
4. S. M. Hwang and D. K. Lieu, Reduction of torque ripple in brushless DC motors, *IEEE Transactions on Magnetics*, 31(6 pt 2), 3737–3739, 1995.
5. S. J. Park, H. W. Park, M. H. Lee et al., New approach for minimum-torque-ripple maximum-efficiency control of BLDC motor, *IEEE Transactions on Industrial Electronics*, 47(1), 109–114, 2000.
6. S. Joong-Ho and C. Ick, Commutation torque ripple reduction in brushless DC motor drives using a single DC current sensor, *IEEE Transactions on Power Electronics*, 19(2), 312–319, 2004.
7. L. Yong, Z. Q. Zhu, and D. Howe, Direct torque control of brushless DC drives with reduced torque ripple, *IEEE Transactions on Industry Applications*, 41(2), 599–608, 2005.
8. N. Ki-Yong, L. Woo-Taik, L. Choon-Man et al., Reducing torque ripple of brushless DC motor by varying input voltage, *IEEE Transactions on Magnetics*, 42(4), 1307–1310, 2006.
9. K. Dae-Kyong, L. Kwang-Woon, and K. Byung-Il, Commutation torque ripple reduction in a position sensorless brushless DC motor drive, *IEEE Transactions on Power Electronics*, 21(6), 1762–1768, 2006.
10. Y. Liu, Z. Q. Zhu, and D. Howe, Commutation-torque-ripple minimization in direct-torque-controlled PM brushless DC drives, *IEEE Transactions on Industry Applications*, 43(4), 1012–1021, 2007.
11. H. Lu, L. Zhang, and W. Qu, A new torque control method for torque ripple minimization of BLDC motors with un-ideal back EMF, *IEEE Transactions on Power Electronics*, 23(2), 950–958, 2008.

Parameter Sensitivity

12. A. K. Wallace and R. Spee, The effects of motor parameters on the performance of brushless DC drives, *Conference Record, IEEE Power Electronics Specialists Conference (Cat. No. 87CH2459-6)*, pp. 591–597, 1987.

Faults and Diagnosis

13. R. Spee and A. K. Wallace, Remedial strategies for brushless DC drive failures, *Conference Record of the 1988 Industry Applications Remedial strategies Society Annual Meeting (IEEE Cat. No. 88CH2565-0)*, pp. 493–499, 1988.
14. A. K. Wallace and R. Spee, Simulation of brushless DC drive failures, *PESC Record—IEEE Power Electronics Specialists Conference*, pp. 199–206, 1988.
15. O. Moseler and R. Isermann, Application of model-based fault detection to a brushless DC motor, *IEEE Transactions on Industrial Electronics*, 47(5), 1015–1020, 2000.
16. M. A. Awadallah and M. M. Morcos, Diagnosis of stator short circuits in brushless DC motors by monitoring phase voltages, *IEEE Transactions on Energy Conversion*, 20(1), 246–247, 2005.
17. M. Dai, A. Keyhani, and T. Sebastian, Fault analysis of a PM brushless DC motor using finite element method, *IEEE Transactions on Energy Conversion*, 20(1), 1–6, 2005.
18. S. Rajagopalan, J. M. Aller, J. A. Restrepo et al., Detection of rotor faults in brushless DC motors operating under nonstationary conditions, *IEEE Transactions on Industry Applications*, 42(6), 1464–1477, 2006.